THE
PHYSICAL REVIEW

A journal of experimental and theoretical physics established by E. L. Nichols in 1893

SECOND SERIES, VOL. 70, NOS. 9 AND 10 NOVEMBER 1 AND 15, 1946

Specific Ionization by Fission Fragments

N. O. LASSEN
Institute for Theoretical Physics, University of Copenhagen, Copenhagen, Denmark
(Received July 15, 1946)

A shallow ionization chamber was used to measure the variation along range of the ionization per unit length by fission fragments. Curves giving this variation for each of the two groups of fission fragments were determined; the two curves were found to intersect each other, the heavy group ionizing more than the light group in the beginning of the path while the opposite was the case in later parts of the path.

AS is well known, the ionization by fission fragments varies along range in quite another way than does the ionization by α-particles. This is in agreement with the fact that the effective charge of the fragments, which is rather high in the beginning of the path, decreases along the path, the fragments capturing electrons as their velocities decrease.[1-4] Bøggild, Brostrøm, and Lauritsen[5] and later Bøggild[6] have investigated the range-velocity relation by use of a cloud chamber, but so far as I know the specific ionization itself has not been directly determined earlier; the present paper contains a preliminary report of a direct measurement of the variation of this quantity along range; a more detailed account will soon be published.

The ionization chamber used is shown in Fig. 1. It consisted of two plates placed parallel to each other at a distance of 5.0 ± 0.1 mm; the particles entered through one of the plates, this being only a framework covered with a thin foil of aluminum or gold. The chamber was enclosed in an airtight box (a 5″ copper tube closed in the ends with flanges) in which was also placed a sort of gun delivering the fission fragments; this gun was made of a piece of mica with a thin layer of uranium (0.33 mg/cm²) evaporated upon it and in front of this a diaphragm consisting of a large number (349) of holes about 10 mm in length and with a diameter of 3 mm, which caused the fragments entering the chamber to move in directions almost perpendicular to the plates. The gun was supported by a brass rod which could be moved from outside, the distance be-

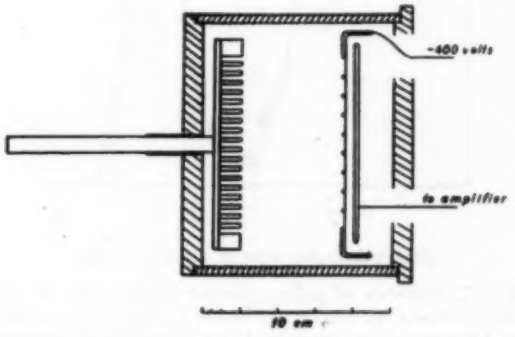

FIG. 1. Experimental arrangement.

[1] N. O. Lassen, Kgl. Danske Vid. Sels. Math.-fys. Medd. 23, No. 2 (1945).
[2] N. O. Lassen, Phys. Rev. 68, 142 (1945).
[3] N. O. Lassen, Phys. Rev. 69, 137 (1946).
[4] N. Bohr, Phys. Rev. 59, 270 (1941).
[5] Bøggild, Brostrøm, and Lauritsen, Kgl. Danske Vid. Sels. Math.-fys. Medd. 18, No. 4 (1940).
[6] J. K. Bøggild, Phys. Rev. 60, 827 (1941).

tween the uranium layer and the ionization chamber thus being varied. In some experiments the mentioned diaphragm was replaced by another one with about 3000 holes of diameter 1.0 mm and length 3.0 mm; in these experiments the foil of the ionization chamber was of gold (0.18 mg/cm²) while in the other experiments an aluminum foil (0.24 mg/cm²) was used. The ionization chamber was placed about 25 cm apart from an internal Be target in the cyclotron of this Institute behind some 5 cm of paraffin. The chamber was connected to a linear amplifier and this in turn to a cathode-ray oscillograph which was photographed on a moving film.

The box was filled with pure argon, and pressures of 75, 150, and 300 mm Hg were used. With these rather low pressures saturation was easily obtained but in order to diminish the background due to coincidences between recoiling argon atoms in the ionization chamber and to the very intense γ-radiation, it was found necessary to make the time constants of the coupling elements between the various stages of the amplifier rather small (5×10^{-5} sec.), and as a consequence the output pulse sizes varied when the potential across the ionization chamber was varied. Thus it was impossible to get absolute measurements while on the other hand careful investigations indicated that the output pulse sizes were proportional to the number of ions produced in the ionization chamber as long as the pressure and the voltage were not varied.

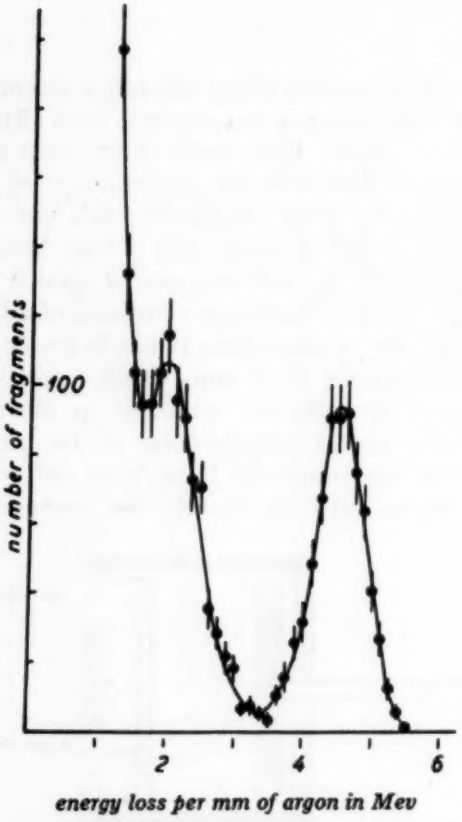

FIG. 2. Number of pulses plotted against size of pulse. Path traversed by fragments inside ionization chamber, 2 mm. Distance from uranium layer to middle of ionization chamber, 10 mm.

Figure 2 refers to the case where the distance a between the uranium layer and the middle of the ionization chamber is equal to 10 mm of argon at atmospheric pressure and the path traversed by the fragments inside the chamber to 2 mm. The curve is obtained by plotting the number of pulses of different sizes against the sizes; concerning the adjustment of the pulse sizes in Mev, see later. As seen, there are a lot of pulses of small sizes corresponding to the background previously mentioned and besides the curve shows two peaks corresponding to the two groups of fission fragments; the light group is seen to be completely separated from the heavy group, while the latter and the background pulses overlap.

For other distances of the uranium layer from the ionization chamber similar curves are obtained, yet when the distance a is increased, the peaks move to the left; for $a=12$ mm the peak corresponding to the heavy group is reduced to a hump on the curve and for $a=14$ mm the heavy group completely disappears in the background. The light group can be seen for $a=12$, 14, and 16, while for $a=18$ it is reduced to a hump on the curve and for $a=20$ it cannot be recognized directly, although the curve is found to be somewhat steeper for $a=22$ than for $a=20$.

When a is decreased the peaks move against higher abscissae and at the same time they approach each other, the peak corresponding to the heavy group moving faster than the other one. For $a=8$ two peaks clearly separated from each other and from the background appear; for $a=6$ the separation from the background is even better but now the heavy group only causes a hump on the left side of the curve for the light group; for $a=4$ the separation between the background and the fission fragments is complete, but

now only one peak is seen; this is valid also for smaller a's, yet for $a=1.5$ the curve has a hump on the right side.

From Fig. 2 the positions of the two maxima can be taken, and, further, the "upper and lower limits" of the light group and the "upper limit" of the heavy group can be determined as the intersection points between the axis of abscissae and the steepest tangents to the curve. By treating the curves corresponding to the various distances in this way and by plotting the values obtained we get the curves on Fig. 3. Here the circles represent the positions of the maxima and the heavily drawn curves thus give the most frequent values of the ionization per mm as a function of the distance traversed, while the thinner drawn curves correspond to the upper and lower limits.

Of course, it is impossible to determine by this method which of the two groups ionize most for $a=1.5$ mm and, hence, whether the two curves intersect each other or not; nevertheless, there are reasons to believe that they really intersect. By the measurements we only get relative figures for the ionization; the adjustment is performed in such a way that the area beneath the curve for the light fragment corresponds to 86 Mev, which figure was chosen because Flammersfeld, Jensen, and Gentner[7] have found 87 Mev for the most frequent value of the total energy and because about 1 Mev is on an average absorbed in the uranium layer. The total energy of the heavy fragment is then found to be 52 Mev in rather good agreement with the value 58 Mev of Flammersfeld, *et al.;* the slight discrepancy may be easily understood regarding that the extrapolation of the curves (the dotted lines) are rather uncertain and, in fact, may be considered to be wrong, as Bøggild, Brostrøm, and Lauritsen[5] found for the mean ranges 18 and 24 mm argon, while the extrapolated curves intersect the axis at the points $a=14.4$ and 22.4.

By drawing the curves in such a way that they do not intersect each other it would be impossible to get agreement with Flammersfeld, *et al.* and other authors[8] concerning the ratio between the energies of the two fragments. It is also interesting that the intersecting of the two curves corresponds to a variation in the effective charge of the two fragments which is at any rate in qualitive agreement with direct measurements of the total charge of the fragments recently published.[2,3] This question, however, will be more closely discussed by Professor Bohr in a forthcoming paper on stopping effects to appear in the Communications of the Copenhagen Academy of Science.

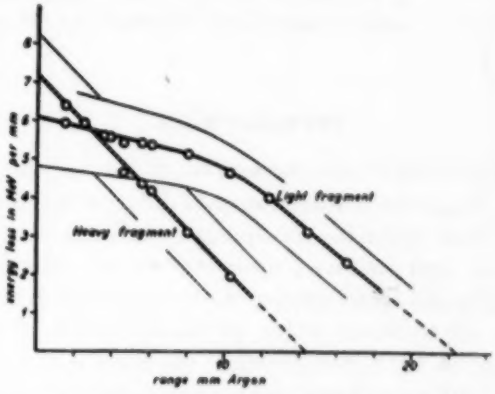

FIG. 3. Ionization per mm as a function of the distance traversed. Upper and lower limits are indicated by light lines.

The writer wishes to express his heartiest thanks to the Director of the Institute, Professor N. Bohr, and to Professor J. C. Jacobsen, for their continued interest in the work.

[7] Flammersfeld, Jensen, and Gentner, Zeits. f. Physik **120**, 450 (1943).

[8] Jentschke and Prankl, Physik. Zeits. **40**, 706 (1939).

Half-Life of Uranium (234)

OWEN CHAMBERLAIN,* DUDLEY WILLIAMS,** AND PHILIP YUSTER***
University of California, Los Alamos Scientific Laboratory, Los Alamos, New Mexico

(Received July 24, 1946)

The half-life of U_{234} has been determined by two independent methods. The first method involves a re-measurement of the relative isotopic abundance of U_{234} and U_{238} in normal uranium; from this measurement the half-life of U_{234} can be obtained in terms of the known half-life of U_{238}. The value obtained by this method is $2.29\pm0.14\times10^5$ years. The second method involves the determination of the specific α-activity of U_{234} from the total specific α-activity and relative isotopic abundances of several enriched uranium samples. The value obtained by this method is $2.35\pm0.14\times10^5$ years. Both values for the half-life are somewhat smaller than the currently accepted value of $2.69\pm0.27\times10^5$ years.

INTRODUCTION

PREVIOUS determinations of the half-life of U_{234} have involved several different methods. The first value for this quantity was reported by Kurie and involved measurement of α-particle ranges and application of the Geiger-Nuttall law[1]; the approximate value so obtained was of the order of 10^4 years. Gratias[2] obtained a value of 1.7×10^5 years from measurements of the specific α-activity of chemically separated U_{234}. The most recent and most accurate value for the half-life of U_{234} is one reported by Nier.[3,4] Nier's method involved an accurate determination of the relative abundance of U_{238} and U_{234} in normal uranium and calculation of the half-life of U_{234} in terms of the known half-life of U_{238}. This calculation assumes that U_{238} and U_{234} are in radioactive equilibrium in normal uranium.

The present report is concerned with a redetermination of the half-life of U_{234} by two independent methods. The first method is similar to Nier's method; the mass spectrograph used in the present work had a somewhat higher resolving power than the one used in Nier's original work on uranium. The second method involves the determination of the specific α-activity of U_{234} from counting measurements and mass spectrographic data on several uranium samples in which the concentration of U_{234} had been increased.

MASS SPECTROGRAPHIC STUDIES OF NORMAL URANIUM

The mass spectrograph used in the present work is an instrument of the Nier type and has been previously described.[5,6] The ions studied were UF_5^+ ions formed by electronic bombardment of uranium hexafluoride vapor.

The spectrum obtained for normal uranium is shown in Fig. 1. The peaks shown at mass positions 333, 330, and 329 correspond to UF_5^+ ions containing U_{238}, U_{235}, and U_{234}, respectively. The 329 peak is re-plotted in the figure with ordinate scale shown at the right. It will be noted that, although resolution of 329 is not complete, the background due to 330 is small. Estimation of the background was made by assuming the shape of the 330 peak to be similar to that of the 333 peak.

Measurement of the relative abundance of U_{234} was made by taking the ratio of ion-beam cur-

TABLE I. Relative abundance of U_{234} in normal uranium.

Data set*	Atomic ratio: U_{238}/U_{234}	Atomic ratio: U_{238}/U_{234}**
1	145	20,200
2	141	19,600
3	139	19,300
4	141	19,600
Average	141.5	19,700

* Each data set represents a different condition of collector slit-width, source tuning, and pressure.
** The observed ratio $U_{238}/U_{235}=139$ is assumed to be correct.

* Present Address: Department of Physics, University of Chicago.
** Present Address: Mendenhall Laboratory of Physics, Ohio State University.
*** Present Address: Department of Chemistry, Washington University, St. Louis.

[1] F. N. D. Kurie, Phys. Rev. **41**, 701 (1932).
[2] O. A. Gratias, Phil. Mag. **17**, 491 (1934).
[3] A. O. Nier, Phys. Rev. **55**, 150 (1939).
[4] G. T. Seaborg, Rev. Mod. Phys. **16**, 1 (1944).
[5] A. O. Nier, Rev. Sci. Inst. **11**, 212 (1940).
[6] D. Williams and P. Yuster, Phys. Rev. **69**, 556 (1946).

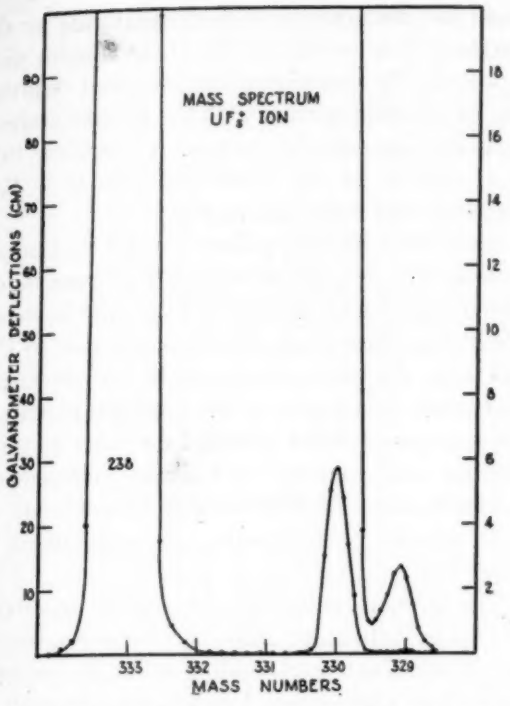

FIG. 1. The mass spectrum of normal uranium hexafluoride in the vicinity of the UF_5 ion. The U_{234} peak as obtained with highest amplifier sensitivity is shown at right; the ion current for this peak was 9×10^{-16} ampere.

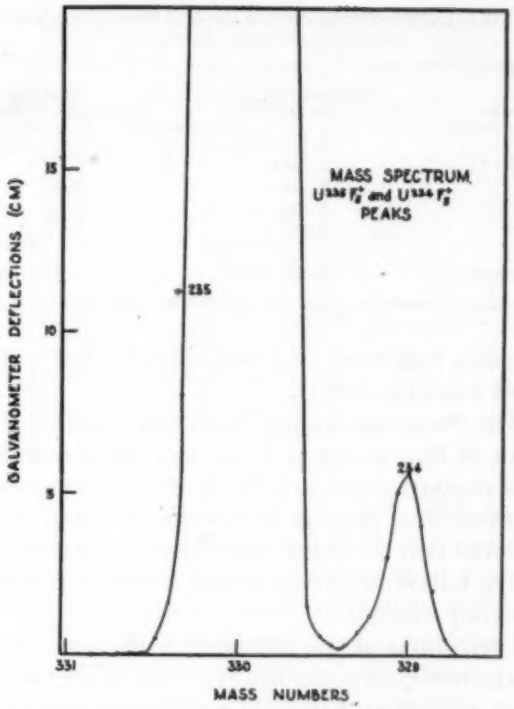

FIG. 2. A portion of the mass spectrum of an enriched uranium sample showing resolution of U_{238} and U_{234} peaks. The ion current for the U_{234} peak was 1.7×10^{-14} ampere.

rents for 330 and 329 under various conditions of collector slit widths and source "tuning." The atomic ratio U_{238} to U_{235} was found to be 139, a result in agreement with Nier's early studies.[3]

The results obtained for the relative abundance of U_{234} are given in Table I. Weighting the data sets equally, one obtains a value of 141.5 for the U_{235}/U_{234} ratio and 19,700 for the U_{238}/U_{234} ratio. After consideration of the deviation of the individual ratios from the above values and the possible sources of instrumental errors, the writers are inclined to believe that the average value is accurate to ±6 percent.

From this value, the half-life T_{234} can be obtained in terms of the known half-life of U_{238} (denoted by T_{238}) from the relation:

$$N_{234}/T_{234}=N_{238}/T_{238}, \qquad (1)$$

where N_{238} and N_{234} are the numbers of atoms of U_{238} and U_{234}, respectively. This relation expresses the fact that U_{238} and U_{234} are in radioactive equilibrium in normal uranium.

The value for T_{238} was taken as 4.51×10^9 years, a value based on the data of Kovarik and Adams.[7,4] Assuming this value to be correct and using 19,700 as the U_{238}/U_{234} ratio, one obtains a value of $2.29\pm0.14\times10^5$ years for the half-life of U_{234}.

MEASUREMENTS OF SPECIFIC ALPHA-ACTIVITY

The U_{234} content of enriched uranium can be determined with greater accuracy than that achieved in measurements on normal uranium, since it is possible to operate the mass spectrograph at lower pressures and hence avoid losses in resolution produced by pressure broadening of the peaks. A typical mass spectrum is shown in Fig. 2. Complete resolution of the 329 peak was achieved at times. At all times the background due to 330 was small.

The counting apparatus used in the present work was of conventional design and utilized electron collection in a counting chamber filled with tank argon at 1.5 atmospheres. The chamber was connected to the input of a conventional linear amplifier with shortest time constant of

[7] A. F. Kovarik and N. I. Adams, J. App. Phys. 12, 296 (1941).

TABLE II. Determinations of the half-life of U_{234} from studies of enriched uranium.

Sample	Disintegrations per sec. per g of U_{234}	Half-life of U_{234} in years
A	2.305×10^{6}	2.45×10^{5}
B	2.501	2.26
C	2.396	2.36
D	2.344	2.41
E	2.487	2.27
Average	2.407×10^{6}	2.35×10^{5}

20 μsec., connected to a discriminator and scale-of-64 counting circuit.

The materials studied were deposited in the form of thin layers of U_3O_8 on 2-mil platinum. The deposits were 3 cm in diameter and varied in mass from 0.6 mg to 1.6 mg of U_3O_8. It is believed that the masses were known to 0.007 mg. Three foils were prepared and counted for each material studied.

Corrections of the following types were made to the observed α-counts: (1) *Coincidence corrections* as high as 3 percent were made necessary by the finite resolving time of the instrument. By adding small samples, it was found that the relation $N=n(1+Tn)$ was valid for small values of Tn, where N is the true counting rate, n the observed counting rate, and T a constant of value 0.76×10^{-6} min. (2) *Thickness correction* for a thickness t mg/cm² is given by the factor $1/(1-0.050t)$. Thickness corrections as high as 1 percent were applied. (3) *Background* counting rates as high as 2.5 percent existed in the chamber at various times. (4) *Efficiency correction* was made to take account of back scattering by the platinum foils on which the U_3O_8 samples were deposited. By comparing the observed counting rate of normal uranium with the specific activity given by Kovarik and Adams,[7] it was found that 51.3 percent of the disintegrations in a thin sample would result in counts.

After the α-disintegration rate and the isotopic constitution of a given sample had been determined, the α-activity due to U_{234} could be determined by subtracting the activities due to U_{238} and U_{235}. In the present study measurements were made on samples of five enriched materials. These measurements included α-counts on three foils for each material and sixteen independent determinations of the isotopic constitution of each sample. The results are summarized in Table II.

The average value for the specific α-activity of U_{234} is 2.407×10^{6} disintegrations per second per gram. The corresponding value of the half-life is 2.35×10^{5} years. From a consideration of the various sources of error, it is believed that the above values are accurate to ±6 percent. Hence, the value of the half-life $2.35\pm0.14\times10^{5}$ years is in satisfactory agreement with the value $2.29\pm0.14\times10^{5}$ years as obtained from the work on normal uranium.

This work was carried out under contract between the University of California and the Manhattan District, Corps of Engineers, War Department. Publication was assisted by the Department of Physics, Ohio State University.

The Neutron-Proton and Neutron-Carbon Scattering Cross Sections for Fast Neutrons

CARL L. BAILEY, WILLIAM E. BENNETT,* THOR BERGSTRALH,** RICHARD G. NUCKOLLS,***
HUGH T. RICHARDS,† AND JOHN H. WILLIAMS
University of Minnesota, Minneapolis, Minnesota

(Received August 5, 1946)

An experimental investigation of the total scattering cross section of hydrogen and carbon for neutrons of energies 0.35 to 6.0 Mev is reported. Neutrons of discrete energies were produced by particle bombardment of lithium, carbon, and heavy water targets. Transmissions of cyclohexane (C_6H_{12}) and graphite scatterers under conditions of good geometry were measured. Results for σ_s(H) are compared with the theoretical interpretations of Bohm and Richman in a later paper and to the experimental results of D. Frisch at lower energies in a companion paper. It is estimated that σ_s(H) and σ_s(C) are determined to approximately five percent.

INTRODUCTION

AN understanding of the interaction between a neutron and proton is fundamental to the basic theory of nuclei. Information on the state of the compound nucleus, the deuteron, exists and serves to determine many of the characteristics of this interaction. On the other hand the scattering of fast neutrons by free protons, where the energy of the system is positive, provides further information necessary to an understanding of the interaction.

A knowledge of the neutron-proton scattering cross sections is also useful as fundamental information in experimental nuclear physics. This may be illustrated by considering the problem of measuring the flux of fast neutrons. If a beam of fast neutrons impinges on a thin foil of hydrogen-containing material, the number of recoil protons observed can be interpreted in terms of the fast neutron flux if the cross section for neutron-proton scattering is known as a function of neutron energy.

The companion paper by D. H. Frisch[1] and a forthcoming report by Bohm and Richman[2] amplify the information given in this report. In the work reported in this paper σ_s(H) and σ_s(C) were measured in the energy range 0.35 to 6.0 Mev. D. H. Frisch[1] has extended the energy range covered down to 0.035 Mev and has made measurements up to 0.50 Mev. In the overlapping region between 0.35 Mev and 0.50 Mev his data are more accurate than those of the present work. Bohm and Richman[2] have used the present data and those of Frisch to interpret the neutron-proton scattering in terms of a potential well of fitted characteristics.

EXPERIMENTAL METHOD

Consider a point source, P, of neutrons of a given energy as illustrated in Fig. 1. Suppose a scatterer, S, in the form of a disk of thickness x and diameter d intercepts a cone of neutrons of angle α. A detector of fast neutrons subtends an angle $\beta \leq \alpha$ at the source P.

If α and β are very small, the observations can be translated into the total cross section by the following expression

$$I/I_0 = e^{-n\sigma x},$$

where I is the intensity of neutrons measured by the detector with the scatterer present, I_0 is the intensity of neutrons measured by the detector when the scatterer is absent, n is the number of

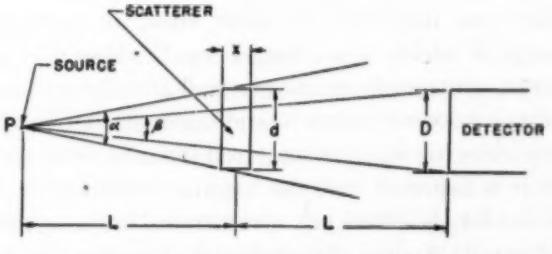

FIG. 1. Geometry of source, scatterer, and detector used in scattering experiment.

* Now at Rice Institute, Houston, Texas.
** U.S.N.R.
*** Now at Naval Research Laboratory, Washington, D. C.
† Now at the University of Wisconsin.
[1] D. H. Frisch, Phys. Rev. **70**, 589 (1946).
[2] Bohm and Richman, Phys. Rev. (forthcoming report).

TABLE I. List of geometrical conditions, transmissions, and cross sections.

E_n	Transmission C_6H_{12}	Transmission C	$2L$ cm	d cm	D cm	x cm	Corrected Transmission C_6H_{12}	Corrected Transmission C	$\sigma_s(C_6H_{12})$ in barns	$\sigma_s(C)$ in barns	$\sigma_s(H)$ Expt in barns	$\sigma_s(H)^a$ Theory in barns
0.35	0.465		36	4.0	2.5	1.5	0.442		104.7 ±2.8	3.15±0.08	7.15±0.24	7.70
		0.450	36	4.0	2.5	3.0		0.444				
0.46	0.490		36	4.0	2.5	1.5	0.469		97.2 ±1.68	3.15±0.10	6.52±0.15	6.70
		0.450	36	4.0	2.5	3.0		0.444				
0.72	0.553		36	4.0	2.5	1.5	0.533		77.76±1.38	2.49±0.06	5.22±0.12	5.21
		0.532	36	4.0	2.5	3.0		0.526				
0.97	0.594		36	4.0	2.5	1.5	0.577		67.80±0.78	2.40±0.03	4.45±0.08	4.43
		0.547	36	4.0	2.5	3.0		0.541				
1.0±0.1	0.444		29	4.0	4.0	2.5	0.408		64.50±1.68	2.38±0.09	4.16±0.15	4.35
		0.410	29	4.0	4.0	4.6		0.399				
1.6	0.516, 0.321		40	4.0	4.0	2.5, 4.0	0.500, 0.299		51.54±0.96	1.90±0.05	3.36±0.08	3.38
		0.484	40	4.0	4.0	4.6		0.479				
2.0	0.402		75	8.0	4.0	4.0	0.364		45.30±0.72	1.63±0.04	2.96±0.07	2.98
		0.535	90	4.0	4.0	4.6		0.534				
2.6	0.433, 0.412		60	4.0	4.0	2.5, 4.0	0.426, 0.403		40.86±0.54	1.60±0.03	2.60±0.05	2.55
		0.540	60	4.0	4.0	4.6		0.538				
2.85		0.607	60	8.0	4.0	4.12		0.600		1.57±0.11		

scattering nuclei per cm³ in the scatterer, x is the length of the scatterer in cm, and σ is the total cross section in cm². In view of the fact that the radiative capture cross section for fast neutrons by H and C is very small, we can assume the scattering cross section is equal to the measured total cross section.

If the conditions are such that α and β are not negligibly small the measured transmission $T=I/I_0$ is greater than that for the ideal "good geometry" condition described above. Neutrons will not be diverted from the detector unless they are deflected by more than an average angle β which is no longer small. Also if α is large, neutrons from the external annular portion of the scatterer which would normally not reach the detector may be scattered into the detector. If it is assumed that the angular distribution of scattering is spherically symmetrical in the center of gravity system of coordinates these two effects can be corrected for. This assumption is justified by experimental observations on light elements[3,4] for neutrons of the energies under discussion. Further justification is evident from the relatively large wave-lengths of the incident neutrons as compared to the nuclear dimensions of the scatterer.

In practice α and β were kept small enough to reduce the corrections outlined in the above paragraph to five percent or less. The geometrical conditions for the scattering measurements are shown in Table I.

It should also be pointed out that the thickness x of the scatterer must be kept small in order that the effects of multiple scattering may be neglected. In practice this means that the transmission T should be as large as convenient since the correction for multiple scattering is proportional to, but much less than, $(1-T)$

[3] Barschall and Kanner, Phys. Rev. **58**, 590 (1940). Coon, Davis, and Barschall, Phys. Rev. **70**, 104 (1946).
[4] Kikuchi, Aoki, and Wakatuki, Proc. Phys. Math. Soc. Jap. **21**, 410 (1939).

TABLE I.—*Continued.*

E_n	Transmission C_6H_{12}	Transmission C	$2L$ cm	d cm	D cm	x cm	Corrected Transmission C_6H_{12}	Corrected Transmission C	$\sigma_s(C_6H_{12})$ in barns	$\sigma_s(C)$ in barns	$\sigma_s(H)$ Expt in barns	$\sigma_s(H)^2$ Theory in barns
	0.445		50	4.0	4.0	4.0	0.432					
3.0		0.520, 0.623	40, 60	4.0, 8.0	4.0	4.6, 4.12		0.515, 0.605	37.56±1.44	1.59±0.08	2.33±0.13	2.34
3.25		0.585	64	8.0	4.0	4.12		0.578		1.69±0.13		
	0.448		45	4.0	4.0	4.0	0.434					
3.5		0.401, 0.464	45, 64	4.0, 8.0	4.0	4.6, 4.12		0.396, 0.456	37.32±1.50	2.39±0.09	2.09±0.09	2.09
3.75		0.461	61	8.0	4.0	4.12		0.452		2.43±0.12		
	0.477		85	4.0	4.0		0.474					
4.0		0.501, 0.550	85, 58	4.0, 8.0	4.0	4.6, 4.12		0.500, 0.542	33.30±0.90	1.85±0.10	1.85±0.09	1.87
4.25		0.502	63	8.0	4.0	4.12		0.494		2.16±0.07		
	0.500		60	8.0	4.0	4.0	0.472					
4.5		0.540	60	8.0	4.0	4.12		0.532	33.60±1.08	1.93±0.06	1.83±0.10	1.69
4.75		0.598	95	8.0	4.0	4.12		0.595		1.60±0.15		
	0.561		85	8.0	4.0	4.0	0.549					
5.0		0.685	85	8.0	4.0	4.12		0.682	26.70±0.60	1.18±0.03	1.63±0.05	1.54
	0.588		85	8.0	4.0	4.0	0.577					
5.5		0.673	85	4.0	4.0	4.6		0.672	24.18±0.67	1.07±0.04	1.48±0.06	1.42
	0.608, 0.603		63, 100	4.0, 8.0	2.0, 4.0	4.0	0.605, 0.599					
6.0		0.698	100	8.0	4.0	4.12		0.696	22.56±1.32	1.11±0.10	1.32±0.12	1.31

times the geometrical correction described above. In none of the work reported in this paper has a correction for multiple scattering been made. Experience gained from this work would lead to a selection of scatterers with smaller x and consequently greater T in future work, although the multiple scattering correction for the present conditions is probably negligible compared to the statistical accuracy of these results.

MEASUREMENTS

The measurements described in this report were made during the winter 1942–43 at the University of Minnesota under an O.S.R.D. contract. The Minnesota pressure-insulated Van de Graaff generator[5] provided monoenergetic ions of energies up to 3 Mev as a primary source of fast neutrons.

In order to cover the neutron energy interval from 0.35 to 6.0 Mev we used the following reactions:

$$Li^7+H^1\rightarrow Be^7+n^1, \quad (1)$$

$$C^{12}+D^2\rightarrow N^{13}+n^1, \quad (2)$$

$$D^2+D^2\rightarrow He^3+n^1. \quad (3)$$

To provide neutrons in the energy interval 0.35 to 0.97 Mev an evaporated thin (about 40 Kev) lithium target was bombarded with protons of discrete energies from 2.10 to 2.68 Mev.

Deuteron bombardment of a thick carbon target provided neutrons of energy 1.0±0.1 Mev which served to check the 0.97 Mev results obtained with neutrons from the Li reaction.

[5] Williams, Rumbaugh, and Tate, Rev. Sci. Inst. **13**, 202 (1942).

Although neutrons of all energies from 0 to 1.15 Mev were emitted in the forward direction when this thick target was bombarded with deuterons of 1.45 Mev, the spectrum was detected by a biased detector whose cut-off was at 0.70 Mev. A study of the response of this detector led us to believe that the average neutron energy to be associated with our measured scattering cross sections was 1.0 ± 0.1 Mev. This point is the only uncertain value on our energy scale. Deuteron bombardment of thin carbon (soot) targets provided neutrons of energies 1.6 and 2.0 Mev.

Reaction (3) is sufficiently exoergic to provide neutrons in the interval from 2.0 to 6.3 Mev with the bombarding energies available to us. Although one would prefer to use thin D^2 targets, time did not allow us to develop this technique. Sufficient work was done to show that it is extremely difficult if not impossible to maintain a thin heavy ice target of a thickness constant to a few percent under deuteron currents of two to five microamperes. Later work at Los Alamos has shown it to be quite feasible to employ gas targets of about 100-Kev stopping power separated from the accelerating tube by thin nickel foils. These gas targets provide sufficient neutron intensity and neutron energy definition for many nuclear problems. We were forced by lack of development time to employ a thick heavy ice target so that it was necessary to use a differential method to select a restricted band of neutron energies. The difference in the number of neutrons, per unit charge of bombarding deuterons, at two neighboring deuteron energies was considered to be the number of neutrons of an energy equal to that produced by the deuterons of energy equal to the mean of the two bombarding energies. The following example illustrated the above statement and the general method of taking the scattering data.

$0=45°$ (angle between d and n in lab system)

$E_1(D)=1.83$ Mev

N_{01B} = number of neutrons detected per unit charge of bombarding deuterons with an empty brass container interposed midway between source and detector

$E_2(D)=2.23$ Mev

N_{02B} similar to N_{01B} but taken with neutrons produced by deuterons accelerated to an energy $E_2(D)$

N_{1B} = number of neutrons detected per unit charge of deuterons with a long paraffin candle between source and detector

N_{2B} similar to N_{1B} but taken with neutrons produced by deuterons accelerated to an energy $E_2(D)$

N_{H1B} = number of neutrons detected per unit charge of deuterons with an identical brass container filled with C_6H_{12} interposed

N_{H2B} similar to N_{H1B} but taken with neutrons produced by deuterons accelerated to an energy $E_2(D)$

The data are calculated as follows:

$N_{01B}-N_{1B}=N_{01}$ = number of neutrons coming directly from the source for $E_1(D)$

$N_{H1B}-N_{1B}=N_{H1}$ = number of neutrons from source at $E_1(D)$ which are transmitted by the scatterer

$N_{02B}-N_{2B}=N_{02}$ = number of neutrons coming directly from the source for $E_2(D)$

$N_{H2B}-N_{2B}=N_{H2}$ = number of neutrons from source at $E_2(D)$ which are transmitted by the scatterer

$N_{02}-N_{01}=N_{02-01}$ = number of neutrons of average energy E_n coming from source

$N_{H2}-N_{H1}=N_{H2-H1}$ = number of neutrons of average energy E_n coming from the source which are transmitted by the cyclohexane scatterer

$$\frac{N_{H2-H1}}{N_{02-01}}=\exp\left[-n\sigma(C_6H_{12})x\right]$$

And E_n is taken as that corresponding to $E=\frac{2.23+1.83}{2}$ $=2.03$ Mev. As $\theta=45°$, $E_n=4.5$ Mev for $E(D)=2.03$ Mev.

Similar data were taken simultaneously on C.

It should be emphasized that the method outlined above is more tedious and less accurate than observations with relatively monoenergetic neutrons from a thin target. Even with a thick target it is difficult to maintain the absolute yield and detection efficiency sufficiently constant for the times of observation necessary to obtain statistically significant differences in the numbers obtained at different bombarding energies. This is particularly true if the heavy ice is not continually replenished. This difficulty was overcome by allowing D_2O vapor to flow continuously on to a liquid-air-cooled target at the overly generous rate of about $\frac{1}{4}$ cc of heavy water per hour. A recovery of about 75 percent of the D_2O was possible if the deuteron current was less than five microamperes. In most of this

work the neutron intensity was monitored by simultaneously counting unscattered neutrons of the same energy with an identical detector placed at a symmetrical angle and at the same distance from the source.

The neutrons from these sources were detected by counting the individual recoil protons in ionization chambers of various designs. For the energy region up to 1 Mev the recoils were obtained from methane at 60 lb./in.^{2} in a chamber 2.5 cm in diameter and 1.0 cm deep. The ionization pulses from the individual recoils were recorded by a linear amplifier and scalar designed by R. G. Nuckolls. By a suitable choice of bias of the detecting equipment it was found possible to exclude the detection of neutrons of energy 100 kev less than the energy under investigation.

The C(d, n) and D(d, n) neutrons were detected by counting recoil protons from a paraffin radiator inside the front face of an argon filled ionization chamber. These chambers were of 2.0 or 4.0 cm diameter, 10 cm long, and filled with argon to pressures up to 100 lb./in.^{2}. The ionization pulse was collected on a central rod of approximately $\frac{1}{8}$-inch diameter. The pressure was usually adjusted to provide sufficient stopping power for the most energetic recoils. Biases were selected to favor the neutron energy studied.

In most cases the fluctuation of individual observations of cross sections from the mean (usually of ten or more observations at a given energy) was not caused by the statistical fluctuations in the number of neutrons recorded but arose from other instrumental effects such as source fluctuations.

The scatterers used in these experiments were C_6H_{12} and C. The cyclohexane was carefully tested for purity and found to be more than 98 percent C_6H_{12}, the remainder being other compounds of carbon and hydrogen. The carbon was especially selected and tested for purity. The liquid cyclohexane was contained in accurately machined copper cylinders. Duplicate empty copper cylinders were necessary to determine the scattering of these containers. Cyclohexane scatterers of diameters 2.0 and 4.0 cm and lengths 1.5, 2.5, and 4.0 cm in corresponding containers were used for appropriate neutron energies. The carbon scatterers were in the form of machined graphite cylinders of radii 4.0 and 8.0 cm and lengths 3.0, 4.12, and 4.6 cm. The multiplicity of sizes of scatterers was required to obtain an appropriate transmission and to make rough tests on the validity of the assumption of spherical symmetry of scattering used in correcting the observations for imperfect geometry.

These scatterers were supported midway between the neutron source (diameter $\sim\frac{1}{4}$ inch) and the detector by fine wire supports. In order to measure the number of neutrons recorded by the detector which did not come directly from the source to the detector in the cone defined by β in Fig. 1, a long cylinder of paraffin of diameter equal to the scatterer was interposed between source and detector. Principally as a result of the directional sensitivity of the paraffin faced recoil detectors the measured "room background" was less than two percent of the primary neutrons recorded. This directional sensitivity was not great enough to influence the relative detection efficiency for neutrons whose incident direction varied by angles of the order of β.

RESULTS

Table I presents a collection of the measured and corrected transmissions of C_6H_{12} and C scatterers of different sizes for different neutron energies. It may be noted that the maximum correction to the measured transmission is less than five percent and for most cases less than one percent. The total cross sections of C_6H_{12} and C are given with probable errors calculated from the deviations of the individual observations of cross section from the mean of several observations.

The value of σ_s(H) is obtained from the above cross sections by taking

$$\sigma_s(\mathrm{H})_{\mathrm{expt}}=\frac{1}{12}\{\sigma_s(C_6H_{12})-6\sigma_s(\mathrm{C})\}.$$

The experimental value is compared to the smooth curve values of Bohm and Richman in the last column of Table I. Plots of σ_s(H) and σ_s(C) as a function of neutron energy are shown in Figs. 2 and 3.

DISCUSSION

An interpretation of the results for σ_s(H) will be given in a later paper by Bohm and Richman. These authors have given us permission to make

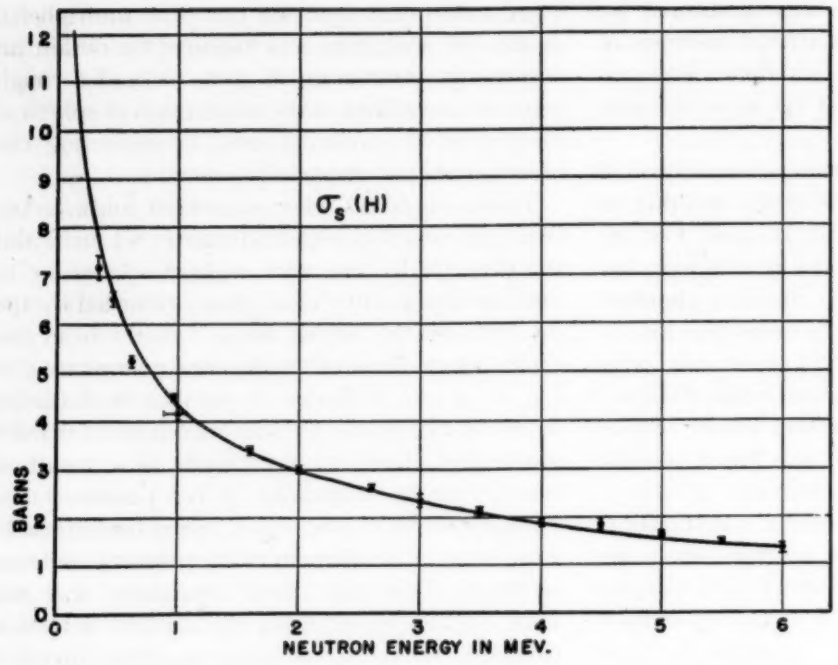

FIG. 2. Scattering cross section of H in barns (10^{-24} cm^2) as a function of neutron energy.

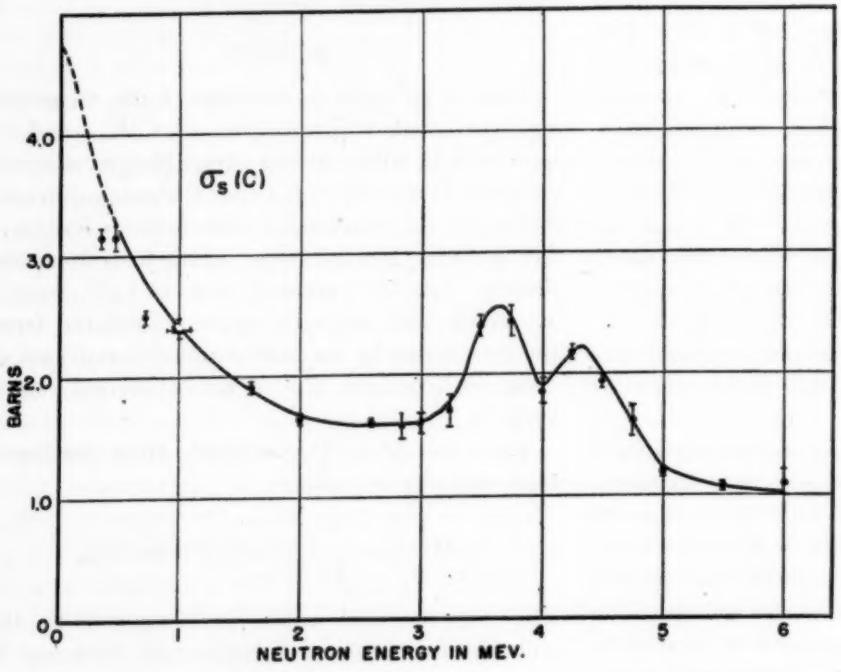

FIG. 3. Scattering cross section of C in barns (10^{-24} cm^2) as a function of neutron energy. The full line is drawn through the experimental results of this paper except below 1 Mev where the more precise work of D. H. Frisch is given preponderant weight.

the following statements about their results. The values of σ_s(H) as a function of neutron energy can be readily understood by assuming a potential function to represent the interaction of neutrons and protons moving with relative velocities covered by the neutron energy range investigated in this report. This potential function is made up of a narrow deep square well and a wide shallow square tail of dimensions necessary to fit the value of the quadrupole moment of the deuteron and the proper values of ^1S scattering. The experimental results fall below the theoretical predictions of Kittel and Breit[6]

[6] Kittel and Breit, Phys. Rev. 56, 744 (1939).

by amounts which increase with neutron energy to a maximum difference of ten percent at 6 Mev. Further studies[7] of σ_s(H) at higher energies show the necessity of a more complex theory to describe the higher energy results.

A comparison of these results with those of former workers[8] is only possible in the energy range between 2.4 and 2.9 Mev. The agreement is well within the statistical errors given by these authors. Further comparison with E. Bretscher, *et al.*,[9] shows that his work and the present study agree to well within the statistical errors of the two studies. Comparison with the results of D. Frisch[1] show that the present results for energies less than 1 Mev are approximately five percent too small.

[7] R. Sherr, Phys. Rev. **66**, 240 (1945).
[8] Aoki, Proc. Phys. Math. Soc. Jap. **21**, 232 (1939); Phys. Rev. **55**, 795 (1939). Zinn, Seely, and Cohen, Phys. Rev. **56**, 260 (1939). Booth and Hurst, Proc. Roy. Soc. **A161**, 248 (1937). Ladenburg and Kanner, Phys. Rev. **52**, 911 (1937).
[9] E. Bretscher, *et al.*—unpublished.

It is probably fair to conclude that the values of σ_s(H) given by the smooth curve of Fig. 2, which is the result of Bohm and Richman's calculation, are correct to within five percent.

With respect to the case of σ_s(C) there is very little that can be said from a theoretical point of view. A comparison with early observations[8] in the 2.5-Mev energy range shows fair agreement. Again a comparison with Bretscher, *et al.*,[9] gives excellent agreement. Frisch's[1] measurements, represented by the dotted line in Fig. 3, show that the present results for energies less than 1 Mev are approximately five percent too small.

Figure 3 shows that a doublet level of the compound nucleus C^{13} exists with energy levels of 8.25 and 8.90 Mev above the ground state. The width of these levels must be much less than indicated in the figure because the differential thick-target technique provided neutrons of from 100 to 300 kev total energy spread in the energy region between 3 and 5 Mev.

PHYSICAL REVIEW VOLUME 70, NUMBERS 9 AND 10 NOVEMBER 1 AND 15, 1946

The Total Cross Sections of Carbon and Hydrogen for Neutrons of Energies from 35 to 490 kev

DAVID H. FRISCH*
Los Alamos Laboratory, Los Alamos, New Mexico
(Received August 8, 1946)

The total cross sections of carbon and hydrogen have been measured at mean neutron energies of 35, 95, 265, and 490 kev.

EXPERIMENTAL ARRANGEMENT

NEUTRONS were produced by the Li(p, n) reaction. (Figure 1.) Protons accelerated by the smaller Wisconsin electrostatic generator at Los Alamos were collimated to a $\frac{3}{32}$" diameter beam of from 20 to 30 microamperes. The proton beam fell on a thin lithium film evaporated on an air-cooled copper target backing 0.020" thick. The stopping power for protons of the lithium film used was measured by observing the energy width of the rise of the neutron yield curve in the forward direction. Targets of 5- to 10-kev stopping power were used.

The nearly monochromatic quality of the neutrons was insured by control of the bombarding proton energy to ±2 kev. The system of corona control used will be described elsewhere by Dr. J. L. McKibben.

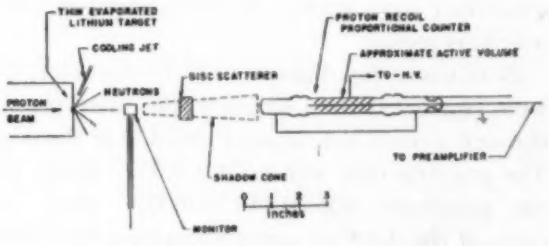

FIG. 1. Arrangement of apparatus.

* Now at the Massachusetts Institute of Technology.

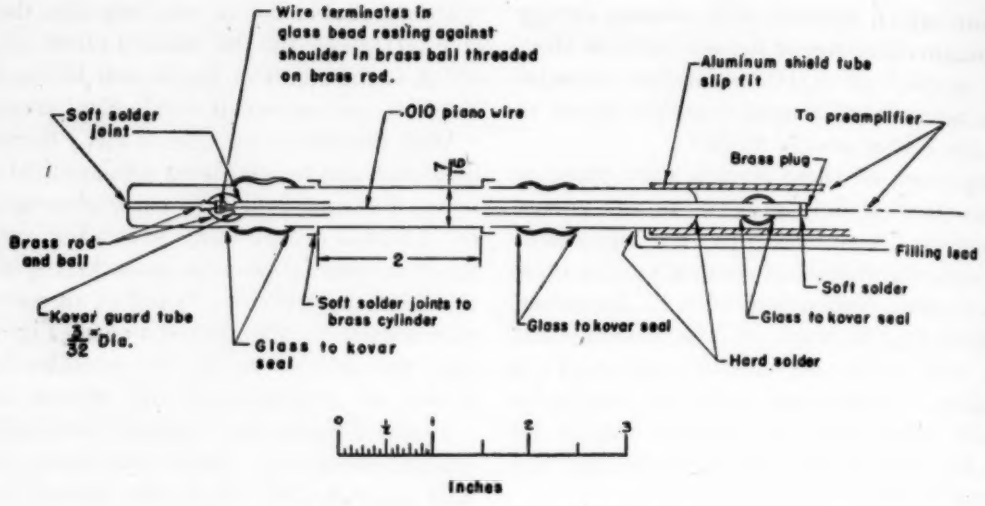

FIG. 2. Construction of neutron detector.

Neutrons for the 35-kev point were made by the "tickling threshold" technique, i.e., setting the proton energy just at the sharp threshold of the neutron-producing reaction. Just at the threshold of this endothermic reaction the neutrons emerge with no velocity in the center of gravity system, and are all carried forward in the room system in a narrow cone with an energy of 29 kev. At a bombarding energy 1 kev above threshold the neutrons get a velocity in the center of gravity system corresponding to only $\frac{1}{8}$ kev, but because of the compounding of velocities those which go forward get an energy of 40 kev in the room system. Those which go backward in the c.g. system are still carried forward in the room and have an energy of 20 kev. Thus in the present case, with a target thick compared to 1 kev, "tickling" at even 1-kev bombarding energy above threshold caused neutrons of all energies from 20 to 40 kev to be present. The mean value of the neutron energy was taken to be 35 ± 5 kev because of the observed change in sensitivity with energy of the neutron detector over this region.

Both scattering disks were $\frac{3}{4}''$ in diameter, and were supported by a single 0.008" wire passing through a small hole along a chord near the edge. The graphite disk was $0.376\pm0.001''$ thick, and the polythene was $0.1465\pm0.001''$ thick. All parts of the detector and preamplifier lay within the shadow of the scatterers. A polythene shadow cone was inserted to measure room scattering and counter background. The densities of the scatters were computed from their dimensions and agreed with the expected values. The commercial polythene used has been analyzed as pure CH_2 to within less than 0.1 percent.

The construction of the neutron detector is shown in detail in Fig. 2. This proton-recoil proportional counter is filled to various pressures of hydrogen (from 50 to 200 cm of mercury) so as to keep the gamma-ray background low compared to the proton recoils in the counter for the various neutron energies used. Details of proportional counter work in this energy region will be published elsewhere.

The intensity of neutrons from the target was monitored by a very small ($\frac{3}{8}''$ diameter and $\frac{5}{16}''$ high) ionization chamber containing uranium (235). This chamber was placed half-way between the target and the scatterer, and thus none of the few neutrons scattered from it could reach the detector without passing through the scatterer. Fissions in the monitor and proton recoils in the detector were amplified by standard amplifiers

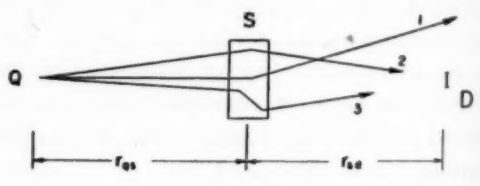

FIG. 3.

designed by M. Sands, and were counted on standard scaling circuits.

INTERPRETATION OF DATA

Backgrounds taken with the polythene cone were never greater than 3 percent, and, in data taken with higher counter-biases, were about 1 percent. This was primarily from neutrons scattered in the room and by parts of the target not shadowed by the cone.

The geometry of this experiment was such that the maximum angle of scattering into the detector was approximately 10°. The cross sections observed with such geometry must be converted into the total cross sections that would be observed with a point source, point scatterer, and point detector. The only correction applied was for single scattering into the chamber because of the finite sizes of the scatterer and detector. (Figure 3, not to scale.) Since this correction was only about 3 percent for hydrogen and 1 percent for carbon, and since multiple scattering corrections are small compared to this, no higher order corrections were made.

A short discussion of the correction may be of interest. Let the distance from source Q to scatterer S be r_{qs} and from scatterer to detector D be r_{sd}. Let ω_{sq} be the fraction of 4π solid angle subtended by the scatterer at the source, ω_{ds} that subtended by the detector at the scatterer, and ω_{dq} that subtended by the detector at the source. The observed fractional transmission of the scatterer is T, its area is A_s, and the area of the detector is A_d. Neutrons scattered at small angles (path 2 in Fig. 3) have a chance of being counted in the detector because of the finite scatterer and detector sizes. The observed $(1-T)$ must be increased by a factor $(1-\omega_{sq}\omega_{ds}/\omega_{dq})$ to give what would be observed if the neutrons were only scattered out of a point detector by a point scatterer (path 1 in Fig. 3). For isotropic scattering in the room system the fractional correction to the observed $(1-T)$ for small ω's is an increase of

$$\frac{A_s(r_{qs}+r_{sd})^2}{4\pi r_{qs}^2 r_{sd}^2}.$$

If $r_{qs}=r_{sd}$, the correction is $A_s/\pi r^2$. For the light elements used, ω_{ds} must be taken in the c.g. system; at small angles the fractional correction is $1.17A_s/\pi r^2$ for carbon and $4A_s/\pi r^2$ for hydrogen.

Transmissions were in the range $0.55 \leq T \leq 0.85$. The basis for the assumption of isotropy of scattering by carbon and hydrogen in the c.g. system is discussed in the companion paper by Bailey, Bennett, Bergstralh, Nuckolls, Richards, and Williams. The uncorrected and corrected data are given in Table I. The corrected hydrogen data are plotted in Fig. 4 along with a theoretical curve by Bohm and Richman,[1] and the corrected carbon data are plotted in Fig. 5 along with data from the companion paper by B.B.B.N.R.W., joined by a smooth curve. Extrapolating from the thermal values on a $1/v$ basis, the capture cross sections of carbon and hydrogen are seen to be negligible at these energies. Thus the observed

TABLE I. Uncorrected and corrected values of σ_H and σ_C.

E_n in kev	σ_H		σ_C	
	Uncorrected	Corrected	Uncorrected	Corrected
35	16.15±0.25	16.74±0.41	4.60±0.14	4.63±0.19
95	13.04±0.26	13.46±0.39	4.62±0.09	4.65±0.14
265	8.87±0.15	9.12±0.24	3.82±0.05	3.85±0.09
490	6.19±0.15	6.33±0.21	3.24±0.07	3.26±0.10

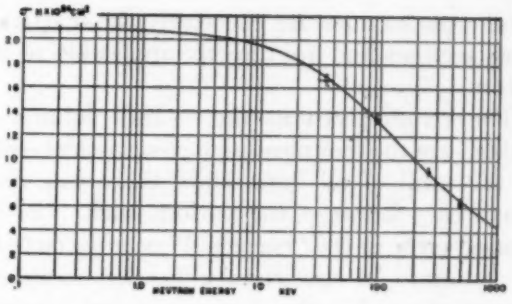

FIG. 4. Neutron-proton cross section. The solid curve is from a theoretical calculation by Bohm and Richman.

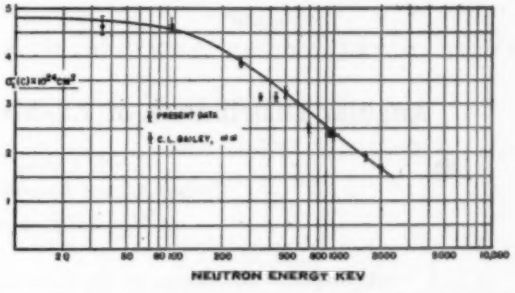

FIG. 5. Corrected data for neutron scattering on carbon.

[1] Bohm and Richman, Phys. Rev., to be published.

total cross sections are effectively the scattering cross sections and are directly applicable to the theory.

The errors given in the "data" column of Table I are the root mean square statistical errors of the total of all data, since there was good consistency between the various runs. The increased error in the "corrected" column includes an estimate of uncertainty in the scattering corrections and in the dimensions and densities of scatterers. The assignment of mean energies (except in the "tickle-threshold" case previously discussed) may be in error by an estimated +5 or −10 kev, the latter error being greater because of possible undetected target thickening.

The author wishes to thank Messrs. C. L. Bailey, D. Greene, R. D. Krohn, R. Perry, and Dr. H. T. Richards for their generous help in taking data and running the electrostatic generator during this experiment.

PHYSICAL REVIEW VOLUME 70, NUMBERS 9 AND 10 NOVEMBER 1 AND 15, 1946

Angular Distribution of 2.5-Mev Neutrons Scattered by Deuterium†

J. H. Coon* and H. H. Barschall*
Los Alamos Laboratory, Los Alamos, New Mexico

(Received July 29, 1946)

The angular distribution of the scattering by deuterium of 2.5-Mev neutrons was measured by analyzing the distribution in energy of the recoiling deuterons in an ionization chamber. In the center of mass system the differential cross section exhibits a maximum for backward scattering of the neutron. The value at the maximum is more than twice the value at angles near 90°. Neutron-proton scattering observed under similar conditions showed a departure of not more than 10 percent from isotropic scattering.

INTRODUCTION

IT was pointed out in an earlier paper[1] that the distribution in angle of scattered fast neutrons could be measured by analyzing the distribution in energy of the recoiling nuclei in an ionization chamber filled with the gas the scattering by which one wishes to investigate. If monoenergetic neutrons are used, the distribution in energy of the recoiling particles in the laboratory system gives a direct measure of the angular distribution of the scattered neutrons in the center of mass system, provided that the dimensions of the chamber are large compared to the range of the most energetic recoiling nuclei.

In order to fulfill this condition very high pressures are required for investigations of the scattering properties of hydrogen or deuterium for fast neutrons. In spite of the application of high collecting fields, difficulties were caused in the earlier work by the slow collection of the ions in the gas at high pressure, resulting in a lack of energy resolution. The lack of resolution was caused partly by the fact that the amplification was not entirely frequency independent for the very slow pulses, partly by the relatively small signal to noise ratio for a slow amplifier, and also by the possible superposition of pulses due to recoils and due to gamma-rays. The earlier work[1] did not give any evidence for an anisotropy in the scattering of 2.5-Mev neutrons by hydrogen or deuterium. It was pointed out in the earlier paper that, because of the lack of resolving power both in energy and angle, deviations from isotropy could have been detected only if they were large and varied slowly with angle. The distribution in energy of the recoiling deuterons showed the unexplained feature that its break at high energy occurred at an energy about 10 percent higher than should have been expected from a comparison with Po alpha-particles. This fact, in addition

† This paper is based on work performed under Contract No. W-7405-Eng-36 with the Manhattan Project at the Los Alamos Scientific Laboratory of the University of California.

* Now at the University of Wisconsin.

[1] H. H. Barschall and M. H. Kanner, Phys. Rev. **58**, 590 (1940).

to an observed small rise of the energy distribution at the high energy end, and observations by Staub[2] of a considerably larger rise at the high energy end of the distribution curve for deuterons, indicated the desirability of repeating the experiments using a method which would yield better resolving power.

It is possible to use considerably lower stopping power if all the recoiling particles originate from a foil. In this case it is also feasible to employ the fast collection of electrons in a pure gas instead of the slow collection of positive ions. Under these conditions it was expected that a very much better resolution in energy and angle could be attained.

EXPERIMENTAL

Figure 1 shows the parallel plate ionization chamber[3] in which a thin radiator of about 50 μg cm^{-2} of evaporated normal or heavy paraffin was located on the high voltage electrode (3300 volts negative for the case of protons and 1900 for deuterons). Neutrons incident normal to the radiator ejected protons or deuterons into the chamber at all angles between 0° and 90°. The chamber was filled with krypton to a pressure such that forward recoils had a range of about 8 or 10 mm in the chamber; this pressure was 9.0 and 4.8 atmospheres, respectively, for protons and deuterons.

A third electrode consisting of a plane grid of fine wire (0.003″ Cu wires spaced at 1.5 mm) was located between and parallel to the two parallel plates and 1.3 cm from the high voltage electrode. The voltage applied to the grid was several hundred volts more negative than the potential which the plane of the grid would have assumed in the absence of the grid. Ionization electrons formed in the region between the grid and high voltage electrode are swept through the grid to the collector plate, thereby inducing a voltage pulse, the magnitude of which is entirely determined by the total charge carried by the electrons and by the distributed capacity of the collecting electrode system. The pulse reaches its full value in the relatively short time determined by the mobility of the electrons. Thus one obtains a fast pulse of magnitude proportional to the number of ion pairs formed, and therefore also to the energy of the ionizing particle. Since the pulse is fast, one can use an amplifier with a relatively narrow-band frequency response at high frequency. Use of such an amplifier has the advantage of reducing circuit noise level, eliminating microphonic troubles, and greatly decreasing the chance of superposition of small pulses due to gamma-rays or recoil gas atoms. In the absence of a grid the space in which the ions are formed is not electrostatically shielded from the collector, and the voltage pulse is the sum of

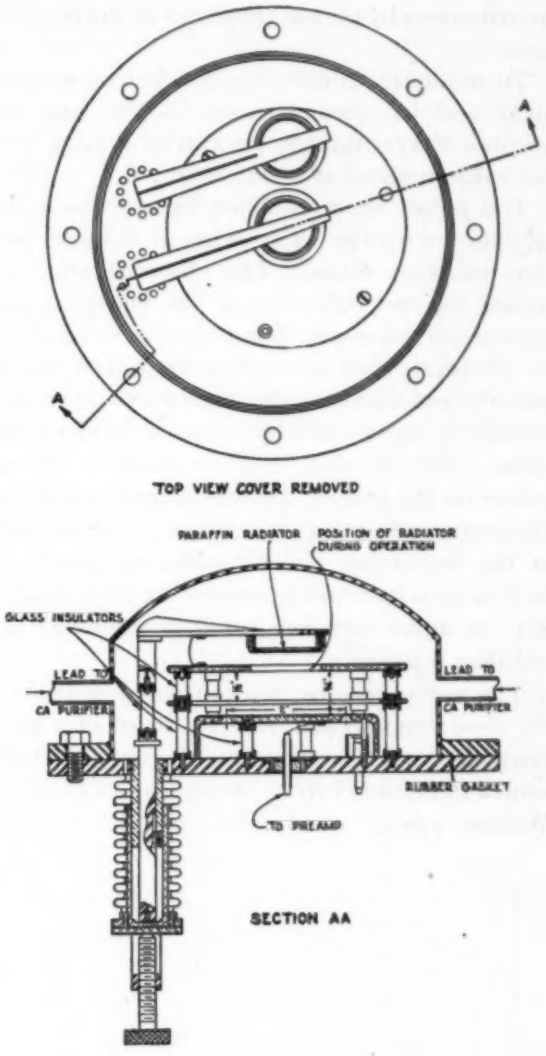

FIG. 1. Parallel plate ionization chamber with thin paraffin radiator.

[2] H. H. Staub, private communication.
[3] This chamber was borrowed from H. H. Staub and D. B. Nicodemus at this laboratory.

contributions by the electrons and by the positive ions.

To minimize trouble due to electron attachment and ion recombination in the gas, the krypton was continually purified by flowing over hot calcium metal at about 350°C.[4]

The pulses were amplified by a linear pulse amplifier[5] with rise time of about 0.5 μsec. and time constant 60 μsec. The observed time required for the collection of the electrons was several microseconds. The pulses were recorded by photographing an oscilloscope screen on 35-mm film and relative pulse heights were measured visually by use of a microfilm reader. An electronic pulse generator was used to impress voltage pulses on the grid of the first amplifier tube for the purpose of testing the constancy and linearity of the amplifying and recording equipment as well as for a standard in comparing pulse heights due to alpha-particles, recoiling protons, and recoiling deuterons.

The monoenergetic neutrons used were from the $d-d$ reaction and were produced in a thick heavy ice target by an analyzed beam of 200-kev atomic deuterium ions accelerated by a Cockcroft-Walton voltage quadrupler. The 1″ diameter radiator in the ionization chamber was located 5″ from the target and at 90° to the deuteron beam. The neutrons incident normal to the radiator had an energy of 2.53 Mev. The energy spread of the neutrons due to the angular range of 12° subtended by the radiator at the target was 110 kev. An additional neutron energy spread of about 30 kev results from the thick heavy ice target. The number of neutrons from the $d-d$ source was monitored by counting protons from the companion reaction $D(d, p)H^3$.

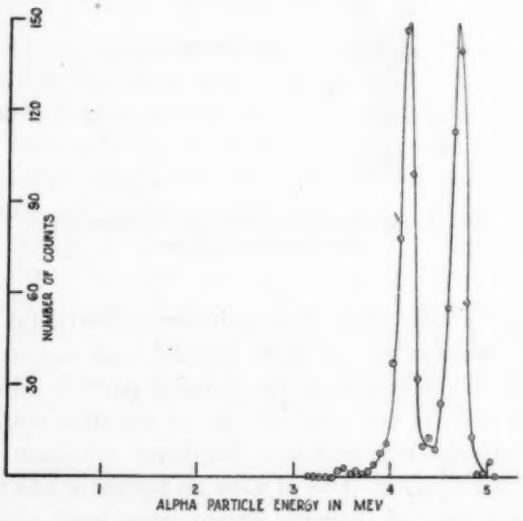

FIG. 2. Distribution in size of pulses due to alpha-particles from a normal uranium foil placed in the ionization chamber.

The paraffin radiator thickness was such that the maximum energy loss of a useful recoil (at maximum angle usable) was about 40 kev for protons and 70 kev for deuterons. Correction was made for the effect of radiator thickness on the energy distribution of the recoiling particles emerging from the radiator. The ratio of the number of deuterium atoms to the number of hydrogen atoms in the heavy paraffin was 62 according to the manufacturer.

For measuring background the Pt foil onto which the radiator was deposited could be replaced by an identical blank Pt foil by means of mechanical controls leading into the ionization chamber through sylphons. The background was minimized by lining the chamber parts with carefully cleaned platinum sheets. The counting rate was about 15 per minute of which 25 percent was background. The pulse height distribution of the background indicated that it was caused mainly by recoiling protons. Data were taken in cycles, the radiator and the blank foil being used alternately.

The best over-all test of the equipment was the counting of alpha-particles from a thin deposit of normal uranium placed in the position normally occupied by the paraffin radiator. Figure 2 shows the pulse height distribution obtained for the two alpha-particle groups. The width of the peaks at half maximum is about 150 kev. This energy resolution indicates that pulse height is independent of direction of the path of the ionizing particle though it is recognized that the relatively short range of the alpha-particle might affect the validity of this test. Comparison of the relative pulse heights due to uranium alpha-particles, and of proton and deuteron recoils of maximum energy gave pulse height values in the same ratio as the energy values with a maximum

[4] E. D. Klema and H. H. Barschall, Phys. Rev. **63**, 18 (1943).

[5] The circuits for this experiment were designed mainly by Matthew Sands and W. A. Higinbotham in this laboratory and were built by the electronics group here.

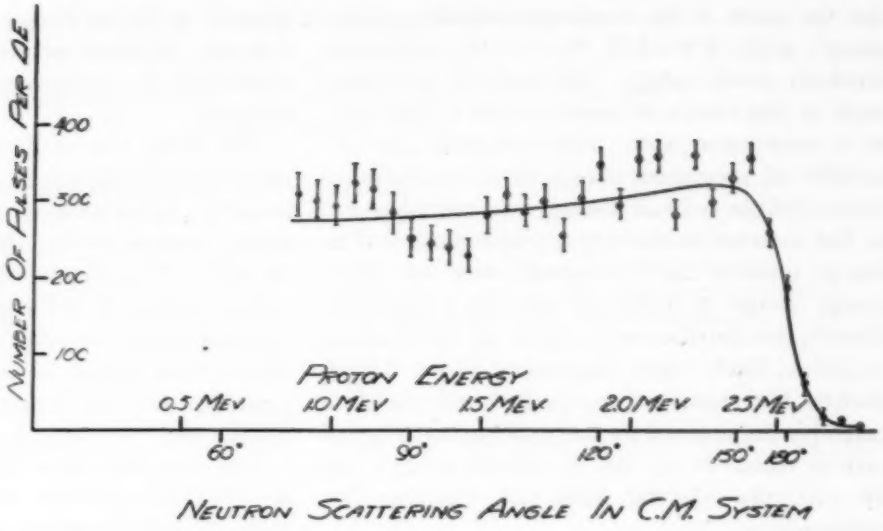

FIG. 3. Distribution in energy and in angle of protons recoiling from 2.53-Mev neutrons. The vertical lines represent standard deviations computed by taking the square root of the sum of the number of counts and the background counts.

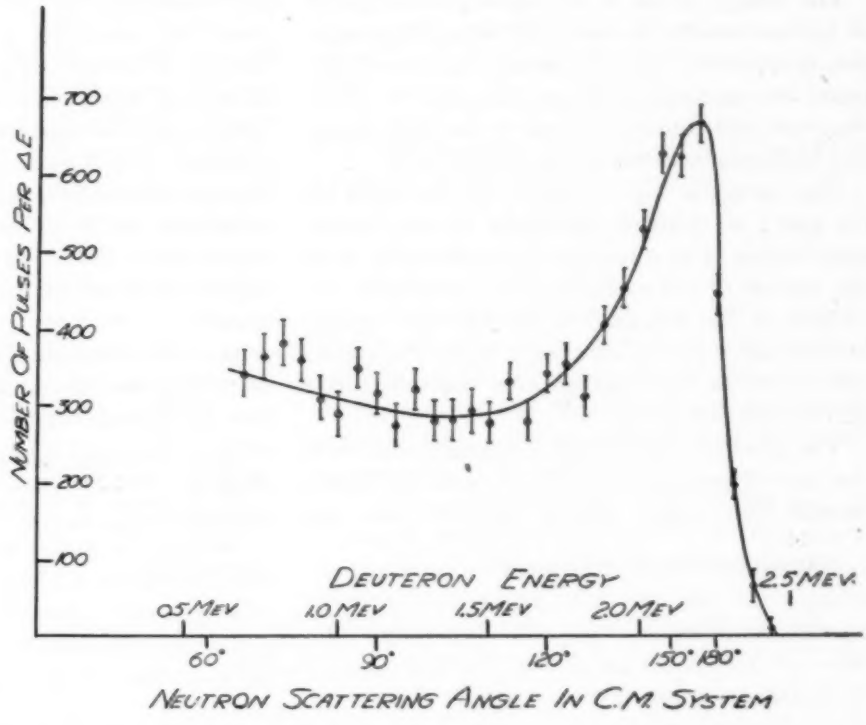

FIG. 4. Distribution in energy and in angle of deuterons recoiling from 2.53-Mev neutrons. The vertical lines represent standard deviations.

difference of 50 kev, which is as good agreement as can be expected from the accuracy of the measurements.

The effectiveness of the grid was tested by using a collimated source of alpha-particles. By changing the distance between source and grid it was determined that if the alpha-particle tracks terminated 2 mm from the grid less than one percent of the pulse height was lost.

Voltage saturation tests showed about a four percent drop in pulse height if the voltage was reduced to half the value used in each case.

RESULTS

Figures 3 and 4 show the pulse height distributions for recoil protons and recoil deuterons, respectively. The abscissae are normalized by taking the neutron energy as 2.53 Mev which is

also the value of the maximum recoiling proton energy, while $8/9\times 2.53$ Mev is the maximum deuteron recoil energy. The neutron scattering angle in the center of mass system is indicated on a non-linear scale. The ordinates are the number of measured pulses (with background subtracted) in a small energy interval ΔE equal to the interval between successive points. The energy interval ΔE is constant over the whole energy range so that the ordinates represent directly the distribution in energy of the recoiling particles. Each curve represents about 12,000 counts. The minimum energy to which the data extend is determined by the maximum energy of carbon recoils or by the maximum energy loss by electrons ejected into the chamber by gamma-rays.

The energy width of the alpha-particle peaks at half-maximum is about 150 kev. The resolution is approximately the same in the case of the recoil measurements, though the rate at which the recoil distributions fall off at the high energy end indicates somewhat better resolution.

The curves in Figs. 3 and 4 are corrected for the effect of radiator thickness[6] on the energy distribution of recoiling particles emerging from the surface of the radiator. The maximum correction in the number of particles per energy interval ΔE is at the low energy end of the curves and amounts to 2 percent for protons and 8 percent for deuterons.

The gradual rise at higher energies shown in the case of protons is hardly outside the experimental uncertainty and is therefore not considered to be in disagreement with the theoretically expected isotropic scattering, which is supported by measurements at higher neutron energies.[7]

The sharp rise at high energy in the case of deuterons implies a preferential backscattering of neutrons by deuterons, with a differential scattering cross section at 180° more than twice that at 110°. Comparison of the area of the high energy hump of the curve with the total area (extrapolating to zero with a horizontal line) shows that about 15 percent of the scattered neutrons are contained in this backscattered maximum.

The cloud-chamber data of Kruger *et al.*[8] for $n-d$ scattering with 2.6-Mev neutrons agrees with the present results in giving a maximum for backscattering of the neutron, though their statistical accuracy is low because the total number of recoils they observed was only 328. According to data of Sherr,[9] the angular distribution of $p-d$ scattering with 2.5-Mev protons exhibits a backscattered maximum similar to, though somewhat larger than, the present measurements on $n-d$ scattering. The Coulomb contribution for $p-d$ scattering at the larger angles involved in backscattering can be neglected.

We wish to thank Mr. R. W. Davis for his help in taking the data and reading the records, and Mr. D. Rhoads for measuring some of the films.

[6] Calculations made by J. L. Magee.

[7] F. C. Champion and C. F. Powell, Proc. Roy. Soc. **A183**, 64 (1944). H. Tatel, Phys. Rev. **61**, 450 (1942).

[8] P. G. Kruger, W. E. Shoupp, R. E. Watson, and F. W. Stallmann, Phys. Rev. **53**, 1014 (1938).

[9] R. Sherr, C. Bailey, M. Blair, and H. Kratz, private communication.

PHYSICAL REVIEW VOLUME 70, NUMBERS 9 AND 10 NOVEMBER 1 AND 15, 1946

Theory of Nuclear Coulomb Energy

E. FEENBERG† AND G. GOERTZEL*
Washington Square College, New York University, New York, New York
(Received August 5, 1946)

The characteristic oscillatory behavior of the Coulomb energy differences for light nuclei is explained in terms of the different values of the average Coulomb interaction between two particles when the wave function is, respectively, symmetrical and antisymmetrical in the space coordinates of the particles. The possible effect of the low binding energy of the least strongly bound particle in $4n+1$ nuclei is discussed. It is shown how the Coulomb energy differences obtained empirically from odd nuclei may be used to estimate Coulomb energy differences for various other cases.

INTRODUCTION

THE Coulomb energy of nuclear systems has been estimated by several distinct methods. These are described briefly in the following paragraphs.

(a) For light nuclei ($A \leqq 16$), single particle wave functions are combined to form Hartree type total wave functions with definite angular momentum and symmetry quantum numbers. These wave functions are used to calculate the expectation value of the electrostatic interaction. Although this procedure does not yield precise quantitative results, it reveals a characteristic oscillatory behavior of the Coulomb energy as a function of atomic number in qualitative agreement with the observations.[1] In the special case of three particle systems (He^3 and H^3), more refined calculations based on models of nuclear forces correlate the Coulomb energy with the assumed range of the force in a satisfactory manner.[2]

(b) The classical energy of a continuous charge distribution spread uniformly throughout a sphere of radius R has the value $3Z^2e^2/5R$, if Ze is the total charge. To obtain the nuclear Coulomb energy, Z^2 is replaced by $Z(Z-1)$ with the result

$$E_c = 3Z(Z-1)e^2/5R. \quad (1)$$

The assumption of constant nuclear density with

$$R = 1.47\times 10^{-13}A^{\frac{1}{3}} \text{ cm} \quad (2)$$

yields[3-5]

$$E_c = 0.592Z(Z-1)/A^{\frac{1}{3}} \text{ Mev}. \quad (3)$$

For odd isobaric nuclei with $N-Z=\pm 1$ the Coulomb energy difference is simply

$$\Delta E_c = E_c(-1) - E_c(+1) = 0.592(A-1)/A^{\frac{1}{3}} \text{ Mev} \quad (4)$$

in excellent agreement with the experimental determinations for A greater than 15, excepting one outstanding discrepancy at $A=27$. Below $A=16$ there are numerous discrepancies, principally because of the oscillatory behaviour of the experimental mass differences.

(c) Attempts have been made to correlate the Coulomb energy differences of odd nuclei with the binding energy of the least strongly bound particle.[5,6] Consider, for example, the systems ${}_4Be^9$ and ${}_5B^9$. The odd particle (neutron or proton) is lightly bound and one might, therefore, expect the effective nuclear radius to exceed the value given by Eq. (2) and the Coulomb energy difference to fall below the value ΔE_c defined by Eq. (4). The qualitative correlation is in the right direction, but no quantitative formulation free from arbitrary assumptions has yet been devised. In view of the extreme nature of these assump-

† Now at Washington University, St. Louis, Missouri.
* This work was carried out while one of us (G. G.) held a fellowship from the Radio Receptor Company, Inc., of New York.
[1] E. Feenberg and M. Phillips, Phys. Rev. **51**, 597 (1937). M. Phillips and E. Feenberg, Phys. Rev. **59**, 400 (1941).
[2] S. S. Share, Phys. Rev. **50**, 488 (1936). William Rarita and R. D. Present, Phys. Rev. **51**, 788 (1937). The application of the calculations in references 1 and 2 to the experimental material involves the assumption that the neutron-neutron and proton-proton interactions differ only in the electrostatic interaction between protons. The same assumption is made in the present analysis of the Coulomb energy problem.
[3] E. Wigner, Phys. Rev. **51**, 947 (1937).
[4] W. Barkas, Phys. Rev. **55**, 694 (1939).
[5] D. R. Elliott and L. D. P. King, Phys. Rev. **60**, 489 (1941).
[6] H. A. Bethe, Phys. Rev. **54**, 436 (1938).

also the value of the maximum recoiling proton energy, while $8/9\times 2.53$ Mev is the maximum deuteron recoil energy. The neutron scattering angle in the center of mass system is indicated on a non-linear scale. The ordinates are the number of measured pulses (with background subtracted) in a small energy interval ΔE equal to the interval between successive points. The energy interval ΔE is constant over the whole energy range so that the ordinates represent directly the distribution in energy of the recoiling particles. Each curve represents about 12,000 counts. The minimum energy to which the data extend is determined by the maximum energy of carbon recoils or by the maximum energy loss by electrons ejected into the chamber by gamma-rays.

The energy width of the alpha-particle peaks at half-maximum is about 150 kev. The resolution is approximately the same in the case of the recoil measurements, though the rate at which the recoil distributions fall off at the high energy end indicates somewhat better resolution.

The curves in Figs. 3 and 4 are corrected for the effect of radiator thickness[6] on the energy distribution of recoiling particles emerging from the surface of the radiator. The maximum correction in the number of particles per energy interval ΔE is at the low energy end of the curves and amounts to 2 percent for protons and 8 percent for deuterons.

The gradual rise at higher energies shown in the case of protons is hardly outside the experimental uncertainty and is therefore not considered to be in disagreement with the theoretically expected isotropic scattering, which is supported by measurements at higher neutron energies.[7]

The sharp rise at high energy in the case of deuterons implies a preferential backscattering of neutrons by deuterons, with a differential scattering cross section at 180° more than twice that at 110°. Comparison of the area of the high energy hump of the curve with the total area (extrapolating to zero with a horizontal line) shows that about 15 percent of the scattered neutrons are contained in this backscattered maximum.

The cloud-chamber data of Kruger *et al.*[8] for $n-d$ scattering with 2.6-Mev neutrons agrees with the present results in giving a maximum for backscattering of the neutron, though their statistical accuracy is low because the total number of recoils they observed was only 328. According to data of Sherr,[9] the angular distribution of $p-d$ scattering with 2.5-Mev protons exhibits a backscattered maximum similar to, though somewhat larger than, the present measurements on $n-d$ scattering. The Coulomb contribution for $p-d$ scattering at the larger angles involved in backscattering can be neglected.

We wish to thank Mr. R. W. Davis for his help in taking the data and reading the records, and Mr. D. Rhoads for measuring some of the films.

[6] Calculations made by J. L. Magee.

[7] F. C. Champion and C. F. Powell, Proc. Roy. Soc. **A183**, 64 (1944). H. Tatel, Phys. Rev. **61**, 450 (1942).

[8] P. G. Kruger, W. E. Shoupp, R. E. Watson, and F. W. Stallmann, Phys. Rev. **53**, 1014 (1938).

[9] R. Sherr, C. Bailey, M. Blair, and H. Kratz, private communication.

Theory of Nuclear Coulomb Energy

E. FEENBERG† AND G. GOERTZEL*
Washington Square College, New York University, New York, New York
(Received August 5, 1946)

The characteristic oscillatory behavior of the Coulomb energy differences for light nuclei is explained in terms of the different values of the average Coulomb interaction between two particles when the wave function is, respectively, symmetrical and antisymmetrical in the space coordinates of the particles. The possible effect of the low binding energy of the least strongly bound particle in $4n+1$ nuclei is discussed. It is shown how the Coulomb energy differences obtained empirically from odd nuclei may be used to estimate Coulomb energy differences for various other cases.

INTRODUCTION

THE Coulomb energy of nuclear systems has been estimated by several distinct methods. These are described briefly in the following paragraphs.

(a) For light nuclei ($A \leqq 16$), single particle wave functions are combined to form Hartree type total wave functions with definite angular momentum and symmetry quantum numbers. These wave functions are used to calculate the expectation value of the electrostatic interaction. Although this procedure does not yield precise quantitative results, it reveals a characteristic oscillatory behavior of the Coulomb energy as a function of atomic number in qualitative agreement with the observations.[1] In the special case of three particle systems (He^3 and H^3), more refined calculations based on models of nuclear forces correlate the Coulomb energy with the assumed range of the force in a satisfactory manner.[2]

(b) The classical energy of a continuous charge distribution spread uniformly throughout a sphere of radius R has the value $3Z^2e^2/5R$, if Ze is the total charge. To obtain the nuclear Coulomb energy, Z^2 is replaced by $Z(Z-1)$ with the result

$$E_c = 3Z(Z-1)e^2/5R. \quad (1)$$

The assumption of constant nuclear density with

$$R = 1.47\times10^{-13}A^{\frac{1}{3}} \text{ cm} \quad (2)$$

yields[3-5]

$$E_c = 0.592Z(Z-1)/A^{\frac{1}{3}} \text{ Mev}. \quad (3)$$

For odd isobaric nuclei with $N-Z=\pm1$ the Coulomb energy difference is simply

$$\Delta E_c = E_c(-1) - E_c(+1) = 0.592(A-1)/A^{\frac{1}{3}} \text{ Mev} \quad (4)$$

in excellent agreement with the experimental determinations for A greater than 15, excepting one outstanding discrepancy at $A=27$. Below $A=16$ there are numerous discrepancies, principally because of the oscillatory behaviour of the experimental mass differences.

(c) Attempts have been made to correlate the Coulomb energy differences of odd nuclei with the binding energy of the least strongly bound particle.[5,6] Consider, for example, the systems $_4Be^9$ and $_5B^9$. The odd particle (neutron or proton) is lightly bound and one might, therefore, expect the effective nuclear radius to exceed the value given by Eq. (2) and the Coulomb energy difference to fall below the value ΔE_c defined by Eq. (4). The qualitative correlation is in the right direction, but no quantitative formulation free from arbitrary assumptions has yet been devised. In view of the extreme nature of these assump-

† Now at Washington University, St. Louis, Missouri.

* This work was carried out while one of us (G. G.) held a fellowship from the Radio Receptor Company, Inc., of New York.

[1] E. Feenberg and M. Phillips, Phys. Rev. **51**, 597 (1937). M. Phillips and E. Feenberg, Phys. Rev. **59**, 400 (1941).

[2] S. S. Share, Phys. Rev. **50**, 488 (1936). William Rarita and R. D. Present, Phys. Rev. **51**, 788 (1937). The application of the calculations in references 1 and 2 to the experimental material involves the assumption that the neutron-neutron and proton-proton interactions differ only in the electrostatic interaction between protons. The same assumption is made in the present analysis of the Coulomb energy problem.

[3] E. Wigner, Phys. Rev. **51**, 947 (1937).

[4] W. Barkas, Phys. Rev. **55**, 694 (1939).

[5] D. R. Elliott and L. D. P. King, Phys. Rev. **60**, 489 (1941).

[6] H. A. Bethe, Phys. Rev. **54**, 436 (1938).

tions, it seems reasonable to conclude that some other effect must be invoked to account for the major part of the experimental periodicity.

(d) The Coulomb energy is an important factor in studies of nuclear structure based on the alpha-particle model.[7] However, it is not likely that estimates of the Coulomb energy can supply evidence for or against the spatial localization suggested by the model. It is satisfactory that a simple estimate agrees fairly well with the experimental determinations.

The present calculation avoids the approximations made in (a) and (b) and yields the characteristic oscillations found in (a) while going over into (b) for sufficiently large values of A. Because of the effect described in (c), certain relations must be interpreted as inequalities for A less than 13. The method of calculation is adapted from that used by Wigner in his theory of nuclear mass defects.[3]

GENERAL FORMULATION

The operator[8]

$$X=\tfrac{1}{4}(1-\tau_{\xi 1})(1-\tau_{\xi 2})P_{12} \tag{5}$$

has the eigenvalues 1, -1, and 0, the first two occurring only when both particles are protons. From the expectation values of the operators

$$\begin{aligned} X_s&=\tfrac{1}{2}(P_{12}+1)X, \\ X_a&=\tfrac{1}{2}(P_{12}-1)X \end{aligned} \tag{6}$$

one obtains the probabilities

$$\begin{aligned} p_s&=(\psi, X_s\psi)=(X_s\psi, X_s\psi), \\ p_a&=(\psi, X_a\psi)=(X_a\psi, X_a\psi) \end{aligned} \tag{7}$$

for the eigenvalues 1 and -1, respectively, of X. Summing Eq. (7) over all pairs of particles yields the result

$$\tfrac{1}{2}A(A-1)(p_s+p_a)=\tfrac{1}{2}Z(Z-1). \tag{8}$$

Thus, $\frac{1}{2}A(A-1)p_s$ may be interpreted loosely as the number of proton pairs for which the wave function is symmetric in the space coordinates of the two protons.

The Coulomb energy, given by the equation

$$E_c=\tfrac{1}{8}\sum{}'\left(\psi, (1-\tau_{\xi i})(1-\tau_{\xi j})\frac{e^2}{r_{ij}}\psi\right), \tag{9}$$

is readily expressed in the form

$$E_c=\tfrac{1}{2}A(A-1)\left[\left(X_s\psi, \frac{e^2}{r_{12}}X_s\psi\right)+\left(X_a\psi, \frac{e^2}{r_{12}}X_a\psi\right)\right]. \tag{10}$$

The quantities L_s and L_a, defined by the equations

$$\begin{aligned} p_sL_s&=\left(X_s\psi, \frac{e^2}{r_{12}}X_s\psi\right), \\ p_aL_a&=\left(X_a\psi, \frac{e^2}{r_{12}}X_a\psi\right), \end{aligned} \tag{11}$$

are interpreted as average values of the Coulomb interaction between two particles when the wave function is, respectively, symmetrical and antisymmetrical in the space coordinates of the particles. In the applications an approximation is introduced by the assumption that L_s and L_a are constant in an isobaric series and vary smoothly as functions of A. A possible limitation on the validity of this assumption is discussed in the concluding section.

It is convenient to replace L_s and L_a by the linear combinations

$$L_c=\tfrac{1}{4}(L_s+3L_a), \quad L'_c=L_s-L_a. \tag{12}$$

Then, using Eqs. (8), (11), and (12), Eq. (10) becomes

$$E_c=\tfrac{1}{2}Z(Z-1)L_c+\tfrac{1}{8}A(A-1)(3p_s-p_a)L'_c. \tag{13}$$

The assumption that the nuclear volume is proportional to the number of particles, as in Eq. (2), implies that $A^{\frac{1}{3}}L_c$ approaches a constant limiting value as A grows larger. For L'_c one expects a very rapid decrease with increasing A. In agreement with this expectation, the empirical data require that L_s and L_a approach equality beyond $A=20$.

[7] L. R. Hafstad and E. Teller, Phys. Rev. **54**, 681 (1938). Harrison Brown and D. R. Inglis, Phys. Rev. **55**, 1182 (1939).

[8] τ_ξ has the value 1 if the particle is a neutron and the value -1 for a proton. The operator P_{12} interchanges the space coordinates of particles 1 and 2. We use a completely antisymmetric wave function (in the space, spin, and charge coordinates of the particles) to obviate the need to distinguish between matrix elements of operators with subscripts 1 and 2 and any other pair of subscripts.

To determine p_s and p_a, some specification of the symmetry properties of the wave function is required. Wigner's first approximation,[3] which yields wave functions belonging to irreducible representations of the symmetric group, is assumed in this discussion.

EVALUATION OF p_s AND p_a

Two procedures will be described. The first may be called intuitive, since it interprets the symmetry properties of the wave function in terms of an alpha-particle structure without, however, specifying the spatial location of the alpha-particles (more properly the "four" groups). The second is a formal and rigorous operator calculation.

1. For a single alpha-particle, there is only one interaction term and the Coulomb energy is represented by $E_c=L_s$. The same formal result is obtained for the systems He^5 and He^6 in their normal states. If a proton is added to the alpha-particle, the spin wave function of the three protons has the form

$$2^{-\frac{1}{2}}\{S_+(1)S_-(2)-S_+(2)S_-(1)\}S_+(3). \quad (14)$$

It is easily seen that the spin state associated with particles 2 and 3 is a linear combination of singlet and triplet with statistical weights one and three, respectively. Consequently, the addition of the proton increases the Coulomb energy by the amount

$$\tfrac{1}{2}(L_s+3L_a). \quad (15)$$

The Coulomb interaction energy between two "four" groups is then evidently L_s+3L_a.

In the $A=4k$ series with $A=2Z$ there are $Z/2$ "four" groups and $Z(Z-2)/8$ pairs of "four" groups. The Coulomb energy has the value

$$\begin{aligned} E_c&=\tfrac{1}{2}ZL_s+Z(Z-2)(L_s+3L_a)/8 \\ &=\tfrac{1}{2}Z(Z-1)L_c+3ZL'_c/8. \end{aligned} \quad (16)$$

The same result holds for all nuclei containing an even number of protons. In the $A=4k+1$ series with $A=2Z-1$ there are $\frac{1}{2}(Z-1)$ "four" groups, $(Z-1)(Z-3)/8$ pairs of "four" groups, and one additional proton. One obtains

$$\begin{aligned} E_c&=\tfrac{1}{2}(Z-1)L_s+(Z-1)(Z-3)(L_s+3L_a)/8 \\ &\qquad +\tfrac{1}{4}(Z-1)(L_s+3L_a) \quad (17) \\ &=\tfrac{1}{2}Z(Z-1)L_c+3(Z-1)L'_c/8 \end{aligned}$$

for these nuclei and for all others containing an odd number of protons.

This simple procedure yields the Coulomb energy without explicit reference to p_s and p_a. These quantities may be inferred from Eqs. (8), (13), (16), and (17). For systems containing an even number of protons,

$$\begin{aligned} A(A-1)p_s&=\tfrac{1}{4}Z(Z+2); \\ A(A-1)p_a&=\tfrac{3}{4}Z(Z-2). \end{aligned} \quad (18)$$

For an odd number of protons

$$\begin{aligned} A(A-1)p_s&=\tfrac{1}{4}(Z-1)(Z+3), \\ A(A-1)p_a&=\tfrac{3}{4}(Z-1)^2. \end{aligned} \quad (19)$$

Equations (16), (17), (18), and (19) are valid only for states with the same symmetry character (the same $(P\,P'\,P'')$) as the normal state.

2. The formal and rigorous derivation starts from the relation

$$P_{ij}=-\tfrac{1}{4}(1+\boldsymbol{\sigma}_i\cdot\boldsymbol{\sigma}_j)(1+\boldsymbol{\tau}_i\cdot\boldsymbol{\tau}_j) \quad (20)$$

which equates the space exchange operator to the negative product of spin and charge spin exchange operators. We wish to evaluate the diagonal matrix elements of the operator

$$\begin{aligned} W&=\tfrac{1}{2}\textstyle\sum_{ij}{}'\,\tfrac{1}{4}(1-\tau_{\xi i})(1-\tau_{\xi j})P_{ij} \\ &=\tfrac{1}{32}\textstyle\sum_{ij}{}'(1+\boldsymbol{\sigma}_i\cdot\boldsymbol{\sigma}_j)(1+\boldsymbol{\tau}_i\cdot\boldsymbol{\tau}_j) \\ &\qquad\qquad \times(1-\tau_{\xi i})(1-\tau_{\xi j}). \end{aligned} \quad (21)$$

It is evident from Eqs. (5)–(7) that

$$\tfrac{1}{2}A(A-1)(p_s-p_a)=(\psi,\,W\psi). \quad (22)$$

With the help of Eq. (8), p_s and p_a can be expressed in terms of the diagonal matrix elements of W.

The triad of relations

$$\tau_\xi\tau_\eta=-i\tau_\zeta; \quad \tau_\eta\tau_\zeta=-i\tau_\xi; \quad \tau_\zeta\tau_\xi=-i\tau_\eta$$

permits the reduction of an arbitrary power series in the variables τ_ξ, τ_η, τ_ζ to a linear function of the same variables. In particular

$$\begin{aligned} &(1+\boldsymbol{\tau}_i\cdot\boldsymbol{\tau}_j)(1-\tau_{\xi i})(1-\tau_{\xi j}) \\ &\qquad\qquad =2(1-\tau_{\xi i})(1-\tau_{\xi j}) \end{aligned} \quad (23)$$

and Eq. (21), defining W, may be replaced by

$$-W=\tfrac{1}{16}\textstyle\sum_{ij}{}'(1+\boldsymbol{\sigma}_i\cdot\boldsymbol{\sigma}_j)(1-\tau_{\xi i})(1-\tau_{\xi j}). \quad (24)$$

The right-hand member of Eq. (24) can be expressed in terms of known quantities by the expedient of adding and subtracting a diagonal term to the sum over i and j:

$$-W=\tfrac{1}{16}\{\textstyle\sum_i(1-\tau_{fi})\}^2 +\tfrac{1}{16}\{\textstyle\sum_i\sigma_i(1-\tau_{fi})\}^2-\tfrac{1}{2}\textstyle\sum_i(1-\tau_{fi}) \quad (25)$$
$$=\tfrac{1}{4}Z^2-Z+S_x^2.$$

Here, S_x^2 is the total proton spin operator. We are concerned with states which are eigenstates of $S_x^2=S'(S'+1)$ with the eigenvalues 0 (Z even) and $\frac{1}{2}(1+\frac{1}{2})$ (Z odd). These are the states with maximum symmetry in the space coordinates of the particles. Equations (18) and (19) are now immediate consequences of Eqs. (8), (22), and (25) combined with the above eigenvalues of S_x^2. In reality the total proton spin does not commute with the Hamiltonian operator and the reference to eigenvalues is inappropriate. However the diagonal matrix elements of S_x^2 cannot differ appreciably from the quoted eigenvalues.

COULOMB ENERGY DIFFERENCES

The formulae for E_c can be put in the following form:

$$E_c=\tfrac{1}{2}Z(Z-1)L_c+\tfrac{3}{8}[Z-\tfrac{1}{2}+\tfrac{1}{2}(-)^Z]L'_c. \quad (26)$$

Now, setting $Z=\frac{1}{2}(A\pm u)$,

$$E_c(A,\pm u)=\tfrac{1}{8}(A\pm u)(A\pm u-2)L_c +\tfrac{3}{16}[A\pm u-1+(-1)^{(A\pm u)/2}]L'_c. \quad (27)$$

Then,

$$\Delta E_c(A,u)=E_c(A,u)-E_c(A,-u) =\tfrac{1}{2}u(A-1)L_c \quad (28)$$
$$+\tfrac{3}{8}[u+\tfrac{1}{2}(-1)^{(A+u)/2}\{1-(-1)^u\}]L'_c.$$

Using Eq. (28), Table I is easily constructed:

TABLE I.

A	$\lvert N-Z\rvert$	$\Delta E_c(A,\lvert N-Z\rvert)$
$4k+1$	1	$\frac{1}{2}(A-1)L_c\equiv F$
$4k+3$	1	$\frac{1}{2}(A-1)L_c+\frac{1}{4}L'_c\equiv G$
$2k$	$2n$	$n(F+G)$; $n=1, 2, 3, \cdots$
$4k+1$	3	$F+2G$
$4k+3$	3	$2F+G$

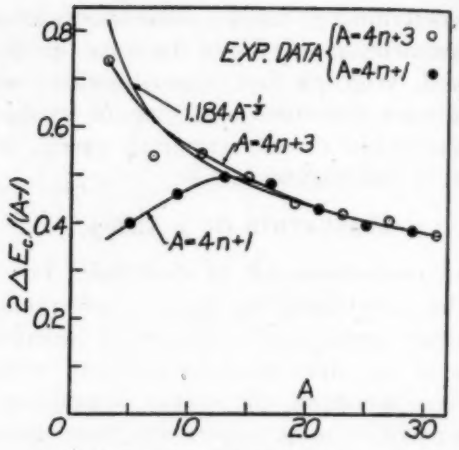

FIG. 1. Plot of experimental Coulomb energy differences against mass number. Ordinates are in Mev and have been multiplied by the factor $2/(A-1)$.

We also include the relations between F, G and L_s, L_a:

$$L_s=G-\frac{A-3}{A-1}F, \quad L_a=-\frac{1}{3}G+\frac{1}{3}\frac{A+5}{A-1}F. \quad (29)$$

Evidently, for $|N-Z|=1$, the alternation of the coefficient of L'_c as one proceeds along the series of odd nuclei causes an oscillatory behavior of the Coulomb energy differences. That is, one expects the data for odd nuclei with $|N-Z|=1$ to fall on two separate curves, marked F and G in the table, rather than on a single curve.

Now, if F and G were smoothly varying functions of the mass number, it would be possible to use the experimental data for the $4n+3$ nuclei to determine G for all A and similarly to use the data for the $4n+1$ nuclei to determine F. With these results and also Table I, Coulomb energy differences could be predicted for many nuclei.

However, F and G may possibly change irregularly with A for the following reason, already mentioned in the introduction under (b). It is likely that the nuclear radius is not a smoothly varying function of mass number below $A=12$, since the binding energy of the least strongly bound particle in this range does not vary smoothly with A. The nuclei of the type $4k+1$ might be expected to have larger radii than would be predicted from the radii of nuclei with neighboring mass numbers. Now it seems likely

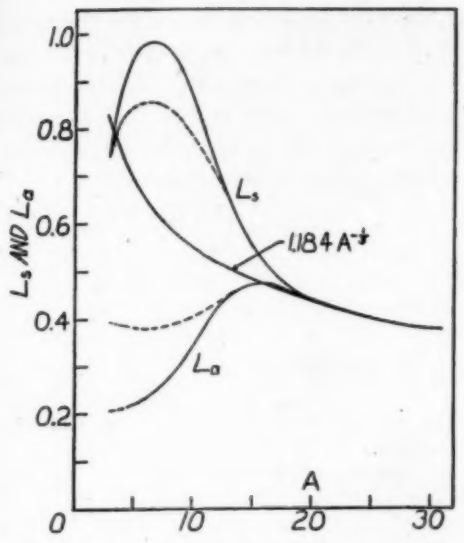

FIG. 2. Plot of L_s and L_a against mass number. Ordinates are in Mev. The dotted curves correspond to the following change in Fig. 1: The $A=4n+1$ curve on Fig. 1 is held constant and equal to 0.497 for A less than 13.

that L_sR and L_aR, where R is the effective nuclear radius, change in a fairly regular manner with mass number, even though possibly L_s and L_a do not. It follows that one expects FR and GR to vary more smoothly with mass number than F and G. This means that the experimentally determined F curve, for A less than 13, applies rigorously only to the $4k+1$ nuclei, while the interpolated points for other nuclei may be too low. Similarly, the G curve is correct for all but the $4k+1$ nuclei, for which it may be too high.

The experimentally determined curves of $2F/(A-1)$ and $2G/(A-1)$ (not corrected for the above possibility) are given in Fig. 1. The experimental points are also indicated there. The derived curves, L_s and L_a, are plotted in Fig. 2. Table II lists the experimental data and the ordinates of the various curves. The Coulomb energy difference computed from Eq. (4) is also included.

Summarizing the preceding discussion, the F curve of Fig. 1 is to be interpreted, for all but the $4k+1$ nuclei, as a lower limit to the correct value to be used in Table I. Similarly, the G curve is, for the $4k+1$ nuclei, an upper limit. The curves for L_a and L_s are lower and upper limits to the correct values for all mass numbers. Above mass 12, all statements concerning upper and lower limits may be replaced by statements concerning equalities.

In order to show the effect of a change in F on the derived curves of Fig. 2, the dotted curves of 2 were plotted. These correspond to the assumption that $2F/(A-1)$ is constant and equal to 0.497 for A less than 13.

It will be possible to determine more accurately the values of F for other than $4k+1$ nuclei when sufficient data are obtained for the Coulomb energy differences of even nuclei. Or, if some estimate is obtained of the variation of nuclear radius with mass number which is sufficiently accurate in this region, the experimental data can be used to determine FR and GR for all A. One then will be in a position to determine more nearly correct values of F and G for all A.

A few words should be said about the experimental values as plotted. Because of the uncertainties of the data, the curves of Fig. 1 are somewhat arbitrary. However, it seems quite clear that the $4k+1$ nuclei fall on a separate curve from the $4k+3$ nuclei. The apparently

TABLE II. Experimental Coulomb energy differences and ordinates of curves plotted in Figs. 1 and 2.

A	ΔE_c (Mev)	References	$\frac{2\Delta E_c}{A-1}$	$\frac{2G}{A-1}$	$\frac{2F}{A-1}$	L_s	L_a	$1.184A^{-\frac{1}{3}}$
3	0.74	a	0.74	0.74	0.37	0.74		0.821
5	0.80	b	0.40	0.67	0.40	0.94	0.22	0.692
7	1.62	c	0.54	0.62	0.43	0.98	0.25	0.619
9	1.84	c	0.46	0.58	0.46	0.93	0.30	0.569
11	2.73	c	0.546	0.55	0.48	0.80	0.38	0.532
13	2.98	c	0.497	0.52	0.50	0.65	0.45	0.504
15	3.5	d	0.50	0.50	0.49	0.55	0.47	0.480
17	3.88	e	0.485	0.48	0.47	0.49	0.47	0.461
19	3.98	f	0.442	0.45	0.45	0.45	0.45	0.444
21	4.32	g	0.432	0.43	0.43	0.43	0.43	0.429
23	4.60	f	0.418	0.42	0.42	0.42	0.43	0.416
25	4.77	f	0.398	0.41	0.41	0.41	0.41	0.405
27	5.32	h	0.408	0.40	0.40	0.40	0.40	0.395
29	5.41	g	0.386	0.39	0.39	0.39	0.39	0.385
31	5.65	i, g	0.377	0.38	0.38	0.38	0.38	0.377

[a] Carl E. Nielsen, Phys. Rev. **60**, 160 (1941). R. D. O'Neal, Phys. Rev. **60**, 359 (1941).
[b] H. Staub and W. E. Stephens, Phys. Rev. **55**, 131 (1939).
[c] R. O. Haxby, W. E. Shoupp, W. E. Stephens, and W. H. Wells, Phys. Rev. **58**, 1035 (1940).
[d] William E. Stephens, Kamal Djanab, and T. W. Bonner, Phys. Rev. **52**, 1079 (1937). W. A. Fowler, L. A. Delsasso, and C. C. Lauritsen, Phys. Rev. **49**, 561 (1936).
[e] Franz N. D. Kurie, J. R. Richardson, and H. C. Paxton, Phys. Rev. **49**, 368 (1936).
[f] M. G. White, L. A. Delsasso, J. G. Fox, and E. C. Creutz, Phys. Rev. **56**, 512 (1939).
[g] M. G. White, E. C. Creutz, L. A. Delsasso, and R. R. Wilson, Phys. Rev. **59**, 63 (1941).
[h] W. H. Barkas, E. C. Creutz, L. A. Delsasso, R. B. Sutton, and M. G. White, Phys. Rev. **58**, 383 (1940).
[i] See reference 5.

anomalous experimental value for $A=7$ is not yet sufficiently well established to justify an attempt at explanation or interpretation.

It is, of course, conceivable that the entire experimental difference $G-F$ is attributable to the variations of R alone, rather than to a combination of causes, including the difference in L_s and L_a. However, there seems to be no plausible excuse for assuming L_s and L_a to be equal. What is surprising is that the experimental evidence requires them to approach equality for relatively low mass number ($A\sim 20$).

PHYSICAL REVIEW VOLUME 70, NUMBERS 9 AND 10 NOVEMBER 1 AND 15, 1946

Elastic Backscattering of $d-d$ Neutrons

J. H. MANLEY,* H. M. AGNEW,** H. H. BARSCHALL,*** W. C. BRIGHT, J. H. COON,*** E. R. GRAVES, T. JORGENSEN,† AND B. WALDMAN††
University of California, Los Alamos Scientific Laboratory, Santa Fe, New Mexico

(Received August 29, 1946)

The backscattering of $d-d$ neutrons was investigated for several materials. A directional thick paraffin detector was used. The detector was sensitive primarily to neutrons which had been scattered elastically or with little energy loss.

INTRODUCTION

THE purpose of the present experiments was to measure the cross sections of various materials for the backward scattering of $d-d$ neutrons which had suffered elastic collisions or inelastic collisions with small energy loss. For this purpose a detector was used, the sensitivity of which is a rapidly increasing function of neutron energy. The detector used the recoils originating from a thick layer of paraffin. Such a detector has a high efficiency, can be made directional, and is most sensitive to the neutrons of highest energy. The directional property of recoil protons eliminates the necessity for a shadow cone usually required to keep the large direct beam from completely masking the small fraction of reflected neutrons.

SOURCE

The neutrons were obtained from the $d-d$ reaction by bombarding a thick D_2O ice target with 50–100 μa of 200-kev unanalyzed ions of deuterium accelerated by means of a Cockcroft-Walton set. The target was cooled with a liquid oxygen refluxing system which required only a small amount of material near the target.

The neutron flux was monitored by counting the protons from the companion $D(d,p)H^3$ reaction.

The deuteron beam was collimated by two tungsten diaphragms with $\frac{3}{8}''$ diameter apertures to define the source on the target. For the conditions of the experiment, the neutron spectrum extends from 2.5 to 3.1 Mev with an energy spread of 0.3 Mev at half-maximum.

The angular distribution of the neutrons from this source for the conditions of the experiment

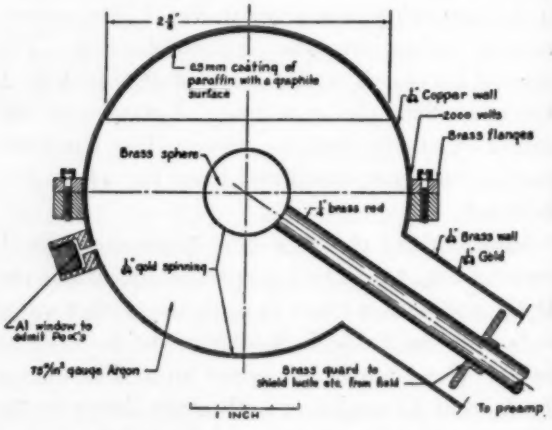

FIG. 1. Spherical ionization chamber. Recoil protons from a thick layer of paraffin are detected.

* Now on leave from Washington University.
** Now at the University of Chicago.
*** Now at the University of Wisconsin.
† Now at the University of Nebraska.
†† Now at the University of Notre Dame.

was assumed to be proportional to $(1+0.7\cos^2\eta)$ where η is the angle between the incident deuterons and the emitted neutron. The scatterer subtended an angle of 34° at the source, corresponding to a variation over the scatterer of 10 percent in neutron intensity and 1 percent in neutron energy.

DETECTOR

The detector used in the experiment is shown in Fig. 1. It consists of a spherical collector electrode, $\frac{3}{4}''$ in diameter, surrounded by a concentric spherical high voltage electrode, 3″ in diameter. The inside surface of a segment of the high voltage electrode was coated with a layer of paraffin, 0.5 mm thick. This layer was covered by graphite to avoid accumulation of charges on the paraffin. The chamber was filled with pure argon to a pressure of 6 atmos.

The chamber was connected to a pulse amplifier by means of a coaxial lead, 18″ long, in order to eliminate scattering material in the neighborhood of the detector. The amplifier had a rise time of 10μ sec. The output of the amplifier was fed through a discriminator into a scale of 64 counter. The operation of the detecting equipment was checked both by means of artificial pulses from an electronic pulse generator and by observing α-particles which could enter the chamber through a window. In order to establish an energy scale the maximum pulse height due to recoiling protons from $d-d$ neutrons was measured in terms of artificial pulses. The assumption was made that the relation between recoil energy and voltage change of the collecting electrode is linear. The artificial pulses were used to set the discriminator to the desired bias. All pulses greater than this bias were counted.

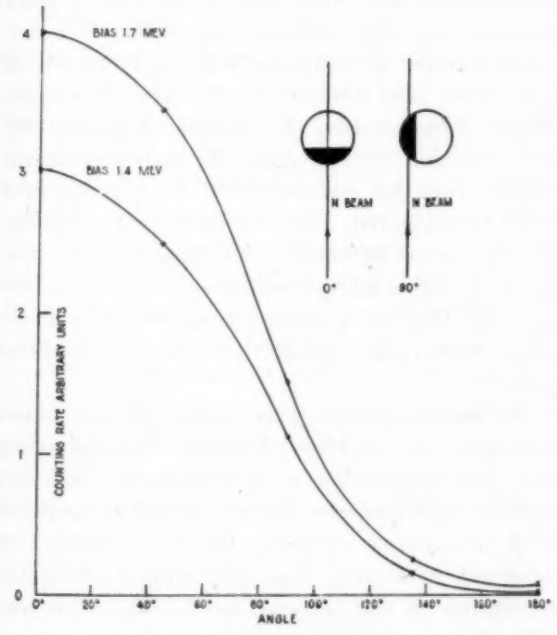

FIG. 2. Response of ionization chamber as a function of angle of incidence of neutron beam.

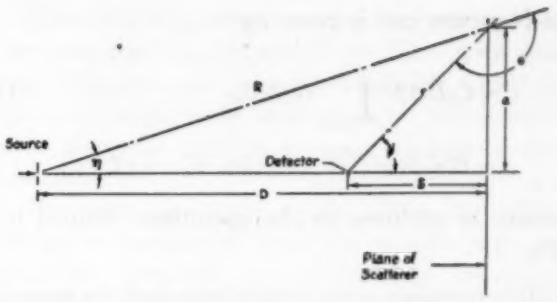

FIG. 3. Geometry for scattering measurements.

As first constructed, the chamber was about 20 times as sensitive to neutrons incident on the convex surface of the radiator as for those incident on the concave. An investigation as to the origin of this background led to the conclusion that it must be due to disintegrations in the copper electrodes of the chamber. Lining the chamber with gold sheet increased the ratio for the two directions of neutron incidence to 100. The counting rate as a function of the angle of incidence is shown in Fig. 2.

GEOMETRY

In order to specify the geometry, the center of the detector is defined as a point $\frac{3}{8}''$ from the pole of the paraffin cap toward the center of the sphere, a point approximately at the center of sensitivity of the detector. The position of the scatterer was taken as its median plane. These points are used to specify the distance, D, from the target to the scatterer, and the distance δ from the scatterer to the detector. The scatterers used were disks, 10″ in diameter.

The geometric relations involved in this experiment are shown in Fig. 3. The counting rate C for this case due to the presence of a scatterer

of N atoms/cm² is given by[1]

$$C = C_0 D_0^2 N \int_{\theta_{min}}^{\pi} I\sigma(\theta) d\omega \qquad (1)$$

$$I = F(\eta)S(\varphi)/(D-\delta)[(Dr/R)-(\delta R/r)],$$

where in addition to the quantities defined by Fig. 3:

$C_0D_0^2$ = counting rate due to direct beam times the square of the distance from the source at which it is measured ($\eta = 0$);

$F(\eta)$ = number of neutrons emitted per unit solid angle by the source normalized to unity at $\eta = 0$;

$S(\varphi)$ = angular sensitivity of the detector (Fig. 2);

$\sigma(\theta)$ = scattering cross section per unit solid angle;

$\theta_{min} = \sin^{-1}\frac{a(D-\delta)}{Rr}$;

$d\omega = 2\pi \sin\theta d\theta$.

For most of the experiments D was chosen to be 16", and $\delta = 1\frac{1}{8}$". These dimensions define a minimum scattering angle $\theta_{min} = 128°$.

Examination of Eq. (1) shows that, in the geometry used, neutrons scattered through various angles θ between θ_{min} and 180° contribute to the measured average scattering cross section according to the geometric weighting factor I. In Fig. 4 I is plotted against θ. The rapid rise of I at the edge of the disk has its origin in the relatively large area subtended by a given $d\theta$ as θ increases. Taking into account the variation of I with θ, the effective average scattering angle used in the experiment was about 137°.

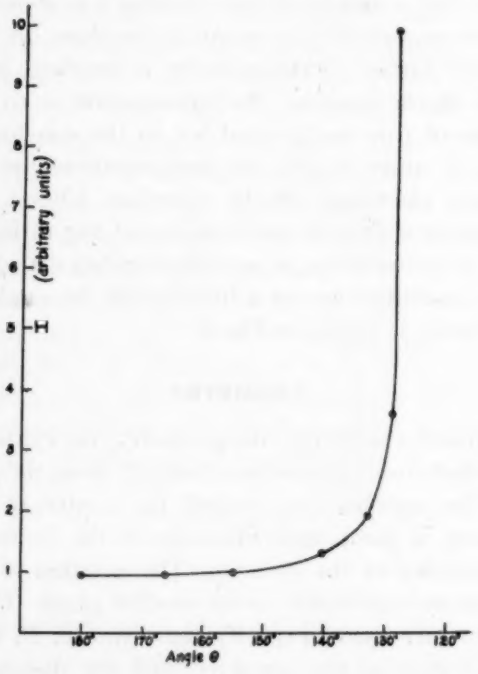

FIG. 4. Weighting factor I as a function of scattering angle θ, showing the relative contribution of different scattering angles to measured average scattering cross section. The plotted points are at radii on disk of 0.5, 1.0, 2.0, 3.0, 4.0, and 5.0 inches.

[1] Calculation by P. Olum.

TABLE I. Samples used in scattering experiments.

Substance	Thickness of sample (cm)	Area cm²	Mass kg	Mol. or atoms/cm³ × 10⁻²⁴
C	3.81	506	3.09	0.306
BeO	6.35	513	5.02	0.235
BeO	4.37	511	3.91	0.185
Al (dural)	2.54	506	3.58	0.153
SiC	4.44	515	3.39	0.099
Fe	5.08	506	20.1	0.428
Fe	2.54	506	10.0	0.214
SiO_2	6.35	512	5.06	0.099
Al_2O_3	6.35	504	4.03	0.0472
Pt	2.54	506	27.6	0.168
Au	2.54	506	24.9	0.150
Pb	2.54	506	14.6	0.0836

The geometric data on the scatterers used are given in Table I.

PROCEDURE

The counting rate C was obtained as the difference between that with a scatterer in place and that with the scatterer removed.

The number of counts with the scatterer was at least twice that without in all cases. C_0 was determined by rotating the chamber through 180° to a position on the axis, D_0 inches from the target. For this measurement the background could be neglected. To secure sufficient statistical accuracy most of observation time was the time for recording scattered neutrons, since the counting rate due to scattered neutrons was never more than 7 percent of that due to the direct beam.

All measurements were taken at two biases (1.4 Mev and 1.7 Mev). It should be emphasized that the sensitivity of the detector increases rapidly with neutron energy and that neutrons with an energy close to the bias energy are detected with very low efficiency. Calling the sensitivity of the detector for 3.1-Mev neutrons 100, the sensitivity of the detector for lower energies for the two biases used is given in

TABLE II. Energy sensitivity of detector.

Neutron energy (Mev) \ Bias (Mev)→	1.4	1.7
3.1	100	100
2.5	46	38
2.0	14	5
1.5	1	0

Table II. The sensitivities are calculated for a thick paraffin radiator, assuming that the hydrogen cross section varies as $E^{-\frac{1}{2}}$ and the range as $E^{\frac{1}{2}}$.

RESULTS

The results of the measurements are listed in Table III. The calculation of the cross section assumes that $\sigma(\theta)$ is constant in the angular range from $\theta_{\min}$ to π. The cross sections are given as $4\pi\sigma(\theta)$ for ease of comparison with total cross sections although it is recognized that the scattering is not isotropic. The results of Table III have not been corrected for energy loss in elastic collisions with light elements, nor for multiple scattering. In the case of compounds the cross sections are given per molecule. The errors listed are average deviations from the mean deduced from the internal consistency of various runs.

In view of the fact that the detector is predominantly sensitive to elastically scattered neutrons, it is surprising to find differences in the data taken at the two biases. In order to see if such effects can be real, the bias effect expected in carbon and aluminum because of energy loss in elastic collisions was calculated from the theoretical energy sensitivity for a thick paraffin radiator, and compared with the observed bias effect. The ratio of the cross sections for the two biases would be expected to be 1.4 and 1.1 for carbon and aluminum, respectively, while 1.6 ± 0.1 and 1.3 ± 0.1 were observed. The difference between theoretical and experimental results which is somewhat greater than the experimental error may be partly explained by multiple scattering. It is believed that in the heavier elements the observed effect is caused by inelastic scattering.

The effect of multiple scattering was studied by using two thicknesses of beryllium oxide and iron. The results are given in Table III. The data are not sufficiently accurate to state more than that the change in cross section is not unreasonable.

The only previously published results which should be comparable with the present ones are those of Barschall and Ladenburg[2] in which helium recoils of energy greater than 1.1 Mev were counted. Their results for iron and lead (Fe: 0.6×10^{-24} cm^2; Pb: 2.5×10^{-24} cm^2) are in good agreement with the results given in Table III, while their results for carbon and aluminum (C: 1.2×10^{-24} cm^2; Al: 1.1×10^{-24} cm^2) are higher than the ones reported in Table III. The difference may be caused by the different energy sensitivity of the detectors used in the two experiments. The results of Wakatuki and Kikuchi[3] cannot be compared with the present work since their detector was sensitive to neutrons of lower energy, and the cross sections would, therefore, include more inelastic scattering.

TABLE III. Cross sections (in units of 10^{-24} cm^2) for backscattering of 3.1-Mev neutrons.

Substance	Cross section	
	1.4-Mev bias	1.7-Mev bias
C	0.79±0.06	0.49±0.03
BeO (sample 6.35 cm thick)	0.80±0.06	0.59±0.05
BeO (sample 4.37 cm thick)	0.68±0.04	0.37±0.03
Al	0.66±0.04	0.53±0.05
SiC	1.5 ±0.1	1.1 ±0.1
Fe (sample 5.08 cm thick)	0.61±0.03	0.54±0.03
Fe (sample 2.54 cm thick)	0.81±0.03	0.62±0.04
Al_2O_3	2.5 ±0.1	2.0 ±0.1
Pt	0.47±0.03	0.44±0.04
Au	0.59±0.04	0.50±0.08
Pb	2.5 ±0.1	2.3 ±0.1

This work was carried out under contract between the University of California and the Manhatten District, Corps of Engineers, War Department.

[2] H. H. Barschall and R. Ladenburg, Phys. Rev. 61, 129 (1942).
[3] T. Wakatuki and S. Kikuchi, Proc. Phys. Math. Soc. Japan 21, 656 (1939).

PHYSICAL REVIEW VOLUME 70, NUMBERS 9 AND 10 NOVEMBER 1 AND 15, 1946

Resonance Reactions

EUGENE P. WIGNER
Princeton University, Princeton, New Jersey

(Received August 1, 1946)

The considerations of a previous note are extended to include the possibility of several resonance levels. It is shown, in the case of resonance scattering, that R, which is the tangent of the phase shift divided by the wave number, is the sum of the reciprocals of linear functions of the energy (Eq. (12)), each term corresponding to one resonance level. All the coefficients in this expression for R are real, energy independent constants. As a result, it appears most natural to write the cross section (Eq. (12a)) as the square of a ratio of two expressions which are themselves fractional expressions of the energy. It is possible to write the cross section also as the square of a single fractional expression of the energy (Eq. (13)). However, the coefficients of the fractional expression are then slowly varying functions of the energy and are not real but subject to other, more involved limitations. The results are quite similar if, in addition to scattering, a reaction is possible also. The cross sections can be represented, most naturally, by means of the squares of the elements of a matrix (Eq. (33)). However, this matrix is the quotient of two matrices which involve the matrix $\Re$ and only $\Re$ is a simple function (Eq. (33a)) of the energy. The cross sections can be evaluated in a simple closed form only if either there is only one pair of reaction products possible (in addition to the reacting pair) (Eqs. (35), (35a)), or if there are only two resonances present. It is shown, however, that the cross sections can be represented also in the usual form (Eq. (42)) but the "constants" of this form are not strictly independent of energy and not real any more but subject to more involved restrictions. It turns out that the cross section becomes zero between consecutive resonances if only elastic scattering is possible. The elastic scattering cross section does not become zero in general for any value of the energy if a nuclear reaction or inelastic scattering is also possible. If the collision can yield, instead of the colliding pair of particles, only another pair, the cross section for the production of this pair will become zero between successive resonances if the product of certain real quantities has the same sign for both resonances. If the collision may result in any of three or more pairs of particles (e.g., $H^2+H^2 \rightarrow H^1+H^3$, or He^3+neutron, or $He^4+\gamma$) no cross section will vanish, in general, for any value of the energy. The considerations of the present paper are restricted to the case in which the relative angular momenta of the reaction products as well as of the reacting particles vanishes.

INTRODUCTION

IT was attempted, in a previous article,[1] to give a derivation of the resonance formula using a minimum of arbitrary assumptions. It was found useful to consider the wave function in that part of the configuration space in which all particles of the two colliding nuclei are close together. This part of the wave function may be called internal wave function. A reasonable generalization of the usual resonance formulae could be obtained by assuming that the internal wave function is, within the resonance region, in first approximation independent of energy and also the same, no matter whether the system was formed by the collision of the two particles appearing on the left side or of the two particles appearing on the right side of the equation describing the nuclear reaction (thus, e.g., that the internal wave function is the same no matter whether the compound state is obtained by the collision of Li^6 with H^2, or of Li^7 with H^1 or of He^4 with He^4). On the basis of this assumption, which is supposed to be valid in the first approximation, the second approximation could be calculated and gave the formulae for scattering and collision cross sections in question. An *a posteriori* justification of the procedure could be obtained by estimating the third approximation. This was found not to affect the results obtained in the second approximation to any appreciable extent if the constants appearing in the second approximation have values similar to those which seem to be, on the present experimental evidence, the usual ones and if the inaccuracy of the wave function in the inside of the internal region is not much greater than on the surface of it. This last assumption restricts the validity of the formulae obtained to a region which is limited by the resonance levels nearest to the one considered.

The present note will deal with the case of several resonance levels with a view, in particular, to obtaining the behavior of the cross sections, etc. in the region between two resonance

[1] E. P. Wigner, Phys. Rev. **70**, 15, 1946. This paper will be referred to as "previous note."

energies.[2] The greater generality of the conditions, from the physical point of view, will be reflected, mathematically, in the assumption that the internal wave function is, in the first approximation, a linear combination, with energy dependent coefficients, of several energy independent wave functions, corresponding to the several resonance levels which play a role. In order to simplify the analysis, it will be further assumed that there are energy values, the so-called resonance levels, for which the phase shift is just π, i.e., for which the outgoing wave has just opposite sign to what would be the outgoing wave if there was no nuclear interaction present between the colliding particles. This assumption will be formulated more sharply later for the case in which the compound state can be obtained from more than one pair of nuclear particles, i.e., for the case in which a nuclear reaction is possible. This assumption was not made in the note referred to above and inasmuch as the final formulae show the existence of an energy value as postulated here, the assumption has been proved in the case of a single resonance level.

RESONANCE SCATTERING

We now proceed with the consideration of the case in which the compound nucleus can disintegrate only in one way which is then the same way in which it was formed. No reaction can take place in this case and the only phenomenon which occurs is that of scattering. We shall assume that the relative angular momentum of the colliding particles is zero. The wave function in the peripheral region of the configuration space (outside the internal region) is then

$$\varphi_1=(4\pi)^{-\frac{1}{2}}r^{-1}u_1^{-1}[\exp(-ik_1r) - U_1\exp(ik_1r)]\psi(i). \quad (1)$$

The same convention is being used here as before: φ_1 is the wave function of the stationary state with energy E_1 and unit flux of the incoming wave, k_1 is the wave vector $v_1=u_1^2=\hbar k_1/M$ the relative velocity of the particles for energy E_1. The $\psi(i)$ is the normalized, real wave function of the internal coordinates of the colliding particles, r is their distance. U_1 is the quantity to be determined; it gives by the equation $U_1=\exp(2i\delta_1)$ the phase shift and hence the scattering cross section at energy E_1. Equation (1) is valid in the peripheral region, i.e., if $r>a$. In the internal region, we define

$$\varphi_1=\Psi_1 \quad (r<a). \quad (2)$$

Integration of the equation $\varphi_2^*H\varphi_1-\varphi_1(H\varphi_2)^*=(E_1-E_2)\varphi_1\varphi_2^*$ (where H is the Hamilton operator) over the internal region gives by means of Green's theorem

$$-\frac{\hbar^2ik_1}{2Mu_1u_2}(\exp(ik_2a)-U_2^*\exp(-ik_2a))(-\exp(-ik_1a)-U_1\exp(ik_1a))$$

$$+\frac{\hbar^2ik_2}{2Mu_1u_2}(\exp(ik_2a)+U_2^*\exp(-ik_2a))(\exp(-ik_1a)-U_1\exp(ik_1a))=(E_1-E_2)\int\Psi_2^*\Psi_1. \quad (3)$$

The last integral, as all integrals of Ψ, has to be extended over the internal region. It was pointed out in the previous note that (3) can be derived also by considering the material balance in the internal region for the wave function

$$\varphi_1\exp(-iE_1t/\hbar)+\varphi_2\exp(-iE_2t/\hbar),$$

which is a non-stationary solution of Schrodinger's equation.

One can eliminate the exponentials from (3) by the substitution

$$\bar{U}=Ue^{2ika}; \quad \bar{\Psi}=\Psi e^{ika}, \quad (4)$$

after which (3) becomes

$$k_1(1-\bar{U}_2^*)(1+\bar{U}_1)+k_2(1+\bar{U}_2^*)(1-\bar{U}_1) = -2iMu_1u_2(E_1-E_2)\hbar^{-2}\int\Psi_2^*\Psi_1. \quad (5)$$

This is quite analogous to Eq. (8) of the preceding note.[1] The reality condition is obtained by noting that the conjugate imaginary of (1) and

[2] P. L. Kapur and R. Peierls, Proc. Roy. Soc. **A166**, 277 (1938); H. A. Bethe and G. Placzek, Phys. Rev. **51**, 450 (1937); F. Kalckar, J. R. Oppenheimer, and R. Serber, Phys. Rev. **52**, 273 (1937); H. A. Bethe, Rev. Mod. Phys. **9**, 71 (1937) (pages 101–117); G. Breit, Phys. Rev. **58**, 1068 (1940); **69**, 472 (1946).

(2) must be, apart from a constant, identical with (1) and (2). The constant is easily seen to be $-U_1^*$. This gives

$$U_1^* U_1 = |U_1|^2 = 1; \quad \Psi_1^* = -U_1^* \Psi_1. \tag{6}$$

Both equations are valid, of course, not only for the quantities with the index 1 but for any other index, corresponding to any other value of the energy, as well. The first shows that, in a stationary state, the intensities of incoming and outgoing waves are equal. Both equations hold equally for the unbarred quantities for which they are written and for the barred quantities of (4).

It was assumed in the previous note that all $\Psi_1, \Psi_2, \cdots$, etc. are multiples of one definite Ψ. This assumption will be generalized now to the assumption that the Ψ are linear combinations, with energy dependent coefficients, of a set of energy independent functions. Evidently, there is a certain arbitrariness in the choice of these functions. It will be assumed that these functions $\Psi_\lambda, \Psi_\mu, \cdots$, etc., are the internal wave functions for energy the values $E_\lambda, E_\mu, \cdots$ for which U becomes -1, i.e., for the various centers of resonance levels. We have, hence,

$$\Psi_1 = \alpha_{1\lambda}\Psi_\lambda + \alpha_{1\mu}\Psi_\mu + \cdots; \tag{7}$$

$$U_\lambda = U_\mu = \cdots = -1; \quad \alpha_{\lambda\mu} = \delta_{\lambda\mu}. \tag{7a}$$

Because of (7a) and (6), the Ψ_λ are real. The assumptions embodied in (7), (7a) do not follow from simple physical postulates. A comparison with the results of the previous note will show, however, that they are reasonable generalizations of the results obtained there. It is also believed that they could be derived, by a little more algebra, in a way similar to that given there, from the same postulates, and that they could be verified afterwards in an entirely similar fashion to that used there.

Applying (5) for $E_1 = E_\lambda$, $E_2 = E_\mu$ and neglecting the difference between barred and unbarred quantities, the left side of (5) vanishes because of (7a) and one has

$$\int \Psi_\mu^* \Psi_\lambda = \delta_{\mu\lambda} c_\lambda, \tag{8}$$

i.e., that the internal wave functions of the various resonance levels are orthogonal. It then follows that, in general,

$$\int \Psi_2^* \Psi_1 = \alpha_{2\lambda}^* \alpha_{1\lambda} c_\lambda + \alpha_{2\mu}^* \alpha_{1\mu} c_\mu + \cdots. \tag{9}$$

Applying now (5) for $E_2 = E_\lambda$ gives

$$2k_1(1+U_1) = -2iMu_\lambda u_1 (E_1 - E_\lambda)\hbar^{-2}\alpha_{1\lambda} c_\lambda$$

or

$$\alpha_{1\lambda} = i\hbar^2 k_1 (1+U_1)/Mu_\lambda u_1 (E_1 - E_\lambda) c_\lambda. \tag{10}$$

Similar equations hold, of course, for $\alpha_{1\mu}$, etc. so that all the α are determined by (10) in terms of the U.

Dividing now (5) by $k_1 k_2 (1+U_1)(1+U_2^*)$ gives because of (9) and (10)

$$\frac{1}{k_2}\frac{1-U_2^*}{1+U_2^*} + \frac{1}{k_1}\frac{1-U_1}{1+U_1} = -\frac{2i\hbar^2(E_1-E_2)}{M}\left\{\frac{1}{v_\lambda c_\lambda (E_1-E_\lambda)(E_2-E_\lambda)} + \frac{1}{v_\mu c_\mu (E_1-E_\mu)(E_2-E_\mu)} + \cdots\right\}$$

$$= 2i\hbar\left\{\frac{1}{k_\lambda c_\lambda}\left(\frac{1}{E_1-E_\lambda} - \frac{1}{E_2-E_\lambda}\right) + \frac{1}{k_\mu c_\mu}\left(\frac{1}{E_1-E_\mu} - \frac{1}{E_2-E_\mu}\right) + \cdots\right\}. \tag{11}$$

It then follows that the R_1 defined by (12) becomes

$$\frac{i}{k_1}\frac{1-U_1}{1+U_1} = R_1$$

$$= \frac{2\hbar}{k_\lambda c_\lambda (E_\lambda - E_1)} + \frac{2\hbar}{k_\mu c_\mu (E_\mu - E_1)} + \cdots + R_\infty, \tag{12}$$

where R_∞ is independent of energy. The real quantities R defined in (12) are $M/\hbar$ times the quantities S defined in the previous note; (12) itself is the generalization of (14a) given there. The c_λ, c_μ, etc., are, because of (8), all positive real quantities, they correspond to $(2/b)^2$ of the previous note. The notation R has been chosen for the quantity appearing in (12) because it has the dimension of a length and because its square is closely related by (13) to the scattering cross section. However, both R and also the

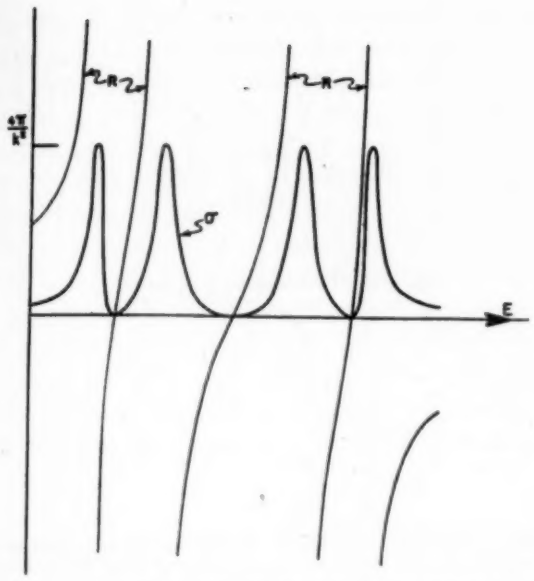

FIG. 1. Resonance scattering. R, i.e., tangent of phase shift divided by the wave number, in arbitrary units and scattering cross section σ in units of maximum possible cross section $4\pi/k^2$ (schematic).

constant R_∞ can be negative as well as positive. From $U=e^{2i\delta}$ and the formula for the cross section in terms of the phase shift δ one obtains for the scattering cross section

$$\sigma(E)=\frac{4\pi}{k^2}\sin^2\delta=\frac{4\pi R^2}{1+k^2R^2}. \tag{12a}$$

This shows that the cross section is $4\pi R^2$ as long as $kR\ll 1$. It assumes its maximum possible value of $4\pi/k^2$ if $R=\infty$.

Figure 1 shows the general trend of R as function of energy and also σ as function of energy. It shows, in the instance represented, the familiar pattern of sharp lines. As long as the lines are as well separated as in Fig. 1, the width of the line at E_λ from half-maximum to half-maximum is given by

$$\Gamma_\lambda=4\hbar/c_\lambda. \tag{12b}$$

Equation (12a) can also be written in the form

$$\sigma(E)=4\pi|S|^2;\quad S=R/(1-ikR). \tag{13}$$

S is the quotient of two rational functions of E, i.e., itself a rational function. Since the degree of its numerator is not higher than the degree of its denominator, it can be written in the form

$$S=S_0+\sum_\nu \frac{s_\nu}{F_\nu-E}. \tag{13a}$$

The sum of (13a) contains as many terms as are resonance levels, i.e., as there are terms in the sum of (12). If R_∞ of (12) vanishes, S_0 will vanish also. Although (13), (13a) are, mathematically, completely equivalent to (12) and (12a) and although they give a simpler expression for the cross section than (12) and (12a) do, the latter seem to me preferable for three reasons. First, the symbols s and F which occur in (13a) are in general complex while those in (12) are all real. Second, there are no restrictions on the constants E_λ, c_λ, except that they are real and the latter ones positive. The s_ν and F_ν of (13c) satisfy complicated equations (not to be given here) which express the fact that $R=S(1+ikS)^{-1}$ is real. Finally, the E_λ, c_λ are strictly independent of energy while s_ν and F_ν depend on the energy through k. They are, of course, slowly varying functions of the energy and their energy dependence is really significant only for very low k, e.g., for neutrons near the thermal region.

A rather good approximation for S is given by

$$S_{\text{appr}}=\sum_\lambda \frac{\frac{1}{2}k\Gamma_\lambda/k_\lambda}{E_\lambda-\frac{1}{2}ik\Gamma_\lambda/k_\lambda-E}, \tag{14}$$

which is an expression often given in the literature.[3] Equation (14) is accurate as long as the energy E is not in the neighborhood of more than one resonance level E_λ, neighborhood meaning a distance of the order Γ_λ. It is always accurate if the energy actually coincides with one of the resonance levels and a good approximation for all E if the resonance levels are all distinct, i.e., their distance is greater than their width. As a result, (14) is, under ordinary conditions, a very good approximation for every E. One

[3] Cf. e.g., H. A. Bethe and G. Placzek, reference 2. The development leading to (13), (13a) is very similar to sections 4 and 5 of G. Breit's last paper (cf. reference 2). Breit already pointed out the limitations of this representation of the resonance formula as they manifest themselves in his model. In particular, he noted that although, in first approximation, the absolute value of our ks_ν is oppositely equal to the imaginary part of F_ν (cf. (14)), this does not hold rigorously and that, in general, the absolute value of ks_ν is greater than the imaginary part of F_ν. This is an inequality which follows from the equations to which the s_ν and F_ν are subject.

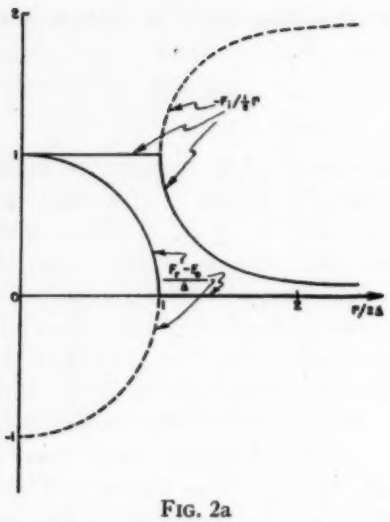

FIG. 2a

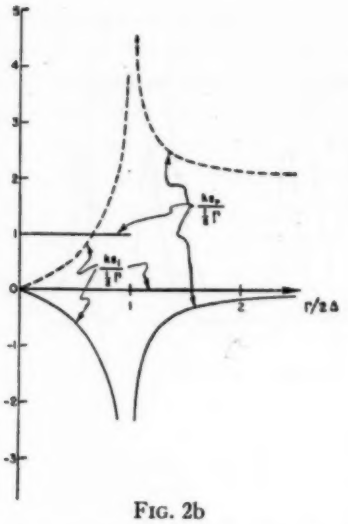

FIG. 2b

FIG. 2. Relation between two descriptions of resonance scattering. Two resonances at $E_0-\Delta$ and $E_0+\Delta$, each of width Γ, give apparent resonances at F. The real parts F_r of the two F are given in Fig. 2a in units of Δ (one of them by a broken line), the negative imaginary parts in units of $\frac{1}{2}\Gamma$. The real parts of the two F are the same for $\Gamma>2\Delta$, the imaginary parts for $\Gamma<2\Delta$. Figure 2b gives the real and imaginary parts s_r and s_i of the strengths of the two apparent resonances in units $\frac{1}{2}\Gamma$.

sees this also by calculating

$$S-S_{\text{appr}}=(1-ikR)^{-1}\times\sum_{\lambda\neq\mu}\frac{\frac{1}{2}k\Gamma_\lambda/k_\lambda}{E_\lambda-\frac{1}{2}ik\Gamma_\lambda/k_\lambda-E}\,\frac{\frac{1}{2}k\Gamma_\mu/k_\mu}{E_\mu-E}. \quad (14a)$$

Because of the $\lambda\neq\mu$ condition, one of the factors after the summation sign is always small if all the resonances are distinct. The second factor can become very large if $E=E_\mu$ but is, in this case, compensated by the factor before the summation sign. In spite of all this, (14) can become grossly inaccurate, e.g., between two levels the width of which is comparable with their distance. In this case (13) with S_{appr} substituted for S can even become larger than the maximum possible width $4\pi/k^2$. The reason is, of course, that the approximate values of s_r and F_r (i.e., $\frac{1}{2}k\Gamma_r/k_r$ and $E_r-\frac{1}{2}ik\Gamma_r/k_r$) which were adopted in (14) do not satisfy the conditions to which the actual s_r and F_r are subject.

Figures 2a and 2b illustrate the behavior of the quantities s_r and F_r in the particularly simple case of only two resonance levels. These are assumed to be at $E_0-\Delta$ and $E_0+\Delta$ and to have both the same width Γ. The energy E_0 is supposed to be so high as compared with Δ or Γ that the variation of k with energy can be neglected. Figure 2a gives the real part and the negative imaginary part of the two $F-E_0$, in units of Δ and $\frac{1}{2}\Gamma$, respectively, both as function of $\Gamma/2\Delta$. The former is ±1 in the approximation in which (14) is valid, the latter 1. One sees that the imaginary part of both F is indeed $-\frac{1}{2}\Gamma$ as long as $\Gamma<2\Delta$ but that this does not hold if $\Gamma>2\Delta$. In the latter case, both F are purely imaginary, the real parts of both having gone to zero as Γ approached Δ. The s are shown in Fig. 2b.They are complex for $\Gamma<2\Delta$ but real for $\Gamma>2\Delta$. The absolute value of ks is always greater than the imaginary part of the corresponding F, a fact which has been recognized already by Breit.[3] It is worth while to note that, in spite of this, the absolute value of kS never exceeds 1. Inasmuch as we believe that the Γ and E_λ are the physically significant quantities, these figures illustrate the somewhat artificial nature of the representation (13), (13a).

RESONANCE REACTIONS

The treatment of the case in which, in addition to elastic scattering a real nuclear reaction (or, at least, inelastic scattering) is possible, differs from the above one in that the peripheral wave function has, instead of (1), the form

$$\varphi_{1j}=\sum_l(4\pi)^{-\frac{1}{2}}r_l^{-1}u_{1l}^{-1}[\delta_{jl}\exp(-ik_{1l}r_l)-U_{1jl}\exp(ik_{1l}r_l)]\psi(i_l). \quad (15)$$

In this as in the following formulae, the indices j, l, $\cdots$ etc. denote pairs of nuclei which can react with each other or appear as products of the reaction. The $\psi(i_l)$ is the product of the real normalized wave functions of the pair l. (E.g., j can denote the pair Li^6+H^2; l the pair Li^7+H^1; m the pair He^4+He^4 etc.) The r_l is the relative distance of the nuclei forming the pair l, the relative velocity of this pair for the energy value E_1 of the total system is denoted by $v_{1l}=u_{1l}^2=\hbar k_{1l}/M_l$, the M_l being the relative mass of the pair l. In (15), because of the δ_{jl}, only nuclei of the pair j approach each other; the U_{1jl} are the elements of the collision matrix. The square $|U_{1jl}|^2$ gives the number of pairs l formed if one pair of the kind j collides.

Equation (15) is valid in the peripheral region. In the internal region, i.e., in the part of the configuration space in which all particles are close together, we have instead of (2)

$$\varphi_{1j}=\Psi_{1j}. \tag{15a}$$

In order to calculate the second approximation we need an equation analogous to (3). This can be obtained again by integration of the equation

$$\varphi_{2j}^*H\varphi_{1l}-\varphi_{1l}(H\varphi_{2j})^*=(E_1-E_2)\varphi_{1l}\varphi_{2j}^*$$

over the internal region. This yields by Green's theorem

$$-\sum_m \frac{\hbar^2 ik_{1m}}{2M_m u_{1m}u_{2m}}[\delta_{jm}\exp(ik_{2m}a)-U_{2jm}^*\exp(-ik_{2m}a)][-\delta_{lm}\exp(-ik_{1m}a)-U_{1lm}\exp(ik_{1m}a)]$$

$$+\sum_m \frac{\hbar^2 ik_{2m}}{2M_m u_{1m}u_{2m}}[\delta_{jm}\exp(ik_{2m}a)+U_{2jm}^*\exp(-ik_{2m}a)][\delta_{lm}\exp(-ik_{1m}a)-U_{1lm}\exp(ik_{1m}a)]$$

$$=(E_1-E_2)\int \Psi_{2j}^*\Psi_{1l}. \tag{16}$$

In order to eliminate the exponentials, one can again introduce barred quantities

$$\bar{\Psi}_l=\Psi_l\exp(ik_la);\quad \bar{U}_{lm}=U_{lm}\exp[i(k_m+k_l)a]. \tag{17}$$

With this substitution, and after multiplication with $\exp[i(k_{1l}-k_{2j})a]$, (16) goes over into

$$ih\sum_m(\delta_{lm}+\bar{U}_{1lm})u_{1m}u_{2m}^{-1}(\delta_{jm}-\bar{U}_{2jm}^*)+ih\sum_m(\delta_{lm}-\bar{U}_{1lm})u_{1m}^{-1}u_{2m}(\delta_{jm}+\bar{U}_{2jm}^*)$$

$$=2(E_1-E_2)\int \bar{\Psi}_{2j}^*\bar{\Psi}_{1l}. \tag{18}$$

This is analogous to Eq. (22) of the previous note. The bars will be left off again forthwith.

We shall now make the assumption mentioned at the end of the Introduction more precise. It will be assumed that there are "resonance energies" E_λ, E_μ, $\cdots$, etc. for which the matrices $\mathfrak{U}_\lambda=\|U_{\lambda lm}\|$ have a characteristic value -1. The corresponding normalized characteristic vectors will be denoted by $\mathfrak{B}_\lambda$ with components $\beta_{\lambda m}$ so that $\mathfrak{U}_\lambda\mathfrak{B}_\lambda=-\mathfrak{B}_\lambda$, or, more in detail,

$$\sum_m U_{\lambda lm}\beta_{\lambda m}=-\beta_{\lambda l}. \tag{19}$$

This amounts to the assumption that, at the resonance energies, there are superpositions of incident waves

$$\sum_l \beta_{\lambda l}(4\pi)^{-\frac{1}{2}}r_l^{-1}u_{\lambda l}^{-1}\exp(-ik_{\lambda l}r_l)\psi(i_l), \tag{20a}$$

for which the outgoing wave has, apart from the sign, the same value which it would have if there was no nuclear reaction or scattering, but that the sign of the outgoing wave is opposite. This means that the outgoing wave for the superposition of incoming waves given by (20a) is

$$\sum_l \beta_{\lambda l}(4\pi)^{-\frac{1}{2}}r_l^{-1}u_{\lambda l}^{-1}\exp(ik_{\lambda l}r_l)\psi(i_l). \tag{20b}$$

The internal wave function for the incoming wave (20a) (and the outgoing wave (20b)) will be denoted by Ψ_λ and it will further be assumed that these are the Ψ_λ, Ψ_μ, $\cdots$ which permit one to express, in first approximation, the internal wave functions linearly for all energies and all incident waves:

$$\Psi_{1j}=\alpha_{1\lambda}{}^j\Psi_\lambda+\alpha_{1\mu}{}^j\Psi_\mu+\cdots. \tag{21}$$

The coefficients α depend both on the energy (E_1 in (21)) and also on the pair of particles (j in (21)) the collision of which is represented by the wave function Ψ_{1j} of (15a). The fact that the internal wave function is Ψ_λ for energy E_λ if the incoming wave is given by (20a) means that

$$\Psi_\lambda = \sum_j \beta_{\lambda j}\Psi_{\lambda j} = \sum_j \beta_{\lambda j}(\alpha_{\lambda\lambda}{}^j\Psi_\lambda + \alpha_{\lambda\mu}{}^j\Psi_\mu + \cdots). \quad (22)$$

This is equivalent with

$$\sum_j \beta_{\lambda j}\alpha_{\lambda\mu}{}^j = \delta_{\lambda\mu}, \quad (23)$$

which is the analogon of the second equation of (7a). Since the $\Psi_\lambda, \Psi_\mu, \cdots$, etc. can be considered as solutions of the same characteristic value problem with the same homogeneous boundary conditions embodied in (20a), (20b), they are mutually orthogonal

$$\int \Psi_\mu{}^*\Psi_\lambda = \delta_{\mu\lambda}c_\lambda; \quad c_\lambda = c_\lambda{}^* > 0, \quad (24)$$

which is the analogon of (8). Equation (24) follows also from the more general equation (18) if one inserts λ for 1, μ for 2 and multiplies it with $\beta_{\lambda l}\beta_{\mu j}{}^*$, sums over l and j and considers (19), the symmetric nature of $\mathfrak{U}$ and the first part of (22).

No assumption analogous to the one contained in (21) was made in the previous note and it is, in fact, believed that this assumption follows from the other more general assumptions made in the Introduction. This was explicitly demonstrated in the previous note for the case of a single resonance level: the energy E_λ was denoted there by E_0 (there was only one E_λ), the corresponding vector $\mathfrak{b}_\lambda$ was denoted there by $\mathfrak{u}_0\mathfrak{b}$ (with components $u_{0l}\beta_l$), and all internal wave functions were the same apart from constant factors. The existence of both the E_0 and the vector $\mathfrak{b}$ was derived there while it is assumed here because it simplifies the analysis to such a great extent.

Since (20b) is the conjugate complex of (20a), (the vector $\mathfrak{b}$ will be shown in (26) to be real) the peripheral wave function is real and the same must hold then for Ψ_λ. This also follows from the more general equations which are the generalizations of (6).

$$\sum_l U_{1jl}{}^*U_{11m} = \delta_{jm}; \quad -\sum_l U_{1jl}{}^*\Psi_{1l} = \Psi_{1j}{}^*. \quad (25)$$

One can easily convince oneself that (25) holds both for the unbarred and also for the barred quantities defined in (17). The first equation of (25) reads, in matrix notation $\mathfrak{U}_1{}^*\mathfrak{U}_1 = 1$ and is, because of the unitary nature of $\mathfrak{U}$, equivalent with the statement that $\mathfrak{U}$ is symmetric. Both (25) and (16) or (18) are rigorous, i.e., do not involve any approximations. However, (21) has only approximate validity.

Introducing now (21) into (18), the right side of this goes over into

$$2(E_1 - E_2)\sum_\lambda \alpha_{2\lambda}{}^{j*}\alpha_{1\lambda}{}^l c_\lambda. \quad (18')$$

We can define the matrix product of two vectors $\mathbf{x}$ and $\mathbf{y}$ as the matrix $\mathbf{x}\times\mathbf{y}$ the j, l element of which is $(\mathbf{x}\times\mathbf{y})_{jl} = x_j y_l$; (18) then becomes in the matrix-vector notation which has been used also in the previous note

$$ih(1+\mathfrak{U}_1)\mathfrak{u}_1\mathfrak{u}_2{}^{-1}(1-\mathfrak{U}_2{}^\dagger) + ih(1-\mathfrak{U}_1)\mathfrak{u}_1{}^{-1}\mathfrak{u}_2(1+\mathfrak{U}_2{}^\dagger) = 2(E_1-E_2)\sum_\lambda c_\lambda(\boldsymbol{\alpha}_{1\lambda}\times\boldsymbol{\alpha}_{2\lambda}{}^*). \quad (18a)$$

All matrices (and vectors) have as many dimensions as there are ways of disintegration for the compound state, the indices 1, 2 give the energy values E_1, E_2 to which the quantities refer, $\mathfrak{u}_1$, $\mathfrak{u}_2$ are diagonal matrices with diagonal elements u_{1l}, u_{2l}, respectively, $\boldsymbol{\alpha}_{1\lambda}$ is a vector with components $\alpha_{1\lambda}{}^l$, etc. Equation (19) then becomes

$$\mathfrak{U}_\lambda\mathfrak{b}_\lambda = -\mathfrak{b}_\lambda, \quad (19a)$$

while (23) goes over into

$$\mathfrak{b}_\lambda\cdot\boldsymbol{\alpha}_{\lambda\mu} = \delta_{\lambda\mu}. \quad (23a)$$

It may be worth while to remark that because of (19a) and the symmetric nature of $\mathfrak{U}_\lambda$, the vectors $\mathfrak{b}_\lambda$ can be chosen to be real and that they can be assumed to be normalized

$$\mathfrak{b}_\lambda = \mathfrak{b}_\lambda{}^*; \quad \mathfrak{b}_\lambda\cdot\mathfrak{b}_\lambda = \sum_l \beta_{\lambda l}{}^2 = 1. \quad (26)$$

One can substitute E_μ for E_2 in (18a) and apply it to the vector $\mathfrak{b}_\mu{}^*$, i.e., substitute E_μ for E_2 in (18), multiply it with $\beta_{\mu j}{}^*$, and sum over j. Because of the symmetry of $\mathfrak{U}_\mu$ and (19), the second term on the left side drops out, the first

simplifies considerably and one has

$$2i\hbar(1+\mathfrak{U}_1)\mathfrak{u}_1\mathfrak{u}_\mu^{-1}\mathfrak{\beta}_\mu^* = 2(E_1-E_\mu)\sum_\lambda c_\lambda(\mathfrak{\alpha}_{1\lambda}\times\mathfrak{\alpha}_{\mu\lambda}^*)\mathfrak{\beta}_\mu^* = 2(E_1-E_\mu)c_\mu\mathfrak{\alpha}_{1\mu}. \quad (27)$$

The last part follows from (23) or (23a) and the general equation

$$(\mathbf{x}\times\mathbf{y})\mathbf{z} = (\mathbf{y}\cdot\mathbf{z})\mathbf{x}. \quad (\mathrm{I})$$

From (27), the vector $\mathfrak{\alpha}_{1\mu}$ becomes

$$\mathfrak{\alpha}_{1\mu} = \frac{i\hbar}{c_\mu(E_1-E_\mu)}(1+\mathfrak{U}_1)\mathfrak{u}_1\mathfrak{u}_\mu^{-1}\mathfrak{\beta}_\mu. \quad (27a)$$

As was pointed out before, $\mathfrak{\beta}_\mu$ can be assumed to be real. Inserting (27a) into (18a) one obtains for the right side of the latter

$$\sum_\lambda \frac{2(E_1-E_2)\hbar^2}{c_\lambda(E_1-E_\lambda)(E_2-E_\lambda)}(1+\mathfrak{U}_1)\mathfrak{u}_1 \times(\mathfrak{u}_\lambda^{-1}\mathfrak{\beta}_\lambda\times\mathfrak{u}_\lambda^{-1}\mathfrak{\beta}_\lambda)\mathfrak{u}_2(1+\mathfrak{U}_2^\dagger) \quad (28)$$

because of the general equation

$$(\mathfrak{a}\mathbf{x}\times\mathfrak{b}\mathbf{y}) = \mathfrak{a}(\mathbf{x}\times\mathbf{y})\mathfrak{b}' \quad (\mathrm{II})$$

valid for all matrices $\mathfrak{a}$, $\mathfrak{b}$ ($\mathfrak{b}'$ being the transposed of $\mathfrak{b}$) and all vectors $\mathbf{x}$, $\mathbf{y}$. Thus (18a) becomes after multiplication with $\mathfrak{u}_1^{-1}(1+\mathfrak{U}_1)^{-1}$ from the left, $(1+\mathfrak{U}_2^\dagger)^{-1}\mathfrak{u}_2^{-1}$ from the right and division by $i\hbar$

$$\mathfrak{u}_2^{-1}(1-\mathfrak{U}_2^\dagger)(1+\mathfrak{U}_2^\dagger)^{-1}\mathfrak{u}_2^{-1}+\mathfrak{u}_1^{-1}(1+\mathfrak{U}_1)^{-1}(1-\mathfrak{U}_1)\mathfrak{u}_1^{-1} - \sum_\lambda\left[\frac{2i\hbar}{c_\lambda(E_1-E_\lambda)}-\frac{2i\hbar}{c_\lambda(E_2-E_\lambda)}\right]\mathfrak{u}_\lambda^{-1}(\mathfrak{\beta}_\lambda\times\mathfrak{\beta}_\lambda)\mathfrak{u}_\lambda^{-1}=0. \quad (29)$$

It then follows that the terms which depend on E_1 (and similarly the terms which depend on E_2) give an energy independent matrix. One can clearly replace in (29) all the diagonal matrices $\mathfrak{u}^{-1}=\mathfrak{v}^{-1}$ by the diagonal matrices $\mathfrak{q}^{-1}=\mathfrak{k}^{-1}$ and obtain for the matrix $\mathfrak{R}_1$

$$\mathfrak{R}_1 = i\mathfrak{q}_1^{-1}(1+\mathfrak{U}_1)^{-1}(1-\mathfrak{U}_1)\mathfrak{q}_1^{-1} = \mathfrak{R}_\infty+\sum_\lambda\frac{2\hbar}{c_\lambda(E_\lambda-E_1)}\mathfrak{q}_\lambda^{-1}(\mathfrak{\beta}_\lambda\times\mathfrak{\beta}_\lambda)\mathfrak{q}_\lambda^{-1}. \quad (30)$$

This is the analogon of the final result (12) for scattering and represents the general solution of our problem just as (36), (36a) of the previous note represented the general solution in the case of a single resonance level. $\mathfrak{R}_\infty$ is an arbitrary real symmetric matrix, the E_λ are arbitrary real energy values, the c_λ are positive real numbers the $\mathfrak{\beta}_\lambda$ real vectors and they can be assumed to be normalized, or, if not, $c_\lambda=1$ can be assumed.

The matrix $\mathfrak{U}_1-1$ can be expressed in terms of $\mathfrak{R}_1$ as

$$\mathfrak{U}_1-1 = 2i\mathfrak{q}_1\mathfrak{R}_1\mathfrak{q}_1/(1-i\mathfrak{q}_1\mathfrak{R}_1\mathfrak{q}_1) \quad (31)$$

and the cross section for the transformation of pair j into pair l is

$$\sigma_{jl}(E_1) = \frac{\pi}{k_{1j}^2}|(\mathfrak{U}_1-1)_{jl}|^2 = \frac{4\pi}{k_{1j}^2}\left|\left(\frac{\mathfrak{q}_1\mathfrak{R}_1\mathfrak{q}_1}{1-i\mathfrak{q}_1\mathfrak{R}_1\mathfrak{q}_1}\right)_{jl}\right|^2. \quad (31a)$$

Although both this expression and that for $\mathfrak{R}_1$ (30) is quite simple, it does not seem possible to express in general the $\sigma_{jl}(E)$ in closed form in terms of the E, k_j, k_l, the energy independent quantities E_λ, $\mathfrak{\beta}_\lambda$, c_λ, and $\mathfrak{R}_\infty$.

HIGHER SPINS

It is easy to generalize (30), (31a) for the case that the nuclei of the pair j, say, have spins j and j', i.e., angular momenta jh and $j'h$, respectively. If our assumption remains valid, that only those states need to be taken into account in which the angular momentum of the motion of the pair around their common center of mass vanishes, one can consider the collision system formed by the pair j as a mixture of states for which the total angular momentum has one of the values

$$J = |j-j'|,\ |j-j'|+1,\ \cdots,\ j+j'-1,\ j+j'. \quad (32)$$

This total angular momentum consists of the vector sum of the spins of the particles making up the pair j since, according to assumption, the relative motion of the particles has no angular momentum. From the wave functions with a definite J only such compound states Ψ can be reached which have the same J. As a consequence, one must consider as many sets of resonance levels as are J in (32) and define for each set an $\mathfrak{R}^J$ according to (30) in which, then, the summation is to be extended only over the compound states with spin J. The total cross section then becomes the weighted sum of expressions (31a), corresponding to the components of the mixture (32)

$$\sigma_{jl}(E)=\frac{4\pi k_l}{k_j}\sum_{J=|j-j'|}^{j+j'} g_J\left|\left(\frac{\mathfrak{R}^J}{1-i\mathfrak{q}\mathfrak{R}^J\mathfrak{q}}\right)_{jl}\right|^2,$$
$$g_J=\frac{2J+1}{(2j+1)(2j'+1)}. \tag{33}$$

The k_j, $\mathfrak{q}$, $\mathfrak{R}^J$ all refer[4] to the energy E in (33). It is, probably, unnecessary to remark that (30) can be written in a somewhat simpler form

$$\mathfrak{R}^J(E)=\mathfrak{R}_\infty{}^J+\sum_\lambda{}^J\frac{\gamma_\lambda\times\gamma_\lambda}{E_\lambda-E}, \tag{33a}$$

where the J on the summation sign indicates that the summation is to be extended only over those λ for which the angular momentum of the compound state Ψ_λ is $J\hbar$. The real vectors γ_λ are, as are the β_λ and the $\mathfrak{R}_\infty{}^J$, independent of energy

$$\gamma_\lambda=(2\hbar/c_\lambda)^{\frac{1}{2}}\mathfrak{q}_\lambda{}^{-1}\beta_\lambda,$$
$$\gamma_{\lambda j}=(2\hbar/c_\lambda)^{\frac{1}{2}}k_{\lambda j}{}^{-\frac{1}{2}}\beta_{\lambda j}. \tag{33b}$$

They are, of course, not normalized.

The $\mathfrak{R}_\infty{}^J$ of (33a) could be, off hand, arbitrary real symmetric matrices. They describe that part of the reaction or scattering which would be present even in the absence of resonance levels. It has been argued, in the previous note, that these $\mathfrak{R}_\infty$ can be considered to be diagonal matrices as long as we can speak of pure resonance reactions. Even if this should not be the case, two remarks will be applicable to the matrix elements $R_{\infty jl}$. First, since they correspond to non-resonance reactions, their order of magnitude will not be greater than the nuclear radius. As a result, their product with $q_jq_l=(k_jk_l)^{\frac{1}{2}}$ will be small compared to 1 except if the energy of both pairs j and l is quite high. Second, $R_{\infty jl}(k_jk_l)^{\frac{1}{2}}$ will be particularly small if either the pair j, or the pair l, consists of a light quantum and a nucleus. If both j and l are such pairs, the process for which $R_{\infty jl}(k_jk_l)^{\frac{1}{2}}$ is responsible is essentially a Compton effect on a nucleus or a similar straight scattering term. Even if only one pair, say j, contains a light quantum, $q_jR_{\infty jl}q_l$ will be a high order correction term which is, e.g., consistently neglected in the usual treatments of light absorption or emission. It therefore appears to be justified to neglect $R_{\infty jl}$ if either of the pairs j or l contains a light quantum.

Since every symmetric matrix can be written as a sum of matrices $(\gamma_\rho\times\gamma_\rho)$, it is possible, formally, to set the $\mathfrak{R}_\infty{}^J$ equal to zero if one admits a few terms in the sum of (33a) for which E_λ is infinite but the γ_λ also infinite in such a way that the corresponding terms give a finite contribution to (33a), replacing $\mathfrak{R}_\infty{}^J$. This is particularly tempting in the case of the (n,γ) reaction. For these reactions, all pairs l, $\cdots$, etc. contain a light quantum (in addition to the normal or excited state of the product nucleus), except one, the initial state j. Because of the remarks made before, all the matrix elements of $\mathfrak{R}_\infty{}^J$ will vanish except the jj element and $\mathfrak{R}_\infty{}^J$ can be replaced by a single term $(\gamma_\infty\times\gamma_\infty)$ with a vector γ_∞ all the components of which vanish, except the j component. Although the elimination of $\mathfrak{R}_\infty{}^J$, which has just been described, is a very formal one, it will be adopted later because it simplifies the formulae at least from a formal point of view. We shall write then

$$\mathfrak{R}^J(E)=\sum_\lambda{}^J\frac{\gamma_\lambda\times\gamma_\lambda}{E_\lambda-E}. \tag{33c}$$

However, when using (33c) we must keep in

[4] Strictly speaking, the matrix in (33) is undefined because $\mathfrak{R}$ and $q\mathfrak{R}q$ do not commute in general. A comparison with (32) shows that the proper definition is

$$\frac{\mathfrak{R}}{1-iq\mathfrak{R}q}=\mathfrak{q}^{-1}\frac{\mathfrak{q}\mathfrak{R}\mathfrak{q}}{1-i\mathfrak{q}\mathfrak{R}\mathfrak{q}}\mathfrak{q}^{-1}. \tag{33'}$$

The fraction on the right side is completely defined since it is a function of a single matrix $\mathfrak{q}\mathfrak{R}\mathfrak{q}$. The right side of (33') will be meant always when the left side is written for brevity.

mind that it has a few (or, in the case of an (n, γ) reaction, one) finite terms with $E_\lambda = \infty$.

EVALUATION OF (33)

Although the preceding formulae give, in principle, a complete solution of our problem, they are unsuited not only to practical calculations but even for obtaining a qualitative picture of the variation of the cross sections. The difficulty in using (33) (or (31a) and (30)) consists in the evaluating of the elements of the matrix $\mathfrak{q}\mathfrak{R}\mathfrak{q}(1-i\mathfrak{q}\mathfrak{R}\mathfrak{q})^{-1}$ if only the matrix elements of $\mathfrak{R}$ are given.

This difficulty can be easily overcome if there are only two states involved, i.e., if only one pair of reaction products is possible. On the whole, this is an exceptional case as even the (n, γ) reaction has several possible end products corresponding to the different excited states of the product nucleus. Examples in question may be, however, some (n, γ) reactions of light elements, and, perhaps, reactions of the kind $Li^7 + n = Be^7 + H^1$.

If there is, in addition to the original pair of nuclei, only one pair of reaction products possible, the matrix $\mathfrak{q}\mathfrak{R}\mathfrak{q}$ becomes two-dimensional and its reciprocal can be found easily. One obtains for

$$\frac{\mathfrak{q}\mathfrak{R}\mathfrak{q}}{1-i\mathfrak{q}\mathfrak{R}\mathfrak{q}} = (1-D-i(S_{jj}+S_{ll}))^{-1} \times \begin{Vmatrix} S_{jj}-iD & S_{jl} \\ S_{jl} & S_{ll}-iD \end{Vmatrix}, \quad (34)$$

in which

$$\begin{aligned} S_{jj} &= k_j\left(R_{jj\infty}+\sum_\lambda \frac{\gamma_{\lambda j}^2}{E_\lambda - E}\right), \\ S_{jl} &= (k_j k_l)^{\frac{1}{2}}\left(R_{jl\infty}+\sum_\lambda \frac{\gamma_{\lambda j}\gamma_{\lambda l}}{E_\lambda - E}\right), \\ S_{ll} &= k_l\left(R_{ll\infty}+\sum_\lambda \frac{\gamma_{\lambda l}^2}{E_\lambda - E}\right), \\ D &= S_{jj}S_{ll} - S_{jl}^2. \end{aligned} \quad (34a)$$

It is assumed that all compound states have the same J. As a result of (34), the cross section for scattering becomes

$$\sigma_{jj} = \frac{4\pi}{k_j^2}\frac{S_{jj}^2 + D}{(1-D)^2 + (S_{jj}+S_{ll})^2} \quad (35)$$

while the reaction cross section is

$$\sigma_{jl} = \frac{4\pi}{k_j^2}\frac{S_{jl}^2}{(1-D)^2 + (S_{jj}+S_{ll})^2}. \quad (35a)$$

The remarkable feature of this last expression is that it goes through zero at least between any two consecutive resonances for which $\gamma_{\lambda j}\gamma_{\lambda l}$ has the same sign since, evidently, S_{jl} goes through zero between two such points. It is similar, in this respect, to the scattering cross section of Fig. 1 which applies if no reaction is possible. However, the scattering cross section given by (35), which applies if a reaction is possible in addition to the scattering, does not exhibit this feature any more, since it can vanish only if both S_{jj} and D vanish for the same E. Even the reaction cross section does not become zero between consecutive maxima if either more than one pair of reaction products are possible or if there are compound states with more than one value of J. The former case will be investigated below. In the latter case the cross section is, according to (33), a weighted average of expressions of the form (35a). This could vanish only if the expression (35a) would vanish for the same E for every J. Such an occurrence has "zero probability."

If several pairs of reaction products are possible, the matrices $\mathfrak{R}$ and $\mathfrak{q}\mathfrak{R}\mathfrak{q}$ have more than two dimensions and the reciprocal of $1-i\mathfrak{q}\mathfrak{R}\mathfrak{q}$ becomes an involved expression. It seems worth while, in that case, to adopt the convention of (33c) to eliminate the constant matrix $\mathfrak{R}_\infty^J$ which occurs in (33a). The J will again be omitted in the following transformation.

Because of (II), one can write for the denominator of the expression in (33)

$$1 - i\mathfrak{q}\mathfrak{R}\mathfrak{q} = 1 - i\sum_\lambda \frac{(\mathfrak{q}\gamma_\lambda \times \mathfrak{q}\gamma_\lambda)}{E_\lambda - E}. \quad (36)$$

We shall try to write for

$$(1-i\mathfrak{q}\mathfrak{R}\mathfrak{q})^{-1} = 1 + i\sum_{\mu\nu} A_{\mu\nu}(\mathfrak{q}\gamma_\mu \times \mathfrak{q}\gamma_\nu). \quad (36a)$$

The $A_{\mu\nu}$ are, of course, functions of the energy. The product of the right sides of (36a) and (36) must give 1. It can be evaluated by means of the general equation

$$(\mathbf{x}\times\mathbf{y})(\mathbf{z}\times\mathbf{w}) = (\mathbf{y}\cdot\mathbf{z})(\mathbf{x}\times\mathbf{w}). \quad (III)$$

One obtains for the $A_{\mu\nu}$ the equations

$$A_{\mu\lambda}-\frac{\frac{1}{2}i}{E_\lambda-E}\sum_\nu A_{\mu\nu}\Gamma_{\nu\lambda}=\frac{\delta_{\mu\lambda}}{E_\lambda-E}, \tag{37}$$

where the $\Gamma_{\nu\lambda}$ are the scalar products

$$\tfrac{1}{2}\Gamma_{\nu\lambda}=(q\gamma_\nu\cdot q\gamma_\lambda)=\sum_j k_j\gamma_{\nu j}\gamma_{\lambda j}. \tag{37a}$$

The Γ with two indices are, in contrast to the Γ of (13a), functions of the energy because of the k which enters (37a). They are, however, slowly varying functions of the energy. The $A_{\mu\nu}$ will turn out to be rapidly varying functions of E.

Both the $\Gamma_{\nu\lambda}$ and the $A_{\mu\lambda}$ are symmetric in their two indices: $\Gamma_{\nu\lambda}=\Gamma_{\lambda\nu}$; $A_{\mu\lambda}=A_{\lambda\mu}$. As a result of (36a), (37), and (III), the matrix in (33) can also be written as[4]

$$\frac{\mathfrak{R}}{1-iq\mathfrak{R}q}=\sum_{\mu\lambda}A_{\mu\lambda}(\gamma_\mu\times\gamma_\lambda). \tag{38}$$

This is how far the transformation of (33) can be carried easily without making approximations.

At this point, the possibility of a transformation similar to that given by (13) should be mentioned. Equation (37) is evidently a matrix equation although the rows and columns of the matrices occurring in it do not refer to the different reaction products as in the case of the matrices $\mathfrak{q}$, $\mathfrak{R}$, etc., but refer to the different resonance levels λ, μ, ν, etc. After multiplication with $E_\lambda-E$, (37) can be written as

$$\mathfrak{a}(\mathcal{E}-E1)-\tfrac{1}{2}i\mathfrak{a}\mathcal{G}=1. \tag{39}$$

In this, $\mathcal{E}$ is the diagonal matrix with the diagonal elements E_λ, E_μ, etc., $\mathfrak{a}$ and $\mathcal{G}$ are symmetric matrices with elements $A_{\mu\nu}$ and $\Gamma_{\mu\nu}$. It follows from (39) that

$$\mathfrak{a}=(\mathcal{E}-\tfrac{1}{2}i\mathcal{G}-E1)^{-1}. \tag{39a}$$

If the symmetric matrix $\mathcal{E}-\frac{1}{2}i\mathcal{G}$ has no double characteristic values—which would be, after all, an exceptional case—it will be possible to bring it into the diagonal form $\mathcal{F}$

$$\mathcal{F}=\mathcal{T}(\mathcal{E}-\tfrac{1}{2}i\mathcal{G})\mathcal{T}^{-1}. \tag{39b}$$

Because of the symmetry of $\mathcal{E}-\frac{1}{2}i\mathcal{G}$, one can assume that $\mathcal{T}$ is a complex orthogonal matrix

$$\mathcal{T}^{-1}=\mathcal{T}'. \tag{39c}$$

One has because of (39b)

$$\mathcal{E}-\tfrac{1}{2}i\mathcal{G}-E1=\mathcal{T}^{-1}(\mathcal{F}-E1)\mathcal{T} \tag{40}$$

and

$$\mathfrak{a}=\mathcal{T}'(\mathcal{F}-E1)^{-1}\mathcal{T}. \tag{40a}$$

The diagonal elements F_ν of $\mathcal{F}$, as well as the elements $T_{\mu\nu}$ of $\mathcal{T}$ will still be slowly varying functions of the energy. However, the elements of $\mathfrak{a}$ will be

$$A_{\mu\lambda}=\sum_\nu T_{\nu\mu}(F_\nu-E)^{-1}T_{\nu\lambda} \tag{40b}$$

at least in the neighborhood of the real part of F_ν, rapidly varying functions of E.

Because of (40b), (38) becomes

$$\begin{aligned}\frac{\mathfrak{R}}{1-iq\mathfrak{R}q}&=\sum_{\mu\lambda}\sum_\nu\frac{T_{\nu\mu}T_{\nu\lambda}}{F_\nu-E}(\gamma_\mu\times\gamma_\lambda)\\&=\sum_\nu\frac{(\mathbf{s}_\nu\times\mathbf{s}_\nu)}{F_\nu-E},\end{aligned} \tag{41}$$

wherein the vector $\mathbf{s}_\nu$ is defined by

$$s_{\nu l}=\sum_\lambda T_{\nu\lambda}\gamma_{\lambda l}. \tag{41a}$$

Finally, (33) gives for the cross section

$$\sigma_{jl}(E)=\frac{4\pi k_l}{k_j}\sum_J g_J\left|\sum_\nu{}^J\frac{s_{\nu j}s_{\nu l}}{F_\nu-E}\right|. \tag{42}$$

There is, of course, a separate set of F_ν and $s_{\nu j}$ for every value of J and the sum of (42) should be taken in this sense. Equation (42) is the analogon of (13), (13a) and is subject to the same kind of limitations as are those equations: the quantities $s_{\nu l}$, $s_{\nu j}$, F_ν are in general complex; they are subject to rather complicated equations which express the fact that the matrices $\mathcal{E}$ and $\mathcal{G}$ are real; they are functions of the energy although slowly varying functions. Except for these limitations (42) is a very concise form of the resonance formula.[5] It should be remembered, however, that the expressions (34), (35) give the cross sections in terms of the $R_{jj\infty}$, $R_{jl\infty}$, $R_{ll\infty}$, E_λ, γ_λ, etc. which are all real, subject to no equations and independent of energy. Of course, they apply only in the case of the simplest re-

[5] Again, Breit's work anticipates many of the results derived here. Although Breit's paper deals with a rather special model, a comparison of his formulae with ours shows that the model used by him already exhibits practically all the features which prevail in the general case.

actions in which only one pair of reaction products is possible.

In order to derive an expression for the cross sections which is not subject to the limitations to which (42) is subject, one will try to avoid the doubtful diagonalization (39b) and try to solve (37) for the $A_{\mu\lambda}$ more directly. If several reaction products are possible, one will obtain a manageable expression only if one resorts to approximations, and it will be assumed that the energy differences are larger than the widths Γ. It will then turn out that the $A_{\mu\mu}$ are, in general, considerably larger than the $A_{\mu\lambda}$ with $\mu \neq \lambda$. One can, therefore, obtain a first approximation for $A_{\mu\mu}$ by using the equation $\lambda=\mu$ of (37) and neglecting the $A_{\mu\nu}$ terms with $\mu \neq \nu$. This gives

$$A_{\mu\mu}=\frac{1}{E_\mu-E-\frac{1}{2}i\Gamma_{\mu\mu}}. \tag{43}$$

One then obtains for $A_{\mu\lambda}$ from (37) by keeping, from the sum, only the terms $\nu=\lambda$ and $\nu=\mu$ and using (43) for the latter

$$A_{\mu\lambda}=\frac{\frac{1}{2}i\Gamma_{\mu\lambda}}{(E_\mu-E-\frac{1}{2}i\Gamma_{\mu\mu})(E_\lambda-E-\frac{1}{2}i\Gamma_{\lambda\lambda})}, \quad (\mu\neq\lambda). \tag{43a}$$

This can be considered to be small as compared with (43) because the energy differences are, in general, larger than the Γ. For this reason, the terms with $\lambda \neq \mu$ may be neglected in first approximation in (38) and one obtains with (33)

$$\sigma_{jl}(E)=\frac{4\pi k_l}{k_j}\sum_J g_J\left|\sum_\mu^J \frac{\gamma_{\mu j}\gamma_{\mu l}}{E_\mu-E-\frac{1}{2}i\Gamma_{\mu\mu}}\right|^2. \tag{44}$$

This equation actually has the form of (42) and constitutes an approximation to it in the same sense as (14) is an approximation to (13c). One sees the analogy between (44) and the customary one level formula, perhaps, most easily if one denotes

$$(q_j\gamma_{\mu j})^2=k_j\gamma_{\mu j}^2=\tfrac{1}{2}\Gamma_{\mu j}, \tag{44a}$$

so that, because of (37a), $\sum_j \Gamma_{\mu j}=\Gamma_{\mu\mu}$. One then sees that $\Gamma_{\mu\mu}$ is what is usually denoted by Γ_μ and that the matrix elements, which are the $q_j\gamma_{\mu j}$, are real. This shows that $s_{\nu j}$ of (42) are also approximately real, i.e., their complex phases are small. However, if the Γ are of the same order of magnitude as the energy differences between resonances, (44) may become grossly inaccurate, just as (14) was inaccurate under similar conditions.

In the next approximation, it is necessary to take the $A_{\mu\mu}$ with $\mu \neq \lambda$ into account. Using (43a) for these, the matrix needed for (33) becomes

$$\frac{\mathfrak{R}}{1-iq\mathfrak{R}q}=\sum_\mu \frac{(\gamma_\mu\times\gamma_\mu)}{E_\mu-E-\frac{1}{2}i\Gamma_{\mu\mu}}+\sum_{\lambda\neq\mu}\frac{\frac{1}{2}i\Gamma_{\mu\lambda}(\gamma_\mu\times\gamma_\lambda)}{(E_\mu-E-\frac{1}{2}i\Gamma_{\mu\mu})(E_\lambda-E-\frac{1}{2}i\Gamma_{\lambda\lambda})}. \tag{45}$$

In this approximation, it is still easy to write (45) in the form (41). The F_μ are the same as in (44)

$$F_\mu=E_\mu-\tfrac{1}{2}i\Gamma_{\mu\mu} \tag{45a}$$

and the s_μ becomes

$$\mathbf{s}_\mu=\gamma_\mu+\sum_{\lambda\neq\mu}\frac{\frac{1}{2}i\Gamma_{\mu\lambda}}{F_\lambda-F_\mu}\gamma_\lambda. \tag{45b}$$

One sees that neither the F nor the $\mathbf{s}$ are entirely independent of the energy. The $\mathbf{s}$ are not real any more as they were in first approximation. However, in the present approximation, i.e., up to terms of the order $\Gamma/(E_\lambda-E_\mu)$, the imaginary part of F_ν is still equal to the square of the length of $q\gamma_\nu$.

The above is intended to show that if one uses equations of the form (42) without taking the restrictions on the F and $\mathbf{s}$ into consideration, one automatically restricts oneself to the case in which the level width is small compared with the spacing of the levels. Under such conditions, the matrix elements are at least approximately real. As one approaches the case in which the Γ are of the same order as the spacing of the levels, the $\mathbf{s}$ become complex in general. However, there remain relations which replace the reality condition which is valid for $\Gamma \ll E_\lambda-E_\mu$. It does not appear justifiable to make statistical statements on the cross sections without taking these conditions into account. Of

course, (33) always remains valid, but it does not seem to be easy to make statistical statements on the basis thereof without resorting to somewhat crude assumptions.

One can calculate the $A_{\mu\mu}$ in the following approximation by taking into account all terms in the Eq. (37) with $\lambda=\mu$ but using for $A_{\mu\nu}$ the approximation (43a). This gives

$$(E_\mu-E-\tfrac{1}{2}i\Gamma_{\mu\mu})A_{\mu\mu}=1-\tfrac{1}{4}\sum_{\nu\neq\mu}\frac{\Gamma_{\nu\mu}^2}{(E_\mu-E-\tfrac{1}{2}i\Gamma_{\mu\mu})(E_\nu-E-\tfrac{1}{2}i\Gamma_{\nu\nu})}.$$

Since the last term herein is a correction term one may write for the right side $1/(1+\frac{1}{4}\sum\cdots)$ where $\sum\cdots$ is the sum on the right side. This gives then

$$A_{\mu\mu}=\frac{1}{E_\mu-E-\tfrac{1}{2}i\Gamma_{\mu\mu}+\frac{1}{4}\sum_\nu{}'\,\Gamma_{\mu\nu}^2/(E_\nu-E-\tfrac{1}{2}i\Gamma_{\nu\nu})}. \tag{46}$$

The term with $\nu=\mu$ has to be omitted in the summation over ν in the denominator. In general, (46) is still approximate. However, one can easily convince oneself that (46) is actually accurate if there is, in addition to μ, only one more resonance level. The approximation corresponding to (46) for $A_{\mu\lambda}$ with $\mu\neq\lambda$ is

$$A_{\mu\lambda}=\frac{\tfrac{1}{2}i\Gamma_{\mu\lambda}^2}{(E_\mu-E-\tfrac{1}{2}i\Gamma_{\mu\mu})(E_\lambda-E-\tfrac{1}{2}i\Gamma_{\lambda\lambda})\left(\Gamma_{\mu\lambda}-\tfrac{1}{2}i\sum_\nu{}''\frac{\Gamma_{\nu\lambda}\Gamma_{\nu\mu}}{E_\nu-E-\tfrac{1}{2}i\Gamma_{\nu\nu}}\right)+\tfrac{1}{4}\Gamma_{\mu\lambda}^3}. \tag{46a}$$

In the summation over ν in the denominator the terms $\nu=\mu$ and $\nu=\lambda$ have to be omitted so that the sum over ν vanishes if there are only two resonance levels, μ and λ. Under this condition (46a) is accurate and differs only by the last term in the denominator from (43a).

Evidently, the last equations are too complicated for being of great practical value. This can hardly to be expected otherwise since our result is quite general except that we assumed only short range forces and considered only collisions in which the angular momentum of the motion of the colliding particles vanishes. Hence (33) should be able to represent the variation of the various cross sections with energy under almost arbitrary conditions. In most cases, if special conditions prevail which are different from those assumed above, it may be easiest to refer back to (33). One property of the cross sections that is of fairly great generality can be, however, easily checked by means of the above formulae, that is that the reaction cross section goes through zero between successive maxima, at least if $\gamma_{\lambda i}\gamma_{\lambda j}$ has the same sign for both, if only two pairs of products are possible but that this does not occur if several products can be formed.

The Average Specific Ionization of Cosmic-Ray Mesons in Hydrogen, Helium, and Argon

LESTER L. SKOLIL
Department of Physics, University of California, Berkeley, California

(Received August 5, 1946)

Counter-controlled, cloud-chamber photographs have been taken of cosmic-ray meson tracks in hydrogen, helium, and argon gases. The chamber was operated in such a way that the average probable ionization could be determined from the counted number of drops that condensed on positive ions. Clusters of droplets that required energy transfers up to 25×(average energy spent per ion pair) were included. The observed results were corrected for the ionization in the alcohol and water vapors used in the chamber. The ionization correction amounted to less than 25 percent for hydrogen and helium gases and less than one percent for argon gas. The average probable ionization per cm at N. T. P. in hydrogen gas was 8.00, in helium gas 9.67, and in argon gas 65.5. The probable error was about seven percent. The results were used to check with theory. There was very good agreement between theory and experiment for hydrogen, argon, and air, but in the case of helium the discrepancy exceeded the estimated experimental error.

INTRODUCTION

THE term, "specific ionization," is applied in a general way to any quantity that represents the number of ion pairs per centimeter of track length. The various methods used in measuring the specific ionization of cosmic-ray particles in gases and the advantages and disadvantages of these methods have been discussed by Johnson,[1] Brode,[2] Hazen,[3] and others.

In the determination by the ionization-chamber method, the ionization is given by an expression essentially of the form $I=N/JL$, where N is the total number of ions per sec. per cm^3 as measured by the ionization chamber, J is the number of particles traversing unit volume per sec., as measured by a counter, and L is the average track length. Since these data are independently collected, there is uncertainty in the interpretation of the results thus obtained.

Using the pulse-ionization-chamber method, one observes the number of ions collected when a single particle passes through the ionization chamber. Since each track will traverse a different path length in the ionization chamber, allowance must be made for the shape of the chamber. Dunlap[4] overcame this limitation by using a counter-controlled, pulse-ionization chamber. In this way the track was confined in direction to the solid angle subtended by the counters and in length to the vertical length of the plates of the chamber.

A cosmic-ray meson in passing through matter produces secondary electrons ejected from molecules. These secondary electrons have sufficient energy, on the average, to produce additional ions. The path of the secondary electrons is usually so short that nearly all the ions lie close together in a group.

If the expansion of the cloud chamber in the determination of the ionization by the cloud-chamber method is performed immediately after the passage of the meson, either a single globule of liquid is formed on the entire group of ions or the individual droplets formed on each ion are so close together that they are not resolved and thus appear as a single globule of liquid. A count of globules per cm of track length gives a measure of the *primary* ionization. If the expansion of the cloud chamber is delayed a few hundredths of a second after the passage of a cosmic-ray meson, the ions will have spread by diffusion so that after expansion each ion will be the nucleus of a drop of liquid, provided the expansion was great enough. An electrical clearing field from the front to the rear of the chamber separates the positive and negative ion-droplets into separate columns. The droplets in these columns, if photographed under favorable conditions, can in most cases be resolved and counted. Occa-

[1] T. H. Johnson, Rev. Mod. Phys. **10**, 193 (1938).
[2] R. B. Brode, Rev. Mod. Phys. **11**, 222 (1939).
[3] W. E. Hazen, Phys. Rev. **65**, 259 (1944); **67**, 269 (1945).
[4] W. C. Dunlap, Jr., Phys. Rev. **67**, 67 (1945).

sionally a secondary electron of exceptionally high energy makes a branch track. If the branch track is short, it is referred to as a cluster. If the ions along all of the branch tracks as well as the ions in the clusters are included, the results thus obtained would give a measure of the total ionization. However, when one uses a cloud chamber at pressures suitable for counting drops, it is not possible to have all the branch tracks within the cloud chamber. With large ionization chambers operated at high pressures the observed results represent nearly the *total* ionization. Finally, the *probable* ionization is defined as the average ionization exclusive of the ions in clusters greater than a certain upper limit.

Cloud-chamber measurements of cosmic-ray ionization in air have been made by Corson and Brode.[5] Using the cloud-chamber method, Hazen[3] has made extensive observation of the average specific ionization of mesons in air at sea level and down to 400 feet underground. The purpose of the present work was to make cloud-chamber measurements of the average probable specific ionization of cosmic-ray mesons in hydrogen, helium, and argon gases.

Cosmic-ray mesons were chosen for this study because they are rather good mono-ionizing particles. This fact may be seen readily from a study of the energy distribution curve and the theoretical ionization curve for mesons. According to theory, the ionization produced by a high speed particle should decrease to a minimum value rather rapidly as the speed of the particle increases up to approximately 95 percent of the velocity of light. This decrease in ionization is caused by the decrease in the time during which the meson can act on the atom. At higher speeds the probable ionization should increase very slowly, approximately as the logarithm of the energy. This increase in ionization is caused by the increase in sharpness of the pulse resulting from the contraction of the electric field in a plane perpendicular to the motion of the particle. It is in this latter region of the energy spectrum, where the ionization is increasing logarithmically, that most of the cosmic-ray mesons occur. Experimental evidence, however, leads to a power law distribution.[6] Thus at the higher energy end of the spectrum we may expect less than 20 percent of the mesons to have an ionization 20 percent greater than the ionization at the maximum of the distribution. At the lower energy end of the spectrum there are few mesons with energies less than 2×10^8 ev, the energy at minimum ionization. In the energy range 1.8×10^8 to 1.5×10^7 ev, Greisen[7] points out that we may expect only eight percent of all mesons. According to Williams,[8] we may expect about four slow mesons out of 10,000 cosmic-ray particles, i.e., mesons with ionization 2.5 times the ionization minimum. Thus we may expect no large variation in the probable ionization of the individual cosmic-ray mesons.

EXPERIMENTAL PROCEDURE

Photographs were taken of diffuse, counter-controlled meson tracks in a cylindrical cloud chamber 30 cm in diameter and 10 cm deep. The front clearing-field electrode consisted of a ring with very thin nickel wires stretched horizontally across the ring three centimeters apart. This electrode was placed immediately behind the front glass and charged to 250 volts, positive with respect to the back of the chamber. The wires were so small and so far out of focus that they did not interfere with the photographing of the drops. From the evidence of the uniformity in separation of the ion columns in a track, we could judge that the clearing field was quite uniform in the region in which tracks were photographed and probably did not give rise to any distortion in the length of the track.

Studies of condensation efficiencies[9] for liquid mixtures[10] of ethyl alcohol and water (70 percent ethyl alcohol) indicate that if 20 percent of the negative-ion drops are present, nearly all of the positive ions are represented by drops. This negative-ion criterion does not change rapidly for ethyl alcohol mixtures from 70 percent down to 40 percent. With mixtures below 40 percent ethyl alcohol, the percentage of nega-

[5] D. R. Corson and R. B. Brode, Phys. Rev. **53**, 773–777 (1938).

[6] H. Jones, Rev. Mod. Phys. **11**, 235 (1939). P. M. S. Blackett, Proc. Roy. Soc. **A159**, 1 (1937).

[7] K. Greisen, Phys. Rev. **63**, 323 (1943).

[8] E. J. Williams, Proc. Roy. Soc. **A172**, 194 (1939).

[9] C. E. Nielsen, Ph.D. Thesis, University of California, Berkeley (1941).

[10] T. N. Gautier and A. E. Ruark, Phys. Rev. **57**, 1040 (1940).

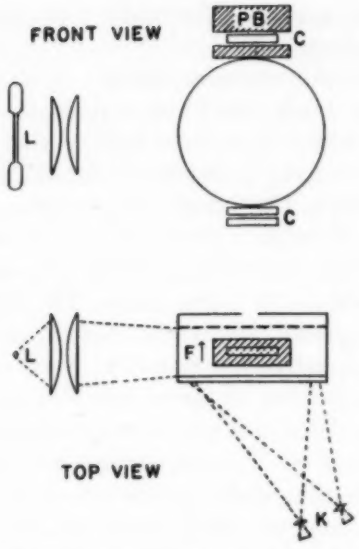

FIG. 1. Schematic diagram showing the cloud chamber and the relative positions of the counters (C), lead (Pb), light source (L), and cameras (K). The clearing field is indicated by F. The light beam through the chamber was made somewhat convergent in order not to illuminate the front glass and to provide nearly constant exposure for tracks on opposite edges of the chamber.

tive-ion drops must be higher than 20 percent in order that one may be quite certain that most of the positive ions are represented by drops. A 50 percent negative-ion criterion was used in this work.

The chamber was evacuated and then filled with the gas and with more than enough of a liquid mixture of ethyl alcohol and water, containing 80 percent ethyl alcohol, to saturate the chamber. The chamber was operated with pools of liquid mixture on the bottom. No trouble was encountered because of electrolysis even with clearing-field electrolysis currents as high as 50 microamperes. During the time required for the performance of the experiment, about three days for each gas, some of the alcohol diffused out through the rubber diaphragm. Therefore the 50 percent criterion was chosen. In most of the tracks the positive and negative ion columns appeared to be equally dense, indicating that the condensation efficiency was certainly nearly 100 percent for positive ions.

Turbulence was avoided by maintaining the room and chamber at as near a constant temperature as possible. None of the observed tracks within the illuminated region of the chamber was noticeably distorted.

The cloud chamber was controlled by a three-counter telescope. Two of the counters were placed below the chamber. The counters were quenched by Neher-Harper quenching circuits, which were coupled to a conventional Rossi coincidence circuit. The tubes used in the above circuits were the triple-grid type 77 except for the trigger tube, which was an 884. With three counters in the telescope more than 99 percent of the pictures yielded visible counter-controlled tracks.

In order to distinguish between electron and meson tracks, a lead block of 10-cm thickness was placed above the top counter. It was very unlikely that an electron could penetrate this lead without producing an electron shower. Photographs with two or more simultaneously occurring tracks were not used. Since additional lead was placed just over the chamber and under the top counter, it was very likely that, out of the few instances where knock-on electrons accompanied the mesons from the lead, both the meson and the electron would be seen.

Two 35-mm Retina cameras with 50-mm lenses were rebuilt to have adjustable tilting of the image plane. This was necessary in order to obtain sharp focus for tracks lying within the volume defined by the counters. The scattering angles for the light that entered the cameras were 60° and 73°, and the corresponding lens apertures that gave satisfactory drop images were f:16 and f:12, respectively. The photographs were taken on Agfa Ultra Speed film. Since grain was not of great importance in studying the number of drop images and since the greatest possible contrast was desired, the films were developed in DK50 for about twice the normal development time.

The cameras were opened at the time of expansion, but a time-delay circuit employing an 885 thyratron was used to delay the flashing of the lights. During the time between the expansion and the flash, the drops grew to a size such that they scattered enough light to be photographed. The cameras were coupled mechanically, and the film was rewound by an electric motor.

The cloud chamber was illuminated by an argon flash tube similar to that described by Hazen.[3] A 450-mf condenser bank at a potential

TABLE I. Ionization by cosmic-ray mesons in gases.

	Hydrogen	Helium	Argon	Air
Observed ionization N.T.P.	11.5	12.6	63.5	
Root-mean-square deviation	0.10	0.11	0.12	
Corrected ionization to dry gas N.T.P.	8.00	9.67	65.5	51
Ratio of ionization to ionization in air	0.160	0.194	1.33	1.0
Ratio of ionization to electron density	4.00	4.84	3.68	3.5
Calculated values of C	0.166	0.215	0.170	0.17
Primary ionization N.T.P.	5.5	6.5	29	21

of 1000 volts was discharged through the flash tube. Crosswise illumination was used, as shown in Fig. 1, in order not to illuminate the front glass or the front clearing-field electrode. As an aid in the focusing of the light source, the region to be illuminated was marked out on the opposite side of the cylinder. A phosphorescent screen was placed over the marked-out region. A flash of the tube produced a phosphorescent glow that lasted long enough for visual observation, thus indicating what adjustments of the light source were necessary.

The drop images were counted on the film with the aid of a microscope that was equipped with a micrometer-motion stage. In some cases both films were counted as a check, particularly when the drop images on one film appeared to be slightly enlarged due to overexposure.

Scratch marks were made on the film to indicate the portion of the track that satisfied the 50 percent negative-ion criterion discussed above. Portions of the track that were crossed by stray tracks were also marked and then omitted.

Secondary rays produced dense clusters of drops which could be counted in most cases. As an aid in obtaining the number of drops in a dense cluster in the positive-ion column, the same cluster was counted in the less dense negative-ion column, and the result was multiplied by the ratio of the plus to minus drops in corresponding adjacent lengths of the track. Clusters were excluded that exceeded the average number of drops for that length of track by more than 25 drops. It was, however, seldom necessary to exclude clusters. Hazen[3] has found that statistical variations from one track to the next were greatly reduced by the exclusion of large clusters.

In order to determine the length of a counted section of track, the films were replaced in the cameras where they were held in their original lateral and axial positions by lateral and backplate springs. The images were reprojected onto a screen through a glass equal in thickness to that through which the photographs were taken and placed at the same angle. The actual projected lengths of the tracks that satisfied the 50 percent negative-ion criterion were measured. The reprojection distance was checked against the original distance between the cameras and the cloud chamber. The reprojection was done with such care that drop images could be made to coincide along the entire track length.

EXPERIMENTAL RESULTS AND DISCUSSION

The total pressure in the chamber for the hydrogen and helium experiments was 152 cm of Hg in each case; for the argon experiment the total pressure was 100 cm of Hg. The observed number of drops per cm of track length was reduced to N.T.P., and corrections were made for the ionization of the alcohol and water vapor mixture. The ionization of the vapor and gas mixture may be given by an expression of the form:

$$I=p_1I_{\text{gas}}+p_2I_{H_2}+(p_2+p_3)I_O+p_3I_{C_2}+p_3I_{H_6}, \quad (1)$$

where I represents the observed number of drops per cm of track length; p_1 represents the partial pressure of the gas, and p_2 and p_3 the partial pressures of the water vapor and alcohol vapor respectively. The values, I_{H_2}, I_{H_6}, I_O, and I_{C_2}, were approximated by assuming that the ionization due to these molecules was proportional to their respective electron densities. For example, in making the correction for helium gas, I_{H_2} equals $2/2\times I_{He}$; $I_{H_6}=3\times I_{He}$; $I_O=8/2\times I_{He}$; and $I_{C_2}=12/2\times I_{He}$. The correction in the case of hydrogen and helium gases was less than 25 percent; for argon the correction was less than one percent.

The corrected values as found in these experiments for the average specific ionization of 25 or more meson tracks in each of the gases are

shown in Table I. Energy transfers greater than η were excluded (η to be explained later).

The observed value shown in Table I for the ionization in argon must be corrected for the overlapping of drop images. Two drop images may be resolved if the overlap is equal to or less than the radius of the drop. The diameter of a correctly exposed and sharply focused drop image was approximately 0.02 mm. The diameter of the drop in the chamber, however, was not equal to the magnification, M, times the image diameter. The track widths measured on the film varied from 0.25 mm to 0.40 mm. In the chamber the drop columns would be M times as wide. The average value of M was 6.1. The correction for the ionization in argon gas amounted to about 4 percent, which should be added to the observed value shown in Table I, i.e., $63.0+0.04(63.0)=65.5$. This correction is a minimum because it was determined on the basis of a random distribution of drops in the track. For hydrogen and helium gases the correction was less than one percent.

The number of drops counted in a track length in helium and hydrogen gases was between 300 and 400 and in argon gas between 400 and 1000. The statistical variation in the ionization of an individual track is determined by the number of primary ionization events. The primary ionization in helium gas is 6.5 primary ion pairs per cm,[11] which gives a ratio of probable to primary ionization of 9.67/6.5 or about 1.5. In the case of hydrogen, this ratio of probable to primary[12] ionization is 8.00/5.5 or about 1.5. The probable statistical deviation is:

$$0.67\frac{(200)^{\frac{1}{2}}}{200}\sim 0.05.$$

The probable error as estimated on the basis of least count and experimental uncertainties is less than five percent.

Block diagrams of the distributions for each of the gases are given in Fig. 2. No slow mesons were observed. The root-mean-square deviation was 11 percent. If these data conform to a normal distribution, then the corresponding most probable error would be 0.67×11 percent or about seven percent. Thus from the experimentally observed spread it is apparent that the mesons were essentially mono-ionizing.

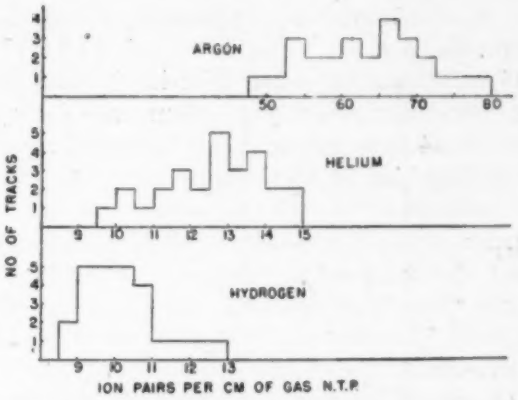

FIG. 2. Block diagram showing frequency distribution of the probable ionization of cosmic-ray mesons in hydrogen, helium, and argon gases. The mean value of the ionization was 11.5 in hydrogen, 12.6 in helium, and 65.5 in argon. The root-mean-square deviation was about 11 percent.

The results of these experiments can be used to check the theory. The energy loss by collision can be given by a theoretical expression[13] of the form:

$$k_\eta(E)=\frac{2C\mu Z}{\beta^2 A}\left(\log\frac{2\mu\eta}{I^2(Z)}\frac{\beta^2}{(1-\beta^2)}-\beta^2\right), \quad (2)$$

where k_η is the energy loss per g/cm^2 by collision with electrons and where the maximum energy transferred is less than η. This last symbol represents $25\times V_0$ where V_0 is the average energy[14] spent per ion pair. $\mu=mc^2=$rest energy of an electron. $I(Z)$ represents a mean energy of excitation of an atom of atomic number Z. According to Bloch's[15] theory of excitation energies, the mean excitation energy for atoms containing many electrons is proportional to the atomic number Z. The most reliable measurement of the constant of proportionality available is $I(Z)=11.5Z$, as determined by Wilson[16] from observations of stopping power. For a hydrogen-like atom Bethe[17] gives $I(Z)=1.1\times J$, where J is

[11] W. E. Hazen, Phys. Rev. **63**, 107 (1943).
[12] Williams and Terroux, Proc. Roy. Soc. **A126**, 289 (1930).
[13] B. Rossi and K. Greisen, Rev. Mod. Phys. **13**, 240 (1941).
[14] Rutherford, Chadwick, and Ellis, *Radiation from Radioactive Substances* (The University Press, Cambridge, England, 1930), p. 81.
[15] F. Bloch, Zeits. f. Physik **81**, 363 (1933).
[16] R. R. Wilson, Phys. Rev. **60**, 749 (1941).
[17] H. A. Bethe, Ann. d. Physik **5**, 325 (1930).

the observed ionization potential. Using this expression for H_2, we have $I(Z)=1.1\times15.9=17.5$. Williams[18] using Wheeler's[19] data for the "stopping power" of helium calculates a value of 44 volts for the mean excitation energy for helium gas. In view of the small spread in the ionization of the individual mesons, it appears that a reasonable effective value of $\gamma^2=1/(1-\beta^2)$ could be taken near the minimum of the theoretical ionization curve, i.e., $\gamma^2=20$, $\beta=0.975$. Fortunately, the value of C calculated with the use of Eq. (2) is not very sensitive to changes in the values of γ^2 or $I(Z)$ since these quantities occur inside the log term. A change of γ^2 by a factor of 10, for instance, affects the value of C by only 7/166 or about 4.5 percent. It is, therefore, not important to know the exact value of γ^2.

The values of C calculated from Eq. (2) for hydrogen and argon gases agree exceptionally well. A value of 0.17 for C is obtained with the use of Hazen's[3] value of 51 ion pairs per cm for the average specific ionization in air and with $I(Z)=11.5\times7.23$, and $A=14.78$. No completely satisfactory explanation has been found for the discrepancy in the case of helium; otherwise there is satisfactory agreement between theory and experiment. Williams[20] suggests the possibility that the experimental value of the energy per ion pair is too low for helium gas. But larger values of V_0 only increase the value of C and, likewise, the discrepancy.

There is another possible explanation for the large value of C. Helium gas has a metastable state of energy corresponding to 19.77 volts. A meson may excite this metastable state. There are some secondary electrons along the meson track that possess insufficient energy to ionize a helium atom but sufficient energy to excite this metastable state. A helium atom thus excited could in turn ionize a vapor molecule by collision with it. This ionization of vapor molecules seems possible since the ionization potential of water is approximately half that of helium. The additional vapor ions thus formed would serve as condensation nuclei for droplets along the track. These droplets would be counted and would tend to increase the observed ionization for the gas and, likewise, the calculated value of C. But this effect is probably not large enough to account for the discrepancy that exists. The ionization potential of helium gas is 24.5 volts, while the average energy spent per ion pair is 27.8 volts. This small difference would indicate that very little energy is lost in helium in excitation.

It is of interest to compare the results of the present work on argon with those obtained by others. Using a counter-controlled ionization chamber under 12 cm of lead, Dunlap[4] obtained a value of 71 ion pairs per cm for the average specific ionization in argon. Energy loss to secondaries by collision are included up to $\eta=3.75\times10^5$ ev. This result represents about 90 percent of the total ionization. Where η is 800 ev, the cloud-chamber method measures about 66 percent of the total ionization. Thus, $(71\times100)/90-0.34\times71=55\pm10$ percent is the calculated value expected as compared to the value 65.5 ± 5 percent observed in the present work. This difference is just within the limits of the probable errors of the experiments.

Clay and Oosthuizen,[21] using an uncontrolled ionization chamber shielded with 12.5 cm of iron, obtained a value of 1.65 for the ratio of the ionization in argon to the ionization in air for all cosmic-ray particles. The results in the present work indicate a corresponding ratio of 65.5/51 or about 1.3.

ACKNOWLEDGMENT

The author is deeply indebted to Professor Wayne E. Hazen, who suggested the problem, for his continued interest, suggestions, and helpful discussions.

[18] E. J. Williams, Proc. Camb. Phil. Soc. **33**, 179 (1937).
[19] J. A. Wheeler, Phys. Rev. **43**, 258 (1933).
[20] E. J. Williams, Proc. Roy. Soc. **A135**, 119 (1932).
[21] J. Clay and K. Oosthuizen, Physica **4**, 527 (1937).

PHYSICAL REVIEW VOLUME 70, NUMBERS 9 AND 10 NOVEMBER 1 AND 15, 1946

The Mass of Cosmic-Ray Mesotrons

WILLIAM B. FRETTER*
Department of Physics, University of California, Berkeley, California
(Received August 13, 1946)

The range of mesotrons in lead as a function of their momentum was determined in an experiment in which two simultaneously expanded counter-controlled cloud chambers were used. The upper chamber was in a magnetic field of 5300 gauss, while the lower, which was vertically in line, contained eight ½-inch thick lead plates. The range of a particle that stopped in one of the plates in the lower chamber, together with the $H\rho$ as measured in the upper chamber, suffice to determine the mass. Data for 26 particles have been obtained which indicate that, within the experimental error, the masses of mesotrons as measured in this experiment are all consistent with a *unique* rest mass of 202 times the rest mass of an electron. Statistical and systematic errors are analyzed.

INTRODUCTION

THE determination of the mass of individual cosmic-ray mesotrons has been accomplished in several ways, all involving measurement of the momentum of the particle and indirect measurement of the velocity or energy. The momentum is found by measuring the curvature of the mesotron track in a cloud chamber in a magnetic field. The velocity is determined by measurement of a quantity such as ionization, range, or momentum loss that theoretically depends on the velocity or energy of the particle. Wheeler and Ladenburg[1] discussed the various methods and gave the results of all observations up to the date of their paper. Subsequently, Johnson and Shutt,[2] Nielsen and Powell,[3] LePrince-Ringuet,[4] D. J. Hughes,[5] and Chaudhuri[6] (with a statistical method) have published additional values of the mass. Most of the values center around approximately 200 electron masses (m_e). The total number of reasonably reliable determinations to date is about 25.

The range-momentum relationship for cosmic-ray mesotrons was first investigated experimentally by J. C. Street[7] during a time when the existence of the particle was being established. He used two cloud chambers, one in a magnetic field of 7000 gauss, the second vertically in line below, and containing three one-cm thick lead plates. Since the apparatus was counter-controlled, he could observe the curvature of a particle in the upper chamber and its range in lead in the simultaneously expanded lower chamber. Between the two chambers there was an additional three cm of lead. With this arrangement, Street was able to show that the penetrating particles had masses much larger than those of electrons, but less than protons. He noticed, however, that "many" of the particles disappeared from view and were apparently stopped before they reached the end of their theoretical range, and he concluded that the mesotrons evidently suffered large anomalous energy losses near the end of their range.

Since measurement of the mass of mesotrons by the comparison of momentum and range depends on the assumption that the individual energy losses are very small compared to the energy of the particle, it seemed worth while to repeat Street's experiment under better conditions in order to verify or disprove the straggling in range that he observed. If the straggling is not observed, the data can be used to determine the masses of the individual particles observed.

THE EXPERIMENTAL APPARATUS

The upper cloud chamber, in which the momentum of the particle was determined, was 12 inches in diameter and three inches deep. It was filled with argon at 1.15 atmospheres and con-

* Whiting Fellow in Physics, University of California.
[1] J. A. Wheeler and R. Ladenburg, Phys. Rev. 60, 754 (1941).
[2] T. H. Johnson and R. P. Shutt, Phys. Rev. 61, 380 (1942).
[3] C. E. Nielsen and W. M. Powell, Phys. Rev. 63, 384 (1943).
[4] LePrince-Ringuet and M. Lheritier, Comptes rendus 219, 618 (1944).
[5] D. J. Hughes, Phys. Rev. 69, 371 (1946).
[6] Chaudhuri, Ind. J. Phys. 18, 57 (1944).
[7] J. C. Street, J. Frank. Inst. 227, 765 (1939).

tained a 1:3 mixture of water and ethyl alcohol in sufficient quantity to keep the expansion ratio at about 10 percent, but the chamber was not saturated with the vapor. The cloud chamber was placed in a magnetic field of 5300 gauss provided by the Carnegie magnet. The clearing field in the chamber was maintained with 67 volts between the slightly aluminized front glass and the metal back plate. The drops that condensed on the positive and negative ions were thus separated into two vertical columns. In order to check the condensation efficiency, two pictures were taken of the upper chamber, one straight on, for the observation of curvature, and one from the side for the observation of the separated ion columns. Light for the photographs was provided by argon-filled capillary flash tubes through each of which condensers of 150 microfarads charged to 1800 volts were discharged. The illuminated region was one inch deep and 12 inches long. The front camera lens was set at f:4.0 for most of the pictures, while the side camera was set at f:6.3. Eastman Super XX or Ansco Ultra-Speed film was used.

It was found that the temperature of the upper cloud chamber had to be maintained uniform within 0.5°C in order to prevent turbulence of the tracks caused by the convection currents. Since the cloud chamber was directly in contact with the back pole-face of the magnet, it was necessary to control the temperature of the magnet as well as a jacket around the main part of the cloud chamber. Residual turbulence was largely responsible for the errors in measurement of curvature.

The lower cloud chamber was 16 inches in diameter and nine inches deep, and contained eight ½-inch thick lead plates. These were placed on 1.5-inch centers so that the length of track visible between each pair of plates was about one inch. The plates were tilted in the chamber so that the camera viewed them edge on in all sections. The camera was a specially made stereoscopic camera using two Leitz f:4.5, 13.5-cm lenses tilted to converge in the illuminated region. The film used was 127 size (1.81 inches), Ansco Superpan Press, obtained in 100-ft. rolls. The pictures thus obtained were square and made use of the full angular field of the lenses. It was necessary to use a 45° front-aluminized mirror

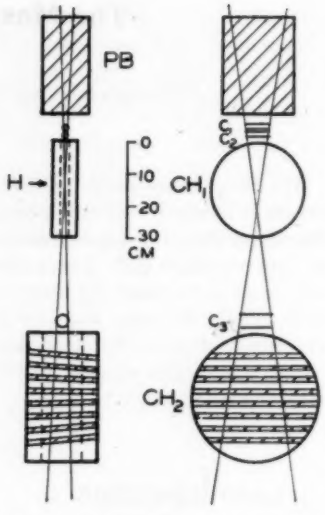

FIG. 1. A schematic drawing of the two cloud chambers Ch_1 and Ch_2. The chambers were simultaneously expanded upon the passage of a particle through counters C_1, C_2, and C_3. The momentum of the particle was determined in the upper chamber, and the range in lead determined in the lower chamber. The dotted lines indicate the extent of the illuminated region.

and to take the picture at 90° from the axis of the chamber because of structural features of the magnet mounting. The clearing field in the lower chamber was maintained by about 20 volts between the plates. It was shorted when the counters tripped but there was a residual field which continued to separate the columns of ions until the ions were fixed by the expansion. This resulted in doubling of horizontal and slanted tracks and doubling of ion clusters along vertical tracks. Measurement of the distance between doubled clusters or tracks gave a very good indication of the age of the track. This distance depends directly on the delay time t and thus permits a more accurate measurement of the track than the width of the diffuse track which depends on $t^{\frac{1}{2}}$.

The illuminated region in the lower chamber was three inches wide at first but was later increased to five inches. The lights were G. E. flash tubes FT22, xenon filled, flashed on 150 μf at 1800 volts.

The over-all experimental set-up is shown in Fig. 1. The chambers were expanded upon the passage of a charged particle through the triple-coincidence Geiger counters, which defined a region in the lower chamber considerably narrower than the light beam. The lead over the

upper counters served to select penetrating particles and to increase the number stopping in the lower chamber. The increase in the number of slow mesotrons was predicted by Rose[8] and is primarily caused by the fact that the decay of mesotrons in the lead is small compared to the decay in an equivalent thickness of air.

OBSERVATIONS

Approximately three pictures per hour were taken with the counter arrangement that was used. Of the approximately 2100 pictures that showed counter-controlled tracks, 83 percent showed particles that went through all of the lead plates in the lower chamber. With few exceptions, these particles were also visible in the upper chamber and had momenta large enough so that the observed penetration was expected. Some of these particles exhibited considerable scattering in the lower cloud chamber, which resulted in a lateral component of range. In some cases the track remained in the illuminated region and could be seen in all segments, but, if the scattering was such as to take the particle out of the illuminated region, the track would be lost to view. Sixteen particles were observed to scatter out the side of the chamber before reaching the last lead plate. Thus it was to be expected that some of the particles would be lost out of the illuminated region, especially in the lower part of the chamber. These could usually be distinguished in the stereoscopic view by the forward or backward direction of the track and the fading due to decreased illumination.

About 7 percent of the singly occurring counter-controlled tracks were observed to terminate in the lower cloud chamber. In most cases, especially in the upper part of the chamber, there was no doubt that the particle did stop. A conclusive observation in some cases was the density of ionization over the plate in which the particle was stopped. If this was noticeably greater than normal, the residual range of the particle was less than the thickness of the lead plate.

In some cases, however, when the ionization was normal but the particle was near the edge of the illuminated region, the scattering in a single plate might have been enough to remove the track from the illuminated region. This was fairly common below the 6th, 7th, and 8th plates and posed a problem in the selection of data. Unless a particle that disappeared under the 6th, 7th, or 8th plates was clearly in the center of the illuminated region or had strong ionization, only a minimum value of its range was given.

Some slow protons were observed. These ionized several times normal in the upper chamber and stopped in the first or second plate of the lower chamber. The heavy ionization and large radius of curvature in the upper chamber were sufficient for easy identification. Of the total of four singly-occurring protons observed, three stopped in the first plate and one in the second. This is evidence for the belief that the slow protons observed at sea level are locally produced and are not part of the tail of an energy distribution; otherwise protons stopping in the other plates might have been expected.

Electrons entering the lower chamber were distinguished by the showers that they made on interaction with the lead. Mesotrons stopping in the first lead plate are indistinguishable from electrons, however, and there is a small but finite probability that an electron might penetrate the first plate and stop in the second without visible multiplication. All data resulting from particles that were stopped in the third plate and were accompanied by other particles were also rejected as possibly being electrons. An example of a mesotron which stopped in the lower chamber is shown in Fig. 2.

REDUCTIONS OF OBSERVATIONS

In order to determine the momentum of the particle in the upper chamber, the magnetic field (H), the radius of the curvature on the film, and the magnification factor of the camera must be measured. The magnetic field was measured by a flip coil of 130 turns-cm^2 connected to a ballistic galvanometer, and was independently checked by a group from the Radiation Laboratory under the direction of W. M. Powell. The magnetic field was uniform to less than 1 percent over a 20-cm diameter, and was measured as a function of the scale reading of an ammeter connected in the field coils. Records of this scale reading were kept during the course of the experiment so that the

[8] M. E. Rose, J. Frank. Inst. **236**, 9 (1943).

magnetic field was known. Its value was approximately 5300 gauss.

The radius of curvature of the track on the film was determined by plotting the coordinates of the track as viewed in a microscope with a traveling stage. If the displacement from a straight line is plotted on a large scale compared to the distance along the track, the resulting curve should be a section of an ellipse. Any deviation from the elliptical shape indicates spurious effects such as turbulence or scattering in the gas. From observation of these curves, it was determined that turbulence was serious if the temperature of the cloud chamber was not carefully controlled. It was difficult to observe zero field tracks because of the thermal equilibrium maintained between the magnet and cloud chamber.

After the track had been plotted and found to conform to the elliptical (or approximately parabolic) curve, the curvature was calculated by smoothing the points and using the sagitta formula or by fitting a curve to the observed points by the method of least squares. If the track departed appreciably from the elliptical curve, it was rejected as unreliable. Several criteria are available to check the reliability of the various tracks. The plotted points were compared with a family of parabolas drawn on transparent plastic, so that even small deviations were easily visible. If many of the points varied from the parabolic shape by more than the usual error of setting the cross-hairs or if a general trend away from the parabolas was shown, it was clear that the track was turbulent. Calculation of the radii of curvature of various sections of the track and comparison of the results was useful in rejecting turbulent tracks. Observation of other tracks on the same strip, including many that were not deviated by the magnetic field, provided another means of checking turbulence. Tracks whose radii of curvature varied along their length by more than 10 percent due to turbulence were rejected in the final analysis of data included in Table I.

Once the curvature on the film was found, it was necessary to know the factor to convert this to curvature in the chamber. The magnification factor of the camera lens was measured by photographing a piece of millimeter cross-section paper back of a 0.5-inch glass plate corresponding

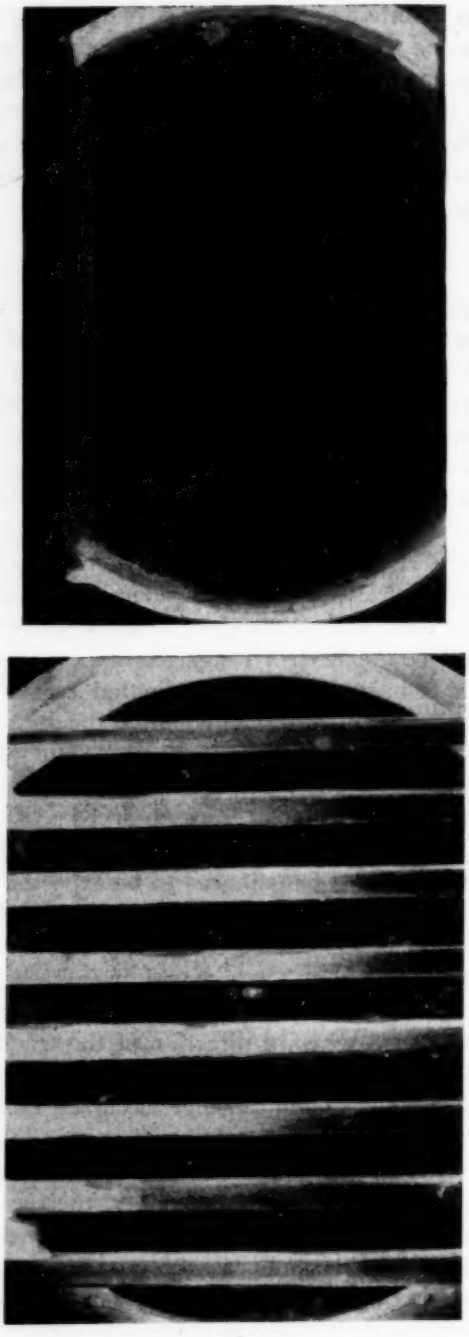

FIG. 2. A mesotron with $H\rho = 820 \times 10^3$ gauss-cm in the upper chamber was stopped in the sixth lead plate with no increase in ionization above the plate. 7.90 cm < range < 9.62 cm. Its mass was 244 ± 37. The slanted tracks appear doubled because of the residual clearing field. The track of the particle in the lower chamber illustrates the possibility of scattering out of the illuminated region if the scattering were toward the front or back instead of toward the side. In the actual apparatus the chambers were separated by a distance equal to two diameters of the upper chamber.

to the front glass. The cross-section paper was placed in the center of the illuminated region, with the chamber removed. Measurement of the pattern on the film gave a factor of 8.05 for conversion of length on the film to length in the cloud chamber. The factor for the side camera varied somewhat over the region and hence was plotted as a function of position in the chamber.

Most of the particles that stopped in the lower chamber had radii of curvature in the chamber of between 1 and 2 meters, or 125 to 250 mm on the film. The displacements of the center of the track from a straight line varied between 0.3 mm and 0.8 mm on the film, depending on the curvature and the length of track usable for measurement.

In order to find the range of the particle after it left the upper chamber, it was necessary to identify the plate in which it appeared to stop and to calculate the amount of lead through which it had gone. There was a considerable amount of material between the chambers: the glass wall, the copper jacket on the upper chamber, the lower counter (which has copper and glass walls), a mirror over the lower chamber, and the glass wall of the lower chamber. By means of the equations for energy loss in various materials given by Rossi and Greisen,[9] it is possible to calculate the thickness of lead equivalent to all of this material. The value obtained was 0.55 inch Pb (equivalent) and this was added to the amount of lead traversed in the lower chamber. A second correction that must be made is for the additional material penetrated when the particle was scattered or went through the lower chamber at an angle. This correction was usually fairly small and was roughly calculated by measuring the projected angles on the film. The residual range of a particle after it entered the plate in which it stopped is of course unknown but observation of the ionization over the plate helped to determine this residual range. If the particle had twice or more normal ionization, it was assumed that it stopped in the first half of the plate. If its ionization was normal, the uncertainty was taken as the full thickness of the plate since an apparent lack of increase of ionization may be caused only by poor illumination.

[9] B. Rossi and K. Greisen, Rev. Mod. Phys. 13, 240 (1941).

RESULTS OF RANGE-MOMENTUM OBSERVATIONS

A graph showing all the particles that stopped or appeared to stop in the chamber is given in Fig. 3. The circles represent particles for which the $H\rho$ and range are both known with relatively high accuracy. The crosses are those for which the range is known but the $H\rho$ is uncertain, because of turbulence. The vertical lines represent particles that disappeared from view under a certain plate but mostly appeared to be scattered or located in such a way that they were leaving the illuminated region. Thus only a lower limit on range was set. It is seen that, for the most part, the particles that were certain in both $H\rho$ and range group together quite well, giving the impression that for most mesotrons the $H\rho$-range relation involves no serious straggling. There were two particles whose range seemed anomalously long for the $H\rho$ measured but in these cases the chamber had been turbulent and the error in the measurement of curvature had been large. These particles are represented by crosses which fall below and to the left of the circles on the graph. Some of the particles represented by vertical lines on the right half of the graph may actually have had anomalously short ranges, but in view of the large angle scattering which has occasionally been observed this is not considered likely. If, on the other hand, these particles had large mass compared to other mesotrons, the ionization before stopping should in all cases be heavier and this was not observed.

The results agree with Street's to the extent that many particles did disappear in the chamber

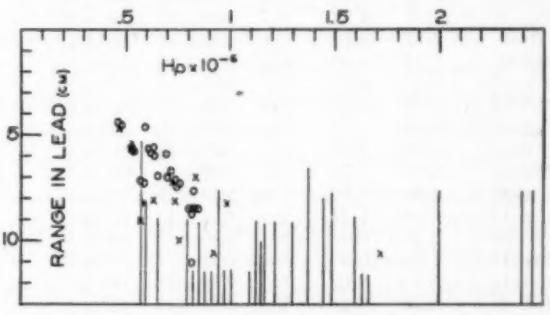

FIG. 3. Graph showing range and $H\rho$ for all particles that *appeared* to stop in the lower chamber. Circles represent particles for which both $H\rho$ and range were accurately determined. Crosses indicate that the $H\rho$ was uncertain, and the vertical lines indicate that the range could only be given a minimum value.

but with the stereoscopic pictures and wide illuminated region in the present experiment it seems possible to attribute most of this effect to scattering in the lead.

MASS DETERMINATION

Since the effect of straggling in range does not seem to be very important, it is possible to make mass determinations for the particles for which $H\rho$ and range are known. A magnified section of the $H\rho$ range plot is shown in Fig. 4. The curves for different masses are the theoretical curves as given by Wheeler and Ladenburg, with constants evaluated from stopping-power experiments. The lines plotted on the diagram are the data for the various stopped particles, with the horizontal projection of each line representing the estimated uncertainty in $H\rho$ and the vertical projection representing the uncertainty in range.

It is seen that, within the experimental error, the masses lie between 142 and 264 electron masses. The weighted average of masses thus determined is 202. In Table I the individual data are given, together with estimated probable errors.

TABLE I. Summary of data.

Track No.	Range in lead (cm) min	max	Ionization increase	$H\rho \times 10^{-3}$ (gauss-cm)	Mass, probable error	Sign
137–19	5.29	5.92	Yes	529±45	160±26	−
165–1	6.50	7.80	No	668±43	199±33	−
165–10	5.25	5.90	Yes	610±60	212±35	−
168–17	5.44	7.24	No	598±43	180±33	−
180–5	6.50	7.80	No	576±43	142±32	+
182–5	3.94	5.21	No	592±27	238±30	+
190–27	4.16	4.85	Yes	480±54	164±38	+
202–26	7.77	9.11	No	840±32	264±28	+
210–6	7.77	9.10	No	830±65	260±42	+
212–8	5.34	6.00	Yes	536±65	163±35	−
215–23	7.80	9.06	No	814±43	250±30	−
218–13	7.90	8.59	Yes	760±21	222±18	+
218–37	6.60	7.35	Yes	700±54	225±32	−
219–25	6.65	8.25	No	749±43	242±37	−
222–31	4.32	5.71	No	530±21	180±26	+
224–30	4.01	4.70	Yes	460±21	157±16	+
226–17	6.60	7.24	Yes	652±43	195±28	+
226–20	5.21	6.48	No	620±27	209±30	−
231–10	5.24	6.55	No	694±21	258±28	+
232–16	6.53	8.05	No	589±21	143±28	+
234–4	5.24	5.86	Yes	633±21	228±19	+
237–8	7.87	9.65	No	809±44	237±35	−
244–11	6.55	7.82	No	760±43	258±35	+
244–20	10.70	11.42	Yes	820±43	183±21	+
244–33	6.75	8.43	No	739±43	230±37	−
245–32	7.90	9.62	No	820±43	244±37	+

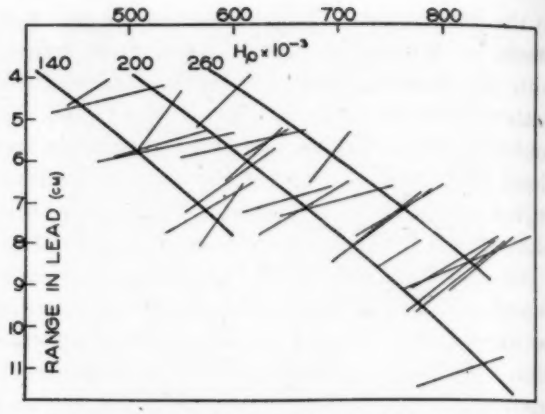

FIG. 4. Graph showing data for particles for which $H\rho$ and range were accurately determined. The curves are the calculated range-momentum relationships for mesotrons of mass 140, 200, and 260 electron masses. Each line represents the data for an individual particle, with the horizontal projection giving the uncertainty in $H\rho$, the vertical projection giving the uncertainty in range.

ERRORS

The errors in the determination of $H\rho$ come from:

1. Measurement of magnetic field. The uncertainty in this measurement is probably about two percent due to all causes: calibration, current measurement, flip coil, etc. The systematic error in H is probably not more than one percent.

2. Measurement of magnification factor. The error in this is less than one percent, but it is also a possible source of systematic error.

3. Measurement of curvature on the film. The statistical error in setting the cross hairs on the track was about two percent. The error due to turbulence in the cloud chamber was in many cases considerably more than this, was very difficult to estimate, and was likely to be systematic. The usual procedure was to observe the appearance of other tracks on the same strip of film, since turbulence was obvious in tracks that were very little bent by the magnetic field. The plotted displacement of the track, which should be nearly parabolic when plotted on a large scale, was also compared with true parabolas to see if there was any skew or off-center motion before the picture was taken.

4. Scattering in the upper chamber. E. J. Williams[10] has given a formula for the spurious radius of curvature produced by scattering in the gas of the upper chamber. If ρ is the true radius of curvature and ρ_s is the apparent radius of curvature due to scattering, the expression reduces to $\rho_s/\rho = H/109$ for the present conditions. Since H is approximately 5300, $\rho_s = 49\rho$. Thus the error caused by scattering in the argon is about two percent, and is not systematic.

The general conclusion was that the uncertainty in $H\rho$ in the majority of the tracks varied

[10] E. J. Williams, Phys. Rev. **58**, 298 (1940).

from ±5 percent to ±10 percent. Tracks with uncertainty greater than this due to turbulence were plotted as crosses on Fig. 3 and rejected for Fig. 4.

The uncertainty in range due to scattering out of the illuminated area has already been discussed, but may cause a systematic error in the final result. For particles that remain in the illuminated area, the uncertainty has been fixed at 0.25 inch of lead for those particles that appear to ionize heavily before they enter the plate and 0.5 inch of lead for those that appear to ionize normally. Those that appear normal may, of course, scatter as they enter the lead and traverse a distance greater than 0.5 inch before stopping. The average angle of scattering of such a particle is about 8° so the correction due to this is not large and has been neglected.

The systematic error introduced by selection of data is more serious. It is possible that some of the particles included in Table I did not actually stop but were scattered out of the illuminated region. This would result in the assignment of a spuriously high mass to those particles, and a resultant systematic error in the average.

The error in mass is thus compounded from the uncertainties in $H\rho$ and range. The maximum value of mass consistent with a given set of data was calculated using the maximum $H\rho$ and minimum range, while the minimum value of mass was calculated using the minimum $H\rho$ and maximum range. Since it is unlikely that the uncertainties in $H\rho$ and range would add in this way, the value assigned to the "probable" error of each observation of mass was about 30 percent less than the maximum error.

CONCLUSIONS

The large straggling of cosmic-ray mesotrons observed by Street has not been confirmed, and it is likely that his results are explained by scattering of particles out of the illuminated region of his lower cloud chamber. Even in the present experiment, with a relatively much larger illuminated region, loss of particles due to scattering is still observed.

Since the momentum of the particles that definitely stop in the lower chamber is known, the masses of the individual particles can be obtained from the range-momentum relationship given by Wheeler and Ladenburg.[1] This gives a number of mass determinations with values ranging from 142 to 264 m_e.

It was of interest to determine whether the data were consistent with a unique mass or whether a distribution of masses must be assumed to explain the spread of values. Let us make use of the criteria of internal and external consistency as given by R. T. Birge.[11] From the estimated errors of individual observations we can assign weights to each observation which are inversely proportional to the square of the estimated error of each observation. We then calculate the weighted average $M=202$. The residuals are calculated by taking the difference between M and the observed value. From these residuals the probable error of a given observation of unit weight based on external consistency can be calculated.

It was found that the ratio of the probable error based on external consistency to the probable "internal" error was very nearly unity. This means that the observations agree among themselves about as well as was to be expected from their individual probable errors.

It is clear, then, that assuming a unique mass of 202 is quite consistent with the data obtained.

The fact that the above statistical analysis of the data can be made is a direct consequence of the fact that a relatively large number of mass determinations have been made in the same experiment. In previous experiments the number of data have been much smaller and no such analysis could be made.

We can now estimate the probable error of the weighted average of all observations. If we use the estimated error for external consistency, the probable error of the weighted average is about ±5.

It should be emphasized, however, that the systematic errors in this experiment are probably somewhat larger than the statistical uncertainty and that, although the uniqueness of the mass seems well established, a more accurate determination of the absolute value of the mass awaits experimental refinements.

The magnet, together with its cloud chamber

[11] R. T. Birge, Phys. Rev. 40, 207 (1932).

and auxiliary equipment, was designed and built by Professor R. B. Brode in 1940 and 1941 expressly for the measurement of the mesotron mass. Funds for this equipment were made available by a grant from the Carnegie Institution of Washington. The lower cloud chamber and its camera were built by Professor W. E. Hazen, who suggested the experiment and to whom I am deeply indebted for constant instruction and encouragement. Professor R. T. Birge was very helpful in connection with the statistical analysis of the data.

PHYSICAL REVIEW VOLUME 70, NUMBERS 9 AND 10 NOVEMBER 1 AND 15, 1946

Low Energy Alpha-Particles from Radium

W. Y. CHANG
Palmer Physical Laboratory, Princeton University, Princeton, New Jersey
(Received July 10, 1946)

The large alpha-ray spectrograph and the sensitive track method of detection, as used for studying the polonium alpha-particles, have been used to investigate the alpha-ray spectrum of radium. Thin and uniform radium sources were freshly prepared by depositing radium carbonate on platinum rods, using a modified method of Hahn and Meitner. Microscopic examination has revealed a line at 4.615 Mev, which is identifiable with that found by Rosenblum. From 0.5 to 0.9 Mev below the main line five previously unknown groups have been found. The intensities of the first line and of these last ones are, respectively, about 1800 and 50–20, if the intensity of the main line is set as 100,000. As in the polonium case, if the particle groups come from the nucleus as all experiments have indicated, the ordinary alpha-decay theory is in serious disagreement with the experiments, for the theoretical intensity varies with energy much more rapidly than the observed intensity. Therefore, a mechanism other than a simple penetration through the static potential barrier may be needed. Attempt has been made to explain these results by assuming a strong interaction between the outgoing particle and the rest of the nucleus. This interaction may imply a transfer of kinetic energy from the particle to the residual nucleus, which will then make the decay probability appear much larger. The total probability of decay and the resultant excitation of the nucleus are discussed in terms of this tentative mechanism.

1. INTRODUCTION

MORE than a year ago we found a series of weak alpha-particle groups[1] in the energy region below the polonium main alpha-ray line. If these alpha-particle groups are assumed to come from within the polonium nuclei, as all experiments have indicated, leaving the lead nuclei in different excited states, they may be then correlated with the gamma-rays from Po. In general the intensities and energies of these groups are found to be of the similar order of magnitude to those of the gamma-ray lines from Po as found by Bothe. However, the intensities of these groups are quite out of line with the predictions of the ordinary alpha-decay theory which assumes penetration through a static potential barrier. For this reason it is of interest to study similar effects in other radioactive nuclei which have different main decay periods and different α-particle energies. The present paper reports the results of an examination of the α-particle spectrum of radium.

[1] W. Y. Chang, Phys. Rev. 69, 60 (1946).

II. EXPERIMENTAL

Because of the longer decay period of radium and the activity of its decay products the work with radium is much more troublesome than with polonium. On the one hand, short exposure times require relatively thick sources entailing α-particle straggling. On the other hand, long exposure with thinner sources introduces difficulties caused by background from contamination of the chamber near the source box and from the α-particles from the decay products. A compromise between these evils was necessary.

To prevent contamination of the whole apparatus with emanation the old radon must be driven out before the preparation of the source and the radon developed in the source during

preparation and exposure must be prevented from escaping into the spectrograph.

Since radium is a less noble element electrochemically, it cannot be deposited on a wire by a purely electrolytic method. A combination of electrolytic and chemical methods is generally used for this purpose. An electric current transports the ions of the substance to the cathode, where they are chemically precipitated and under suitable conditions form a coherent deposit on the cathode. On this principle, we have adopted and somewhat modified a method of Hahn and Meitner[2] in preparing our line source of radium.

Two mg of radium bromide (about 95 percent pure) were dissolved in 20 cc of distilled water. The solution was heated continuously for three or four hours in a boiling water bath to drive off the radon gas already generated and to let the corresponding active products decay completely. Two platinum wires about 0.8 mm in diameter and 40 mm long were horizontally immersed in the solution about 5 mm below the solution surface. The solution was then saturated with CO_2 gas until the milky radium carbonate was redissolved (instead of bubbling CO_2 gas through the solution only during deposition). In this way we have sufficient carbonate ions throughout the whole solution for future precipitation and have sufficient acidity (but not too strong) caused by carbonate acid for conducting the electric current. A current of about 20 ma was passed through the solution. Because of the weakness of the acidity there is an extensive alkaline zone around the cathode and in the immediate neighborhood of the cathode the acidity must be smaller than at any other part of the zone because of liberation of hydrogen gas from this part of the solution. The radium carbonate formed in this region would not be dissolved but instead would be deposited on the cathode (presumably partly caused by the remaining velocity toward the cathode of the radium ions). The evolution of the hydrogen gas at the cathode would drive off any radon gas newly formed. In a period of about an hour about $\frac{1}{8}$ to 1/20 mc could be deposited uniformly on the wire. The source was then washed carefully with distilled water and heated gently to red heat in a Pyrex tube. In this way radon was driven off[3] and the deposit made to adhere more firmly to the wire then possibly in non-emanating state. The source prepared in this way was practically free from decay products. Only an extremely small number of the 7-cm alpha-particles were emitted as checked with the alpha-ray counter.

When the solution had no other acidity than that caused by carbonate acid, about 45 volts were required to send the above current through the solution (the two wires were about 2 cm apart). In this case a white uniform coating was formed on the wire. When the solution had traces of hydrochloric acid, the required voltage dropped to two or three volts and under these circumstances a black coating having practically no radioactivity was formed on the wire. Therefore the solution before being saturated with CO_2 must be practically neutral. The source after use could be dissolved in the original solution with very dilute HCl acid. After this the solution had to be gently heated to dryness two or three times before the above procedure was repeated, in order to be sure that the solution was free from acid. The platinum electrodes could not be left in the solution when not in use; otherwise, under the attack of the radiations, platinum would pass into the solution,[4] and this might interfere with the deposition.

The experimental arrangements, i.e., the spectrograph and the disposition of the Lucite chamber slits, etc., were exactly the same as in the experiments on the polonium alpha-particles. The technique of employing the track method to record the alpha-particles was also the same. In each of the experiments the time of exposure was four hours. It may be mentioned again that, in this case as well as in the polonium case, the number of irregular tracks on each plate is, under favorable conditions, negligibly small in the region near the main line and is only a small percentage of the corresponding number of regular tracks in the region further away. From blank

[2] O. Hahn and L. Meitner, Zeits. f. Physik **26**, 161 (1924); F. Tödt, Zeits. f. physik Chemie **113**, 329 (1924).

[3] Only a very small percentage of the radon gas can escape from even an untreated solid radium source, if it is not heated strongly. In our spectrograph the source-box is quite near to the opening connected to the pumping system; hence any traces of radon gas given off can be drawn into the pump almost immediately.

[4] Mme Curie, le Radium **4**, 349 (1907); E. Rutherford, *Radioactive Substances and their Radiations* (Cambridge University Press, England, 1913), pp. 314–315.

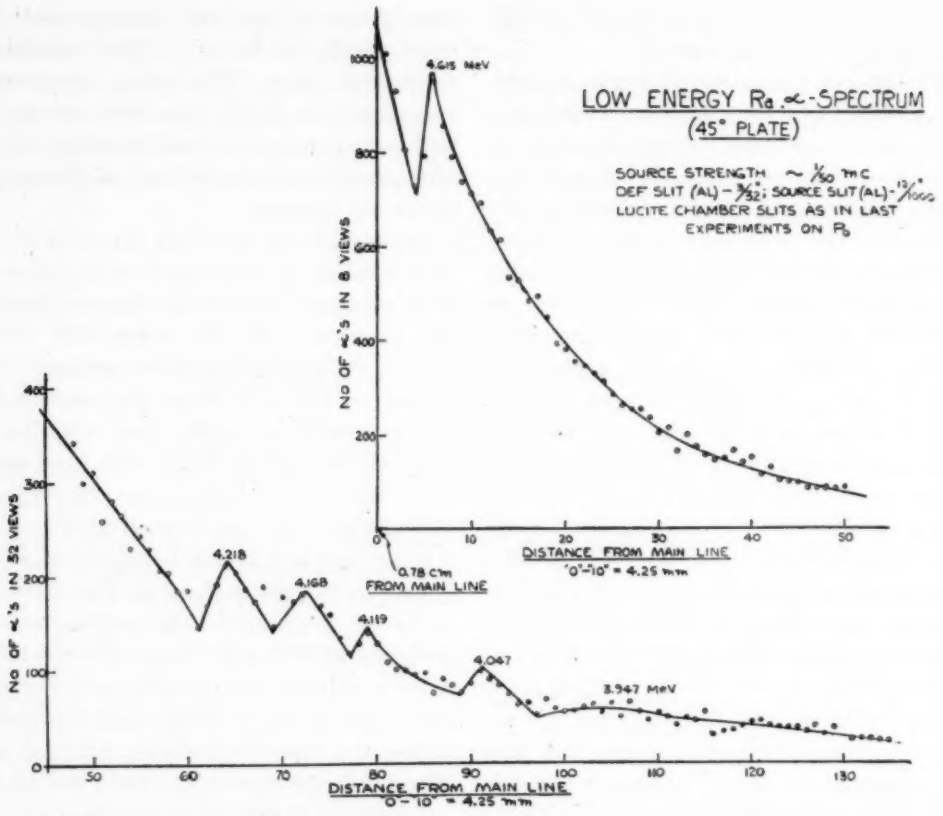

FIG. 1. Low energy-number distribution of the radium alpha-particles. Lower curve is an energy continuation of the upper one. The first group is identifiable with that found by Rosenblum. In the still lower energy region some less prominent groups seem to appear.

experiments the background due to contamination of the chamber was found also negligibly small in comparison with the respective small group intensity.

III. RESULTS

Figure 1[5] shows the low energy distribution of the radium alpha-particles. It was obtained by exposing in the spectrograph plates inclined at 45° to the alpha-particle beam from a radium source of about 1/50 mc. The lower curve is a continuation (in energy) of the upper one. The intensity axes have however different scales; each figure on the upper vertical axis represents track population in 8 views, while that on the lower one is for 32 views. It is seen that near the main group (not shown) is a prominent line, the energy of which is 4.615 Mev and may therefore be identified with the line, 4.612 Mev, found by Rosenblum.[6] Below this group no distinct groups seem to exist until one reaches the lower curve, where four or five groups seem to appear. However, since the peak intensities of these lines relative to the background are not much larger than their respective statistical fluctuations, it cannot be certain that they are real. To be sure about their existence we took another exposure with a stronger source and examined the plates only in this portion of the curve.

Figure 2 represents the energy-intensity distribution so obtained with a source which was about five times stronger than that used for Fig. 1. The discrete groups, as can be seen from the curve, appear here much more distinctly than in Fig. 1;

[5] To be sure that the existence of the discrete groups is not caused by "psychological prejudice," the two halves along the length of the plate were independently examined in two separate periods, i.e., one being examined in the first week while the other in the fourth week. The two curves so obtained are very similar to each other. Curve 1 is the result of these two.

[6] S. Rosenblum and J. Perrin, Comptes rendus **195**, 317 (1932).

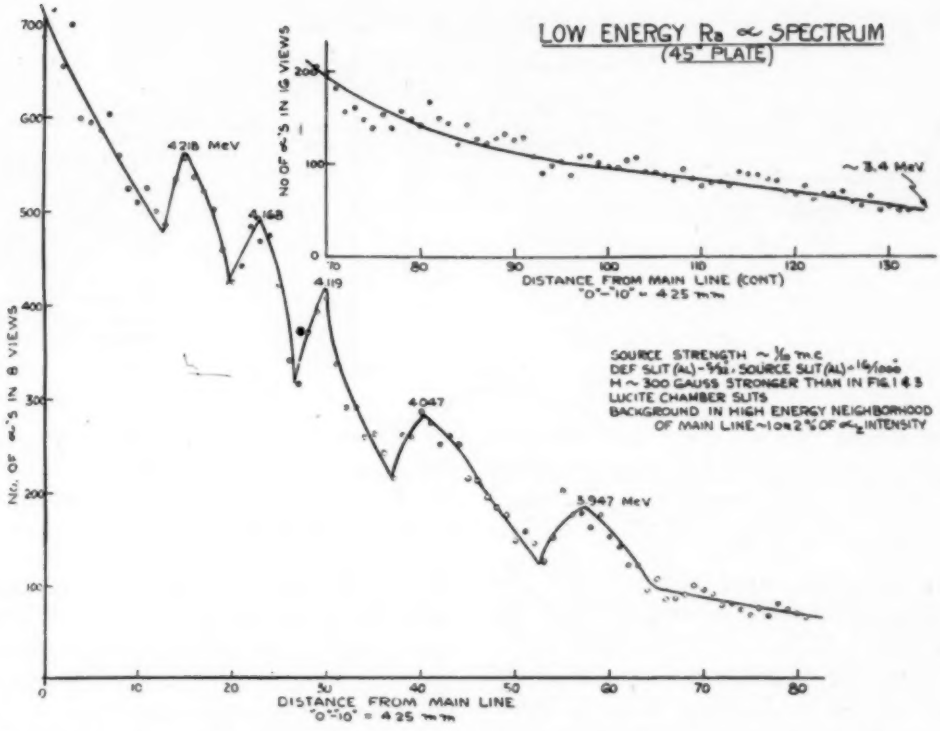
LOW ENERGY Ra α SPECTRUM
(45° PLATE)
NO OF α'S IN 16 VIEWS
~3.4 MeV
DISTANCE FROM MAIN LINE (CONT)
"0"-"10" = 4.25 mm
SOURCE STRENGTH ~ 1/10 mc
DEF SLIT (AL) - 5/32, SOURCE SLIT (AL) = 16/1000
H ~ 300 GAUSS STRONGER THAN IN FIG. 1 & 3
LUCITE CHAMBER SLITS
BACKGROUND IN HIGH ENERGY NEIGHBORHOOD
OF MAIN LINE ~ 10 ± 2 % OF α2 INTENSITY
NO. OF α'S IN 8 VIEWS
4.218 MeV
4.168
4.119
4.047
3.947 MeV
DISTANCE FROM MAIN LINE
"0"-"10" = 4.25 mm

FIG. 2. The last part of the curve in Fig. 1 (and its still lower extension) repeated with a stronger radium source (about five times stronger). The less prominent groups appear more distinctly in this curve. No distinct groups seem to appear in the still lower region.

their peak intensities are several times larger than the respective statistical fluctuations. The positions of the corresponding groups in these two different curves may agree with one another to within about 0.02 Mev. Allowing for the difference in number of the microscopic views counted and in the width of the source and defining slits used, the intensities of any one group in these two curves are about in the same ratio as the relative strengths of the two sources. The microscopic examination has been extended down to a region about 1.5 Mev below the main line. There is no indication of any prominent alpha-particle groups in this region. This is shown in the upper curve of Fig. 2, a continuation of the lower one.

It may be interesting to see if the form of the distribution curve will change after a radium source is left in air for a period of time. Figure 3 was obtained after the same source as used for Fig. 2 was left in air for 30 hours. It is seen that the groups have become broader and less prominent, particularly the lines 4.168 Mev and 3.947 Mev. This must be because of (1) the change in surface condition of the source and (2) the increase in background caused by the growth of the decay products from radium. However, the second effect in this low energy region of the spectrum must be very small, for the energies of the alpha-particles from all the decay products are greater than that of the alpha-particles from radium and experiment shows that the background even in the high energy neighborhood of the radium main line is only about five percent of the α_2 intensity. Therefore, the change in the distribution form may be chiefly caused by the change in surface condition of the source.

As in the polonium case,[1] the energies of these groups have been calculated by comparison with that of the main group, the latter being taken as 4.793 Mev. The relativistic correction has been neglected as before. The results and probable errors are summarized in Table I. The energy value of each group in the table (as well as on the curves) represents the average of two corresponding values from Figs. 1 and 2, which were obtained with the two radium sources. The rela-

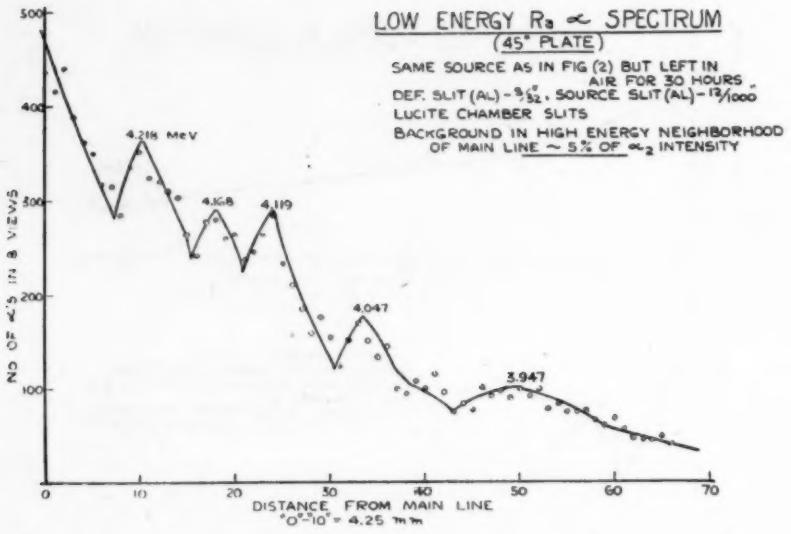
LOW ENERGY R_a α SPECTRUM
(45° PLATE)
SAME SOURCE AS IN FIG (2) BUT LEFT IN AIR FOR 30 HOURS
DEF. SLIT (AL) - 5/52". SOURCE SLIT (AL) - 13/1000"
LUCITE CHAMBER SLITS
BACKGROUND IN HIGH ENERGY NEIGHBORHOOD OF MAIN LINE ~ 5% OF α_2 INTENSITY
4.216 MeV
4.168
4.119
4.047
3.947
NO OF α'S IN 8 VEWS
DISTANCE FROM MAIN LINE
0°-10° = 4.25 mm

FIG. 3. Same portion of the curve showing the weak low energy groups, obtained with the same radium source after it was left in air for about 30 hours. The weak groups appear broader and less prominent.

tive integral intensities were estimated after the general backgrounds were subtracted from the peak intensities, as in the case of polonium alpha-particles, according to the natural trend of the background of the first group in each curve. These are in the last column of Table I, each figure also representing the average of two corresponding values from Figs. 1 and 2. It must be pointed out that in this case the general backgrounds are much larger and the lines are broader than in the polonium case, presumably caused by the straggling of the alpha-particles through a much greater thickness of the source. Therefore, it is more difficult to find the energy positions and particularly to estimate the relative integral intensities. In the latter case the values can be easily off by a factor of two or more, and the listed intensities may perhaps be on the larger side.

IV. DISCUSSION

In the case of polonium we performed several experiments under different experimental conditions, to see if the weak alpha-particle groups did actually come from within the polonium nucleus. From these tests, we are inclined to believe that the polonium alpha-particle groups do have a nuclear or atomic origin. For such an origin further evidence is furnished by a comparison of the radium alpha-ray spectrum with that of polonium. If the weak particle groups were caused by some external effects inherent in the instruments, one would expect the radium alpha-particles to have the same spectrum as (or at least similar spectrum to) the polonium alpha-particles, for the experiments on radium alpha-particles were done under the same conditions as the last experiments on polonium alpha-particles. However, the two spectra of radium and polonium are entirely different from each other as can be seen in Fig. 4. In this figure the horizontal axis represents the group energies relative to that of the main group, and the figures above the vertical lines are the corresponding relative integral intensities. The upper spectrum is for polonium while the lower one is for radium. It is seen that the radium groups so far observed occur only within one-Mev energy difference, whereas several polonium groups occur beyond one-Mev difference. Besides, no coincident groups (i.e. having the same energy positions) have been found.

As in the polonium case, if the particle groups do actually come from the nucleus, the emission of an alpha-particle must leave the residual

TABLE I. Group energy of radium alpha-particles.

Group	Group energy in Mev	$E_n = a_0 - a_n$ in Mev	Relative integral intensity
a_0	4.793	0	10^5
a_1	4.615±0.015	0.178	1800
a_2	4.218±0.015	0.575	45
a_3	4.168±0.015	0.625	33
a_4	4.119±0.015	0.674	35
a_5	4.047±0.015	0.746	25
a_6	3.947±0.015	0.846	18

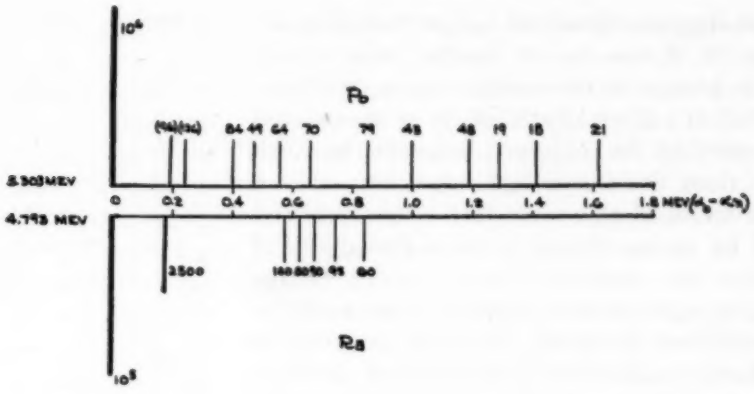

FIG. 4. A comparison of the spectra, respectively, from Po and Ra. They were obtained under the same experimental conditions but are thus shown to be quite different.

nucleus, i.e., $_{86}Rn^{222}$ in the present case, in an excited state. The differences between the main group energy and the individual group energies give the corresponding energy states thus excited of the product nucleus, neglecting the effect of the recoil energy on the excitation energy. These are in the third column of Table I. The gamma-ray line, 0.178 Mev (to be expected from the transition between the first excited state and the ground state), agrees within the experimental error with the line, 0.189 Mev, as observed by Hahn and Meitner.[7] Other gamma-ray lines of much smaller intensities must be expected as a result of transitions from the higher levels to the lower ones. Actual measurements of these lines would certainly be complicated by the presence of the very much stronger lines emitted from the decay products of radium. Moreover, a method of detection for these weak gamma-ray lines must have a sensitivity comparable with that of the track method for the alpha-particles. However, it is fortunate for the possibilities of future experimentation in this direction that a very much stronger (and hence thicker) source can be used for the gamma-ray measurements than for the alpha-particle measurements, on account of the very much higher penetrating power of the gamma-rays.

TABLE II. Theoretical spin changes in different Ra alpha-transformations.

Type of alpha-transformation	$\lambda_b \times 10^{15}$ sec.$^{-1}$	$v_b(1+4/222) \times 10^{-9}$ cm/sec.	$r_{eff} \times 10^{13}$ cm	j_b
a_0	14000	1.547	0.720	9
a_1	252	1.519	0.702	10
a_2	6.3	1.452	0.764	8
a_3	4.6	1.443	0.792	6
a_4	4.7	1.435	0.812	5
a_5	3.5	1.422	0.844	4
a_6	2.5	1.405	0.876	0

[7] O. Hahn and L. Meitner, Zeits. f. Physik 26, 161 (1924).

The same difficulty as in the case of polonium also exists in the present case, when one tries to apply the current alpha-decay theory to the observed energy-intensity relation. In the first place, the unacceptably large spin changes as calculated from the theory in the usual way for the different alpha-transformations here occur again as can be seen from Table II. The values vary from 10 to 0 as the alpha-transformation is changed from the 'normal-normal' one to the 'normal-highest' one. Since both radium and radon have even mass numbers as well as even charge numbers, both of them are expected to have zero spins in their respective ground states; but the spin change in the corresponding transformation as calculated from the theory is 9. Secondly, this disagreement between theory and experiment can be revealed more clearly from the Geiger-Nutall curves as is shown in Fig. 5. The line joining the crosses is for the members of the radium family and can generally be described by the theory. For the convenience of discussion we may take it as a theoretical curve. It is seen that the departure of the observed intensities of the radium groups becomes larger as the energy separation from the main group energy gets larger just as in the case of the polonium groups, and that the two curves except the initial portions for the polonium and radium groups are practically parallel.

One way out of the difficulty mentioned above

may be suggested from the Geiger-Nutall curves in Fig. 5, if one has to ascribe these alpha-particle groups to the nuclear origin. We have seen that at a given kinetic energy of the emitted alpha-particle the observed intensity is much larger than the theoretical value. One can of course speak of this same fact in another way round by saying that at a given probability of emission the observed kinetic energy of the emerging alpha-particle is smaller than would be expected from the theory. Therefore, according to this latter version one may say that a certain amount of the particle's kinetic energy is lost during emission by some process which has a mechanism other than the simple penetration through the static potential barrier. As mentioned once before,[8] it may be reasonable to assume tentatively that the outgoing particle, even when it is almost completely free of the potential barrier, may interact strongly with the residual nucleus. And as a result of this interaction, it may transfer to the latter a certain portion of its kinetic energy beside the recoil energy. The energy so imparted may then become the energy of some internal mode of motion of the residual nucleus, the product nucleus consequently being excited to different quantum states. Hence, at a given probability of the alpha-emission, the observed kinetic energy of the particle should be smaller than would be expected from the alpha-decay theory. In other words, the observed intensity would then appear greater for the observed kinetic energy, as can be seen from the Geiger-Nutall curves in Fig. 5. The experimental results may thus be explained in general terms.

On the basis of the above interpretation, one may be able to say something about the relative order of magnitude of the effects for two different types of nuclei, which emit two different main groups of alpha-particles. Alpha-particles from a decay process of low energy will have to traverse a thicker wall of the potential barrier than those from a decay process of higher energy. Consequently a larger interaction and hence a greater portion of the kinetic energy to be given back to the residual nucleus may be expected. As a result of this the intensity of a weak group (relative to

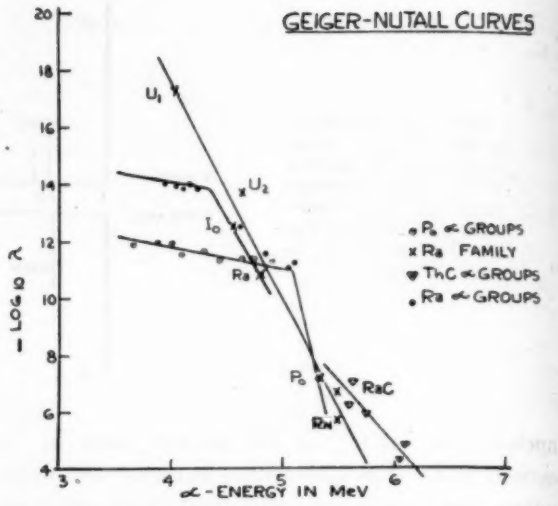

FIG. 5. The Geiger-Nutall curves of the Ra and P_o groups as compared with those for the members of the Ra-family and for the ThC-groups.

the main intensity) at a given energy separation from the main line would appear larger in this case than in the case of higher main group energy. A comparison of the relative intensities of the weak groups of polonium and radium, respectively, at about the same energy separation from the main lines seems to bear out this interpretation.

The probability of the alpha-decay may then be a result of the probabilities of the following three processes, namely (1) the probability of formation of the alpha-particles within the nucleus (according to Bethe),[9] (2) the probability of penetration through the potential barrier (according to Gamow),[10] and (3) the probability apparently contributed by the interaction in the manner as described in general terms above. It is obvious that, on account of the interaction between the emerging alpha-particle and the residual nucleus, the effective form of the potential barrier may be much more complicated than has been usually assumed in the current alpha-decay theory, and it may not be at all a static one. Instead, it may be a complicated dynamical one. Furthermore, for the emission of alpha-particle groups of much lower energy than the main group energy from the same nucleus, the third process has to play a much more important role than the

[8] W. Y. Chang, Phys. Rev. 69, 254 (1946).

[9] H. A. Bethe, Rev. Mod. Phys. 9, 163 (1937).

[10] G. Gamow, *Structure of Atomic Nuclei* etc. (Oxford University Press, New York, 1937).

first two processes in order to give agreement with the experimental results.

As to the excitation of the residual nucleus, we may have two fairly distinct steps: (1) "Internal Excitation"—the alpha-particle may leave the interior of the nucleus with different possible energies, leaving the nucleus in the corresponding "partial excited states," and (2) "External Excitation"—the emerging alpha-particle may interact with the nucleus while it is traversing the potential barrier and consequently it may excite the residual nucleus to different possible modes of motion as already mentioned above. The final likelihood of excitation of the product nucleus may then be the resultant of these two "partial excitations"; indeed, we will expect from the general principles of quantum mechanics that it will be, not the probabilities themselves, but the probability amplitudes for these two processes which will be additive. There seems no reason to believe that alpha-particles will leave the nuclear interior all with one energy, putting the responsibility of exciting the nucleus entirely to the second step. Besides, it may be reasonable to say that step (1) takes place independently whether alpha-particles inside the nucleus already exist as sub-units or whether they are created at the instant of emission. Generally, one may assume in terms of Bohr's idea of many-body model that of the maximum amount of energy available within the nucleus the alpha-particle may leave the nucleus with the whole amount or with a certain definite portion. However, higher states of the nucleus will be excited more easily by the interaction process, if the above explanation ("external excitation") is reasonably correct.

A few exposures have been taken for the alpha-ray spectra of RaC, RaC′, RdTh, ThC, ThC′ etc., and microscopic analysis of the plates has been in progress. We hope that the present difficult problem can be revealed more clearly and definitely, when we get more results for these elements.*

I should like to express my sincere thanks to Professor R. Ladenburg, Professor E. P. Wigner, and Professor J. A. Wheeler for their kind interest and useful discussion in this work, and to Mr. Thomas Coor for his assistance in some of the experiments.

* *Note added to the proof on the integral intensities of the weak alpha-particle groups:* In a previous paper (Phys. Rev. 69, 72 (1946)) we mentioned that the integral intensities of the weak groups were obtained by subtracting the general background which was determined by the natural trend of the first weak group's background in each curve, and that this subtraction of the background is very arbitrary. Recently we have found in the Po case that the values of the intensities (except α_1 and α_2) relative to α_0 will become about $\frac{1}{2}$ to $\frac{1}{3}$ of the corresponding previous values listed in the above mentioned paper, if the area of each small group is measured down only to the minima of the curve. This is because of the fact that the base and hence the area of each group becomes considerably larger as we go further down below the minima. Similarly in the present case of radium the values (except α_1) relative to α_0 will become about $\frac{1}{2}$ of the corresponding values in Table I. Therefore, one may not be surprised if the integral intensities of any small group relative to the main group intensity, as given previously, is off by a factor of three. For comparison with gamma-ray intensities in the case of polonium, reference should be made to a letter by Professor N. Feather in Phys. Rev. 70, 88 (1946).

PHYSICAL REVIEW VOLUME 70, NUMBERS 9 AND 10 NOVEMBER 1 AND 15, 1946

Beta-Rays from H^3

RICHARD J. WATTS† AND DUDLEY WILLIAMS†
Los Alamos Scientific Laboratory, Los Alamos, New Mexico
(Received August 2, 1946)

The upper limit of the β-ray spectrum of H^3 has been re-determined by a method involving the acceleration of β-particles through a thin window into a Geiger counter. The effective window thickness was determined by acceleration of electrons from a hot filament. The value obtained for the upper limit is 11 ± 2 kev.

I. INTRODUCTION

As a result of the extremely low energies involved, many difficulties have been encountered in studies of the β-rays from H^3. However, numerous attempts have been made to determine the upper limit of the β-ray spectrum. The results of these studies are summarized in Table I. It will be noted that most of the previously published results were obtained by methods involving absorption in gases.

In the present study a somewhat different method was employed. This method involved the use of a counter with a thin window, the minimum thickness of which was determined by accelerating electrons from a hot filament until they were just able to penetrate the window. After the window thickness had been determined, the source of β-rays was mounted on a suitable electrode in vacuum near the window of the counter and accelerating or retarding potentials were applied to the electrode until the β-rays were just able to penetrate the window. From the measured window thickness and the potential necessary to stop the β-rays, the upper limit of the spectrum can be determined.

II. EXPERIMENTAL METHOD

The counter windows consisted of several layers of collodion film. The film was prepared by dropping an amyl-acetate solution of collodion upon a water surface and allowing the solvent to evaporate; the resulting film was removed from the water on a metal frame. Although the thickness of different films varied considerably, the average thickness of the films used was approximately 0.07 mg/cm². In preparing the counter window the films were supported on a brass plate in which holes approximately 1 mm in diameter had been drilled. These holes were confined to a circular area of $\frac{1}{2}''$ diameter on the plate; the drill holes were spaced in such a manner as to give the area transparency of more than 50 percent. When supported in this manner, four layers of film could usually withstand atmospheric pressure. However, eight layers were used in the window employed in the work described below.

In determining window thickness, electrons from a tungsten filament were accelerated toward the brass plate supporting the window and electrons passing through the window were collected by an electrode biased positively with respect to the brass support. It was found to be desirable to have the window mounted between the brass supporting plate and a coarse copper gauze grounded to the plate. Plate and collector currents were read from galvanometers of the appropriate sensitivity.

The high voltage supply consisted of a 10-kv bank of dry cells and a 10-kv electronic supply. These supplies were arranged in such a manner as to give a range of potentials from $+20$ kv to -20 kv.

In Fig. 1 is given a typical set of data on the thickness of the window. It will be noted that at 12 kv the electrons begin to penetrate the window. As the accelerating potential is increased, more and more electrons pass through. These data were reproduced several times under somewhat different conditions of filament current, and it is believed that the minimum thickness is 12.0 ± 0.5 kv. However, for large plate currents, the results were more erratic than those shown in the figure. The dotted curve in the figure shows the collector current when the brass supporting plate was introduced without a collodion window; this curve was obtained with a low filament

† Now at Ohio State University, Columbus, Ohio.

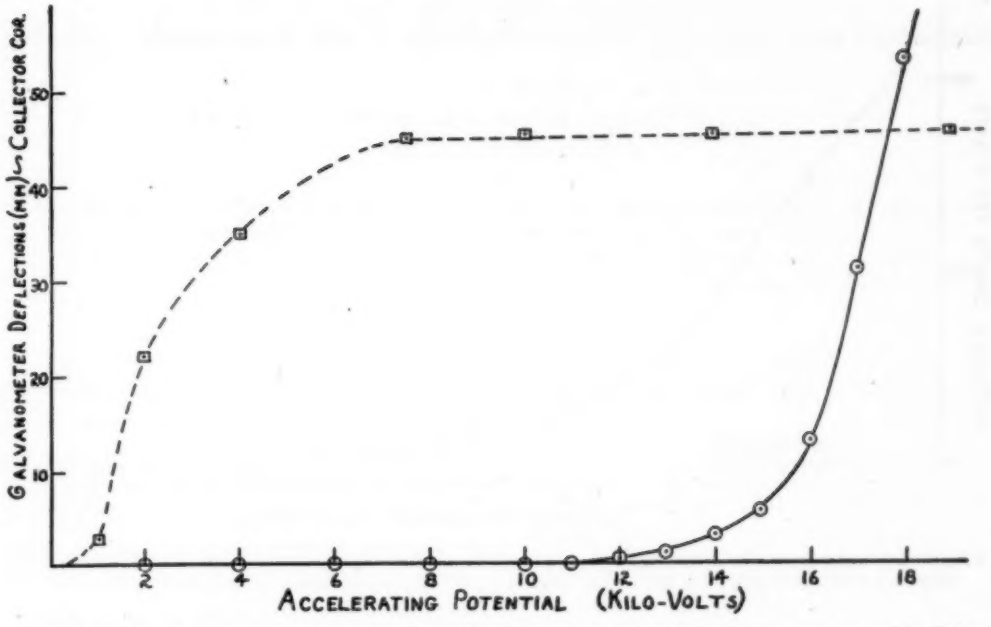

FIG. 1. Collector current as a function of accelerating voltage. Solid curve: Current transmitted by window. Dotted curve: Current transmitted by perforated brass support without window (at lower filament current).

TABLE I. Previous studies of H^3 beta-rays.

Investigators	Method	Upper limit kev	Reference
Libby and Lee	Magnetic	13±5	Phys. Rev. **55**, 245 (1939)
Alvarez and Cornog	Ion pairs per unit volume of gas	18*	Phys. Rev. **57**, 248 (1940)
O'Neal and Goldhaber	Range in argon-alcohol mixture	15±3	Phys. Rev. **58**, 574 (1940) Phys. Rev. **60**, 359 (1941)
Brown	Range in helium	9.5±2	Phys. Rev. **59**, 954 (1941)
Nielsen	Droplets in cloud chamber	14.5±1 (11.7)*	Phys. Rev. **60**, 160 (1941)

* Values obtained on Fermi theory from observed value for mean energy.

current. In both examples shown the plate current was emission limited.

In obtaining the data on the H^3 β-rays, a long counter with a 0.001″ tungsten wire as the high voltage electrode was used. The gas employed was argon at atmospheric pressure. This argon was allowed to flow through a flask containing absolute alcohol. With a sufficiently high voltage, satisfactory performance as a fast Geiger counter was attained. The brass plate supporting the window was mounted in a port in the side wall of the counter. This brass plate with a wax seal also served to seal one end of the glass vacuum system in which the β-ray source was mounted. The pressure in the vacuum system at all times was 10^{-5} mm of mercury or less.

The source was prepared by R. M. Potter and consisted of a thin layer of aluminum oxide hydrated with water containing $H_2{}^3O$. In the preparation of the source, a freshly polished aluminum disk $\frac{3}{4}$″ in diameter was heated to 600°C in an atmosphere of oxygen. After the disk had cooled in vacuum, water vapor containing $H_2{}^3O$ was admitted to the system and was allowed to react with the thin oxide coating of the disk. Sources prepared in this manner proved satisfactory. The water in the hydrated oxide coat showed no appreciable tendency to be removed by subsequent pumping.

The aluminum disk supporting the source served as an electrode to which accelerating and retarding potentials could be applied. The disk was mounted approximately $\frac{1}{2}$″ from the brass plate supporting the window. Previous tests had

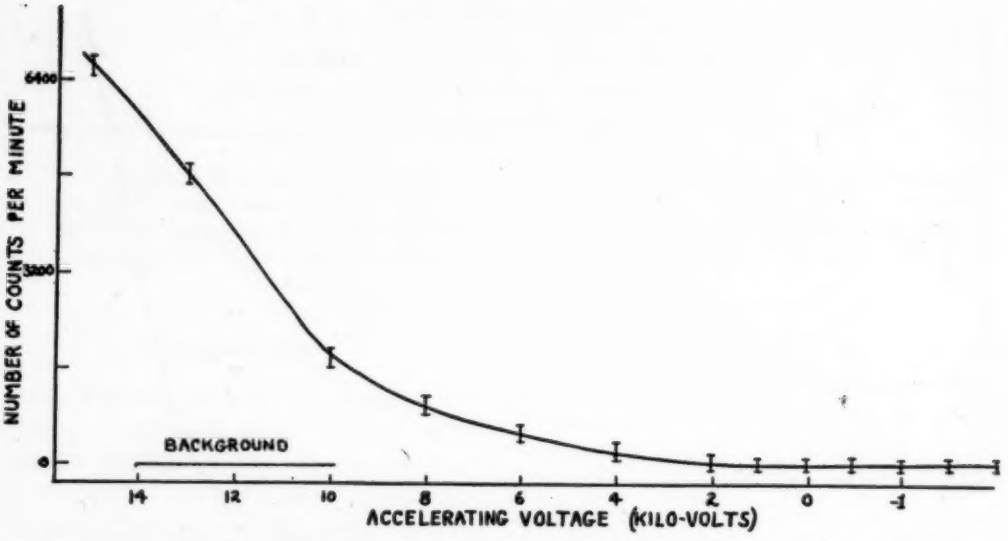

FIG. 2. Counting rate above background as a function of the acceleration voltage. The limits of error shown for the counting rate are three times the probable error. Background: 2133±20 c/min.

revealed no spurious effects in the counter when an uncoated brass disk had been mounted similarly and subjected to accelerating potentials. In obtaining the β-ray data, a scale-of-64 circuit and a mechanical register were employed. Data were taken for three-minute intervals at various accelerating potentials and the background observed for zero accelerating potential was checked for three minutes between each observation interval. The background was remarkably constant throughout the entire period during which measurements were in progress.

The observed counting data are shown in Fig. 2. It will be noted that the counting rate is high for large accelerating potentials and becomes indistinguishable from the background when the accelerating potential is reduced to 1 kv. Further reduction in accelerating potential is without observable effect, although it is possible that the use of a stronger source might have yielded more accurate data on this point. However, it is believed that the observed end point is within ±1.5 kv of the true value.

III. DISCUSSION OF RESULTS

Taking the observed value for minimum window thickness as 12 kv and the accelerating potential necessary for penetration as 1 kv, one is led to a value of 11 kev for the upper limit of the β-ray spectrum of H^3. With the worst possible combination of errors, the limits can be set as 11±2 kev.

This value is somewhat below the value of 15±3 kev obtained by O'Neal and Goldhaber and above the value 9.5±2 kev reported by Brown. However, in both cases the extreme limits of error overlap the values obtained in the present study. The value 14.5±1 kev Nielsen obtained by linear extrapolation is definitely higher than the present results; however, the value for the upper limit obtained on the basis of the Fermi theory from Nielsen's value of 6.5 kev for the mean energy is 11.7 kev, a value in excellent agreement with the present results.

In connection with the results obtained in the present work, one perhaps serious weakness should be noted especially. The results are based on a series of careful measurements with a single counter window, and the writers feel that if sufficient time had been available a more accurate value could have been obtained by measurements involving several different window thicknesses. It is also suggested by the writers that a repetition of the present experiment with an electron multiplier in place of the counter would be desirable, since, in this case, a window would not be used and the upper limit could be obtained directly from the retarding potentials.

This work was carried out under contract between the University of California and the Manhattan District, Corps of Engineers, War Department. Publication was assisted by the Department of Physics of the Ohio State University.

PHYSICAL REVIEW VOLUME 70, NUMBERS 9 AND 10 NOVEMBER 1 AND 15, 1946

Secondary Structure in the K Absorption Limit of Germanium Tetrachloride

C. H. SHAW*
Rowland Physical Laboratory, Johns Hopkins University, Baltimore, Maryland
(Received August 2, 1946)

An experimental determination of the fine structure of the K absorption limit of $GeCl_4$ has been made under conditions of high resolving power with the two-crystal spectrometer. Both position and magnitude of the structure were obtained for comparison with the theory of Hartree, Kronig, and Petersen and with their theory as modified by Corson (following paper).

CONSIDERABLE secondary structure appears in the x-ray absorption edges of solids, liquids, and gases within a few volts of the edge. In the spectral region in which work on gases has been done the resolving power on an energy scale must be high if the experiments are to show the natural structure. The photographic spectrometers used for studies of gases have had rather low resolving power, with the result that data have not been gathered near the absorption limit with this equipment.[1,2]

With the development of accurate means of low x-ray intensity measurement, the application of the two-crystal spectrometer became practicable and it was possible not only to determine the position of the fine structure, but to measure its intensity through the absorption limit.[3-5]

The theory of the fine structure as developed by Kronig[6] and Petersen[7] has been applied most rigorously to gaseous $GeCl_4$.[8] This gas was chosen by these authors for several reasons: The absorption limit of germanium is in a convenient x-ray region, the gas is stable and easily handled, the chlorines are sufficiently massive to provide good scattering of the ejected photoelectrons, the molecule is symmetrical, and the Hartree field has been calculated accurately for chlorine.

The present work is a study of the fine structure of the germanium K absorption limit in gaseous $GeCl_4$, and a comparison with theory of both the position and intensity of the fine structure.

EXPERIMENTAL

The double-crystal spectrometer and G-M counter intensity recorder are described in former communications.[4,9] A slight change, however, was made in recording the data. Repeated tests have shown the x-ray intensity to be constant to about two percent over a period of several hours. The remainder of the equipment likewise is stable enough that the spectral distribution curve with absorber in may be obtained and then a determination of the incident radiation made with absorber out. The necessity for moving the rather bulky absorption cell between each reading is thereby eliminated.

A gold target electroplated on a copper target base served as the source of continuous radiation. With the "perfect" calcite crystals of Class I[10] used in these experiments the continuous spectrum at 35 kv and 20 ma gave about 15,000 counts per minute in the G-M counter.

The absorption cell was the in-blown glass window type, with an absorption path of some 7 cm. It was mounted in a thermally insulated envelope in such a way that its temperature could be maintained at about 65°C by a stream of thermostatically regulated air. At this temperature, the vapor pressure of $GeCl_4$ is about 390 mm.[11] To insure that no droplets of liquid were gathered on the cell windows, streams of the warm air were made to play directly on the windows. The temperature of the cell was measured by a thermocouple placed in contact with the cell itself.

* Now at Ohio State University, Columbus, Ohio.
[1] D. Coster and G. H. Klamer, Physica 1, 889 (1934).
[2] T. Drynski and R. Smoluchowski, Physica 6, 929 (1939).
[3] B. Cioffari, Phys. Rev. 51, 630 (1937).
[4] C. H. Shaw, Phys. Rev. 57, 877 (1940).
[5] T. M. Snyder and C. H. Shaw, Phys. Rev. 57, 881 (1940).
[6] R. de L. Kronig, Zeits. f. Physik 75, 468 (1932).
[7] H. Petersen, Zeits. f. Physik 80, 258 (1933).
[8] D. R. Hartree, R. de L. Kronig, and H. Petersen, Physica 1, 895 (1934). Referred to hereafter as HKP.
[9] J. A. Bearden and C. H. Shaw, Phys. Rev. 48, 18 (1935).
[10] L. G. Parratt, Rev. Sci. Inst. 6, 387 (1935).
[11] *International Critical Tables* 3, 232 (1928).

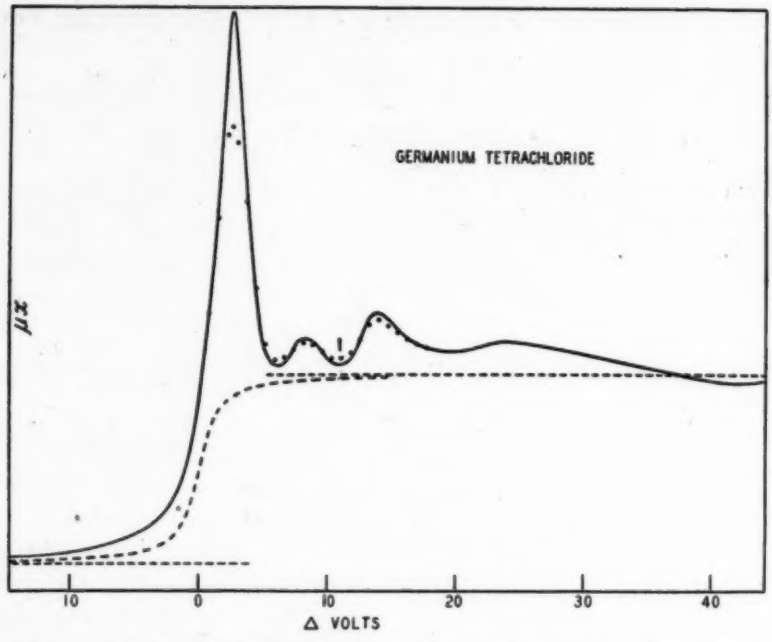

FIG. 1. The absorption coefficient in arbitrary units for the K absorption limits of the free germanium atom (dashed line) and of the germanium atom in $GeCl_4$ (solid line) as a function of energy separation from the edge.

As a final check that the temperature and hence the gas pressure were constant throughout the run, the intensity at a chosen wave-length was observed periodically. Three runs were made with absorber in, and two with absorber out. The intensity of the incident radiation varied with wave-length considerably, because of emission lines from the gold target. Calibrated aluminum absorbers were used to reduce the intensity when the counting rate rose above the linear region of the counter.

Absorption of x-rays in the windows of the cell was measured with the $GeCl_4$ frozen out by air cooled to dry ice temperature.

Former work has shown that at this wave-length the correction for second-order radiation from the target is unnecessary.[12]

RESULTS

The absorption coefficient as a function of energy as shown in Fig. 1 was obtained as follows: The two experimental curves of incident intensity and transmitted intensity as a function of wave-length were plotted and the average curve in each case drawn through the experimental points. The necessary corrections for counter base line and absorption in windows were made on these curves, and the logarithm of the quotient of the curves was taken. The dots in Fig. 1 represent this curve where it differs from the solid line which was obtained after correction of the data for the diffraction pattern of the spectrometer crystals.[10] The short vertical line indicates the estimated experimental error. Figure 1 shows experimental results to 40 volts from the absorption edge. The remainder to 180 volts is shown in Fig. 1 of the succeeding paper by E. M. Corson.

Kronig's theory gives the relation between the absorption coefficient of an atom bound in a molecule to that of the free atom. In order to compare experiment with theory, correction must be made for the absorption by the chlorines in the $GeCl_4$. This is most readily accomplished by using the experimental values of the absorption jump as determined by S. J. M. Allen[13] to locate the germanium absorption base line. The absorption jump for germanium was interpolated to be 7.95 from the data given for adjacent

[12] W. W. Beeman and H. Friedman, Phys. Rev. 56, 392 (1939).

[13] Compton and Allison, *X-Rays in Theory and Experiment* (D. Van Nostrand Company, New York, 1934), pp. 804, 805.

atomic numbers. The base line for germanium absorption is the abscissa of Fig. 1.

Since no GeH_4 was available, it was not possible to determine the shape of the absorption edge for the germanium atom directly, but there is no reason to expect that it would be much different from that for the bromine or krypton atom. On the assumption that the true absorption edge width for the germanium atom is 2.10 volts, the average of those for bromine and krypton,[4] the dashed curve in Fig. 1 was constructed. The relative positions of the absorption edges were fixed arbitrarily. It is obvious that the large absorption peak introduces uncertainty in the position of the edge. In fact if a shift of the initial rise for the molecule of about 6 volts toward lower energies were assumed, the discrepancy between experiment and theory for the major peak intensity (following paper) disappears without very much affecting the remainder of the structure. Had GeH_4 been available, a measure of the shift would have been made experimentally.

Because of the high resolving power, structure appears which has not been detected previously. This structure, of finer detail than the remainder, appears within some 15 volts of the absorption edge.

The ratio of the absorption coefficient of the germanium atom in $GeCl_4$ to that of the free atom is given in Fig. 1 of the following paper to an ejection energy of 180 volts, together with the theoretical results of HKP and the theoretical modification of Corson. Experiment and theory agree for the position of the fine structure from 80 to 180 volts. In contrast with the results of Coster and Klamer[3] the experimental and predicted positions of the absorption minimum α fail to coincide by practically 20 volts. A decrease in resolving power would have the effect of shifting the observed absorption minimum α to larger voltages, which would account for these authors' better agreement with theory.

The following paper reconsiders the Kronig-Petersen theory in the light of different assumptions for the distribution of the chlorine atoms in the molecule.

The author is indebted to the Chemistry Department of Cornell University for the germanium tetrachloride and to Professor J. A. Bearden for the use of his equipment.

PHYSICAL REVIEW VOLUME 70, NUMBERS 9 AND 10 NOVEMBER 1 AND 15, 1946

The Theory of the Fine Structure of X-Ray Absorption Limits in Polyatomic Molecules†

E. M. CORSON*
Rowland Physical Laboratory, Johns Hopkins University, Baltimore, Maryland
(Received August 2, 1946)

The theory of the fine structure of x-ray absorption limits in polyatomic molecules is developed in a form which takes molecular configuration into account, and it is found that the Petersen formula represents a limiting case. The fine structure of the *K*-absorption limit is calculated for several molecular models, in particular that of Ge in $GeCl_4$, for which comparison is made with the previous calculation of Hartree, Kronig, and Petersen, and the newer experimental results obtained by Shaw.

INTRODUCTION

X-RAY fine structure, which in the case of polyatomic molecules may extend over a region of several hundred volts on the high frequency side of the edge, was first explained by Kronig[1] on the basis of the interference between the direct wave representing the ejected photoelectron, and the components scattered by the partner atoms. This interference modifies the amplitude of the wave, and thereby the transition

† This article is part of a dissertation submitted to the Board of University studies of the Johns Hopkins University in conformity with the requirement for the degree of Doctor of Philosophy.

* Since 1943, Research Physicist, The Electrometallurgical Company. At present on leave of absence at The Institute for Advanced Study, Princeton, New Jersey.

[1] R. De L. Kronig, Zeits. f. Physik **75**, 468 (1932).

probability, with the result that the absorption coefficient increases or decreases as the interference is constructive or destructive.

The direct problem involves certain difficulties, both with respect to the physical picture which one must consider, and the mathematical formulation. Therefore, instead of calculating the Einstein absorption coefficient $B_{jj'}$ directly, Kronig[1] considered the inverse process, i.e., the emission of a photon when an electron is captured by an atom with an empty K-level, which amounts to the simpler problem of calculating $A_{j'j}$, where

$$A_{j'j}=\frac{8\pi h\nu^3_{j'j}}{c^3}B_{j'j}=\frac{64\pi^4\nu^3_{j'j}}{3hc^3}$$
$$\times\{|M_x(j'j)|^2+|M_y(j'j)|^2+|M_z(j'j)|^2\} \quad (1)$$

in the usual notation. The problem is further simplified by calculating not the absorption coefficient itself, but the absorption coefficient ratio $\chi(W)$, namely, the ratio of the absorption coefficient for the atom in question, when bound in the molecule to the absorption coefficient of the same atom when free. This device achieves a twofold simplification, in that it avoids an explicit representation of the final state, the K-level in question, permitting a symbolic treatment, and eliminates arbitrary constants in making comparison with experiment.

In this picture of the inverse process, it is readily evident that the probability of absorption of the electron in the K-level, with accompanying photon emission, is dependent upon the resultant amplitude at the atom in question, which varies with the phase difference between the direct and scattered electron waves. The phase difference depends upon the following factors: (1) the interatomic distance ρ, (2) the energy W of the electron, (3) the angle θ between the axis of the atom-pair considered and the incident wave-normal, (4) the phase difference δ_l between the asymptotic solutions

$$R_0\sim\sin\left(Kr-\frac{l\pi}{2}\right);\quad R_1\sim\sin\left(Kr-\frac{l\pi}{2}+\delta_l\right)$$

of the equation

$$\frac{d^2R}{dr^2}+\left[K^2-\frac{8\pi^2m}{h^2}V(r)-\frac{l(l+1)}{r^2}\right]R=0 \quad (2)$$

for the field free case, and when $V(r)$ corresponds to the field of the scattering partner atom.

For the diatomic case Kronig[2] obtained

$$\frac{A_{j'j}(\text{bound})}{A_{j'j}(\text{free})}=|1+q\cos\theta|^2+|q\sin\theta|^2$$
$$=1+qq^*+(q+q^*)\cos\theta \quad (3)$$

and

$$\chi(W)-1=\tfrac{1}{2}\int_0^\pi[qq^*+(q+q^*)\cos\theta]\sin\theta d\theta, \quad (4)$$

where $q=C(\rho,\theta)e^{i\tau(1-\cos\theta)}/\rho$ in which $C(\rho,\theta)$ is the amplitude of the scattered spherical wave, and $\tau=2\pi\rho(2mW)^{\frac{1}{2}}/h$ or $(2W)^{\frac{1}{2}}\rho$ in atomic units.

To obtain $\chi(W)$ explicitly, q must be evaluated. Using a technique similar to that developed by Faxen and Holtsmark[3] in another connection, Petersen[4] obtained

$$q_s=\sum_{l=0}^{\infty}(2l+1)\sin\delta_l[(-1)^lf_{-l-1}(\tau)+if_l(\tau)]$$
$$\times P_l(\mu_s)\exp\left[-i\left(2\pi\alpha\rho\mu_s-\delta_l-\frac{l\pi}{2}\right)\right] \quad (5)$$

where $f_l(\tau)=(\pi/2\tau)^{\frac{1}{2}}J_{l+\frac{1}{2}}(\tau)$; $\alpha=(2mW)^{\frac{1}{2}}/h$;

$$\mu_s=\cos\theta_s,$$

and

$$\chi_s(W)-1=\sum_{l=0}^{\infty}\{(2l+1)\sin^2\delta_l[f_{-l-1}^2+f_l^2]$$
$$+2\sin\delta_l[(-1)^lf_{-l-1}\sin\delta_l+f_l\cos\delta_l]$$
$$\times[(l+1)f_{l+1}-lf_{l-1}]\}. \quad (6)$$

Corresponding to Eqs. (3) and (4) Petersen[5] found in the polyatomic case

$$1+\sum_s[q_sq_s^*+(q_s+q_s^*)\cos\theta_s]$$
$$+\sum_{s\neq t}\sum(q_sq_t^*+q_s^*q_t)\cos(\theta_s-\theta_t)$$
$$=A_{j'j}(\text{bound})/A_{j'j}(\text{free}), \quad (7)$$

$s, t=1, 2, \cdots n$, where n is the number of partner atoms (e.g., $n=4$ for $GeCl_4$) and

$$\chi(W)-1=\sum_s[\chi_s(W)-1]=n[\chi_s(W)-1] \quad (8)$$

under the assumption that the terms in the

[2] R. de L. Kronig, Zeits. f. Physik **75**, 468 (1932).
[3] H. Faxen and J. Holtsmark, Zeits. f. Physik **45**, 307 (1927).
[4] H. Petersen, Zeits. f. Physik **80**, 258 (1933).
[5] H. Petersen, Dissertation. Groningen Arch. Neerl **14**, 165 (1933).

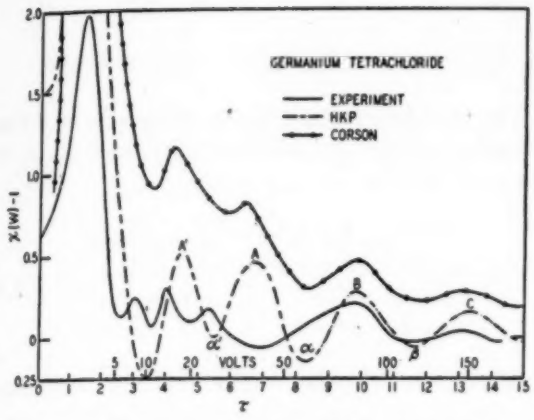

FIG. 1. $\chi(W)-1$ as a function of the energy separation from the absorption edge in units of $\tau=2\rho W^{\frac{1}{2}}$. The maximum ordinate for the H.K.P. curve is 9.2, while that for the author's is 12.5.

double sum, and the angular interdependence, may be neglected in Eq. (8).

GERMANIUM TETRACHLORIDE

Hartree, Kronig, and Petersen[6] (referred to as H.K.P.) calculated the fine structure for the K-absorption of Ge in $GeCl_4$, assuming $\chi(W)-1=4[\chi_a(W)-1]$ with the above-mentioned restrictions. Their result was considered in fairly good agreement with the experiments of Coster and Klamer,[7] but more recent and accurate experiments performed by Shaw[8] indicate that there is considerable disagreement between theory and experiment both as to positions of maxima and minima, and the general character of the $\chi(W)-1$ curve from about 100 volts down to the edge. (See Fig. 1.)

Among the several factors which might contribute to this discrepancy perhaps the most obvious is the assumption of angular independence, which was made in deriving Eq. (8). This amounts to saying that all molecules with the same interatomic distances and number of atoms will give the same result for $\chi(W)-1$ regardless of structure. This can hardly be the case, and in the following $\chi(W)-1$ is calculated, taking molecular structure into account.

CALCULATIONS FOR $GeCl_4$

According to Wierl[9] the Cl-atoms are located at the apices of a regular tetrahedron, with the Ge-atom at the center and $\rho_{Ge-Cl}=2.10$A.

The immediate problem is to obtain the $\cos\theta_s$ where the angles are those between the unit vectors to the four Cl-atoms and the incident wave normal, in a form which will automatically satisfy the constraints imposed by the model, and facilitate integration.

The most convenient choice of body fixed axes is the set of symmetry axes, and relative to these the unit vectors to the four Cl-atoms are

$$\begin{aligned} r_1&=\frac{1}{\sqrt{3}}(i+j-k),\\ r_2&=\frac{-1}{\sqrt{3}}(i+j+k),\\ r_3&=\frac{1}{\sqrt{3}}(-i+j+k),\\ r_4&=\frac{1}{\sqrt{3}}(i-j+k). \end{aligned} \tag{9}$$

Relative to wave axes whose Z' direction is that of the wave normal, and whose origin coincides with that of the symmetry axes, the same unit vectors are

$$\begin{aligned} r_1&=(\sin\theta_1\cos\varphi_1 i'+\sin\theta_1\sin\varphi_1 j'+\cos\theta_1 k'),\\ r_2&=(\sin\theta_2\cos\varphi_2 i'+\sin\theta_2\sin\varphi_2 j'+\cos\theta_2 k'), \end{aligned} \tag{10}$$

etc.

The most convenient specification of direction cosines between the two systems of axes is by means of Euler's angles. In which case, the usual relations are:

$$\begin{aligned} i&=(\cos\theta\cos\psi\cos\varphi-\sin\varphi\sin\psi)i'-(\cos\theta\cos\varphi\sin\psi+\sin\varphi\cos\psi)j'+\sin\theta\cos\varphi k',\\ j&=(\cos\theta\cos\psi\sin\varphi+\cos\varphi\sin\psi)i'+(\cos\psi\cos\varphi-\cos\theta\sin\varphi\sin\psi)j'+\sin\theta\sin\varphi k',\\ k&=-\cos\theta\cos\psi i'+\sin\psi\sin\theta j'+\cos\theta k'. \end{aligned} \tag{11}$$

[6] D. R. Hartree, R. de L. Kronig, and H. Petersen, Physica **1**, 895 (1934).
[7] D. Coster and G. H. Klamer, Physica **1**, 890 (1934).
[8] C. H. Shaw, Phys. Rev. **70**, 643 (1946).
[9] R. Wierl, Ann. d. Physik **8**, 521 (1931).

From these relations it follows with $\mu=\cos\theta$:

$$\cos\theta_1=\frac{1}{\sqrt{3}}[(1-\mu^2)^{\frac{1}{2}}(\cos\varphi+\sin\varphi)-\mu],$$

$$\cos\theta_2=\frac{-1}{\sqrt{3}}[(1-\mu^2)^{\frac{1}{2}}(\cos\varphi+\sin\varphi)+\mu],$$

$$\cos\theta_3=\frac{-1}{\sqrt{3}}[(1-\mu^2)^{\frac{1}{2}}(\cos\varphi-\sin\varphi)-\mu], \tag{12}$$

$$\cos\theta_4=\frac{1}{\sqrt{3}}[(1-\mu^2)^{\frac{1}{2}}(\cos\varphi-\sin\varphi)+\mu].$$

The Legendre polynomials $P_l(\cos\theta_s)$ $(s=1, 2, 3, 4)$ will also be required and for this purpose we consider the addition theorem for spherical harmonics.

$$P_l(\cos\gamma)=P_l(\cos\theta)P_l(\cos\theta')+\sum_{m=1}^{l}\frac{(l-m)!}{(l+m)!}P_l^m(\cos\theta)P_l^m(\cos\theta')\times[e^{im(\varphi-\varphi')}+e^{-im(\varphi-\varphi')}],$$

where

$$\cos\gamma=\sin\theta\sin\theta'\cos(\varphi-\varphi')+\cos\theta\cos\theta'.$$

The relations for $\cos\theta_s$ are of this form if the following values are assigned to θ' and φ', with $\cos\lambda=1/\sqrt{3}$. For:

$$\begin{array}{lll}\cos\theta_1, & \theta'=\lambda+\pi, & \varphi'=-3\pi/4,\\ \cos\theta_2, & \theta'=\lambda+\pi, & \varphi'=\pi/4,\\ \cos\theta_3, & \theta'=\lambda, & \varphi'=3\pi/4,\\ \cos\theta_4, & \theta'=\lambda, & \varphi'=-\pi/4.\end{array} \tag{13}$$

λ above is half the angle between any pair of unit vectors. Then one finds, with $P_l^m(\pm)=P_l^m(\pm 1/\sqrt{3})$

$$P_l(\mu_1)=P_l(\mu)P_l(-)+\sum_{m=1}^{l}\frac{(l-m)!}{(l+m)!}P_l^m(\mu)P_l^m(-)\times[e^{im(\varphi+3\pi/4)}+e^{-im(\varphi+3\pi/4)}] \tag{14}$$

with similar relations for μ_2, μ_3, μ_4.

As an illustration q_1 takes the form

$$q_1=\sum_{l=0}^{\infty}(2l+1)\sin\delta_l[(-)^l f_{-l-1}+if_l]P_l(\mu)P_l(-)e^{-i\gamma}+\sum_{l=1}^{\infty}\sum_{m=1}^{l}(2l+1)\frac{(l-m)!}{(l+m)!}\times\sin\delta_l[(-)^l f_{-l-1}+if_l]P_l^m(\mu)P_l^m(-)[e^{i\{m(\varphi+3\pi/4)-\gamma\}}+e^{-i\{m(\varphi+3\pi/4)+\gamma\}}], \tag{15}$$

where

$$\gamma=2\pi\alpha\rho\mu_1-\delta_l-\tfrac{1}{2}l\pi.$$

From Bauer's formula

$$e^{2\pi i\alpha\rho\mu_1}=\sum_{l=0}^{\infty}(2l+1)i^l f_l P_l(\mu_1) \tag{16}$$

and

$$q_1+q_1^*=2\sum_{l=0}^{\infty}(2l+1)\sin\delta_l P_l(\mu)P_l(-)[(-)^l f_{-l-1}\cos\gamma+f_l\sin\gamma]+2\sum_{l=1}^{\infty}\sum_{m=1}^{l}(2l+1)\frac{(l-m)!}{(l+m)!}\times\sin\delta_l P_l^m(\mu)P_l^m(-)[(-)^l f_{-l-1}(\cos k_1+\cos k_2)+f_l(\sin k_2-\sin k_1)], \tag{17}$$

where

$$k_1=m(\varphi+3\pi/4)-\gamma,\quad k_2=m(\varphi+3\pi/4)+\gamma.$$

Evidently, $\chi(W)-1$ takes the form

$$\chi(W)-1=\frac{1}{4\pi}\sum_{s=1}^{4}\int_{-1}^{1}\int_{0}^{2\pi}[q_s q_s^*+(q_s+q_s^*)\mu_s]d\mu d\varphi. \tag{18}$$

The actual integrations are rather lengthy, and must necessarily be omitted here, except for a brief illustrative sketch of the method for q_1.

The integral

$$\frac{1}{4\pi}\int_{-1}^{1}\int_{0}^{2\pi} q_1 q_1^* d\mu d\varphi$$

is fairly straightforward, and requires no amplification.

For the integral involving $(q_1+q_1^*)\mu_1$ consider just the first summation as given in (18). Then the explicit integral of this part is

$$\frac{2}{4\pi\sqrt{3}}\sum_{l=0}^{\infty}(2l+1)\sin\delta_l P_l(-)\int_{-1}^{1}\int_{0}^{2\pi} P_l(\mu)\{(-)^l f_{-l-1}\cos\gamma+f_l\sin\gamma\}$$
$$\times\left\{\frac{(1-\mu^2)^{\frac{1}{2}}}{2}[(1+i)e^{-i\varphi}+(1-i)e^{i\varphi}]-\mu\right\}d\mu d\varphi, \quad (19)$$

where the value of μ_1 is given in (12). This integral may be written as

$$\frac{2}{4\pi\sqrt{3}}\sum_{l=0}^{\infty}(2l+1)\sin\delta_l P_l(-)[(-)^l f_{-l-1}A^{11}+f_l A_{12}], \quad (20)$$

where

$$A_{12}{}^{11}=\begin{matrix}Re\\Im\end{matrix}\left[e^{-i(\delta_l+l\pi/2)}\int_{-1}^{1}\int_{0}^{2\pi} P_l(\mu)e^{2\pi i\alpha\rho\mu_1}\left\{\frac{(1-\mu^2)^{\frac{1}{2}}}{2}[(1+i)e^{-i\varphi}+(1-i)e^{i\varphi}]-\mu\right\}d\mu d\varphi\right]. \quad (21)$$

The value of $\exp(2\pi i\alpha\rho\mu_1)$ as given in (16) may be inserted, and the integral evaluated using recursion formulae for the ordinary and associated Legendre polynomials. Proceeding in this manner, one finally obtains:

$$\chi(W)-1=4\sum_{l=0}^{\infty}\sum_{m=-l}^{l}(2l+1)\frac{(l-|m|)!}{(l+|m|)!}[f_{-l-1}{}^2+f_l{}^2]\left[P_l{}^{|m|}\left(\frac{1}{\sqrt{3}}\right)\right]^2\sin^2\delta_l\frac{-8}{\sqrt{3}}\sum_{l=0}^{\infty}\sum_{m=-l}^{l}\left[\frac{(l-|m|)!}{(l+|m|)!}\right]$$
$$\times P_l{}^{|m|}(+)\sin\delta_l[(-)^l f_{-l-1}\sin\delta_l+f_l\cos\delta_l]$$
$$\times[(l+|m|)f_{l-1}P_{l-1}{}^{|m|}(+)-(l-|m|+1)f_{l+1}P_{l+1}{}^{|m|}(+)]. \quad (22)$$

The corresponding expression used by H.K.P. is:

$$\chi(W)-1=4\sum_{l=0}^{\infty}(2l+1)\sin^2\delta_l[f_{-l-1}{}^2+f_l{}^2]-8\sum_{l=0}^{\infty}\sin\delta_l[(-)^l f_{-l-1}\sin\delta_l+f_l\cos\delta_l][lf_{l-1}-(l+1)f_{l+1}]. \quad (23)$$

These expressions are plotted with the experimental curve in Fig. 1.

It is evident that, although the new curve maintains much the same trend as the experimental, there is still considerable disagreement at the principal maximum ($\tau=1.2$) as regards amplitude, and a section of the experimental curve between 5 and 7 on the τ scale appears to have been shifted laterally away from the edge by about one unit. In addition, the first minimum of the experimental curve is entirely absent.

A clearer picture of configuration dependence, and the additional factors which contribute to these differences, is obtained if we consider first, several intermediate structures leading to Petersen's limiting case.

Case I

According to Coster and Klamer[10] the molecule $AsCl_3$ is a regular pyramid, with the As-atom at the top, and the three Cl-atoms at equal distances from it. It is estimated that ρ_{As-Cl} is about 2.20A.

[10] D. Coster and G. H. Klamer, Physica 1, 890 (1934).

Proceeding as for $GeCl_4$, but with the changes appropriate to this model, there results

$$\chi(W)-1=3\sum_{l=0}^{\infty}\Big\{(2l+1)\sin^2\delta_l[f_{-l-1}{}^2+f_l{}^2][P_l(-)]^2+\frac{2}{3\sqrt{3}}\sin\delta_l P_l(-)$$
$$\times[(-)^l f_{-l-1}\sin\delta_l+f_l\cos\delta_l][f_{l+1}P^1{}_{l+1}(-)+f_{l-1}P^1{}_{l-1}(-)]$$
$$+2(\tfrac{2}{3})^{\frac{1}{2}}\sin\delta_l P_l(-)[(-)^l f_{-l-1}\sin\delta_l+f_l\cos\delta_l][lf_{l-1}P_{l-1}(-)-(l+1)f_{l+1}P_{l+1}(-)]\Big\}$$

$$+6\sum_{l=1}^{\infty}\sum_{m=1}^{l}\Big\{(2l+1)\frac{(l-m)!}{(l+m)!}\sin^2\delta_l[f_{-l-1}{}^2+f_l{}^2][P_l{}^m(-)]^2+\frac{1}{3\sqrt{3}}\frac{(l-m)!}{(l+m)!}\sin\delta_l P_l{}^m(-)$$
$$\times[(-)^l f_{-l-1}\sin\delta_l+f_l\cos\delta_l][f_{l+1}P_{l+1}{}^{m+1}(-)+f_{l-1}P_{l-1}{}^{m+1}(-)$$
$$-(l+m)(l+m-1)f_{l-1}P_{l-1}{}^{m-1}(-)-(l-m+1)(l-m+2)f_{l+1}P_{l+1}{}^{m-1}(-)]$$
$$+2(\tfrac{2}{3})^{\frac{1}{2}}\frac{(l-m)!}{(l+m)!}\sin\delta_l P_l{}^m(-)[(-)^l f_{-l-1}\sin\delta_l+f_l\cos\delta_l]$$
$$\times[(l+m)f_{l-1}P_{l-1}{}^m(-)-(l-m+1)f_{l+1}P_{l+1}{}^m(-)]\Big\}, \quad (24)$$

where $P_l{}^m(-)=P_l{}^m[-(2/3)^{\frac{1}{2}}]$.

The curve for $AsCl_3$ is not drawn since the only experimental curve available appears to be that of Coster and Klamer[10] which gives the absorption coefficient for $AsCl_3$ rather than the ratio $\chi(W)$, and is therefore unsuitable for comparison with the theoretical result.

The interesting feature of the result for $AsCl_3$ is the relation one finds between $\chi(W)-1$ of $GeCl_4$ and $AsCl_3$, which will be denoted by $\chi(G)-1$ and $\chi(A)-1$, respectively.

$$\frac{\chi(A)-1}{\chi(G)-1}=\frac{3}{4}+8\sum_{l=0}^{\infty}\frac{\sin\delta_l[f_{-l-1}\sin\delta_l+f_l\cos\delta_l][(l+1)f_{l+1}-lf_{l-1}]}{3[\chi(G)-1]}, \quad (25)$$

where ρ AsCl has been taken as 2.10A to simplify the relation.

Petersen's equation would predict just the constant term.

Case II

Imagine a flat model YCl_4, with the Cl atoms located by the unit vectors, $i, j, -i, -j$. This case approaches the physical conditions corresponding to Petersen's average over independent angles. Then

$$\chi(W)-1=4\sum_{l=0}^{\infty}\{(2l+1)\sin^2\delta_l[f_{-l-1}{}^2+f_l{}^2](P_l)^2+2\sin\delta_l P_l[(-)^l f_{-l-1}\sin\delta_l+f_l\cos\delta_l]$$
$$\times[f_{l+1}P^1{}_{l+1}+f_{l-1}P^1{}_{l-1}]\}+8\sum_{l=1}^{\infty}\sum_{m=1}^{l}\Big\{(2l+1)\frac{(l-m)!}{(l+m)!}\sin^2\delta_l[f_{-l-1}{}^2+f_l{}^2][P_l{}^m]^2$$
$$+\frac{(l-m)!}{(l+m)!}\sin\delta_l P_l{}^m[(-)^l f_{-l-1}\sin\delta_l+f_l\cos\delta_l][f_{l+1}P_{l+1}{}^{m+1}+f_{l-1}P_{l-1}{}^{m+1}$$
$$-(l+m)(l+m-1)f_{l-1}P_{l-1}{}^{m-1}-(l-m+1)(l-m+2)f_{l+1}P_{l+1}{}^{m-1}]\Big\}, \quad (26)$$

where the argument of $P_l{}^m$ is 0. The resultant curve is practically identical with the curve obtained by H.K.P.

Case III

The limiting case is obtained when one considers all the scattering atoms placed at one point, and the atom in question at the origin. From Eqs. (9)–(11), it is evident that with the assumed choice of axes this corresponds to locating all the atoms by the unit vector $\mathbf{k}$, in which case one simply obtains a linear superposition amounting to four diatomic molecules.

In each of the cases considered, the inclusion of the constraints imposed by the molecular model has introduced a characteristic parameter of the molecule as argument of the Legendre polynomials in the expression for $\chi(W)$. Thus for the tetrahedral model of $GeCl_4$ the argument is $1/\sqrt{3}$, which is the cosine of half the angle between unit vectors, whereas the flat model (Case II) introduces the cosine of the angle between unit vectors as argument. Comparison of the results for the different models indicates that the configuration dependence has considerable influence on the magnitude of the $\chi(W)$ curve, but does not affect the position of the maxima and minima appreciably.

We note in passing that the configuration dependence of the fine structure may, in certain cases, decide between possible molecular structures, although this application will depend to some extent on how well the remaining discrepancies can be explained.

SOURCES OF ERROR

It need hardly be mentioned that an accurate determination of the phases δ_l with a truly representative field is vital to all such calculations. In the present case, the phases were determined by H.K.P. for the Hartree field of Cl by direct numerical integration of Eq. (2), which in atomic units becomes

$$\frac{d^2R}{dr^2}+\left[2(E-V)-\frac{l(l+1)}{r^2}\right]R=0. \qquad (27)$$

For $E=V=0$, the solution of (27) goes to zero at the origin as r^{l+1} (no nodes), and the value of $\delta_l/\pi(E=0)$ is therefore given by the number of nodes present when $V=V(r)$, i.e., the number of half-waves which pass a fixed radius as V is increased from zero to its final value.

Inasmuch as a bound $(3p)$ wave function in the Cl atom tends asymptotically to the r-axis and has only one node, one might expect $\delta_1(E=0)$ to be 2π. This would certainly be the case if the field used for calculating the wave function for the limiting case of an incident electron of energy $E_i=0$, $l=1$ were the same as that for the bound $(3p)$ electron ($E_b<0$). If Eq. (27) is written in the form

$$\left[-\frac{R''}{R}=2(E-V)-\frac{l(l+1)}{r^2}\right],$$

it is evident that in passing from the bound to the free case ($E_b<0\leq E_i$) the curvature increases with E, and R cuts the axis to form a second node. However, this picture is incomplete because the free electron interacts with one more electron than does a member of the Cl $(3p)^5$ group.

If the potential energies of a bound and free electron be denoted by V_b, V_i, respectively, then V_i-V_b is positive—so that in going from V_b to V_i, the effect on the curvature of the wave function is opposite in direction to that caused by the corresponding increase in E. In the present case, the change in V is greater than that in E, and the radial function for the incident electron has only one node for $E_i=0$.

The huge peak at low energies appears to be caused by this rather unexpected shift of $\delta_1(E=0)$ from 2π to π. On the other hand, we can readily see that the polarization effect will tend to reduce the difference between V_i and V_b so that $\delta_1(E=0)$ may return to 2π.

In the absence of a corrected Hartree field for Cl, we may use the following device to estimate the polarization effect, although it must be emphasized that the result can only be indicative of the trend.

Henneberg[11] showed on the basis of the W.J.B.K. method and the Fermi-Thomas field that, with some restrictions, the phases δ_l for any atom could be obtained from the known values for some one atom. Taking Holtsmark's[12] values of the δ_l for the polarization corrected Hartree field of Kr, it is found that the correction to δ_1(Cl) is of the order of π.

The absence of the first minimum which appears in the experimental curve perhaps is caused

[11] W. Henneberg, Zeits. f. Physik **83**, 555 (1933).
[12] J. Holtsmark, Zeits. f. Physik **66**, 49 (1930).

by this same effect, but more generally the above result emphasizes the fact that the uncorrected Hartree field is not sufficiently accurate for such calculations, particularly at small energies.

The almost uniform vertical displacement of the theoretical curve is probably due to the neglect of the double summation terms in Eq. (7) which take into account the secondary interference between the electron waves scattered by the different partner atoms. It is important to distinguish this effect from the primary interference between the direct wave and the wave scattered by each partner atom taken separately, as described by the single summation in (7), and multiple scattering which is entirely neglected in this treatment.

An exact evaluation of these terms is extremely difficult, but approximate calculation indicates that their contribution will be small, and mainly negative. It would be of interest to obtain a complete expression for these terms since mixed factors such as $f_l f_{l'} \sin \delta_l \sin \delta_{l'} \cos (\delta_l - \delta_{l'})$ will appear, and might affect the positions of maxima and minima to some degree. Physically it is quite clear that the secondary terms $q_s^* q_t$ must be much less important than the terms $q_s q_s^*$ because $q_s q_s^*$ is always positive while $q_s^* q_t$ will change sign, and the factors $q_s^* q_t$ do not attain their maxima simultaneously. It is only necessary to visualize the tetrahedral model of $GeCl_4$ to see that at least one atom of a given pair s, t will be scattering through a large angle, which results in a correspondingly small amplitude.

In the discussion of Case III it was shown that the H.K.P. calculation of $\chi(W)$ is formally equivalent to a superposition of four diatomic molecules, and it is clear that the secondary interference terms cannot be neglected in this limiting case. In fact, all q's become identical, and every term $q_s^* q_t$ is positive and equal to $q_s^* q_s$. If these cross terms are included the first maximum of the H.K.P. curve ($\tau = 1.2$, $\chi(W) - 1 = 9.26$) increases to approximately 50, and the curve is distorted and shifted vertically off the scale of Fig. 1. Starting from this oversimplified model, the scattering atoms may be rearranged in various more complex models, and as the actual physical configuration is approached, the contribution from the secondary terms decreases until the closest approximation to the experimental curve is obtained.

Thus, when the atoms are separated as in Case II, the secondary terms contribute an amount of the order of that due to the primary terms, and the first maximum drops to about half the value found above.

Electron exchange has not been considered because of the additional complication introduced, and the fact that the various approximations, including the several implicit in Kronig's original formulation, would make such considerations of doubtful significance.

CONCLUSION

Figure 1 indicates that the relative amplitudes of Corson's curve agree better with experiment than do those of the H.K.P. curve, which vary too sharply. This is also true of the absolute amplitudes if one takes into account the secondary terms, as indicated in the discussion. However, the most significant result of the present investigation is that the molecular configuration plays an important role in determining the absorption fine structure.

ACKNOWLEDGMENT

Thanks are due Dr. C. H. Shaw, who suggested this investigation, for assistance and encouragement and to Dr. G. H. Dieke for his advice and helpful criticism.

The Isotopic Constitution of Tungsten, Silicon, and Boron

MARK G. INGHRAM
Department of Physics, University of Chicago, Chicago, Illinois

(October 1, 1945)

The isotopic constitutions of tungsten, silicon, and boron have been determined. Five isotopes of tungsten were observed at masses 180, 182, 183, 184, and 186 with abundances of 0.122 percent, 25.77 percent, 14.24 percent, 30.68 percent, and 29.17 percent, respectively. Three isotopes of silicon were observed at masses 28, 29, and 30 with abundances of 92.28 percent, 4.67 percent, and 3.05 percent, respectively. Two isotopes of boron were observed at masses 10 and 11 with abundances of 18.83 percent and 81.17 percent, respectively. Upper limits for the existence of other hypothetical normal isotopes in the immediate neighborhood of the known isotopes are given.

INTRODUCTION

THIS paper is a report on a mass spectrometric study of the isotopes of tungsten, silicon, and boron. This study was undertaken to: verify the existence of the rare mass 180 isotope of tungsten, to make accurate determinations of the isotopic constitution of these elements, and to search the mass numbers in the immediate vicinity of the known isotopes for possible rare isotopes and, if they cannot be detected, to place upper limits for the existence of these hypothetical isotopes.

APPARATUS

The mass spectrometer used in this investigation was a Nier type, 60°, 6-inch radius of curvature, single focusing mass spectrometer.[1] The gas to be analyzed was introduced through a capillary leak to the ionization chamber of the source, and ionized by a 0.5-ma beam of electrons of 85-volts energy. The ions formed were collimated into an ion beam of 2000-volt energy by the collimating plates of the source, and directed normally into a wedge-shaped magnetic field. This magnetic field resolved the ion beam into its various mass components and refocused a beam of one mass component through the collector slit to a collector plate. The collector plate was surrounded by an electron repelling field of 22½ volts, so that secondary electrons formed at the collector plate by positive ion bombardment could not leave that plate. Ion currents were measured by either of two methods: (1) the conventional FP-54 electrometer tube method[2] in which the voltage developed across the input resistor is canceled by an equal and opposite voltage supplied from a Leeds and Northrup type K-2 potentiometer, or (2) the 100 percent inverse feedback method[3] in which the amplifier drives a standard Brown Electronik Strip Chart Recorder so that permanent records of actual peak shapes are obtained. The latter of these methods was used for the major portion of the work here reported, and the first only as a check.

The pumping system consisted of a two-stage, glass, mercury diffusion pump, backed by a Welch Duo-Seal fore pump. A liquid air trap was used between the diffusion pump and the mass spectrometer tube to trap out vapors. The pumping speed of the system at the tube was 2.5 liters per second. The mass spectrometer tube was wrapped with a furnace so that the entire system could be baked out at a temperature of 450°C. With proper precautions this system could be maintained at 1×10^{-7} mm of mercury pressure.

DISCUSSION OF ABSOLUTE MEASUREMENTS

Before proceeding to the results, some of the possible systematic errors which bear on the interpretation of absolute isotopic measurements will be discussed.

Magnetic Field Variation

Either of two basic methods can be used to bring the ion beam of desired mass to focus on the fixed collector. This can be seen by referring

[1] A. O. C. Nier, Rev. Sci. Inst. 11, 212 (1940).
[2] D. B. Penick, Rev. Sci. Inst. 6, 115 (1935).
[3] A. O. C. Nier, E. P. Ney, and M. G. Inghram, to be published.

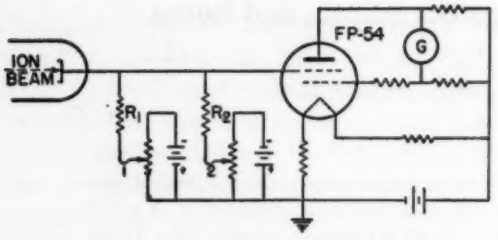

FIG. 1. Circuit used for determining the degree of non-linearity of high resistors in the low voltage range.

to the familiar Eq. (1) which gives the radius of curvature of the ions in a magnetic field.

$$\frac{m}{e}=4.82\times10^{-8}\frac{H^2r^2}{V}. \qquad (1)$$

In this equation m is the mass of the ion in atomic mass units, e is the number of electronic charges on the ion, H is the magnetic field in gauss, r is the radius of curvature of the ions in the magnetic field in cm, and V is the energy of the ions in volts. Thus to bring ions of different m/e to focus on the fixed collector, i.e., fixed r, either H or V must be changed. With the machine used in the present investigation, measurement of the isotopic ratio by changing the ion energy gave, for conditions of poor focus in the source, variations as large as ±20 percent for a 10 percent difference in mass. This variation is explained as caused by a change in efficiency of the source, as the voltage across it is changed. On the other hand, measurements of the isotopic ratio when the ion trajectories were changed by varying the magnetic field varied by less than ±0.5 percent for a 10 percent difference in mass for widely different fields. For this reason, all measurements reported in the present work were obtained by varying the magnetic field to bring the different mass ions to focus on the fixed collector.

To verify that stray magnetic fields in the source region had no influence on the results, isotopic ratios were obtained with and without a 300-gauss magnetic field around the source. The maximum difference observed was one percent in the ratio for a 10 percent difference in mass. Since the stray field from the main magnet was always less than $\frac{1}{10}$ of this test 300-gauss field, it may be concluded that when no source magnet is used the systematic error introduced by stray magnetic fields in the source region should not exceed 0.1 percent of the ratio for a 10 percent difference in mass. In all cases where sufficient ion intensity could be obtained without the use of a source magnet, the magnet was not used.

Ion Measurements

To check possible non-linearities in the ion measurement circuits two methods of ion measurement were used. In using the FP-54 electrometer[2] the voltage developed across the input resistor was cancelled by an equal and opposite voltage supplied by a type K-2 potentiometer, so that the ratio of any two ion beams was determined as the ratio of the voltages supplied by the potentiometer to cancel out those ion currents, With the 100 percent inverse feedback amplifier and the Brown Electronik Strip Chart Recorder. the voltage developed across the input resistor was recorded by the recorder, and the ratio of any two ion currents was determined as the ratio of the two peak heights recorded on the recorder. Within the limits of experimental error, ±0.3 percent, no systematic effect could be observed between the two methods of measurement. The major question remaining in the linearity of the detecting circuits is then the non-ohmic response of the input resistor which is common to both methods of measurement.

Linearity of Resistors

To measure the non-linearity of the high resistors (4×10^{10} ohms) in the low voltage range (0.001 to 10 volts) the circuit shown in Fig. 1 was devised. The operation of this circuit can be understood from the following considerations. If the potentials applied to the points 1 and 2 are zero with respect to ground, and a small ion current sufficient to produce one millivolt across the input resistors is allowed to strike the collector, a deflection D_1 will be observed on the galvanometer. If now a potential of one volt is applied to point 1, and minus one volt to point 2, the potential on the grid of the FP-54 will still be at ground. Now allowing the same ion current to fall on the collector as was used with the potentials of points 1 and 2 at ground, a second deflection D_2 of the galvanometer will be produced. The ratio of D_1 to D_2 will then be the ratio of the effective resistances of the high resistors at

0.001 and 1.00 volts, respectively, across the resistors. By repeating this procedure for other voltages applied to the points 1 and 2, a curve can be drawn for the effective resistance of a set of resistors for any voltage across them. By proper use of three resistors, the effective resistance of a single resistor, with any predetermined voltage across it, can be found. Using this method it was found that most IRC MG-6 resistors are ohmic in the range 0.001 to 10 volts within ± 0.2 percent of their value. Some other resistors exhibited marked non-linearities and polarizations in this range. The measurements reported here were made with resistors which showed no non-ohmic response.

Secondary Electrons

That the errors due to secondary electron emission from the collector plate were negligible can be seen from Fig. 2. This curve is a plot of the current measured by the collector as a function of the voltage supplied to suppress the secondary electrons. This curve shows that below -15 volt less than one percent of the total ion current was caused by secondary electrons. Since $22\frac{1}{2}$ volts was used as the supressor voltage and the potential on the collector plate never changed by more than 0.01 volt in the present measurements, it may be concluded that the secondary electron contribution to the measured ion currents was less than one percent for all measurements here reported. Curves for the variation of secondary electron emission with the mass of the bombarding ion show that very roughly the emission varies by 0.7 times the variation in mass for the surfaces used in these experiments. We may conclude that the systematic error in isotopic ratio due to secondary electron emission should be less than 0.03 percent for a 10 percent difference in mass. This is completely negligible. The importance of suppressing secondary electrons can be seen from the fact that if they had not been suppressed, the error would have been 3 percent in the ratio for a 10 percent difference in mass.

Various Other Possible Errors

Systematic discriminations were looked for that might be caused by the various accelerating and focusing plates in the source region. The maximum variation obtained, with wide changes in the potentials of these plates, when no source magnet was used, was 0.3 percent of the ratio for a 10 percent difference in mass.

In view of possible space charge effects, the ratios were studied as a function of ionizing electron current. The variations observed when the currents were changed by a factor of 5 was less than 0.3 percent of the ratio for a 10 percent difference in mass.

A change of isotopic abundance due to passage of the gas through the leak is another factor which must be considered as a source of systematic error. In the cases of tungsten hexafluoride, silicon tetrafluoride, and boron trifluoride, the maximum change that would be expected in the isotopic ratio would be 1.00 percent, 0.95 percent, and 0.74 percent, respectively. In the operating region, the peak height in the spectrometer varied approximately as the pressure of the gas behind the leak to the 1.4 power. The fractionation of the leak should therefore be appreciably below the maximum.

In the case of the analysis of tungsten by using the gas tungsten hexafluoride, a small systematic error will be introduced if the concentration of the isotopes in the vapor phase is different from the concentration of the isotopes of the solid phase with which it is in equilibrium. The order of magnitude of this error is below a few tenths of one percent. The silicon tetrafluoride and the boron trifluoride were completely in the vapor phase so that no error could be introduced from this effect in these cases. The errors resulting

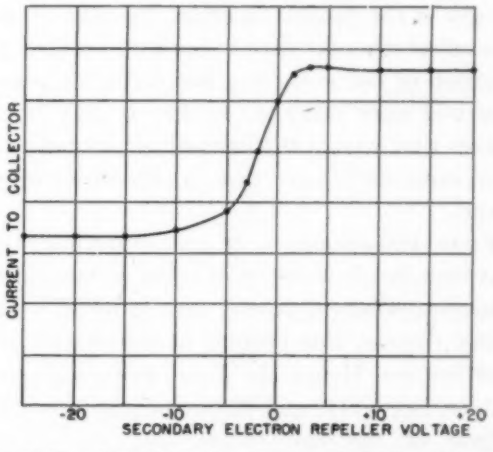

FIG. 2. Graph showing the energy and number of secondary electrons produced by collision of ions of 2000 volts energy with the collector plate.

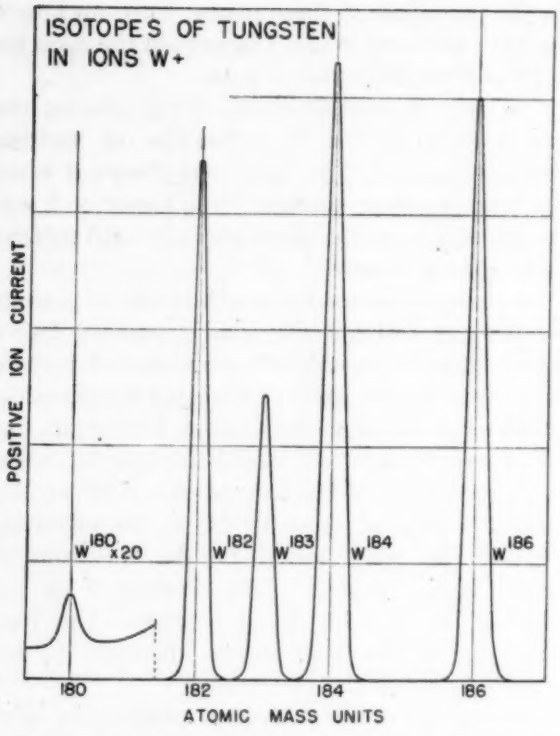

FIG. 3. Recorder tracing of the isotopes of tungsten as observed in the W^+ ion position. The region about mass 180 is recorded at 20 times the sensitivity used for the rest of the tracing.

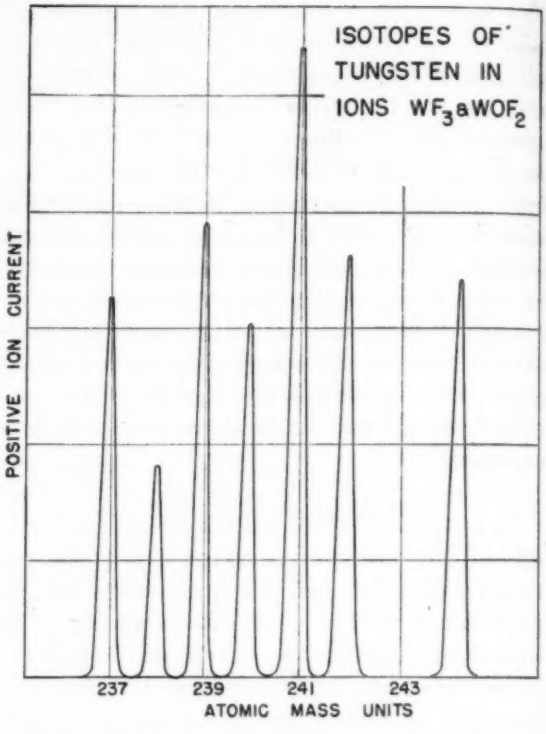

FIG. 4. Recorder tracing of the isotopes of tungsten as observed in the WF_3^+ position. The presence of the compound WOF_2^+ is apparent.

from the chemical preparation of the samples cannot be evaluated, but are undoubtedly less than a few tenths percent.

If the peak shape for peaks of widely differing intensities are not identical, the slit systems could discriminate systematically according to the intensity of the peaks. To check the magnitude of this effect the Si^{28}/Si^{30} ratio was studied as a function of the collecting slit width. The errors observed were random, so that it may be concluded that within 0.2 percent of the ratio there is no error introduced due to differences in peak shape.

From consideration of the systematic error uncertainties it is felt that none of the absolute abundances here reported can be relied upon to better than ± one percent of the abundance of that isotope. Hence the final answers quoted in Tables IV, VIII, and XI, are quoted with the largest of the two errors, i.e., the standard deviation of the actual results or the systematic error uncertainty.

EXPERIMENTAL RESULTS

Tungsten

Tungsten was first studied by Aston[4] using tungsten hexacarbonyl as the source of tungsten. By photographic methods he detected isotopes of mass 182, 183, 184, and 186 with abundances of 22.6 percent, 17.3 percent, 30.1 percent, and 29.8 percent, respectively. Later Dempster[5] working with a spark source discovered a rare isotope of mass 180 and estimated its relative abundance as one percent of the 183 isotope, or approximately 0.17 percent.

In the present investigation the isotopic constitution was studied by using a mixture of WF_6 and WOF_4. Figure 3 shows a curve obtained on the Brown recorder of the tungsten spectrum in the W^+ position, and Fig. 4 shows the same type of curve taken in the WF_3^+ position. The existence of the peaks due to WOF_2^+ is apparent in the latter. Calculations of the isotopic constitution can be made directly from the heights

[4] F. W. Aston, Proc. Roy. Soc. **A132**, 491 (1931).
[5] A. J. Dempster, Phys. Rev. **52**, 1074 (1937).

of the peaks in Fig. 3, and from Fig. 4 by resolving the spectra due to the two compounds. Using these techniques the isotopic constitution of tungsten was determined in the WF_5^+, WF_4^+, WF_3^+, WF_2^+, W^+, WF_2^{++}, and W^{++} positions. The abundances obtained, for the moment neglecting the rare isotope at mass 180, are given in Table I. No accurate determinations were possible in the WF^+ or WF^{++} positions, due to mercury backgrounds which interfere in these positions. Similarly results in the WF_4^{++}, and WF_3^{++} positions were unreliable due to other large interfering impurities.

The data were taken over a three-week period. The consistency of any one run was much better than the comparison between runs. For this reason a direct average, rather than a weighted average, was used in determining the standard deviations given.

The rare isotope of tungsten at mass 180 discovered by Dempster[5] was verified by studying the WF_5^+, W^+, WF_4^{++}, and W^{++} positions. It could not be determined accurately in the other positions due to interference of the WOF_n peaks. The results obtained are tabulated in Table II.

The existence of the rare isotope of tungsten at mass 180 is proved by the facts that, in all of the nine positions studied, a peak was present to about 0.122 percent which could not be accounted for by known impurities. It would be very unlikely that this would have been the case if the peak corresponding to the 180 mass observed had been an impurity. The fact that the mass is lighter than any other mass in the tungsten spectrum shows that it cannot be an impurity in which tungsten is a part. Another proof results from the observation that varying the electron accelerating potentials gave the same appearance potentials for the 180 mass as for the other four isotopes of tungsten. It must therefore be concluded that tungsten has a stable isotope of mass 180.

The regions in the immediate neighborhood of the known isotopes were searched for other possible rarer isotopes. In some cases peaks were found which could correspond to unknown rare isotopes, but in every case a search in the other ion positions showed that these peaks were impurities. Table III gives the upper limits set on the existence of hypothetical isotopes together with the ion position in which this limit was determined. The fourth column of this table gives the tentative mass assignments given the artificially produced radioactive isotopes of tungsten as given by Seaborg.[6]

Thus, the isotopic constitution of tungsten as determined in the present work as compared with those given by Aston and Dempster is given in Table IV. The errors given are the systematic error uncertainties.

Calculating the chemical atomic weight from these abundances using the value of 1.8×10^{-4} for

TABLE I. Abundances of tungsten isotopes other than rare isotope at 180.

Ion studied	% 182	% 183	% 184	% 186	No. of measurements
WF_5^+	26.02	14.22	30.74	29.00	68
WF_4^+	25.80	14.14	30.89	29.17	10
WF_3^+	25.73	14.46	30.54	29.24	12
WF_2^+	25.83	14.34	30.88	29.00	20
W^+	25.76	14.14	30.83	29.26	97
WF_2^{++}	25.57	14.41	30.59	29.41	57
W^{++}	25.87	14.09	30.71	29.44	31
Average	25.80±0.13	14.26±0.14	30.74±0.13	29.22±0.16	

TABLE II. Abundance of W^{180}.

Ion studied	% 180	No. of measurements
WF_5^+	0.119	16
W^+	0.121	16
WF_4^{++}	0.124	16
W^{++}	0.122	25
Average	0.122±0.002	

TABLE III. Upper limit for abundances of tungsten isotopes not found.

Mass No.	Upper limit on existence	Ion studied	Artificial radioactivity[a]
174	0.001%	WF_4^+	
175	0.001	WF_4^+	
176	0.001	WF_4^+	
177	0.001	WF_4^+	
178	0.002	WF_4^+	
179	0.005	W^+	
181	0.01	W^{++}	
		W^{++}	
185	0.01	W^{++}	β^-, 77 day
187	0.02	WF_5^+	β^-, 24 hour
188	0.006	WF_5^+	
189	0.002	WF_5^+	
190	0.002	WF_5^+	
191	0.001	WF_5^+	
192	0.001	WF_5^+	

[a] See reference 6 in text.

[6] G. T. Seaborg, Rev. Mod. Phys. 16, 1 (1944).

the packing fraction of tungsten[7] and the factor 1.000275 in converting from the physical to the chemical atomic weight gives 183.89, which is in good agreement with the chemically determined value of 183.92.

The relative intensities of the various ion fragments observed in this mass spectrometer when WF_6 was bombarded by electrons of 85-volts energy are given in Table V.

Silicon

Silicon was first studied by Aston[8] using the ions formed in SiF_4 gas. He showed with the photographic method that the main isotope had a mass of 28 and that there was a second weak isotope at mass 29. He noted a line at mass 30, but the possibilities of hydrogen compounds made this inconclusive. Later[9] he proved the existence of the mass 30 isotope during his work on zirconium. The latest determination of the isotopic constitution is that of McKellar[10] in which he used photometry on the bands of SiN. He gives the abundances of masses 28, 29, and 30 as 89.6 percent, 6.2 percent, and 4.2 percent respectively. No limits have been set on the existence of other hypothetical normal isotopes of silicon.

The isotopic constitution of silicon was determined in this investigation by studying the SiF_3^+ ions formed by electron bombardment of SiF_4 gas. The other positions are unreliable due to impurities of boron trifluoride, carbon dioxide, and nitrogen. Figure 5 is a recording taken on the Brown recorder of the silicon isotopes in the SiF_3^+ position. Table VI gives the isotopic composition of silicon as determined in this position by the two different measurement techniques. The errors given with the averages are the standard deviations.

Following the method described for establishing lower limits on the existence of rare isotopes of tungsten, the results obtained for silicon are given in Table VII.

The isotopic constitution determined in the

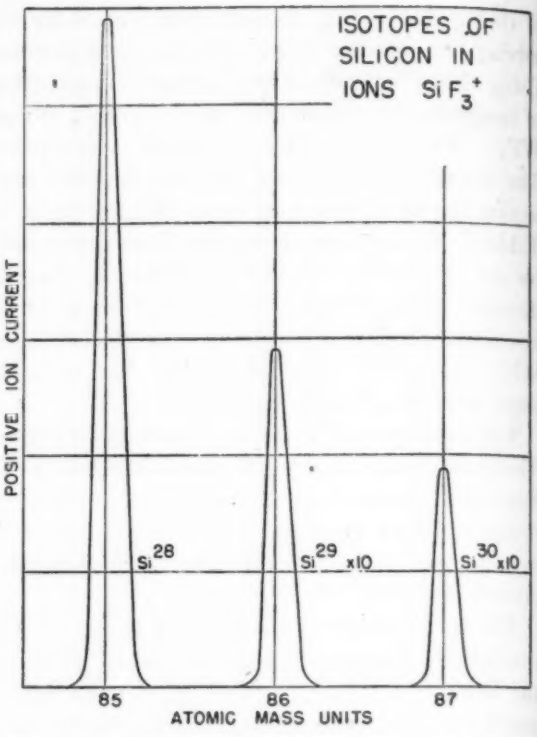

FIG. 5. Recorder tracing of the isotopes of silicon as observed in the SiF_3^+ position. The region about masses 86 and 87 are recorded at ten times the sensitivity used in recording the 85.

TABLE IV. Isotopic constitution of tungsten.

Investigator	%180	%182	%183	%184	%186
Aston	—	22.6	17.3	30.1	29.8
Dempster	~0.17	—	—	—	—
Present work	0.122 ±0.002	25.77 ±0.3	14.24 ±0.2	30.68 ±0.3	29.17 ±0.3

TABLE V. Relative intensities of ion fragments when WF_6 is bombarded by 85 ev electrons.

Ion	Intensity	Ion	Intensity
WF_6^+	0.5	WF_6^{++}	0.5
WF_5^+	100	WF_5^{++}	0.5
WF_4^+	22	WF_4^{++}	20
WF_3^+	32	WF_3^{++}	17
WF_2^+	51	WF_2^{++}	16
WF^+	36	WF^{++}	15
W^+	33	W^{++}	14

TABLE VI. Isotopic composition of Si.

Method	28	29	30	No. of measurements
Recording spectrometer	92.31	4.67	3.02	17
FP-54 Electrometer	92.25	4.68	3.08	10
Average	92.28±0.03	4.67±0.01	3.05±0.03	

[7] A. J. Dempster, Phys. Rev. **53**, 869 (1938).
[8] F. W. Aston, Phil. Mag. **40**, 628 (1920).
[9] F. W. Aston, Phil. Mag. **49**, 1198 (1925).
[10] A. McKellar, Phys. Rev. **45**, 761 (1934).

present work compared with the values of McKellar are given in Table VIII. The errors given are the systematic error uncertainties.

It should be noted that the ratio of the 29 to the 30 obtained in the present work is very close to that obtained by McKellar; the main difference in the two determinations is in the ratio of the two small isotopes to the 28.

Calculating the chemical atomic weight from the abundances using the packing fractions of 4.86×10^{-4}, 4.54×10^{-4}, and 5.68×10^{-4} for the masses 28, 29, and 30, respectively, as given by Pollard[11] and the factor 1.000275 in converting from the physical to the chemical atomic weight gives 28.086 which is in good agreement with the chemically determined value of 28.06.

Boron

Boron was first studied by Aston using the ions characteristic of BF_3 gas.[12] He noted two masses at mass 10 and 11. Since that time there have been several other investigations of the isotopic ratios using photometry methods.[13–15] The latest value was obtained by Ornstein and Vreeswijk.[16]

In the present investigation the isotopic constitution of boron was determined by using the ions formed by electron bombardment of BF_3 and $BO(CH_3)_3$. The latter material is more convenient to handle in the mass spectrometer since it does not form addition compounds with the walls of the spectrometer as readily as does BF_3. The source of boron used was tank BF_3 supplied by the Harshaw Chemical Company. The results of the analyses are tabulated in Table IX.

Following the method used for establishing upper limits on the existence of hypothetical isotopes of tungsten, the upper limits set on the existence of possible rare isotopes of boron are tabulated in Table X.

The intensities of the peaks observed in BF_3 when bombarded by electrons of 85 volts energy are 3.8, 5.6, 90.5, and 0.2 for the B^+, BF^+, BF_2^+, and BF_3^+, respectively.

Thus the isotopic composition as determined in this work as compared with the results of other investigators is given in Table XI. The errors

TABLE VII. Upper limits of abundances of Si isotopes not found.

Mass No.	Upper limit on existence	Ion studied	Artificial radioactivity[a]
24	0.002%	SiF_3^+	
25	0.003	SiF_3^+	
26	0.006	SiF_3^+	
27	0.006	SiF_3^+	β^+, 4.9 sec.
31	0.005	SiF_3^+	β^-, 170 min.
32	0.003	SiF_3^+	
33	0.002	SiF_3^+	
34	0.002	SiF_3^+	
35	0.002	SiF_3^+	

TABLE VIII. Isotopic constitution of silicon.

Investigator	%28	%29	%30
McKellar	89.6	6.2	4.2
Present work	92.28±0.08	4.67±0.05	3.05±0.03

[11] E. Pollard, Phys. Rev. **57**, 1186 (1940).
[12] F. W. Aston, Phil. Mag. **40**, 628 (1920).
[13] F. W. Aston, Proc. Roy. Soc. **A132**, 490 (1931).
[14] A. Elliot, Nature **126**, 845 (1930).
[15] Paton and Almy, Phys. Rev. **37**, 1710 (1931).
[16] Ornstein and Vreeswijk, Zeits. f Physik **80**, 57 (1933).

TABLE IX. Isotopic constitution of boron.

Ion studied	% 10	% 11	No. of measurements
BF_2^+	18.89	81.11	10
BF_2^+	18.83	81.17	20
BF^+	18.87	81.13	10
B^+ from BF_3	18.73	81.27	20
B^+ from $BO(CH_3)_3$	18.81	81.19	20
Average	18.83±0.06	81.17±0.06	

TABLE X. Upper limits for abundances of isotopes of boron not found.

Mass No.	Upper limit on existence	Ion studied	Artificial radioactivity[a]
7	0.003%	B^+	
8	0.003	B^+	
9	0.006	B^+	
12	0.003	BF_2^+	β^-, 0.022 sec.
13	0.0003	BF_2^+	
14	0.0003	BF_2^+	

[a] See reference 6 in text.

TABLE XI. Isotopic constitution of boron.

Investigator	Method	%10	%11
Aston[a]	Mass spectra	19.8	80.2
Elliot[b]	Band spectra	21.6	78.4
Paton and Almy[c]	Band spectra	17.1	82.9
Ornstein and Vreeswijk[d]	Line spectra	18.4	81.6
Present work	Mass spectra	18.83±0.2	81.17±0.2

[a] Reference 13 in text.
[b] Reference 14 in text.
[c] Reference 15 in text.
[d] Reference 16 in text.

quoted for the present work are the systematic error uncertainties.

Calculating the chemical atomic weight from the abundances determined in this investigation using the packing fractions determined by Bainbridge[17] of 16.3×10^{-4} and 11.8×10^{-4} for the masses 10 and 11, respectively, and the factor 1.000275 in converting from the physical to the chemical atomic weight, gives 10.821 which is in good agreement with the chemically determined value of 10.82.

The author takes pleasure in acknowledging his indebtedness to Professor A. J. Dempster and Professor A. O. C. Nier for their suggestions, and to B. M. Rustad and J. L. Curtain for their assistance in this work.

[17] K. T. Bainbridge, Phys. Rev. **51**, 385 (1937).

PHYSICAL REVIEW VOLUME 70, NUMBERS 9 AND 10 NOVEMBER 1 AND 15, 1946

The Energy Spectrum of Cascade Electrons

I. TAMM AND S. BELENKY
P. N. Lebedev Physical Institute, Academy of Sciences of the U.S.S.R., Moscow

(Received July 1, 1946)

The theoretical investigations on the energy spectrum of shower electrons by Rossi and Klapman and by Bhabha and Chakrabarty are analyzed and compared with the theory previously developed by the present authors.

THEORETICAL investigations on the energy spectrum of shower electrons have been published lately by Rossi and Klapman[1] and by Bhabha and Chakrabarty.[2] The present note contains an analysis of these investigations and a comparison of their results with the results previously obtained by us.

1

Some years ago we derived[3] simple analytical expressions for the number and energy distribution of shower electrons integrated over the total length of the shower. This distribution function differs only by a constant factor from the "track length" of shower electrons defined by Rossi and Klapman.[1]

We obtained also analytical expressions for the energy spectrum of electrons (in equilibrium with mesons), generated both by knock-on processes and by the disintegration of mesons. Somewhat later we calculated the energy spectrum of shower electrons and photons as a function of the depth.[4] These calculations indicated that the approximations, which are usually made in shower theory as regards the collision losses (e.g., in the papers of Bhabha,[5] Arley[6] and others), lead to serious errors in the energy spectrum of shower particles near to and below the "critical" energy. It was found that the number of low energy electrons is much greater than was usually supposed, a result important for the interpretation of many cosmic-ray experiments.

In the present note we shall show that the results of numerical integrations, carried out by Rossi and Klapman, fully corroborate our theory, and will give a criticism of the theory, developed by Bhabha and Chakrabarty.

2

Rossi and Klapman[1] by a numerical integration of the shower theory equations computed the integral track length of electrons in a shower in air, initiated by a primary electron of arbitrary energy. Owing to difficulties of the numerical

[1] B. Rossi and S. Klapman, Phys. Rev. **61**, 414 (1942).
[2] H. J. Bhabha and S. K. Chakrabarty, Proc. Roy. Soc. **181**, 267 (1943).
[3] Ig. Tamm and S. Belenky, J. Phys. U.S.S.R. **1**, 177 (1939).
[4] S. Belenky, Comptes rendus Acad. Sci. U.S.S.R. **30**, 608 (1941).
[5] H. J. Bhabha, Proc. Roy. Soc. **164**, 257 (1938).
[6] N. Arley, Proc. Roy. Soc. **168**, 519 (1938).

integrations the authors were not able to obtain the complete energy spectrum of the electrons, i.e., the track length of electrons of energies exceeding any prescribed value of E, and have contented themselves with one point of the spectrum ($E=10^7$ ev). On the other hand all processes, which may play any appreciable role during the passage of the shower particles through matter, were taken into account in their calculations and exact expressions for the probabilities of these processes were used instead of the usual asymptotic ones. The results thus obtained were used to calculate the number of electrons having energy exceeding 10^7 ev in showers, initiated in the atmosphere by collisions and by disintegrations of mesons.

In our calculations of the electron spectrum a number of simplifications were made (asymptotic expressions for the probabilities of radiation loss and pair production were used, Compton effect was disregarded, some approximations were made in the diffusion equations of the shower theory, etc.). Thus a comparison of our formulas with the results obtained by numerical integration for $E=10^7$ ev (i.e., for 1/10 of the critical energy in air) seems to be very desirable and provides a valuable check of accuracy of our analytical expressions for the electron spectrum.

The expression obtained by us for the total (integrated over the length of the shower) number of electrons of energy $>E$ in a shower, initiated by a primary electron of energy E_m, is (see formulas (8, 9) T-B*)

$$N(E_m, E)=E_m\phi(\epsilon_m, \epsilon)/\beta, \tag{1}$$

where

$$\phi(\epsilon_m, \epsilon)=1-\epsilon e^{\epsilon}\int_{\epsilon}^{\epsilon_m}\frac{e^{-x}}{x}dx-\frac{\epsilon e^{\epsilon-\epsilon_m}}{\epsilon_m}. \tag{2}$$

β is the collision loss of the electrons per radiation length; $\epsilon=2.4E/\beta$, $\epsilon_m=2.4E_m/\beta$. The quantity $N(E_m, E)$ is closely related to the integral electron track length $Z(E_m, E)$, defined by Rossi and Klapman

$$Z(E_m, E)=N(E_m, E)\cdot X_0\cdot\rho, \tag{3}$$

where X_0 is the shower unit of length (see T-B (2, 1)) and ρ the density of the material traversed.

* In the future our paper, reference 3, will be referred to as T-B.

Substituting in (3) the value (1) of $N(E_m, E)$ one obtains:

$$Z(E_m, E)=\frac{A}{\pi LZN_0r_0^2}\left(\frac{E_m}{2mc^2}\right)\phi(\epsilon_m, \epsilon). \tag{4}$$

Here A is the atomic weight of the material, Z its atomic number, N_0 Avogadro's number, $r_0=e^2/mc^2$, and L is an averaged value of the logarithm, appearing in the formula for the collision loss.

If $\epsilon_m\gg 1$ and $\epsilon\ll\epsilon_m$, then

$$\phi(\epsilon_m, \epsilon)=1+\epsilon e^{\epsilon}\mathcal{E}_i(-\epsilon), \tag{2a}$$

where $\mathcal{E}_i(-\epsilon)$ is the exponential integral.

Using the formula (1) or carrying out the necessary calculations independently (as was done in T-B) one can determine $N_e(E_m, E)$ and $N_d(p, E)$, $N_e(E_m, E)$ being the number of electrons with energy exceeding E arising from collision processes of mesotrons with maximum transferable energy E_m, and $N_d(p, E)$ being the number of electrons with energy exceeding E arising from the disintegration of mesotrons with momentum p. Both quantities are referred to one incident mesotron.

According to (4, 5) and (4, 6) T-B, the function $N_e(E_m, E)$ is equal to

$$N_e(E_m, E)=\frac{1}{L}\epsilon e^{\epsilon}\int_{\epsilon}^{\epsilon_m}\frac{e^{-x}}{x^2}\left\{\frac{c^2}{v^2}\ln\left(\frac{x}{\epsilon_m}\right)+1-\frac{x}{\epsilon_m}\right\}dx, \tag{5}$$

where c is velocity of light and v is the velocity of the mesotron.

If $\epsilon_m\gg 1$, $\epsilon\ll\epsilon_m$ and $v\sim c$, we obtain from the Eq. (5) (see (4, 16), T-B):

$$N_e(E_m, E)=\frac{1}{L}\left\{\left(\ln\frac{E_m}{E}-2\right)(1+\epsilon e^{\epsilon}\mathcal{E}_i(-\epsilon))+\psi(\epsilon)\right\}, \tag{6}$$

where

$$\psi(\epsilon)=\epsilon e^{\epsilon}\left\{\ln\epsilon\cdot\mathcal{E}_i(-\epsilon)+\int_{\epsilon}^{\infty}\frac{e^{-x}}{x}\ln x\cdot dx\right\}. \tag{7}$$

The function $\psi(\epsilon)$ is tabulated in the paper of T-B. The maximum value of $\psi(\epsilon)$ does not exceed 0.3 and therefore for $\epsilon\ll\epsilon_m$ the term $\psi(\epsilon)$

is small in comparison with the first term in brackets of formula (6).

According to (7, 6), T-B, the number of disintegration electrons (including their shower progeny) in equilibrium with a mesotron of momentum p, mass M and rest life time τ_0 is expressed by the following formulas:

$$N_d(p, E)=\frac{x_0 M\beta}{2\tau_0 cp^2}\cdot\frac{1}{q^2}\cdot\epsilon e^{\epsilon}\int_{\epsilon}^{\epsilon_2} e^{-x}\left(\frac{\epsilon_2^2}{x^2}-1\right)dx, \quad (8)$$

if $\epsilon_1<\epsilon<\epsilon_2$,

$$N_d(p, E)=\frac{x_0 M\beta}{2\tau_0 cp^2}\cdot\frac{1}{q^2}\cdot\epsilon e^{\epsilon}\left\{(\epsilon_2^2-\epsilon_1^2)\right.$$
$$\left.\times\int_{\epsilon}^{\epsilon_1}\frac{e^{-x}}{x^2}dx+\int_{\epsilon_1}^{\epsilon_2} e^{-x}\left(\frac{\epsilon_2^2}{x^2}-1\right)dx\right\},$$

if $\epsilon<\epsilon_1$,

where $q=2.4$ and

$$\epsilon_{1,2}=\frac{qc}{2\beta}\{(c^2M^2+p^2)^{\frac{1}{2}}\mp p\}. \quad (8a)$$

If $p\gg cM$, $\epsilon_2\gg 1$ and $\epsilon\ll\epsilon_2$, then

$$N_d(p, E)=\frac{x_0 Mc}{2\tau_0\beta}[1+\epsilon e^{\epsilon}\mathcal{E}_i(-\epsilon)]. \quad (9)$$

Following Rossi and Klapman, we may denote by $K_0=\frac{1}{2}Mc/\tau_0\rho$ the average energy transferred to the disintegration electrons per one mesotron per 1 g/cm². With the help of this notation formula (9) may be rewritten as follows:

$$N_d(p, E)=\frac{A}{\pi LZN_0 r_0^2}\left(\frac{K_0}{2mc^2}\right)$$
$$\times[1+\epsilon e^{\epsilon}\mathcal{E}_i(-\epsilon)]. \quad (9a)$$

Let us compare our results with those obtained by Rossi and Klapman for the number of electrons in air with energies exceeding $E=10^7$ ev. Let us at first assume that $\epsilon_m\gg 1$ and $\epsilon_2\gg 1$ (this corresponds to E_m or $pc\gg\beta/2.4=4.1\times10^7$ ev); in this case we can apply formulae (4) and (2a), (5) and (9a). Integrating in these formulae the Rossi and Greisen's[7] value of $\beta=9.8\times10^7$ ev for air and $E=10^7$ ev, we obtain

$$Z(E_m, 10^7\text{ ev})=3.2\left(\frac{E_m}{10^7}\right)\frac{g}{cm^2};$$
$$N_e(E_m, 10^7\text{ ev})=0.035+0.024\ln(E_m/2\cdot10^8);$$
$$N_d(p, 10^7\text{ ev})=3.2(K_0/10^7). \quad (10)$$

According to the computations of Rossi and Klapman these quantities are equal to

$$Z(E_m, 10^7\text{ ev})=3.06\left(\frac{E_m}{10^7}\right)\frac{g}{cm^2};$$
$$N_e(E_m, 10^7\text{ ev})=0.035+0.0234\ln(E_m/2\cdot10^8);$$
$$N_d(p, 10^7\text{ ev})=3.06(K_0/10^7). \quad (11)$$

$Z(E_m, 10^7\text{ ev})$ and $N_e(E_m, 10^7\text{ ev})$ for smaller values of the energy E_m (i.e., for $E_m\sim$ and $<4.1\times10^7$ ev) are given in Rossi and Klapman's papers only graphically. Using for this range of E_m our Eqs. (2), (4), and (5), we have obtained values of Z and N_e which, within the accuracy of these graphs, practically coincide with those obtained by Rossi and Klapman.

Thus numerical integration of the shower theory equations, carried out by Rossi and Klapman, confirms the validity of the approximations underlying our derivation of analytical expressions for the energy spectrum of cascade electrons. On the other hand the result obtained previously by other authors (Bhabha[5] and Arley[6]) regarding the number of electrons with energies of the order or below the critical energy, are in complete disagreement with the calculations of Rossi and Klapman.

3

Bhabha and Chakrabarty[2,*] have developed a modification of the theory of showers intended to take a better account of the collision losses of electrons than was done in most of previous theories. In their theory radiation processes and pair production are as usual described by asymptotic formulas for complete screening and the collision losses are assumed to be independent of the energy of electrons. B-Ch obtain under these assumptions a solution of the equation of the shower theory in the form of a series and

[7] B. Rossi and K. Greisen, Rev. Mod. Phys. 13, 240 (1941).

* Further referred to as B-Ch.

show, that for energies greater than one-third of the critical energy, it is sufficient to retain only the first term of this series. At lower energies it is insufficient to take into consideration only the first or even several of initial terms of the series. However, B-Ch, in the opinion that the contribution of low energy electrons to the total number of particles is relatively small, take into account in their final formulae only the first term of the series.

The solution of the equations of the shower theory obtained by B-Ch satisfies exactly the boundary conditions and the authors regard this as a definite advantage over the well-known solution obtained by Snyder[8] and Serber,[9] which satisfies these conditions only approximately. The cascade curve (total number of electrons in its dependence on depth) given by B-Ch[10] differs considerably from the cascade curves of Snyder and Serber.

B-Ch have also calculated the energy spectrum of shower electrons and have arrived at the conclusion, that the collision losses exercise a marked influence on this spectrum; even the number of electrons with energies above the critical energy is considerably diminished.

Further applications of this theory to a number of problems in the shower theory were made by Bhabha and Chakrabarty.[10,11] Bhabha and Chakrabarty's theory is quite satisfactory for energies of the order of or above the critical energy and corrects in this region previous investigations of Bhabha and of Arley. However the assumption of B-Ch, that the number of low energy electrons (below one-third of the critical energy) is comparatively insignificant, is erroneous, and as a consequence their cascade curve as well as their energy spectrum in the low energy region are incorrect.

In order to show this let us at first calculate on the theory of B-Ch as well as on the theory developed by one of us[4] the energy distribution of shower electrons at a depth corresponding to the maximum of the cascade curve and in the neighborhood of or below the critical energy.

Henceforth it will be assumed that the energy E_0 of the primary electron initiating a shower is so high that not only E_0/β, but even $\ln(E_0/\beta)$, is much greater than 1.

Using the formulae of B-Ch[2] one can obtain the following expression for the number of electrons of energy exceeding E (the notations are those of B-Ch)

$$N(E,t)=\frac{1}{2\pi i}\int_{s-i\infty}^{s+i\infty}\left[\frac{E_0}{E_0+\beta g(s_1 t)}\right]^{s-1}\times\frac{1}{s-1}\frac{D-\lambda_s}{\mu_s-\lambda_s}\exp(-\lambda_s t)ds. \quad (12)$$

Carrying out the integration of this expression by the saddle point method one obtains at the shower maximum (for energies of the order of or below β)

$$N_{\max}(E)=\frac{1}{(-2\pi\lambda_2''\cdot\ln E_0/\beta)^{\frac{1}{2}}}\cdot\frac{E_0}{\beta}\cdot\frac{1}{(E/\beta)+g(2,t)}\cdot\frac{D}{\mu_2}. \quad (13)$$

Inserting from the table given in Bhabha-Chakrabarty's paper the numerical values for λ_2'', D, μ_2, and $g(2,\infty)$ (since $\ln(E_0/\beta)\gg 1$, therefore $t\gg 1$) we obtain

$$N_{\max}(E)=\frac{0.31E_0/\beta}{(\ln(E_0/\beta))^{\frac{1}{2}}}\cdot n_1(\epsilon), \quad (14)$$

where $\epsilon=2.4E/\beta$ and

$$n_1(\epsilon)=1/(0.95\epsilon+1.87). \quad (14_1)$$

On the other hand integrating by the saddle method expression (14) of our paper,[4] which gives the number of particles of energy exceeding a given value of E as a function of the depth, we obtain at maximum of the shower:

$$N_{\max}(E)=\frac{0.31E_0/\beta}{(\ln(E_0/\beta))^{\frac{1}{2}}}\cdot n_2(\epsilon), \quad (15)$$

where

$$n_2(\epsilon)=1+\epsilon e^{\epsilon}\mathcal{E}_i(-\epsilon). \quad (15_1)$$

Spectrum (15_1) coincides with the "equilibrium spectrum" of shower particles [see Eq. (2a) of the present paper].

[8] H. Snyder, Phys. Rev. **53**, 960 (1938).
[9] R. Serber, Phys. Rev. **54**, 317 (1938).
[10] S. K. Chakrabarty, Ind. J. Phys. **16**, 377 (1942).
[11] H. J. Bhabha and S. K. Chakrabarty, Proc. Ind. Acad. Sci. **15**, 464 (1942). This paper was not available to us.

TABLE I. Values of $n_1(\epsilon)$ and $n_2(\epsilon)$.

ϵ	0	0.25	0.5	1	2	3	$\epsilon \gg 1$
n_1	0.534	0.473	0.425	0.353	0.264	0.211	$\frac{1.05}{\epsilon}\left(1-\frac{1.97}{\epsilon}\right)$
n_2	1	0.665	0.536	0.404	0.277	0.214	$\frac{1}{\epsilon}\left(1-\frac{2}{\epsilon}\right)$

Values of $n_1(\epsilon)$ and n_2 for various ϵ are given in Table I.

It will be seen from this table that for energies of the order of or above the critical one the results of Bhabha-Chakrabarty's theory practically coincide with ours. However, there is a considerable discrepancy at energies below the critical energy. As a result, our value for the total number of electrons is almost two times greater than the value calculated on the theory of B-Ch. In fact, according to Eq. (14), the total number of electrons at the maximum of the shower is

$$N_{\max}(0)=\frac{0.165}{(\ln (E_0/\beta))^{\frac{1}{2}}}\cdot\frac{E_0}{\beta}, \tag{16}$$

while according to our Eq. (15)

$$N_{\max}(0)=\frac{0.31}{(\ln (E_0/\beta))^{\frac{1}{2}}}\cdot\frac{E_0}{\beta}. \tag{17}$$

Our value (17) for $N_{\max}(0)$ coincides with the value calculated by Serber.[9] The correctness of this value is further supported by a paper of Landau.[12] It was shown by Landau that abstaining from any detailed analysis of the low energy part of the electron spectrum and using only arguments of a very general kind (e.g., using the relation

$$\int_0^\infty N(0, t)dt=E_0/\beta,$$

which is an expression of the law of conservation of energy) one can prove that, in the case $\ln (E_0/\beta)\gg 1$, $N_{\max}(0)$ must be equal to the value given by Eq. (17).

It is easy to understand, why the solution of B-Ch fails to satisfy the relation (17), proved by Landau. It was previously mentioned that this solution is mathematically justified only for energies not lower than a third of the critical energy. An extrapolation of this solution to lower energies would be possible if the low energy region were of no appreciable significance. However, according to the last row of Table I, more than a half of the particles have energies $<\beta/3$ (i.e., $\epsilon<0.8$) and thus belong to the region for which the solution of B-Ch is invalid.

In connection with this point we should like to mention that B-Ch's statement (p. 293 of their paper), that for $E\to 0$ the differential number of particles $P(E)=-\partial N/\partial E$ tends to a finite limit, is also erroneous. Differentiating (15) with respect to E we obtain (for $\epsilon\ll 1$): $P(E)=C\ln\epsilon$, where C is independent of E. The logarithmic divergence of the differential electron spectrum at low energies has been independently confirmed by calculations carried out by Bethe, the results of which are discussed in Rossi and Greisen's review.[7]

In conclusion it should be noted that, contrary to the contention of Bhabha and Chakrabarty, Snyder and Serber's theory yields a correct expression for the total number of particles as a function of depth. We have shown[4] that the terms, which should be added to Serber's expression in order to exactly satisfy the boundary conditions, are important only for electron energies E close to the energy E_0 of the primary. These terms contribute to the total number of particles a fraction which is proportional in the first approximation to β/E_0 and which already at $\beta/E_0\sim 0.1$ becomes negligible.

[12] L. Landau, J. Phys. U.S.S.R. **3**, 237 (1940).

The Ammonia Spectrum and Line Shapes Near 1.25-cm Wave-Length

CHARLES HARD TOWNES
Bell Telephone Laboratories, Murray Hill, New Jersey

(Received August 2, 1946)

The ammonia "inversion" lines near 1.25-cm wave-length are resolved, their widths being decreased at low pressures to 200 kilocycles. Line shapes, intensities, and frequencies are measured and correlated with theory. Calculated intensities and Lorentz-type broadening theory fit experimental results if frequency of collision is fifteen times greater than that measured by viscosity methods. Splitting due to rotation is in fair agreement with a recalculation of theoretical values. A saturation effect is observed with increase of power absorbed per molecule and an interpretation made.

SINCE the measurements of Cleeton and Williams[1] on ammonia absorption in the 1-centimeter region techniques for producing and measuring 1-centimeter radiation have improved markedly. The fine structure of this line can now be resolved and line frequencies and shapes measured with exactness. This affords a more accurate check on pressure broadening theory than can be obtained in the infra-red region, as well as additional information about the ammonia molecule. There are some small differences between the results presented here and those of Bleaney and Penrose[2] and of Good[3] which were published after the present work was largely complete, and their work is extended in certain respects.

GENERAL THEORY

The ammonia absorption at approximately 1.25-cm wave-length is caused by the ability of the ammonia molecule to "turn inside out," the nitrogen atom going through the plane of the hydrogens. Various functions[4] for the potential of the nitrogen atom as it goes through the plane of the hydrogens have been found which satisfactorily fit the frequency of this inversion line as well as the frequency of the similar line for the first excited vibration state. Sheng, Barker, and Dennison[4] calculated the additional splitting of the first vibrational state due to the fact that the molecules may be in different rotational states each of which has a slightly different inversion frequency and found agreement with experimental determinations. They also calculated the splitting of the inversion line in the ground state which is the line discussed here, but had no experimental data accurate enough for a comparison. Their formula for frequency is given by

$$\nu/hc=(W_0^a-W_0^s)/hc$$
$$+(A_0^a-A_0^s)(J^2+J-K^2)+(C_0^a-C_0^s)K^2, \quad (1)$$

where J and K are the usual angular momentum quantum numbers. A definition of the other quantities and their calculated values may be found in their paper. Substituting these values,

$$\nu/hc=0.66-0.0011(J^2+J-K^2)$$
$$+0.0005K^2 \text{ cm}^{-1}. \quad (2)$$

It may be seen from this formula that an angular momentum about the symmetry axis (K) tends to force the hydrogens apart and allow the nitrogen to pass through their plane more freely, thus increasing ν, whereas an angular momentum perpendicular to the symmetry axis $(J^2+J-K^2)^{\frac{1}{2}}$ creates a centrifugal force which retards this motion and decreases ν. Cleeton and Williams[1] observed the combined effects of all of these lines since their measurements were at atmospheric pressure where the lines were very broad and superimposed.

The intensity and shape of each of these lines assuming collisions are the main cause of line broadening is predicted theoretically by Van Vleck and Weisskopf[5] to be

[1] Cleeton and Williams, Phys. Rev. **46**, 235 (1934).
[2] Bleaney and Penrose, Nature **157**, 339 (1946).
[3] Good, Phys. Rev. **69**, 539 (1946).
[4] Sheng, Barker, and Dennison, Phys. Rev. **60**, 786 (1941); Dennison and Uhlenbeck, Phys. Rev. **41**, 313 (1932).
[5] Van Vleck and Weisskopf, Rev. Mod. Phys. **17**, 227 (1945).

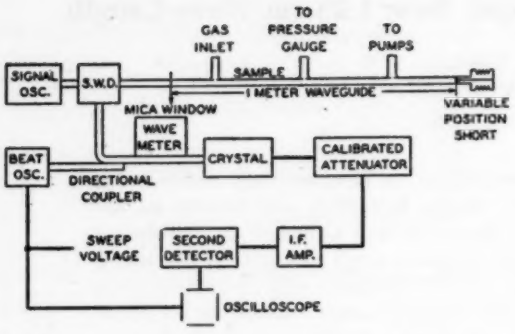

FIG. 1. Schematic diagram of apparatus used for ammonia pressures ≥ 0.27 mm Hg.

$$\gamma=\frac{2\pi^2 Nf}{3ckT}|\mu_{ij}|^2\nu^2 \left[\frac{1/2\pi\tau}{(\nu-\nu_0)^2+(1/2\pi\tau)^2}+\frac{1/2\pi\tau}{(\nu+\nu_0)^2+(1/2\pi\tau)^2}\right], \quad (3)$$

where

γ = the absorption in nepers/cm
N = the density of molecules
f = the fraction of molecules in the rotational state considered
μ_{ij} = the matrix element of dipole moment
ν = the frequency
ν_0 = the resonant frequency and $h\nu_0 \ll kT$
τ = the time between collisions which produce a large change of phase of the oscillation
c, k, T = velocity of light, Boltzman constant, and absolute temperature, respectively.

As long as the second term is small, this formula predicts that the half-width of the line is directly proportional to pressure and that the intensity at resonance ($\nu=\nu_0$) is constant independent of pressure. Thus within the approximations of the formula, that is neglecting the natural width of the line, the Doppler effect, collisions of molecules with the walls of the container, and saturation effects which will be discussed below, the lines are expected to become narrower with decreasing pressure but to stay constant in intensity at the resonant frequency. This conclusion is in contrast, however, with some measurements[6] in the infra-red region which indicate that the intensity at the resonant frequency is proportional approximately to the square root of the pressure.

[6] For a summary see W. M. Elsasser, Harvard Meteorological Studies No. 6 (1942), pp. 45–48.

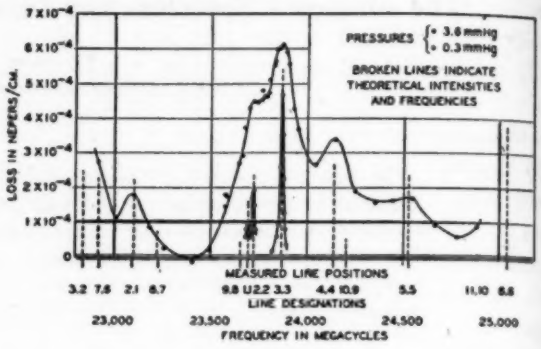

FIG. 2. Envelope of the NH_3 absorption spectrum at 3.6 mm Hg.

LINE SHAPES AND INTENSITY—APPARATUS AND RESULTS

To resolve the ammonia lines and measure their shapes and intensities the apparatus shown schematically in Fig. 1 was used. The ammonia was contained in a one-meter wave guide with small pinhole outlets so that the gas pressure could be measured and changed but the radiation could not leak out. One-mil mica windows inserted in the wave guide isolated the ammonia from atmospheric pressure. The signal and beat oscillators used were type 2K33, the beat oscillator being swept over approximately 10 megacycles by applying a sine wave to its reflector. The standing wave detector (S.W.D.) is a probe which may be moved several wave-lengths along the wave guide and thus pick up the maxima and minima of the standing wave. The intensity of the detected signal was adjusted by means of the calibrated attenuator so that it gave a standard deflection on the oscilloscope. The difference in attenuator settings with the standing wave de-

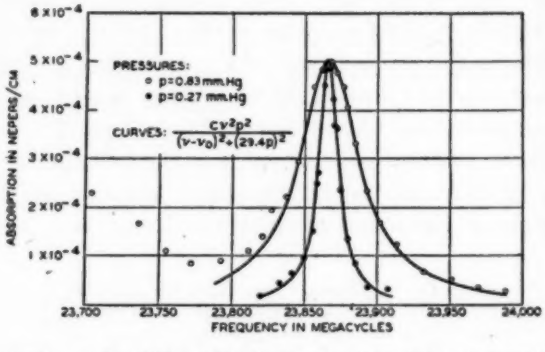

FIG. 3. The NH_3 (3.3) absorption line. The absorption in wave guide is shown here and in Fig. 1. Absorption in free space may be obtained by multiplying by 0.8.

tector at maxima and minima allows a determination of the attenuation undergone by the radiation which travels down the wave guide to the variable position short and back again. Measurements were made with two settings of the variable position short one-quarter wavelength apart. An average of these two measurements cancels out certain types of errors such as that due to a small reflection at the mica window. The evacuated wave guide showed an attenuation of approximately 6×10^{-4} neper per cm. This was of the same order as the absorption due to ammonia and was subtracted from the total measured attenuation after the ammonia gas was let in. The wave meter is a tunable resonant cavity with small coupling to the wave guide. It was calibrated from 23,500 megacycles to 24,500 megacycles against a second wave-meter which had been calibrated in the same region by comparison with multiples of a standard 100-kilocycle frequency. Frequencies outside this range were determined by a semi-theoretical extrapolation of this calibration. Attenuation measured in this way is thought to be accurate in absolute value to approximately 2×10^{-5} neper per cm and reproducible to half of this. The wave-meter calibration is thought to have a probable error of 2 megacycles in the range directly calibrated and 5 megacycles in the extrapolated range.

An envelope of the ammonia absorption at 3.6 millimeters of mercury pressure is shown in Fig. 2 as well as measurements of 3 lines at 0.3 millimeter pressure. The most intense single line later identified as $J=3$ and $K=3$ was examined in some detail at 0.83- and 0.27-mm Hg as shown in Fig. 3. The formula given above for the line shape was fitted to the points obtained and as may be seen from this figure agrees within experimental error. The intensity at resonance does indeed stay constant. The second term of this formula was negligible at the pressures used. On the low frequency side of the 3, 3 line another interfering line may be seen at 0.83-mm pressure.

The half-width obtained by fitting the theoretical formula (3) to these curves shows that the time between collisions τ equals $6.7\times10^{-9}p$, where p is the pressure in mm Hg. Thus collisions affecting this oscillation are fifteen times more frequent than the collisions found by ordinary kinetic measurements. As pointed out by Bleaney and Penrose,[2] the long range dipole-dipole forces

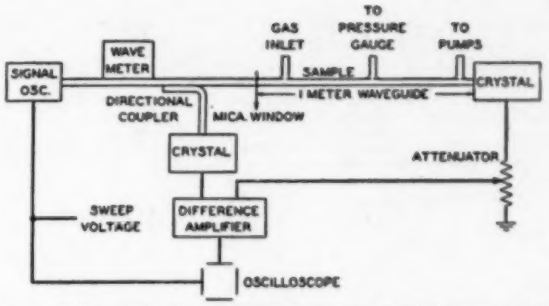

FIG. 4. Schematic diagram of apparatus used for ammonia pressures less than 0.27 mm Hg.

may effect this transition although they are ineffective in transferring linear momentum which is essential for most kinetic processes. Using the experimentally determined half-width of the 3, 3 line, and a value 0.0637 calculated for f, the fraction of molecules in the $J=3$, $K=3$ state at 25°C, the peak intensity of this line may be calculated from the expression (3). If the dipole moment $|\mu_{ij}|$ is 1.45×10^{-18} e.s.u., the peak intensity should be 4.9×10^{-4} neper/cm. The experimental value is 5.0×10^{-4} neper/cm in wave guide, or 4.0×10^{-4} neper/cm for a plane wave.[7] This value is considerably higher than the 0.18 db/meter or 2.1×10^{-4} neper/cm given by Good.[8] The probable error of the measurement is thought to be $\pm0.2\times10^{-4}$ neper/cm. The calculated value 4.9×10^{-4} has a probable error of about five percent due to an uncertainty in the pressure at which the line breadth was measured and in addition a few percent error due to uncertainties in the value of $|\mu_{ij}|$. The discrepancy of 20 percent between measured and calculated attenuations thus is slightly larger than expected from the estimated errors.*

As a check on the nature of the forces producing such a large half-width, argon was mixed with ammonia to determine the consequent line broadening. The resulting line when 0.5 millimeter of ammonia and 9.5 millimeters of argon were mixed was symmetrical and its peak frequency unchanged. Its half-width was only twice as great as that for 0.5-millimeter ammonia alone. This indicates the frequency of collision between ammonia and argon is approximately the same as

[7] W. D. Hershberger, J. App. Phys. **17**, 495 (1946).

* In computing the theoretical intensities, $|\mu_{ij}|^2$ was erroneously taken equal to the square at the dipole moment μ rather than to $K^2\mu^2/J(J+1)$ [see D. M. Dennison, Rev. Mod. Phys. **3**, 280 (1931)]. The corrected theoretical intensity for the $J=3$, $K=3$ line is 3.7×10^{-4} neper/cm which is in good agreement with the experimental value.

TABLE I. Absorption lines of NH_3 in frequency range 22,800 to 25,100 megacycles.

Line designation J	K	Calculated intensity nepers $\times 10^{-4}$/cm	Frequency in megacycles Experiment	From formula (4)	Difference
1	1	1.65	23,693	23,699	+6
2	2	2.41	23,722	23,725	+3
3	3	5.50	23,870	23,869	−1
4	4	2.74	24,137	23,134	−3
5	5	2.42	24,529	24,522	−7
6	6	3.86	25,046	25,039	−7
2	1	2.28	23,097	23,108	+11
3	2	2.53	22,840	22,843	+3
7	6	2.32	22,927	22,920	−7
8	7	0.77	23,231	23,224	−7
9	8	0.47	23,656	23,650	−6
10	9	0.54	24,202	24,202	0
11	10	0.14	24,877	24,890	+13

obtained by kinetic measurements and that the large number of collisions between ammonia molecules is probably caused by dipole-dipole forces.

LINE FREQUENCIES—APPARATUS, RESULTS, AND RECALCULATION OF THEORY

The technique described above and shown schematically in Fig. 1 could not be used at pressures much lower than 0.3 mm Hg because the signal oscillator was not stabilized in frequency and would drift an appreciable distance on the curve during a single measurement. For these lower pressures a second technique was used as shown in Fig. 4. A single oscillator was swept over approximately 10 megacycles and its output sampled by one crystal before entering the wave guide containing ammonia and by a second crystal after traversing the ammonia. The difference between the signals from these two crystals was amplified and put on the vertical plates of an oscilloscope whose horizontal sweep is synchronized with the oscillator sweep. If the oscillator frequency is centered near an ammonia absorption line, a pip corresponding to the line then appears on the oscilloscope. As the pressure is decreased the line becomes narrower but remains of constant peak intensity as predicted until it reaches a width of approximately 500 kilocycles when it begins to fade out. Causes for decrease in intensity at this point will be discussed below. The narrow and weak lines may be detected by this method more easily than by the first, and frequencies can be more accurately measured. The frequency of the line is measured by tuning the wave-meter until it produces a pip on the oscilloscope. Its pip may be superimposed on that due to an ammonia line to an accuracy of a fraction of a megacycle.

Thirteen lines were detected in the frequency range 22,800 to 25,100 megacycles, their identification and frequencies being given in Table I. The "hyperfine structure" reported by Good[3] was not observed. The frequencies may be fitted to a formula of the same form as (2) but having somewhat different constants. Such a formula is

$$\nu = 0.79356_6 - 5.015_8\times 10^{-3}(J^2+J-K^2) + 1.964_6\times 10^{-3}K^2 + 6.3\times 10^{-7} \times[-5.02(J^2+J-K^2)+1.96K^2]^2 \text{ cm}^{-1} \quad (4)$$

or

$$\nu = 23{,}790.5 - 150.34_1(J^2+J-K^2) + 58.87_8K^2 + 2.1\times 10^{-5}[-150(J^2+J-K^2) + 59K^2]^2 \text{ megacycles.}$$

Here a higher order term is included which is not given by Sheng, Barker, and Dennison,[4] but whose form and magnitude is obtained immediately from their theory as a term in an exponential expansion. It will be noted from Table I and from Fig. 2 that the frequencies given by this formula and the theoretical intensities fit well with experimental observations, but also show some systematic deviations. This formula is to be compared with the results of Bleaney and Penrose[2]

$$\nu = 0.7940 - 0.0050(J^2+J-K^2) + 0.0020K^2 + 0.63[-0.005(J^2+J-K^2)+0.002K^2]^2 \text{ cm}^{-1}$$

and of Good[3*]

$$\nu = 0.7932 - 4.8\times 10^{-3}(J^2+J-K^2) + 2.0\times 10^{-3}K^2 \text{ cm}^{-1}.$$

Bleaney and Penrose also find the higher order term useful in fitting the experimental data. Another higher order term of the same magnitude should be included, however, if theory is to be considered this accurate. It is $-(\Delta/h)[2\mu|\delta V-\delta E|]^{\frac{1}{2}}\delta y_1$ in the notation of Sheng, Barker, and Dennison. This term is calculated to be $-0.590|J^2+J-1.56K^2|^{\frac{1}{2}}(J^2+J$

* Good has informed me privately that his more recent results are in good agreement with formula (4).

$-1.56K^2$) megacycles. Its inclusion results, however, in a definitely worse fit than if it is omitted. Since both this term and the higher order term included in (4) are only a few percent as large as the main term, it is hardly to be expected that the approximate theory which has been used will predict them correctly.

The line shapes, intensities, and spacing ratios therefore agree reasonably well with theoretical expectations, the main discrepency being in the magnitude of the line spacing. It appeared possible that a numerical error had been made in calculating the line splitting in the ground vibration state so a recalculation was made with the same theory and potential function used by Sheng, Barker, and Dennison.[4]

The quantities desired are given within sufficient approximation by

$$A_0-A_s(\mathrm{cm}^{-1})=-\frac{\Delta_0}{2\pi}\left(\frac{\mu h}{2c}\right)^{\frac{1}{2}}\times\int_0^{y_1}\frac{\dfrac{1}{\mu r^2\sin^2\alpha+3/2mr^2\cos^2\alpha}-\dfrac{1}{\mu r_0^2\sin^2\alpha_0+3/2mr_0^2\cos^2\alpha_0}}{\left[66{,}551\ \mathrm{sech}^4\left(\dfrac{y}{0.09586(h/c\mu)^{\frac{1}{2}}}\right)-109{,}519\ \mathrm{sech}^2\left(\dfrac{y}{0.09586(h/c\mu)^{\frac{1}{2}}}\right)+44{,}642\right]^{\frac{1}{2}}}dy,$$

$$C_0-C_s(\mathrm{cm}^{-1})=-\frac{\Delta_0}{2\pi}\left(\frac{\mu h}{2c}\right)^{\frac{1}{2}}\times\int_0^{y_1}\frac{\dfrac{1}{3mr^2\cos^2\alpha}-\dfrac{1}{3mr_0^2\cos^2\alpha_0}}{\left[66{,}551\ \mathrm{sech}^4\left(\dfrac{y}{0.09586(h/c\mu)^{\frac{1}{2}}}\right)-109{,}619\ \mathrm{sech}^2\left(\dfrac{y}{0.09586(h/c\mu)^{\frac{1}{2}}}\right)+44{,}642\right]^{\frac{1}{2}}}dy,$$

where

$$\alpha=\alpha_0 y/y_0$$

and

$$r=r_0[1-0.05\alpha_0+0.05\alpha_0(y/y_0)^2].$$

The basis for these expressions and definitions of quantities involved may be found in the above-mentioned article. The expressions were evaluated both for the first excited state and the ground state and although results for the excited state are in essential agreement with those previously found, there is a significant difference for the ground state as shown by Table II. The recalculated quantities agree much more closely with experiment. The remaining discrepancy between experiment and theory can probably be eliminated by using a somewhat modified potential function which will still be consistent with other observed data.

SATURATION EFFECTS

Calculation shows that the Doppler effect and collisions between molecules and the wave-guide walls should make the formula (3) above for the line shape begin to break down at about 150 kilocycles total width at half-maximum, and should prevent the low pressure width of the lines from decreasing below about 75 kilocycles. However, on first examination the lines began to decrease in peak intensity when they were still wider than 1000 kilocycles, and would not become narrower than about 500 kilocycles. A closer investigation showed that the fraction of power absorbed and the apparent width of the absorption line depends on the amount of power sent through the absorbing tube. Thus under certain conditions an increase of power through the

TABLE II. Recalculated values of the ground state and first excited vibrational state of NH_3.

	Calculated value Sheng, Barker, and Dennison[a]		Experimental value		Recalculated value	
	A^a-A^s	C^a-C^s	A^a-A^s	C^a-C^s	A^a-A^s	C^a-C^s
Ground state	−0.0011	0.0005	−0.005015	0.001964	−0.00330	0.00175
First excited vibrational state	−0.162	0.06	−0.17	0.06	−0.156	0.066

[a] See reference 4 in text.

absorbing tube by a factor of ten increases the power absorbed at the resonance frequency by only a factor of two or three, and broadens the apparent width of the line by about the same amount. At somewhat higher pressures and the same amounts of power this phenomenon does not occur. By decreasing the power level, lines of total width at half-maximum of 200 kilocycles were obtained. A further reduction of power to obtain still narrower lines was not practical with the experimental setup used.

Three possible causes for this dependence of absorption coefficient on power presented themselves.

1. A simple increase in temperature of the gas due to the power absorbed.

2. A disturbance of the distribution of molecules between the ground and excited states by their absorbing quanta faster than they can dispose of the energy, depleting the supply of molecules capable of absorbing.

3. A decrease in the lifetime of both upper and lower states of the molecule due to very rapid induced transitions. This broadens the line and decreases the absorption at resonance.

The first effect can be shown to be negligible, since for the powers used ($\sim$1 mw) the increase in temperature is of the order of 1 degree. The results of the second and third effect are derived below and their magnitudes agree with the somewhat rough observations made.

The expression for the absorption coefficient, neglecting the non-resonant term, may be written using (3) above

$$\gamma=\frac{4\pi^2}{3}\frac{(n_0-n_1)}{hc}|\mu_{ij}|^2\frac{\omega^2}{\omega_0}\times\left[\frac{\frac{1}{\tau}+\frac{1}{2\tau_0'}+\frac{1}{2\tau_e'}}{(\omega-\omega_0)^2+\left(\frac{1}{\tau}+\frac{1}{2\tau_0'}+\frac{1}{2\tau_e'}\right)^2}\right]. \quad (5)$$

Here $\omega=2\pi\nu$ and $\omega_0=2\pi\nu$. $1/2\tau_0'$ and $1/2\tau_e'$ have been added to allow for the frequency of disturbance of the ground and excited states respectively by processes other than collisions. n_0-n_1 is the difference between the number of molecules in the lower and the upper states of the particular transition in question. If n_q represents the rate at which each of these molecules makes transitions due to the radiation present, then

$$n_0-n_1=\frac{Nfh\nu_0/2kT}{1+n_q t},$$

where N and f are defined in formula (3), and t is the relaxation time of the molecule, or the average time required to get rid of one absorbed quantum independently of the radiation field. n_q may be shown to be

$$\frac{I\gamma}{Nh\nu f/2kT-I\gamma t}$$

if I is the intensity of incident radiation in quanta per second per square centimeter. Since $1/\tau_0'=1/\tau_e'=n_q$, formula (5) becomes

$$\gamma=\frac{\pi}{3}\frac{Nf}{ckT}|\mu_{ij}|^2\omega^2\left[1-\frac{I\gamma t}{Nh\nu f/2kT}\right]\times\left[\frac{\frac{1}{\tau}+\frac{I\gamma}{Nh\nu f/2kT-I\gamma t}}{(\omega-\omega_0)^2+\left(\frac{1}{\tau}+\frac{I\gamma}{Nh\nu f/2kT-I\gamma t}\right)^2}\right]. \quad (6)$$

Thus saturation effects set in when either

$$\frac{I\gamma t}{(Nh\nu f/2kT)} \text{ approaches 1}$$

or

$$\frac{I\gamma}{[(Nh\nu f/2kT)-I\gamma t]} \text{ approaches } 1/\tau.$$

For $I\to\infty$, $I\gamma\to Nh\nu f/2kTt$. Observations show that saturation sets in when $I\gamma/(Nh\nu f/2kT)$, the rate of transition per molecule assuming the distribution is undisturbed is approximately equal to the rate of collision. Thus for 1.8 milliwatts into the absorption tube (cross section 10.7 mm$\times$4.3 mm) at a pressure of 4×10^{-3} mm Hq, the effect just becomes noticeable. For this condition $I\gamma/(Nh\nu f/2kT)\approx3\times10^6$ and $1/\tau\approx6.4\times10^6$. This indicates also that $t\approx\tau$, or that molecules lose their excitation on almost every collision, otherwise saturation effects would show up at somewhat smaller power values. Observation is in agreement with the above

theory that the power at which saturation effects occur decreases as the square of the pressure.

ACKNOWLEDGMENT

This work has benefited from the contributions of many members of the Bell Laboratories. Mention should be made especially of the aid and encouragement of Dr. S. O. Morgan, of the considerable laboratory help of Messrs. W. H. Hewitt and F. R. Merritt, and of the work of the computing staff which obtained the values given in Table II and assisted in other calculations.

PHYSICAL REVIEW VOLUME 70, NUMBERS 9 AND 10 NOVEMBER 1 AND 15, 1946

Helium Molecular Energy States as Detected by Collisions of the Second Kind in Helium

ROLAND MEYEROTT
Sloane Physics Laboratory, Yale University New Haven, Connecticut
(Received August 12, 1946)

From a survey of the literature on spectra enhanced by collisions of the second kind, which take place in helium, evidence is presented for the existence in measurable concentrations of both the helium molecule-ion and the helium metastable molecule. From the intensity distribution of the enhanced spectra, the repulsive energy between two helium atoms at separations of 1.052A and 1.090A is derived to be 6.8 volts and 5.8 volts, respectively. The rates of formation of the molecular states are discussed in the special case of a steady-state discharge and the molecular states are shown to be very probable at high pressures. From this it is shown that the ion whose mobility is found to be 21.4 cm²/sec. volt is probably that of He_2^+ in helium and, hence, the discrepancy between the theoretical and experimental values of the mobilities can be removed by such an interpretation. The existence of neon molecules is also suggested.

INTRODUCTION

DIFFICULTY in interpreting certain types of experiments in electrical discharges in gases has led to the conclusion that processes which take place under such conditions are exceedingly complex and that little can be gained by their study. In helium, the simplest of all gases, we find numerous examples. The experimental value for the mobility of He^+ in He, 21.4 cm²/volt sec., as measured by Tyndall and Powell,[1] is almost double the theoretical value, 12 cm²/volt sec., calculated by Massey and Mohr.[2] The rate of decay of metastable helium atoms in pure helium is much larger than can be accounted for by the theory, or by comparison with the other noble gases.[3] Selective excitation of impurities in helium discharges is in disagreement with theory. Duffendack and Smith,[4] Takahashi,[5] and others[6] have had difficulty in accounting for the enhanced spectra produced in helium. They assume the helium metastable atoms in the $1s2s^1S$ and $1s2s^3S$ states, and the helium ion, He^+, to be the carriers of the excitation energy. This requires in some cases an assumption of changes in kinetic energy in collisions of the second kind of 3 to 5 ev, which theory hardly permits. Experiments by Richardson[7] and others on the effect of helium on the hydrogen molecular spectra has led to the belief that, in the H_2 triplet spectrum, helium merely enhances the o,o bands with little or no effect on the states of higher vibrational energy. These results have led Smith[8]

[1] A. M. Tyndall and C. F. Powell, Proc. Roy. Soc. **A134**, 125 (1931).
[2] Massey and Mohr, Proc. Roy. Soc. **A144**, 188 (1934).
[3] See Mitchell and Zemansky, *Resonance Radiation and Excited Atoms* (The Macmillan Company, New York, 1934), pp. 236–250.
[4] O. S. Duffendack and H. L. Smith, Phys. Rev. **34**, 68 (1929).
[5] Y. Takahashi, Ann. d. Physik **3**, 49 (1929).
[6] For complete list consult Bibliography in references 4 and 5. See also L. S. Headrick and O. S. Duffendack, Phys. Rev. **37**, 736 (1931).
[7] For summary, see Richardson, *Molecular Hydrogen and its Spectrum* (Yale University Press, New Haven, Connecticut, 1934), pp. 194–218.
[8] N. D. Smith, Phys. Rev. **49**, 345 (1936).

to assume that the hydrogen continuum produced in a discharge containing an excess of helium would be caused by the molecules in the zero vibrational level in the upper state. His results on measurements of the intensity distribution of the continuous spectrum differs considerably both from theory and the later results of Coolidge,[9] indicating the presence of excitation in vibrational levels with $v'>0$. In atomic spectra the excitation of a large number of levels of NI and H by means of a helium discharge is usually attributed to retardation of recombination by the relatively high helium pressure. However, since the atomic hydrogen or nitrogen is present only as a slight impurity, it seems evident that this interpretation also is incorrect.

It has been suggested by the author[10] that the molecule ion, He_2^+, might be the ion whose mobility was measured by Tyndall and Powell and, hence, the above disagreement in mobility could be expected. It now appears from an extensive but by no means exhaustive survey of the literature of spectra enhanced in helium that not only He_2^+ is present in larger concentrations than He^+ in certain types of discharges, but that the metastable molecule, He_2^*, is more abundant than the atomic metastables, He*. By assuming the presence of the above molecular states in helium, not only can all the above mentioned difficulties be removed, but the best of these data can be used to measure the repulsive energy between two normal helium atoms in the neighborhood of 1A.

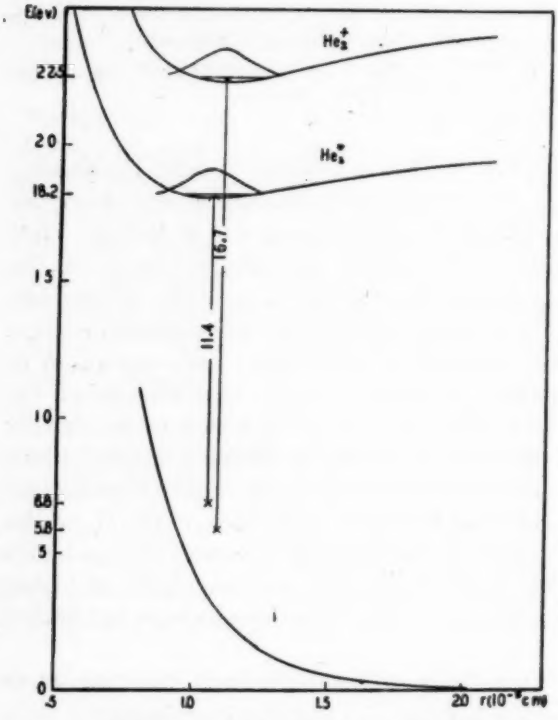

FIG. 1. Morse curves for He_2^+ and He_2^*. Repulsion energy as calculated by Slater. The energies 6.8 ev and 5.8 ev are obtained for the points $r=1.052$A and $r=1.090$A, respectively.

THEORY

The theory of resonance collision and a discussion of the results can be found in Mott and Massey.[11] The characteristic feature of these processes is that the cross sections become very large, perhaps ten times the kinetic theory cross sections for collisions which require no change in kinetic energy of the particles. Changes in energy other than that which can arise through the polarizability or Van der Waals forces between the particles are very improbable. An estimation of the energy due to the polarizability of an atom or molecule in the field of an ion at closest distance of approach shows that this is not likely to exceed 0.5 ev or 4000 cm^{-1}. Thus the atomic ion, He^+, can become neutralized on collision with an impurity if the impurity has an energy level above its ground state (or in some cases above a metastable state) within ± 4000 cm^{-1} of the ionization energy of helium, 198,298 cm^{-1}. If this energy state is not the ground state of the impurity ion or a metastable state, we can expect to observe the spectra of very small quantities of the impurity. In the same way, the metastable helium atom in the $1s2s^3S$ state, which we shall call He*, can excite energy levels on collision of $159{,}884\pm 4000$ cm^{-1}. We shall, for simplicity, neglect the singlet metastable $1s2s^1S$ state as being too short lived compared with the ^3S to have an appreciable effect on the enhanced spectra, although its effects have been observed.

The molecular states are slightly more complicated than the above atomic states. The ground state of the helium molecule is, of course, a repulsive state. In Fig. 1 are shown Morse curves

[9] A. S. Coolidge, Phys. Rev. **65**, 236 (1944).
[10] R. Meyerott, Phys. Rev. **66**, 242 (1944).
[11] N. F. Mott and H. S. W. Massey, *The Theory of Atomic Collisions* (Oxford University Press, New York, 1933), pp. 236–243.

TABLE I. Spectra enhanced by presence of helium.

1			2					3					4		5				6					7		
$N_2^+ C-X^2\Sigma$			N_2^+ neg. bands $B-X^2\Sigma$					CO⁺ first neg. bands					CO⁺ comet tail bands		N_2 sec. pos. $C^3\Pi_u-B^3\Pi_g$				H. Lyman and Balmer							
v'	I	Energy above N_2	v'	IN_2	IHe	$\frac{IN_2}{IHe}$	Energy above N_2	v'	ICO	IHe	Energy above CO		v'	I	Energy above CO	v'	IN_2	IHe	Energy above N_2	n	L	B	Energy above H	NI $n s^3P_{1/2,3/2}$	n	I	Energy above NI (Aver. of $\frac{1}{2}$ and $\frac{3}{2}$ states)
8	32	196,317	0	16	29	1.8	151,240	0	35	33	157,651		0	7	133,309	0	38	38	88,591	2	SS		82,296		3	20	86,150
9	25	198,308	1	13	22	1.7	153,616	1	51	23	159,423		1	12	134,845	1	38	37	90,585	3	SS	100	97,492		4	20	104,153
10	15	200,267	2	9	29	3.2	155,950	2	45	5	161,046		2	14	136,353	2	36	36	92,525	4	SS	31.8	102,822		5	10	110,054
11	8	202,232	3	3	18	6.0	158,242	3	38	3	162,620		3	9	137,832	3	28	17	94,214	5	S	6.8	105,291		6	4	112,731
12	1	204,134	4	1	24	24.0	160,493	4	27		164,146		4	7	139,284	4	21	6	96,249	6	5.0	1.03	106,631		7	4	114,093
13	1	206,036	5	1	3	3.0	162,700	5	16		165,623		5	5	140,707					7	4.3	0.184	107,439		8	3	114,924
													6	2	142,102					8	3.4		107,963		9	2	115,446
													7		143,469					9	3.0		108,324		10	1.5	115,865
													8		144,808					10	2.8		108,581		11	1	116,074
																				11	2.6		108,771		12	0.5	116,273
																				12	0.6		108,916		13	0.5	116,435

IN_2 denotes intensity in N_2, etc.

for the molecule ion, He_2^+, and the metastable molecule, He_2^*. The curve for the repulsive state shown was calculated from Slater's[12] formula

$$E = 4.8 \times 10^2 e^{-4.6r} \text{ ev},$$
$$r \text{ in A}.$$

The wave functions for the lowest vibrational states of the stable molecules are also indicated. If we apply the Franck-Condon principle, we see that the most probable value of the energy, E_p, will be that corresponding to a transition when r is near r_e. Transitions for r greater or less than r_e will be less probable but will occur, hence, we have available a continuous range of energies. Judging from Fig. 1, this range will extend approximately 25,000 cm^{-1} on either side of E_p. This, of course, neglects the ± 4000 cm^{-1} which can arise due to polarizability or Van der Waals forces mentioned previously. For a transfer of excitation to be probable, we must have an impurity having energy levels in the range $E_p \pm 25{,}000$ cm^{-1}.

The intensity distribution in these energy levels of the impurity will depend on the transition probabilities of the impurities as well as those for helium. For simplicity, it will be assumed here that the maximum intensity will occur in those levels in the impurity which have energy in closest resonance with E_p, corresponding to the equilibrium distance, r_e, of the helium molecules in question. This, we shall see, is not in variance with the present experimental evidence.

In the above discussion we have neglected possible excitation of the helium molecules in vibrational states above the ground state. This is justified to some extent by the fact that very little intensity is ever observed in the higher vibrational states of He_2, in fact, so little that the dissociation energies of helium molecules are not easily derived from the data. While this may cause some error in the repulsive energy, we can at least set a lower limit to this energy from the data to be considered.

Thus far, no assumption has been made about selection rules for energy transfer other than that the states are nearly in resonance. Some restriction must be placed on this. It is obvious that a collision between a helium ion and an impurity must result in ionization of the impurity, if energy transfer is to take place. For collisions with either of the metastable states considered here, the metastables make a triplet to singlet transition, hence, in order to preserve the total spin, the impurity must suffer a change in spin. If the impurity has doublet states, no difficulties will be encountered. If it has only singlets and triplets, then transitions which occur on collision must be triplet to singlet, or *vice versa*. In the case of ionization by collision with a metastable state, the spin can be preserved by ejecting an electron with the proper spin.

EXCITATION BY THE ATOMIC STATES, He^+ AND He^*

In Table I is shown a number of spectra enhanced in helium discharges. From the considerable mass of data that has come to the author's attention, this list was selected as

[12] J. C. Slater, Phys. Rev. 32, 349 (1928).

representative of the processes taking place. Data from enhanced molecular spectra have been used whenever available, since transitions to various vibrational levels of a given electronic state are more likely to depend only on the energy, E_p, than transitions to different states in atoms. Also, the energy separation between vibrational levels in molecules is likely to be less than between different energy states in atoms, and hence, we obtain a more nearly continuous measure of the energy states in helium.

Evidence for the atomic ion, He^+, and the allowable range of excitation is shown in column 1. Here is shown the sum of the intensities in all the upper, v', levels of N_2^+, $C-X^2\Sigma$ system enhanced in helium, as measured by Watson and Koontz.[13] The greatest intensity occurs in the $v'=8$ and 9 levels having energies, respectively, 1981 cm^{-1} smaller and 5 cm^{-1} larger than the ionization energy of He^+. It can be seen that there is still considerable intensity in the $v'=11$ state, 3929 cm^{-1} greater than this ionization energy. Probable transitions having $v'<8$, unfortunately, are confused by the tail of the $v'=8$ band and, hence, are not observed. This may account for the greater intensity in the $v'=8$ level than the $v'=9$, which is more nearly resonant with the helium ion.

The metastable atom, He^*, is responsible for most of the enhancement of the N_2^+ negative bands shown in the second column of Table I. These data of Merton and Pilley[14] were obtained with a Tesla coil discharge through helium containing N_2 impurity. For comparison is shown the excitation of this system in pure N_2 under identical conditions. The intensity in the $He-N_2$ mixture cuts off sharply at 160,493 cm^{-1}, 609 cm^{-1} above the excitation energy, 159,884 cm^{-1}, of He^* and can be identified as caused by He^*. The considerable intensity present in the lower levels may be caused by several effects. The process involves ionization and the electron may carry away the excess energy, almost 1 ev in this case, the N_2 concentration may be large enough to contribute to the excitation by electron impact, or perhaps the transition probabilities are such to give this, more or less, uniform distribution of intensity. In connection with the last two suggestions, it may be significant that the ratio of the intensity in He to that in pure N_2 rises to a sharp maximum at the correct energy as shown in Table I, Some intensity in the $v'=0$ level can also be caused by He_2^+, as we shall see later.

In column 3 is shown the intensity of CO^+ first negative bands $B^2\Sigma\rightarrow X^2\Sigma$ enhanced in He as compared with those in pure CO. The intensities in He are my own estimate as Johnson[15] apparently estimates the intensities in He from the head of the band, which is usually overexposed. The energies in this case were calculated, using $I(CO)=14.0$ ev. The agreement between the energy of $v'=1$, 159,423 cm^{-1}, is taken as a measure of the correctness of this value for I(CO). The limits of error are not likely to be greater than ± 0.1 ev. This is in agreement with the value, 14.1 ± 0.2 ev, as given by Sponer,[16] but in disagreement with the recent value of 14.55 ev of Amand, quoted by Gaydon and Penney.[17] In any case, we have a measure of I(CO) to be used in connection with He_2^+ and it is not likely to be in error by more than 0.5 ev.

EXCITATION BY THE MOLECULAR STATES IN HELIUM, He_2^+ AND He_2^*

The best example of enhancement by the molecule ion, He_2^+, is found in the comet tail bands of CO^+, the $A^2\Pi\rightarrow X^2\Sigma$ system. The work by Duffendack and Smith[4] in remeasuring the intensities of these bands gives us an excellent measure of the energy of the repulsive ground state of He_2 and a check on our earlier predictions. Column 4 of Table I shows the intensity distribution in the upper state of the comet tail system and the corresponding energies above the ground state of CO, using the value for $I(CO)=14.0$ ev as discussed previously. The increase in intensity up to the level $v'=2$ and subsequent decrease with higher energies well illustrates what we anticipated. We take the corresponding energy 136,000 cm^{-1} to be E_p, the energy obtained in a transition between He_2^+ and He_2 repulsive state

[13] W. W. Watson and P. G. Koontz, Phys. Rev. **46**, 32 (1934).
[14] T. R. Merton and J. G. Pilley, Phil. Mag. **50**, 195 (1925).
[15] R. C. Johnson, Proc. Roy. Soc. **A108**, 343 (1925).
[16] H. Sponer, *Molekulspectren* (Verlagsbuchhandlung, Julius Springer, Berlin, 1935).
[17] A. G. Gaydon and W. G. Penney, Proc. Roy. Soc. **A183**, 374 (1944).

with electron capture, at the equilibrium distance, 1.090A, for He_2^+. The limits of excitation by He_2^+ are by no means restricted to the values given in the table. With longer exposures, Johnson[15] obtains excitation to $v'=9$. The $v'=0$ level of N_2^+ negative bands, having energy 151,000 cm^{-1}, can also be excited by He_2^+.

The N_2 second positive band system enhanced in helium would be an excellent example for resonance with He_2^* since the excitation potential is nearly correct, but the bands break off at $v'=4$ and, hence, we cannot follow the intensities as we did in the case of the comet tail bands. In column 5 of Table I are shown the intensities of this system in pure N_2 and in He. The intensities in He are my own eye estimates. It would be difficult to tell, without very careful measurement, whether the decrease in intensity indicated in the column is real or only apparent. To supplement this information we have shown the intensities of excitation in helium of the Lyman and Balmer series of atomic hydrogen in column 6 and the principal series of NI in column 7. The Lyman series up to $n=6$ is usually strongly over exposed. Estimates of intensities from $n=6$ to $n=12$ are from Rao and Badami[18] and indicate merely the range of excitation to be expected. The Balmer series has been measured carefully by Merton and Nicholson[19] and the intensities listed are absolute. This distribution may be affected somewhat by transition from higher levels and, hence, the sharp decrease with increasing n is not too significant. The lowest observed line at 97,492 cm^{-1} is much stronger than the rest.

In NI, column 7, the result is similar. These data taken from Kamiyama[20] show the lines having excitation energies 86,150 cm^{-1} as much stronger (although probably overexposed) than the remaining lines. The range of excitation is almost the same as that in hydrogen. It is perhaps significant that the only members of the $sp^4\,{}^4P$ series which appear have excitation energy 88,000 cm^{-1} and appear with maximum intensity 10. (The intensity 20, as indicated in the table, is a result of two transitions.) It might be noted, parenthetically, that Duffendack, Henshaw, and Goyer[21] have measured strong excitation of Mg^+ in He at an energy 12.02 volts $\sim$96,000 cm^{-1} above the ground state of Mg, but only the strong lines are given so that we cannot observe the trend.

In all cases the maximum enhancement seems to occur from 85,000 cm^{-1} to 100,000 cm^{-1}, hence we shall take the decrease in intensity of the N_2 second positive system at $v'=3$ as representing a decrease in excitation probability, and $v'=2$ with an energy of 92,000 cm^{-1} as corresponding to E_p, the transition energy between He_2^* and He_2 at $r_e=1.052$A. This is not likely to be in error by more than the energy, 2000 cm^{-1}, corresponding to one vibrational jump in N_2 or there would be a slightly different distribution of intensities relative to the $v'=0$ and $v'=1$ states. This error is not serious when we consider that the Van der Waals energies can be at least that large.

REPULSIVE ENERGY BETWEEN TWO NORMAL HELIUM ATOMS

In order to determine the repulsive energy of the ground state of the helium molecule we need to know, in addition to the above energy differences, the energy of the stable molecules above that of two unexcited helium atoms at infinite distance of separation. A knowledge of the dissociation products, their excitation potentials, and the dissociation energy is sufficient for this purpose. From spectroscopic data we know that He_2^* dissociates into $He^*(^3S)$, the atomic metastable (excitation energy of 159,884 $cm^{-1}=19.81$ ev) and He, the normal helium atom. Similarly, He_2^+ dissociates into the normal ion He^+ (ionization potential 198,298 $cm^{-1}=24.58$ ev) and a normal helium atom. Also, from the Rydberg series in He_2, we know the ionization potential of He_2^*, relative to He_2^+ to be 34,302 $cm^{-1}=4.25$ ev. Hence, the dissociation energy of He_2^* or He_2^+ is all that is required. Unfortunately, the experimental values of these are very inaccurate because $v'=2$ is the highest vibrational state observed in any of the molecules. From this Weizel[22] estimates the dissociation energies of the helium molecules to be around 2.5 ev. We shall take the recent theoretical value for $D_e=2.22$ ev for He_2^+

[18] Rao and Badami, Proc. Roy. Soc. **A138**, 540 (1932).
[19] T. R. Merton and J. W. Nicholson, Proc. Roy. Soc. **A96**, 112 (1919).
[20] M. Kamiyama, Sci. Pap., I.P.C.R. **36**, 375 (1939).
[21] O. S. Duffendack, C. L. Henshaw, and M. Goyer, Phys. Rev. **34**, 132 (1929).
[22] W. Weizel, *Bandenspektren* (Akad, Verlagsges, m.b.z., Leipzig, 1931), pp. 255, 270.

obtained by Weinbaum[23] as being more nearly correct, since his values of the total energy and internuclear distance compare favorably with experimental values. Using this value and the cycle

$$D_e(He_2^*)+I(He^{*3}S)=I(He_2^*)+D_e(He_2^+),$$

we obtain $D_e(He_2^*)=4.25+2.22-4.77=1.70$ ev. Errors in these values greater than 0.2 ev are very unlikely.

These values for D_e were used to construct the Morse curves for He_2^* and He_2^+ in Fig. 1. The molecule ion is seen to have an energy of 22.4 ev electronic energy plus 0.1 ev vibrational energy or 22.5 ev in its lowest vibrational state. Subtracting the previously determined value for the most probable energy, $E_p=136{,}000$ cm$^{-1}=16.7$ ev, 5.8 ev is obtained for the repulsive energy at $r=1.090$A. Likewise, He_2^* is found to have 18.2 ev energy. Subtracting the value 92,000 cm^{-1} $=11.4$ ev, the repulsive energy at $r=1.052$A is found to be 6.8 ev. If our assumptions for determining the most probable value of the energy, E_p, are correct, these values are probably accurate to better than ± 0.5 ev. These points have been indicated in Fig. 1.

These results are in disagreement with the theoretical values and with other experiments. Slater's potential, which he indicates should represent the repulsive energy for distances greater than 1A, is only about half as large as those obtained here. Rosen[24] obtains values still lower. Amdur and Pearlman[25] from scattering experiments suggest still a softer potential. However, in their experiments they measure scattering of neutralized ions in helium, which, even if extreme purity conditions are satisfied, are confused by the presence of the molecule ion He_2^+.

It seems unlikely that this disagreement is caused by the methods employed in this paper since none of the other results are capable of the accuracy quoted here. If transitions from He_2^* and He_2^+ in higher vibrational levels occur, then E_p would be measured down from some higher point on the curves. This would make a positive correction to the repulsive energy and, hence, increase the discrepancy. (The values quoted here correspond to the lower limit of the energy.) The perturbation methods employed by Slater, Rosen, and others in determining the repulsive energy are likely to be inferior to the variation method employed by Weinbaum in calculating the binding energy of He_2^+. The employment of two variation parameters instead of one as used by Pauling[26] only changed D_e by 0.2 ev. On the other hand, Rosen[24] and Slater,[12] using slightly different charge distributions, obtain results which agree only in the neighborhood of 3A but diverge at smaller distances. At $r=1.43$A, the smallest distance given by Rosen, Slater obtains 0.67 ev compared with 0.39 ev obtained by Rosen. A final check on this curve would be the measurement of the intensity distribution of the helium continuum in the spectral region of 600A to 1200A. To date this has not been done.

The present method is not limited to the determination of the repulsive energy at two points as was done here, but can be extended to include most of the interesting range if careful intensity measurements are made in helium mixtures under controlled conditions. It should be possible to evaluate the energy from a molecular combination as simple as He_2^* and H. It may even be possible to treat He_2^+ and CO which produce the comet tail bands. More will be said about the experimental conditions in the next section.

FORMATION OF THE MOLECULAR STATES OF HELIUM

Since helium is a monatomic gas, the question arises as to the mechanism responsible for the molecular states. Some clue to this is suggested by the work of Ebbinghaus discussed by Mitchell and Zemansky[3] on the rate of decay of metastable atoms, He*. The differential equation for the number, n, of He* per cc

$$dn/dt=-\beta n^2, \qquad (1)$$

where β is an experimentally determined constant. Metastable atoms are removed from the gas by diffusion to the walls and by collisions with other atoms. The first process varies inversely with the pressure, the second proportional to the pressure.

[23] S. Weinbaum, J. Chem. Phys. **3**, 547 (1935).
[24] N. Rosen, Phys. Rev. **38**, 255 (1931).
[25] Amdur and Pearlman, J. Chem. Phys. **9**, 503 (1941).
[26] L. Pauling, J. Chem. Phys. **1**, 56 (1933).

(It may be some higher power of p.) Mitchell and Zemansky give the following value for β,

$$\beta = 1350/p + 107p, \qquad (2)$$

where p is expressed in mm of Hg. From the first term, the cross section for diffusion of He* in He is found to be 11.1×10^{-16} cm², while from the second, the cross section for decay by collisions with helium atoms is found to be 0.000059×10^{-16} cm².

The assumption is made that this cross section, 0.000059×10^{-16} cm², is that of the following reaction,

$$\mathrm{He}(^3S)+\mathrm{He}+0.78 \text{ volt} = \mathrm{He}(^1S)+\mathrm{He},$$

where the 0.78-volt energy is supposed to arise from the thermal energy of the gas. Not only is this a very large cross section for a process which requires this amount of energy, as is stated by Mitchell and Zemansky, but it requires a change in spin on collision, which is very improbable.

In line with the other evidence presented in this paper, it is suggested that this might be the cross section for the formation of the helium metastable molecule, He_2^*. Comparing this cross section with that for diffusion, one can say roughly that one collision in 10^5 effective in diffusion produces a molecule He_2^*. This hypothesis is susceptible to verification by measuring simultaneously the rates of decay of the atom, He*, and the molecule, He_2^*.

EXPERIMENTAL CONDITIONS FOR OBSERVING MOLECULAR STATES

The optimum experimental conditions for the production of any spectra enhanced in helium are determined by the formation of He_2^*. If the helium pressure is too high, enhancement of spectra of an impurity by He* may not take place because of molecule formation, while if it is too low the concentration of He* is diminished by diffusion to the walls of the vessel. On the other hand, if the spectra are enhanced by He_2^*, at too low pressure, He_2^* will not be formed, or if the impurity destroys He*,† too high a partial pressure of the impurity will also hinder the production of He_2^*.

Some insight into the optimum pressures for a given process can be had from the data of Ebbinghaus. He used a rectangular gas absorption tube, length 5.2 cm and thickness 1.65 cm. These dimensions are not much different than those of discharge tubes, hence his coefficients will at least be of the correct order of magnitude. We shall take the term $1350n'/p$ to represent the diffusion of He_2^*, while the term $107pn$ to represent the rate of increase of He_2^* due to collisions, where n' = number of He_2^* per cc. Other processes for production of He_2^* involving higher excited states are very likely operating, so that the term here only corresponds to a lower limit. The equation for the rate of change of He_2^* in time is then,

$$dn'/dt = 107pn - 1350n'/p. \qquad (3)$$

In a steady-state discharge, as an uncondensed or Corona discharge, n and n' do not change with time. For this case we can equate $dn'/dt=0$ and obtain the following relation between the concentrations of He_2^* and He*

$$\frac{n'}{n} = \frac{107p^2}{1350} = 10^{-1}p^2.$$

For $p=0.1$ mm, $n'/n=10^{-3}$ while for $p=100$ mm, $n'/n=10^3$.

These results are in qualitative agreement with experiment. Helium molecular spectra are produced best in wide bore tubes at pressures above one cm. The measurements of NI and N_2 second positive spectrum enhanced by He_2^* given in Table I, are for helium pressures of 4 cm and 30 cm, respectively. The helium pressure for enhancement by both He_2 and He in the same discharge (where pressure is given) seems to average several millimeters.

In the light of the present discussion, perhaps this theory, while not completely correct, may serve as a guide to the selection of the proper conditions under which to observe a given spectrum.

HELIUM IONS IN HELIUM

In attempting to decide which ion, He^+ or He_2^+, is most likely to be present at high helium

† In N_2-He mixtures this is likely to occur. R. Bernard, Ann. de Physique 13, 1 (1940), using controlled electron impact in mixtures containing 5 to 20 percent N_2 did not observe any unusual enhancement of the N_2 second positive system and hence states that the enhancement of N_2 in He is limited to the production of N_2^+ first negative system due to He. A partial pressure of N_2 of say one part per 10^3 will likely hinder the production of He_2 molecules due to the formation of N_2^+ first negative system.

pressures, we have in addition to the above results, the following information. First: in the mass spectrograph, at pressures from 10^{-4} cm to 4×10^{-4} cm, Arnot and M'Ewen[27] find He_2^+ present and that its concentration increases relative to that of He^+ with pressure. Second: the Comet tail bands of CO^+ produced by He_2^+ appear readily at helium pressures of about one cm. Johnson[15] obtained these bands in an uncondensed discharge while Duffendack and Smith[4] used controlled electron impact in helium. This indicates the presence of measureable concentrations of He_2^+ at higher pressures. On the other hand, Watson and Koontz[13] and more recently Takamine, Suga, and Tanka[28] found a strongly condensed discharge at helium pressures from 0.01 cm to 1.8 cm and relatively long exposures necessary to bring out the $C-X^2\Sigma$ system of N_2^+, which indicates the presence of He^+. Third: Tyndall and Powell using a corona discharge at helium pressures of 30 cm find only *one* ion present (they can detect the presence of several ions with their method). Thus we know that He_2^+ is present at very low pressures and that the concentration increases with pressure relative to that of He^+. He_2^+ appears more easily than He^+ at high pressures as evidenced by collisions of the second kind.

These experiments at least demonstrate that He_2^+ should be produced by the ion source used by Tyndall and Powell. The fact that only one ion is found using this source would lead us to believe that the He^+ ion was present in insufficient concentration to be detected. If the previous calculations on the ratio of the concentrations of He_2^* to He^* are correct, this result is to be expected. Ionization in such a discharge is likely to be a step process with metastables first produced and then ionized. Production of He_2^+ from He_2^* is favored over that of He^+ from He^* by electron impact in the same gas, both by having a lower ionization potential and, probably, a larger cross section. The ionization potential of He_2^* is 4.25 ev as compared with 4.77 ev for He^*. Since He_2^* is a molecule consisting of two atoms separated by 1A, in a state analogous to He^*, geometrical considerations alone would predict a larger cross section. Thus, the presence of He_2^+ to the exclusion of He^+ in the corona discharge at high pressures seems accounted for.

[27] F. L. Arnot and M. B. M'Ewen, Proc. Roy. Soc. **A171**, 106 (1939).

[28] Takamine, Suga, and Tanka, Sci. Pap. I.P.C.R. **36**, 437 (1939).

THE MOBILITY OF He_2^+ AND He^+ IN HELIUM

The interpretation of the data presented in this paper gives strong support to the earlier suggestion by the author[10] that the value 21.4 cm²/sec. volt for the mobility of helium ions produced by a positive corona source refer to that of the molecule ion He_2^+. The theoretical value of the mobility of He^+ in helium calculated by Massey and Mohr,[2] 12 cm²/sec. volt, and perhaps confirmed by earlier measurements by Tyndall and Powell[29] using an α-particle ion source, is much smaller than that of He_2^+. We have here what on first sight appears to be a paradoxical situation in which a "clustered" ion, He_2^+, has a larger mobility and, hence, a smaller cross section for diffusion than the unclustered one. This paradox results from the fact that the possibility of charge exchange exists in collision of He^+ with a helium atom which is absent in the case of He_2^+. This charge exchange can be interpreted as a large angle scattering and, hence, a large cross section. Massey and Mohr[2] have shown that without taking charge exchange into account, the theoretical mobility of He^+ in He would be 24 cm²/sec. volt while taking it into account, the value of the mobility is reduced to 12 cm²/sec. volt. When these exchange forces are small, the mobility is determined by the polarizability of the helium atom in the field of the ion. If this is assumed to be the case for He_2^+ in helium, and the value 24 cm²/sec. volt is corrected for the fact that He_2^+ has a mass 8 instead of 4, to which the above value would refer, we obtain 22 cm²/sec. volt as an approximate theoretical value of the mobility of He_2^+ in He. The agreement between this value and the experimental value 21.4 cm²/sec. volt is the best yet reported in this field.

H_2 SPECTRA EXCITED IN HELIUM

The H_2 spectrum excited in helium discharges has been subjected to extensive investigation and the results have been summarized by Richardson.[7] In the triplet spectrum, the excitation is practically confined to the low vibrational levels of H_2.

[29] A. M. Tyndall and C. F. Powell, Proc. Roy. Soc. **A129**, 162 (1930).

The action of the helium in this case is usually interpreted as quenching the higher vibrational levels of the excited molecules before they radiate. This is feasible, since the masses of the H_2 molecule and the He atom in this case are nearly equal. This is not the complete explanation, however. The observations have all been made on the transitions where the initial levels are all about 112,000 cm^{-1} above the ground state of H_2. Reference to column 7, Table I, will show that this is about the limit of the excitation of He_2^*. Since the vibrational levels are separated by about 2000 cm^{-1}, the excitation of the various electronic states in the range of 112,000 cm^{-1} is more probable than excitation of higher vibrational levels of a low-lying electronic state.

The level $1s\sigma 2s\sigma^3\Sigma_g^+$, 95,226 cm^{-1} above the ground state of H_2, which is responsible for the hydrogen continuum, may have many vibrational levels excited. This coupled with the "quenching" action of helium may account for discrepancy between Smith's[8] measurements of the intensity distribution of the hydrogen continuum produced in helium and hydrogen mixtures, and those of Coolidge[9] produced in pure hydrogen by controlled electron impact.

NEON MOLECULES

In most of the references listed in this paper, data of enhanced spectra in neon mixtures are also given. Enhancement appears at energies slightly higher than that caused by He_2^* and possibly over a longer range of energies. This is probably caused by neon metastable molecules. However, discussion of these effects must be deferred until more information is available, about either the attractive or the repulsive state in neon.

ACKNOWLEDGMENT

The author wishes to express his thanks to Professors W. W. Watson and H. Margenau of Yale University for valuable discussions and criticisms during the preparation of this paper.

PHYSICAL REVIEW VOLUME 70, NUMBERS 9 AND 10 NOVEMBER 1 AND 15, 1946

The Determination of X-Ray Diffraction Line Widths

C. G. SHULL*
Beacon Research Laboratory, The Texas Company, Beacon, New York
(Received June 20, 1946)

The methods which have been suggested for correcting x-ray diffraction line widths for geometrical effects are reviewed. Experimental data are presented for two samples of finely-divided NiO and MgO which show that neither the Warren nor the Jones correction method is valid for *these particular specimens*. A direct Fourier transform procedure is given which permits calculation of the corrected diffraction line width for all experimental cases.

INTRODUCTION

IT is well known in x-ray diffraction studies that the size of the diffracting crystals determines to a certain extent the sharpness or diffuseness of the observed diffraction line. With the usual type of diffraction cameras, the diffraction broadening is noticeable with crystal sizes in the range of 400–500A and becomes more pronounced as the crystal size is reduced. Numerous applications of this broadening have been made in the past in determining the crystal sizes present in experimental systems.

It has been shown[1–3] that the angular breadth β of a diffraction line should be given by

$$\beta = C\lambda/L\cos\theta, \qquad (1)$$

where C is a constant, λ the x-ray wave-length, L the size of the crystal, and θ the Bragg angle corresponding to the diffraction line under study. In this expression, either the "half-width" (total width at half maximum) or the "integral width"

* Now at Clinton Laboratories, Oak Ridge, Tennessee.

[1] P. Scherrer, *Kolloidchemie* (Zsigmondy, 1920), third edition, p. 387.
[2] W. H. and W. L. Bragg, *Crystalline State* (The Macmillan Company, New York, 1933), p. 189.
[3] A. L. Patterson, Phys. Rev. 56, 972–982 (1939).

(area under diffraction peak divided by peak maximum) definitions of β can be used. The value of the constant C (commonly referred to as the Scherrer constant) will depend upon the definition of β, as Patterson[3] and others have shown.

The most recent and reliable calculations of the Scherrer constant for crystals of cubic symmetry have been made by Patterson,[3] Stokes and Wilson,[4,5] and Murdock.[6] These investigators have shown C to depend upon the crystal shape and the diffraction line indices, and in all cases to be not far removed from unity.

Before applying Eq. (1) to experimental data, it is necessary to correct the observed diffraction line widths for geometrical effects (finite specimen size, divergence in incident x-ray beam, absorption in specimen, etc.) which contribute to the observed broadening. Some of the earlier proposed methods for making these corrections have been reviewed by Clark.[7] These correction procedures are incomplete in spite of being rather involved and lead to the possibility of considerable error in the final result.

More recently Jones[8] has suggested a mixture method which furnishes a direct experimental determination of the necessary geometrical corrections. In the Jones method, the material (A) of unknown crystal size is intermixed with a second material (B) whose crystals are very large (larger than 1000A) and hence whose diffraction broadening is negligible. The widths of the diffraction lines of (B) can then be considered the geometrical width contributing to the observed width of (A). This is so because the same geometrical conditions were present during the simultaneous irradiation of both (A) and (B). There are certain precautions which must be taken to insure the equivalence of geometrical effects for (A) and (B) as Taylor[9] has pointed out. These include: (1) a mass absorption coefficient for (B) not far removed from that of (A) and (2) a crystal size for (B) which is not large enough that its diffracted radiation would suffer an absorption (including extinction) different from that characterized by the mixture composition.

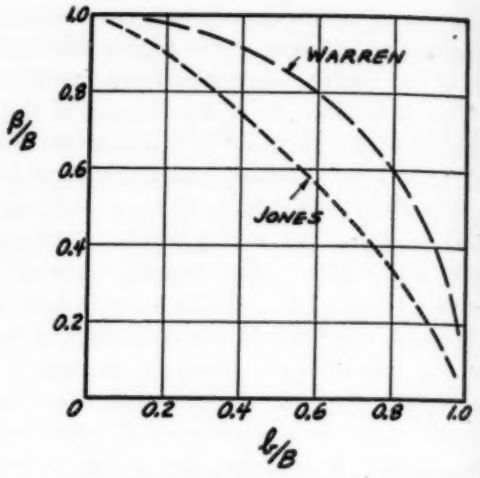

FIG. 1. Curves for correcting observed diffraction line width for geometrical width.

Jones[8] has worked out a procedure for applying the corrections obtained by this mixture method. After correcting all of the diffraction line widths for the presence of the $K\alpha$ doublet, the pure diffraction width β is obtained from the true width[10] B of material (A) and from the true width b of material (B) through use of a correction curve. This correction curve is shown as the Jones curve in Fig. 1. Since B and b are known from experimental data, the pure diffraction width β can be evaluated from the curve in this figure.

Warren,[11] on the other hand, has proposed a different correction curve from that by Jones and his is also included in Fig. 1. In comparing the two curves, it is seen that a considerable difference in results can be obtained by the two methods, especially if the experimental data fall in the range of b/B values above 0.4. Unfortunately with samples of crystal size 100A or larger and with the usual cylindrical type of diffraction camera, the experimental data generally fall in this unfavorable region of b/B and hence there is uncertainty in the result because of the differences in the correction curves.

The present paper deals with observations on two samples of finely divided materials, NiO and

[4] A. R. Stokes and A. J. C. Wilson, Proc. Camb. Phil. Soc. **38**, 313 (1942).
[5] A. R. Stokes and A. J. C. Wilson, Proc. Camb. Phil. Soc. **40**, 197–198 (1944).
[6] C. C. Murdock, Phys. Rev. **63**, 223 (1943).
[7] G. L. Clark, *Applied X-Rays* (McGraw-Hill Book Company, Inc., New York, 1940), third edition, pp. 490–499.
[8] F. W. Jones, Proc. Roy. Soc. **166A**, 16–43 (1938).
[9] A. Taylor, Phil. Mag. **35**, 215–229 (1944).
[10] True width corresponds to the diffraction line width after the doublet correction has been applied to the observed width.
[11] B. E. Warren and J. Biscoe, J. Am. Ceramic Soc. **21**, 49 (1938).

MgO, and is intended to show the differences between the results obtained by the two correction methods. It is seen in Fig. 1 that the two curves show a different dependence upon b/B values and this suggests a means for selecting one over the other. Since for any sample the true diffraction broadening β should be independent of experimental conditions, a study of β_W (calculated according to the Warren curve) and β_J (calculated according to the Jones curve) should indicate a preference between the two methods.

In addition to the Warren and Jones procedures for correcting the observed diffraction line for geometrical effects, there is a resolution procedure available which enables a direct evaluation of the diffraction width. Such an evaluation has been carried out for the present materials and comparisons will be made in a later section with the results obtained by the correction methods. We proceed first to a study of the direct resolution procedure for evaluating the pure diffraction width.

DIRECT EVALUATION OF THE DIFFRACTION WIDTH

Jones[8] has shown that the function $k(x)$ representing the observed intensity of diffraction as a function of the distance x from the center of the diffraction line can be obtained from

$$k(x)=\int_{-\infty}^{\infty} g(u)f(x-u)du, \tag{2}$$

where g represents the distribution of intensity across a line possessing no diffraction broadening and f corresponds to the intensity distribution which would have been obtained with an infinitely narrow and perfectly collimated x-ray beam and an infinitely small specimen. The function k would, for example, represent the observed profile of the diffraction line of material (A) above, while g would represent the material (B) line profile. It is desired to evaluate the function f from experimental data for k and g. This can be performed conveniently by use of Fourier transform theory.[12]

We let K, G, and F be the Fourier transforms of k, g, and f as defined by equations of the form

$$K(t)=(2/\pi)^{\frac{1}{2}}\int_0^{\infty} k(x)\cos xtdx. \tag{3}$$

Only the cosine transforms need be considered here since all of these functions are symmetrical about their origin points. It follows from Eq. (2) that[13]

$$F(t)=K(t)/G(t) \tag{4}$$

and hence

$$f(x)=(2/\pi)^{\frac{1}{2}}\int_0^{\infty} F(t)\cos xtdt. \tag{5}$$

Thus when k and g are known, a straightforward process is available for determining the function f from which the diffraction width can be easily obtained. The general process is rather cumbersome since it involves finding transforms for three functions which are known only numerically and not analytically. However, it has been found from experimental data that the functions k and g can be closely approximated by simple analytical functions (within experimental error) and this serves to simplify the numerical work greatly. Several special cases are given in the following.

Case I: When

$$g(x)=\exp(-m^2x^2)+\sigma\exp(-n^2x^2)$$

and

$$k(x)=\exp(-p^2x^2)+\tau\exp(-q^2x^2). \tag{6}$$

It follows that

$$G(t)=\frac{1}{\sqrt{2}m}\exp\left(-\frac{t^2}{4m^2}\right)+\frac{\sigma}{\sqrt{2}n}\exp\left(-\frac{t^2}{4n^2}\right) \tag{7a}$$

and

$$K(t)=\frac{1}{\sqrt{2}p}\exp\left(-\frac{t^2}{4p^2}\right)+\frac{\tau}{\sqrt{2}q}\exp\left(-\frac{t^2}{4q^2}\right), \tag{7b}$$

and hence $f(x)$ can be obtained by insertion of

[12] The present problem is very similar to that encountered in determining the shape of x-ray emission lines from the rocking curves obtained with double crystal spectrometers. A general treatment of the spectrometer problem has been given by L. P. Smith (Phys. Rev. **46**, 343–351 (1934)) and the present treatment can be considered as a simplified and specialized one applicable to the conditions found in this type of investigation.

[13] E. C. Titchmarsh, *Introduction to the Theory of Fourier Integrals* (Oxford University Press, New York, 1937), p. 51.

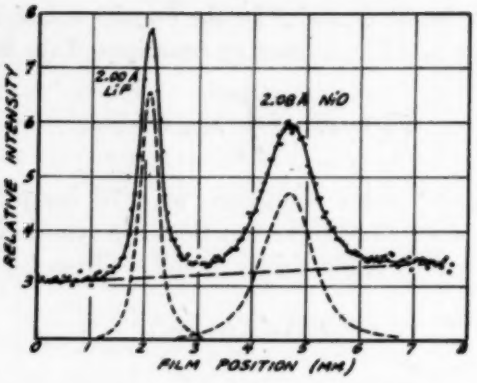

FIG. 2. Intensity distribution over typical NiO and LiF diffraction lines.

Eq. (7) into Eq. (4) followed by the evaluation of Eq. (5).

For this particular case F can be evaluated directly from the parameters given in Eq. (6) and hence only one transformation is necessary. If additional exponential terms are needed to represent either k or g above, the solution is still available after carrying out one transformation.

Case II: When

$$g(x)=\exp(-m^2x^2)$$

and

$$k(x)=\exp(-p^2x^2)+\tau\exp(-q^2x^2). \quad (8)$$

It follows that

$$F(t)=\frac{m}{p}\left\{\exp(-r^2t^2)+\frac{\tau p}{q}\exp(-s^2t^2)\right\} \quad (9)$$

where

$$r^2=\frac{m^2-p^2}{4m^2p^2} \quad \text{and} \quad s^2=\frac{m^2-q^2}{4m^2q^2},$$

and hence

$$f(x)=\frac{m}{\sqrt{2}p}\left\{\frac{1}{r}\exp\left(-\frac{x^2}{4r^2}\right)+\frac{\tau p}{q}\frac{1}{s}\exp\left(-\frac{x^2}{4s^2}\right)\right\}. \quad (10)$$

Thus the function representing the diffraction line profile free of geometrical contributions can be written directly in terms of the parameters of (8). Moreover if our interest is confined to the integral width of this diffraction line, this can also be obtained directly as

$$\beta=\frac{1}{f(0)}\int_{-\infty}^{\infty}f(x)dx$$

$$=2\sqrt{\pi}rs\left[\frac{1+\tau p/q}{s+r\tau p/q}\right]. \quad (11)$$

Thus the pure diffraction width may be obtained by mere evaluation of the parameters describing the observed diffraction lines.

Case III: When

$$g(x)=\exp(-m^2x^2)$$

and

$$k(x)=\exp(-p^2x^2). \quad (12)$$

It follows that

$$f(x)=\frac{m}{\sqrt{2}p}\frac{1}{r}\exp\left(-\frac{x^2}{4r^2}\right) \quad (13)$$

and that

$$\beta=2\sqrt{\pi}r. \quad (14)$$

This expression for the integral width is identical with that obtained by the Warren correction method with B and b obtained from Eq. (12).

EXPERIMENTAL TECHNIQUE

Samples of finely divided NiO and MgO were used as specimens in the present study. Both oxide samples were prepared by heating in air the respective carbonates, one hour at 750°F for NiO and six hours at 1200°F for MgO. A series of x-ray photograms for each of these samples was taken under various experimental conditions. Most of the photograms were taken in cylindrical type diffraction cameras (radii 28.8 and 71.7 mm) with powder specimens packed into small glass capillaries.

Pulverized LiF and NaCl were used as calibration materials to provide diffraction lines possessing no diffraction broadening. These calibration materials were obtained by grinding single crystal fragments of the halide until microscopic examination showed the final powder particle size to be of the order of one micron and smaller. Crystals of such size would, of course, produce no observable diffraction broadening. Careful mixing

of the calibrating material with the oxide samples was performed to insure equivalence of geometrical effects during the x-ray examination.

Thin-walled glass capillaries of various diameters between 0.3 and 0.8 mm were used as specimen holders along with different conditions of primary x-ray beam collimation. Filtered radiation from both copper and cobalt target x-ray tubes was used. By changing the conditions of beam collimation, specimen size, x-ray wavelength and camera radius, it was possible to obtain data covering quite a range of b/B values. Some data were also taken in a Brentano "focusing" spectrometer type of instrument and these data combined with those taken in the cylindrical cameras covered a b/B range from 0.25 to about 0.8.

Specimen mixtures of NiO-LiF and MgO-NaCl were used in the experimental investigation. With the NiO-LiF mixture, the 2.08A-NiO diffraction line (200) and the 2.00A-LiF diffraction line were selected for study. These two lines were sufficiently close together so that the width of the LiF line could be considered the geometrical width present at the NiO line position. A microphotometer trace showing the intensity distribution across a typical pair of these lines is given in Fig. 2. After resolving the individual peaks from the background, the observed widths b_0 and B_0 (using Jones' notation) were determined for the LiF and NiO peaks, respectively. Similar data were taken for the 2.10A-MgO line and the 1.99A-NaCl line in MgO-NaCl specimen mixtures.

Integral peak widths (in which the area under the peak is divided by the peak maximum) have been used exclusively in the present investigation. It has been found that such widths are to be preferred experimentally to half-width values because of their greater internal consistency.

TABLE I. Results of Fourier transform determinations of the diffraction width.

NiO (All values expressed in terms of 10^{-2} radians)	MgO
$\beta = 1.33$	1.57
1.40	1.34
1.40	1.61
1.34	1.37
1.31	1.20
1.41	1.43
1.51	1.38
Average = 1.39 ± 0.05	1.41 ± 0.10

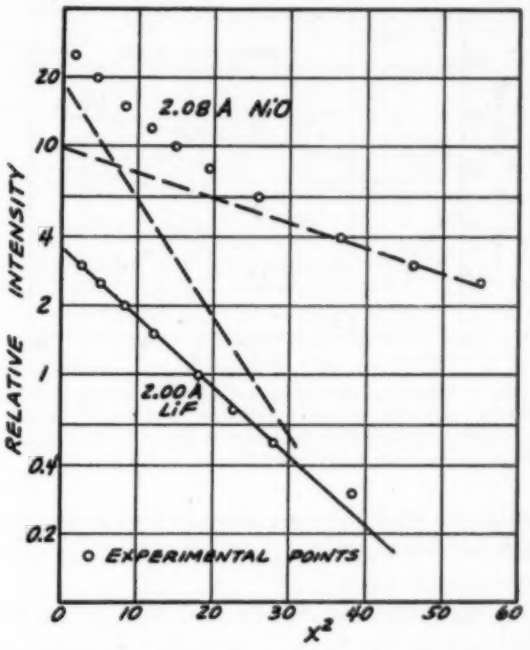

FIG. 3. Graph showing relative intensity *versus* distance from center of line squared (arbitrary units) for NiO and LiF diffraction lines.

Moreover integral widths would appear to be of more significance when a distribution of crystal sizes is encountered in the specimen. All crystal sizes would be contributing to the integral width value in a known degree of weighting[8] whereas this would not be the case with half-width values.

ANALYSIS OF EXPERIMENTAL DATA

The data analysis by the Fourier transform procedure will be considered first. It has been found that the experimental curves, such as given in Fig. 2, can be represented sufficiently closely by the analytical functions (8) corresponding to Case II above. Figure 3 shows a semi-logarithmic plot of the intensity *versus* distance squared from center of line for a pair of NiO-LiF diffraction lines. The representation of the NiO line by the sum of two straight lines and the LiF line by one straight line indicates the applicability of the conditions described in Case II.

The Fourier transform analysis has been applied to fourteen sets of data (covering a wide range of geometrical conditions) for the two specimens with the results given in Table I. The standard deviations have been calculated from the internal consistency of the data. It is purely

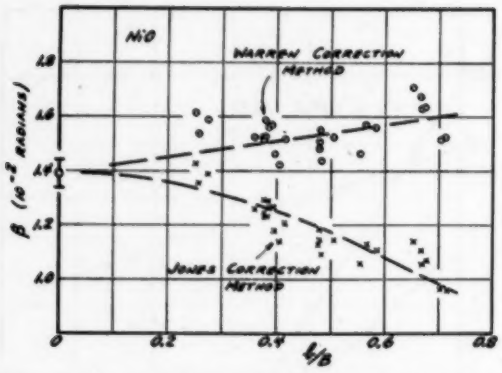

FIG. 4. Variation of the pure diffraction width of 2.08A-NiO line with geometrical conditions. The point plotted on the ordinate axis is that taken from Table I. All values are on the basis of an x-ray wave-length of 1.54A.

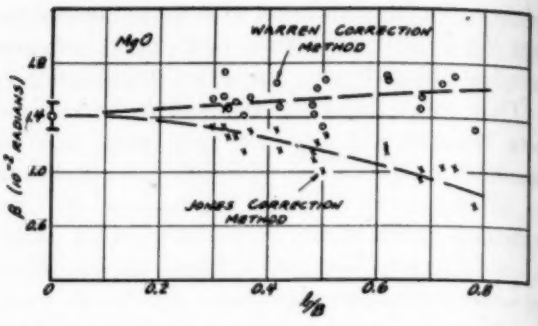

FIG. 5. Variation of the pure diffraction width of the 2.10A-MgO line with geometrical conditions. The point plotted on the ordinate axis is that taken from Table I. All values are on the basis of an x-ray wave-length of 1.54A.

fortuitous that the two average values are close together since there is no connection between their crystal sizes.

In applying the Warren and Jones correction methods to the data, it was first necessary to correct for the presence of the $K\alpha$ doublet. This was done by the method outlined by Jones.[8] In general this correction was small because of the small separation of the doublet components at these angles of diffraction. These corrected width values, b and B, were then used to determine the pure diffraction widths β_W and β_J from the curves of Fig. 1.

Figures 4 and 5 show the pure diffraction widths for the 2.08A-NiO line and the 2.10A-MgO line plotted against b/B values. There is considerable spread among the experimental points but nevertheless definite trends in the data can be seen. Also shown in Figs. 4 and 5 along the ordinate axes are the average values for the pure diffraction widths as given in Table I. Since both the Warren and Jones correction curves intersect at a common value along the ordinate axis, the data calculated by the correction methods should likewise show the trend toward a common intersection representing the true diffraction width. The curves through the experimental points in these figures have been drawn with this in mind although the data are not sufficiently significant to warrent selection of a particular curve shape. The intersection point would be, of course, the value to be inserted into Eq. (1) in determining the crystal size.

DISCUSSION OF RESULTS

It would appear from the sequence of data shown in Figs. 4 and 5 that neither the Warren nor the Jones correction curve was the most suited *for these particular specimens*. An intermediate correction curve would have been more suitable. Such a correction curve, applicable for all cases covered by the conditions given in Eq. (8), could of course be constructed. If the diffraction lines had been of shape characterized by Case III above, the Warren method would have been acceptable. It is to be emphasized that other specimens may show diffraction line shapes different from those for the present specimens because of differences in crystal size distribution. Thus the optimum correction curve depends upon the particular line shapes encountered experimentally.

Of course, the best procedure in determining crystal sizes is that of obtaining experimental data under conditions where the correction to be applied is small, namely, small values of b/B. If this is not possible or feasible, as is the case with crystal sizes in the upper range of measurable sizes, then it would appear necessary for best results to study the diffraction line shapes. In any event the Fourier transform procedure is a direct one applicable to all cases.

ACKNOWLEDGMENTS

Grateful acknowledgment is accorded to Dr. L. C. Roess for helpful discussions and to Miss Sybil Cumming for assistance in accumulating experimental data.

The Orientation of Electrical Breakdown Paths in Single Crystals

J. W. DAVISSON*
Laboratory for Insulation Research, Massachusetts Institute of Technology, Cambridge, Massachusetts
(Received July 8, 1946)

The effect of temperature on the orientation of electrical breakdown paths in the alkali halide crystals has been investigated. The results obtained suggest the existence of a path sequence

random→[100]→[111]→[110]→[*xxy*]

assumed by the direction of breakdown as the lattice energy or temperature increases. Star patterns of 12 non-primitive lattice directions were observed in LiCl and LiF. Mixed and impure crystals grown from the melt tend to exhibit high temperature path patterns at low temperatures. By extending the study at room temperature to crystals possessing different bonding and symmetry properties, general laws governing path orientation are established. It is shown that the possible path directions depend upon the macroscopic symmetry prevailing and are apparently not influenced by the type of lattice bond.

I. INTRODUCTION

THAT electrical breakdown through single crystals can result in the formation of breakdown paths orientated in distinct crystallographic directions was discovered independently and almost simultaneously by L. Inge,[1] A. von Hippel,[2] and J. Lass.[3] A comprehensive survey of the phenomenon in the alkali halide crystals by von Hippel,[4] using homogeneous and inhomogeneous fields, gave direction laws as partly summarized in Table I. In NaCl at room temperature, for instance, with the field orientated in the [100] direction, the paths proceeded from the anode in the [110] direction, but were apt to change to [111] before reaching the cathode, thus forming characteristic tetrahedral pyramids resting with their bases on the cathode plane (Fig. 1).

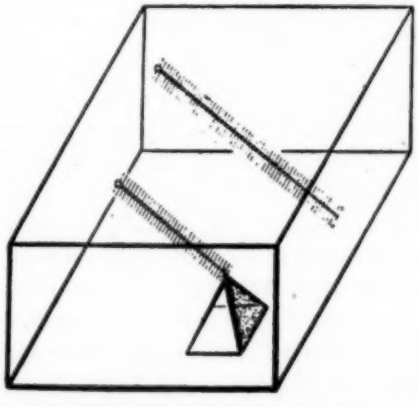

FIG. 1. Breakdown of NaCl (paths starting at the anode in the [110] direction and splitting near the cathode into [111] paths).

It was also found that the direction laws for breakdown through the volume of the crystal reappear in the direction which discharge paths may take on its surface,[4] and that addition agents influence the selection of path directions in the volume and surface breakdown in a similar manner.[5] Surface patterns on less symmetrical crystals have been observed by Kreft and Steinmetz.[6]

TABLE I. Appearance and direction of the breakdown path in the alkali-halide crystals.

Crystal	Appearance	Direction (the field direction is [100])
LiF, NaF, NaCl	sharp	primary [110], secondary [111]
KCl, RbCl	sharp	[110] and [100]
NaBr	a little blurred	[110], but also [111], [100] and random
KBr, KI, RbBr, RbI	blurred	[100] and random

* This communication is an abstract of a thesis submitted (1943) in partial fulfillment of the requirements for the degree of Doctor of Philosophy in Physics at the Massachusetts Institute of Technology.

[1] L. Inge and A. Walther, Zeits. f. Physik **64**, 830 (1930); **71**, 627 (1931).

[2] A. von Hippel, Zeits. f. Physik **67**, 707 (1931); **68**, 309 (1931).

[3] J. Lass, Zeits. f. Physik **69**, 313 (1931).

[4] A. von Hippel, Zeits. f. Physik **75**, 145 (1932); Ergeb. d. exakt. Naturwiss. **14**, 104 (1935); J. App. Phys. **8**, 815 (1937).

[5] A. von Hippel, Zeits. f. Physik **88**, 364 (1934).

[6] F. Kreft and H. Steinmetz, Zeits. f. angew. Min. **1**, 144 (1937). H. Steinmetz, Naturwiss. **22**, 314 (1934).

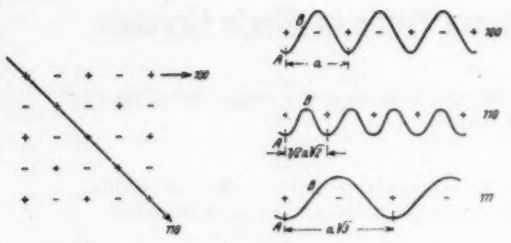

FIG. 2. Potential structure of NaCl.

If breakdown is initiated at the cathode, the path orientation is not the same as in the anodic phenomenon; thus [100] instead of [110] paths are formed in NaCl at room temperature.[1-3]

Metallic dendrites (of Na metal in NaCl crystals, etc.) may be grown from the cathode in the alkali halide crystals at elevated temperatures and show again characteristic crystallographic orientations.[7]

By measuring the breakdown strength of the alkali halides quantitatively, von Hippel[4] was able to formulate a tentative theory of the breakdown process. This assumes that excess electrons, produced by some ionizing process or introduced into the structure from the outside, are accelerated by the applied field after overcoming the friction barrier of the lattice vibrations, and produce impact ionization, avalanche formation, and breakdown. The direction laws follow from the assumption that the electrons take the paths offering the least friction, and that these paths are determined by the potential structure of the material. For NaCl the [110] direction offers the lowest potential barriers (Fig. 2), the [111] direction the flattest potential modulation and smallest number of ions per unit length of path, while the [100] direction is most unfavorable in both respects.

A difficulty arose when the breakdown strength of NaCl was measured as a function of the orientation of the crystal relative to the field.[8] No dependence of the strength on orientation was found. This suggested that in traversing the maximum of the vibration barrier the electrons are still moving so slowly that their long wavelength makes it impossible for them to discern the lattice structure; only after sufficient acceleration will the electrons move in selective directions. This fact made it very doubtful that the potential structure was a decisive factor in determining the breakdown direction, because the electrons were apparently able to cross the potential barriers in all directions without noticing their existence. Consequently, the research here reported was undertaken to obtain more information concerning the mechanism of path formation.

[7] A. von Hippel, Zeits. f. Physik **98**, 580 (1936).
[8] A. von Hippel and J. W. Davisson, Phys. Rev. **57**, 156 (1940).

II. APPARATUS AND PROCEDURE

The simplest and most satisfactory device used to produce breakdown paths was an ordinary leak-tester such as is commonly used in testing vacuum systems.[4]

A section (about $\frac{1}{4}$ cm thick) of crystal to be treated was placed on a metallic plate in the bottom of a vessel filled with a suitable insulating medium with the tester in contact with the upper surface. The insulating medium prevented the spark discharge from taking place in the air or over the surface of the crystal. Breakdown paths at different temperatures were obtained by using the following insulating media: (1) liquid air, (2) dry ice and butanol, (3) transformer oil, (4) transformer oil heated to 200°C, (5) boiling sulphur, and (6) electrical heating inside a vacuum.

Since the tester provided an alternating positive and negative voltage of unknown magnitude, the path orientations were checked in several cases by means of a steady d.c. voltage by using ivory electrodes.[4] The ivory electrode sample holder consisted of two highly polished and slightly rounded ivory electrodes between which a thin (2- to 8-mil) section was placed. The system was inserted in a bomb containing nitrogen at 100 atmospheres to suppress corona, and a steady d.c. voltage from a suitably filtered power source was applied. The ivory electrodes provided a homogeneous field across the sample and limited the current at breakdown so that secondary destruction did not obliterate initial breakdown effects.

In most instances the path directions obtained by the two methods were identical, i.e., in sulphur, baryte, aragonite, calcite, fluorite, sphalerite, and the majority of the alkali halides. The peculiar breakdown obtained in fluorite at room temperature (V, 1, B), however, was obtained

only with the leak-tester in thick samples. It should be remarked that breakdown paths are characteristically an inhomogeneous field phenomenon, since the positive space charge existing along the path channels acts as an auxiliary electrode that renders the field inhomogeneous within the crystal even when homogeneous fields are applied.[4]

The tester, in addition to its convenience in allowing the use of thick samples and a simple method of temperature control, also permitted visual observation of path formation so that intricate patterns could be grown without actual failure through the sample taking place. The path growth could also be halted or made to progress very slowly, thus, the effect of weak and strong fields upon path orientation could be studied in detail.

The patterns obtained by the above methods were examined under the microscope and the angular coordinates of the paths θ, φ measured. The inclination angle θ was measured against the normal to the section, and the azimuthal angle φ between the horizontal path projection and a "datum line" on the surface. In Fig. 3 the lower diagram represents a crystal section of orientation (hkl) whose unit normal is represented in the unit sphere of the upper diagram by the vector n. The dotted vector in the crystal, represented by n_2, is a unit vector in the direction of the breakdown path. n_3 is directed along the surface projection of the path, and n_1 is a unit vector directed along the "datum line" which is usually parallel to a crystal edge. φ is the angle between n_1 and n_3, and θ is the acute angle between n and n_2.

The angular coordinates θ, φ were transformed into zonal parameters $[uvw]$, which are components of the path directions upon the crystallographic axes, and thus the path directions could be correlated with symmetry properties and atomic structure of the crystal. The zonal parameters $[uvw]$ are related to the Miller indices (hkl) and to the unit cell through the expression

$$H=ua_1+va_2+wa_3=hb_1+kb_2+lb_3,$$

where H is any vector direction, the a vectors are unitary lattice vectors defining the unit cell, and the b vectors are the associated reciprocal unitary lattice vectors. The transformation equations for θ, $\varphi \rightarrow [uvw]$ may be represented (Fig. 3) by

$$n_1 \cdot n_2 = \cos\varphi \sin\theta,$$
$$n \cdot n_2 \times n_1 = \sin\varphi \sin\theta,$$

where n_1 (the datum line)

$$= u_1a_1+v_1a_2+w_1a_3/|u_1a_1+v_1a_2+w_1a_3| \text{ etc.}$$

The above equations may be expanded in each crystal system to yield the transformation equations desired.

In the isometric (cubic) system the direction $[hkl]$ is always normal to the plane (hkl).

According to the laws of crystal symmetry a direction $[uvw]$ is a member of a set of equivalent directions $[[uvw]]$ which can be derived from the first one by macroscopic symmetry operations.[5] By analyzing the path patterns observed the extent to which the path directions conform to one or more sets of equivalent directions was investigated.

III. BREAKDOWN PATHS IN THE ALKALI HALIDE CRYSTALS*

1. Rubidium and Potassium Halides

As Table III shows, the rubidium and potassium halides exhibit the following transitions in their breakdown path patterns as the temperature increases:

$$\text{random} \rightarrow [100] \rightarrow [110].$$

Thus, at liquid air temperature, for KBr, KI, RbBr, and RbI the paths are without orientation and resemble breakdown paths in amorphous media. As the temperature is raised, first [100] paths form and at more elevated temperatures [110] companion paths appear. Figures 4 and 5 illustrate the transition from random at -180°C to [100] at 20°C in RbBr.

In RbCl at -180°C random paths exhibit a strong tendency to orientate in the [100] directions, and KCl exhibits complete [100] orienta-

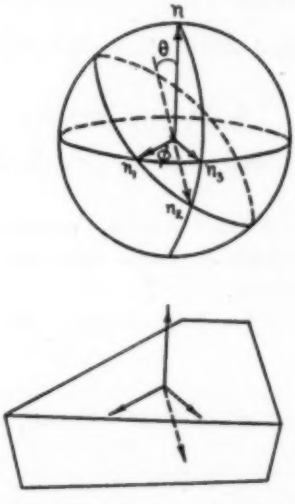

FIG. 3. Breakdown path coordinates.

[5] See Davey, *Crystal Structure and its Applications*, International Series in Physics (McGraw-Hill Book Company, Inc., New York, 1934).

* The alkali halide crystals prepared for this investigation were grown from the melt by the Kyropoulos method. (S. Kyropoulos, Zeits. f. Anorg. u. angew Chemie 154, 308 (1926).) LiF crystals were obtained from the Harshaw Chemical Company, Cleveland, Ohio.

FIG. 4. Random RbBr −180°C.

tion at −180°C. Thus increase of lattice energy tends to influence the path patterns in the same way as increase of temperature.

2. Sodium Halides

The sodium salts exhibit the same type of thermal dependence of path orientation as shown by the rubidium and potassium halides. In addition, however, [111] paths are observed which, on the basis of inconclusive evidence, seem to belong between [100] and [110]. The tentative path sequence is

random→[100]→[111]→[110].

The individual salts behave as follows:

A. Sodium Bromide

a. 20°C—random paths (see, however, Table I).

b. 150°C—[111] paths transforming into [110] in regions of weak field strength; [110] paths dominant.

c. 500°C—[110] dominant; [111] not observed.

B. Sodium Chloride

a. Liquid air temperature—

pure NaCl—random paths favoring the [100] directions for all orientations of the crystal (Fig. 6). The [100] orientation tendency seems to be more pronounced in strong than in weak fields.

thin sections of pure NaCl subjected to overvoltage—[100] paths usually accompanied by fractures (Fig. 7).

thin sections of mixed (NaCl+4.6 mole percent AgCl) crystals subjected to overvoltage—sharp [110] paths accompanied by (110) fracture planes.

mixed (NaCl+1 mole percent AgCl) crystals—sharp [100] and [110] paths.

b. Room temperature—

pure NaCl—sharp [110] paths (Fig. 8) for all orientations of crystal.

thin sections pure NaCl subjected to overvoltage—sharp [111] paths usually accompanied by factures (Fig. 9).

mixed (NaCl+AgCl) crystals—precise [110] paths.

cathodic breakdown in (100) and (110) sections of pure NaCl takes place in the [100] direction.

c. At 500°C—precise [110] breakdown paths in all samples of pure and mixed crystals. The patterns form with greater facility than at room temperature so that elaborate constructions involving secondary and tertiary branch paths are formed.

d. At 800°C—[110] breakdown paths in precise orientation apparently form up to the melting point.

FIG. 5. [100] (100) RbBr 20°C.

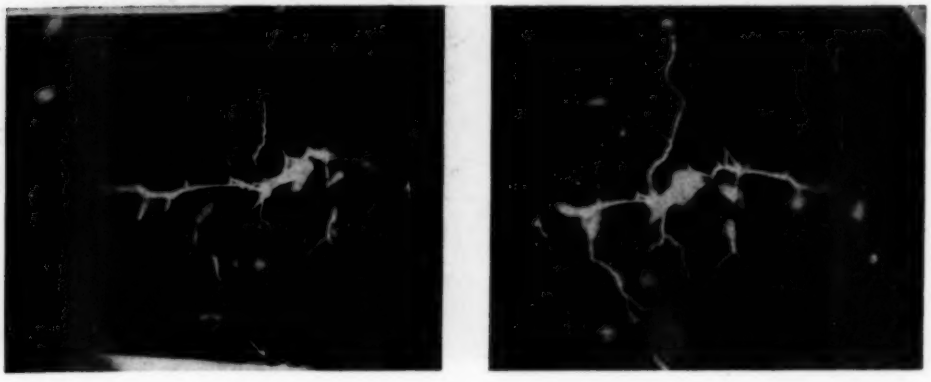

FIG. 6. [100] & R in (110) NaCl at −180°C.

C. Sodium Fluoride

a. At −180°C—sharp [111] paths.

b. At 200°C—[111] paths dominant with [110] companion paths.

3. Lithium Halides

The high temperature path pattern of the lithium salts examined is a temperature dependent 'star' formed by 12 equivalent paths in the non-primitive directions [xxy]. The projection of the 'star' observed in LiCl upon a cube face is shown in Fig. 10. In this design a path projection exists for every 22½° except in the directions of the cube edges. The paths which project into the 45° diagonals have an inclination that is different from the others. In the general case, since the parameters are temperature dependent, the projection figure will not be quite as regular. The 45° projection lines will not change though the inclination of the corresponding paths will. The non-diagonal lines will all be shifted equally toward or away from the diagonals.

FIG. 7. [100] thin (100) NaCl at −180°C overvoltage.

The low temperature pattern in these salts is [110], hence the thermal transitions observed may be represented by

$$[110] \leftrightharpoons [xxy]_T.$$

The individual salts behave as follows:

*A. Lithium Chloride**

a. At −180°C—indications of [110] and star path formation.

b. At 20°C and at 500°C—the star pattern [552] in sharp orientation (Fig. 10).

B. Lithium Fluoride

a. At −180°C—sharp [110] paths.

b. At 20°C—[110] and star paths occur together.

c. At elevated temperatures—the star pattern alone appears and, as Table II shows, the parameters are temperature dependent. Thus at 150°C the pattern (Fig. 11) is accurately represented by the parameters [133] and at 450°C approximately by [122].

It should be remarked that the patterns above are reproducible at least to the extent that in a single experiment the same path directions are obtained from any portion of the crystal surface.

IV. DISCUSSION OF THE ALKALI HALIDE EXPERIMENTS

The breakdown path orientation observed in the alkali halide crystals fall, according to the

* The lithium chloride crystal became contaminated by a speck of rust that fell into the melt during growth.

FIG. 8. [110] (100) NaCl 20°C.

data just presented, into the general sequence

$$\text{random} \leftrightarrow [100] \leftrightarrow [111] \leftrightarrow [110] \leftrightarrow [xxy],$$

where Fig. 12,

[100] = 3 equivalent cube-edge directions,
[111] = 4 equivalent body-diagonal directions,
[110] = 6 equivalent face-diagonal directions,
[xxy] = 12 equivalent non-primitive directions such that two components are equal.

The position of the [111] paths in the sequence above is uncertain, since they were never observed in the potassium or rubidium halides (Table III). In NaF, however, [111] paths appear alone at −180°C, and dominant [111] with [110] companion paths appear at elevated temperatures (III, 2, C).

Change of temperature of an alkali halide crystal influences breakdown paths in three ways: it (*a*) affects the rigor of orientation, (*b*) influences the tendency to form branch paths, (*c*) allows patterns of different orientation to appear.

The orientation of the paths becomes more rigorous, and the tendency to form branch paths increases with increase of temperature. Paths in precise orientation apparently form up to the melting point of the crystal.

The influence of temperature upon breakdown path orientation is summarized in Table III where it will be noted that the transition from one dominant path orientation to the next takes place gradually over a temperature range of several hundred degrees. Increase of temperature favors transitions to the right in the sequence above.

Increase of lattice energy, as shown by Table IV, acts in the same sense as increasing the temperature. It should be noted, however, that [111] paths were observed only in sodium salts and [xxy] paths only in lithium salts; thus the path directions may also be conditioned by the nature of the ions. It would be of interest to

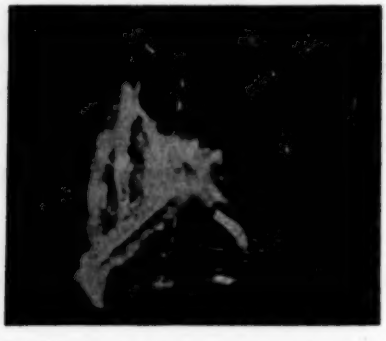

FIG. 9. [111] thin (100) NaCl at 20°C overvoltages.

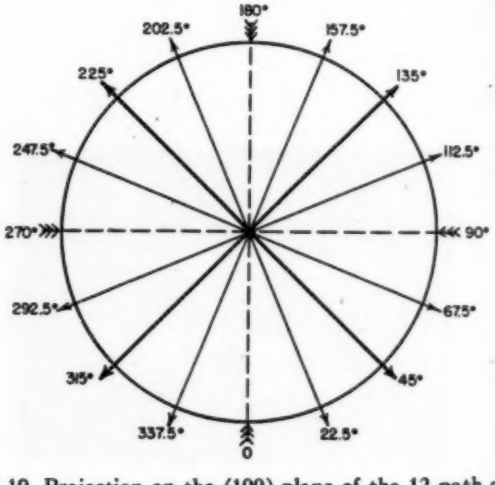

FIG. 10. Projection on the (100) plane of the 12 path star pattern in LiCl.

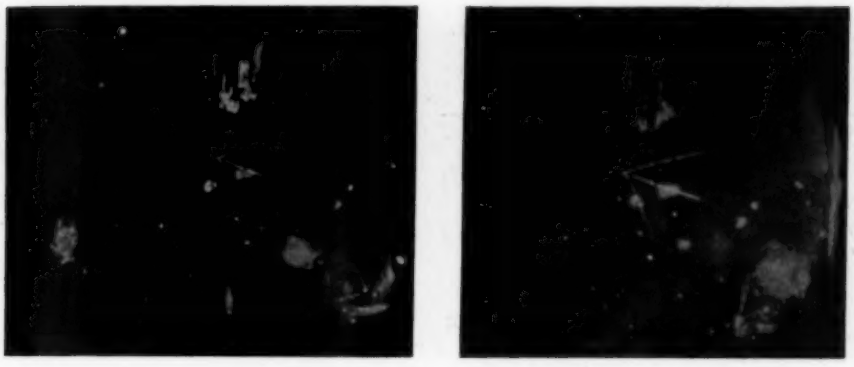

FIG. 11. [133] star LiF 150°C.

examine the patterns in LiI (Table IV), since a star pattern would not be expected if lattice energy is decisive.

Addition agents influence the pattern sequence in the same sense as increase of temperature. Thus, although pure NaCl at −180°C yields random paths favoring the [100] direction, the mixed NaCl+4.6 mole percent AgCl crystal exhibits precise [110] paths at all temperatures investigated. When less AgCl is admitted to the lattice, precise [100] and [110] paths are formed at −180°C, while at elevated temperatures only [110] paths are observed. Iron contamination in LiCl seems to have shifted the path pattern at lower temperatures from [110] to [*xxy*].

The type of applied voltage also influences the selection of the patterns. Thus in thick sections of pure NaCl at room temperature, [110] paths and not [111] paths are obtained with the tester (Fig. 8); but in thin (1-mil) sections, however, [110] or [111] paths may be produced at will depending upon whether an overvoltage is applied or not. With overvoltage, [111] paths are always formed (Fig. 9). With ivory electrodes [110] and [111] paths are observed in thick sections, but the [111] paths as shown in Fig. 1 tend to form near the cathode plane as branches from [110] paths. At −180°C random paths favoring the [100] directions are observed in thick sections of pure NaCl for all orientations of the crystal (Fig. 6), and in thin (100) sections [100] paths are observed when overvoltage is applied (Fig. 7). In the mixed (NaCl+AgCl) crystals at −180°C, [110] paths are observed when overvoltage is applied to thin sections. With a negative point electrode [100] paths are formed in NaCl at room temperature. These results confirm von Hippel's contention that [111] paths are favored in excess fields in NaCl at room temperature, and show further that the favored direction is temperature dependent, since [100] and not [111] paths are formed at −180°C. A tentative conclusion is that excess

TABLE II. Star path patterns in lithium fluoride. φ_0 observed azimuthal angle against cube edge; φ_c calculated azimuthal angle; θ_0 observed inclination angle; θ_c calculated inclination angle.

[133] pattern at 150°C				[122] pattern at 450°C			
φ_0	φ_c	θ_0	θ_c	φ_0	φ_c	θ_0	θ_c
18.7	18.5	47.3	46.6	28.0	26.6	50.1	48.3
71.0	71.5	45.3	46.6	64.0	63.4	47.2	48.3
109.5	108.5	46.7	46.6	115.5	116.6	47.2	48.3
198.5	198.5	47.7	46.6	134.0	135.0	71.5	71.6
251.5	251.5	48.2	46.6	154.0	153.4	46.7	48.3
288.5	288.5	47.6	46.6	207.0	206.6	50.5	48.3
341.5	341.5	47.2	46.6	224.0	225.0	70.0	71.6
				316.0	315.0	70.3	71.6
				335.0	333.4	47.7	48.3

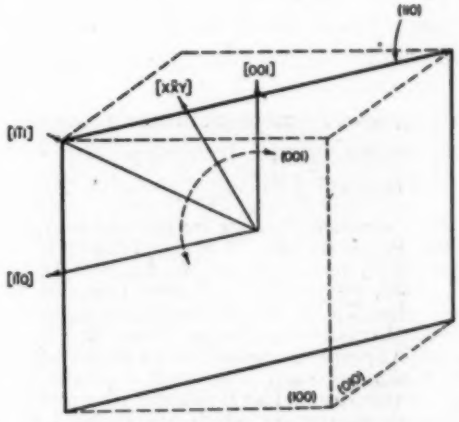

FIG. 12. Directions assumed by breakdown paths in the alkali halides.

TABLE III. Breakdown path orientation in alkali-halide crystals.*

	T°C	F	Cl	Br	I
Li	−180	110	?		
	20	110 & *xxy*	552		
	200	133	552		
	450	122	552		
Na	−180	111	100 & *R*	*R*	
	20	111 & 110	110 & 111	*R* & 100, 111, 110	
	200	110 & 111	110	110 & 111	
	450		110	110	
K	−180		100	*R*	*R*
	20		100	100	*R*
	200		100 & 110	100	100 & *R*
	450		110 & 100	100 & 110	
Rb	−180		100 & *R*	*R*	*R*
	20		100 & 110	100	*R*
	200		100 & 110	100 & 110	100
	450			100 & 110	100 & 110

* The symbol *R* stands for random paths, i.e., without orientation.

fields tend to shift the pattern observed to lower temperature forms. A definite field influence has been observed only in sodium salts.

V. BREAKDOWN PATHS IN CRYSTALS OF DIFFERENT SYMMETRIES

1. Isometric (cubic) System*

A. Periclase (MgO) '32; O_h' [[110]]

Periclase possesses an NaCl structure and a lattice energy of 940 kg cal./mole, as compared with 240 kg cal./mole for LiF.[10] Patterns of the type [*xxy*] or [*xyz*] might, therefore, be anticipated (Table IV), but up to 500°C from (100) faces [110] paths only were observed.

B. Fluorite (CaF_2) '32; O_h' [[110]]

Observations on (111) fluorite are in complete accord with those of Kreft and Steinmetz.[6] At room temperature, although [110] paths develop from the point electrode of the tester, the actual failure of the sample usually takes place abruptly with the formation of a single winding and deviating, unorientated channel that is free from accompanying crystal fractures. This behavior occurred in several different samples that ranged in color from deep violet to clear amber. At elevated temperatures, breakdown paths form more readily and failure takes place in the [110] breakdown path direction. In thin sections, with ivory electrodes, failure in the [110] direction takes place at room temperature, and elaborate [110] surface patterns are sometimes formed. (Fig. 13.)

* The 32 symmetry classes are grouped into 7 systems as follows: 1–2 triclinic; 3–5, monoclinic; 6–8, orthorhombic; 9–15, tetragonal; 16–20, trigonal; 21–27, hexagonal; 28–32, cubic. The symmetry increases with the number; thus, No. 27 denotes the most symmetrical form of hexagonal crystal, etc. The class number together with the familiar Schönflies symbol, which represents the symmetry elements present, is included after the name and formula of the crystal. This is followed by a representation of the path parameters which are enclosed in double brackets to signify that the complete pattern is present.

[10] F. Seitz, *Modern Theory of Solids* (McGraw-Hill Book Company, Inc., New York, 1940), p. 88.

TABLE IV. Breakdown paths in relation to electrical and thermal properties, where U=lattice energy in kg cal./mole—Seitz, *Modern Theory of Solids*, p. 80; E_m =maximum breakdown strength$\times(10)^6$ volts/cm—von Hippel (reference 4); $h\nu$=Reststrahl$\times(10)^{-3}$ volt—von Hippel (reference 4). The dash under the path parameter indicates the dominant pattern at room temperature.

Salt	U	E_m	$h\nu$	Path patterns observed				
LiF	240	4.0	7.2				110	*xxy*
NaF	215	2.4	3.3			111	110	
LiCl	193							*xxy*
KF	190		3.0					
LiBr	183							
NaCl	180	1.6	2.4		100	111	110	
NaBr	172	0.8	1.8	*R*		111	110	
LiI	171							
KCl	164	1.0	1.9		100		110	
RbCl	159	0.8	1.7	*R*	100		110	
KBr	158	0.7	1.5	*R*	100		110	
RbBr	152	0.6	1.15	*R*	100		110	
RbI	144	0.5	1.05	*R*	100		110	

C. Sphalerite (ZnS) '31; T_d' [[110]]

In sphalerite the Zn and S atoms are each arranged in face-centered lattices in such a way that a diamond structure would result, if all the atoms were the same. [110] breakdown paths developed in (100) and (110) sections. No temperature effects were noted.

D. Sodium Chlorate ($NaClO_3$) '28; T' [[552]]

This crystal type contains no reflection planes or center of symmetry. The path pattern, which has been described by Kreft and Steinmetz,[6] is identical with [552] star pattern observed in LiCl (Fig. 10). The same pattern was obtained in liquid air and at 200°C.

2. Tetragonal System

A. Apophyllite ($KCa_4(Si_2O_3)\cdot 8H_2O$) '15; D_{4h}' [[110]]

Apophyllite was chosen for investigation because it is a crystallographically symmetrical

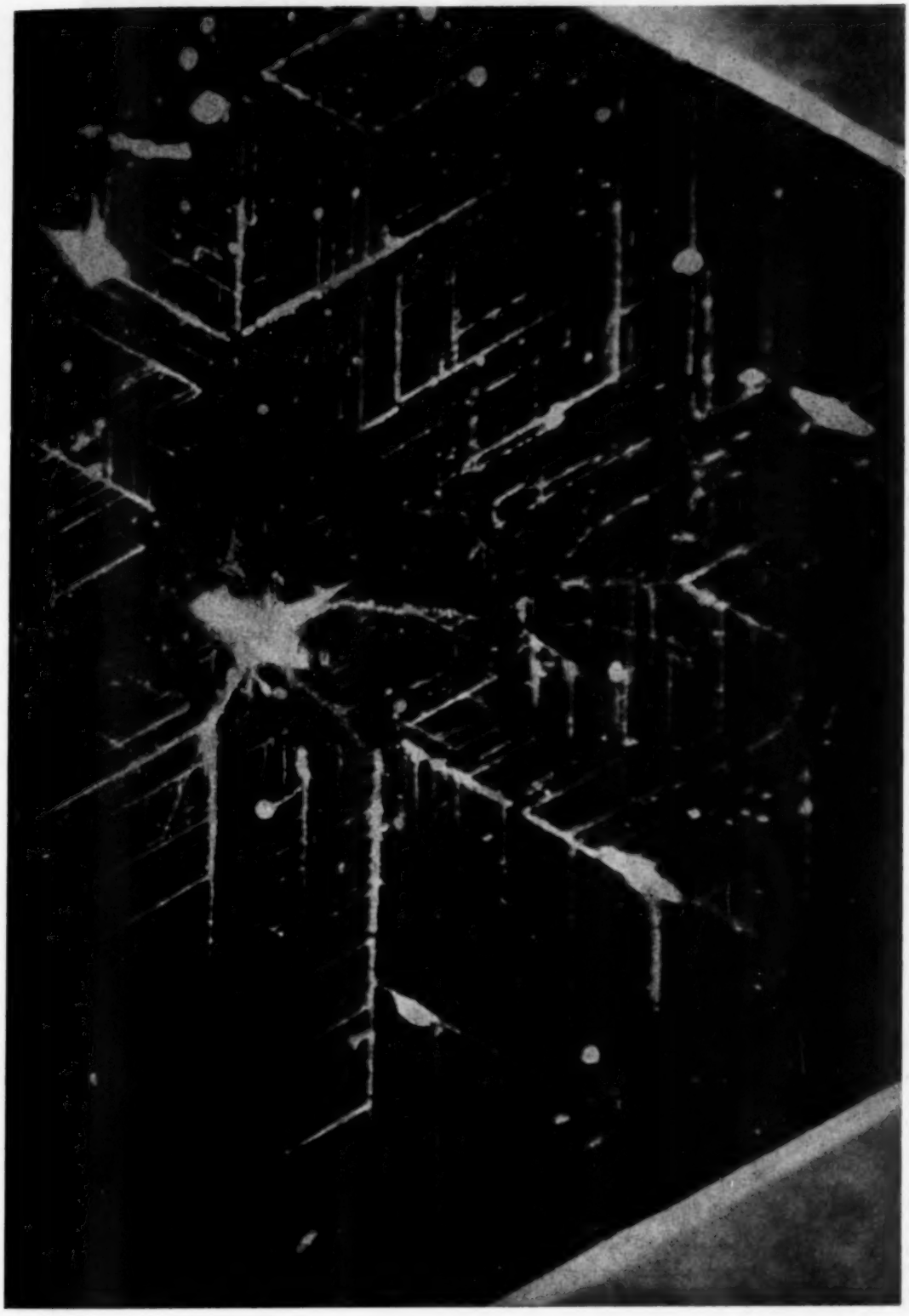

FIG. 13. [110] surface breakdown paths on (111) fluorite.

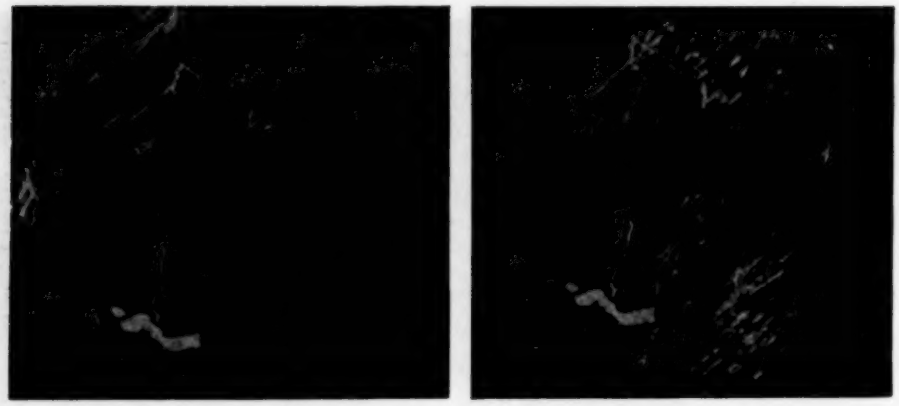

FIG. 14. Pattern in (100) KH_2PO_4.

crystal possessing a complex and distorted atomic structure. It has been described as a distorted layer lattice consisting of alternating puckered silicate rings of 4 and 8 silicon atoms per ring, respectively.[11]

The paths observed in apophyllite are of a simple degenerate nature.

In a (100) section—symmetrical forks lying in the basal (001) plane and inclining at 45°.
In a (010) section—complimentary forks in the (001) plane.
In a (001) section—[001] paths straight through sample.
In a (111) section—the three directions above and no others appear.

The complete pattern, therefore, consists of the paths:

[110] [1$\bar{1}$0] [001]

TABLE V. The path pattern of potassium dihydrogen phosphate.

[uvw]	θ calculated	φ	θ observed	φ
20, 9, 16	41.1	329	41.5	328
$\bar{2}0$, $\bar{9}$, 16	41.1	149	41.6	149
$\bar{9}$, 20, 16	70.1	307	70.2	307
9, $\bar{2}0$, 16	70.1	127	70.2	129
15, 4, 7	26.9	33	26.8	33
$\bar{1}5$, $\bar{4}$, 7	26.9	213	27.7	213
$\bar{4}$, 15, 7	76.2	66	74.1	67
4, $\bar{1}5$, 7	76.2	246	76.2	246

[11] W. H. Taylor and St. Naray, Szabo. Zeits. f. Krist. **77**, 150 (1931); Bragg, *Atomic Structure of Minerals* (Cornell University Press, Cornell, New York, 1937), p. 26.

B. Potassium dihydrogen phosphate (KH_2PO_4) *'11; V_d'* [[20, 9, 16]] [[15, 4, 7]]

Since there are only four equivalent points associated with this crystal, and eight path directions were observed, it follows that two sets of patterns are present at room temperature as Table V show. (Fig. 14).

3. Hexagonal System

A. Beryl ($Be_3Al_2(SiO_3)_6$) *'27; D_{6h}'* [[100]], [[001]]

In beryl the breakdown paths are observed to lie along the coordinate axes at room temperature. No change in the pattern was observed at 500°C.

B. Apatite ($Ca_5F(PO_4)_3$) *'25; C_{6h}'* [[9, 14, 11]]

The observed and calculated angles for the path directions are shown in Table VI. The [5, 9, 11] paths do not appear because they possess large inclination angles.

4. Trigonal System

A. Calcite ($CaCO_3$) *'20; D_{3d}'* [[2, 1, 1.45]] [[10, 5, 2]] [[001]]

The observations of Kreft and Steinmetz[6] are confirmed. In basal sections the paths proceed

TABLE VI. The path pattern of apatite.

[uvw]	θ calculated	φ	θ observed	φ
9, 14, 11	34.2	194	35	194
9, 14, $\bar{1}1$	34.2	346	34.6	347
14, 5, 11	57.6	49	57	48.6
14, 5, $\bar{1}1$	57.6	131	56.2	131
5, $\bar{9}$, 11	73.7		not observed	
5, $\bar{9}$, $\bar{1}1$	73.7		not observed	

along the c axis unless one applies only the minimum voltage required for path formation. With caution a trigonal set of paths is obtained which lie within vertical reflection planes that bisect the horizontal coordinate axes and are inclined at 54° to the c axis. The parameters obtained for the trigonal set are [2, 1, 1.45] which, when transformed into Miller indices, become (705), the direction quoted by Kreft and Steinmetz. In oblique sections additional path directions appear; [10, 5, 2] was observed in cleavage sections, and in (010) sections the path sets [2, 1, 1.45] and [110] but not [10, 5, 2] were observed. A correlation between path directions in different oblique sections was not obtained, but in all of them the basal section paths were identified. The path indexing seems to show that the additional paths are contained within reflection planes and that they possess large inclination angles with the c axis which may explain why they are not observed in basal sections. In aragonite (V, 5, C) no additional paths are observed in oblique sections.

B. Quartz (SiO_2) *'18; D_3'* [[*101*]]

The trigonal path set observed in a basal section of quartz (Fig. 15) lies within the vertical planes that contain the horizontal coordinate axes and are inclined at 42° to the c axis. They seem to lie parallel to the intersections of alternate pyramidal faces. Excess voltage applied at room temperature did not produce other paths. In liquid air, however, the paths appear to go straight through. Paths in addition to the trigonal set appear in prismatic sections.

5. Orthorhombic System

The breakdown paths observed in crystals of the orthorhombic system all lie within principal planes as shown schematically in Fig. 16. All the crystals examined belong to the normal symmetry class '8; V_h.'

A. Baryte ($BaSO_4$) [[*0, 9, 11*]], [[*100*]]

Measurements and observations of von Hippel[2] are confirmed. The complete pattern consists of the paths:

[0, 9, 11] [0, $\bar{9}$, 11] [100]

FIG. 15. Trigonal path set in basal quartz.

B. Sulphur (S_{12S}) [[*021*]], [[*100*]]

The following path directions were observed at room temperature:

In a (100) section—[100] paths directed straight through.
In a (010) section—symmetrical fork paths in (100) plane and inclining at 47°.
In a (001) section—complimentary forks in (100) plane.
In (110) and (111) sections—[100] paths only (Fig. 17).

Both the tester and the ivory electrode methods were used to produce paths. The [100] or a-paths form more readily than the fork paths as shown by the behavior in (110) and (111) sections. The complete pattern consists of the paths:

[021] [0$\bar{2}$1] [100]

C. Aragonite ($CaCO_3$) [[*670*]] [[*001*]]

The following path directions were observed:

In a (100) section—symmetrical fork paths lying in the (001) plane and inclining at 62°, and [001] surface paths.
In a (010) section—complimentary fork paths inclining at 28° in (001) plane, and surface [001] paths.
In a (001) section—[001] paths through section.
In a (110) section—a single path in the (001) plane at 30° inclination, and surface [001] paths.
In an oblique (0, 2.4, 1) section—three paths observed: one inclining at 60° and the other two constituting a symmetrical oblique fork inclining at 41°.

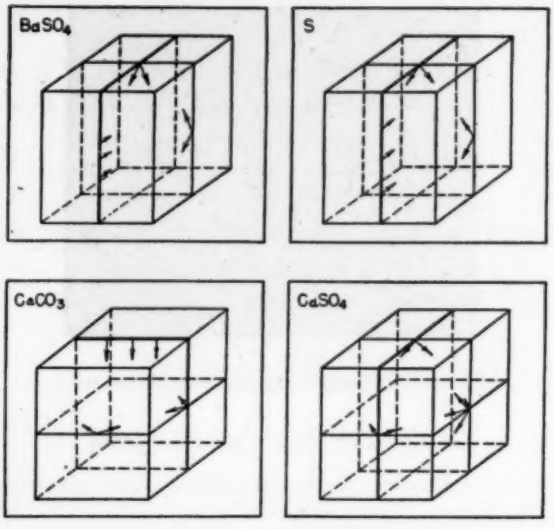

FIG. 16. Breakdown path directions in orthorhombic crystals.

Paths with parameters [670] and [6$\bar{7}$0] should appear as symmetrical forks inclining at 62° and 28° in (100) and (010) sections. They should incline at 30° and 86° in (110) sections, and should also appear as a symmetrical oblique fork inclining at 40.1° in the oblique (0, 2.4, 1) section. The [001] path should incline at 60° in the oblique section. The complete pattern for all orientations of aragonite is, therefore:

[670] [6$\bar{7}$0] [001]

D. Anhydrite ($CaSO_4$) [[*580*]] [[*087*]]

Using the experimental angles obtained by Kreft and Steinmetz[6] for the path directions in anhydrite, the above path parameters are obtained. The pattern is different from those observed in other crystals of this system in that there are two sets of fork paths instead of only one; thus, from a (010) face a path quartet is observed. The four paths in the pattern are the following:

[580] [5$\bar{8}$0] [087] [0$\bar{8}$7]

VI. DISCUSSION OF EXPERIMENTAL RESULTS

The breakdown path directions are not dependent upon the orientation of the crystal relative to the field. The paths in oblique sections of sodium chloride, apophyllite, sulphur, aragonite, and in calcite are in the same directions as in prismatic cuts. The existence of additional path directions in oblique cuts that do not appear in basal sections of crystals such as calcite and quartz does not violate the rule stated above, since these paths possess large inclination angles in the basal section. (V, 4, A, B.)

Breakdown paths obey the laws of macroscopic crystal symmetry; that is, given one path, the orientations of all the remaining paths in the pattern may be predicted from symmetry considerations.

Breakdown paths tend to lie within reflection planes and therefore tend to form degenerate patterns whenever such planes exist. A degenerate pattern, recognized by the presence of zeros or repeated numbers in the path parameters, is one that exhibits fewer allowed path directions than the maximum number of directions permitted by the symmetry class under consideration. For instance, (a) in the isometric system, the sequence of patterns [100]→[111]→[110] →[*xxy*] observed in the alkali halides represents a sequence of decreasing degeneracy. It will be observed (Fig. 12) that all the above directions are contained within (110) reflection planes. The [110] paths observed in fluorite and sphalerite (V, 1, B, C) are contained within (110) reflection planes. In sodium chlorate (V, 1, D) the [552] pattern is non-degenerate since the tetartohedral class possesses only 12 equivalent points and contains no reflection planes. (b) In the tetragonal system, KH_2PO_4 exhibits the non-degenerate patterns [20, 9, 16] and [15, 4, 7] in the absence of reflection planes, whereas apophyllite possesses five reflection planes and shows a degenerate path pattern. (c) In the hexagonal system, beryl with seven reflection planes belongs to the most symmetrical class of this system. The paths, which are directed along the coordinate axes, are the most degenerate possible. Apatite is an exception for it shows a non-degenerate pattern in the presence of a single basal reflection plane (V, 3, B). (d) In the trigonal system, quartz reveals a degenerate set in the absence of reflection planes (V, 4, B). The trigonal set of paths observed in basal sections of calcite (V, 4, A) are degenerate and lie within the only reflection planes that the crystal possesses. In oblique cuts the additional paths that appear seem to lie within these same

reflection planes. A complete indexing of these paths, however, was not carried out. (e) In the orthorhombic system, the paths in every instance were observed to lie within reflection planes (V, 5, A, B, C, D).

The type of lattice bond does not seem to influence the path patterns in a characteristic way. The path pattern observed in sulphur (V, 5, B), a crystal that exhibits covalent and molecular bonding, is similar to the patterns observed in aragonite and baryte (V, 5, A, C) which are essentially ionic in nature, but belong to the same symmetry class.

The breakdown path directions do not appear to be related in a directly obvious manner to the atomic positions in the lattice. This is most convincingly demonstrated by the path patterns observed in sulphur (V, 5, B). The structure, as shown by Warren and Burwell,[12] is similar in appearance in the (a) and (b) directions and is quite different in the (c) or [001] direction. Looking at the structure from (a) or (b) one observes lines of sulphur rings extending diagonally through the crystal at *ca.*±45° to the line of sight in the [110] and [1$\bar{1}$0] directions, i.e., parallel to the base. The lines are not meshed; thus, in one layer the lines all run in the [110] direction, in the next [1$\bar{1}$0], etc. Each ring, which consists of 8 sulphur atoms, stands on end in the (c) direction and faces *ca.*±45° to the observer at (a) or (b). From (c) one views the sulphur rings end-on; thus, the structure looks different and more open.

On the basis of the structure one might expect similar patterns for (100) and (010) cuts, and a different one for (001). Furthermore, the existence of the 45° line of sulphur rings might lead to the prediction of the following pattern.

In a (100) section—symmetrical fork paths inclining at 45° and lying in the (001) plane.
In a (010) section—complimentary fork paths in the (001) plane.
In a (001) section—[001] paths through sample.

This does not agree with the pattern observed which in (010) and (001) cuts shows symmetrical fork paths at approximately±45° lying in the (100) plane and [100] paths in (100) and oblique sections.

In the alkali halides the sequence of path patterns observed suggests that the path directions may change according to the sequence of decreasing interplanar distances, but the [111] paths seem to be out of position, and the parameters of the star paths do not fit closely to the scheme. Further investigation, however, may show more conformity.

VII. CONCLUSIONS

Before considering a mechanism for breakdown path orientation one should be familiar with related electronic phenomena in crystals. A review of pertinent information has recently been presented by von Hippel[13] who discusses the problem of breakdown path orientation in the frame of his general theory on the breakdown of solid dielectrics. The mechanism which he has evolved is based on the assumption that the

FIG. 17. [100] paths in (111) sulphur at 20°C paths appear double due to refraction.

[12] B. E. Warren and J. T. Burwell, J. Chem. Phys. **3**, 6 (1935).

[13] A. von Hippel, Proc. Faraday Soc., Conference on Dielectrics, Bristol, 1946.

paths mark directions for which there is least transfer of energy from excess electrons, which are accelerated by the applied field, to the lattice. The path directions are believed to depend upon the wave-length, and hence upon the velocity of excess electrons. The orientating mechanism proposed by him is electron wave interaction with the lattice that results in scattering into preferential lattice directions.

The experimental foundation for an exact theory, however, is not yet complete. We are working further on this problem.

ACKNOWLEDGMENT

The author wishes to thank Professor Arthur von Hippel for the use of his personal equipment and mineral collection as well as for his help and encouragement throughout this investigation.

PHYSICAL REVIEW VOLUME 70, NUMBERS 9 AND 10 NOVEMBER 1 AND 15, 1946

The System of Microstresses in Cold-Worked Metal

NELSON M. BLACHMAN*
Case School of Applied Science, Cleveland, Ohio
(Received July 1, 1946)

Smith and Stickley have measured the x-ray line widths from specimens of cold-worked α-brass and tungsten as functions of Bragg angle and x-ray wave-length. Their results accord with the microstress theory of broadening. They find that with α-brass, which is elastically anisotropic, the line width depends upon crystallographic direction in a systematic manner, while with tungsten, which is elastically isotropic, it does not. For several very simple theoretical models of internal-stress systems the variation in line width with crystallographic direction is computed here. The one which fits the above results best, though poorly, is that which assumes that the homogeneously strained domains suffer uniform normal stress of random magnitude. A plausible model for the microstress system and a very good fit are obtained by superposing upon this model any of the other models considered and thus obtaining the proper amount of anisotropy.

INTRODUCTION

CONSIDERABLE attention has been given in the last twenty-five years to the generally observed broadening of the x-ray diffraction lines of polycrystalline metal by cold work. The microstress theory of x-ray line broadening assumes a system of internal stresses (microstresses) in a piece of cold-worked metal which are in some manner random in magnitude and direction and are constant only over domains very small compared with the sample. If we apply Bragg's law, $\lambda = 2d_{hkl} \sin \theta_{hkl}$, to one of these homogeneously stressed and, therefore, homogeneously strained domains, we find upon logarithmic differentiation, taking λ constant, the following relation between the microstrain $e_{hkl} = \Delta d_{hkl}/d_{hkl}$ in the direction normal to the (hkl) planes and the angular displacement of the hkl reflection to which it gives rise,

$$\Delta\theta_{hkl} = -e_{hkl} \tan \theta_{hkl}.$$

The displaced reflections coming from all the various crystallites which are in position to reflect combine to form a broadened line, in which the root-mean-square displacement of the Bragg angle is evidently $\tan \theta_{hkl}$ times the r.m.s. value of e_{hkl}, which we shall denote by E_{hkl}.

Smith and Stickley find $B_{hkl}/\tan \theta_{hkl}$ (B = corrected half-intensity breadth of line) to be independent of λ, in agreement with this prediction of the microstress theory.[1] With cold-worked tungsten, which is elastically isotropic, they found it also independent of crystallographic direction, but not with α-brass, which is elasti-

* Now at Cruft Laboratory, Harvard University, Cambridge, Massachusetts.

[1] Charles S. Smith and E. E. Stickley, Phys. Rev. 64, 191 (1943).

cally anisotropic. Their observations with cold-worked α-brass are presented in Table I.

The half-intensity breadth B is the range of scattering angle (2θ) corresponding to that part of the line over which the intensity is at least half that at the center of the line. On the assumption that the microstresses obey a Gaussian law, the distribution of intensities over each line is Gaussian, and the corresponding r.m.s. microstrain is $E=(B/\tan\theta)/2^2\times 1.175=(B/\tan\theta)/4.70$, where the 2's are accounted for by the doubling of angles due to reflection and to taking both right and left halves of the lines. This E is also tabulated in Table I. It may be in error by a constant factor close to one if the microstress distribution is not Gaussian, but that is of little consequence for the following arguments.

The table includes the orientation factor $\Gamma=(k^2l^2+l^2h^2+h^2k^2)/(h^2+k^2+l^2)^2$, upon which Young's modulus for the various directions depends.[2]

For cold-worked tungsten, Smith and Stickley obtain the value 14.00×10^{-3} radian for $B/\tan\theta$, whence $E=2.980\times10^{-3}$.

It is the purpose of this paper to determine the implications of these values of E concerning the system of internal stresses existing in the cold-worked brass and tungsten. The method used will be to postulate various theoretical models of internal-stress systems, to compute the corresponding values of E with particular reference to metals of the cubic system, to which both α-brass and tungsten belong, and to compare these values with the empirical data.

FIRST MODEL. UNIFORM NORMAL STRESS

The first model to be considered is the microstress system in which all parts of the cold-worked sample are assumed to suffer uniform normal stress whose magnitude is random, of mean value zero, and constant throughout only small domains.

For materials of the cubic system the inverse of Hooke's law, reduced by symmetry considerations, gives the relations[3]

$$\left.\begin{aligned} e_{xx}&=s_{11}X_x+s_{12}Y_y+s_{12}Z_z,\\ e_{yy}&=s_{12}X_x+s_{11}Y_y+s_{12}Z_z,\\ e_{zz}&=s_{12}X_x+s_{12}Y_y+s_{11}Z_z,\\ e_{yz}&=s_{44}Y_z,\\ e_{zx}&=s_{44}Z_x,\\ e_{xy}&=s_{44}X_y,\end{aligned}\right\} \quad (1)$$

between the stress and strain existing at any point, where e_{xx}, e_{yy}, e_{zz} are the normal components of strain in the directions of the crystallographic axes, being positive for extension, and e_{yz}, e_{zx}, e_{xy} are the shearing components of strain associated with the subscripted axes; e_{yz} is, for example, approximately the change in angle between two lines originally parallel to the y and z axes, and is positive for a decrease in that angle. X_x, Y_y, Z_z are the normal components of stress in the directions of the crystallographic axes, being positive for tension, and Y_z $(=Z_y$ because there is no resultant torque), for example, is the shearing component of stress acting in the direction of the z axis on a plane whose directed normal is the positive y axis. The s's are called the elastic moduli for the material with respect to the crystallographic axes.

For uniform normal stress of magnitude n, $X_x=Y_y=Z_z=n$, $Y_z=Z_x=X_y=0$. Substitution into Eqs. (1) yields $e_{xx}=e_{yy}=e_{zz}=(s_{11}+2s_{12})n$,

TABLE I. The results of Smith and Stickley with α-brass.

Line	Radiation	$B/\tan\theta$	Direction	E	Γ
200	Fe	13.09×10^{-3} radian	[100]		0.0000
400	Cu	11.65			
	Ni	12.72			
	Co	13.49			
Average		12.74		2.714×10^{-3}	
311	Cu	11.05	[311]		0.1570
	Ni	10.55			
	Co	10.72			
	Fe	11.41			
Average		10.93		2.328	
420	Cu	10.91	[210]	2.322	0.1600
220	Ni	9.40	[110]		0.2500
	Co	10.00			
	Fe	10.45			
Average		9.95		2.106	
331	Cu	9.23	[331]		0.2741
	Ni	9.65			
Average		9.44		2.008	
222	Cu	7.44	[111]		0.3333
	Ni	8.15			
	Co	7.55			
	Fe	8.07			
Average		7.80		1.660	

[2] a. W. Voigt, *Lehrbuch der Kristallphysik* (B. G. Teubner, Leipzig, 1910), pp. 589, 739; b. W. A. Wooster, *A Textbook of Crystal Physics* (Cambridge University Press, London, 1938), p. 252; c. C. S. Barrett, *Structure of Metals* (McGraw-Hill Book Company, Inc., New York, 1943), p. 455.

[3] a. Reference 2a, page 586ff.; b. Reference 26, page 248; c. Reference 2c, page 454.

$e_{yz}=e_{zz}=e_{zy}=0$. Thus, the resultant strain is a uniform dilatation. Hence, the normal strain in any direction $[hkl]$ is independent of h, k, l, and its r.m.s. value must be

$$E=(s_{11}+2s_{23})N, \tag{2}$$

where N is the r.m.s. value of n. This result and those below hold whether or not the distributions are Gaussian.

Since its right side is independent of crystallographic direction, Eq. (2) fits the measurements on tungsten within the experimental error, but it yields a 40 percent error at best for α-brass. For tungsten $s_{11}=2.573\times10^{-13}$ cm^2/dyne, $s_{23}=-0.729\times10^{-13}$ cm^2/dyne, $s_{44}=6.604\times10^{-13}$ cm^2/dyne.[4] Putting these values into Eq. (2) and setting $E=2.980\times10^{-3}$, one finds $N=2.675\times10^{10}$ dynes/cm^2. For α-brass $s_{11}=19.4\times10^{-13}$ cm^2/dyne, $s_{23}=-8.35\times10^{-13}$ cm^2/dyne, $s_{44}=13.9\times10^{-13}$ cm^2/dyne.[4] Taking E as 2.12×10^{-3}, one gets an order of magnitude $N=7.80\times10^9$ dynes/cm^2.

SECOND MODEL. RANDOM PRINCIPAL STRESSES

In the second model it is assumed that the principal stresses[5] existing at any point of cold-worked metal are random in orientation and random and independent in magnitude, being constant throughout only small domains, and each on the average zero. Because of the linearity of Eqs. (1), the normal strain in the $[hkl]$ direction is the sum of the $[hkl]$ strains produced by each of the three principal stresses separately. Its mean-square value is, thus, the sum of the mean-square values of these three components, since, because of the independence, the cross-products average to zero. Suppose that these three principal stresses all have the same r.m.s. value T. Because of their randomness of orientation, each one on the average produces the same r.m.s. $[hkl]$ strain. Thus, E^2 is three times the mean-square $[hkl]$ strain produced by a single normal stress of random magnitude and random direction.

If the magnitude of such a single normal stress is t, and its orientation with respect to the crystallographic axes is specified by the direction cosines l, m, n, then[6]

$$\left.\begin{aligned} X_x&=l^2t, & Y_z&=mnt,\\ Y_y&=m^2t, & Z_x&=nlt,\\ Z_z&=n^2t, & X_y&=lmt. \end{aligned}\right\} \tag{3}$$

The normal strain in the $[hkl]$ direction due to this stress is[7]

$$e=H^2e_{xx}+K^2e_{yy}+L^2e_{zz}+KLe_{yz}+LHe_{zx}+HKe_{xy}, \tag{4}$$

where H, K, L are the direction cosines for this direction, $H=h/(h^2+k^2+l^2)^{\frac{1}{2}}$, etc. Combining Eqs. (1), (3), and (4), one obtains

$$e=[s_{23}+(s_{11}-s_{23})(H^2l^2+K^2m^2+L^2n^2)+s_{44}(KLmn+LHnl+HKlm)]t,$$

which is to be squared and averaged over all directions l, m, n. This averaging is performed by transforming to spherical coordinates, taking $l=\sin\theta\cos\phi$, $m=\sin\theta\sin\phi$, $n=\cos\theta$. The probability that θ lies between θ and $\theta+d\theta$ is $\frac{1}{2}\sin\theta d\theta$; the probability that ϕ lies between ϕ and $\phi+d\phi$ is $d\phi/2\pi$. The result is

$$(e^2)_{Av}=(1/15)t^2\{[3s_{11}^2+4s_{11}s_{23}+8s_{23}^2]+[s_{44}^2-4(s_{11}-s_{23})^2]\Gamma\},$$

where

$$\Gamma=K^2L^2+L^2H^2+H^2K^2=\tfrac{1}{2}-\tfrac{1}{2}(H^4+K^4+L^4).$$

Thus,

$$E=T(1/5)^{\frac{1}{2}}\{[3s_{11}^2+4s_{11}s_{23}+8s_{23}^2]+[s_{44}^2-4(s_{11}-s_{23})^2]\Gamma\}^{\frac{1}{2}}. \tag{5}$$

Because for an elastically isotropic metal[8] $s_{44}=2(s_{11}-s_{23})$, this E is independent of direction for such a metal, in accord with the observations on tungsten. To fit the observed value of E for tungsten, Eq. (5) requires that $T=3.34\times10^9$ dynes/cm^2. For α-brass (5) becomes

$$E=T(208-577\Gamma)^{\frac{1}{2}}\times10^{-13}\text{ cm}^2/\text{dyne}.$$

Γ lies between 0 for [100] and $\frac{1}{3}$ for [111]. Thus, $E_{100}/E_{111}=3.7$, which considerably exceeds the variation exhibited in Table I.

[4] a. E. Schmid and W. Boas, *Kristallplastizität* (Verlagsbuchhandlung, Julius Springer, Berlin, 1935), p. 200; b. F. Seitz and T. A. Read, J. App. Phys. 12, 100 (1941).
[5] A. E. H. Love, *Mathematical Theory of Elasticity* (Cambridge University Press, London, 1927), p. 81.
[6] Reference 5, p. 80.
[7] Reference 5, p. 43.
[8] Reference 2a, p. 589.

THIRD MODEL. RANDOM SHEARING STRESSES

In the next model there is at each point a set of orthogonal coordinate axes with respect to which the normal components of stress all vanish. In such a model there is nowhere any dilatation. Suppose, as before, that the orientation of these axes is random and that the magnitudes of the three shearing components of stress are random and independent, all having the same r.m.s. value S. It is again only necessary to consider the effect of one of these three shearing stresses. Its magnitude will be designated by s and the direction cosines with respect to the crystallographic axes of the two axes with which it is associated by l_1, m_1, n_1; l_2, m_2, n_2, with $l_1l_2+m_1m_2+n_1n_2=0$, i.e., the two axes perpendicular. Thus,[6]

$$\left.\begin{aligned} X_x&=2l_1l_2s, & Y_z&=(m_1n_2+n_1m_2)s,\\ Y_y&=2m_1m_2s, & Z_x&=(n_1l_2+l_1n_2)s,\\ Z_z&=2n_1n_2s, & X_y&=(l_1m_2+m_1l_2)s. \end{aligned}\right\} \quad (6)$$

Combining Eqs. (1), (4), and (6), one finds

$$e=\{2(s_{11}-s_{22})(H^2l_1l_2+K^2m_1m_2+L^2n_1n_2)+s_{44}[KL(m_1n_2+n_1m_2)+LH(n_1l_2+l_1n_2)+HK(l_1m_2+m_1l_2)]\}S.$$

To average the square of this e with respect to direction, one may transform the direction l_1, m_1, n_1 to spherical coordinates and add another angular coordinate ψ to specify the position of direction l_2, m_2, n_2 about the direction l_1, m_1, n_1. The probability that ψ lies between ψ and $\psi+d\psi$ is $d\psi/2\pi$. We write $l_1=\sin\theta\cos\phi$, $m_1=\sin\theta\sin\phi$, $n_1=\cos\theta$; $l_2=\sin\psi\sin\phi-\cos\psi\cos\theta\cos\phi$, $m_2=-\sin\psi\cos\phi-\cos\psi\cos\theta\sin\phi$, $n_2=\cos\psi\sin\theta$. Thus, the square root of three times the mean-square value of the above e is

$$E=S(1/5)^{\frac{1}{2}}\{4(s_{11}-s_{22})^2+3[s_{44}^2-4(s_{11}-s_{22})^2]\Gamma\}^{\frac{1}{2}}. \quad (7)$$

Like (5), (7) fits the observations on tungsten for which one obtains $S=10.10\times10^9$ dynes/cm². For α-brass (7) becomes

$$E=S(716-732\Gamma)^{\frac{1}{2}}\times10^{-13}\ \text{cm}^2/\text{dyne}.$$

This yields $E_{100}/E_{111}=4.0$, which again far exceeds the observed ratio, 1.635.

SLIP

The next two models include the phenomenon of slip.[9] The shearing stress in a crystal of α-brass or any other face-centered-cubic metal on a (111) plane in a $[10\bar{1}]$ direction cannot exceed a certain critical value, which probably is less than $\frac{1}{2}\times10^8$ dynes/cm²,[10] without the crystal's slipping on that plane in that direction. This stress is small compared to the stresses that have been found in this work. Thus, it will be assumed that slip relieves essentially all of the shearing stress on the slip plane in the slip direction. For tungsten and other body-centered-cubic metals the slip direction is [111], but the slip plane is indefinite.

Fourth Model. Random Principal Stresses

The fourth model will be like the second except that it will be assumed that in each domain slip occurs once, relieving all of the corresponding shearing stress. As the mechanism for this relief one may assume that the previously existing stress system is modified so as to leave no resultant shearing stress on the plane of slip in the slip direction but not to change any other of the six stress components referred to axes coinciding with the slip. It will be assumed that this slip occurs in a random one of the 24 possible ways. However, the crystallographic axes can be chosen in each domain so that the normal to the slip plane and the slip direction always have the same direction cosines, say a, b, c, and A, B, C, respectively, where on account of the perpendicularity of the slip plane and direction $aA+bB+cC=0$. The normal $[hkl]$ strain due to the original principal stress t acting in the direction with cosines l, m, n, plus that caused by a set of stresses, which relieves the shearing stress related to the directions with cosines a, b, c, and A, B, C, but does not alter the other stress components as determined with respect to a set of orthogonal axes of which two have these directions, is

---

[9] See references 4a; 2b, p. 39; 2c, p. 288.

[10] Compare E. Schmid, *International Conference on Physics, Vol. II, The Solid State of Matter* (Phys. Soc., London, 1935).

$$e=\{s_{23}+(s_{11}-s_{23})(H^2l^2+K^2m^2+L^2n^2)+s_{44}(KLmn+LHnl+HKlm)$$
$$-[2(s_{11}-s_{23})(H^2aA+K^2bB+L^2cC)+s_{44}(KL[bC+cB]+LH[cA+aC]+HK[aB+bA])]$$
$$\cdot[aAl^2+bBm^2+cCn^2+(bC+cB)mn+(cA+aC)nl+(aB+bA)lm]\}t.$$

Because the crystallographic axes have been oriented with respect to the slip rather than the reflecting plane, the latter is equally likely to be any plane of the form $\{hkl\}$. Thus, it is necessary to average not only over l, m, n, but also over all permutations and changes of sign of H, K, L. Squaring the above e, taking these two averages, and averaging over t, whose r.m.s. value we write as T', tripling, and extracting the square root, one obtains

$$E=T'(1/15)^{\frac{1}{2}}\{[9s_{11}^2+12s_{11}s_{23}+24s_{23}^2]$$
$$+[2s_{44}^2-12(s_{11}-s_{23})^2]\Gamma$$
$$-(a^2A^2+b^2B^2+c^2C^2)[4(s_{11}-s_{23})^2$$
$$-(2s_{44}^2+12[s_{11}-s_{23}]^2)\Gamma]\}^{\frac{1}{2}}. \quad (8)$$

For a metal which slips on (111), $a^2A^2+b^2B^2+c^2C^2=\frac{1}{3}(A^2+B^2+C^2)=\frac{1}{3}$. Similarly for one which slips in direction [111] this quantity is $\frac{1}{3}$. Thus, the indefiniteness of the slip plane in tungsten is of no consequence. Under these circumstances Eq. (8) becomes

$$E=T'(1/45)^{\frac{1}{2}}\{[23s_{11}^2+44s_{11}s_{23}+68s_{23}^2]$$
$$+[8s_{44}^2-24(s_{11}-s_{23})^2]\Gamma\}^{\frac{1}{2}}. \quad (9)$$

This E is seen to depend on Γ even for isotropic materials. For tungsten (9) becomes

$$E=T'(2.35+1.93\Gamma)^{\frac{1}{2}}\times10^{-13}\ \text{cm}^2/\text{dyne},$$

giving $E_{100}/E_{111}=0.89$ instead of 1.00. For α-brass (9) is

$$E=T'(139-377\Gamma)^{\frac{1}{2}}\times10^{-13}\ \text{cm}^2/\text{dyne},$$

whence $E_{100}/E_{111}=3.2$ as compared with the empirical value 1.635.

Fifth Model. Random Shearing Stresses

If slip is added to the third model just as it was above to the second, one gets by a process similar to the above

$$E=S'(1/15)^{\frac{1}{2}}\{12(s_{11}-s_{23})^2$$
$$+6[s_{44}^2-6(s_{11}-s_{23})^2]\Gamma$$
$$+(a^2A^2+b^2B^2+c^2C^2)[-4(s_{11}-s_{23})^2$$
$$+6(s_{44}^2+2[s_{11}-s_{23}]^2)\Gamma]\}^{\frac{1}{2}}, \quad (10)$$

where S' is the r.m.s. value of s here. If $a^2A^2+b^2B^2+c^2C^2=\frac{1}{3}$,

$$E=S'(8/45)^{\frac{1}{2}}\{4(s_{11}-s_{23})^2$$
$$+3[s_{44}^2-4(s_{11}-s_{23})^2]\Gamma\}^{\frac{1}{2}}. \quad (11)$$

Although the E in Eq. (10) is not in general independent of Γ for isotropic materials, in the particular case of (11) it is. For tungsten (11) is $E=S'\times2.786\times10^{-13}$ cm^2/dyne, which requires $S'=10.70\times10^9$ dynes/cm^2 to fit the observations. For α-brass (11) is

$$E=S'(676-1540\Gamma)^{\frac{1}{2}}\times10^{-13}\ \text{cm}^2/\text{dyne},$$

from which $E_{100}/E_{111}=4.06$ where 1.635 is observed.

Sixth Model. Random Crystallographic Stresses

In this model the magnitudes of the six stress components determined with respect to the crystallographic axes in each domain are assumed random, independent, and of mean value zero. If the r.m.s. values of the three normal components are all P, and those of the three shearing components are all Q, we have from (1) and (4)

$$E=\{(s_{11}+2s_{23})^2P^2+[s_{44}^2Q^2$$
$$-2(s_{11}-s_{23})^2P^2]\Gamma\}^{\frac{1}{2}}. \quad (12)$$

This E is independent of Γ for isotropic materials only if $P^2=2Q^2$. Applying it to tungsten, for $E=2.980\times10^{-3}$, one must have $P=10.8\times10^9$ dynes/cm^2, $Q=7.6\times10^9$ dynes/cm^2. For brass a considerable variety of results can be obtained, depending upon P/Q. This point is considered at greater length below.

Synthesis

It is not an accident that Eqs. (2), (5), (7)–(9), and (12) all exhibit E as a function of Γ of the same form,

$$E=E_0(1-R\Gamma)^{\frac{1}{2}}. \quad (13)$$

Any theory involving stresses which on the average act symmetrically with respect to the six crystallographic axes (three positive and three

negative) necessarily yields such a result. This is a consequence of the fact that the strain in the direction $[hkl]$ is a quadratic function of H, K, L. Its mean-square value is, therefore, an even symmetric quartic function of H, K, L. Thus, it can contain no odd powers of these quantities. It can contain no quadratic terms, for all even, symmetric, homogeneous, quadratic functions of H, K, L are multiples of $H^2+K^2+L^2=1$. And all even, symmetric, homogeneous, quartic functions of H, K, L are made up of multiples of $K^2L^2+L^2H^2+H^2K^2=\Gamma$ and $H^4+K^4+L^4=1-2\Gamma$. Thus, E^2 must be a linear function of Γ, and E must be of the foregoing form.

One should, therefore, determine the E_0 and R which fit the observations best. For tungsten R is obviously zero and $E_0=2.980\times10^{-3}$. In the case of α-brass we want the R for which the quantity $E_{obs}/(1-R\Gamma)^{\frac{1}{2}}$ is most nearly constant, E_{obs} being the E of Table I. This quantity is tabulated for several values of R in Table II. It is seen to be very nearly constant for R between 1.50 and 1.65. The [111] value does not seem to fit well, possibly because the low intensity of 222 reflection resulted in poor breadth measurements for this line. In what follows it will be assumed that the best fit is given by $R=1.58$, $E_0=2.70\times10^{-3}$, for which the corresponding values of (13),

$$E=2.70\times10^{-3}(1-1.58\Gamma)^{\frac{1}{2}},$$

have been tabulated in Table II.

For the case of α-brass, only one of the foregoing models can, when the corresponding E is written in the form of (13), take on the value of 1.58 for R, namely, the sixth. Eq. (12) is transformed into Eq. (14) for $P=9.8\times10^{5}$ dynes/cm², $Q=6.0\times10^{9}$ dynes/cm². For the first model, $R=0$, while for the second to fifth, inclusive, R is at least 2.7. (Note that R cannot exceed 3.) However, one can readily get four more models by superposing a stress system for which R exceeds 1.58 upon a system (the first model) for which R is less than 1.58. On the assumption that the superposed internal-stress systems are independent, the squares of the corresponding E's add directly, i.e., the radicands of the E's themselves add directly, and the resultant E is, of course, still of the form (13).

TABLE II. Determination of E_0 and R for α-brass.

		$\frac{E}{(1-R\Gamma)^{\frac{1}{2}}}$					$(1-1.58\Gamma)$
Γ	E	$R=1.50$	1.55	1.60	1.65	1.70	$\times2.70\times10^{-3}$
0.0000	2.714×10^{-3}	2.714×10^{-3}	2.714	2.714	2.714	2.714	2.70×10^{-3}
0.1570	2.328	2.662	2.678	2.692	2.704	2.720	2.34
0.1600	2.322	2.668	2.680	2.692	2.708	2.724	2.32
0.2500	2.106	2.668	2.694	2.720	2.748	2.780	2.10
0.2741	2.008	2.620	2.652	2.684	2.716	2.750	2.02
0.3333	1.660	2.346	2.386	2.426	2.472	2.522	1.86

Two parameters are then available, and the desired values for both E_0 and R can be obtained.

One of these parameters is N; the other is T, S, T', or S'. It may be added that three or more different internal-stress systems can be superposed, but the amount of each required then becomes indeterminate. The following combinations are found to yield the desired result of $R=1.58$ and $E_0=2.70\times10^{-3}$:

$N=6.6\times10^{9}$ dynes/cm², $T=14.2\times10^{9}$ dynes/cm²;
$N=5.8\times10^{9}$ dynes/cm², $S=8.2\times10^{9}$ dynes/cm²;
$N=6.5\times10^{9}$ dynes/cm², $T'=17.6\times10^{9}$ dynes/cm²;
$N=5.6\times10^{9}$ dynes/cm², $S'=8.6\times10^{9}$ dynes/cm².

CONCLUSIONS

The fact that the fit shown in Table II is rather good, being based on Eq. (13), which applies to any system of microstresses, constitutes strong evidence in favor of the microstress theory. It not only accounts for the observed constancy of $B/\tan\theta$ with respect to wavelength, as Smith and Stickley concluded,[1] but also for its observed variation with direction.

Although the sixth model and the several superposition models all fit the data, they must be examined with regard to their reasonableness. On this basis the sixth model is immediately eliminated, since it is not reasonable that the three normal stresses in the directions of the crystallographic axes should be independent of each other. The combination of the first and fourth models might be thrown out because the latter does not fit the observations on tungsten. However, with as small a ratio of T' to N as has been found here for α-brass, the predicted variation of E with direction would be less than four percent, which may well be smaller than the experimental error.

The combinations with the models involving random shearing stress are quite plausible, since

any system of stresses can be resolved into the sum of three shearing stresses acting on mutually orthogonal planes and a uniform normal stress.[11] The models in which uniform normal stress and random principal stresses are combined (superposition of first and second and superposition of first and fourth) are quite reasonable. It is implausible that the principal stresses should be either all equal, as in the first model, or all independent, as in the second. Something intermediate is rather to be expected, because when one of the principal stresses is positive, for example, the Poisson contraction prejudices the others toward being positive also. Superposition of the two systems (second or fourth on first) yields a model in which the coefficient of correlation between any two principal stresses is $N^2/(N^2+T^2)$. It is evident that no one simple model by itself appears reasonable.

One may object to our treatment of slip, for actually which of the 24 possible slip mechanisms comes into play is not a matter of random choice but of the one on which the greatest shearing component acts. Moreover, there may be multiple slip and even twinning in a single domain. Had these considerations been taken into account, however, the calculation would have become very difficult. The point may be raised that Table I lists $B/\tan\theta$ only for those members of each family of planes which were in position to reflect. For the other planes E may be different from the tabulated values. However, no satisfactory way of taking this into account has been devised except to assume that the tabulated values are typical.

It is to be noted that the values of N listed in the preceding section are all close to 6.0×10^9 dynes/cm^2, while those of T, S, T', and S' are all much smaller. We may conclude that the microstress system in the α-brass is indeed essentially like that of the first model but with the admixture of a small amount of anisotropic stress of any variety, the exact form of the description of the latter being possibly immaterial.

The problem of the internal energy change associated with cold-work and its relation to the x-ray diffraction effects has been reviewed by others.[12,13] The present microstress systems lead to the same order of r.m.s. strain and hence to the same order of energy as was reported by Hayworth. This energy value, 0.05 cal./g, is far less than the only measured values of 1 cal./g, and the generally accepted implication is that the difference is associated with distortions on an atomic scale, e.g., Taylor dislocations.

ACKNOWLEDGMENT

I want to thank Dr. Charles S. Smith, who suggested this work and under whose guidance it was carried out.

[11] Reference 5, p. 83.

[12] F. Seitz and T. A. Read, J. App. Phys. 12, 177–178 (1941).

[13] F. E. Hayworth, Phys. Rev. 52, 618 (1937).

PHYSICAL REVIEW VOLUME 70, NUMBERS 9 AND 10 NOVEMBER 1 AND 15, 1946

Properties of Monoclinic Crystals

W. P. MASON
Bell Telephone Laboratories, Inc., Murray Hill, New Jersey
(Received August 15, 1946)

Two crystals of the monoclinic sphenoidal class have been found which have modes of vibration with zero temperature coefficients of frequency, and this property together with the high electromechanical coupling and the high Q's make it appear probable that these crystals may have considerable use as a substitute for quartz which is difficult to obtain in large sizes. These crystals are ethylene diamine tartrate ($C_6H_{14}N_2O_6$) and dipotassium tartrate ($K_2C_4H_4O_6$, $\frac{1}{2}H_2O$). Complete measurements of the elastic, piezoelectric, and dielectric constants of the dipotassium tartrate (DKT) crystal are given in this paper. The crystal has 4 dielectric constants, 8 piezoelectric constants, and 13 elastic constants. A discussion is given in the appendix of the method of measuring these constants by the use of 18 properly oriented crystals.

I. INTRODUCTION

As part of the program for investigating promising piezoelectric crystals, measurements have been made of a number of piezoelectric crystals occurring in the various crystallographic classes. It has been found that the less symmetric classes give greater possibilities in obtaining low temperature coefficients because with the larger number of elastic constants a greater possibility exists of balancing temperature coefficients between the various constants and obtaining zero temperature coefficient crystals. In particular two crystals of the monoclinic sphenoidal class have been found which have modes of vibration with zero temperature coefficients of frequency, and this property together with the high electromechanical coupling and the high Q's (or low internal dissipation) make it appear likely that these crystals may have considerable use as substitutes for quartz, which is difficult to obtain in large sizes. These two crystals are ethylene diamine tartrate* (which has been given the designation EDT) and dipotassium tartrate (which has been given the designation DKT).

It is the purpose of this paper to derive the fundamental constants for a monoclinic crystal and to show how they are measured. This process is illustrated completely for one of these crystals, dipotassium tartrate ($K_2C_4H_4O_6$, $\frac{1}{2}H_2O$). This crystal forms in the monoclinic sphenoidal class which has as its only element of symmetry the b or Y crystallographic axis, which is an axis of binary symmetry. As a consequence there are four dielectric constants, eight piezoelectric constants, and thirteen elastic constants. To obtain all of these constants requires measuring the properties of eighteen carefully oriented crystal cuts. Since this is the first time that all of the properties of a monoclinic crystal have been measured by dynamic methods, a complete description of the process is given in the appendix.

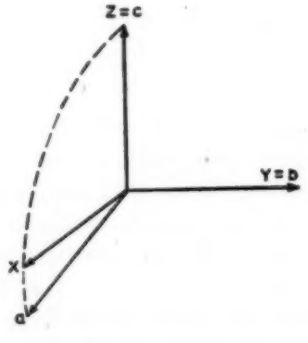

FIG. 1. Method of relating rectangular X, Y, Z axes to a, b, c crystallographic axes of a monoclinic crystal.

II. MONOCLINIC CRYSTALS AND THEIR RESULTING PIEZOELECTRIC EQUATIONS

Monoclinic crystals are characterized by having two crystallographic axes b and c at right angles to each other, and a third axis a which makes an angle different from 90° with the other two. The c axis lies along the shortest direction of the unit cell while the b axis is the axis of twofold symmetry. In measuring the properties of a crystal, the calculation comes out much more

* A paper on the properties of this crystal is in course of preparation.

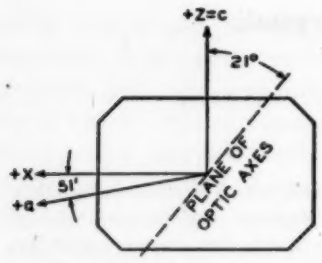

FIG. 2. Relation of $+X$ and $+Z$ axes to plane of optic axes.

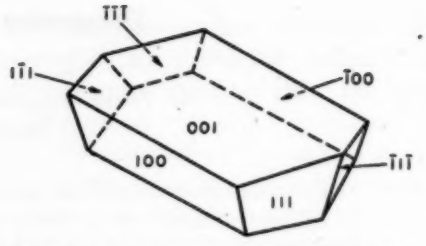

FIG. 3. Crystal habit for DKT crystals.

simply for a right-angled system of coordinates. As shown by Fig. 1, the method chosen[1] for relating the right-angled X, Y, Z system of axes to the a, b, c crystallographic axes of the crystallographer is to make Z coincide with c, Y with b, and to have the X axis lie in the plane of the b axis and at an angle of 51′ above a for DKT.

The X, Y, Z axes form a right-angled system of axes. Since b is the binary axis, it is necessary to have a convention for specifying which end of the axis is positive. As shown in a companion paper by W. L. Bond[2] this can be done by locating the optic axis of the crystal. A monoclinic crystal is a biaxial crystal and the plane that contains these axes is found to be parallel to the b or Y crystallographic axis. As shown by Fig. 2, the plane of the optic axes lies at a clockwise direction of 21° from the c or Z crystallographic axis. Since X lies at a counterclockwise angle of 90° from c and $(+b=+Y)$ makes a right-angle system of coordinates with the X and Z axes, the measurement determines the positive directional of all three axes. Oriented crystal cuts are usually specified by x-ray orientation procedures as discussed in the above paper.[2]

These crystals were grown from a supersaturated solution by A. N. Holden. Holden finds that the water of crystallization in DKT is quite tightly bound and experimentally it has been found that no noticeable dehydration takes place at 80°C over a week's time. At about 150°C the vapor pressure of DKT reaches atmospheric and will cause bubbling in an oil bath. The usual crystal habit is that shown by Fig. 3. The crystal has two cleavage planes lying along planes determined by the three crystallographic axes. However, these cleavages are not sufficiently bad to cause much trouble in processing these crystals.

The Voigt form of writing the piezoelectric equations for a monoclinic sphenoidal crystal is as shown in Eq. (1). In this equation T_1 to T_6 represent the six stresses and S_1 to S_6, the six strains. σ represents the electric displacement $D/4\pi$ in the interior of the crystal and the normal component of σ is the surface charge.

$$
\begin{aligned}
S_1&=s_{11}^E T_1+s_{12}^E T_2+s_{13}^E T_3+s_{15}^E T_5+d_{21}E_y,\\
S_2&=s_{12}^E T_1+s_{22}^E T_2+s_{23}^E T_3+s_{25}^E T_5+d_{22}E_y,\\
S_3&=s_{13}^E T_1+s_{23}^E T_2+s_{33}^E T_3+s_{35}^E T_5+d_{23}E_y,\\
S_4&=s_{44}^E T_4+s_{46}^E T_6+d_{14}E_x+d_{34}E_z,\\
S_5&=s_{15}^E T_1+s_{25}^E T_2+s_{35}^E T_3+s_{55}^E T_5+d_{25}E_y,\\
S_6&=s_{46}^E T_4+s_{66}^E T_6+d_{16}E_x+d_{36}E_z,\\
\sigma_x&=\frac{\epsilon_{11}^T E_x}{4\pi}+\frac{\epsilon_{13}^T E_z}{4\pi}+d_{14}T_4+d_{16}T_6,\\
\sigma_y&=\frac{\epsilon_{22}^T E_y}{4\pi}+d_{21}T_1+d_{22}T_2+d_{23}T_3+d_{25}T_5,\\
\sigma_z&=\frac{\epsilon_{13}^T E_x}{4\pi}+\frac{\epsilon_{33}^T E_z}{4\pi}+d_{34}T_4+d_{36}T_6,
\end{aligned}
\qquad (1)
$$

where the superscripts E over the elastic compliances indicate that they are to be measured with the applied fields held constant or zero. When there are two applied fields both of these fields have to be held constant or zero to obtain the Voigt elastic compliances. The superscripts T for the dielectric constants indicate that they are to be measured for no stresses applied, i.e., that they are the "free" dielectric constants.

[1] This system of relating rectangular axes to crystallographic axes has been standardized by a committee on piezoelectric crystals of the Institute of Radio Engineers, under the chairmanship of Professor W. G. Cady. They have also standardized the symbols and nomenclature used in this paper.

[2] Paper in course of preparation.

TABLE I. *X* cut crystals of DKT.

Temperature in degrees C	Shear mode: Length along *Z*, *L* = 20.20 mm, *W* = 4.25 mm, *T* = 0.91 mm		Longitudinal modes: Length 22.5° from *Y*, *L* = 20.01 mm, *W* = 3.21 mm, *T* = 0.896 mm		Length 45° from *Y*, *L* = 19.65 mm, *W* = 3.2 mm, *T* = 0.90 mm		Length 67.5° from *Y*, *L* = 21.0 mm, *W* = 3.23 mm, *T* = 0.912 mm	
	f_R	Δf	f_R	Δf	f_R	Δf	f_R	Δf
+80	235300	1000	89160	180	85100	280	81000	150
+70	236350		89560		85500		81370	
+60	237500	1000	89980	170	85980	270	81750	150
+50	238600		90380		86340		82120	
+40	239600	1000	90800	170	86760	260	82480	140
+30	240650		91240		87210		82860	
+20	241750	975	91690	160	87670	250	83260	140
+10	242750		92100		88030		83610	
0	243800	975	92440	160	88390	240	83940	130
−10	244700		92770		88690		84280	
−20	245600	960	93100	150	89030	220	84520	130
−30	246500		93400		89350		84850	
−40	247400	930	93690	150	89630	220	85120	120
−50	248250		93960		89940		85420	
−60	249100	930	94270	130	90240	210	85700	110
−70	249950		94570		90610		85980	
−80	250700	930	94860	140	90910	210	86260	110

TABLE II. *Z* cut crystals of DKT.

Temperature in degrees C	Shear mode: Length along *Y*, *L* = 19.84 mm, *W* = 4.27 mm, *T* = 0.90 mm		Longitudinal modes: Length 22.5° from *Y*, *L* = 19.61 mm, *W* = 3.21 mm, *T* = 0.863 mm		Length 45° from *Y*, *L* = 19.96 mm, *W* = 3.13 mm, *T* = 0.910 mm		Length 67.5° from *Y*, *L* = 19.96 mm, *W* = 3.32 mm, *T* = 0.886 mm	
	f_R	Δf	f_R	Δf	f_R	Δf	f_R	Δf
+80	257500	5600	91030	920	88225	1600	101840	1110
+70	257600		91290		88300		102040	1130
+60	257600	5750	91520	980	88375	1775	102180	1200
+50	257500		91760		88450		102280	
+40	257400	5900	92000	1020	88500	1900	102380	1400
+30	257200		92200		88550		102450	
+20	257000	6400	92420	1100	88600	2000	102540	1600
+10	256700		92620		88630		102620	
0	256450	7000	92810	1200	88660	2125	102680	1720
−10	256150		92990		88660		102720	
−20	255850	7400	93150	1300	88650	2275	102740	1880
−30	255500		93310		88640		102760	
−40	255100	7900	93450	1400	88610	2450	102780	2000
−50	254700		93600		88560		102800	
−60	254250	8400	93720	1500	88490	2650	102800	2150
−70	253800		93840		88425		102770	
−80	253300	8900	93960	1600	88350	2875	102740	2200

TABLE III. *Y* cut crystals of DKT.

Temperature in degrees C	Shear mode: Length along *Z*, *L* = 14.52 mm, *W* = 2.95 mm, *T* = 1.05 mm		Longitudinal modes: Length 22.5° from *X*, *L* = 19.95 mm, *W* = 3.71 mm, *T* = 1.03 mm		Length 45° from *X*, *L* = 20.32 mm, *W* = 4.03 mm, *T* = 1.05 mm		Length 67.5° from *X*, *L* = 12.75 mm, *W* = 2.51 mm, *T* = 1.02 mm	
	f_R	Δf	f_R	Δf	f_R	Δf	f_R	Δf
+80	401500	1000	123760	780	101460	1030	135950	950
+70	402850		124000		101660		136550	
+60	404000	1000	124210	750	101880	1010	137150	940
+50	405000		124440		102080		137700	
+40	406100	1000	124650	730	102300	990	138200	930
+30	407100		124860		102500		138710	
+20	408200	1000	125100	710	102700	980	139240	920
+10	409200		125300		102900		139770	
0	410100	950	125510	700	103120	970	140350	910
−10	411100		125730		103320		140820	
−20	412050	950	125950	680	103530	960	141220	900
−30	413000		126160		103720		141610	
−40	413950	950	126370	670	103940	960	142000	880
−50	414950		126600		104140		142400	
−60	415900	950	126810	640	104340	930	142800	870
−70	416900		127040		104650		143220	
−80	417850	950	127250	620	104750	910	143650	850

TABLE IV. Oblique cuts of DKT.

Temperature in degrees C	Width parallel to *Z* − length and thickness 45° from *X* and *Y*. Shear mode, *L* = 20.28 mm, *W* = 3.18 mm, *T* = 0.895 mm		Width parallel to *X* − length 45° from *Y* and *Z*. Longitudinal mode, *L* = 11.13 mm, *W* = 3.20 mm, *T* = 0.90 mm		Orientation. See Fig. 9, *L* = 20.09 mm, *W* = 3.195 mm, *T* = 0.90 mm		Length along *Y* width 45° from *X* and *Y*. Face shear mode, *L* = 20.29 mm, *W* = 3.2 mm, *T* = 0.89 mm	
	f_R	Δf	f_R	Δf	f_R	Δf	f_R	Δf
+80	328100	900	149900	365	86220	280	335000	7350
+70	329500		150810		86440		336100	
+60	330700	900	151600	365	86650	310	336600	6800
+50	331800		152400		86870		337900	
+40	332950	930	153100	370	87100	350	338500	7100
+30	334000		153800		87350		339500	
+20	334950	930	154500	380	87575	350	340500	7350
+10	335900		155200		87800		341200	
0	336850	950	155800	385	88000	385	341900	8000
−10	337800		156400		88200		342600	
−20	338250	1000	156950	415	88390	385	343300	8470
−30	339700		157510		88575		344000	
−40	340600	1050	158050	430	88750	420	344600	9000
−50	341550		158550		88925		345000	
−60	342500	1060	159050	435	89050	490	345520	9640
−70	343400		159500		89175		346000	
−80	344400	1120	159900	450	89300	525	346400	10200

For ferroelectric type crystals it has been found that equations which relate the piezoelectric effect to the electrical displacement or the surface charge (the normal component displacement $D/4\pi$ equals the surface charge at the crystal surface) are more fundamental than those based on the field. By eliminating the fields from the first six equations of (1), by substituting in the displacements from the last three equations we have

$$
\begin{aligned}
S_1 &= s_{11}^{D}T_1 + s_{12}^{D}T_2 + s_{13}^{D}T_3 + s_{15}^{D}T_5 + g_{21}\sigma_y,\\
S_2 &= s_{12}^{D}T_1 + s_{22}^{D}T_2 + s_{23}^{D}T_3 + s_{25}^{D}T_5 + g_{22}\sigma_y,\\
S_3 &= s_{13}^{D}T_1 + s_{23}^{D}T_2 + s_{33}^{D}T_3 + s_{35}^{D}T_5 + g_{23}\sigma_y,\\
S_4 &= s_{44}^{D}T_4 + s_{46}^{D}T_6 + g_{14}\sigma_x + g_{34}\sigma_z,\\
S_5 &= s_{15}^{D}T_1 + s_{25}^{D}T_2 + s_{35}^{D}T_3 + s_{55}^{D}T_5 + g_{25}\sigma_y, \qquad (2)\\
S_6 &= s_{46}^{D}T_4 + s_{66}^{D}T_6 + g_{16}\sigma_x + g_{36}\sigma_z,\\
E_x &= 4\pi\beta_{11}^{T}\sigma_x + 4\pi\beta_{13}^{T}\sigma_z - g_{14}T_4 - g_{16}T_6,\\
E_y &= 4\pi\beta_{22}^{T}\sigma_y - g_{21}T_1 - g_{22}T_2 - g_{23}T_3 - g_{25}T_5,\\
E_z &= 4\pi\beta_{13}^{T}\sigma_x + 4\pi\beta_{33}^{T}\sigma_z - g_{34}T_4 - g_{36}T_6,
\end{aligned}
$$

TABLE V. Free dielectric constants of DKT.

Temperature in degrees C	Dielectric constant normal to X	Dielectric constant normal to Y	Dielectric constant normal to Z	Dielectric constant normal to a plane making 45° angle with X and Z
+80	6.64	5.97	6.53	6.57
+70	6.61	5.94	6.52	6.55
+60	6.57	5.91	6.51	6.53
+50	6.54	5.89	6.51	6.52
+40	6.51	5.86	6.50	6.50
+30	6.48	5.83	6.49	6.48
+20	6.44	5.80	6.49	6.47
+10	6.41	5.78	6.48	6.45
0	6.38	5.75	6.47	6.43
−10	6.35	5.72	6.47	6.41
−20	6.31	5.69	6.46	6.39
−30	6.28	5.66	6.45	6.38
−40	6.25	5.64	6.45	6.36
−50	6.22	5.61	6.46	6.34
−60	6.19	5.58	6.47	6.34
−70	6.15	5.55	6.48	6.33
−80	6.12	5.52	6.50	6.32
−90	6.09	5.49	6.52	6.31
−100	6.05	5.47	6.54	6.31

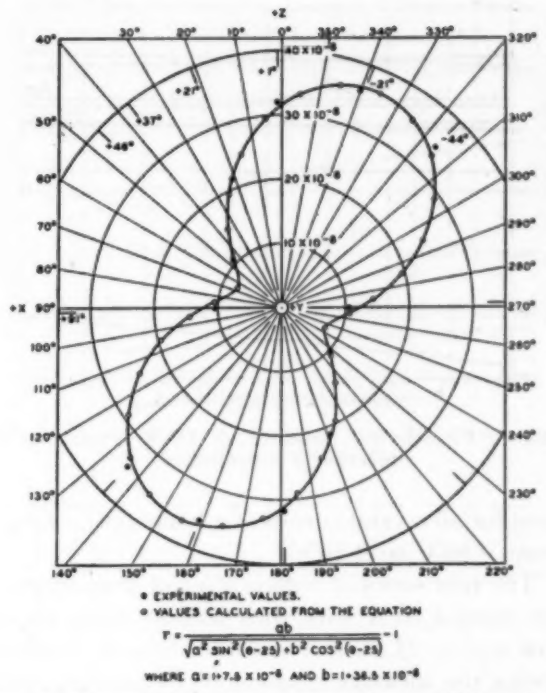

FIG. 4. Average temperature expansion coefficient for DKT crystals in the XZ plane.

where the β_{ij}^{T} constants are the "free" dielectric impermeabilities, which are related to the dielectric constants ϵ_{ij}^{T} by the equations

$$
\begin{aligned}
\beta_{11}^{T} &= \frac{\epsilon_{33}^{T}}{\epsilon_{11}^{T}\epsilon_{33}^{T} - (\epsilon_{13}^{T})^2}; \quad \beta_{13}^{T} = \frac{-\epsilon_{13}^{T}}{\epsilon_{11}^{T}\epsilon_{33}^{T} - (\epsilon_{13}^{T})^2};\\
\beta_{22}^{T} &= \frac{1}{\epsilon_{22}^{T}}; \quad \beta_{33}^{T} = \frac{\epsilon_{11}^{T}}{\epsilon_{11}^{T}\epsilon_{33}^{T} - (\epsilon_{13}^{T})^2}.
\end{aligned} \qquad (3)
$$

The relations between the displacement and field elastic compliances and between the d and g piezoelectric constants are discussed in detail in the appendix.

III. MEASUREMENT OF THE PROPERTIES OF DKT

The preferred orientations for measuring crystal properties and the elastic, piezoelectric, and dielectric constants associated with each cut have been discussed in detail in the appendix, Section VI. It is the purpose of this section to record the measured results for the cuts and to give the final constants as calculated from the measurements. The resonant and anti-resonant frequencies, the resistance at resonance and the capacitance at low frequencies have been meas-

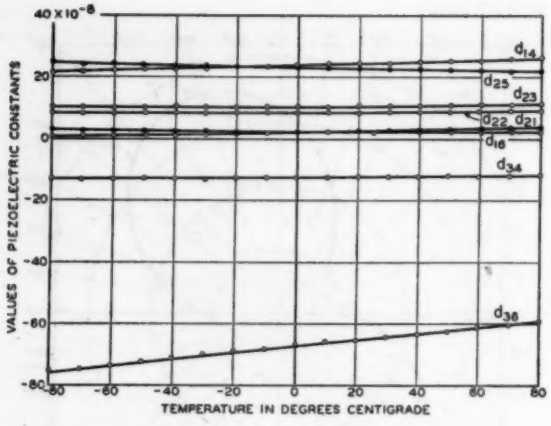

FIG. 5. Piezoelectric constants of DKT crystals as a function of temperature.

ured for all crystal cuts over a temperature range from −80°C to +80°C.

The first series of cuts is a set of four crystals cut normal to X with their lengths along the Z axis and at 22.5°, 45°, and 67.5° from Z. Table I shows the measured resonance frequencies, and the separation of the resonant and anti-resonant frequencies all made in a holder which is shielded so that no stray capacity has to be allowed for. Table II shows similar data for Z cut crystals and Table III for Y cut crystals. In order to complete the measurements several double orientation crystals have to be used and the orientations and data are given by Table IV. Finally Table V shows a measurement of the dielectric constants of four crystals. These are measured at 1000 cycles and represent the "free" dielectric constants. From these data and the data of the temperature[3] expansion coefficients shown by Fig. 4 all of the properties of the crystal can be determined.

In order to illustrate the method, calculations are made at room temperature of all of the constants. From Table I we find that the resonant frequency and the separation of resonant and anti-resonant frequency for a crystal cut normal to the X axis, with its length 45° from the Y and Z axes and with the dimension $L=19.65$ mm; $W=3.2$ mm; $T=0.90$ mm, are at 20°C, $f_R=87670$, $(f_A-f_R)=250$ cycles. From Table V the free dielectric constant for this crystal is 6.44. From Eq. (50) of the appendix the coefficient of coupling k is equal to

$$k=\frac{\pi}{2}\left(\frac{\Delta f}{f_R}\right)^{\frac{1}{2}}=\frac{\pi}{2}\left(\frac{250}{87670}\right)^{\frac{1}{2}}=0.084. \quad (4)$$

The frequency constant for the plated crystal is $f_R l=172.1$ kc cm$=f_M{}^E$. Since the density is 1.988, this gives a value for the elastic compliance at constant field along the X axis equal to

$$s_{22_{45°}}{}^{E'}=\frac{1}{(2f_M{}^E)^2\rho}=4.24\times10^{-12}\ \text{cm}^2/\text{dyne}. \quad (5)$$

From this value and the free dielectric constant (6.44) we have from Eq. (17) of the appendix

$$d_{12}'=\left(\frac{\epsilon_{11}{}^T}{4\pi}s_{22}{}^E\right)^{\frac{1}{2}}k=\pm12.35\times10^{-8}\ \text{c.g.s. unit}. \quad (6)$$

But from Eq. (91) of the appendix $d_{12}'=d_{14}/2$ so that the fundamental constant $d_{14}=\pm24.7\times10^{-8}$. As will be shown later this sign is positive, and the value of d_{14} calculated over a temperature range is shown plotted by Fig. 5. Performing the same operations on the crystals cut at 22.5° from Y and 67.5° from Y, we find

$$s_{22_{22.5}}{}^E=3.73\times10^{-12};\quad s_{22_{67.5}}{}^E=4.09\times10^{-12}. \quad (7)$$

Since from Eq. (84) in the appendix, the elastic constant $s_{22}{}^{E'}$ satisfies the equation

$$s_{22}{}^{E'}=s_{22}{}^E\cos^4\theta+(2s_{23}{}^E+s_{44}{}^E)\sin^2\theta\cos^2\theta+s_{33}{}^E\sin^4\theta, \quad (8)$$

these three values are enough to determine the fundamental constants $s_{22}{}^E$, $s_{33}{}^E$, $(2s_{23}{}^E+s_{44}{}^E)$. The formulae are

$$\begin{aligned}s_{22}{}^E&=1.707s_{22_{22.5}}{}^E-s_{22_{45}}{}^E+0.293s_{22_{67.5}}{}^E;\\ s_{33}{}^E&=0.293s_{22_{22.5}}{}^E-s_{22_{45}}{}^E+1.707s_{22_{67.5}}{}^E;\\ (2s_{23}{}^E+s_{44}{}^E)&=6s_{22_{45}}{}^E-2(s_{22_{22.5}}{}^E+s_{22_{67.5}}{}^E).\end{aligned} \quad (9)$$

From these formulae and the values of Eq. (7) we obtain

$$\begin{aligned}s_{22}{}^E=3.395\times10^{-12};\quad s_{33}{}^E=3.907\times10^{-12};\\ (2s_{23}{}^E+s_{44}{}^E)=9.684\times10^{-12}.\end{aligned} \quad (10)$$

The first crystal of Table I is a face shear vibrating crystal whose frequency is determined

[3] The temperature expansion coefficients of DKT crystals have been measured by Miss E. J. Armstrong.

by the width of the crystal. From Eqs. (105) and (106) of the appendix, the frequency is determined by

$$f=\frac{1}{2l_w}\left(\frac{c_{44}{}^{c,E}}{\rho}\right)^{\frac{1}{2}} \tag{11}$$

and the fundamental elastic constant $s_{44}{}^{E}$ by the equation

$$s_{44}{}^{E}=1/c_{44}{}^{c,E}. \tag{12}$$

From the measured values of Table I,

$$\begin{aligned} c_{44}{}^{c,E}&=8.35\times10^{10}\ \text{dynes/cm}^2;\\ k&=0.100;\quad \epsilon_{11}{}^{T}=6.44. \end{aligned} \tag{13}$$

Hence

$$\begin{aligned} s_{44}{}^{E}&=11.9\times10^{-12}\ \text{cm}^2/\text{dyne};\\ d_{14}&=24.7\times10^{-8}. \end{aligned} \tag{14}$$

This checks the value of d_{14} obtained from the 45° X cut crystal. It also shows that the shear mode driven by a shear elastic constant has a higher coupling than a 45° longitudinal cut driven by the same shear constant.

When these constants are measured over a wide temperature range, it is necessary to take account of the coefficients of temperature expansion. This changes not only the length of the frequency determining direction, but also changes the density ρ since the total volume of the crystal changes with temperature. The average of the temperature coefficients measured from −40° to +80°C are shown by Fig. 4. In the XZ plane, the coefficient follows the dumbbell shape with its major axis at an angle of about −26 degrees from the Z axis. This shape represents the difference between a circle at 25°C and the ellipse that the circle expands into at different temperatures. The temperature coefficient along the Y axis is 44.8 parts per million per degree centigrade. When it is desired to obtain the temperature expansion coefficient for any other angle, say in a plane containing the Y axis and making an angle θ with the Z axis, with the direction making an angle φ with the Y axis, the coefficient is obtained by reading the coefficient T_θ for the angle θ in the XY plane and substituting in the formula

$$T_l=T_\theta\sin^2\varphi+T_y\cos^2\varphi, \tag{15}$$

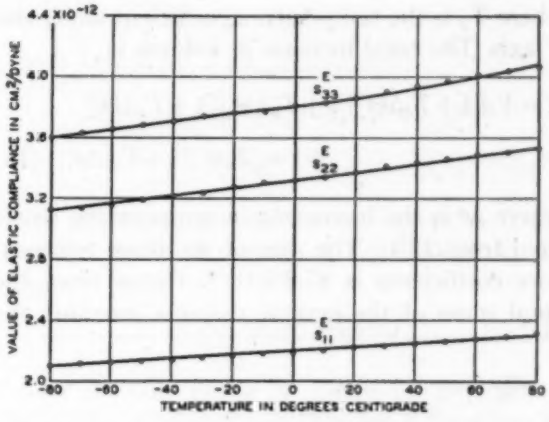

FIG. 6. Three extensional moduli of compliance measured as a function of temperature.

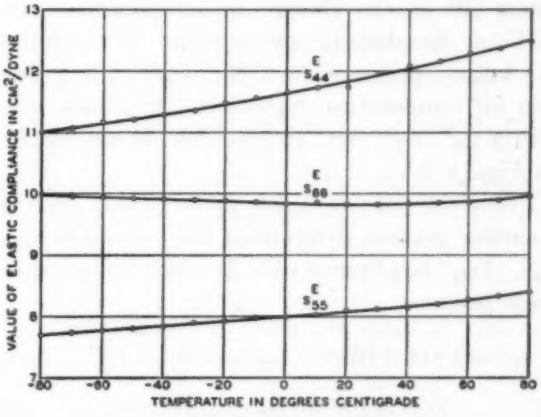

FIG. 7. Three shearing moduli of compliance for DKT measured as a function of temperature.

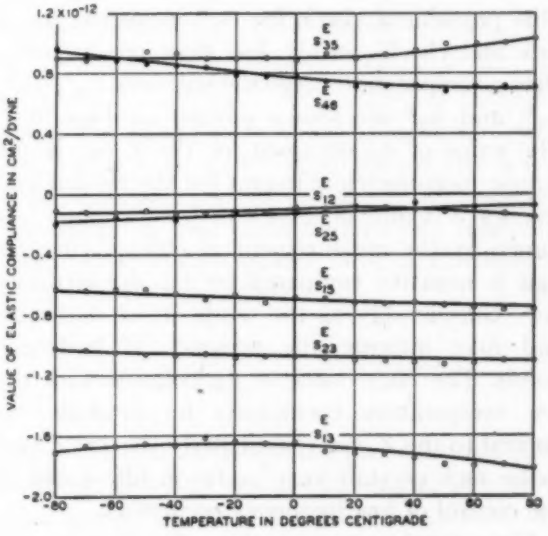

FIG. 8. Seven cross coupling moduli of compliances measured as a function of temperature.

where T_y is the temperature coefficient along the Y axis. The total increase in volume is

$$V=V_0[1+T_x\Delta\Theta][1+T_y\Delta\Theta][1+T_z\Delta\Theta]$$
$$\doteq 1+(T_x+T_y+T_z)\Delta\theta, \quad (16)$$

where $\Delta\theta$ is the increment in temperature measured from 25°C. The sum of the three temperature coefficients is 87.8×10^{-6}. Hence since the total mass of the crystal remains constant the temperature coefficient of density is

$$T_\rho=-87.8\times10^{-6} \text{ per °C.} \quad (17)$$

From the frequency equation for a longitudinal mode

$$f=\frac{1}{2l}\left(\frac{1}{\rho s}\right)^{\frac{1}{2}} \quad (18)$$

the correction to the elastic compliance s is

$$s=\frac{1}{\rho(2lf)^2}=\frac{1}{\rho_0[1-87.8\times10^{-6}\Delta\Theta][2fl_0(1+T_l\Delta\Theta)]^2}=\frac{1+(87.8-2T_l)\times10^{-6}\Delta\Theta}{\rho_0(2fl_0)^2}, \quad (19)$$

where $\Delta\Theta$ is the change in temperature from 25°C, ρ_0 the density measured at 25°C, and l_0 the length measured at 25°C. With this correction for temperature coefficient, the elastic constants s_{22}^E, s_{33}^E, s_{44}^E, and s_{23}^E are shown plotted on Figs. 6–8.

From the data of Table II for Z cut crystals a similar process determines the constants s_{11}^E, s_{22}^E, $(2s_{12}^E+s_{66}^E)$ and s_{66}^E. At room temperature these become

$$s_{11}^E=2.218\times10^{-12}; \quad s_{22}^E=3.404\times10^{-12};$$
$$2s_{12}^E+s_{66}^E=9.64; \quad s_{66}^E=9.81; \quad (20)$$
$$s_{12}^E=-0.085.$$

This provides a check for s_{22}^E measured for Z cuts and checks within less than one percent. Over a temperature range the values of s_{11}^E, s_{22}^E, s_{12}^E, and s_{66}^E are shown plotted on Figs. 6–8. The value of d_{36} obtained for the Z cut is the largest piezoelectric constant for the crystal and reaches a value of 66.4×10^{-8} c.g.s. unit. As shown by the measurement of oblique cuts, its sign is negative compared to d_{14}. d_{36} increases very considerably as the temperature decreases and may indicate the presence of hydrogen bonds. The large value of d_{36} coupled with the low temperature coefficients for crystals cut normal to the Z axis (particularly the 45° Z cut) make such crystals very useful in filters and in the control of low frequency oscillators.

For crystals cut normal to the Y axis of a monoclinic crystal, the longitudinal elastic constant varies with angle according to the equation

$$s_{33}'^E=s_{33}^E\cos^4\psi+2s_{35}^E\cos^3\psi\sin\psi$$
$$+(2s_{13}^E+s_{55}^E)\sin^2\psi\cos^2\psi$$
$$+2s_{15}^E\sin^3\psi\cos\psi+s_{11}^E\sin^4\psi. \quad (21)$$

The derivation of this equation is given in the appendix, Eq. (86). The values of s_{33}^E and s_{11}^E are given in Fig. 6 so that the data for the three longitudinal crystals are sufficient to determine s_{35}^E, $(2s_{13}^E+s_{55}^E)$ and s_{15}^E which are shown plotted on Figs. 7 and 8. The equation for the piezoelectric constants of longitudinal crystals cut normal to the Y axis is

$$d_{12}'=d_{21}\sin^2\psi+d_{23}\cos^2\psi+\frac{d_{25}}{2}\sin 2\psi. \quad (22)$$

From the values of coupling and the dielectric constants for the three crystals, we find

$$d_{21}=+2.2\times10^{-8}; \quad d_{23}=+10.4\times10^{-8};$$
$$d_{25}=+22.4\times10^{-8}. \quad (23)$$

All constants have the same sign. The sign of d_{23} was determined by squeeze tests on the crystal to be a positive charge delivered along the positive Y axis for an extension along the Z axis.

The two remaining elastic cross constants s_{25}^E and s_{46}^E have to be evaluated by employing oblique cuts that do not lie along or normal to any of the three crystallographic axes. s_{46}^E can be determined by using the face shear mode of a crystal cut with its length along Y and its width

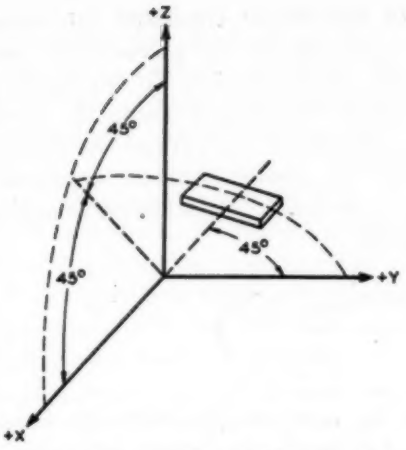

FIG. 9. Doubly oriented DKT crystal.

at 45° between the positive X and Z axes, for as shown by Eqs. (105)–(107) of the appendix, the frequency of the unplated crystal determines the elastic constant

$$s_{66}^{E\prime}=\frac{s_{66}^{E}-2s_{46}^{E}+s_{44}^{E}}{2}. \tag{24}$$

From the data of the last crystal of Table IV, we find $s_{46}^{E}=0.74\times10^{-12}$ at 20°C. The electromechanical coupling factor as calculated from the resonant and anti-resonant frequencies is

$$k=0.225. \tag{25}$$

Since from Eq. (108) the piezoelectric constant driving this mode is

$$d_{14}'=\frac{(d_{14}+d_{16}-d_{24}-d_{36})}{2} \tag{26}$$

and the dielectric constant from Table V is 6.47, we find

$$d_{14}'=52.6\times10^{-8}. \tag{27}$$

Since d_{14} and d_{36} have been found equal to 24.7×10^{-8} and -66.4×10^{-8}, we find

$$d_{16}-d_{24}=14\times10^{-8}. \tag{28}$$

The constant s_{25}^{E} was determined by measuring the resonant frequency of a crystal oriented as shown by Fig. 9. It is shown in the appendix, Eq. (87), that the frequency of a plated crystal is given by

$$f=\frac{1}{2l}\left(\frac{1}{\rho s_{22}^{E}}\right)^{\frac{1}{2}}, \tag{29}$$

where

$$s_{22}^{E\prime}=\tfrac{1}{16}[s_{11}^{E}+s_{33}^{E}+(s_{55}^{E}+2s_{13}^{E})]+\tfrac{1}{8}[s_{15}^{E}+s_{35}^{E}+s_{46}^{E}+(s_{44}^{E}+2s_{23}^{E})+(s_{66}^{E}+2s_{12}^{E})]+\tfrac{1}{4}[s_{22}^{E}+s_{25}^{E}].$$

Since all the values are known except s_{25}^{E}, the data for the third crystal of Table IV yield the value

$$s_{25}^{E}=-0.12\times10^{-8}. \tag{30}$$

The second crystal of Table IV provides a check on the elastic constant for a direction in the YZ plane halfway between the two axes. The value found is 4.19×10^{-12} dyne/cm² which checks the value for a 45° X cut crystal shown by Table I. The piezoelectric constant driving this mode is from Eq. (97) of the appendix

$$d_{12}'=0.3535[d_{23}+d_{22}-d_{24}]. \tag{31}$$

From the data of Table IV, $d_{12}'=11.1\times10^{-8}$ and since d_{23} is known, we have

$$d_{22}-d_{24}=21.0\times10^{-8}. \tag{32}$$

This value together with the data of Eq. (28) gives

$$d_{22}-d_{16}=7.0\times10^{-8}. \tag{33}$$

The first crystal of Table IV should have a longitudinal mode driven by the piezoelectric constant (from Eq. (99) of appendix)

$$d_{12}'=-0.3535[d_{21}+d_{22}-d_{16}]. \tag{34}$$

From the values given above this should result in a value of 3.2×10^{-8} which should give a very low coupling. This was verified for no resonance was found for this mode. Driven in a face shear mode this crystal should have a piezoelectric shear constant equal to

$$d_{14}'=\frac{(d_{14}+d_{25})}{2}=23.5\times10^{-8}. \tag{35}$$

From the data of Table IV, the measured value is about 20×10^{-8} which verifies the sign of d_{14} with respect to d_{25}.

Finally the driving constant of the double oriented crystal, Number 3 of Table IV should

be according to Eq. (102) of the appendix

$$d_{12}'=0.1768[d_{21}+d_{23}+d_{25}+2d_{22} -(d_{14}+d_{16}+d_{34}+d_{36})]. \quad (36)$$

From the values and signs assigned, we find $d_{12}'=18.5\times10^{-8}$. The measured value from Table IV is 15×10^{-8}, which verifies the sign of d_{36}.

All of the elastic constants are determined except s_{55}^E and all the piezoelectric constants except d_{22} (or d_{16} or d_{34}). To determine s_{55}^E we make use of the data of Table III on the face shear mode of a Y cut crystal. As shown in the appendix the elastic constant controlling this mode is a "coupled" constant and the frequency is given by

$$f=\frac{1}{2l_w}\left(\frac{c_{11}^{c,E}+c_{55}^{c,E}-[(c_{11}^{c,E}-c_{55}^{c,E})^2+4c_{15}^{c,E^2}]^{\frac{1}{2}}}{2\rho}\right)^{\frac{1}{2}}. \quad (37)$$

The method of calculating s_{55}^E from the measured value of the shear mode and the other elastic constants is explained in the appendix. The resultant obtained from the data is

$$s_{55}^E=8.15\times10^{-12}. \quad (38)$$

The values over a temperature range are shown by Fig. 7. With this value s_{13} can be determined and all the elastic constants are given by Figs. 6–8.

To determine the remaining piezoelectric constants, requires measuring the properties of a thickness mode. Either of the two shears S_6 or S_4 can be used or the thickness longitudinal mode. Of these the mode with the largest coupling is the S_4 mode, which is obtained by measuring a Z cut crystal, dimensioned so that it has a single mode. This crystal had a coupling of 4.9 percent giving a value of $d_{34}=-12.1\times10^{-8}$. Hence the remaining values are

$$d_{22}=8.9\times10^{-8}; \quad d_{16}=1.9\times10^{-8}.$$

Both of these constants are too small to drive modes appreciably, and none were observed. The complete values of the piezoelectric constants over a range of temperature are plotted on Fig. 5.

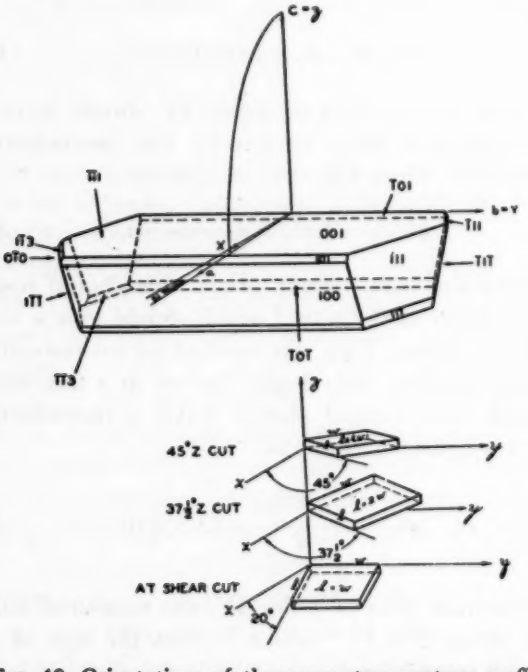

FIG. 10. Orientations of three zero temperature coefficient crystals with respect to the mother crystal. 45° Z cut and 37.5° Z cut are longitudinal modes. AT shear cut is a face shear mode.

IV. DISCUSSION OF PROPERTIES OF DKT CRYSTALS

This crystal has properties that make it a possible substitute for quartz for a number of applications. Three cuts have been found for which large electromechanical couplings are associated with zero temperature coefficients of frequency. These cuts are all perpendicular or nearly perpendicular to the Z axis and two of the modes are longitudinal and one a face shear mode. While the coefficient can be made zero at a specified temperature, the deviation from the frequency at the zero temperature coefficient is parabolic as in most zero coefficient quartz crystals. The curvature is several times larger than for quartz crystals. Figure 10 shows these three cuts in relation to the natural crystal.

This crystal shows some evidence of hydrogen bond type of coupling at low temperatures. Figure 11 shows a plot of the inverse of d_{36} for dipotassium tartrate, and indicates only a uniform increase in d_{36} as the temperature is lowered.

Such a curve might be accounted for by a hydrogen bond type of dipole at low temperatures such as occurs for potassium dihydrogen phosphate,[4] and a frozen dipole liberated at a high temperature such as occurs in sodium chlorate and sodium bromate.[5] However, the range in temperature is too small to make this interpretation certain. All the other piezoelectric constants vary less than does d_{36}. The contributions of the different types of dipoles to the dielectric constant is too uncertain to test out the relation found for ammonium dihydrogen phosphate, potassium dihydrogen phosphate, sodium chlorate and sodium bromate, that the piezoelectric stress was proportional to the dipole polarization.

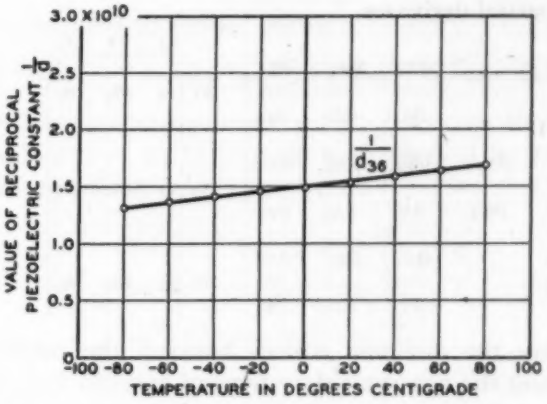

FIG. 11. Inverse of d_{36} plotted over a temperature range.

APPENDIX. CALCULATION OF THE RESONANT FREQUENCIES OF A MONOCLINIC CRYSTAL

I. Introduction

For monoclinic or triclinic crystals, the applied fields and the resulting charge displacements are usually not in the same direction and hence a somewhat extended discussion has to be given for them. It turns out that the piezoelectric constants that are directly measured are the d_{ijm} piezoelectric constants which relate strains to the applied fields. This follows from the fact that the electrical boundary conditions are that the tangential components of the fields of a plated crystal are zero.

It is the purpose of this appendix to investigate the frequencies of longitudinal modes and limiting cases of face shear modes for the purpose of relating the measured frequencies and capacities to the elastic, piezoelectric, and dielectric constants of the crystal. In order to facilitate the calculation the piezoelectric equations are expressed in tensor form, since by doing so, long summation terms are avoided. A short discussion is given of the tensor method of writing the piezoelectric equations.

II. Piezoelectric Equations in Tensor Form

The stress components acting on a unit cube of a solid body are symmetrical and can be written in the form

$$\begin{vmatrix} T_1 & T_6 & T_5 \\ T_6 & T_2 & T_4 \\ T_5 & T_4 & T_3 \end{vmatrix}. \tag{1}$$

These are the three longitudinal stresses and the three shearing stresses. These components form a tensor of the second rank as will be shown. To conform to the usual tensor notation we shall write these components as

$$T_{kl} = \begin{vmatrix} T_{11} & T_{12} & T_{13} \\ T_{12} & T_{22} & T_{23} \\ T_{13} & T_{23} & T_{33} \end{vmatrix} = \begin{vmatrix} T_1 & T_6 & T_5 \\ T_6 & T_2 & T_4 \\ T_5 & T_4 & T_3 \end{vmatrix}. \tag{2}$$

These nine terms form a symmetrical tensor of the second rank for, if we transform them to a rotated system of axes, this transformation takes place according to the tensor transformation formula

$$T_{ij}' = \frac{\partial x_i'}{\partial x_k} \frac{\partial x_j'}{\partial x_l} T_{kl}. \tag{3}$$

In this equation

$$x_i' = x_1', x_2', x_3'$$

are the coordinates of the rotated set of axes and

$$x_k = x_1, x_2, x_3$$

are the coordinates of the original axes. The

[4] W. P. Mason, Phys. Rev. 69, 173–194 (1946).
[5] W. P. Mason, "Elastic, piezoelectric, and dielectric properties of sodium chlorate and sodium bromate," Phys. Rev. 70, 529 (1946).

partial derivates

$$\frac{\partial x_1'}{\partial x_k}=\begin{vmatrix} \frac{\partial x_1'}{\partial x_1} & \frac{\partial x_1'}{\partial x_2} & \frac{\partial x_1'}{\partial x_3} \\ \frac{\partial x_2'}{\partial x_1} & \frac{\partial x_2'}{\partial x_2} & \frac{\partial x_2'}{\partial x_3} \\ \frac{\partial x_3'}{\partial x_1} & \frac{\partial x_3'}{\partial x_2} & \frac{\partial x_3'}{\partial x_3} \end{vmatrix} \quad \begin{array}{c} \\ x_1' \\ x_2' \\ x_3' \end{array} \quad \begin{array}{c} x_1 \quad x_2 \quad x_3 \\ \begin{vmatrix} l_1 & m_1 & n_1 \\ l_2 & m_2 & n_2 \\ l_3 & m_3 & n_3 \end{vmatrix} \end{array} \tag{4}$$

are the direction cosines between the rotated and the non-rotated systems of axes. In Eq. (3) another tensor convention is used, namely that when an index is repeated on one side of an equation, a summation with respect to the indices 1, 2, 3 is indicated. Both k and l are repeated in Eq. (3). For example in expanded form, letting i' and j' each equal 1, Eq. (3) will expand into

$$T_{11}'=\left(\frac{\partial x_1'}{\partial x_1}\right)^2 T_{11}+2\left(\frac{\partial x_1'}{\partial x_1}\frac{\partial x_1'}{\partial x_2}\right)T_{12}+2\left(\frac{\partial x_1'}{\partial x_1}\frac{\partial x_1'}{\partial x_3}\right)T_{13}+\left(\frac{\partial x_1'}{\partial x_2}\right)^2 T_{22}+2\frac{\partial x_1'}{\partial x_2}\frac{\partial x_1'}{\partial x_3}T_{23}+\left(\frac{\partial x_1'}{\partial x_3}\right)^2 T_{33}. \tag{5}$$

In ordinary elastic terminology this would be expressed as

$$T_1'=l_1^2T_1+2l_1m_1T_6+2l_1n_1T_5+m_1^2T_2+2m_1n_1T_4+n_1^2T_3 \tag{6}$$

which is the expression given by Love for the transformations of stress from one system of axes to another system. Hence since the stress system is a collection of nine quantities which transfer from one system of axes to another system by the tensor transformation equation, the stress system is a tensor of the second order.

The strain components are usually defined as

$$S_1=\frac{\partial \xi}{\partial x_1};\quad S_2=\frac{\partial \eta}{\partial x_2};\quad S_3=\frac{\partial \zeta}{\partial x_3};$$
$$S_6=\left(\frac{\partial \eta}{\partial x_1}+\frac{\partial \xi}{\partial x_2}\right);\quad S_5=\left(\frac{\partial \xi}{\partial x_3}+\frac{\partial \zeta}{\partial x_1}\right);\quad S_4=\left(\frac{\partial \zeta}{\partial x_2}+\frac{\partial \eta}{\partial x_3}\right), \tag{7}$$

where ξ, η, ζ are, respectively, the displacements of the body along the x_1, x_2, x_3 axes, respectively. This set of 9 quantities, however, is not a tensor for it does not satisfy the tensor transformation equation. If, however, we define new strain components as

$$S_{11}=S_1=\frac{\partial \xi}{\partial x_1};\quad S_{22}=S_2=\frac{\partial \eta}{\partial x_2};\quad S_{33}=S_3=\frac{\partial \zeta}{\partial x_3};$$
$$S_{12}=S_{21}=\frac{S_6}{2}=\frac{1}{2}\left(\frac{\partial \eta}{\partial x_1}+\frac{\partial \xi}{\partial x_2}\right);$$
$$S_{13}=S_{31}=\frac{S_5}{2}=\frac{1}{2}\left(\frac{\partial \xi}{\partial x_3}+\frac{\partial \zeta}{\partial x_1}\right); \tag{8}$$
$$S_{23}=S_{32}=\frac{S_4}{2}=\frac{1}{2}\left(\frac{\partial \zeta}{\partial x_2}+\frac{\partial \eta}{\partial x_3}\right),$$

the symmetrical nine components

$$\begin{vmatrix} S_{11} & S_{12} & S_{13} \\ S_{12} & S_{22} & S_{23} \\ S_{13} & S_{23} & S_{33} \end{vmatrix} \tag{9}$$

will form a tensor of the second rank.

The generalized Hooke law between the stresses and the strains can be written

$$S_{ij}=s_{ij,kl}T_{kl}, \tag{10}$$

since $s_{ij,kl}$ or s_{ijkl} is a tensor of the fourth rank. The right-hand side of the equation being the product of a fourth rank tensor by a second rank tensor is a sixth rank tensor, but since it is contracted twice by having k and l in both terms, the resultant of the right-hand side is a second rank tensor. A tensor of the fourth rank will ordinarily have 81 terms, but since S_{ij} and T_{kl} are both symmetrical, only 21 independent terms exist in s_{ijkl}. If we examine this expression and compare term by term with the usual way of writing Hooke's law, given by Eq. (11)

$$\begin{aligned} S_1=S_{11}&=s_{11}T_1+s_{12}T_2+s_{13}T_3+s_{14}T_4+s_{15}T_5+s_{16}T_6, \\ &\cdots\cdots\cdots \\ S_6=2S_{12}&=s_{16}T_1+s_{26}T_2+s_{36}T_3+s_{46}T_4+s_{56}T_5+s_{66}T_6 \end{aligned} \tag{11}$$

and noting that $S_6=2S_{12}$, etc., the usual two

index compliances correspond to the four index symbol s_{ijkl} provided we replace

$$\begin{array}{lll} 1 \text{ by } 11, & 2 \text{ by } 22, & 3 \text{ by } 33, \\ 4 \text{ by } 23, & 5 \text{ by } 13, & 6 \text{ by } 12. \end{array} \tag{12}$$

However, for any number 4, 5, or 6 the elastic constant s_{ij} has to be divided by two to equal the corresponding s_{ijkl} constant, and if 4, 5, or 6 occurs twice, the diviser has to be 4.

The adiabatic form of Voigt's piezoelectric equations can thus be written in tensor form

$$\begin{aligned} S_{ij} &= s_{ijkl}{}^{E} T_{kl} + d_{mij} E_m, \\ \sigma_n &= \frac{\epsilon_{mn}{}^{T}}{4\pi} E_m + d_{nkl} T_{kl}, \end{aligned} \tag{13}$$

where E_m are the three applied fields, σ_n the surface charges normal to the three axes, d_{ijm} the third rank piezoelectric tensor relating the strains to the applied fields or the electric displacement to the applied stresses. In a similar way to the elasticities, the two index piezoelectric symbols are related to the three index symbols if we replace the ij terms

$$\begin{array}{l} 1 \text{ by } 11, \ 2 \text{ by } 22, \quad 3 \text{ by } 33, \\ 4 \text{ by } 23, \quad 5 \text{ by } 13 \quad \text{and} \quad 6 \text{ by } 12. \end{array} \tag{14}$$

For any number 4, 5, or 6, the piezoelectric constant d_{im} has to be divided by 2 to equal the corresponding d_{ijm} constant.

To find the form of the piezoelectric equations for which the electric displacement $D/4\pi$ is the independent variable, the following derivation can be used. Let us first consider the dielectric "impermeability" tensor $\beta_{mn}{}^{T}$ which is formed from the dielectric constant tensor $\epsilon_{mn}{}^{T}$ by means of the relation

$$\beta_{mn}{}^{T} = (-1)^{(m+n)} \Delta\epsilon_{mn}{}^{T} / \epsilon_{mn}{}^{T}, \tag{15}$$

where $\epsilon_{mn}{}^{T}$ is the dielectric constant tensor

$$\begin{vmatrix} \epsilon_{11}{}^{T}, & \epsilon_{12}{}^{T}, & \epsilon_{13}{}^{T} \\ \epsilon_{12}{}^{T}, & \epsilon_{22}{}^{T}, & \epsilon_{23}{}^{T} \\ \epsilon_{13}{}^{T}, & \epsilon_{23}{}^{T}, & \epsilon_{33}{}^{T} \end{vmatrix} \tag{16}$$

and $\Delta\epsilon_{mn}{}^{T}$ is the determinant formed from this tensor by suppressing the mth row and nth column. We next multiply both sides of the last of Eq. (13) by $4\pi\beta_{mn}{}^{T}$ giving

$$4\pi\beta_{mn}{}^{T}\sigma_n = E_m[\beta_{mn}{}^{T}\epsilon_{mn}{}^{T}] + 4\pi\beta_{mn}{}^{T} d_{nkl} T_{kl}. \tag{17}$$

If we take the product $\epsilon_{mn}{}^{T}\beta_{mn}{}^{T}$ for the three values of m, we have as the multipliers of E_1, E_2, E_3, respectively,

$$\begin{aligned} &\epsilon_{11}{}^{T}\beta_{11}{}^{T} + \epsilon_{12}{}^{T}\beta_{12}{}^{T} + \epsilon_{13}{}^{T}\beta_{13}{}^{T}, \\ &\epsilon_{21}{}^{T}\beta_{21}{}^{T} + \epsilon_{22}{}^{T}\beta_{22}{}^{T} + \epsilon_{23}{}^{T}\beta_{23}{}^{T}, \\ &\epsilon_{31}{}^{T}\beta\pi_1{}^{T} + \epsilon_{32}{}^{T}\beta_{32}{}^{T} + \epsilon_{33}{}^{T}\beta_{33}{}^{T}. \end{aligned} \tag{18}$$

But by virtue of the definition of $\beta_{mn}{}^{T}$ given by Eq. (15) it is obvious that the value of each term is unity so that Eq. (17) can be written

$$\begin{aligned} E_m &= 4\pi\beta_{mn}{}^{T}\sigma_n - 4\pi\beta_{mn}{}^{T} d_{nkl} T_{kl} \\ &= 4\pi\beta_{mn}{}^{T}\sigma_n - g_{mkl} T_{kl}, \end{aligned} \tag{19}$$

where the new piezoelectric constants g_{mkl} relating the fields to the applied forces or the strains to the electric displacement is given in terms of the d_{nkl} piezoelectric constants and the "free" dielectric impermeability by the tensor equation

$$g_{mkl} = 4\pi\beta_{mn}{}^{T} d_{nkl}. \tag{20}$$

Introducing the value of E_m into the first of Eqs. (13) we find

$$S_{ij} = s_{ijkl}{}^{D} T_{kl} + g_{mij}\sigma_n, \tag{21}$$

where the open circuit or zero charge elastic compliances are given by

$$s_{ijkl}{}^{D} = s_{ijkl}{}^{E} - d_{mij} g_{mkl}. \tag{22}$$

Hence the complete piezoelectric equation can be written

$$\begin{aligned} S_{ij} &= s_{ijkl}{}^{D} T_{kl} + g_{mij}\sigma_n, \\ E_m &= 4\pi\beta_{mn}{}^{T}\sigma_n - g_{mkl} T_{kl}. \end{aligned} \tag{23}$$

III. Equations of Motion of a Piezoelectric Crystal

The equation of motion of a piezoelectric crystal or any aeolotropic body can be derived from Newton's laws of motion and the piezoelectric Eqs. (13). Newton's law can be written in the tensor form

$$\rho \frac{\partial^2 \xi_k}{\partial t^2} dx_1 dx_2 dx_3 = F_k, \tag{24}$$

where ξ_k are the displacements of the elementary cube $dx_1dx_2dx_3$ in the x_1, x_2, x_3 directions, F_k are the components of force in these directions exerted on the elementary cube, and ρ is the density of the material within the cube. From elastic theory we have that the total resultant force along the x_1 direction is the partial derivatives of the stresses in this direction or

$$F_1=+\left[\frac{\partial T_{11}}{\partial x_1}+\frac{\partial T_{12}}{\partial x_2}+\frac{\partial T_{13}}{\partial x_3}\right]dx_1dx_2dx_3$$

$$=+\frac{\partial T_{1l}}{\partial x_l}dx_l. \quad (25)$$

For the forces in any direction we can write the general tensor relations

$$F_k=+\frac{\partial T_{kl}}{\partial x_l}dx_l. \quad (26)$$

Hence the equations of motion become

$$\rho\frac{\partial^2\xi_k}{\partial t^2}=+\frac{\partial T_{kl}}{\partial x_l}. \quad (27)$$

Into this equation we can insert expressions for the strains in terms of the stresses and applied charges and obtain the partial differential equations for any mode of motion. However, before doing this it is desirable to discuss the boundary condition that such crystals have to satisfy.

The elastic conditions for a crystal free to vibrate are that the stresses normal to the free edges are zero. For a surface whose normal has the direction cosines l_1, l_2, l_3 with respect to the X_1, X_2, X_3 axes, respectively, the conditions reduce to

$$\begin{aligned}T_x&=T_{11}l_1+T_{12}l_2+T_{13}l_3=T_{ij}l_j=0,\\ T_y&=T_{21}l_1+T_{22}l_2+T_{23}l_3=T_{2j}l_j=0,\\ T_z&=T_{31}l_1+T_{32}l_2+T_{33}l_3=T_{3j}l_j=0,\end{aligned} \quad (28)$$

where T_x, T_y, and T_z are the stresses along the X_1, X_2, X_3 axes. If we denote these by T_i, the boundary conditions can be abbreviated into

$$T_i=T_{ij}l_j=0. \quad (29)$$

The electrical boundary conditions are determined by whether plating is placed on the surface of the crystal or not. If any plating is a long distance from the crystal, then the surface charge σ_i is necessarily zero since no path exists for conducting charge to this surface. If, on the other hand, a plating is integral with the surface normal to the x_1 axis, the surface charge σ_1 will not be zero but will be a function of the other two directions x_2 and x_3. In the interior of the crystal, the electrical condition is expressed by determining the electrical induction D. At every point of the interior the divergence of the electric induction vector is equal to zero, or

$$\frac{\partial D_1}{\partial x_1}+\frac{\partial D_2}{\partial x_2}+\frac{\partial D_3}{\partial x_3}=\frac{\partial D_i}{\partial x_i}=0. \quad (30)$$

At the surface of the crystal the normal component of the electric induction divided by 4π is equal to the surface charge. At the plated surface the electric field starts out normal to the surface since the tangential components of the field on crossing a boundary are continuous, and for a plated surface the tangential component of the field is zero. These equations are sufficient to determine the electrical as well as the mechanical reactions of the crystal.

IV. Equation for Simple Longitudinal Vibrations

In obtaining the elastic and piezoelectric constants of a crystal, it is necessary to vibrate the crystal in a simple mode of motion and determine the constants from the measured resonant and anti-resonant frequencies, and the capacities of the crystal. The simplest mode of motion and the one most easily related to the elastic constants is the simple longitudinal mode of motion. If we take x_1 as the thickness direction and apply plating to these surfaces of the crystal, the only value of surface charge different from zero will be σ_1 since no electrical connection is made to the other surfaces. Since x_1 is assumed small, the voltage gradient $\partial E_1/\partial x_1$ will be a constant throughout the thickness of the crystal. Also, since the plating is an equipotential surface

$$\frac{\partial E_1}{\partial x_2}=\frac{\partial E_1}{\partial x_3}=0. \quad (31)$$

We take the length along the x_2 axis and the width along the x_3 axis. For sides normal to the

thickness, the boundary conditions are

$$T_{11}=T_{12}=T_{13}=0. \tag{32}$$

Since the thickness is taken as small and all the stresses are zero on the two surfaces normal to x_1, these stresses cannot differ appreciably from zero in the interior and hence we can set

$$T_{11}=T_{12}=T_{13}=0 \tag{32}$$

for all elements of the crystal. Similarly since the width is considered very small, the stresses

$$T_{31}=T_{32}=T_{33}=0. \tag{33}$$

For the length, the only finite dimension, the stresses on the surface are

$$T_{21},\ T_{22},\ T_{23}. \tag{34}$$

Of these $T_{21}=T_{12}$ and $T_{23}=T_{32}$ have already been found to be zero so that the only stress different from zero in the interior is T_{22}.

Inserting this condition in Eq. (27) the only equation of motion resulting is

$$\rho\frac{\partial^2\xi_2}{\partial t^2}=+\frac{\partial T_{22}}{\partial x_2}. \tag{35}$$

Since T_{22} is the only stress, the corresponding strains are given by Eq. (13), first part. For the case of interest here, $k=l=2$ and since a charge is developed only in the x_1 direction, $n=1$. Hence we have

$$S_{ij}=s_{ij22}{}^{E}T_{22}+d_{1ij}E_1. \tag{36}$$

In particular the stress T_{22} can be specified by a single strain, all the other strains being related dependently to this one. Taking the strain S_{22} since it is simply related to the displacement ξ_2, we can write

$$S_{22}=s_{2222}{}^{E}T_{22}+d_{122}E_1$$

or

$$T_{22}=+\frac{S_{22}}{s_{2222}{}^{E}}-\frac{d_{122}E_1}{s_{2222}{}^{E}}. \tag{37}$$

The electrical relations of (13) reduce to the form

$$\sigma_n=4\pi\epsilon_{n_1}{}^{T}E_1+d_{n22}T_{22}$$

$$=\left(4\pi\epsilon_{n_1}{}^{T}-\frac{d_{n22}d_{122}}{s_{2222}{}^{E}}\right)E_1-\frac{d_{n22}}{s_{2222}{}^{E}}S_{22}. \tag{38}$$

The only charge of interest is the one in the x_1 direction which is the direction of the applied field. Hence

$$\sigma_1=\left[4\pi\epsilon_{11}{}^{T}-\frac{d_{122}{}^{2}}{s_{2222}{}^{E}}\right]E_1+\frac{d_{122}}{s_{2222}{}^{E}}S_{22}. \tag{39}$$

Finally we call the expression

$$4\pi\epsilon_{11}{}^{T}-\frac{d_{122}{}^{2}}{s_{2222}{}^{E}}=4\pi\epsilon_{11}{}^{LC}=4\pi\epsilon_{11}{}^{S_{22}}, \tag{40}$$

indicating that it is the longitudinally clamped dielectric constant which relates the potential and surface charge when the crystal is clamped so that S_{22} disappears.

In terms of the more usual two index symbols, the two piezoelectric and elastic relations can be written

$$\rho\frac{\partial^2\xi_2}{\partial t^2}=\frac{1}{s_{22}{}^{E}}\frac{\partial^2\xi_2}{\partial x_2{}^{2}}-\frac{d_{12}}{s_{22}{}^{E}}\frac{\partial E_1}{\partial x_2},$$
$$\sigma_1=4\pi\epsilon_{11}{}^{LC}E_1-\frac{d_{12}}{s_{22}{}^{E}}\frac{\partial\xi_2}{\partial x_2}. \tag{41}$$

To solve this equation we note that E_1 is a constant independent of x_2 since the plating forms an equipotential surface. Hence the equation of motion becomes

$$\rho\frac{\partial^2\xi_2}{\partial t^2}=\frac{1}{s_{22}{}^{E}}\frac{\partial^2\xi_2}{\partial x_2{}^{2}}. \tag{42}$$

The equations of motion (41) and (42) have been solved several times in published papers[6] so that only the final results will be given. From this analysis it can be shown that the admittance of the free crystal is

$$\frac{1}{Z}=\frac{i}{E}=\frac{i}{E_1l_t}$$
$$=\frac{j\omega l_w l\epsilon_{11}{}^{LC}}{4\pi l_t}\left[1+\frac{4\pi d_{12}{}^{2}}{\epsilon_{11}{}^{LC}s_{22}{}^{E}}\left(\frac{\tan\omega l/2v}{\omega l/2v}\right)\right]. \tag{43}$$

At very low frequencies this admittance reduces to the capacitance reactance

$$\frac{j\omega l_w l\epsilon_{11}{}^{T}}{4\pi l_t}=j\omega C_0 \tag{44}$$

[6] See W. P. Mason, Phys. Rev. 69, 173 (1946).

so that the low frequency measurement of the capacitance C_0 determines the "free" dielectric constant $\epsilon_{11}{}^T$. When the tangent

$$\tan\frac{\omega l}{2v}=\infty \quad \text{or} \quad \frac{\omega l}{2v}=\frac{\pi}{2};$$
$$f_R=\frac{v}{2l}=\frac{1}{2l(\rho s_{22}{}^E)^{\frac{1}{2}}}. \tag{45}$$

A resonant frequency is obtained whose value is determined by the elastic compliance $s_{22}{}^E$, the density ρ, and the length of the crystal.

The anti-resonance occurs when the expressions in brackets in Eq. (43) equals zero or when

$$1+\frac{4\pi d_{12}{}^2}{\epsilon_{11}{}^{LC}s_{22}{}^E}\left(\frac{\tan\omega_A l/2v}{\omega_A l/2v}\right)=0$$

or

$$\frac{\omega_A l}{2v}\cot\frac{\omega_A l}{2v}=-\frac{4\pi d_{12}{}^2}{\epsilon_{11}{}^{LC}s_{22}{}^E}. \tag{46}$$

Defining the coefficient of electromechanical coupling as

$$k=\frac{d_{12}}{\left(\frac{\epsilon_{11}{}^T}{4\pi}s_{22}{}^E\right)^{\frac{1}{2}}}, \tag{47}$$

and substituting the value of $\epsilon_{11}{}^{LC}$ from Eq. (40) in Eq. (46) this becomes

$$\frac{\omega_A l}{2v}\cot\frac{\omega_A l}{2v}=-\left(\frac{k^2}{1-k^2}\right). \tag{48}$$

We wish now to obtain an expression for evaluating the coupling factor k in terms of the measured resonant and anti-resonant frequencies f_R and f_A. Their difference is usually small so that we can write

$$f_A=f_R+\Delta f; \quad \omega_A=\omega_R+2\pi\Delta f. \tag{49}$$

Inserting this expression in (48) and expanding by the multiple angle formula, we have after solving for k^2

$$k^2=\frac{\pi^2}{4}\frac{\Delta f}{f_R}\left[1+\left(\frac{4-\pi^2}{4}\right)\frac{\Delta f}{f_R}+\left(\frac{\pi^2-4}{4}\right)\left(\frac{\pi^2}{4}\right)\left(\frac{\Delta f}{f_R}\right)^2+\cdots\right]. \tag{50}$$

Hence when the frequency difference between resonance and anti-resonance is measured, the coupling coefficient k can be obtained by substituting in the above formula. Usually the first term is sufficient. Having the coupling, the elastic constant $s_{22}{}^E$, which can be calculated from the resonant frequency, and $\epsilon_{11}{}^T$ which is obtained by low frequency capacity measurements, the piezoelectric constant d_{12} can be evaluated. By using these constants for rotated cuts, all the independent elastic constants not involving pure shear, most of the piezoelectric constants, and all of the dielectric constants can be evaluated.

V. Evaluation of Shearing Constants from Face Shear Vibrations

A measurement of various orientations of the crystal in longitudinal vibration will evaluate all of the elastic constants except the shearing constants. To measure the shearing elastic constants requires setting up a vibration in which a pure shear is the predominant motion. A choice can be made of a thickness shear mode or a face shear mode and the latter was chosen since the mode is simpler and is more easily dimensioned and because the fundamental constants can be directly measured by a single orientation. It is the purpose of this section to derive the resonant frequencies of a face shear mode.

This is a more general contour mode than the longitudinal mode considered and involves satisfying boundary conditions along four edges. We consider a crystal cut normal to the Z or X_3 axis and assume that the thickness is so small that the stresses determined by the X_3 direction can be set equal to zero. Hence

$$T_{31}=T_{32}=T_{33}=0. \tag{51}$$

The remaining stresses

$$T_{11},\ T_{12},\ \text{and}\ T_{22} \tag{52}$$

are all finite throughout the crystal but vanish at the edges. The vanishing of the stresses in Eq. (51) simplifies the equations of motion for it results in only three independent strains, i.e., the other three strains have a definite ratio to the independent strains. Since the field E is parallel to the Z axis at the surface, and the

thickness is assumed small, the only component of the field will be E_3. Then Eq. (13) can be written

$$\begin{aligned}
S_{11}=S_1&=s_{11}^{E}T_1+s_{12}^{E}T_2+s_{16}^{E}T_6+d_{31}E_3,\\
2S_{12}=S_6&=s_{16}^{E}T_1+s_{26}^{E}T_2+s_{66}^{E}T_6+d_{36}E_3,\\
S_{22}=S_2&=s_{12}^{E}T_1+s_{22}^{E}T_2+s_{26}^{E}T_6+d_{32}E_3,\\
\sigma_3&=\frac{\epsilon_{33}^{T}E_3}{4\pi}+d_{31}T_1+d_{32}T_2+d_{36}T_6.
\end{aligned}\tag{53}$$

All the other stresses disappear by virtue of (51)

For inserting in the equations of motion it is desirable to express the stress in terms of the strain. This can be done by solving Eq. (53) simultaneously, giving

$$\begin{aligned}
T_1&=c_{11}^{c,E}S_1+c_{12}^{c,E}S_2+c_{16}^{c,E}S_6-e_{31}^{c}E_3,\\
T_2&=c_{12}^{c,E}S_1+c_{22}^{c,E}S_2+c_{26}^{c,E}S_6-e_{32}^{c}E_3,\\
T_6&=c_{16}^{c,E}S_1+c_{26}^{c,E}S_2+c_{66}^{c,E}S_6-e_{36}^{c}E_3,\\
\sigma_3&=E_3\left[\frac{\epsilon_{33}^{T}}{4\pi}-(d_{31}e_{31}^{c}+d_{32}e_{32}^{c}+d_{36}e_{36}^{c})\right]\\
&\qquad+e_{31}^{c}S_1+e_{32}^{c}S_2+e_{36}^{c}S_6.
\end{aligned}\tag{54}$$

In these equations $c_{ij}^{c,E}$ designate the field contour elastic constants that apply when a contour mode occurs for a very thin crystal. These constants are given in terms of the elastic compliances at constant field by the formula

$$c_{ij}^{c,E}=\frac{(-1)^{k+l}\Delta_{kl}}{\Delta}(k,l=1,2,3),\tag{55}$$

where Δ is the determinant

$$\Delta=\begin{vmatrix} s_{11}^{E}, & s_{12}^{E}, & s_{16}^{E}\\ s_{12}^{E}, & s_{22}^{E}, & s_{26}^{E}\\ s_{16}^{E}, & s_{26}^{E}, & s_{66}^{E}\end{vmatrix}$$

and Δ_{kl} is the minor obtained by suppressing the kth row and lth column. The piezoelectric moduli applying to a contour mode of motion are given by

$$\begin{aligned}
e_{31}^{c}&=d_{31}c_{11}^{c,E}+d_{32}c_{12}^{c,E}+d_{36}c_{16}^{c,E},\\
e_{32}^{c}&=d_{31}c_{12}^{c,E}+d_{32}c_{22}^{c,E}+d_{36}c_{26}^{c,E},\\
e_{36}^{c}&=d_{31}c_{16}^{c,E}+d_{32}c_{26}^{c,E}+d_{36}c_{66}^{c,E},
\end{aligned}\tag{56}$$

while the contour clamped dielectric constant is given by the equation

$$\epsilon_{33}^{c,S}=\epsilon_{33}^{T}-(d_{31}e_{31}^{c}+d_{32}e_{32}^{c}+d_{36}e_{36}^{c})4\pi.\tag{57}$$

The superscripts c,S indicate that this is the dielectric constant if the crystal is free from contour strains, but not for thickness modes.

Inserting Eqs. (54) in the equations of motion (27) noting that

$$\partial E_3/\partial x_1=\partial E_3/\partial x_2=0,$$

since the plating is an equipotential surface, the equations of motion become

$$\begin{aligned}
\rho\frac{\partial^2\xi_1}{\partial t^2}&=c_{11}^{c,E}\frac{\partial^2\xi_1}{\partial x_1^2}+2c_{16}^{c,E}\frac{\partial^2\xi_1}{\partial x_1\partial x_2}+c_{66}^{c,E}\frac{\partial^2\xi_1}{\partial x_2^2}+c_{16}^{c,E}\frac{\partial^2\xi_2}{\partial x_1^2}+(c_{12}^{c,E}+c_{66}^{c,E})\frac{\partial^2\xi_2}{\partial x_1\partial x_2}+c_{26}^{c,E}\frac{\partial^2\xi_2}{\partial x_2^2},\\
\rho\frac{\partial^2\xi_2}{\partial t^2}&=c_{16}^{c,E}\frac{\partial^2\xi_1}{\partial x_1^2}+(c_{12}^{c,E}+c_{66}^{c,E})\frac{\partial^2\xi_1}{\partial x_1\partial x_2}+c_{26}^{c,E}\frac{\partial^2\xi_1}{\partial x_2^2}+c_{66}^{c,E}\frac{\partial^2\xi_2}{\partial x_1^2}+2c_{26}^{c,E}\frac{\partial^2\xi_2}{\partial x_1\partial x_2}+c_{22}^{c,E}\frac{\partial^2\xi_2}{\partial x_2^2}.
\end{aligned}\tag{58}$$

For simple harmonic motion, Eqs. (58) reduce to the form

$$\begin{aligned}
c_{11}\frac{\partial^2\xi_1}{\partial x_1^2}+2c_{16}\frac{\partial^2\xi_1}{\partial x_1\partial x_2}+c_{66}\frac{\partial^2\xi_1}{\partial x_2^2}+c_{16}\frac{\partial^2\xi_2}{\partial x_1^2}+(c_{12}+c_{66})\frac{\partial^2\xi_2}{\partial x_1\partial x_2}+c_{26}\frac{\partial^2\xi_2}{\partial x_2^2}+\omega^2\rho\xi_1=0,\\
c_{16}\frac{\partial^2\xi_1}{\partial x_1^2}+(c_{12}+c_{66})\frac{\partial^2\xi_1}{\partial x_1\partial x_2}+c_{26}\frac{\partial^2\xi_1}{\partial x_2^2}+c_{66}\frac{\partial^2\xi_2}{\partial x_1^2}+2c_{26}\frac{\partial^2\xi_2}{\partial x_1\partial x_2}+c_{22}\frac{\partial^2\xi_2}{\partial x_2^2}+\omega\rho\xi_2=0,
\end{aligned}\tag{59}$$

where the elastic constants are understood to be the contour, potential constants.

For experimental purposes it is found that the best measurements are obtained when the crystal is long compared to its width or thickness. This is further accentuated by taking a high harmonic of this mode which in effect makes the unit cell longer compared to its width. Hence the solution of interest is one where the crystal is infinitely long in the x_1 direction and with a finite width in the x_2 direction. For the infinitely long crystal, there should be no variation of the displacements ξ_1 or ξ_2 along the length of the crystal and hence

$$\frac{\partial^2\xi_1}{\partial x_1}=\frac{\partial^2\xi_1}{\partial x_1\partial x_2}=\frac{\partial^2\xi_2}{\partial x_1^2}=\frac{\partial^2\xi_2}{\partial x_1\partial x_2}=0 \tag{60}$$

this leaves only the terms

$$c_{66}\frac{\partial^2\xi_1}{\partial x_2^2}+c_{26}\frac{\partial^2\xi_2}{\partial x_2^2}+\omega^2\rho\xi_1=0, \quad c_{26}\frac{\partial^2\xi_1}{\partial x_2^2}+c_{22}\frac{\partial^2\xi_2}{\partial x_2^2}+\omega^2\rho\xi_2=0. \tag{61}$$

The solution of these equations represents two coupled motions controlled by the x_2 dimension. If $c_{26}=0$ these two motions are a shear vibration and a longitudinal vibration existing independently, but with c_{26} finite, the shear and the longitudinal motions are coupled so that there is no pure shear or pure longitudinal motion. To show this we can eliminate ξ_2 from the above equation and obtain one fourth-order equation

$$\frac{\partial^4\xi_1}{\partial x_2^4}+\omega^2\rho\left[\frac{c_{22}+c_{66}}{c_{22}c_{66}-c_{66}^2}\right]\frac{\partial^2\xi_2}{\partial x_2^2}+\frac{\omega^4\rho^2\xi_1}{c_{22}c_{66}-c_{26}^2}=0. \tag{62}$$

A solution of this equation is

$$\xi_1=A\cos\alpha x_2+B\sin\alpha x_2+C\cos\beta x_2+D\sin\beta x_2,$$

where

$$\begin{aligned}\alpha&=\omega\left(\frac{(c_{22}+c_{66})\rho}{2(c_{22}c_{66}-c_{26}^2)}\right)^{\frac{1}{2}}\left(1+\left[\frac{(c_{22}-c_{66})^2+4c_{26}^2}{(c_{22}+c_{66})^2}\right]^{\frac{1}{2}}\right)^{\frac{1}{2}},\\ \beta&=\omega\left(\frac{(c_{22}+c_{66})\rho}{(c_{22}c_{66}-c_{26}^2)}\right)^{\frac{1}{2}}\left(1-\left[\frac{(c_{22}-c_{66})^2+4c_{26}^2}{(c_{22}+c_{66})^2}\right]^{\frac{1}{2}}\right)^{\frac{1}{2}}.\end{aligned} \tag{63}$$

If $c_{26}=0$

$$\alpha=\omega(\rho/c_{66})^{\frac{1}{2}}; \quad \beta=\omega(\rho/c_{22})^{\frac{1}{2}},$$

and the two vibrations would exist independently.

The value of ξ_2 is obtained by a substitution of the value of ξ_1 in the last of Eq. (61) and is

$$\xi_2=\left(\frac{\alpha^2c_{26}}{\omega^2\rho-\alpha^2c_{22}}\right)[A\cos\alpha x_2+B\sin\alpha x_2]+\left(\frac{\beta^2c_{26}}{\omega^2\rho-\beta^2c_{22}}\right)[C\cos\beta x_2+D\sin\beta x_2]. \tag{64}$$

The boundary conditions to be satisfied are

$$\begin{aligned}T_2&=c_{22}\frac{\partial\xi_2}{\partial x_2}+c_{26}\frac{\partial\xi_1}{\partial x_2}-e_{31}{}^cE_3=0 \quad \text{when} \quad x_2=0 \quad \text{and} \quad x_2=l_w,\\ T_6&=c_{26}\frac{\partial\xi_2}{\partial x_2}+c_{66}\frac{\partial\xi_1}{\partial x_2}-e_{36}{}^cE_3=0 \quad \text{when} \quad x_2=0 \quad \text{and} \quad x_2=l_w,\end{aligned} \tag{65}$$

where l_w is the width of the crystal. These conditions determine the four independent constants A,

B, C, and D. In terms of E_3 these constants are

$$A=-\left[\frac{(\omega^2\rho-\alpha^2c_{22})\tan\alpha l_w/2}{\alpha[\beta^2-\alpha^2][c_{22}c_{66}-c_{26}^2]}\right]\left[e_{36}{}^cE_3-e_{32}{}^cE_3\left[\frac{\omega^2\rho c_{66}-\beta^2(c_{22}c_{66}-c_{26}^2)}{\omega^2\rho c_{26}}\right]\right],$$

$$B=\left[\frac{(\omega^2\rho-\alpha^2c_{22})}{\alpha[\beta^2-\alpha^2][c_{22}c_{66}-c_{26}^2]}\right]\left[e_{36}{}^cE_3-e_{32}{}^cE_3\left[\frac{\omega^2\rho c_{66}-\beta^2(c_{22}c_{66}-c_{26}^2)}{\omega^2\rho c_{26}}\right]\right],$$

$$C=\left[\frac{(\omega^2\rho-\beta^2c_{22})\tan\beta l_w/2}{\beta(\beta^2-\alpha^2)(c_{22}c_{66}-c_{26}^2)}\right]\left[e_{36}{}^cE_3-e_{32}{}^cE_3\left[\frac{\omega^2\rho c_{66}-\alpha^2(c_{22}c_{66}-c_{26}^2)}{\omega^2\rho c_{26}}\right]\right], \tag{66}$$

$$D=-\left[\frac{(\omega^2\rho-\beta^2c_{22})}{\beta(\beta^2-\alpha^2)(c_{22}c_{66}-c_{26}^2)}\right]\left[e_{36}{}^cE_3-e_{32}{}^cE_3\left[\frac{\omega^2\rho c_{66}-\alpha^2(c_{22}c_{66}-c_{26}^2)}{\omega^2\rho c_{26}}\right]\right].$$

To obtain the electrical admittance of the crystal, we make use of the last of Eqs. (54) which for this limiting case becomes

$$\sigma_3=\frac{E_3\epsilon_3{}^{c,S}}{4\pi}+e_{32}{}^c\frac{\partial\xi_2}{\partial x_2}+e_{36}{}^c\frac{\partial\xi_1}{\partial x_2}. \tag{67}$$

Integrating this equation over the length and width, noting that E_3 does not vary over the surface and ξ_2 and ξ_1 are not functions of x_1, we have

$$Q=\frac{E_3l_wl\epsilon_3{}^{c,S}}{4\pi}+e_{32}{}^cl[\xi_{22}-\xi_{21}]+e_{36}{}^cl[\xi_{12}-\xi_{11}] \tag{68}$$

where the displacements are the displacements at the two edges, and Q is the total charge on the surface. Introducing the displacements from Eq. (63), (64), and (66) and noting that the current to enter the crystal is $j\omega Q$, the admittance of the crystal becomes

$$\frac{i}{E}=\frac{j\omega ll_w\epsilon_{33}{}^{c,S}}{4\pi l_t}\left[1-\frac{e_{32}{}^24\pi}{\epsilon_{33}{}^{c,S}}\left[\frac{\alpha^2[\omega^2\rho c_{66}-\beta^2(c_{22}c_{66}-c_{26}^2)]}{(\beta^2-\alpha^2)(c_{22}c_{66}-c_{26}^2)\omega^2\rho}\left(\frac{\tan\alpha l_w/2}{\alpha l_w/2}\right)\right.\right.$$

$$\left.-\frac{\beta^2[\omega^2\rho c_{66}-\alpha^2(c_{22}c_{66}-c_{26}^2)]}{[(\beta^2-\alpha^2)(c_{22}c_{66}-c_{26}^2)\omega^2\rho]}\times\frac{\tan\beta l_w/2}{\beta l_w/2}\right]+\frac{4\pi e_{36}{}^2}{\epsilon_{33}{}^{c,S}}\left[\left[\frac{(\omega^2\rho-\alpha^2c_{22})\left(\frac{\tan\alpha l_w/2}{\alpha l_w/2}\right)}{(\beta^2-\alpha^2)(c_{22}c_{66}-c_{26}^2)}\right]\right.$$

$$\left.\left.-\left[\frac{(\omega^2\rho-\beta^2c_{22})\left(\frac{\tan\beta l_w/2}{\beta l_w/2}\right)}{(\beta^2-\alpha^2)(c_{22}c_{66}-c_{26}^2)}\right]\right]-\frac{4\pi e_{32}e_{36}}{\epsilon_{33}{}^{c,S}}\left[\left[\frac{c_{66}(\omega^2\rho-\alpha^2c_{22})(\omega^2\rho-\beta^2c_{22})-\alpha^2\beta^2c_{22}c_{26}{}^2}{(\beta^2-\alpha^2)(c_{22}c_{66}-c_{26}^2)\omega_2\rho c_{26}}\right]\right.\right.$$

$$\left.\left.\times\left[\frac{\tan\alpha l_w/2}{\alpha l_w/2}-\frac{\tan\beta l_w/2}{\beta l_w/2}\right]+\left(\frac{c_{26}}{c_{22}c_{66}-c_{26}^2}\right)\left[\frac{\tan\alpha l_w/2}{\alpha l_w/2}+\frac{\tan\beta l_w/2}{\beta l_w/2}\right]\right]\right]. \tag{69}$$

At low frequencies

$$\frac{\tan\alpha l_w}{\alpha l_w/2}\xrightarrow{\quad}\frac{\tan\beta l_w/2}{\beta l_w/2}\xrightarrow{\quad}1, \tag{70}$$

and the admittance is a capacity

$$C=\frac{ll_w\epsilon_{33}^{c,S}}{4\pi l_t}\left[1+\frac{4\pi e_{22}^2}{\epsilon_{33}^{c,S}}\left[\frac{c_{66}}{c_{22}c_{66}-c_{26}^2}\right]+\frac{4\pi e_{36}^2}{\epsilon_{33}^{c,S}}\left[\frac{c_{22}}{c_{22}c_{66}-c_{26}^2}\right]-\frac{4\pi e_{22}e_{26}}{\epsilon_{33}^{c,S}}\left(\frac{2c_{26}}{c_{22}c_{66}-c_{26}^2}\right)\right]. \tag{71}$$

This capacitance is the "free" dielectric capacitance.

If $c_{26}=0$, the impedance reduces to that for two uncoupled modes, and is

$$\frac{i}{E}=\frac{j\omega ll_w\epsilon_{33}^{c,S}}{4\pi l_t}\left[1+\frac{4\pi e_{22}^2}{\epsilon_{33}^{c,S}c_{22}}\left[\frac{\tan\omega\left(\frac{\rho}{c_{22}}\right)^{\frac{1}{2}}\frac{l_w}{2}}{\omega\left(\frac{\rho}{c_{22}}\right)^{\frac{1}{2}}\frac{l_w}{2}}\right]+\frac{4\pi e_{22}^2}{\epsilon_{33}^{c,S}}\left[\frac{\tan\omega\left(\frac{\rho}{c_{22}}\right)^{\frac{1}{2}}\frac{l_w}{2}}{\omega\left(\frac{\rho}{c_{22}}\right)^{\frac{1}{2}}\frac{l_w}{2}}\right]\right]. \tag{72}$$

For the general case where c_{26} is not zero, Eq. (69) is the admittance of two coupled modes. The resonant frequencies occur when the admittance is infinite (impedance zero) and hence occur when

$$\tan\alpha l_w/2=\infty \quad \text{or} \quad \tan\beta l_w/2=\infty\,. \tag{73}$$

These are satisfied for the first modes when

$$\begin{aligned} f_1&=\frac{1}{2l_w}\left(\frac{(c_{22}+c_{66})-[(c_{22}-c_{66})^2+4c_{26}^2]^{\frac{1}{2}}}{2\rho}\right)^{\frac{1}{2}},\\ f_2&=\frac{1}{2l_w}\left(\frac{(c_{22}+c_{66})+[(c_{22}-c_{66})^2+4c_{26}^2]^{\frac{1}{2}}}{2\rho}\right)^{\frac{1}{2}}. \end{aligned} \tag{74}$$

Since the frequency f is equal to the velocity of propagation $v/2l_w$, we find that the two values of the velocity satisfy the determinant

$$\begin{vmatrix} \rho v^2-c_{22}, & c_{26} \\ c_{26}, & \rho v^2-c_{66} \end{vmatrix}=0. \tag{75}$$

VI. Elastic, Piezoelectric, and Dielectric Constants of Rotated Crystals

We have so far calculated the resonant and anti-resonant frequencies of longitudinal crystals cut normal to the X or X_1 axis of the crystal and with the length along the Y or X_2 axis, and the frequencies of a face shear mode cut normal to the Z or X_3 axis with the width (frequency controlling dimension) along the Y or X_2 axis. To measure all the properties of a crystal requires a number of different orientations for both longitudinal and shear vibrations. To make the solutions given previously hold for any of these oriented crystals, we use a system of rotated axes which are rotated from the reference axes by three rotations for the most general case.

Starting with the reference axes, the elastic constants for any rotated cuts are given by the general tensor formula

$$s_{ijkl}'=\frac{\partial x_i'}{\partial x_m}\frac{\partial x_j'}{\partial x_n}\frac{\partial x_k'}{\partial x_o}\frac{\partial x_l'}{\partial x_p}s_{mnop}, \tag{76}$$

where the partial derivatives are the direction cosines defined by Eq. (4). In a similar manner, the peizoelectric and dielectric tensors are given by the formulae

$$d_{ijk}'=\frac{\partial x_i'}{\partial x_l}\frac{\partial x_j'}{\partial x_m}\frac{\partial x_k'}{\partial x_n}d_{lmn}, \tag{77}$$

$$\epsilon_{ij}'=\frac{\partial x_i'}{\partial x_k}\frac{\partial x_j'}{\partial x_l}\epsilon_{kl}. \tag{78}$$

For a monoclinic crystal, with the Y axis taken as the axis of twofold symmetry, the three tensors have the form shown below when the

axes chosen are the X, Y, and Z axes as defined in the text

$$\epsilon_{kl}=\begin{vmatrix}\epsilon_{11}, & 0, & \epsilon_{13}\\ 0, & \epsilon_{22}, & 0\\ \epsilon_{13}, & 0, & \epsilon_{33}\end{vmatrix}, \tag{79}$$

$$d_{lmn}=\begin{vmatrix}0, & 0, & 0, & d_{123}, & 0, & d_{112}\\ d_{211}, & d_{222}, & d_{233}, & 0, & d_{213}, & 0\\ 0, & 0, & 0, & d_{323}, & 0, & d_{312}\end{vmatrix}. \tag{80}$$

Here the first number denotes the direction of the field and the last two numbers the resulting strain. The elastic tensor has the form

$$s_{mnop}=\begin{vmatrix}s_{1111}, & s_{1122}, & s_{1133}, & 0, & s_{1113}, & 0,\\ s_{1122}, & s_{2222}, & s_{2233}, & 0, & s_{2213}, & 0,\\ s_{1133}, & s_{2233}, & s_{3333}, & 0, & s_{3313}, & 0,\\ 0, & 0, & 0, & s_{2323}, & 0, & s_{2312}\\ s_{1113}, & s_{2213}, & s_{3313}, & 0, & s_{1313}, & 0,\\ 0, & 0, & 0, & s_{2312}, & 0, & s_{1212}\end{vmatrix}. \tag{81}$$

For longitudinal crystals the rotated elastic constant of interest is the s_{2222}' constant since this is the inverse of Young's modulus along the length Y' or X_2'. The piezoelectric constant driving this mode is d_{122}'. Introducing the tensor terms is the tensor Eq. (76), the rotated constant s_{2222}' becomes

$$s_{2222}'=\frac{\partial x_2'}{\partial x_m}\frac{\partial x_2'}{\partial x_n}\frac{\partial x_2'}{\partial x_o}\frac{\partial x_2'}{\partial x_p}s_{mnop}=l_2^4s_{1111}+l_2^2m_2^2(2s_{1122}+4s_{1212})+l_2^2n_2^2(2s_{1133}+4s_{1313})+4l_2^3n_2s_{1113}$$
$$+m_2^4s_{2222}+m_2^2n_2^2(2s_{2233}+4s_{2323})+4n_2^3l_2s_{3313}+n_2^4s_{3333}+m_2^2l_2n_2[4s_{2213}+4s_{2312}]. \tag{82}$$

In terms of the equivalent two index symbols the equation becomes

$$s_{22}'=l_2^4s_{11}+l_2^2m_2^2(2s_{12}+s_{66})+l_2^2n_2^2(2s_{13}+s_{55})+2l_2^3n_2s_{15}+m_2^4s_{22}+m_2^2n_2^2(2s_{23}+s_{44})+2n_2^3l_2s_{35}$$
$$+n_2^4s_{33}+m_2^2l_2n_2[2s_{25}+s_{46}]. \tag{83}$$

Hence by cutting nine oriented longitudinally vibrating crystals five elastic constants can be determined and four relations obtained between the other eight elastic constants. Eight of these cuts can be obtained by having the length in the YZ, ZX, and XY planes. For a crystal cut with its length in the YZ plane, with the angle measured from Y equal to θ, we have

$$l_2=0, \quad m_2=\cos\theta, \quad n_2=\sin\theta,$$

hence

$$s_{22}'=s_{22}\cos^4\theta+(2s_{23}+s_{44})\sin^2\theta\cos^2\theta+s_{33}\sin^4\theta(YZ \text{ plane}). \tag{84}$$

For the XY plane, measuring the length from Y

$$l_2=\sin\varphi, \quad m_2=\cos\varphi, \quad n_2=0,$$

and

$$s_{22}'=s_{22}\cos^4\varphi+(2s_{12}+s_{66})\sin^2\varphi\cos^2\varphi+s_{11}\sin^4\varphi(XY \text{ plane}). \tag{85}$$

For the ZX plane with ψ measured from positive Z in the direction of positive X, as defined in the text, $l_2=\sin\psi$, $n_2=\cos\psi$, $m_2=0$, and

$$s_{22}'=s_{33}\cos^4\psi+2\cos^3\psi\sin\psi\,s_{35}+\sin^2\psi\cos^2\psi(2s_{13}+s_{55})+2\sin^3\psi\cos\psi\,s_{15}+\sin^4\psi\,s_{11}. \tag{86}$$

Three crystals each in the YZ plane and XY plane and five in the XZ plane will determine eight relations and give three checks between the constants s_{11}, s_{22}, and s_{33}. To determine the ninth relation requires a crystal with a double orientation and for this purpose the crystal shown by Fig. 9 was used. In this case $l_2=0.5$, $m_2=-0.707$; $n_2=0.5$ and

$$s_{22}'=\tfrac{1}{16}[s_{11}+s_{55}+s_{33}]+\tfrac{1}{8}[s_{13}+s_{15}+s_{44}+s_{35}+s_{66}+s_{46}]+\tfrac{1}{4}[s_{12}+s_{22}+s_{23}+s_{25}]. \tag{87}$$

The piezoelectric constant for driving these longitudinal crystals, d_{122}' is given in terms of the

developed tensor equation

$$d_{122}'=\frac{\partial x_1'}{\partial x_l}\frac{\partial x_2'}{\partial x_m}\frac{\partial x_2'}{\partial x_n}d_{lmn}=2\frac{\partial x_1'}{\partial x_1}\frac{\partial x_2'}{\partial x_2}\frac{\partial x_2'}{\partial x_3}d_{123}+2\frac{\partial x_1'}{\partial x_1}\frac{\partial x_2'}{\partial x_1}\frac{\partial x_2'}{\partial x_2}d_{112}+\frac{\partial x_1'}{\partial x_2}\left(\frac{\partial x_2'}{\partial x_1}\right)^2 d_{211}+\frac{\partial x_1'}{\partial x_2}\left(\frac{\partial x_2'}{\partial x_2}\right)^2 d_{222}$$
$$+\frac{\partial x_1'}{\partial x_2}\left(\frac{\partial x_2'}{\partial x_3}\right)^2 d_{233}+2\frac{\partial x_1'}{\partial x_2}\frac{\partial x_2'}{\partial x_1}\frac{\partial x_2'}{\partial x_3}d_{213}+2\frac{\partial x_1'}{\partial x_3}\frac{\partial x_2'}{\partial x_2}\frac{\partial x_2'}{\partial x_3}d_{323}+2\frac{\partial x_1'}{\partial x_3}\frac{\partial x_2'}{\partial x_1}\frac{\partial x_2'}{\partial x_2}d_{312}. \quad (88)$$

In terms of the two index symbols and the direction cosines this equation becomes

$$d_{12}'=l_1m_2n_2d_{14}+l_1l_2m_2d_{16}+m_1l_2^2d_{21}+m_1m_2^2d_{22}$$
$$+m_1n_2^2d_{23}+m_1l_2n_2d_{25}+n_1m_2n_2d_{34}$$
$$+n_1l_2m_2d_{36}. \quad (89)$$

For crystals cut in the YZ plane with the thickness in the X_1 direction, the direction cosines are

$$\begin{vmatrix} l_1=1, & m_1=0, & n_1=0 \\ l_2=0, & m_2=\cos 0, & n_2=\sin\theta \\ l_3=0, & m_3=-\sin\theta, & n_3=\cos\theta \end{vmatrix} \quad (90)$$

and the piezoelectric constants driving this mode are

$$d_{12}'=d_{14}\sin\theta\cos\theta=\frac{d_{14}}{2}\sin 2\theta. \quad (91)$$

Hence a measurement of the 45° X cut crystal will determine the piezoelectric constant d_{14}. Its sign can be determined from polarity tests. For the XY plane with the thickness along $Z=X_3$, the direction cosines become

$$\begin{vmatrix} l_1=0; & m_1=0; & n_1=-1 \\ l_2=\cos\varphi; & m_2=\sin\varphi; & n_2=0 \\ l_3=-\sin\varphi; & m_3=+\cos\varphi; & n_3=0 \end{vmatrix} \quad (92)$$

and the piezoelectric constant driving this mode is

$$d_{12}'=-d_{36}\sin\varphi\cos\varphi=-\frac{d_{36}}{2}\sin 2\varphi. \quad (93)$$

In the XZ plane with the thickness along the Y axis, the direction cosines are

$$\begin{vmatrix} l_1=0; & m_1=1; & n_1=0 \\ l_2=\sin\psi; & m_2=0; & n_2=\cos\psi \\ l_3=\cos\psi; & m_3=0; & n_3=-\sin\psi \end{vmatrix} \quad (94)$$

and the piezoelectric constant driving this mode is

$$d_{12}'=d_{21}\sin^2\psi+d_{23}\cos^2\psi+\frac{d_{25}}{2}\sin 2\psi. \quad (95)$$

Two more single angle orientations, which will give information on the piezoelectric constants but not on the elastic constants are orientations for which the length and thickness axes both lie in the YZ and XZ planes, respectively. For the first case with the angle θ measured between the length and the Y axis, the direction cosines are

$$\begin{vmatrix} l_1=0; & m_1=\sin\theta; & n_1=-\cos\theta \\ l_2=0; & m_2=\cos\theta; & n_2=\sin\theta \\ l_3=1; & m_3=0; & n_3=0 \end{vmatrix} \quad (96)$$

and the piezoelectric constant d_{12}' is

$$d_{12}'=\sin\theta[(d_{22}-d_{34})\cos^2\theta+d_{23}\sin^2\theta]. \quad (97)$$

Hence if a crystal is cut with its length 45° between the Y and Z axis and its width along the X axis, the piezoelectric constants $(d_{22}-d_{34})$ can be evaluated and compared in sign with d_{23}, which has already been determined from Eq. (95). The second orientation with the length and thickness in the XY plane and with the width along the Z axis, the direction cosines are

$$\begin{vmatrix} l_1=\sin\varphi; & m_1=-\cos\varphi; & n_1=0 \\ l_2=\cos\varphi; & m_2=\sin\varphi; & n_2=0 \\ l_3=0; & m_3=0; & n_3=1 \end{vmatrix} \quad (98)$$

and the piezoelectric constant d_{12}' is given by

$$d_{12}'=-\cos\varphi[d_{21}\cos^2\varphi+(d_{22}-d_{16})\sin^2\varphi]. \quad (99)$$

Hence a crystal cut at 45° between the X and Y axes and with its width along the Z axis will

determine the value of $(d_{22}-d_{16})$ since d_{21} is already known.

A check on the piezoelectric constants and their signs is obtained by using one double orientation crystal. The one selected on account of the ease of cutting is the one shown by Fig. 9. From the figure it is readily shown that the direction cosines are

$$\begin{vmatrix} l_1=0.707\sin\theta; & m_1=\cos\theta; & n_1=0.707\sin\theta \\ l_2=0.707\cos\theta; & m_2=-\sin\theta; & n_2=0.707\cos\theta \\ l_3=0.707; & m_3=0; & n_3=-0.707 \end{vmatrix}. \quad (100)$$

With these values the piezoelectric constant for driving this mode is

$$d_{12}'=\frac{(d_{21}+d_{23}+d_{25})}{2}\cos^3\theta + \left[d_{22}-\frac{(d_{14}+d_{16}+d_{34}+d_{36})}{2}\right]\sin^2\theta\cos\theta. \quad (101)$$

Hence by taking $\theta=45°$ this becomes

$$d_{12}'=0.1768[d_{21}+d_{23}+d_{25}] + 0.1768[2d_{22}-(d_{14}+d_{16}+d_{34}+d_{36})]. \quad (102)$$

To separate d_{22} from d_{16} and d_{34} requires the measurement of one thickness vibration crystal. The one chosen for DKT was a crystal cut normal to Z, which gave an S_4 shear. This determined the constant d_{34}. From this all the values can be calculated.

To evaluate the shear elastic constants, four crystal cuts are made all of which vibrate in the face shear mode. Three of these are cut normal to the X, Y, and Z axes, respectively, with their width (the frequency determining dimension) along the Z, X, and Y axes, respectively. The fourth cut is made with the thickness direction halfway between the X and Z axes and the width along the Y axis. The frequency of a Z cut crystal has been discussed at some length in Section V and since s_{26} is zero for a monoclinic crystal the shear vibration frequency is determined by

$$f=\frac{1}{2l_w}\left(\frac{c_{66}^{c,E}}{\rho}\right)^{\frac{1}{2}}. \quad (103)$$

Then since

$$c_{66}^{c,E}=\begin{vmatrix} s_{11}^E & s_{12}^E \\ s_{12}^E & s_{22}^E \end{vmatrix}\Big/\begin{vmatrix} s_{11}^E & s_{12}^E & 0 \\ s_{12}^E & s_{22}^E & 0 \\ 0 & 0 & s_{66}^E \end{vmatrix}=\frac{1}{s_{66}^E}, \quad (104)$$

the fundamental elastic constant s_{66}^E can be evaluated from the measurements.

The frequency of an X cut crystal with its width along Z can in a similar manner be determined since it can be shown that the mode of motion is a simple shear, and the frequency is given by

$$f=\frac{1}{2l_w}\left(\frac{c_{44}^{c,E}}{\rho}\right)^{\frac{1}{2}} \quad (105)$$

and

$$s_{44}^E=1/c_{44}^{c,E}. \quad (106)$$

An oriented cut is necessary to evaluate s_{46}^E. If we cut a crystal with the width and thickness both in the ZX plane and the length of the crystal along the Y axis, it can be shown that the shearing modulus $s_{66}'^E$ is equal to

$$s_{66}'^E=s_{66}^E\cos^2\theta-s_{46}^E\sin 2\theta+s_{44}^E\sin^2\theta. \quad (107)$$

At the same time $s_{26}'^E$ is equal to zero so that the resonant frequency of such a plate is determined by $c_{66}^{c,E'}$. The driving piezoelectric constant d_{14} is equal to

$$d_{14}'=d_{14}\cos^2\theta+\frac{(d_{16}-d_{34})}{2}\sin 2\theta-d_{36}\sin^2\theta. \quad (108)$$

Hence for a crystal cut with its thickness direction 45° from X, the elastic constant

$$\frac{1}{s_{66}^{E'}}=\frac{2}{(s_{66}^E-2s_{46}^E+s_{44}^E)}=c_{66}^{c,E'}. \quad (109)$$

The dielectric constants ϵ_{11}^T, ϵ_{22}^T, ϵ_{33}^T can be evaluated by measuring the capacities at low frequencies along the X, Y, and Z axes, respectively, while the dielectric constant ϵ_{13}^T can be evaluated by measuring the capacity of the above crystal which as shown involves the values

$$\frac{(\epsilon_{11}^T+2\epsilon_{13}^T+\epsilon_{33}^T)}{2}. \quad (110)$$

Hence all of the constants can be evaluated as explained above except the shear elastic constant s_{55}^E. This is more complicated since it involves measuring a coupled mode. For a Y cut crystal with its width or frequency determining direction along X, the shear coupling coefficient cannot be neglected and the shear resonant frequency is given by the equation

$$f=\frac{1}{2l_w}\left(\frac{(c_{11}^{c,E}+c_{55}^{c,E})-[(c_{11}^{c,E}-c_{55}^{c,E})^2+4c_{15}^{c,E^2}]^{\frac{1}{2}}}{2\rho}\right)^{\frac{1}{2}}$$

or

$$\frac{c_{11}^{c,E}+c_{55}^{c,E}-[(c_{11}^{c,E}-c_{55}^{c,E})^2+4(c_{15}^{c,E})^2]^{\frac{1}{2}}}{2}=(2l_wf)^2\rho. \tag{111}$$

Finally we have from Eq. (55) transformed to the Y axis

$$c_{ij}^{c,E}=\frac{(-1)^{k+l}\Delta_{kl}}{\Delta}(k,l,=1,2,3), \tag{112}$$

where Δ is the determinant

$$\Delta=\begin{vmatrix} s_{11}^E, & s_{13}^E, & s_{15}^E \\ s_{13}^E, & s_{33}^E, & s_{35}^E \\ s_{15}^E, & s_{35}^E, & s_{55}^E \end{vmatrix}.$$

Since all the s_{ij}^E values have been determined but s_{55}^E, the two relations can be solved simultaneously for s_{55}^E and all the elastic constants can be determined.

PHYSICAL REVIEW VOLUME 70, NUMBERS 9 AND 10 NOVEMBER 1 AND 15, 1946

Second Quantization and Representation Theory

E. M. CORSON
The Institute for Advanced Study, Princeton, New Jersey

(Received August 2, 1946)

The formalism of the second quantization is developed entirely within the framework of the Dirac-Jordan representation theory. The equivalence of this formalism and the methods of ordinary coordinate-spin space is shown, and the equations of "connection" are fully developed. It is shown that the "creation" and "annihilation" operators, and indeed all operators which do not commute with the quantized Hamiltonian and hence whose representatives cannot be explicitly given in a configuration space of a fixed number of dimensions are easily treated in terms of the general representation theory and arise quite naturally. Both types of statistics are considered, and the Fock-Dirac density matrix and self-consistent field are treated as a simple illustration.

WE consider the general properties of a system of n-indistinguishable particles, and compare the description of the system by two different operator sets x_r and $\mathbf{E}_r$ associated with the rth particle ($r=1, 2, \cdots n$). The operators $\mathbf{x}_r$ and $\mathbf{E}_r$ will in general stand for a complete commuting set of observables for each particle; thus for electrons for example we may take $\mathbf{x}_r=(\mathbf{x}_r, \mathbf{y}_r, \mathbf{z}_r, \sigma_r)$; $\sigma_r=\sigma_{sr}$ and $\mathbf{E}_r=(\mathbf{H}_r, \mathbf{m}_r^2, \mathbf{m}_r, \sigma_r)$; $\mathbf{m}_r=\mathbf{m}_{sr}$. However, for our general calculations we need only consider that the operators $\mathbf{E}_r$ have discrete spectra, without specifying their specific form beyond the condition that the operators (both $\mathbf{x}_r$ and $\mathbf{E}_r$) of any one particle commute with those of any other. All the $\mathbf{x}$'s together form a complete $\mathbf{x}$-representation and likewise the $\mathbf{E}$'s form an $\mathbf{E}$-representation.

Now any arbitrary physical state $|;t\rangle$ can be expanded in terms of the eigen-$|\rangle$ of either of these

complete representations, and we have

$$|\,;t\rangle=\begin{cases}\int\cdots\int|x_1'x_2'\cdots x_n'\rangle dx'\langle x_1'\cdots x_n'|\,;t\rangle & \text{or}\\ \sum\{E_1'\cdots E_n'\}\,|E_1'E_2'\cdots E_n'\rangle\langle E_1'\cdots E_n'|\,;t\rangle.\end{cases}\tag{1}*\dagger$$

The two representatives $\langle x_1'\cdots x_n'|\,;t\rangle$ and $\langle E_1'\cdots E_n'|\,;t\rangle$ of a state $|\,;t\rangle$ are connected by the equation

$$\begin{aligned}\langle x_1'\cdots x_n'|\,;t\rangle&=\sum\{E_1'\cdots E_n'\}\langle x_1'\cdots x_n'|E_1'\cdots E_n'\rangle\langle E_1'\cdots E_n'|\,;t\rangle\\&=\sum\{E_1'\cdots E_n'\}\langle x_1'|E_1'\rangle\langle x_2'|E_2'\rangle\cdots\langle x_n'|E_n'\rangle\langle E_1'\cdots E_n'|\,;t\rangle,\end{aligned}\tag{2}$$

this last step being possible only because of the specified independence of the operators describing each particle.[1]

In the Schroedinger picture (to which we have implicitly referred in the indicated time dependence of the state $|\,;t\rangle$) the equation of motion of our state vector is

$$ih\frac{\partial}{\partial t}|\,;t\rangle=\mathbf{H}|\,;t\rangle,^2\tag{3}$$

and in the **x** and **E**-representations, we have the Schroedinger "wave equations."

$$ih\frac{\partial}{\partial t}\langle x_1'\cdots x_n'|\,;t\rangle=\int\cdots\int\langle x_1'\cdots x_n'|\mathbf{H}|x_1''\cdots x_n''\rangle dx''\langle x_1''\cdots x_n''|\,;t\rangle,\tag{4}$$

$$ih\frac{\partial}{\partial t}\langle E_1'\cdots E_n'|\,;t\rangle=\sum\{E_1''\cdots E_n''\}\langle E_1'\cdots E_n'|\mathbf{H}|E_1''\cdots E_n''\rangle\langle E_1''\cdots E_n''|\,;t\rangle.\tag{5}$$

Suppose now that

$$\mathbf{H}=\mathbf{U}+\mathbf{V}=\textstyle\sum_r\mathbf{u}(\mathbf{x}_r)+\sum_{r<s}\mathbf{v}(\mathbf{x}_r,\mathbf{x}_s).$$

We shall require the representative of **H** in the **E**-representation.

Consider the part **U** of **H**, then

$$\begin{aligned}\langle E_1'\cdots E_n'|\textstyle\sum_r\mathbf{u}(\mathbf{x}_r)|E_1''\cdots E_n''\rangle=\int\cdots\int\langle E_1'\cdots E_n'|x_1'\cdots x_n''\rangle dx'\\ \times\langle x_1'\cdots x_n'|\textstyle\sum_r\mathbf{u}_r|x_1''\cdots x_n''\rangle dx''\langle x_1''\cdots x_n''|E_1''\cdots E_n''\rangle.\end{aligned}\tag{6}$$

Now

$$\langle x_1'\cdots x_n'|\textstyle\sum_r\mathbf{u}_r|x_1''\cdots x_n''\rangle=\sum_r\langle x_r'|\mathbf{u}_r|x_r''\rangle\prod_{j\neq r}^{n}\delta(x_j'-x_j'').$$

Hence

$$\begin{aligned}\langle E_1'\cdots E_n'|\mathbf{u}_r|E_1''\cdots E_n''\rangle=\int\cdots\int\langle E_1'\cdots E_n'|x_1'\cdots x_n'\rangle dx'\langle x_r'|\mathbf{u}_r|x_r''\rangle dx_r''\\ \times\langle x_1'\cdots x_{r-1}'x_r''x_{r+1}'\cdots x_n'|E_1'\cdots E_n'\rangle.\end{aligned}\tag{7}$$

---

* The summation indices are enclosed by the brace immediately following.

† The prime tilted to the right indicates the complete commuting set, including spin variables if any; e.g. $dx'=dx_1'dx_2'\cdots dx_n'$.

[1] If the operators are those of electrons as specified above, the functions $\langle x_r'|E_r'\rangle$ may be considered as the ordinary Schroedinger eigenfunctions of a central field problem in zero approximation without interaction. However, the specific zero-order problem need not be restricted any further.

[2] **H** here need not be at all related to the $\mathbf{H}_r$ previously mentioned.

Furthermore $\langle E_1' \cdots E_n' | x_1' \cdots x_n' \rangle = \prod_j^n \langle E_j' | x_j' \rangle$ and $\left\{ \begin{array}{l} \int \langle E_l' | x_j' \rangle dx_j' \langle x_j' | E_m' \rangle = \delta(E_l', E_m') \\ \sum\{E_j'\} \langle x' | E_j' \rangle \langle E_j' | x'' \rangle = \delta(x' - x'') \end{array} \right\}$

therefore

$$\langle E_1' \cdots E_n' | \mathbf{u}_r | E_1'' \cdots E_n'' \rangle = \prod_{j \neq r}^n \delta(E_j', E_j'') \int\int \langle E_r' | x_r' \rangle dx_r' \langle x_r' | \mathbf{u}_r | x_r'' \rangle dx_r'' \langle x_r'' | E_r'' \rangle$$

$$= \prod_{j \neq r}^n \delta(E_j', E_j'') \langle E_r' | \mathbf{u}_r | E_r'' \rangle.^3 \quad (8)$$

Therefore

$$\sum\{E_1'' \cdots E_n''\} \langle E_1' \cdots E_n' | \textstyle\sum_r \mathbf{u}_r | E_1'' \cdots E_n'' \rangle \langle E_1'' \cdots E_n'' | ; t \rangle$$

$$= \sum_{r=1}^n \sum\{E_r''\} \langle E_r' | \mathbf{u}_r | E_r'' \rangle \langle E_1' \cdots E_{r-1}' E_r'' E_{r+1}' \cdots E_n' | ; t \rangle. \quad (9)$$

Here the summation includes the case $E_r'' = E_r'$, and we could split the sum into a diagonal term, plus sum over non-diagonal, i.e., $E_r'' \neq E_r'$.

Writing $\mathbf{v}(\mathbf{x}_r, \mathbf{x}_s) = \mathbf{v}_{rs}$

$$\langle x_1' \cdots x_n' | \mathbf{v}_{rs} | x_1'' \cdots x_n'' \rangle = \langle x_r' x_s' | \mathbf{v}_{rs} | x_r'' x_s'' \rangle \prod_{j \neq r,s}^n \delta(x_j' - x_j'') \quad (10)$$

and

$$\begin{aligned} \langle E_1' \cdots E_n' | \mathbf{v}_{rs} | E_1'' \cdots E_n'' \rangle &= \int \cdots \int \langle E_1' \cdots E_n' | x_1' \cdots x_n' \rangle dx' \langle x_1' \cdots x_n' | \mathbf{v}_{rs} | x_1'' \cdots x_n'' \rangle \\ &\quad \times dx'' \langle x_1'' \cdots x_n'' | E_1'' \cdots E_n'' \rangle \\ &= \int \cdots \int \langle E_1' \cdots E_n' | x_1' \cdots x_n' \rangle dx' \langle x_r' x_s' | \mathbf{v}_{rs} | x_r'' x_s'' \rangle \\ &\quad \times dx_r'' dx_s'' \langle x_1' \cdots x_{r-1}' x_r'' x_{r+1}' \cdots x_{s-1}' x_s'' x_{s+1}' \cdots x_n' | E_1'' \cdots E_n'' \rangle \\ &= \prod_{j \neq r,s}^n \delta(E_j', E_j'') \int \cdots \int \langle E_r' | x_r' \rangle \langle E_s' | x_s' \rangle \\ &\quad \times dx_r' dx_s' \langle x_r' x_s' | \mathbf{v}_{rs} | x_r'' x_s'' \rangle dx_r'' dx_s'' \langle x_r'' | E_r'' \rangle \langle x_s'' | E_s'' \rangle \\ &= \prod_{j \neq r,s} \delta(E_j', E_j'') \langle E_r' E_s' | \mathbf{v}_{rs} | E_r'' E_s'' \rangle, \end{aligned} \quad (11)$$

$$\sum\{E_1'' \cdots E_n''\} \langle E_1' \cdots E_n' | \mathbf{v}_{rs} | E_1'' \cdots E_n'' \rangle \langle E_1'' \cdots E_n'' | ; t \rangle$$

$$= \sum\{E_r'', E_s''\} \langle E_r' E_s' | \mathbf{v}_{rs} | E_r'' E_s'' \rangle \langle E_1' \cdots E_{r-1}' E_r'' E_{r+1}' \cdots E_{s-1}' E_s'' E_{s+1}' \cdots E_n' | ; t \rangle. \quad (12)$$

Therefore (5) becomes

$$\sum_{r=1}^n \sum\{E_r''\} \langle E_r' | \mathbf{u}_r | E_r'' \rangle \langle E_1' \cdots E_{r-1}' E_r'' E_{r+1}' \cdots E_n' | ; t \rangle$$

$$+ \sum_{r<s} \sum\{E_r'', E_s''\} \langle E_r' E_s' | \mathbf{v}_{rs} | E_r'' E_s'' \rangle \langle E_1' \cdots E_{r-1}' E_r'' E_{r+1}' \cdots E_{s-1}' E_s'' E_{s+1}' \cdots E_n' | ; t \rangle$$

$$- i\hbar \frac{\partial}{\partial t} \langle E_1' \cdots E_n' | ; t \rangle = 0. \quad (13)$$

[3] Here as usually occurs in a continuous representation, one integral is fictitious because of δ-functions in the matrix element $\langle x_k' | \mathbf{u}_k | x_k'' \rangle$.

SYMMETRY PROPERTIES

I. Symmetric Functions

For a symmetric wave function $\langle E_1' \cdots E_n' | \rangle$ we can specify each point in the domain of the function by giving the sequence $n_1', n_2', \cdots n_k', \cdots$, which numbers specify the number of times the various eigenvalues $E^{(1)}, E^{(2)}, \cdots E^{(k)}, \cdots$, respectively, occur in $\langle E_1' \cdots E_n' | \rangle$. Here the sequence $E^{(1)}, E^{(2)}, \cdots$ is the eigenvalue spectrum of an $\mathbf{E}$ (the same for all $\mathbf{E}_r$) ordered in any convenient manner. Thus the representative of states may be expressed as functions of the variables $n_1', n_2', \cdots n_k' \cdots$ instead of $E_1', \cdots E_n'$, the change being essentially a transformation to a new representation in which the rows and columns of matrices are labeled by the observables $\mathbf{n}_1, \mathbf{n}_2, \mathbf{n}_3, \cdots \mathbf{n}_k, \cdots$ (infinite set) which are the numbers of particles or systems with $\mathbf{E}$'s having the values $E^{(1)}, E^{(2)}, \cdots E^{(k)} \cdots$, respectively. We may also speak of them as *occupation* observables whose eigenvalues tell us how many particles are in the cell $E^{(1)}, E^{(2)}, \cdots$.[4]

The new observables are function (non-analytic) of the observables $\mathbf{E}_1, \mathbf{E}_2, \cdots \mathbf{E}_n$ so that the transformation consists essentially of a re-labeling of the rows and columns, and the only significant change to be made in the representative of a state will be that arising from the change in the weights of the different points of its domain (i.e., normalization).

A given sequence $n_1', n_2', \cdots n_k', \cdots$[5] defines a definite set of eigenvalues (or sets of values) $E_1', E_2', \cdots E_n'$ without regard to the sequence of the latter e.g., for $n=3$. Suppose $n_4'=2$, $n_5'=1$ all other n_i''s $=0$, then

$$\langle E_1^{(4)}, E_2^{(4)}, E_3^{(5)} | \rangle = P\langle E_1^{(4)}, E_2^{(4)}, E_3^{(5)} | \rangle \sim \langle n_1', n_2', n_3', n_4', n_5', \cdots | \rangle = \langle 0, 0, 0, 2, 1, 0, 0, \cdots | \rangle, \quad (14)$$

where P is any permutation of the sub-indices of the E''s.

We normalize according to

$$\sum \{n_1', n_2' \cdots\} |\langle n_1' n_2' \cdots | \rangle|^2 = \sum \{E_1' \cdots E_n'\} |\langle E_1' \cdots E_n' | \rangle|^2, \quad (15)$$

from which we can infer that $|\langle n_1' n_2' \cdots | \rangle|^2 = \sum |\langle E_1' \cdots E_n' | \rangle|^2$, where the latter summation is over all values of the E''s such that n_1' of them are equal to $E^{(1)}$, n_2' equal to $E^{(2)}$, etc. The number of terms in the sum is then $n!/n_1'!n_2'! \cdots$, and they are all equal since $\langle E_1' \cdots E_n' | \rangle$ is symmetrical, hence we must take

$$\langle n_1' n_2' \cdots | \rangle = [n!/\textstyle\prod_j n_j'!]^{\frac{1}{2}} \langle E_1' E_2' \cdots E_n' | \rangle \quad (16)$$

neglecting a possible phase factor.

We must now obtain the transformation law for the representatives of dynamical variables from the $\mathbf{E}$ to the $\mathbf{n}$ representations. Suppose $\mathbf{U} = \sum_r \mathbf{u}_r$, $\mathbf{u}_r$ being a function of the variables describing the rth particle, and the form of $\mathbf{u}_r$ being the same for all as it must be if $\mathbf{U}$ is to be of physical significance. The representative of $\mathbf{U}$ has already been determined in the $\mathbf{E}$ representation (e.g. (8)); and a convenient way of transforming this representaive to the $\mathbf{n}$ representation is to take the equation

$$|2\rangle = \mathbf{U}|1\rangle \text{ and transform its representatives.} \quad (17)$$

In the $\mathbf{E}$ representation (17) becomes

$$\langle E_1', E_2' \cdots E_n' | 2 \rangle = \sum_r \sum \{E_r''\} \langle E_r' | \mathbf{u}_r | E_r'' \rangle \langle E_1' \cdots E_{r-1}' E_r'' E_{r+1}' \cdots E_n' | 1 \rangle. \quad (18)$$

Now in the symmetric case, the wave function $\langle E_1' E_2' \cdots E_n' | \rangle$ may contain a number of equal arguments, e.g., $\langle E^{(p)}, E^{(p)}, E^{(p)}, E^{(q)}, E^{(q)}, E^{(v)}, \cdots E^{(z)} | \rangle$ the number of times $E^{(p)}$ occurs as argu-

[4] We speak of "cell" here rather than state, which is used in a somewhat different sense.

[5] Obviously for a fixed number of systems or particles n, at most n of the numbers in this infinite set are non-zero.

ment being n_p' (variable) by definition. For this particular illustrative selection of E''s, we have

$$\langle E^{(p)}, E^{(p)}, E^{(p)}, E^{(q)}, E^{(q)}, \cdots |2\rangle = \sum\{E_1''\}\langle E^{(p)}|\mathbf{u}|E_1''\rangle\langle E_1'' E^{(p)}E^{(p)}E^{(q)}E^{(q)}\cdots|1\rangle + \cdots$$
$$+\sum\{E_4''\}\langle E^{(q)}|\mathbf{u}|E_4''\rangle\langle E^{(p)}E^{(p)}E^{(p)}E_4''E^{(q)}\cdots|1\rangle + \cdots + \sum\{E_n''\}\cdots. \quad (19)$$

Thus we see that in general there are n_p' terms[6] on the right in which $E_r' = E^{(p)}$ ($r = 1, 2, 3$; $n_p' = 3$ in this special case) is replaced by $E_r'' = E^{(m)}$ say, ($E_r'' = E^{(m)}$ being a prototype value for E_r'', and all these terms are equal since the wave functions are symmetrical. Similarly there are n_q' terms in which $E_r' = E^{(q)}$ ($r = 4, 5$; $n_q' = 2$ in this illustrative case) is replaced by $E_r'' = E^{(m)}$, and again we group these equal terms together. Thus (19) may be written as

$$\sum_m \langle E^{(p)}|\mathbf{u}|E^{(m)}\rangle n_p'[n_1'!\cdots(n_p'-1)!\cdots(n_m'+1)!\cdots/n!]^{\frac{1}{2}}\langle n_1'\cdots n_p'-1\cdots n_m'+1\cdots|1\rangle + \cdots,$$
$$+\sum_m \langle E^{(q)}|\mathbf{u}|E^{(m)}\rangle n_q'[n_1'!\cdots(n_q'-1)!\cdots(n_m'+1)!\cdots/n!]^{\frac{1}{2}}\langle n_1'\cdots n_q'-1\cdots n_m'+1\cdots|1\rangle + \cdots, \quad (20)$$

where the summation index m taken on all integer values. The wave function $\langle n_1'\cdots n_p'-1\cdots n_m'+1\cdots|\rangle$, for example, appears because the corresponding wave function in the $\mathbf{E}$ representation differs from $\langle E_1'\cdots E_n'|\rangle$ only in that E_r'' replaces E_r' so that the number of particles in the "cell" $E_r'(=E^{(p)})$ is reduced by one, while the number in the cell $E_r''(=E^{(m)})$ is increased by one, and correspondingly it is necessary to give the wave function its appropriate normalization factor $[n_1'!\cdots(n_p'-1)!\cdots(n_m'+1)!\cdots/n!]^{\frac{1}{2}}$.

We can further simplify (20) and write

$$\sum_k \sum_m \langle k|\mathbf{u}|m\rangle n_k'[n_1'!\cdots(n_k'-1)!\cdots(n_m'+1)!\cdots/n!]^{\frac{1}{2}}\langle n_1'\cdots n_k'-1\cdots n_m'+1\cdots|1\rangle, \quad (21)$$

where $\langle E^{(k)}|\mathbf{u}|E^{(m)}\rangle$ is written as $\langle k|\mathbf{u}|m\rangle$ for convenience, and now k also takes on all values, since superfluous terms are eliminated by the presence of the factor n_k'.

Combining (18) and (21) after cancelling like members in the respective normalization factors, we have

$$\langle n_1'n_2'\cdots|2\rangle = \sum_{k,m}\langle k|\mathbf{u}|m\rangle[n_k'(n_m'+1-\delta_{km})]^{\frac{1}{2}}\langle n_1'\cdots n_k'-1\cdots n_m'+1\cdots|1\rangle.^{7} \quad (22)$$

For an operator such as $\mathbf{V} = \sum_{r,s}\mathbf{v}_{r,s}$ involving pairs of particles we have from (13)

$$|2\rangle = \mathbf{V}|1\rangle, \quad (23)$$

$$\langle E_1'\cdots E_n'|2\rangle = \sum_{r<s}\sum\{E_r'', E_s''\}\langle E_r'E_s'|\mathbf{v}_{rs}|E_r''E_s''\rangle\langle E_1'\cdots E_{r-1}'E_r''E_{r+1}'\cdots E_{s-1}'E_s''E_{s+1}'\cdots E_n'|1\rangle. \quad (24)$$

Considering again the illustrative wave function $\langle E^{(p)}E^{(p)}E^{(p)}E^{(q)}E^{(q)}E^{(v)}\cdots|\rangle$ it is evident that the number of equal terms in (24) in which $E^{(p)}$ in this function is replaced by $E_s'' = E^{(n)}$ say, and $E_r'' = E^{(m)}$ is just $\frac{1}{2}n_p'(n_p'-1)$, i.e., the number of ways of choosing s such that $E_s' = E^{(p)}$, $E_s'' = E^{(n)}$ and r such that $E_r' = E^{(p)}$, $E_r'' = E^{(m)}$ with $r<s$.

Further, there will be $n_p'n_q'$ equal terms in which $E_r' = E^{(p)}$ is replaced by $E_r'' = E^{(m)}$ and $E_s' = E^{(q)}$ by $E_s'' = E^{(n)}$, etc. Thus collecting equal terms, (24) may be written as

$$\sum_{m,n}\{\langle pp|\mathbf{v}|mn\rangle\tfrac{1}{2}n_p'(n_p'-1)[n_1'!\cdots(n_p'-2)!\cdots(n_m'+1)!\cdots(n_n'+1)!\cdots/n!]^{\frac{1}{2}}$$
$$\times\langle n_1'\cdots n_p'-2\cdots n_m'+1\cdots n_n'+1\cdots|1\rangle + \cdots$$
$$+\langle pq|\mathbf{v}|mn\rangle n_p'n_q'[n_1'!\cdots(n_p'-1)!\cdots(n_q'-1)!\cdots(n_m'+1)!\cdots(n_n'+1)!\cdots/n!]^{\frac{1}{2}}$$
$$\times\langle n_1'\cdots n_p'-1\cdots n_q'-1\cdots n_m'+1\cdots n_n'+1\cdots|1\rangle + \cdots$$
$$+\langle qq|\mathbf{v}|mn\rangle\tfrac{1}{2}n_q'(n_q'-1)[n_1'!\cdots(n_q'-2)!\cdots(n_m'+1)!\cdots(n_n'+1)!\cdots/n!]^{\frac{1}{2}}$$
$$\times\langle n_1'\cdots n_q'-2\cdots n_m'+1\cdots n_n'+1\cdots|1\rangle + \cdots + \cdots\} \quad (25)$$

[6] The number of ways of choosing r and E_r'' such that $E_r' = E^{(p)}$ and $E_r'' = E^{(m)}$ is just n_p', i.e., the number of ways of choosing r such that $E_r' = E^{(p)}$ since there is always only one way of choosing $E_r'' = E^{(m)}$.

[7] $\langle n_1'\cdots n_k'-1\cdots n_m'+1\cdots|\rangle$ is understood as $\langle n_1'\cdots n_k'\cdots|\rangle$ for $k=m$.

or simply as

$$\tfrac{1}{2}\sum_{k,l,m,n}\langle kl|\mathrm{v}|mn\rangle n_k'(n_l'-\delta_{kl})[n_1'!\cdots(n_k'-1)!\cdots(n_l'-1)!\cdots(n_m'+1)!\cdots(n_n'+1)!/n!]^{\frac{1}{2}}$$
$$\times\langle n_1'\cdots n_k'-1\cdots n_l'-1\cdots n_m'+1\cdots n_n'+1\cdots|1\rangle \quad (26)$$

with the previously mentioned convention that for coincident summation indices, both the normalization factor and the wave function above are to be taken accordingly, e.g., for $k=l$, these would be $[n_1'!\cdots(n_k'-2)!\cdots(n_m'+1)!\cdots(n_n'+1)!\cdots/n!]^{\frac{1}{2}}\langle n_1'\cdots n_k'-2\cdots n_m'+1\cdots n_n'+1\cdots|1\rangle$.

Keeping this point in mind, (26) and (24) combine to give as a final result

$$\langle n_1'n_2'\cdots|2\rangle=\tfrac{1}{2}\sum_{klmn}\langle kl|\mathrm{v}|mn\rangle[n_k'(n_l'-\delta_{kl})(n_m'+1-\delta_{km}-\delta_{lm})(n_m'+1+\delta_{mn}-\delta_{kn}-\delta_{ln})]^{\frac{1}{2}}$$
$$\times\langle n_1'\cdots n_k'-1\cdots n_l'-1\cdots n_m'+1\cdots n_n'+1\cdots|1\rangle \quad (27)$$

where the factor under the root sign which remains after clearing the normalization constants is readily verified by considering (25) and (26), and the effect of various coincident summation indices on the normalization factor to be chosen in (26).

The eigenvalues of our new dynamical variables $\mathbf{n}_1$, $\mathbf{n}_2$, $\cdots$ are the integers 0, 1, 2, $\cdots$ and are thus apart from the factor h, the same as those of the action variable $\mathbf{J}$ in the problem of the simple harmonic oscillator.*

$$\mathbf{H}=\frac{1}{2m}(\mathbf{p}^2+m^2w^2\mathbf{q}^2);\quad \mathbf{J}=\mathbf{H}/w-h/2.$$

In the Heisenberg representation for the oscillator the matrix of $\mathbf{J}$ is

$$\langle|\mathbf{J}|\rangle\sim\begin{vmatrix}0&0&0&0&\cdots\\0&1&0&0&\\0&0&2&0&\\0&0&0&3&\\\cdot&\cdot&\cdot&\cdot&\end{vmatrix} \quad (28)$$

and one can introduce the angle variable $\mathbf{w}$ defined by the Heisenberg matrices of $\exp(i\mathbf{w})$ and $\exp(-i\mathbf{w})$, i.e.,

$$\begin{vmatrix}0&0&0&0&\cdots\\1&0&0&0&\\0&1&0&0&\cdots\\0&0&1&0&\cdots\\\cdot&\cdot&\cdot&\cdot&\cdots\end{vmatrix} \quad \text{and} \quad \begin{vmatrix}0&1&0&0&\cdots\\0&0&1&0&\\0&0&0&1&\cdots\\\cdot&\cdot&\cdot&\cdot&\cdots\\\cdot&\cdot&\cdot&\cdot&\cdots\end{vmatrix}.$$

From the matrix representatives we see that $\exp(i\mathbf{w})$ and $\exp(-i\mathbf{w})$ are not truly reciprocal since $\exp(-i\mathbf{w})\exp(i\mathbf{w})=1$, $\exp(i\mathbf{w})\exp(-i\mathbf{w})\neq 1$. Further we observe that

$$\mathbf{J}\exp(i\mathbf{w})=\exp(i\mathbf{w})(\mathbf{J}+h) \quad \text{and} \quad \mathbf{J}\exp(-i\mathbf{w})=\exp(-i\mathbf{w})(\mathbf{J}-h). \quad (29)$$

Comparing the above, with the relations for $\mathbf{q}$, $\mathbf{p}$ i.e.,

$$\exp(ic\mathbf{q})\mathbf{p}-\mathbf{p}\exp(ic\mathbf{q})=-ch\exp(ic\mathbf{q}) \quad \text{or} \quad \mathbf{p}\exp(ic\mathbf{q})=\exp(ic\mathbf{q})(\mathbf{p}+ch) \quad (30)$$

with $c=\pm 1$ we see that at least formally Eq. (29) are consistent with the view that $\mathbf{J}$ and $\mathbf{w}$ are a pair of canonically conjugate dynamical variables satisfying the quantum condition $\mathbf{wJ}-\mathbf{Jw}=ih$. This relation is really meaningless since we can only define $\exp(\pm i\mathbf{w})$ but not $\mathbf{w}$ itself, and furthermore we know that to be canonically conjugate the dynamical variables must have continuous

* Dirac, *Quantum Mechanics* (Oxford University Press, Cambridge, England, 1935).

spectra which $\mathbf{J}$ has not. Nonetheless, the analogy is suggestive, and we shall make use of it with proper reservations.

It is readily verified from the matrix forms that

$$\begin{gathered}\mathbf{J}^{\frac{1}{2}}\exp(i\mathbf{w})=\exp(i\mathbf{w})(\mathbf{J}+\hbar)^{\frac{1}{2}},\quad \exp(-i\mathbf{w})\mathbf{J}^{\frac{1}{2}}=(\mathbf{J}+\hbar)^{\frac{1}{2}}\exp(-i\mathbf{w}),\\ \mathbf{J}^{\frac{1}{2}}\exp(i\mathbf{w})\exp(-i\mathbf{w})\mathbf{J}^{\frac{1}{2}}=\mathbf{J},\\ \exp(-i\mathbf{w})\mathbf{J}^{\frac{1}{2}}\mathbf{J}^{\frac{1}{2}}\exp(i\mathbf{w})=(\mathbf{J}+\hbar)^{\frac{1}{2}}\exp(-i\mathbf{w})\exp(i\mathbf{w})(\mathbf{J}+\hbar)^{\frac{1}{2}}=\mathbf{J}+\hbar.\end{gathered}\tag{31}$$

These results hold in spite of the inequality $\exp(i\mathbf{w})\exp(-i\mathbf{w})\neq 1$ and show that when we deal with the quantities $\mathbf{J}^{\frac{1}{2}}\exp(i\mathbf{w})$ and $\exp(-i\mathbf{w})\mathbf{J}^{\frac{1}{2}}$ we can consider $\exp(i\mathbf{w})$ and $\exp(-i\mathbf{w})$ as truly reciprocal, without getting into difficulties.

By analogy we introduce $\exp(\pm i\mathbf{w}_k)$ for each of our variables $\mathbf{n}_k$, and corresponding to (29), we now have

$$\exp(i\mathbf{w}_k)\mathbf{n}_k=(\mathbf{n}_k-1)\exp(i\mathbf{w}_k)\quad\text{and}\quad\exp(-i\mathbf{w}_k)\mathbf{n}_k=(\mathbf{n}_k+1)\exp(-i\mathbf{w}_k),^{8}\tag{32}$$

and $\exp(i\mathbf{w}_k)$, $\exp(-i\mathbf{w}_k)$ and $\mathbf{n}_k$ commute with $\exp(i\mathbf{w}_l)$, $\exp(-i\mathbf{w}_l)$ and $\mathbf{n}_l$ for $k\neq l$.

These results are in accord with the formal relation

$$\mathbf{w}_k\mathbf{n}_k-\mathbf{n}_k\mathbf{w}_k=\mathrm{i}.\tag{33}$$

From the commutators (32) we have the selection rules

$$(n_k''-n_k'+1)\langle n_k'|\exp(i\mathbf{w}_k)|n_k''\rangle=0\quad\text{and}\quad(n_k''-n_k'-1)\langle n_k'|\exp(-i\mathbf{w}_k)|n_k''\rangle=0\tag{33'}$$

and the explicit forms of these representatives are given by (28), namely

$$\langle n_1'n_2'\cdots|\exp(i\mathbf{w}_k)|n_1''n_2''\cdots\rangle=\delta(n_k',n_k''+1)\prod_{j\neq k}\delta(n_j',n_j''),\tag{34a}$$

$$\langle n_1'n_2'\cdots|\exp(-i\mathbf{w}_k)|n_1''\cdots\rangle=\delta(n_k',n_k''-1)\prod_{j\neq k}\delta(n_j',n_j'').\tag{34b}$$

These relations mean that $\exp(i\mathbf{w}_k)$ operating on a $|\rangle$ whose representative is $\langle n_1'n_2'\cdots n_k'\cdots|\rangle$ gives a resultant whose representative is

$$\begin{cases}\langle n_1'\cdots n_k'-1\cdots|\rangle & n_k'\geqslant 1\\ 0 & n_k'=0\end{cases}\tag{35a}$$

and $\exp(-i\mathbf{w}_k)|\rangle$ for this same $|\rangle$ has the representative

$$\langle n_1'\cdots n_k'+1\cdots|\rangle\tag{35b}$$

as may be readily verified by expressing $\exp(\pm i\mathbf{w}_k)|\rangle$ in the $\mathbf{n}$ representation.

Equation (33) suggests another equivalent definition of $\exp(\pm i\mathbf{w}_k)$, namely

$$\begin{cases}\text{If}\quad|\rangle=\sum\{n_1'\cdots\}\,|n_1'\cdots n_k'\cdots\rangle\langle n_1'\cdots n_k'\cdots|\rangle,\quad\text{then}\\ \exp(\pm i\mathbf{w}_k)|\rangle=\sum\{n_1'\cdots\}\,|n_1'\cdots n_k'\cdots\rangle\exp(\mp\partial/\partial n_k')\langle n_1'\cdots n_k'\cdots|\rangle,\end{cases}\tag{36}$$

since by Taylor's theorem

$$\exp(\partial/\partial n_k')f(n_k')=\sum_{r=0}\frac{1}{r!}\left(\frac{\partial}{\partial n_k'}\right)^r f=f(n_k'+1),\quad\text{etc.}$$

It is here that the formal analogy of (33) to the commutator $[\mathbf{q},\mathbf{p}]=i\hbar$ is useful.

We can now see that Eq. (22) is just the representative of

$$|2\rangle=\sum_{k,m}\langle k|\mathbf{u}|m\rangle(\mathbf{n}_k)^{\frac{1}{2}}(\mathbf{n}_m+1-\delta_{km})^{\frac{1}{2}}\exp(i\mathbf{w}_k)\exp(-i\mathbf{w}_m)|1\rangle.\tag{37}$$

[8] In general, $\exp(i\mathbf{w})\mathbf{f}(\mathbf{n})=\mathbf{f}(\mathbf{n}-1)\exp(i\mathbf{w})$, $\exp(-i\mathbf{w})\mathbf{f}(\mathbf{n})=\mathbf{f}(\mathbf{n}+1)\exp(-i\mathbf{w})$.

Equation (37) must hold whenever $|2\rangle = \mathbf{U}|1\rangle$ holds, and hence

$$\begin{aligned}\mathbf{U} &= \sum_{k,m} \langle k|\mathbf{u}|m\rangle \mathbf{n}_k^{\frac{1}{2}}(\mathbf{n}_m+1-\delta_{km})^{\frac{1}{2}} \exp(i\mathbf{w}_k) \exp(-i\mathbf{w}_m) \\ &= \sum_{k,m} \langle k|\mathbf{u}|m\rangle \mathbf{n}_k^{\frac{1}{2}} \exp(i\mathbf{w}_k)(\mathbf{n}_m+1)^{\frac{1}{2}} \exp(-i\mathbf{w}_m),\end{aligned} \tag{38}$$

where we have used Eqs. (32) in the last step.

The result (38) is the required expression of $\mathbf{U}$ in terms of the operators $\mathbf{n}$, and gives us immediately the $\mathbf{n}$ representative of $\mathbf{U}$. The $\langle k|\mathbf{u}|m\rangle$ here are of course just numerical coefficients.

The result (38) can be put into simpler form by introducing the dynamical variables

$$\begin{cases} \xi_k = (\mathbf{n}_k+1)^{\frac{1}{2}} \exp(-i\mathbf{w}_k) = \exp(-i\mathbf{w}_k)\mathbf{n}_k^{\frac{1}{2}}, \\ \xi_k^* = \exp(i\mathbf{w}_k)(\mathbf{n}_k+1)^{\frac{1}{2}} = \mathbf{n}_k^{\frac{1}{2}} \exp(i\mathbf{w}_k). \end{cases} \tag{39}$$

These operators satisfy the commutation conditions.

$$[\xi_k, \xi_l]_- = 0, \quad \xi_k\xi_k^* = \mathbf{n}_k+1; \quad [\xi_k^*, \xi_l^*]_- = 0, \quad \xi_k^*\xi_k = \mathbf{n}_k; \quad [\xi_k, \xi_l^*]_- = \delta_{kl}. \tag{40}$$

In terms of these new variables, Eq. (38) takes the simple form

$$\mathbf{U} = \sum_{k,m} \xi_k^* \langle k|\mathbf{u}|m\rangle \xi_m. \tag{41}$$

Similarly (27) is the representative of

$$|2\rangle = \tfrac{1}{2} \sum_{k,l,m,n} \langle kl|\mathbf{v}|mn\rangle [\mathbf{n}_k(\mathbf{n}_l-\delta_{kl})(\mathbf{n}_m+1-\delta_{km}-\delta_{lm})(\mathbf{n}_n+1+\delta_{mn}-\delta_{kn}-\delta_{ln})]^{\frac{1}{2}} \times \exp(i\mathbf{w}_k) \exp(i\mathbf{w}_l) \exp(-i\mathbf{w}_m) \exp(-i\mathbf{w}_n)|1\rangle. \tag{42}$$

Here we require the relations

$$\begin{aligned} &\text{a.} \quad \exp(i\mathbf{w}_k)(\mathbf{n}_l+1)^{\frac{1}{2}} = (\mathbf{n}_l+1-\delta_{kl})^{\frac{1}{2}} \exp(i\mathbf{w}_k). \\ &\text{b.} \quad \exp(i\mathbf{w}_k)(\mathbf{n}_l)^{\frac{1}{2}} = (\mathbf{n}_l-\delta_{kl})^{\frac{1}{2}} \exp(i\mathbf{w}_k). \\ &\text{c.} \quad \exp(-i\mathbf{w}_k)(\mathbf{n}_l+1)^{\frac{1}{2}} = (\mathbf{n}_l+1+\delta_{kl})^{\frac{1}{2}} \exp(-i\mathbf{w}_k). \end{aligned} \tag{43}$$

Applying (43a, b) to $\mathbf{w}_k$ in (42) for example, we obtain

$$[\xi_k^*(\mathbf{n}_l)^{\frac{1}{2}}(\mathbf{n}_m+1-\delta_{lm})^{\frac{1}{2}}(\mathbf{n}_n+1+\delta_{mn}-\delta_{ln})^{\frac{1}{2}}] \exp(i\mathbf{w}_l) \exp(-i\mathbf{w}_m) \exp(-i\mathbf{w}_n). \tag{44}$$

Repeating the operation for $\mathbf{w}_l$ and $\mathbf{w}_m$ we obtain as the final form of $\mathbf{V}$

$$\mathbf{V} = \tfrac{1}{2} \sum_{k,l,m,n} \xi_k^*\xi_l^* \langle kl|\mathbf{v}|mn\rangle \xi_m\xi_n. \tag{45}$$

II. Antisymmetric Functions

Introduce $\mathbf{n}$ representation defined as before. $\mathbf{n}_k$ = number of $\mathbf{E}$'s having the value $E^{(k)}$, etc., except that in this case since the wave function $\langle E_1'E_2'\cdots E_n'|\rangle$ is antisymmetric, the $\mathbf{n}$'s may take on only the eigenvalues 0,1, otherwise the above wave function would vanish identically (which property of course characterizes the antisymmetric case).

To each set of values of the $\mathbf{E}$'s there will be a definite set of values for the $\mathbf{n}$'s and conversely, but when a set of n''s is given we do not know which E''s have the values associated with the given n'-sequence and of course the sign of the function is affected by the order of the E''s. Thus when we pass to the representatives $\langle n_1'n_2'\cdots|\rangle$ we can only infer that

$$\langle E_1'E_2'\cdots E_n'|\rangle = \pm\langle n_1'n_2'\cdots|\rangle.^9 \tag{46}$$

The normalization factor is not required now since the eigenvalues of the **n**'s are restricted to 0 and 1.

We must now set up a rule for specifying the sign in any particular case, and this can be done by ordering the eigenvalue spectrum of an **E** (the same for each **E**) in some arbitrarily chosen way so as to establish first a "standard sequence." This is most conveniently done by taking the standard sequence as

$$E^{(1)}, E^{(2)}, E^{(3)}, \cdots \tag{47}$$

which is the same as the order in which the n''s are written in $\langle n_1'n_2'n_3'\cdots|\rangle$ and we then require that the (+) sign in (46) shall be taken when the E''s in $\langle E_1'E_2'\cdots E_n'|\rangle$ which form a particular selection of n different members from the total set (47) can be brought into the order in which they appear in the standard sequence (gaps omitted) by an even number of interchanges, and the (−) sign for an odd number (i.e., according to whether or not the actual order of the E''s is an even or odd permutation of the standard order, with gaps omitted).

Thus suppose we write the standard sequence as

$$E^{(1)}<E^{(2)}<E^{(3)}<\cdots<E^{(i)}<E^{(j)}<E^{(k)}<E^{(l)}<\cdots.$$

Then for $n=5$, if $\langle E_1'E_2'E_3'E_4'E_5'|\rangle=\langle E^{(6)}, E^{(k)}, E^{(3)}, E^{(l)}, E^{(2)}|\rangle$ i.e., $E_1'=E^{(6)}$, $E_2'=E^{(k)}$, etc., the natural order for this selection of 5 members from (47) is $E^{(2)}, E^{(3)}, E^{(6)}, E^{(k)}, E^{(l)}$. The number of interchanges required to achieve this natural order is 6, and consequently

$$\langle E_1^{(6)}, E_2^{(k)}, E_3^{(3)}, E_4^{l}, E_5^{(2)}|\rangle=\langle n_1'n_2'\cdots n_6'\cdots n_k'\cdots|\rangle=\langle 0, 1, 1, 0, 0, 1, \cdots 0, 1, \cdots 1, \cdots|\rangle.$$

For convenience in determining the correct sign in (46) let us introduce a comparison sequence (indicated by an underline)

$$\underline{E_1'E_2'E_3'\cdots E_n'} \tag{48}$$

defined by the condition that whatever the values of the E''s in (48) (i.e., for *any* selection of n members from the set (47)), the arguments in (48) are automatically arranged in the order of the standard sequence. (It may happen that one or another member is not underlined, and these exceptions will be explained as they arise.)

By definition

$$\underline{\langle E_1'E_2'\cdots E_r'\cdots E_n'|\rangle}=+\langle n_1'n_2'\cdots n'_{E_r'}\cdots n'_{E_s'}\cdots|\rangle. \tag{49}$$

Thus the underline indicates the operation of ordering, and in particular makes possible a unique definition of position of the E_i''s for the given selection of n, counting from the left. Thus in (49) E_r' is at the normal[10] ordered position

$$r'=n_1'+n_2'+\cdots+n'_{E_r'} \tag{50}$$

and E_s' at the position

$$s'=n_1'+n_2'+\cdots+n'_{E_s'}. \tag{51}$$

We must now obtain the transformation law for dynamical variables from the **E** to the **n** representation.

Following the procedure in the symmetric case we write

$$|2\rangle=\mathbf{U}|1\rangle;\quad \mathbf{U}=\sum_{r=1}^{n}\mathbf{u}_r \tag{52}$$

or

$$\langle E_1'E_2'\cdots E_n'|2\rangle=\sum_{r=1}^{n}\sum\{E_r''\}\langle E_r'|\mathbf{u}_r|E_r''\rangle\langle E_1'\cdots E_{r-1}'E_r''E_{r+1}'\cdots E_n'|1\rangle. \tag{53}$$

[9] We must emphasize that the indices of the arguments on the left refer to the eigenvalues of the first, second, $\cdots n$th observable while those on the right are the numbers of **E**'s equal to $E^{(1)}$, i.e., n_1', etc., and there is obviously no correspondence of indices intended.

[10] We say normal rather than standard to indicate that there will in general be gaps.

In the **n** representation (53) becomes

$$\langle n_1' n_2' \cdots | 2 \rangle = \sum_{r=1}^{n} \sum \{E_r''\} \pm \langle E_r' | \mathbf{u} | E_r'' \rangle \langle n_1' \cdots n'_{E_r'} - 1 \cdots n'_{E_r''} + 1 \cdots | 1 \rangle.^{11} \tag{54}$$

With regard to the ambiguity of sign in (54) it is clear that we must take the $(-)$ sign in those cases where a $(-)$ sign appears in one and only one of the equations

$$\begin{aligned} &\text{a.} \quad \langle E_1' \cdots E_r' \cdots E_n' | \rangle = \pm \langle n_1' n_2' \cdots n'_{E_r'} \cdots | \rangle. \\ &\text{b.} \quad \langle E_1' \cdots E_{r-1}' E_r'' E_{r+1}' \cdots E_n' | \rangle = \pm \langle n_1' \cdots n'_{E_r'} - 1 \cdots n'_{E_r''} + 1 \cdots | \rangle. \end{aligned} \tag{55}$$

We may standardize the procedure for determining the sign in (54) by the following device. First we observe that when E_r' in (55a) and E_r'' in (55b) are shifted to the first place the resultant sign in (54) is not affected, so that we may write consistently[12]

$$\begin{aligned} &\text{a.} \quad \langle E_r' E_1' \cdots E_{r-1}' E_{r+1}' \cdots E_n' | \rangle = \pm \langle n_1' \cdots n'_{E_r'} \cdots | \rangle. \\ &\text{b.} \quad \langle E_r'' E_1' \cdots E_{r-1}' E_{r+1}' \cdots E_n' | \rangle = \pm \langle n_1' \cdots n'_{E_r'} - 1 \cdots n'_{E_r''} + 1 \cdots | \rangle. \end{aligned} \tag{56}$$

Now if we order the E''s in (56a, b) in standard sequence except for E_r', E_r'', respectively,[13] which remain at first place, we have

$$\begin{aligned} &\text{a.} \quad \underline{\langle E_r' E_1' \cdots E_{r-1}' E_{r+1}' \cdots E_n' | \rangle} = \pm \langle n_1' \cdots n'_{E_r'} \cdots | \rangle. \\ &\text{b.} \quad \underline{\langle E_r'' E_1' \cdots E_{r-1}' E_{r+1}' \cdots E_n' | \rangle} = \pm \langle n_1' \cdots n'_{E_r'} - 1 \cdots n'_{E_r''} + 1 \cdots | \rangle. \end{aligned} \tag{57}$$

Now:

$$\begin{aligned} &\text{a.} \quad \underline{\langle E_r' E_1' \cdots E_{r-1}' E_{r+1}' \cdots E_n' | \rangle} = -(-)^{r'} \underline{\langle E_1' \cdots E_{r-1}' E_r' E_{r+1}' \cdots E_n' | \rangle} \\ &\qquad\qquad = -(-)^{r'} \langle n_1' \cdots n'_{E_r'} \cdots | \rangle. \\ &\text{b.} \quad \underline{\langle E_r'' E_1' \cdots E_{r-1}' E_{r+1}' \cdots E_n' | \rangle} = -(-)^{r''} \underline{\langle E_1' \cdots E_{r-1}' E_r'' E_{r+1}' \cdots E_n' | \rangle} \\ &\qquad\qquad = -(-)^{r''} \langle n_1' \cdots n'_{E_r'} - 1 \cdots n'_{E_r''} + 1 \cdots | \rangle. \end{aligned} \tag{58}$$

Equation (58a), results from the observation that shifting E_r' from its ordered position r' (in the middle term) to first place introduces a factor $-(-)^{r'}$; and the definition (49), Similarly for (58b).

Combining (55)–(58) we see that the sign in (54) is determined by the signature function $(-)^{r'+r''}$ or $(-)^{|r'-r''|}$ where r', r'' are defined for these sequences as in (50) and (51). From the nature of the signature as a power of (-1) it is clearly immaterial whether we take $(-)^{r'+r''}$ or $(-)^{|r'-r''|}$, the only difference being in the way we define and handle the signature operators to be introduced later. We shall use the latter definition in our calculation.[14, 15]

Equation (54) may be written as

$$\langle n_1' n_2' \cdots | 2 \rangle = \sum_{r=1}^{n} \langle E_r' | \mathbf{u}_r | E_r' \rangle \langle n_1' n_2' \cdots | 1 \rangle + \sum_r \sum \{E_r'' \neq E_r'\} \pm \langle E_r' | \mathbf{u}_r | E_r'' \rangle \langle n_1' \cdots n'_{E_r'} - 1 \cdots n'_{E_r''} + 1 \cdots | 1 \rangle. \tag{59}$$

---

[11] Here $\langle n_1' \cdots n'_{E_r'} - 1 \cdots n'_{E_r''} + 1 \cdots | \rangle$ is undetsood simply as $\langle n_1' \cdots n'_{E_r'} \cdots | \rangle$ for $E_r'' = E_r'$.

[12] We note that the steps (56), (57) below change the sign relations of both parts a and b consistently if at all, thus not affecting the resultant sign in (54).

[13] Which explains why E_r' and E_r'' are not underlined here.

[14] The former is used by: Jordan-Wigner, Zeits. f. Physik **47**, 631 (1928). Fock, Zeits. f. Physik **75**, 622 (1932).

[15] We could immediately obtain the signature in the present case by noting that the condition (55) for the $\pm$ sign is the same as the condition that the numbers of E''s on the left in (55) that lie between E_r' and E_r'' (not inclusive) shall be $\begin{matrix}\text{even}\\ \text{odd}\end{matrix}$ i.e., that $\Sigma_\epsilon n_\epsilon'$ where the sum is over all ϵ for which $E^{(\epsilon)}$ lies between E_r' and E_r'', i.e., $|r'-r''|$. We develop the above procedure here since it is required later when considering operators more complicated than **U**.

In the first sum a typical matrix element is $\langle E^{(k)}|\mathbf{u}|E^{(k)}\rangle$ or simply $\langle k|\mathbf{u}|k\rangle$,[16] and it appears a number of times equal to the number of ways of choosing r such that $E_r'=E^{(k)}$, which is $n'_{E^{(k)}}=n_k'$. In the second sum a typical matrix element $\langle E^{(k)}|\mathbf{u}|E^{l}\rangle$ or $\langle k|\mathbf{u}|l\rangle$ appears a number of times equal to the number of ways of choosing r and E_r'' such that $E_r'=E^{(k)}$ and $E_r''=E^{(l)}$ which is also n_k', and we have then

$$\langle n_1'n_2'\cdots|2\rangle=\sum_k\langle k|\mathbf{u}|k\rangle n_k'\langle n_1'n_2'\cdots|1\rangle+\sum_{k\neq l}\sum\pm\langle k|\mathbf{u}|l\rangle\langle n_1'\cdots n_k'-1\cdots n_l'+1\cdots|1\rangle. \tag{60}$$

The factor n_k' does not appear in the second term since $\langle n_1'\cdots n_k'-1\cdots n_l'+1\cdots|\rangle$ is non-vanishing only for $n_k'=1$, $n_l'=0$.

The observable $1-2\mathbf{n}_k$ formed from $\mathbf{n}_k$ has the eigenvalues 1, -1 and from our previous acquaintance with the spin operators it is natural to write

$$1-2\mathbf{n}_k=\boldsymbol{\sigma}_{zk}. \tag{61}$$

In analogy with the symmetric case we introduce the "step" operators $\frac{1}{2}(\boldsymbol{\sigma}_{xk}+i\boldsymbol{\sigma}_{yk})$ and $\frac{1}{2}(\boldsymbol{\sigma}_{xk}-i\boldsymbol{\sigma}_{yk})$ associated with $\boldsymbol{\sigma}_{zk}$, which play the part of angle variable analogous to $\exp(-i\mathbf{w}_k)$ and $\exp(i\mathbf{w}_k)$, respectively, and are represented in a $\boldsymbol{\sigma}_{zk}$ or $\mathbf{n}_k$ diagonal representation by

$$\begin{pmatrix}0&1\\0&0\end{pmatrix}\quad\text{and}\quad\begin{pmatrix}0&0\\1&0\end{pmatrix},\quad\text{respectively.} \tag{62}$$

There will be a set $\boldsymbol{\sigma}_{xk}$, $\boldsymbol{\sigma}_{yk}$, $\boldsymbol{\sigma}_{zk}$ for each k, and the members of one set will commute with the members of any other.

The form of the representatives (62) show that when $\frac{1}{2}(\boldsymbol{\sigma}_{xk}-i\boldsymbol{\sigma}_{yk})$ or $\frac{1}{2}(\boldsymbol{\sigma}_{xk}+i\boldsymbol{\sigma}_{yk})$ is applied to a $|\rangle$ whose representative is $\langle n_1'\cdots n_k'\cdots|\rangle$, the representative of the product is $\langle n_1'\cdots n_k'-1\cdots|\rangle$ and $\langle n_1'\cdots n_k'+1\cdots|\rangle$, respectively, with obvious restrictions on n_k'.

For convenience we introduce the suggestive notation

$$\boldsymbol{\sigma}_{zk}=\boldsymbol{\sigma}_k,\quad \tfrac{1}{2}(\boldsymbol{\sigma}_{xk}-i\boldsymbol{\sigma}_{yk})=\boldsymbol{\partial}_k=\boldsymbol{\partial}_k^-,\quad \tfrac{1}{2}(\boldsymbol{\sigma}_{xk}+i\boldsymbol{\sigma}_{yk})=\boldsymbol{\partial}_k^*=\boldsymbol{\partial}_k^+. \tag{63}$$

One can readily verify that these satisfy the relations

$$\begin{aligned}
&\boldsymbol{\sigma}_k^2=1,\quad \boldsymbol{\partial}_k^{2-}=\boldsymbol{\partial}_k^{2+}=0,\\
&\boldsymbol{\sigma}_k\boldsymbol{\partial}_k^-=-\boldsymbol{\partial}_k^-,\quad \boldsymbol{\sigma}_k\boldsymbol{\partial}_k^+=\boldsymbol{\partial}_k^+,\\
&\boldsymbol{\partial}_k^-\boldsymbol{\sigma}_k=\boldsymbol{\partial}_k^-,\qquad \boldsymbol{\partial}_k^+\boldsymbol{\sigma}_k=-\boldsymbol{\partial}_k^+,\\
&\left.\begin{aligned}\boldsymbol{\partial}_k^+\boldsymbol{\partial}_k^-&=1-\mathbf{n}_k\\ \boldsymbol{\partial}_k^-\boldsymbol{\partial}_k^+&=\mathbf{n}_k\end{aligned}\right\}\quad[\boldsymbol{\partial}_k^+,\boldsymbol{\partial}_k^-]_+=1.
\end{aligned} \tag{64}$$

In this notation, the step operator $\boldsymbol{\partial}_k^-$ for example, has the representative

$$\langle n_1'\cdots|\boldsymbol{\partial}_k^-|n_1''\cdots\rangle=\langle n_k'|\boldsymbol{\partial}_k^-|n_k''\rangle\prod_{j\neq k}\delta(n_j',n_j''), \tag{65}$$

where $\langle n_k'|\boldsymbol{\partial}_k^-|n_k''\rangle=\delta(n_k',n_k''+1)$ with the obvious restriction $n_k'\geqslant 1$.

Apropos of the above remarks on the properties of the step operators, we have

$$\begin{aligned}
\langle n_1'\cdots|\boldsymbol{\partial}_k^-|1\rangle&=\langle n_1'\cdots|\boldsymbol{\partial}_k^-\sum\{n_1'',n_2''\cdots\}|n_1''n_2''\cdots\rangle\langle n_1''\cdots|1\rangle\\
&=\sum\{n_1''\cdots\}\langle n_1'\cdots|\boldsymbol{\partial}_k^-|n_1''\cdots\rangle\langle n_1''\cdots|1\rangle\\
&=\begin{cases}\langle n_1'\cdots n_k'-1\cdots|1\rangle & n_k'=1\\ 0 & n_k'=0.\end{cases}
\end{aligned} \tag{66}$$

[16] We can write the matrix element this way because $\mathbf{u}_r$ is of the same form for all r, and $\langle E_r'|\mathbf{u}_r|E_r''\rangle$ is a matrix independent of r.

Hence we see that (60) is the representative of

$$|2\rangle=\sum_k \langle k|\mathbf{u}|k\rangle \mathbf{n}_k|1\rangle+\sum_{j\neq k}\sum \pm\langle k|\mathbf{u}|l\rangle \partial_k^-\partial_l^+|1\rangle. \tag{67}$$

Since this holds whenever (52) holds, we must have

$$\mathbf{U}=\sum_k\langle k|\mathbf{u}|k\rangle\mathbf{n}_k+\sum_{j\neq k}\sum \pm\langle k|\mathbf{u}|l\rangle\partial_k^-\partial_l^+. \tag{68}$$

The $\pm$ sign in (68) is an awkward feature, and to remove it we need a "signature" operator which will automatically introduce the proper sign.

To this end we introduce the variables

$$\xi_l=\prod_{j=1}^{l-1}\sigma_j\partial_l^+=\mathbf{v}_l\partial_l^+,\quad \xi_k^*=\prod_{j=1}^{k-1}\partial_k^-\sigma_j=\partial_k^-\mathbf{v}_k, \tag{69}$$

where the numbering is as in the standard sequence, and obviously all factors in the definition of a ξ or ξ^* commute.

From the properties listed in (64), we see that

$$\xi_k^*\xi_l=\partial_k^-\begin{cases}\sigma_k\sigma_{k+1}\cdots\sigma_{l-1} & k<l\\ \sigma_l\sigma_{l+1}\quad\sigma_{k-1} & k>l\end{cases}\partial_l^+ \tag{70}$$

where as indicated we take the upper bracket for $k<l$ and the lower for $k>l$. Further since $\sigma_l\partial_l^+=\partial_l^+$ and $\partial_k^-\sigma_k=\partial_k^-$ we can omit the factor σ_k in the upper and σ_l in the lower bracket, which may now be written as

$$\xi_k^*\xi_l=\partial_k^-\partial_l^+\begin{cases}(1-2\mathbf{n}_{k+1})(1-2\mathbf{n}_{k+2})\cdots(1-2\mathbf{n}_{l-1}) & k<l\\ (1-2\mathbf{n}_{l+1})(1-2\mathbf{n}_{l+2})\cdots(1-2\mathbf{n}_{k-1}) & k>l.\end{cases} \tag{71}$$

For the eigenvalue $n'=0$, each factor is 1; and for $n'=1$, it is -1. Hence in each line the number of factors $(-)$ is equal to the number of non-zero n''s which is the number of E''s actually found to lie between $E^{(k)}$ and $E^{(l)}$ in any given sequence. This is just the required sign convention, agreeing with our previous result in giving $(-)$ to power $\sum_s n_s'=|r''-r'|$ as signature when $\xi_k^*\xi_l$ operates on a $|\rangle$. Thus (68) becomes

$$\mathbf{U}=\sum_k\langle k|\mathbf{u}|k\rangle\mathbf{n}_k+\sum_{k\neq l}\sum\xi_k^*\langle k|\mathbf{u}|l\rangle\xi_l. \tag{72}$$

From the relations (64) one may readily obtain the commutation relation for the ξ's, namely

$$\begin{aligned}&[\xi_k^*,\xi_l^*]_+=0,\quad \xi_k^*\xi_k=\mathbf{n}_k,\\ &[\xi_k,\xi_l^*]_+=\delta_{kl},\quad \xi_k\xi_k^*=1-\mathbf{n}_k.\end{aligned} \tag{73}$$

Thus (72) simplifies to

$$\mathbf{U}=\sum_{k,l}\xi_k^*\langle k|\mathbf{u}|l\rangle\xi_l. \tag{74}$$

We must now consider the $\mathbf{E}$ and $\mathbf{n}$ representatives of a more general operator

$$\mathbf{V}=\sum_{r<s}\mathbf{v}_{rs} \tag{75}$$

for which we may write $|2\rangle=\mathbf{V}|1\rangle$ and

$$\begin{aligned}\langle E_1'\cdots E_n'|2\rangle=\tfrac{1}{2}\sum_{r\neq s}\sum\{E_r'',E_s''\}&\langle E_r'E_s'|\mathbf{v}_{rs}|E_r''E_s''\rangle\\ &\times\langle E_1'\cdots E_{r-1}'E_r''E_{r+1}'\cdots E_{s-1}'E_s''E_{s+1}'\cdots E_n'|1\rangle,\end{aligned} \tag{76}$$

and in the **n** representation

$$\langle n_1' n_2' \cdots | 2 \rangle = \tfrac{1}{2} \sum_{r \neq s} \sum \{E_r'', E_s''\} \pm \langle E_r' E_s' | v_{rs} | E_r'' E_s'' \rangle \times \langle n_1' \cdots n'_{E_r'} - 1 \cdots n'_{E_s'} - 1 \cdots n'_{E_r''} + 1 \cdots n'_{E_s''} + 1 \cdots | 1 \rangle. \quad (77)$$

Here again the $(-)$ sign in (77) is to be taken when there is a $(-)$ in only one of the relations

$$\begin{aligned} &\text{a.} \quad \langle E_1' \cdots E_n' | \rangle = \pm \langle n_1' \cdots | \rangle, \\ &\text{b.} \quad \langle E_1' \cdots E_{r-1}' E_r'' E_{r+1}' \cdots E_{s-1}' E_s'' E_{s+1}' \cdots E_n' | \rangle \\ &\qquad = \pm \langle n_1' \cdots n'_{E_r'} - 1 \cdots n'_{E_s'} - 1 \cdots n'_{E_r''} + 1 \cdots n'_{E_s''} + 1 \cdots | \rangle. \end{aligned} \quad (78)$$

By the definition of the comparison sequence

$$\begin{aligned} &\text{a.} \quad \underline{\langle E_1' \cdots E_{r-1}' E_r' E_{r+1}' \cdots E_{s-1}' E_s' E_{s+1}' \cdots E_n' | \rangle} = + \langle n_1' \cdots n'_{E_r'} \cdots n'_{E_s'} \cdots | \rangle, \\ &\text{b.} \quad \underline{\langle E_1' \cdots E_{r-1}' E_r'' E_{r+1}' \cdots E_{s-1}' E_s'' E_{s+1}' \cdots E_n' | \rangle} \\ &\qquad = + \langle n_1' \cdots n'_{E_r'} - 1 \cdots n'_{E_s'} - 1 \cdots n'_{E_r''} + 1 \cdots n'_{E_s''} + 1 \cdots | \rangle. \end{aligned} \quad (79)$$

Furthermore

$$\begin{aligned} &\text{a.} \quad \underline{\langle E_r' E_s' E_1' \cdots E_{r-1}' E_{r+1}' \cdots E_{s-1}' E_{s+1}' \cdots E_n' | \rangle} = -(-)^{r'+s'} \\ &\text{b.} \qquad (-)^{r'+s'} \times \left\{ \underline{\langle E_1' \cdots E_{r-1}' E_r' E_{r+1}' \cdots E_{s-1}' E_s' E_{s+1}' \cdots E_n' | \rangle} \right\}_{s' < r'}^{s' > r'} \end{aligned} \quad (80)$$

since shifting E_r' from its ordered position r' to first place multiplies the function by $-(-)^{r'}$, and in this process E_s' remains at its ordered position s' if $E_s' > E_r'$ or moves one place to the right to $s'+1$ if $E_s' > E_r'$. Shifting E_s' to second place now introduces another factor $(-)^{s'}$ or $-(-)^{s'}$ in these two cases.

Similarly

$$\begin{aligned} &\text{a.} \quad \underline{\langle E_r'' E_s'' E_1' \cdots E_{r-1}' E_{r+1}' \cdots E_{s-1}' E_{s+1}' \cdots | \rangle} = -(-)^{r''+s''} \\ &\text{b.} \qquad (-)^{r''+s''} \times \left\{ \underline{\langle E_1' \cdots E_{r-1}' E_r'' E_{r+1}' \cdots E_{s-1}' E_s'' E_{s+1}' \cdots E_n' | \rangle} \right\}_{s'' < r''}^{s'' > r''} \end{aligned} \quad (81)$$

By a previous argument, replacing (78a, b) by

$$\begin{aligned} &\text{a.} \quad \underline{\langle E_r' E_s' E_1' \cdots E_{r-1}' E_{r+1}' \cdots E_{s-1}' E_{s+1}' \cdots E_n' | \rangle} = \pm \langle n_1' n_2' \cdots | \rangle \\ &\text{b.} \quad \underline{\langle E_r'' E_s'' E_1' \cdots E_{r-1}' E_{r+1}' \cdots E_{s-1}' E_{s+1}' \cdots E_n' | \rangle} \\ &\qquad = \pm \langle n_1' \cdots n'_{E_r'} - 1 \cdots n'_{E_s'} - 1 \cdots n'_{E_r''} + 1 \cdots n'_{E_s''} + 1 \cdots | \rangle \end{aligned} \quad (82)$$

will not affect the resultant sign in (77), and we again combine equations (78)–(82) to determine

the signature, and with our definition (69) of the signature operators we have four cases to consider, i.e.,

Case	signature	conditions
I	$(-)^{s'-r'+s''-r''}$	$E_s'>E_r'$, $E_s''>E_r''$
II	$(-)^{r'-s'+r''-s''}$	$E_s'<E_r'$, $E_s''<E_r''$
III	$-(-)^{s'-r'+r''-s''}$	$E_s'>E_r'$, $E_s''<E_r''$
IV	$-(-)^{r'-s'+s''-r''}$	$E_s'<E_r'$, $E_s''>E_r''$.

(83)

If as in (59) we change notation to $E^{(k)}=E_r'$, $E^{(l)}=E_s'$, $E^{(m)}=E_r''$, $E^{(n)}=E_s''$, we see that the transition from $\langle n_1'\cdots|\rangle$ to $\langle n_1'\cdots n_k'-1\cdots n_l'-1\cdots n_m'+1\cdots n_n'+1\cdots|\rangle$ is achieved by operating on $|\rangle$ by

$$\partial_k^-\partial_l^-\partial_n^+\partial_m^+. \tag{84}$$

That the order of the factors ∂^- and ∂^+ is correct may be readily verified by considering (77) for the special cases $E_r''=E_r'$, $E_s''=E_s'$ $(k=m,\ l=n)$ and $E_r''=E_s'$, $E_s''=E_r'$ $(m=l,\ n=k)$ with the definitions (64).

Combining (83) and (84) we have

$$\begin{matrix} \text{I} \\ \text{II} \\ \text{III} \\ \text{IV} \end{matrix}\begin{matrix} (-)^{s'-r'} \\ (-)^{r'-s'} \\ -(-)^{s'-r'} \\ -(-)^{r'-s'} \end{matrix}\left\{\begin{matrix} \\ \\ \\ \\ \end{matrix}\right.\partial^{-E_r'}\partial^{-E_s'}\partial^{+E_s''}\partial^{+E_r''}\left.\begin{matrix} (-)^{s''-r''} \\ (-)^{r''-s''} \\ (-)^{r''-s''} \\ (-)^{s''-r''} \end{matrix}\right\} = \begin{matrix} (-)^{l-k} \\ (-)^{k-l} \\ -(-)^{l-k} \\ -(-)^{k-l} \end{matrix}\left\{\begin{matrix} \\ \\ \\ \\ \end{matrix}\right.\partial^-{}_k\partial_l^-\partial_n^+\partial_m^+\left.\begin{matrix} (-)^{n-m} \\ (-)^{m-n} \\ (-)^{m-n} \\ (-)^{n-m}. \end{matrix}\right\} \tag{85}$$

The use of k, l, m, n as exponents of $(-)$ in (85) should cause no difficulty on comparing with the equivalent expressions on the left.

Now we introduce

$$\xi_l=\prod_{j=1}^{l-1}\sigma_j\partial_l^+=\nu_l\partial_l^+, \tag{86}$$

etc., and we find

I, III	$\nu_k\nu_l=\sigma_k\sigma_{k+1}\cdots\sigma_{l-1}$,	I, IV	$\nu_m\nu_n=\sigma_m\sigma_{m+1}\cdots\sigma_{n-1}$,
II, IV	$\nu_k\nu_l=\sigma_l\sigma_{l+1}\cdots\sigma_{k-1}$,	II, III	$\nu_m\nu_n=\sigma_n\sigma_{n+1}\cdots\sigma_{m-1}$.

From (86) the expression for $\xi_k^*\xi_l^*\xi_n\xi_m$ becomes

$$\xi_k^*\xi_l^*\xi_n\xi_m=\begin{matrix} k>l \\ l>k \end{matrix}\left\{\begin{matrix} -\sigma_{l+1}\sigma_{l+2}\cdots\sigma_{k-1} \\ \sigma_{k+1}\sigma_{k+2}\cdots\sigma_{l-1} \end{matrix}\right.(\partial_k^-\partial_l^-\partial_n^+\partial_m^+)\left\{\begin{matrix} \sigma_{m+1}\sigma_{m+2}\cdots\sigma_{n-1} \\ -\sigma_{n+1}\sigma_{n+2}\cdots\sigma_{m-1} \end{matrix}\right.\begin{matrix} n>m \\ m>n \end{matrix} \tag{87}$$

where conditions (83) or (85) are obtained by taking combinations of upper and lower brackets (one at each end) as indicated.

If we rewrite (69) in terms of the operators $(1-2\mathbf{n})$, we find that these equations provide just the required signature in all cases, and our final result is

$$\mathbf{V}=\tfrac{1}{2}\sum_{k,\,l,\,m,\,n}\xi_k^*\xi_l^*\langle kl|\mathbf{v}|mn\rangle\xi_n\xi_m \tag{88}$$

and

$$\mathbf{H}=\textstyle\sum_r \mathbf{u}_r+\sum_{r<s}\mathbf{v}_{rs}=\sum_{k,\,l}\xi_k^*\langle k|\mathbf{u}|l\rangle\xi_l+\tfrac{1}{2}\sum_{k,\,l,\,m,\,n}\xi_k^*\xi_l^*\langle kl|\mathbf{v}|mn\rangle\xi_n\xi_m. \tag{89}$$

Equation of Motion

We list here for convenience the commutators:

$$\begin{aligned}
&\xi_j\xi_k+\epsilon\xi_k\xi_j=0, \quad \epsilon=+1 \text{ Fermi Dirac statistics.}\\
&\xi_j\xi_k^*+\epsilon\xi_k^*\xi_j=\delta_{jk}, \quad \epsilon=-1 \text{ Bose Einstein statistics.}\\
&\xi_j^*\xi_j=\mathbf{n}_j,\\
&\xi_j\xi_j^*=1-\epsilon\mathbf{n}_j,
\end{aligned} \tag{90}$$

If we consider the systems or particles of the assembly (in either statistics) to be moving under the action of some external field of force without interaction between individual systems, the total Hamiltonian will be of the form $\mathbf{U}$ (e.g., (7)). Then the equations of motions* for the ξ's will be

$$ih\frac{d}{dt}\xi_j=[\xi_j,\mathbf{H}]_-=\sum_{k,l}\langle k|\mathbf{u}|l\rangle[\xi_j,\xi_k^*\xi_l]_-=\sum_l\langle j|\mathbf{u}|l\rangle\xi_l. \tag{91}$$

The Schroedinger wave equation for one system alone with Hamiltonian $\mathbf{u}$, say is

$$ih\frac{d}{dt}\langle E^j|\rangle=\sum_l\langle E^j|\mathbf{u}|E^l\rangle\langle E^l|\rangle=\sum_l\langle j|\mathbf{u}|l\rangle\langle E^l|\rangle. \tag{92}$$

Furthermore, it is readily shown that the operator ξ_j and the wave function $\langle E^j|\rangle$ obey the same transformation law in passing from one representation to another. The analogy is further enhanced by the fact that the interpretation for $\xi_j^*\xi_j$ is very similar to that of $|\langle E^j|\rangle|^2$, particularly if we normalize the latter to n (the total number of particles) so that $\sum_j|\langle E^j|\rangle|^2=n$ and $|\langle E^j|\rangle|^2$ is then the probable number of particles in the "state" $E^{(j)}$.

Thus we may say that the transition from the wave function procedure to that of the operators ξ corresponds to assuming that the wave functions $\langle E^j|\rangle$ describing a single system is not a numerical function of the parameter $E^{(j)}$, but is an operator for each $E^{(j)}$, satisfying the quantum conditions (90). It is essentially this transcription which suggests the descriptive term "second quantization."

We may further note that the initial transcription from the $\mathbf{x}$ to the $\mathbf{E}$ representation, which has been here used for illustrative purposes is not essential, and one may pass directly from either to the $\mathbf{n}$ representation, with appropriate changes of sums to integrals in the former case.

III. Quantized Wave Functions

We obtain a convenient expression for the Hamiltonian $\mathbf{H}$ (89), for both symmetric and antisymmetric particles by introducing the quantized wave functions ψ, ψ^* defined by the equations

$$\text{a.}\quad \psi(x)=\sum_r\langle x|E^r\rangle\xi_r, \quad \text{b.}\quad \psi^*(x')=\sum_r\xi_r^*\langle E^r|x'\rangle, \quad \text{c.}\quad \mathbf{n}=\sum_r\xi_r^*\xi_r=\int\psi^*(x)dx\psi(x). \tag{93}$$

Using (90) it is readily seen that these operators satisfy the commutation relations

$$\begin{aligned}
&\text{a.}\quad \psi(x')\psi^*(x'')+\epsilon\psi^*(x'')\psi(x')=\delta(x'-x'')\mathbf{I},\\
&\text{b.}\quad \psi(x')\psi(x'')+\epsilon\psi(x'')\psi(x')=0,\\
&\text{c.}\quad \mathbf{n}\psi-\psi\mathbf{n}=-\psi, \quad \langle n'|\psi|n''\rangle(n'-n''+1)=0,\\
&\text{d.}\quad \mathbf{n}\psi^*-\psi^*\mathbf{n}=\psi^*, \quad \langle n'|\psi^*|n''\rangle(n'-n''-1)=0,\\
&\text{e.}\quad \mathbf{n}_j\psi-\psi\mathbf{n}_j=-\langle x'|E^j\rangle\xi_j,\\
&\text{f.}\quad \mathbf{n}_j\psi^*-\psi^*\mathbf{n}_j=\xi_j^*\langle E^j|x'\rangle.
\end{aligned} \tag{94}$$

* The unitary transformation from the Schroedinger to Heisenberg picture generated by the unitary operator $\mathbf{U}=\exp(i\mathbf{H}t/\hbar)$ is implicitly understood, but by custom not explicitly indicated by any additional new subscripts to the operators, vectors, etc.

From the definitions (93), and the commutation properties, $\mathbf{H}$ takes the form

$$\mathbf{H}=\int\int \psi^*(x')dx'\langle x'|\mathbf{u}|x''\rangle dx''\psi(x')+\tfrac{1}{2}$$
$$\times\int\int\int\int \psi^*(x')\psi^*(x'')dx'dx''\langle x'x''|\mathbf{v}|x'''x^{\mathrm{iv}}\rangle dx'''dx^{\mathrm{iv}}\psi(x^{\mathrm{iv}})\psi(x'''), \quad (95)$$

where we have used $\langle E^rE^s|x'x''\rangle=\langle E^r|x'\rangle\langle E^s|x''\rangle$ and since the $\mathbf{x}$'s are homologous $\langle x_r'|\mathbf{u}_r|x_r''\rangle$ and $\langle x_r'x_s'|\mathbf{v}_{rs}|x_r''x_s''\rangle$ are written as $\langle x'|\mathbf{u}|x''\rangle$, $\langle x'x''|\mathbf{v}|x'''x^{\mathrm{iv}}\rangle$, respectively. Here, we may again note that $\langle x'|\mathbf{u}|x''\rangle=u(x')\delta(x'-x'')$, and $\langle x'x''|\mathbf{v}|x'''x^{\mathrm{iv}}\rangle=v(x',x'')\delta(x'-x''')\delta(x''-x^{\mathrm{iv}})$.

The selection rules (94c, d, e, f) hold for both symmetry cases, but for definiteness we shall now consider ψ and ψ^* for the symmetric case, so that

$$\text{a.}\quad \psi=\sum_k\langle x'|E^k\rangle(\mathbf{n}_k+1)^{\frac{1}{2}}\exp(-i\mathbf{w}_k),\quad \text{b.}\quad \psi^*=\sum_k\langle E^k|x'\rangle(\mathbf{n}_k)^{\frac{1}{2}}\exp(i\mathbf{w}_k), \quad (96)$$

and in the complete $\mathbf{n}$ representation, the representatives are

$$\begin{aligned}&\text{a.}\quad \langle n_1'\cdots|\psi|n_1''\cdots\rangle=\sum_k\langle x'|E^k\rangle(n_k'+1)^{\frac{1}{2}}\delta(n_k',n_k''-1)\prod_{i\neq k}\delta(n_i',n_i''),\\ &\text{b.}\quad \langle n_1'\cdots|\psi^*|n_1''\cdots\rangle=\sum_k\langle E^k|x'\rangle(n_k')^{\frac{1}{2}}\delta(n_k',n_k''+1)\prod_{i\neq k}\delta(n_i',n_i'').\end{aligned} \quad (97)$$

From these, the representatives of the equations $|2\rangle=\psi|1\rangle$ and $|2\rangle=\psi^*|1\rangle$ are, respectively,

$$\begin{aligned}&\text{a.}\quad \langle n_1'\cdots|2\rangle=\sum_k\langle x'|E^k\rangle(n_k'+1)^{\frac{1}{2}}\langle n_1'\cdots n_k'+1\cdots|1\rangle,\\ &\text{b.}\quad \langle n_1'\cdots|2\rangle=\sum_k\langle E^k|x'\rangle(n_k')^{\frac{1}{2}}\langle n_1'\cdots n_k'-1\cdots|1\rangle.\end{aligned} \quad (98)$$

Both these equations differ from our previous equations of this type (e.g. (22), (27), 60)) in that the total number of particles (as given by the sums of the function arguments on the right) is not conserved. Thus, ψ applied to a $|\rangle$ whose representative is $\langle n_1'n_2'\cdots|\rangle$ in n-particle space gives a product with representative $\sim\langle n_1'\cdots n_k'+1\cdots|\rangle$ i.e., in $n+1$-particle space, and the representative of $\psi^*|\rangle$; $\sim\langle n_1'\cdots n_k'-1\cdots|\rangle$ in $n-1$-particle space.

Hence we see, as in already implicit in the selection rules (94c, d), that operators which do not commute with $\mathbf{n}$ are of a type for which we cannot obtain a representative in a representation with a fixed number of observables diagonal, or as we may say, in a configuration space of a fixed number of dimensions

Nevertheless, the general representation theory permits us to transcribe Eqs. (98a, b) to other representations, by a procedure which is essentially the inverse of the method used in developing the equations of the second quantization, and this is sufficient for all practical purposes.

Equation (98a) is the $\mathbf{n}$ transcription of

$$\text{a.}\quad \langle E_1'\cdots E_n'|2\rangle=(n+1)^{\frac{1}{2}}\sum_E\langle x'|E'\rangle\langle E'E_1'\cdots E_n'|1\rangle=\sum_k\langle x'|E^k\rangle\langle E^kE_1'E_2'\cdots E_n'|1\rangle,^{17} \quad (99)$$

and in the $\mathbf{x}$ representation thus becomes

$$\begin{aligned}\text{a.}\quad \langle x_1'x_2'\cdots x_n'|2\rangle&=(n+1)^{\frac{1}{2}}\sum\{E_1'\cdots E_n'\}\sum_E\langle x'|E'\rangle\langle x_1'|E_1'\rangle\cdots\langle x_n'|E_n'\rangle\langle E'E_1'\cdots E_n'|1\rangle\\ &=(n+1)^{\frac{1}{2}}\langle x'x_1'\cdots x_n'|1\rangle.\end{aligned} \quad (100)$$

[17] The factor $(n+1)^{\frac{1}{2}}$ here is necessary because in the transition to (98a) the appropriate normalization factor appears as $[n_1'!n_2'!\cdots(n_k'+1)!\cdots/(n+1)!]^{\frac{1}{2}}$.

Equation (98b) however, arises from the equation

$$\text{b.}\quad \langle E_1'\cdots E_n'|2\rangle=\frac{1}{(n)^{\frac{1}{2}}}\{\langle E_1'|x'\rangle\langle E_2'E_3'\cdots E_n'|1\rangle+\langle E_2'|x'\rangle\langle E_1'E_3'E_4'\cdots E_n'|1\rangle+\cdots$$
$$+\langle E_n'|x'\rangle\langle E_1'\cdots E_{n-1}'|1\rangle\}\quad(99)$$
$$=\frac{1}{(n)^{\frac{1}{2}}}\sum_{j=1}^{n}\langle E_j'|x'\rangle\langle E_1'\cdots E_{j-1}'E_{j+1}'\cdots E_n'|1\rangle,$$

since a typical wave function on the right above, say $\langle E^k|x'\rangle$ appears n_k' times, and the factor $1/(n)^{\frac{1}{2}}$ is required because in the transition to (98b) the normalization factor appears as $[n_1'!\cdots(n_k'-1)!\cdots/(n-1)!]^{\frac{1}{2}}\langle n_1'\cdots n_k'-1\cdots|1\rangle$.

In the **x** representation this becomes (see (2) and the orthogonality conditions (7))

$$\text{b.}\quad \langle x_1'\cdots x_n'|2\rangle=\frac{1}{(n)^{\frac{1}{2}}}\sum_{j=1}^{n}\delta(x_j'-x')\langle x_1'\cdots x_{j-1}'x_{j+1}'\cdots x_n|1\rangle.\quad(100)$$

Let us now consider (A) $|2\rangle=\psi^*(x)\psi(x')|1\rangle$ and (B) $|2\rangle=\psi(x')\psi^*(x)|1\rangle$.

(A)

$$\text{a.}\quad \langle n_1'\cdots|2\rangle=\sum\{n_1''\cdots\}\sum\{n_1'''\cdots\}\sum_k(n_k')^{\frac{1}{2}}\langle E^k|x\rangle\delta(n_k',n_k'''+1)\prod_{i\neq k}\delta(n_i',n_i''')$$
$$\times\sum_j(n_j'''+1)^{\frac{1}{2}}\langle x'|E^j\rangle\delta(n_j''',n_j''-1)\prod_{l\neq j}\delta(n_l''',n_l'')\langle n_1''n_2''\cdots|1\rangle\quad(101)$$
$$=\sum_{k,j}(n_k')^{\frac{1}{2}}(n_j'+1-\delta_{jk})^{\frac{1}{2}}\langle E^k|x\rangle\langle x'|E^j\rangle\langle n_1'\cdots n_k'-1\cdots n_j'+1\cdots|1\rangle,$$

which is the **n**-transcription of

$$\text{b.}\quad \langle E_1'E_2'\cdots E_n'|2\rangle=\sum_{r=1}^{n}\sum\{E_r''\}\langle E_r'|x\rangle\langle x'|E_r''\rangle\langle E_1'\cdots E_{r-1}'E_r''E_{r+1}'\cdots E_n'|1\rangle,$$

or

$$\text{c.}\quad \langle x_1'x_2'\cdots x_n'|2\rangle=\delta(x_1'-x)\langle x'x_2'x_3'\cdots x_n'|\rangle+\delta(x_2'-x)\langle x_1'x'x_3'\cdots x_n'|\rangle+\cdots$$
$$+\delta(x_n'-x)\langle x_1'\cdots x_{n-1}'x'|\rangle$$
$$=\sum_{r=1}^{n}\delta(x_r'-x)\langle x_1'\cdots x_{r-1}'x'x_{r+1}'\cdots x_n'|1\rangle,$$

hence

$$\text{d.}\quad \langle x_1'\cdots x_n'|\psi^*(x)\psi(x')|x_1''\cdots x_n''\rangle=\sum_{r=1}^{n}\delta(x_r'-x)\delta(x_r''-x')\prod_{i\neq r}\delta(x_r''-x_i').$$

(B)

$$\text{a.}\quad \langle n_1'\cdots|2\rangle=\sum\{n_1''\cdots\}\sum\{n_1'''\cdots\}\sum_j(n_j'+1)^{\frac{1}{2}}\langle x'|E^j\rangle\delta(n_j',n_j'''-1)$$
$$\times\prod_{i\neq j}\delta(n_i',n_i''')\sum_k(n_k''')^{\frac{1}{2}}\langle E^k|x\rangle\delta(n_k''',n_k''+1)\prod_{l\neq k}\delta(n_l''',n_l'')\langle n_1''n_2''\cdots|1\rangle,\quad(102)$$
$$=\sum\langle x'|E^j\rangle\langle E^k|x\rangle(n_j'+1)^{\frac{1}{2}}(n_k'+\delta_{jk})^{\frac{1}{2}}\langle n_1'\cdots n_i'+1\cdots n_k'-1\cdots|1\rangle,$$

which is the **n** transcription of

b. $\langle E_1'\cdots E_n'|2\rangle=\sum_{E'}\langle x'|E'\rangle\langle E'|x\rangle\langle E_1'\cdots E_n'|1\rangle$

$$+\sum_{r=1}^{n}\sum\{E_r''\}\langle x'|E_r''\rangle\langle E_r'|x\rangle\langle E_1'E_2',\cdots E_{r-1}'E_r''E_{r+1}'\cdots E_n'|1\rangle,$$

or

c. $$\langle x_1'\cdots x_n'|2\rangle=\delta(x'-x)\langle x_1'\cdots x_n'|1\rangle+\sum_{r=1}^{n}\delta(x_r'-x)\langle x_1'\cdots x_{r-1}'x'x_{r+1}'\cdots x_n'|1\rangle.$$

From these results we find that the representative of $\{\psi(x)\psi^*(x')-\psi^*(x')\psi(x)\}|1\rangle$ is

$$\langle x_1'\cdots x_n'|2\rangle=\delta(x'-x)\langle x_1'\cdots x_n'|1\rangle \tag{103}$$

which merely verifies the relation (94a).

Similarly the representative of $|2\rangle=\{\psi(x')\psi(x)-\psi(x)\psi(x')\}|1\rangle$ is

$$\langle x_1'\cdots x_n'|2\rangle=[(n+2)(n+1)]^{\frac{1}{2}}\{\langle x'xx_1'\cdots x_n'|1\rangle-\langle xx'x_1'\cdots x_n'|1\rangle\}=0 \tag{104}$$

and verifies the relation (94b).

The same results may be readily obtained for the antisymmetric case; the only difference being in the change of sign in the appropriate places. We may further note that the operators ψ, ψ^* do not affect the symmetry properties of the wave functions.

From (101c) with $x=x'$, the representative of $|2\rangle=\psi^*(x)\psi(x)|1\rangle$ is

$$\langle x_1'\cdots x_n'|2\rangle=\sum_{r=1}^{n}\delta(x_r'-x)\langle x_1'\cdots x_{r-1}'xx_{r+1}'\cdots x_n'|1\rangle=\sum_{r=1}^{n}\delta(x_r'-x)\langle x_1'\cdots x_r'\cdots x_n'|1\rangle,^{18} \tag{105}$$

hence

$$\langle x_1'\cdots x_n'|\psi^*\psi|x_1''\cdots x_n''\rangle=\prod_{i=1}^{n}\delta(x_i''-x_i')\sum_{r=1}^{n}\delta(x_r'-x). \tag{106}$$

We shall also require the **x** representative of $\psi^*(x')\psi^*(x'')\psi(x'')\psi(x')$. This can be calculated directly in the **x** representation by first applying the commutation rules (94a, b) to obtain its equivalent, $\psi^*(x')\psi(x')\psi^*(x'')\psi(x'')-\psi^*(x')\psi(x'')\delta(x'-x'')\cdot\mathbf{I}$ and then using (101c, d) with x' and x'' for x. We thus obtain the equation

$$\begin{aligned}\langle x_1'\cdots x_n'|2\rangle&=\delta(x'-x'')\sum_{r=1}^{n}\delta(x_r'-x')\langle x_1'\cdots x_{r-1}'x''x_{r+1}'\cdots x_n'|1\rangle\\&\quad+\sum_{r\neq s}\delta(x_s'-x')\delta(x_r'-x'')\langle x_1'\cdots x_{s-1}'x'x_{s+1}'\cdots x_{r-1}'x''x_{r+1}'\cdots x_n'|1\rangle\\&\quad-\delta(x'-x'')\sum_{r=1}^{n}\delta(x_r'-x')\langle x_1'\cdots x_{r-1}'x''x_{r+1}'\cdots x_n'|1\rangle,^{19}\\&=\sum_{s\neq r}\delta(x_s'-x')\delta(x_r'-x'')\langle x_1'\cdots x_{s-1}'x'x_{s+1}'\cdots x_{r-1}'x''x_{r+1}'\cdots x_n'|1\rangle,\end{aligned} \tag{107}$$

and

$$\begin{aligned}&\langle x_1'\cdots x_n'|\psi^*(x')\psi^*(x'')\psi(x'')\psi(x')|x_1''\cdots x_n''\rangle\\&\qquad=\sum_{r\neq s}\delta(x_s'-x')\delta(x_r'-x'')\delta(x_s''-x')\delta(x_r''-x'')\prod_{i\neq r,s}\delta(x_i''-x_i').\end{aligned} \tag{108}$$

---

[18] $\delta(x_r'-x)f(x)=\delta(x_r'-x)f(x_r')$.

[19] $\langle x_1'\cdots x_n'|\mathbf{I}\delta(x'-x'')|x_1'''\cdots x_n'''\rangle=\delta(x'-x'')\prod_{i=1}^{n}\delta(x_i'''-x_i')$.

The use of these results allows us rather more flexibility in passing from the $\mathbf{x}$ to the $\mathbf{n}$ representation and conversely. In fact, we are now in a position to make the transition at any desired point in our calculations. To illustrate the preceding work we shall consider a few examples.

The Coulomb-potential operator which arises in the first part of $\mathbf{H}$ (e.g., (95)) reduces to [20]

$$\mathbf{U}(x_0)=\int \frac{\psi^*(x')\psi(x')dx'}{|\mathbf{x}_0-\mathbf{x}'|} \tag{109*}$$

and from (105), (106)

$$\begin{aligned}\langle x_1'\cdots x_n'|\,\mathbf{U}(x_0)\,|x_1''\cdots x_n''\rangle &= \int \frac{\langle x_1'\cdots x_n'|\,\psi^*(x')\psi(x')\,|x_1''\cdots x_n''\rangle dx'}{|\mathbf{x}_0-\mathbf{x}'|} \\ &= \int \sum_{k=1}^{n}\frac{\delta(x_k'-x')}{|\mathbf{x}_0-\mathbf{x}'|}dx' \prod_{i=1}^{n}\delta(x_i''-x_i') = \sum_{k=1}^{n}\frac{1}{|\mathbf{x}_0-\mathbf{x}_k'|}\prod_i \delta(x_i''-x_i')\end{aligned} \tag{110}$$

and $|2\rangle=\mathbf{U}|1\rangle$ becomes

$$\langle x_1'\cdots x_n'|2\rangle=\sum_{k=1}^{n}\frac{1}{|\mathbf{x}_0-\mathbf{x}_k'|}\langle x_1'\cdots x_n'|1\rangle, \tag{111}$$

which brings us back essentially to our starting point; part I.

IV. The Self-Consistent Field

The development of the second quantization thus far has laid emphasis on the operational aspect of the method, and its place in the general representation theory. It should be clear, however, that from a purely mathematical point of view the central theme is the expansion of a symmetric or antisymmetric function of n variables (in particular eigenfunctions of the Hamiltonian) in terms of a complete set of orthonormal functions, i.e., in terms of symmetrized or antisymmetrized product functions whose individual members are the $\langle x'|E^r\rangle$ of (2), (93), etc. Except for the orthonormality conditions these functions have been essentially arbitrary, and thus appeared in a subsidiary role. In order to apply our result to the determination of the eigenfunctions and eigenvalues it is necessary to compute the matrix components of the latter, and apply the variation principle. In particular if we consider only one of the infinite set of antisymmetrized product functions we are led to the equations of the self-consistent field, which will of course include "exchange."

We write the Hamiltonian (95) in the form

$$\mathbf{H}=\mathbf{H}_1+\mathbf{H}_2. \tag{112}$$

Introduce

$$\begin{aligned}\rho\langle x', x''\rangle &= \langle H'|\,\psi^*(x')\psi(x'')\,|H'\rangle \\ &= \int\cdots\int\langle H'|x_1'\cdots x_n'\rangle dx'\langle x_1'\cdots x_n'|\,\psi^*(x')\psi(\mathbf{x}'')\,|x_1''\cdots x_n''\rangle dx''\langle x_1''\cdots x_n''|H'\rangle.\end{aligned} \tag{113}$$

Using (101c, d) we obtain

$$\begin{aligned}\rho\langle x', x''\rangle &= \sum_{r=1}^{n}\int\cdots\int\langle H'|x_1'\cdots x_{r-1}'x'x_{r+1}'\cdots x_n'\rangle \\ &\qquad \times dx_1'\cdots dx_{r-1}'dx_{r+1}'\cdots dx_n'\langle x_1'\cdots x_{r-1}'x''x_{r+1}'\cdots x_n'|H'\rangle \\ &= n\int\cdots\int\langle H'|x'x_2'\cdots x_n'\rangle dx_2'\cdots dx_n'\langle x''x_2'\cdots x_n'|H'\rangle,\end{aligned} \tag{114}$$

[20] $\langle x'|\mathbf{u}|x''\rangle=u(x')\delta(x'-x'')$.

* In this and the equations following, the quantities in the denominator are to be understood as vectors.

where the last step follows from the symmetry properties of the eigenfunction. Therefore.

$$\langle H'|\mathbf{H}_1|H'\rangle=\int\int\rho(x',x'')\langle x'|\mathbf{u}|x''\rangle dx'dx''=\int\rho(x',x')u(x')dx'. \tag{115}$$

If the electron interaction term includes only the Coulomb-potential, the representative is given by

$$\langle x'x''|\mathbf{v}|x'''x^{\mathrm{iv}}\rangle=\delta(x'-x''')\delta(x''-x^{\mathrm{iv}})\frac{e^2}{|\mathbf{x}'-\mathbf{x}''|},$$

and

$$\mathbf{H}_2=\frac{e^2}{2}\int\int\frac{\psi^*(x')\psi^*(x'')\psi(x'')\psi(x')dx'dx''}{|\mathbf{x}'-\mathbf{x}''|}. \tag{116}$$

With (108) we find

$$\begin{aligned}&\langle H'|\psi^*(x')\psi^*(x'')\psi(x'')\psi(x')|H'\rangle\\&=\sum_{r\neq s}\int\cdots\int|\langle x_1'\cdots x_{s-1}'x'x_{s+1}'\cdots x_{r-1}'x''x_{r+1}'\cdots x_n'|H'\rangle|^2dx_1'\cdots dx_{s-1}'dx_{s+1}'\cdots dx_{r-1}'dx_{r+1}'\cdots dx_n'\\&=n(n-1)\int\cdots\int|\langle x'x''x_3'\cdots x_n'|H'\rangle|^2dx_3'\cdots dx_n'.\end{aligned} \tag{117}$$

The equations thus far are exact, and the self-consistent field approximation is obtained by introducing the approximate eigenfunction of H' given by

$$\langle x_1'\cdots x_n'|H'\rangle=A[(x_1'|1)(x_2'|2)\cdots(x_n'|n)], \tag{118}$$

where A is the antisymmetrizer

$$\frac{1}{(n!)^{\frac{1}{2}}}\sum_P\epsilon_pP\ ^{21}\quad\text{and}\quad\int(r|x)dx(x|s)=\delta_{rs}.$$

Denoting the approximate "density" by $\rho(x',x'')$[22] we find

$$\rho(x',x'')=\sum_{r=1}^{n}(r|x')(x''|r). \tag{119}$$

With the approximation (118), the right-hand term of (117) becomes

$$\rho(x',x')\rho(x'',x'')-|\rho(x',x'')|^2 \tag{120}$$

and finally

$$H'=\int\rho(x',x')\mathbf{u}(x')dx'+\frac{e^2}{2}\int\int\frac{[\rho(x',x')\rho(x'',x'')-|\rho(x',x'')|^2]}{|\mathbf{x}'-\mathbf{x}''|}dx'dx''. \tag{121}$$

[*Note added in proof.*]

The operators $\psi(x)$, $\psi(x)\psi(x')$, $\psi(x)\psi(x')\psi(x'')$, etc., may be described by the statement that applied to a $|\rangle$ whose representative is $\langle x_1'x_2'\cdots x_n'|\rangle$ the representative of the resultant is a function of $n+1$, $n+2$, $n+3$, $\cdots$, etc., variables,

---

[21] ϵ_p is the signature of the permutation P. $\epsilon_p^2=1$. $\epsilon_p\epsilon_q=\epsilon_{pq}$.

[22] Quantities in the approximate method are denoted by rounded brackets.

respectively, those numbering beyond n being unsigned. Considered in terms of various dimensions n, we may set up the following matrix correspondences.

(1)

$$\psi(x): \begin{Bmatrix} \text{const.} \\ \langle x_1' | \rangle \\ \langle x_1' x_2' | \rangle \\ \cdot \\ \cdot \\ \cdot \end{Bmatrix} \rightarrow \begin{Bmatrix} \langle x | \rangle \\ \sqrt{2}\langle x x_1' | \rangle \\ \sqrt{3}\langle x x_1' x_2' | \rangle \\ \cdot \\ \cdot \\ \cdot \end{Bmatrix}$$

(2)

$$\psi(x)\psi(x'): \begin{Bmatrix} \text{const.} \\ \langle x_1' | \rangle \\ \langle x_1' x_2' | \rangle \\ \cdot \\ \cdot \\ \cdot \end{Bmatrix} \rightarrow \begin{Bmatrix} (2\cdot 1)^{\frac{1}{2}}\langle x x' | \rangle \\ (3\cdot 2)^{\frac{1}{2}}\langle x x' x_1' | \rangle \\ (4\cdot 3)^{\frac{1}{2}}\langle x x' x_1' x_2' | \rangle \\ \cdot \\ \cdot \\ \cdot \end{Bmatrix}$$

etc.

The writer wishes to express his appreciation to Professor J. A. Wheeler of Princeton University, and Dr. V. Bargmann of the Institute for Advanced Study for several interesting and helpful discussions on the subject of this paper.

PHYSICAL REVIEW VOLUME 70, NUMBERS 9 AND 10 NOVEMBER 1 AND 15, 1946

Phenomenological Theory of Transport Processes in Fluids

BORIS LEAF*
Sterling Chemistry Laboratory, Yale University, New Haven, Connecticut
(Received August 5, 1946)

In this article a general theory of transport processes in fluids, developed from equations of hydrodynamics and thermodynamics which have been generalized for application to multicomponent systems, is presented. The equations for the flow of entropy and masses of components of the fluid, obtained from the local entropy dissipation, are used to treat the processes of viscosity, mobility, diffusion, electrical and thermal conductance, thermal transpiration, thermal diffusion, and the homogeneous thermoelectric effect. Reciprocal relations and other properties of the coefficients associated with each process are obtained and also inter-relationships between the coefficients of the various processes. The special conditions for the steady state, the state of pure thermal conduction, and the state of equilibrium are considered. Investigation of the steady state in thermal diffusion indicates that mass flow may persist, contrary to the usual assumption in treatment of experimental data.

VARIOUS attempts have been made to provide a phenomenological theory of specific, irreversible processes in fluids. One of the most recent appears in the thesis of S. R. de Groot.[1] The method there employed appeared susceptible to generalization into an inclusive theory of transport phenomena in fluids. Such a theory is presented here. In its development will be found results differing materially from those of de Groot.

DERIVATION OF THE EXPRESSION FOR ENTROPY DISSIPATION

Let us consider the hydrodynamic motion of a fluid composed of several constituents. The equation of continuity for the ith constituent is

$$\partial\rho_i/\partial t+\nabla\cdot\rho_i\mathbf{v}_i=0, \tag{1}$$

or

$$d\rho_i/dt+\rho_i\nabla\cdot\mathbf{v}_i=0, \tag{2}$$

* Frank B. Jewett Fellow 1945–6. Present address: Department of Physics, Kansas State College, Manhattan, Kansas.

[1] S. R. de Groot, *L'Effet Soret. Diffusion Thermique dans Les Phases Condenseés* (N. V. Noord-Hollandsche Uitgevers Maatschappij, Amsterdam, Holland, 1945).

where

$$d/dt=\partial/\partial t+\mathbf{v}_i\cdot\nabla \tag{3}$$

is the "mobile operator" or time derivative following the motion of the ith constituent, which has a density ρ_i and velocity $\mathbf{v}_i$ relative to the containing vessel.

In order to write the equation of motion we shall need the expression for the partial stress tensor for the ith constituent. This will be obtained by a generalization of the method for determining the stress tensor for a one-component fluid.[2] The total stress tensor Ψ is given by the sum of the partial stress tensors Ψ_i for the various constituents in the fluid. Also for each constituent we write down a rate-of-pure-strain tensor Φ_i.

$$\Psi_i=\begin{pmatrix} P_i & W_i & V_i \\ W_i & Q_i & U_i \\ V_i & U_i & R_i \end{pmatrix}$$

and

$$\Phi_i=\begin{pmatrix} a_i & \frac{1}{2}h_i & \frac{1}{2}g_i \\ \frac{1}{2}h_i & b_i & \frac{1}{2}f_i \\ \frac{1}{2}g_i & \frac{1}{2}f_i & c_i \end{pmatrix} \tag{4}$$

where

$$a_i=\partial v_{ix}/\partial x,\quad b_i=\partial v_{iy}/\partial y,\quad c_i=\partial v_{iz}/\partial z,$$
$$h_i=\partial v_{ix}/\partial y+\partial v_{iy}/\partial x,$$
$$g_i=\partial v_{iz}/\partial z+\partial v_{ix}/\partial x,$$
$$f_i=\partial v_{iy}/\partial z+\partial v_{iz}/\partial y.$$

For an isotropic fluid, by proper orientation of axes, all the symmetrical tensors Ψ_i and Φ_i can be diagonalized simultaneously. We define the partial mean hydrostatic pressure for the ith constituent as

$$-3p_i=P_i+Q_i+R_i, \tag{5}$$

so that $\sum_i p_i=p$, the total hydrostatic pressure. The natural generalization for a system of several constituents of the relationships between the components of the stress tensor and the components of the rate-of-pure-strain tensor is

$$\begin{aligned} P_i&=-p_i+\textstyle\sum_j \lambda_{ij}(a_j+b_j+c_j)+\sum_j 2\eta_{ij}a_j, \\ Q_i&=-p_i+\textstyle\sum_j \lambda_{ij}(a_j+b_j+c_j)+\sum_j 2\eta_{ij}b_j, \\ R_i&=-p_i+\textstyle\sum_j \lambda_{ij}(a_j+b_j+c_j)+\sum_j 2\eta_{ij}c_j, \end{aligned} \tag{6}$$

since motion imparted to constituent i will be accompanied by motion of the other constituents in the same direction. Therefore

$$\lambda_{ij}=-\tfrac{2}{3}\eta_{ij}$$

so that

$$\Psi_i=-p_i\mathbf{I}+\textstyle\sum_j 2\eta_{ij}(\Phi_j-\frac{1}{3}\mathbf{I}\nabla\cdot\mathbf{v}_j), \tag{7}$$

where $\mathbf{I}$ is the unit tensor. Let us write

$$\Psi_i=-p_i\mathbf{I}+\mathbf{X}_i, \tag{8}$$

where the tensor $\mathbf{X}_i$ is given by

$$\mathbf{X}_i=\textstyle\sum_j 2\eta_{ij}(\Phi_j-\frac{1}{3}\mathbf{I}\nabla\cdot\mathbf{v}_j). \tag{9}$$

It can readily be shown that

$$(\mathbf{X}_i\cdot\nabla)\cdot\mathbf{v}_i=\textstyle\sum_j 2\eta_{ij}\{(a_i-\frac{1}{3}\nabla\cdot\mathbf{v}_i)(a_j-\frac{1}{3}\nabla\cdot\mathbf{v}_j)+(b_i-\frac{1}{3}\nabla\cdot\mathbf{v}_i)(b_j-\frac{1}{3}\nabla\cdot\mathbf{v}_j)$$
$$+(c_i-\frac{1}{3}\nabla\cdot\mathbf{v}_i)(c_j-\frac{1}{3}\nabla\cdot\mathbf{v}_j)+\tfrac{1}{2}(h_ih_j+g_ig_j+f_if_j)\} \tag{10}$$

which reduces in the case of a one-component fluid to twice the Rayleigh dissipation function for viscosity.[3]

The equation of motion for the ith constituent can now be written:

$$\rho_i d\mathbf{v}_i/dt=\rho_i\mathbf{F}_i+\nabla\cdot\Psi_i, \tag{11}$$

from which we obtain the energy equation,

$$\rho_i\frac{dv_i^2/2}{dt}=\mathbf{F}_i\cdot\rho_i\mathbf{v}_i+\mathbf{v}_i\cdot(\nabla\cdot\Psi_i)=\mathbf{F}_i\cdot\rho_i\mathbf{v}_i+\nabla\cdot(\Psi_i\cdot\mathbf{v}_i)-(\Psi_i\cdot\nabla)\cdot\mathbf{v}_i. \tag{12}$$

In these equations Ψ_i is the partial stress tensor of Eqs. (7) and (8) and $\mathbf{F}_i$ is the external force acting on unit mass of substance i in the fluid.

Consider now the three terms on the right of Eq. (12) contributing to the increase of the kinetic

[2] See L. Page, *Introduction to Theoretical Physics* (D. Van Nostrand Company, Inc., New York, 1935), second edition, p. 254.

[3] Lord Rayleigh, *The Theory of Sound* (Dover Publications, New York, 1896), second revised edition, Vol. II, p. 315.

energy of the fluid element. The first, $\mathbf{F}_i \cdot \rho_i \mathbf{v}_i$, gives the rate at which external forces perform work on the element. If $\mathbf{F}_i$ is derivable from a potential function, then this term gives simply the rate of decrease of potential energy. For an element of volume τ, the second term can be written

$$\int_\tau \nabla \cdot (\mathbf{\Psi}_i \cdot \mathbf{v}_i) d\tau = \int_\sigma \mathbf{v}_i \cdot \mathbf{\Psi}_i \cdot d\boldsymbol{\sigma}. \tag{13}$$

But $\mathbf{\Psi}_i \cdot d\boldsymbol{\sigma}$ is the force acting on surface $d\sigma$ as a result of the partial stress $\mathbf{\Psi}_i$, so that $\mathbf{v}_i \cdot \mathbf{\Psi}_i \cdot d\boldsymbol{\sigma}$ is the work done per unit time on $d\sigma$ moving with the fluid, without change in size or shape of the fluid element. On the other hand, the third term, $(\mathbf{\Psi}_i \cdot \nabla) \cdot \mathbf{v}_i$, represents work done on the element in a thermodynamic sense, tending to increase the internal energy E_i by changing size and shape. If we consider as a thermodynamic system a unit mass of constituent i in the fluid, we may therefore write

$$\rho_i dE_i/dt + \nabla \cdot \mathbf{Q}_i = (\mathbf{\Psi}_i \cdot \nabla) \cdot \mathbf{v}_i, \tag{14}$$

where E_i is the internal energy per unit mass of substance i in the fluid and $\mathbf{Q}_i$ is the heat flow vector for this thermodynamic system. According to Eq. (8)

$$(\mathbf{\Psi}_i \cdot \nabla) \cdot \mathbf{v}_i = -p_i \nabla \cdot \mathbf{v}_i + (\mathbf{X}_i \cdot \nabla) \cdot \mathbf{v}_i, \tag{15}$$

where the second term on the right is given by Eq. (10). Thus,

$$\rho_i dE_i/dt + \nabla \cdot \mathbf{Q}_i = -p_i \nabla \cdot \mathbf{v}_i + (\mathbf{X}_i \cdot \nabla) \cdot \mathbf{v}_i. \tag{16}$$

Using Eqs. (14), (12), and (8), we obtain

$$\rho_i dE_i/dt + \nabla \cdot \mathbf{Q}_i = \mathbf{F}_i \cdot \rho_i \mathbf{v}_i - \nabla \cdot (p_i \mathbf{v}_i) + \nabla \cdot (\mathbf{X}_i \cdot \mathbf{v}_i) - \rho_i \frac{dv_i^2/2}{dt}. \tag{17}$$

At this point it is necessary to introduce partial pressures as thermodynamic functions and to develop the relations for the individual constituents of a multi-component system using these convenient functions. The energy E and entropy S per unit mass of system can be written as

$$\rho E = \sum_i \rho_i E_i, \quad \rho S = \sum_i \rho_i S_i, \tag{18}$$

where E_i is the energy; S_i, the entropy, per unit mass of substance i; and $\rho = \sum_i \rho_i$ is the total density. But

$$dE = TdS - pd(1/\rho) + \sum_i \mu_i d(\rho_i/\rho), \tag{19}$$

where μ_i is the chemical potential or free energy per unit mass of substance i. Therefore,

$$d(\textstyle\sum_i \rho_i E_i/\rho) = Td(\sum_i \rho_i S_i/\rho) - pd(1/\rho) + \sum_i \mu_i d(\rho_i/\rho). \tag{20}$$

Define partial pressure p_i so that

$$E_i = TS_i - p_i(1/\rho_i) + \mu_i. \tag{21}$$

Then

$$\textstyle\sum_i \rho_i E_i/\rho = T \sum_i \rho_i S_i/\rho - \sum_i p_i(1/\rho) + \sum_i \mu_i \rho_i/\rho, \tag{22}$$

$$d(\textstyle\sum_i \rho_i E_i/\rho) = Td(\sum_i \rho_i S_i/\rho) - \sum_i p_i d(1/\rho) + \sum_i \mu_i d(\rho_i/\rho) + (\sum_i \rho_i S_i/\rho) dT - 1/\rho \sum_i dp_i + \sum_i (\rho_i/\rho) d\mu_i. \tag{23}$$

It is, therefore, consistent to let

$$\textstyle\sum_i p_i = p \tag{24}$$

so that from Eqs. (20), (23), and (18),

$$SdT - (1/\rho)dp + \textstyle\sum_i (\rho_i/\rho) d\mu_i = 0, \tag{25}$$

which is the well-known Gibbs-Duhem equation. We shall identify the thermodynamic partial pres-

sures defined by Eq. (21) with the hydrostatic partial pressures of Eq. (5). Differentiation of Eq. (21) gives

$$dE_i = TdS_i - p_i d(1/\rho_i) + S_i dT - (1/\rho_i)dp_i + d\mu_i. \tag{26}$$

But

$$dE_i = TdS_i - p_i d(1/\rho_i) \tag{27}$$

so that

$$S_i dT - (1/\rho_i)dp_i + d\mu_i = 0. \tag{28}$$

From Eqs. (2) and (27) we obtain

$$\rho_i dE_i/dt = \rho_i T dS_i/dt - p_i \nabla \cdot \mathbf{v}_i. \tag{29}$$

Let

$$\begin{aligned} H_i &= E_i + p_i/\rho_i = \mu_i + TS_i, \\ A_i &= E_i - TS_i = \mu_i - p_i/\rho_i, \\ F_i &= E_i - TS_i + p_i/\rho_i = \mu_i, \end{aligned} \tag{30}$$

where H_i, A_i, and F_i are the partial enthalpy, work function, and free energy, respectively, per unit mass of substance i in the system. According to Eq. (27)

$$\begin{aligned} dH_i &= TdS_i + (1/\rho_i)dp_i, \\ dA_i &= -S_i dT - p_i d(1/\rho_i), \\ dF_i &= -S_i dT + (1/\rho_i)dp_i. \end{aligned} \tag{31}$$

The conditions for exactness of the differentials in Eqs. (27) and (31) require that

$$\begin{aligned} (\partial S_i/\partial p_i)_{\rho i} &= 1/\rho_i^2 (\partial \rho_i/\partial T)_{S_i}, \\ (\partial S_i/\partial \rho_i)_{p i} &= -1/\rho_i^2 (\partial p_i/\partial T)_{S_i}, \\ (\partial S_i/\partial \rho_i)_T &= -1/\rho_i^2 (\partial p_i/\partial T)_{\rho i}, \\ (\partial S_i/\partial p_i)_T &= 1/\rho_i^2 (\partial \rho_i/\partial T)_{p i}, \end{aligned} \tag{32}$$

so that a set of Maxwell's relations holds for each substance i in the system.

Returning now to consideration of motion of a fluid we combine Eqs. (16) and (17) with Eq. (29).

$$\rho_i T dS_i/dt + \nabla \cdot \mathbf{Q}_i = (\mathbf{X}_i \cdot \nabla) \cdot \mathbf{v}_i = \mathbf{F}_i \cdot \rho_i \mathbf{v}_i - \mathbf{v}_i \cdot \nabla p_i + \nabla \cdot (\mathbf{X}_i \cdot \mathbf{v}_i) - \rho_i \frac{dv_i^2/2}{dt} \tag{33}$$

so that

$$\begin{aligned} T\{\rho_i dS_i/dt + \nabla \cdot (\mathbf{Q}_i/T)\} &= -(\mathbf{Q}_i/T) \cdot \nabla T + (\mathbf{X}_i \cdot \nabla) \cdot \mathbf{v}_i \\ &= -(\mathbf{Q}_i/T) \cdot \nabla T - \mathbf{v}_i \cdot (\nabla p_i - \rho_i \mathbf{F}_i) + \nabla \cdot (\mathbf{X}_i \cdot \mathbf{v}_i) - \rho_i \frac{dv_i^2/2}{dt}. \end{aligned} \tag{34}$$

But the entropy flow vector is defined by

$$\mathbf{S}_i = \mathbf{Q}_i/T. \tag{35}$$

Therefore, if $2\theta_i$ is the local entropy dissipation per unit mass,

$$2\rho_i T\theta_i \equiv T(\rho_i dS_i/dt + \nabla \cdot \mathbf{S}_i). \tag{36}$$

According to the second law of thermodynamics, θ_i cannot assume negative values. Hence,

$$2\rho_i T\theta_i = -\mathbf{S}_i \cdot \nabla T + (\mathbf{X}_i \cdot \nabla) \cdot \mathbf{v}_i \geq 0, \tag{37a}$$

$$2\rho_i T\theta_i = -\mathbf{S}_i \cdot \nabla T - \mathbf{v}_i \cdot (\nabla p_i - \rho_i \mathbf{F}_i) + \nabla \cdot (\mathbf{X}_i \cdot \mathbf{v}_i) - \rho_i \frac{dv_i^2/2}{dt} \geq 0. \tag{37b}$$

Subtraction of Eq. (37b) from Eq. (37a) gives

$$\mathbf{v}_i \cdot (\nabla p_i - \rho_i \mathbf{F}_i - \nabla \cdot \mathbf{X}_i + \rho_i d\mathbf{v}_i/dt) = 0, \tag{38}$$

a result which can also be obtained by combination of Eq. (8) with Eqs. (11) or (12). Summing over the index i we obtain the general relations for local entropy dissipation for hydrodynamic flow. The total dissipation per unit mass of solution at a given point in time and space is the sum of the dissipations for the individual flowing constituents whose motions are confluent at that point. Thus,

$$\rho\theta=\sum_i \rho_i\theta_i. \tag{39}$$

Therefore

$$2\rho T\theta=T(\textstyle\sum_i \rho_i dS_i/dt+\nabla\cdot\mathbf{S})\geq 0 \tag{40a}$$

$$=-\mathbf{S}\cdot\nabla T+\textstyle\sum_i(\mathbf{X}_i\cdot\nabla)\cdot\mathbf{v}_i\geq 0 \tag{40b}$$

$$=-\mathbf{S}\cdot\nabla T-\textstyle\sum_i \mathbf{v}_i\cdot(\nabla p_i-\rho_i\mathbf{F}_i)+\sum_i\nabla\cdot(\mathbf{X}_i\cdot\mathbf{v}_i)-\sum_i\rho_i\dfrac{dv_i^2/2}{dt}\geq 0, \tag{40c}$$

where we have written $\sum_i \mathbf{S}_i=\mathbf{S}$, the total entropy flow vector. According to Eq. (35), the total heat flow vector is given by $\mathbf{Q}=T\mathbf{S}$.

We shall use the term "energy dissipation" to indicate the function $T\theta$. The total energy dissipation for an element of fluid of volume τ is obtained from Eq. (40c):

$$-\int_\tau\{\mathbf{S}\cdot\nabla T+\textstyle\sum_i \mathbf{v}_i\cdot(\nabla p_i-\rho_i\mathbf{F}_i)\}d\tau+\sum_i\int_\sigma \mathbf{v}_i\cdot\mathbf{X}_i\cdot d\boldsymbol{\sigma}-\sum_i\int_\tau\rho_i\frac{dv_i^2/2}{dt}d\tau\geq 0. \tag{41}$$

It can be considered as arising out of three processes. The first volume integral represents dissipation related to transport of heat and mass in the fluid. The other volume integral expresses dissipation associated with deceleration of the fluid element—distribution of its kinetic energy of macroscopic motion among the molecules of the fluid. Finally, the surface integral gives the work done by the viscous forces, acting on the fluid element as though it were a rigid body, i.e., without change in size or shape. (See the interpretation of the surface integral in Eq. (13).)

We now restrict our further discussion by the following assumptions:

(1) $$\int_\sigma \mathbf{v}_i\cdot\mathbf{X}_i\cdot d\boldsymbol{\sigma}=\int_\tau\rho_i\frac{dv_i^2/2}{dt}d\tau \tag{42a}$$

or

$$\nabla\cdot(\mathbf{X}_i\cdot\mathbf{v}_i)=\rho_i\frac{dv_i^2/2}{dt}. \tag{42b}$$

We are assuming here essentially that the entire acceleration of any fluid element is produced by viscous forces alone, acting on the element as though it were rigid. Thus, we shall not consider the phenomena of "pressure flow" or bulk motion of the fluid, but rather those associated with diffusion of the fluid constituents, generally referred to as transport processes.

(2) The external force is derivable from a potential.

$$\mathbf{F}_i=-\nabla\phi_i. \tag{43}$$

Equation (38) now becomes

$$-\mathbf{v}_i\cdot(\nabla p_i+\rho_i\nabla\phi_i)=(\mathbf{X}_i\cdot\nabla)\cdot\mathbf{v}_i, \tag{44}$$

and the energy dissipation of Eq. (40c) becomes

$$2\rho T\theta=-\mathbf{S}\cdot\nabla T-\textstyle\sum_i \mathbf{v}_i\cdot(\nabla p_i+\rho_i\nabla\phi_i)\geq 0. \tag{45}$$

Define

$$\mathbf{J}_i\equiv\rho_i\mathbf{v}_i \quad\text{and}\quad \Pi_i\equiv\mu_i+\phi_i. \tag{46}$$

Then, using Eq. (28) we obtain

$$2\rho T\theta=-(\mathbf{S}+\textstyle\sum_i S_i\mathbf{J}_i)\cdot\nabla T-\sum_i \mathbf{J}_i\cdot\nabla\Pi_i\geq 0. \tag{47}$$

This expression appears in the form of Onsager's dissipation function for the case of interacting, simultaneous transport processes.[4] Let

$$\mathbf{J}_i=-\textstyle\sum_j a_{ij}\nabla\Pi_j-b_i\nabla T, \tag{48}$$

$$\mathbf{S}+\textstyle\sum_i S_i\mathbf{J}_i=-\sum_i b_i\nabla\Pi_i-c\nabla T, \tag{49}$$

where we employ the same coefficients b_i in both equations in conformity with Onsager's reciprocal relations. According to these relations, furthermore,

$$a_{ij}=a_{ji}. \tag{50}$$

[4] L. Onsager, Phys. Rev. 37, 405 (1931); 38, 2265 (1931).

Substitution into Eq. (47) gives

$$\sum_{ij} a_{ij}\nabla\Pi_i\cdot\nabla\Pi_j+2\sum_i b_i\nabla\Pi_i\cdot\nabla T +c(\nabla T)^2\geq 0, \quad (51)$$

so that, since the relation must hold for any choice of $\nabla\Pi_i$ and ∇T, the determinant

$$\begin{vmatrix} a_{11} & a_{12} & \cdots & a_{1n} & b_1 \\ a_{12} & a_{22} & \cdots & a_{2n} & b_2 \\ \cdots & & & & \\ a_{1n} & a_{2n} & \cdots & a_{nn} & b_n \\ b_1 & b_2 & \cdots & b_n & c \end{vmatrix} \geq 0 \quad (52)$$

and each of its principal minors must likewise be non-negative. Let

$$b_i=\sum_j a_{ij}\sigma_j. \quad (53)$$

Then

$$\begin{aligned} \mathbf{J}_i &= -\sum_j a_{ij}(\nabla\Pi_j+\sigma_j\nabla T), \\ \mathbf{S} &= \sum_i(\sigma_i-S_i)\mathbf{J}_i-(c-\textstyle\sum_{ij}a_{ij}\sigma_i\sigma_j)\nabla T, \quad (54) \\ \mathbf{Q} &= \sum_i TS_i^*\mathbf{J}_i-\lambda\nabla T, \end{aligned}$$

where $S_i^*=\sigma_i-S_i$ is the entropy of transport per unit mass of substance i and $\lambda=T(c-\sum_{ij}a_{ij}\sigma_i\sigma_j)$ is the coefficient of thermal conductivity. We may easily show by Eq. (52) that $\lambda\geq 0$. Expansion of the determinant in terms of the elements of its last row and last column gives

$$-\sum_i b_i(\sum_j b_j a_{ij}^*)+c|a_{mn}|\geq 0,$$

where the asterisk denotes the co-factor of the element a_{ij} in the determinant $|a_{mn}|$. But from Eq. (53),

$$\sigma_i=\sum_j b_j a_{ij}^*/|a_{mn}|,$$

so that $c\geq\sum_i b_i\sigma_i=\sum_{ij}a_{ij}\sigma_i\sigma_j$ and therefore $\lambda\geq 0$. Elimination of the coefficients σ_i and c gives

$$\mathbf{J}_i=-\sum_j a_{ij}\{\nabla\Pi_j+(S_j+S_j^*)\nabla T\}, \quad (55)$$

$$\mathbf{Q}=-T\sum_{ij}a_{ij}S_i^*\nabla\Pi_j -\{T\sum_{ij}a_{ij}S_i^*(S_j+S_j^*)+\lambda\}\nabla T. \quad (56)$$

Alternatively, using Eq. (28) we may write

$$\mathbf{J}_i=-\sum_j a_{ij}\{(\nabla p_j)/\rho_j+\nabla\phi_j+S_j^*\nabla T\}, \quad (57)$$

$$\mathbf{Q}=-T\sum_{ij}a_{ij}S_i^*\{(\nabla p_j)/\rho_j+\nabla\phi_j\} -(T\sum_{ij}a_{ij}S_i^*S_j^*+\lambda)\nabla T. \quad (58)$$

The physical interpretation of the coefficients a_{ij} is apparent if we write

$$\mathbf{v}_i=-\sum_j a_{ij}/\rho_i\{\nabla\Pi_j+(S_j+S_j^*)\nabla T\}. \quad (59)$$

We perceive that

$$a_{ij}=\rho_i U_{ij}, \quad (60)$$

where U_{ij} is the mobility of the ith constituent when the jth constituent is subject to unit force per unit mass. The force on a unit mass of constituent j arising from its presence in a temperature gradient is $-(S_j+S_j^*)\nabla T$ when Π_j is uniform. According to Eq. (52), the determinant $|U_{ij}|=|a_{ij}|/\rho_1\rho_2\cdots\rho_n\geq 0$ and any of its principal minors are likewise non-negative. From Eq. (50), $\rho_i U_{ij}=\rho_j U_{ji}$.

From Eqs. (47), (55), and (54) we find

$$2\rho T\theta=-\sum_i\mathbf{J}_i\cdot\{\nabla\Pi_i+(S_i+S_i^*)\nabla T\} +\lambda/T(\nabla T)^2\geq 0,$$

$$2\rho T\theta=\sum_{ij}\mathbf{J}_i\cdot\mathbf{J}_j a_{ij}^*/|a_{mn}|+\lambda/T(\nabla T)^2\geq 0,$$

where a_{ij}^* is the co-factor of a_{ij} in the determinant $|a_{mn}|$. The elements of the adjoint determinant

$$r_{ij}=a_{ij}^*/|a_{mn}| \quad (61)$$

are coefficients of flow resistance. The determinant $|r_{ij}|$ and each of its principal minors are non-negative. Also $r_{ij}=r_{ji}$.

$$2\rho T\theta=\sum_{ij}r_{ij}\mathbf{J}_i\cdot\mathbf{J}_j+\lambda/T(\nabla T)^2\geq 0. \quad (62)$$

SPECIAL STATES OF THE SYSTEM

An important condition of a flowing fluid is the so-called steady state. From Eqs. (40a) and (47),

$$T(\sum_i\rho_i dS_i/dt+\nabla\cdot\mathbf{S}) =-(\mathbf{S}+\sum_i S_i\mathbf{J}_i)\cdot\nabla T-\sum_i\mathbf{J}_i\cdot\nabla\Pi_i \quad (63)$$

so that, acording to Eqs. (3) and (30),

$$T\sum_i\rho_i\partial S_i/\partial t=-\nabla\cdot\mathbf{Q}-\sum_i\mathbf{J}_i\cdot\nabla(H_i+\phi_i). \quad (64)$$

Also from Eq. (1),

$$\partial\rho_i/\partial t=-\nabla\cdot\mathbf{J}_i. \quad (65)$$

In the steady state $\partial S_i/\partial t=0$ and $\partial\rho_i/\partial t=0$. These conditions defining the steady state are sufficient to require that every property at a given point in the system be independent of time. Therefore

$$\nabla\cdot\mathbf{J}_i=0 \text{ and } \nabla\cdot\{\mathbf{Q}+\sum_i\mathbf{J}_i(H_i+\phi_i)\}=0. \quad (66)$$

In the case of a closed system the components of $\mathbf{J}_i$ normal to the surface of the fluid must vanish

a result which can also be obtained by combination of Eq. (8) with Eqs. (11) or (12). Summing over the index i we obtain the general relations for local entropy dissipation for hydrodynamic flow. The total dissipation per unit mass of solution at a given point in time and space is the sum of the dissipations for the individual flowing constituents whose motions are confluent at that point. Thus,

$$\rho\theta=\sum_i \rho_i\theta_i. \tag{39}$$

Therefore

$$2\rho T\theta=T(\textstyle\sum_i \rho_i dS_i/dt+\nabla\cdot\mathbf{S})\geq 0 \tag{40a}$$

$$=-\mathbf{S}\cdot\nabla T+\textstyle\sum_i(\mathbf{X}_i\cdot\nabla)\cdot\mathbf{v}_i\geq 0 \tag{40b}$$

$$=-\mathbf{S}\cdot\nabla T-\textstyle\sum_i \mathbf{v}_i\cdot(\nabla p_i-\rho_i\mathbf{F}_i)+\sum_i \nabla\cdot(\mathbf{X}_i\cdot\mathbf{v}_i)-\sum_i \rho_i\dfrac{dv_i^2/2}{dt}\geq 0, \tag{40c}$$

where we have written $\sum_i \mathbf{S}_i=\mathbf{S}$, the total entropy flow vector. According to Eq. (35), the total heat flow vector is given by $\mathbf{Q}=T\mathbf{S}$.

We shall use the term "energy dissipation" to indicate the function $T\theta$. The total energy dissipation for an element of fluid of volume τ is obtained from Eq. (40c):

$$-\int_\tau\{\mathbf{S}\cdot\nabla T+\textstyle\sum_i \mathbf{v}_i\cdot(\nabla p_i-\rho_i\mathbf{F}_i)\}d\tau+\sum_i\int_\sigma \mathbf{v}_i\cdot\mathbf{X}_i\cdot d\sigma-\sum_i\int_\tau \rho_i\dfrac{dv_i^2/2}{dt}d\tau\geq 0. \tag{41}$$

It can be considered as arising out of three processes. The first volume integral represents dissipation related to transport of heat and mass in the fluid. The other volume integral expresses dissipation associated with deceleration of the fluid element—distribution of its kinetic energy of macroscopic motion among the molecules of the fluid. Finally, the surface integral gives the work done by the viscous forces, acting on the fluid element as though it were a rigid body, i.e., without change in size or shape. (See the interpretation of the surface integral in Eq. (13).)

We now restrict our further discussion by the following assumptions:

(1) $$\int_\sigma \mathbf{v}_i\cdot\mathbf{X}_i\cdot d\sigma=\int_\tau \rho_i\dfrac{dv_i^2/2}{dt}d\tau \tag{42a}$$

or

$$\nabla\cdot(\mathbf{X}_i\cdot\mathbf{v}_i)=\rho_i\dfrac{dv_i^2/2}{dt}. \tag{42b}$$

We are assuming here essentially that the entire acceleration of any fluid element is produced by viscous forces alone, acting on the element as though it were rigid. Thus, we shall not consider the phenomena of "pressure flow" or bulk motion of the fluid, but rather those associated with diffusion of the fluid constituents, generally referred to as transport processes.

(2) The external force is derivable from a potential.

$$\mathbf{F}_i=-\nabla\phi_i. \tag{43}$$

Equation (38) now becomes

$$-\mathbf{v}_i\cdot(\nabla p_i+\rho_i\nabla\phi_i)=(\mathbf{X}_i\cdot\nabla)\cdot\mathbf{v}_i, \tag{44}$$

and the energy dissipation of Eq. (40c) becomes

$$2\rho T\theta=-\mathbf{S}\cdot\nabla T-\textstyle\sum_i \mathbf{v}_i\cdot(\nabla p_i+\rho_i\nabla\phi_i)\geq 0. \tag{45}$$

Define

$$\mathbf{J}_i\equiv\rho_i\mathbf{v}_i \quad\text{and}\quad \Pi_i\equiv\mu_i+\phi_i. \tag{46}$$

Then, using Eq. (28) we obtain

$$2\rho T\theta=-(\mathbf{S}+\textstyle\sum_i S_i\mathbf{J}_i)\cdot\nabla T-\sum_i \mathbf{J}_i\cdot\nabla\Pi_i\geq 0. \tag{47}$$

This expression appears in the form of Onsager's dissipation function for the case of interacting, simultaneous transport processes.[4] Let

$$\mathbf{J}_i=-\textstyle\sum_j a_{ij}\nabla\Pi_j-b_i\nabla T, \tag{48}$$

$$\mathbf{S}+\textstyle\sum_i S_i\mathbf{J}_i=-\sum_i b_i\nabla\Pi_i-c\nabla T, \tag{49}$$

where we employ the same coefficients b_i in both equations in conformity with Onsager's reciprocal relations. According to these relations, furthermore,

$$a_{ij}=a_{ji}. \tag{50}$$

[4] L. Onsager, Phys. Rev. 37, 405 (1931); 38, 2265 (1931).

Substitution into Eq. (47) gives

$$\sum_{ij} a_{ij}\nabla\Pi_i\cdot\nabla\Pi_j+2\sum_i b_i\nabla\Pi_i\cdot\nabla T+c(\nabla T)^2\geq 0, \quad (51)$$

so that, since the relation must hold for any choice of $\nabla\Pi_i$ and ∇T, the determinant

$$\begin{vmatrix} a_{11} & a_{12} & \cdots & a_{1n} & b_1 \\ a_{12} & a_{22} & \cdots & a_{2n} & b_2 \\ \cdots & & & & \\ a_{1n} & a_{2n} & \cdots & a_{nn} & b_n \\ b_1 & b_2 & \cdots & b_n & c \end{vmatrix} \geq 0 \quad (52)$$

and each of its principal minors must likewise be non-negative. Let

$$b_i=\sum_j a_{ij}\sigma_j. \quad (53)$$

Then

$$\begin{aligned} \mathbf{J}_i &= -\sum_j a_{ij}(\nabla\Pi_j+\sigma_j\nabla T), \\ \mathbf{S} &= \sum_i(\sigma_i-S_i)\mathbf{J}_i-(c-\textstyle\sum_{ij}a_{ij}\sigma_i\sigma_j)\nabla T, \quad (54) \\ \mathbf{Q} &= \sum_i TS_i^*\mathbf{J}_i-\lambda\nabla T, \end{aligned}$$

where $S_i^*=\sigma_i-S_i$ is the entropy of transport per unit mass of substance i and $\lambda=T(c-\sum_{ij}a_{ij}\sigma_i\sigma_j)$ is the coefficient of thermal conductivity. We may easily show by Eq. (52) that $\lambda\geq 0$. Expansion of the determinant in terms of the elements of its last row and last column gives

$$-\sum_i b_i(\sum_j b_j a_{ij}^*)+c|a_{mn}|\geq 0,$$

where the asterisk denotes the co-factor of the element a_{ij} in the determinant $|a_{mn}|$. But from Eq. (53),

$$\sigma_i=\sum_j b_j a_{ij}^*/|a_{mn}|,$$

so that $c\geq\sum_i b_i\sigma_i=\sum_{ij}a_{ij}\sigma_i\sigma_j$ and therefore $\lambda\geq 0$. Elimination of the coefficients σ_i and c gives

$$\mathbf{J}_i=-\sum_j a_{ij}\{\nabla\Pi_j+(S_j+S_j^*)\nabla T\}, \quad (55)$$

$$\mathbf{Q}=-T\sum_{ij}a_{ij}S_i^*\nabla\Pi_j-\{T\sum_{ij}a_{ij}S_i^*(S_j+S_j^*)+\lambda\}\nabla T. \quad (56)$$

Alternatively, using Eq. (28) we may write

$$\mathbf{J}_i=-\sum_j a_{ij}\{(\nabla p_j)/\rho_j+\nabla\phi_j+S_j^*\nabla T\}, \quad (57)$$

$$\mathbf{Q}=-T\sum_{ij}a_{ij}S_i^*\{(\nabla p_j)/\rho_j+\nabla\phi_j\}-(T\sum_{ij}a_{ij}S_i^*S_j^*+\lambda)\nabla T. \quad (58)$$

The physical interpretation of the coefficients a_{ij} is apparent if we write

$$\mathbf{v}_i=-\sum_j a_{ij}/\rho_i\{\nabla\Pi_j+(S_j+S_j^*)\nabla T\}. \quad (59)$$

We perceive that

$$a_{ij}=\rho_i U_{ji}, \quad (60)$$

where U_{ij} is the mobility of the ith constituent when the jth constituent is subject to unit force per unit mass. The force on a unit mass of constituent j arising from its presence in a temperature gradient is $-(S_j+S_j^*)\nabla T$ when Π_j is uniform. According to Eq. (52), the determinant $|U_{ij}|=|a_{ij}|/\rho_1\rho_2\cdots\rho_n\geq 0$ and any of its principal minors are likewise non-negative. From Eq. (50), $\rho_i U_{ij}=\rho_j U_{ji}$.

From Eqs. (47), (55), and (54) we find

$$2\rho T\theta=-\sum_i\mathbf{J}_i\cdot\{\nabla\Pi_i+(S_i+S_i^*)\nabla T\}+\lambda/T(\nabla T)^2\geq 0,$$

$$2\rho T\theta=\sum_{ij}\mathbf{J}_i\cdot\mathbf{J}_j a_{ij}^*/|a_{mn}|+\lambda/T(\nabla T)^2\geq 0,$$

where a_{ij}^* is the co-factor of a_{ij} in the determinant $|a_{mn}|$. The elements of the adjoint determinant

$$r_{ij}=a_{ij}^*/|a_{mn}| \quad (61)$$

are coefficients of flow resistance. The determinant $|r_{ij}|$ and each of its principal minors are non-negative. Also $r_{ij}=r_{ji}$.

$$2\rho T\theta=\sum_{ij}r_{ij}\mathbf{J}_i\cdot\mathbf{J}_j+\lambda/T(\nabla T)^2\geq 0. \quad (62)$$

SPECIAL STATES OF THE SYSTEM

An important condition of a flowing fluid is the so-called steady state. From Eqs. (40a) and (47),

$$T(\sum_i\rho_i dS_i/dt+\nabla\cdot\mathbf{S})=-(\mathbf{S}+\sum_i S_i\mathbf{J}_i)\cdot\nabla T-\sum_i\mathbf{J}_i\cdot\nabla\Pi_i \quad (63)$$

so that, acording to Eqs. (3) and (30),

$$T\sum_i\rho_i\partial S_i/\partial t=-\nabla\cdot\mathbf{Q}-\sum_i\mathbf{J}_i\cdot\nabla(H_i+\phi_i). \quad (64)$$

Also from Eq. (1),

$$\partial\rho_i/\partial t=-\nabla\cdot\mathbf{J}_i. \quad (65)$$

In the steady state $\partial S_i/\partial t=0$ and $\partial\rho_i/\partial t=0$. These conditions defining the steady state are sufficient to require that every property at a given point in the system be independent of time. Therefore

$$\nabla\cdot\mathbf{J}_i=0 \text{ and } \nabla\cdot\{\mathbf{Q}+\sum_i\mathbf{J}_i(H_i+\phi_i)\}=0. \quad (66)$$

In the case of a closed system the components of $\mathbf{J}_i$ normal to the surface of the fluid must vanish

at the surface, so that

$$\int_\tau \nabla \cdot \mathbf{Q} d\tau = 0 \tag{67}$$

when integrated over the entire fluid. However, it is important to note that flow of mass in the interior of the fluid and tangential to the surface is not excluded and, moreover, there may even be sources and sinks of heat flow, whose total contribution must, however, vanish. If the system is also adiabatically insulated only tangential components of $\mathbf{Q}$ as well as of $\mathbf{J}_i$ are possible at the surface. The energy dissipation, of course, need not vanish in the steady state but continues to be given by Eqs. (40b), (47), or (62). Equation (40a) becomes

$$2\rho T\theta = T(\textstyle\sum_i \mathbf{J}_i \cdot \nabla S_i + \nabla \cdot \mathbf{S}) \geq 0. \tag{68}$$

The condition $\mathbf{J}_i = 0$ throughout the fluid will occur, according to Eqs. (55) and (57) only when

$$\nabla \Pi_j + (S_j + S_j^*)\nabla T = (\nabla p_j)/\rho_j + \nabla \phi_j + S_j^* \nabla T = 0 \tag{69}$$

for every j such that $a_{ij} \neq 0$. When every $\mathbf{J}_i = 0$, Eq. (69) must hold for all values of j. The system is then in a state of pure thermal conduction. According to Eq. (54),

$$\mathbf{Q} = -\lambda \nabla T \tag{70}$$

which is Fourier's law of heat conduction. From Eq. (63),

$$T(\textstyle\sum_i \rho_i \partial S_i/\partial t + \nabla \cdot \mathbf{S}) = -\mathbf{S} \cdot \nabla T \geq 0, \tag{71}$$

so that

$$T \textstyle\sum_i \rho_i \partial S_i/\partial t = -\nabla \cdot \mathbf{Q} = \nabla \cdot (\lambda \nabla T). \tag{72}$$

But

$$\partial S_i/\partial t = (C_{p_i}/T)\partial T/\partial t + 1/\rho_i^2 (\partial \rho_i/\partial T)_{p_i} \partial p_i/\partial T \tag{73}$$

where C_{p_i} is the partial specific heat at constant partial pressure.

$$\nabla \cdot (\lambda \nabla T) = \textstyle\sum_i \rho_i C_{p_i} \partial T/\partial t + \sum_i 1/\rho_i^2 (\partial \rho_i/\partial T)_{p_i} \partial p_i/\partial T. \tag{74}$$

In the steady state $\nabla \cdot (\lambda \nabla T) = 0$. If ∇T is small, λ can be considered constant so that in the steady state the temperature must satisfy Laplace's equation. The state of pure thermal conduction is analogous to the condition of a solid in a temperature gradient but must be relatively rare in a fluid.

It is instructive to consider the case of a pure gas in a temperature gradient in the absence of external forces. If $\mathbf{J} = 0$, according to Eq. (69),

$$\nabla p = -\rho S^* \nabla T. \tag{75}$$

If we assume the relation $p = \rho RT$, we find

$$\nabla \ln p = -(S^*/R)\nabla \ln T. \tag{76}$$

Let us suppose the gas is contained in a straight cylindrical tube along whose length is the temperature gradient. Then, as is well known, the phenomenon of thermal transpiration occurs if pressure is sufficiently low so that the mean free path of the molecules is greater than the diameter of the tube. A pressure gradient is established so that

$$d(\ln p)/d(\ln T) = \tfrac{1}{2}. \tag{77}$$

Therefore at this low pressure $S^* = -R/2$. (R is the gas constant per unit mass.) Furthermore, S^* will be constant along the radius of the tube since the properties of the gas are determined throughout by collisions with the wall and not by the infrequent collisions between gas molecules. Now if we increase the pressure of gas in the tube, the wall will affect only a small surface layer of the gas and we can no longer expect S^* to be constant along the radius. With the increase in pressure the thermal transpiration effect disappears. In such a situation Eq. (75) cannot be satisfied and $\mathbf{J}$ does not vanish. Instead, a circulation of the gas occurs with the surface layer flowing toward the hot end of the tube and a return flow in the interior. All stages between the extremes of maximum pressure gradient with no flow and maximum flow with no pressure gradient are possible depending on the radial variation of S^*. Since we may write

$$\nabla \rho = (\partial \rho/\partial p)\nabla p + (\partial \rho/\partial T)\nabla T, \tag{78}$$

clearly the density gradient should depend only on the coefficient of thermal expansion in the case of $\nabla p = 0$. For a liquid we would likewise expect a difference between S^* in the surface and

in the interior and the consequent circulation. However, for a liquid we may not be justified in neglecting external forces, particularly in the surface.

The condition of a fluid in which no energy dissipation occurs at any point is the state of equilibrium. According to Eq. (51) this requires that everywhere, for each species i

$$\nabla\Pi_i=0 \quad \text{and} \quad \nabla T=0. \tag{79}$$

The temperature and each potential Π_i must be constant throughout the system. This of course implies that $\mathbf{Q}$ and $\mathbf{J}_i$ vanish everywhere. Equilibrium is a special case of the steady state. Equation (79) requires

$$\nabla\mu_i=-\nabla\phi_i \quad \text{or} \quad \nabla p_i=-\rho_i\nabla\phi_i. \tag{80}$$

If, for example, $\nabla\phi_i=g\mathbf{k}$ where $\mathbf{k}$ is the unit vector in the upward Z direction and g is the acceleration of gravity, there results the well-known formula

$$dp_i/dz=-\rho_i g \quad \text{or} \quad dp/dz=-\rho g. \tag{81}$$

Similarly if $\Delta\phi_i=e_i\Delta\psi$ where e_i is the electrical charge per unit mass of substance i and ψ, the electrostatic potential

$$\nabla\psi=-(1/e_i)\nabla\mu_i=-(1/e_i\rho_i)\nabla p_i$$
$$=-(1/e\rho)\nabla p, \tag{82}$$

where $e=\sum_i e_i\rho_i/\rho$ is the total electrical charge per unit mass of fluid.

As is well known, a thermodynamically reversible process is one which occurs without energy dissipation, i.e., the system is in equilibrium throughout the process. Therefore, if we consider two points in the system, A and B, at each moment

$$\Pi_{ia}=\Pi_{ib} \quad \text{and} \quad T_a=T_b \tag{83}$$

or

$$d\Pi_{ia}=d\Pi_{ib} \quad \text{and} \quad dT_a=dT_b \tag{84}$$

so that

$$-S_{ia}dT+(1/\rho_{ia})dp_{ia}+d\phi_{ia}$$
$$=-S_{ib}dT+(1/\rho_{ib})dp_{ib}+d\phi_{ib}. \tag{85}$$

Thus, consider an isothermal system of two fluid phases A and B where A is the vapor in equilibrium with liquid B. In the absence of external forces

$$(1/\rho_{ia})dp_{ia}=(1/\rho_{ib})dp_{ib}. \tag{86}$$

The general equations of state relating partial pressures and densities are not known. For ideal gases we write

$$p_{ia}=\rho_{ia}RT/M_i \tag{87}$$

and for ideal liquids

$$p_{ia}=p^0{}_{ia}x_{ib} \text{ (Raoult's law)}, \tag{88}$$

where R is the gas constant per mole; M_i, the molecular weight of substance i; x_{ib}; its mole fraction in the liquid phase; and $p^0{}_{ia}$, its vapor pressure in the pure state. From Eqs. (86) and (88)

$$dp_{ib}=(\rho_{ib}/\rho_{ia})p^0{}_{ia}dx_{ib} \tag{89}$$

which relates the partial pressure of a component of an ideal liquid solution to its mole fraction in the liquid.

Data obtained for non-ideal solutions are generally expressed in the form

$$d\Pi_i=(RT/M_i)d(\ln\rho_i\gamma_i), \tag{90}$$

where γ_i is an appropriate activity coefficient chosen so that under those conditions for which the solution approaches ideality, γ_i approaches unity. Lumped into the factor γ_i may be the effect of external forces, as in the treatment of electrolytes, for example. In this case

$$\phi_i=e_i\psi. \tag{91}$$

In the Debye-Hückel theory for dilute electrolytes the identification

$$e_i d\psi=(RT/M_i)d(\ln\gamma_i)$$

is made, so that

$$d\mu_i=(RT/M_i)d(\ln\rho_i),$$

i.e., apart from interionic attractions and repulsions the solution is considered as ideal. It would appear that the use of Eq. (90) for expressing experimental data with an arbitrarily defined "activity coefficient" does much toward obscuring the nature of the quantities measured. A more direct method would be to seek equations of state of the form

$$\Pi_i=\Pi_i(\rho_1, \rho_2, \cdots \rho_n, T), \tag{92}$$

which in the absence of external forces is equivalent to

$$\mu_i=\mu_i(\rho_1, \rho_2, \cdots \rho_n, T)$$

or

$$p_i=p_i(\rho_1, \rho_2, \cdots \rho_n, T), \tag{93}$$

and in the presence of external forces requires also knowledge of

$$\phi_i=\phi_i(\rho_1, \rho_2, \cdots \rho_n, T). \tag{94}$$

APPLICATION TO PARTICULAR TRANSPORT PROCESSES

Let us now turn to consideration of particular transport processes. We start with isothermal processes. For an isothermal fluid, according to Eqs. (40b) and (10) the energy dissipation is given by

$$\begin{aligned}\sum_{ij} 2\eta_{ij}\{&(a_i-\tfrac{1}{3}\nabla\cdot\mathbf{v}_i)(a_j-\tfrac{1}{3}\nabla\cdot\mathbf{v}_j)\\&+(b_i-\tfrac{1}{3}\nabla\cdot\mathbf{v}_i)(b_j-\tfrac{1}{3}\nabla\cdot\mathbf{v}_j)\\&+(c_i-\tfrac{1}{3}\nabla\cdot\mathbf{v}_i)(c_j-\tfrac{1}{3}\nabla\cdot\mathbf{v}_j)\\&+\tfrac{1}{2}(h_ih_j+g_ig_j+f_if_j)\}\geq 0,\end{aligned} \tag{95}$$

or, if we write $\mathbf{B}_i=\mathbf{\Phi}_i-\frac{1}{3}\mathbf{I}\nabla\cdot\mathbf{v}_i$, the dissipation becomes

$$\sum_{ij} 2\eta_{ij}\mathbf{B}_i:\mathbf{B}_j\geq 0, \tag{96}$$

where $\mathbf{B}_i:\mathbf{B}_j$ is the double product of the two tensors, i.e., the sum of the principal diagonal elements of the tensor which is the product of $\mathbf{B}_i$ and $\mathbf{B}_j$. Therefore, if we use Eqs. (51) and (62),

$$\begin{aligned}\sum_{ij} r_{ij}\mathbf{J}_j\cdot\mathbf{J}_j&=\sum_{ij} a_{ij}\nabla\Pi_i\cdot\nabla\Pi_j\\&=\sum_{ij} 2\eta_j\mathbf{B}_i:\mathbf{B}_j=\sum_{ij} 2\eta_{ij}\mathbf{b}_i\cdot\mathbf{b}_j\geq 0,\end{aligned} \tag{97}$$

where $\mathbf{b}_i$ is the vector formed from the three principal diagonal components of $\mathbf{B}_i$ when the coordinate axes are oriented so as to diagonalize $\mathbf{B}_i$. Thus, $\mathbf{b}_i$ is the vector whose components are $a_i-\frac{1}{3}\nabla\cdot\mathbf{v}_i$, $b_i-\frac{1}{3}\nabla\cdot\mathbf{v}_i$, and $c_i-\frac{1}{3}\nabla\cdot\mathbf{v}_i$ referred to a properly oriented set of coordinate axes. Let

$$\mathbf{b}_i=\sum_l w_{il}\mathbf{J}_l=-\sum_{lm} w_{il}a_{lm}\nabla\Pi_m, \tag{98}$$

where w_{il} is a quantity with dimensions of (length)^2/mass. Then

$$r_{lm}=\sum_{ij} 2\eta_{ij}w_{il}w_{jm}. \tag{99}$$

Since $r_{ij}=r_{ji}$, it follows that $\eta_{ij}=\eta_{ji}$. Furthermore, we see from Eq. (97) that the determinant $|\eta_{ij}|$ and each of its principal minors are non-negative. In particular, for a one-component fluid the viscosity coefficient is non-negative.

Following Onsager[5] we write the generalized form of Fick's law of diffusion for a system of several components as

$$\mathbf{J}_i=-\sum_j D_{ij}\nabla\rho_j, \tag{100}$$

where D_{ij} are the coefficients of diffusion. According to Eq. (55) for an isothermal system

$$\mathbf{J}_i=-\sum_j a_{ij}\nabla\Pi_j, \tag{101}$$

so that, using a relation of the type of Eq. (92), we obtain

$$D_{ij}=\sum_l a_{il}\partial\Pi_l/\partial\rho_j. \tag{102}$$

Therefore,

$$\partial\Pi_l/\partial\rho_j=\sum_i r_{li}D_{ij}=\sum_{imn} 2\eta_{mn}w_{ml}w_{ni}D_{ij}. \tag{103}$$

It is interesting to consider this result for the case of self-diffusion of a single perfect gas in the absence of external forces. We find from Eq. (87)

$$\partial\Pi/\partial\rho=2\eta w^2D=RT/M\rho, \tag{104}$$

so that

$$D=RT/2M\rho w^2\eta. \tag{105}$$

The similarity in form of this equation to the equations of Stokes-Einstein[6] and Eyring[7] is at once apparent. From Eqs. (50) and (102) we obtain the reciprocal relations

$$\sum_i(\partial\Pi_i/\partial\rho_m)D_{ij}=\sum_i(\partial\Pi_i/\partial\rho_j)D_{im}. \tag{106}$$

The dissipation function for isothermal flow may be written

$$\sum_{ijkl} r_{ij}D_{ik}D_{jl}\nabla\rho_k\cdot\nabla\rho_l\geq 0. \tag{107}$$

Closely related to fluid flow is electrolytic conduction. If species i carries an electrical charge e_i per unit mass, then the current density associated with flow of that species is

$$\begin{aligned}\mathbf{I}_i=e_i\mathbf{J}_i&=-\sum_j e_ie_ja_{ij}\nabla(\Pi_j/e_j)\\&=-\sum_j L_{ij}\nabla(\Pi_j/e_j).\end{aligned} \tag{108}$$

The coefficients L_{ij} are the coefficients of con-

[5] L. Onsager, Ann. N. Y. Acad. Sci. **46**, 241 (1945).
[6] A. Einstein, Ann. d. Physik **19**, 289 (1906).
[7] S. Glasstone, K. J. Laidler, and H. Eyring, *Theory of Rate Processes* (McGraw-Hill Book Company, Inc., 1941), first edition, p. 519.

ductance. The dissipation function becomes

$$\sum_{ij}(r_{ij}/e_ie_j)\mathbf{I}_i\cdot\mathbf{I}_j=\sum_{ij}(r_e)_{ij}\mathbf{I}_i\cdot\mathbf{I}_j\geq 0, \quad (109)$$

which is a generalization of the Joule heat. The coefficients $(r_e)_{ij}$ are the coefficients of electrical resistance. Now

$$\nabla\Pi_i/e_i=\sum_j(r_e)_{ij}\mathbf{I}_j, \quad (110)$$

so that if we let $\phi_i=e_i\psi$ where ψ is the electrostatic potential,

$$\nabla(\mu_i/e_i+\psi)=(\nabla p_i)/\rho_ie_i+\nabla\psi=\sum_j(r_e)_{ij}\mathbf{I}_j, \quad (111)$$

which is the generalized form of Ohm's law for fluid solutions. Obviously the determinants $|L_{ij}|$ and $|(r_e)_{ij}|$ as well as each of their principal minors must be non-negative. Also $L_{ij}=L_{ji}$ and $(r_e)_{ij}=(r_e)_{ji}$.

The above conductance equations were obtained under the assumption that every diffusing species carried an electrical charge. More generally, if electrically neutral species are also diffusing, for a charged species i,

$$\mathbf{I}_i=-\sum_j L_{ij}\nabla\Pi_j/e_j-\sum_k e_ia_{ik}\nabla\Pi_k, \quad (112)$$

where $\sum_j$ indicates summation over charged species and $\sum_k$, over neutral. The dissipation function becomes

$$\sum_{ij}(r_e)_{ij}\mathbf{I}_i\cdot\mathbf{I}_j+\sum_{ik}(r_{ik}/e_i)\mathbf{I}_i\cdot\mathbf{J}_k+\sum_{kl}r_{kl}\mathbf{J}_k\cdot\mathbf{J}_l\geq 0. \quad (113)$$

The motion of uncharged constituents as well as that of charged constituents may influence the conduction of electricity in fluids. Thus, Eq. (111) becomes

$$\nabla(\mu_i/e_i+\psi)=(\nabla p_i)/\rho_ie_i+\nabla\psi=\sum_j(r_e)_{ij}\mathbf{I}_j+\sum_k(r_{ik}/e_i)\mathbf{J}_k. \quad (114)$$

The condition for cessation of current was given in Eq. (82). If the fluid is electrically neutral, we see that although there may be gradients in the chemical potentials and partial pressures of individual species there can be no total pressure gradient. We may write

$$\nabla\psi=-1/e_i\sum_j(\partial\mu_i/\partial\rho_j)\nabla\rho_j, \quad (115)$$

where index j is summed over all components, charged or neutral. Thus in general, we must allow the possibility that existence of a gradient of electrostatic potential in a solution will be accompanied by concentration gradients in neutral as well as charged species.

Let us now consider transport phenomena in non-isothermal systems. Using Eq. (92) we write the mass flow vector of Eq. (55) as

$$\mathbf{J}_i=-\sum_{jl}a_{ij}(\partial\Pi_j/\partial\rho_l)\nabla\rho_l-\sum_j a_{ij}(\partial\Pi_j/\partial T+S_j+S_j^*)\nabla T. \quad (116)$$

We may define the thermal diffusion coefficients D_i^T by the equation

$$\mathbf{J}_i=-\sum_j D_{ij}\nabla\rho_j-D_i^T\nabla T. \quad (117)$$

Therefore,

$$D_i^T=\sum_j a_{ij}(\partial\Pi_j/\partial T+S_j+S_j^*)=\sum_j a_{ij}[(1/\rho_j)(\partial p_j/\partial T)+\partial\phi_j/\partial T+S_j^*] \quad (118)$$

and

$$D_{ij}=\sum_l a_{il}\partial\Pi_l/\partial\rho_j$$

as in the isothermal case (Eq. (102)), or

$$a_{ij}=\sum_l D_{il}\partial\rho_l/\partial\Pi_j \quad (119)$$

where

$$\rho_l=\rho_l(\Pi_1,\ \Pi_2,\ \cdots\Pi_n,\ T).$$

Substituting Eq. (119) into Eq. (118) we obtain

$$D_i^T=\sum_{jl}D_{il}(\partial\rho_l/\partial\Pi_j)(\partial\Pi_j/\partial T+S_j+S_j^*)=\sum_l D_{il}\{-(\partial\rho_l/\partial T)u_j+\sum_j(\partial\rho_l/\partial\Pi_j)(S_j+S_j^*)\}. \quad (120)$$

If we define the thermal diffusion ratios as

$$k_l^T=-(\partial\rho_l/\partial T)u_j+\sum_j(\partial\rho_l/\partial\Pi_j)(S_j+S_j^*) \quad (121)$$

we find

$$D_i^T=\sum_l k_l^TD_{il} \quad (122)$$

and

$$\mathbf{J}_i=-\sum_l D_{il}(\nabla\rho_l+k_l^T\nabla T). \quad (123)$$

Under conditions such that mass flow vanishes, i.e., $\mathbf{J}_i=0$ for all species i, in the presence of a temperature gradient (the state described as pure thermal conduction in Eq. (70)), we find the simple relation

$$k_i^T=-d\rho_i/dT \quad (124)$$

so that the thermal diffusion ratios can be determined directly from the observed density

gradients, or knowing the ratios one may calculate the density gradients and thus the extent of separation of the components in a temperature gradient. It has been assumed by some authors[8] that in the steady state of gas mixtures subject to a temperature gradient the condition $\mathbf{J}_i=0$ will hold. But, as we have seen, the steady state need not be a state of pure thermal conduction, so that the $\mathbf{J}_i$ need not vanish. Hence, measurements made on the steady state and interpreted by the theory for the state of pure thermal conduction may well lead to erroneous conclusions. We considered earlier the behavior of a single gas in a temperature gradient in the absence of external forces and found that at normal pressures a circulation of the gas occurs in the steady state so that no pressure gradient is established as in the case of thermal transpiration. As an extreme possibility for a gas mixture we may suppose a similar circulation of each component occurs with the result that the gradients of the individual partial pressures vanish in the steady state. In such an event

$$\nabla\rho_i=\sum_j(\partial\rho_i/\partial p_j)\nabla p_j+(\partial\rho_i/\partial T)\nabla T$$
$$=(\partial\rho_i/\partial T)\nabla T,$$

and the density gradient of each component would depend only on its thermal expansion in the fluid. More likely, a steady-state condition intermediate between the extremes of no flow and of no partial pressure gradients occurs for the various components. The question requires experimental investigation. The general expression for the density gradients, from which the thermal diffusion separation can be calculated, is

$$\nabla\rho_i=-\sum_j d_{ij}\mathbf{J}_j-k_i^T\nabla T, \quad (125)$$

where $d_{ij}=D_{ji}^*/|D_{lm}|$, the asterisk denoting the adjoint of the element D_{ji} in the determinant $|D_{lm}|$.

Another transport process which may appear in non-isothermal fluids is the homogeneous thermoelectric effect. From Eq. (57) we find

$$\nabla\phi_i=-\sum_j r_{ij}\mathbf{J}_j-(1/\rho_i)\nabla p_i-S_i^*\nabla T. \quad (126)$$

For $\phi_i=e_i\psi$, where ψ is the electrostatic potential,

$$\nabla\psi=-\sum_j(r_{ij}/e_i)\mathbf{J}_j$$
$$-(\nabla p_i)/\rho_i e_i-(S_i^*/e_i)\nabla T \quad (127)$$

so that

$$\rho e\nabla\psi=-\sum_{ij}\rho_i r_{ij}\mathbf{J}_j-\nabla p-\rho S^*\nabla T, \quad (128)$$

where e is the total electric charge and S^*, the total entropy of transport per unit mass of solution. If the solution is electrically neutral then

$$\nabla p=-\rho S^*\nabla T-\sum_{ij}\rho_i r_{ij}\mathbf{J}_j. \quad (129)$$

Under conditions for which $\mathbf{J}_j=0$ this result reduces to Eq. (75); we would expect a total pressure gradient to be evident. However, here again we point out that the steady-state condition is $\nabla\cdot\mathbf{J}_j=0$ and not necessarily $\mathbf{J}_j=0$.

ACKNOWLEDGMENT

The author wishes to thank the trustees of the Frank B. Jewett Fellowships for the award of a fellowship during whose tenure the present investigation was performed. He is also grateful for the hospitality of the Sterling Chemistry Laboratory and the Sloane Physics Laboratory of Yale University.

[8] S. Chapman and T. G. Cowling, *The Mathematical Theory of Non-Uniform Gases* (Cambridge University Press, London, 1939), p. 252.

PHYSICAL REVIEW VOLUME 70, NUMBERS 9 AND 10 NOVEMBER 1 AND 15, 1946

On the Expansibility of Solutions in Powers of the Interaction Constants

H. J. BHABHA
Tata Institute of Fundamental Research, Bombay 26, India
(Received October 22, 1946)

IT is usual in quantum theory to treat the interaction of particles with fields as a small perturbation which gives rise to transitions from one state to another of the unperturbed system. Even when all approximations higher than the first one in which a given effect appears are infinite on the present method of calculation, it is usual to assume that this first approximation is a good approximation to the exact solution for sufficiently small values of the interaction constant, and that it is increasingly good the smaller its value. Underlying this procedure is the tacit assumption that the exact solution is a continuous function of the interaction constant for vanishingly small values of it, and can therefore be expanded as a series in ascending powers of the interaction constant. The purpose of this note is to show that in the classical theory, where the equations can be solved exactly in certain circumstances, there are exact solutions of the fundamental equations which do not possess this property, and their study leads to a deeper understanding of the whole problem.

As an example, consider the interaction of an electron of mass m and charge e with the electromagnetic field. The exact classical equations of motion of a point electron have been given by Dirac (1938) and are

$$m\dot{v}_k-\tfrac{2}{3}e^2\left(\frac{d\dot{v}_k}{d\tau}+v_k\dot{v}^2\right)=eF_{kl}{}^{in}v^l, \qquad (1)$$

where $F_{kl}{}^{in}$ is the ingoing field acting on the electron, v_k is the four-velocity of the particle and a dot denotes differentiation with respect to the proper time τ. The important point about Eq. (1) is that it contains higher derivatives of v_k than the first, and hence the solution of the equation is not uniquely determined if only the position and velocity of the electron are specified at any given instant of time. Taking the simplest case of a free electron for which the right side of (1) is zero, Dirac has shown that the equation has two types of solutions, the first type being of the well-known form

$$v_k=\text{constant}, \qquad (2)$$

and the second type of the form

$$v_0=\cosh\,(e^{a\tau}+b), \qquad (3)$$

where $a=3m/2e^2$ and b is an arbitrary constant. In solutions of the second type the velocity of the electron tends extremely rapidly to infinity even in the absence of an external field, and we have therefore to exclude such solutions as non-physical ones. Solutions of the first type may be called the physical solutions. The distinction between physical and non-physical solutions persists in the presence of an external field. Equation (1) possesses solutions of both types, however small e may be, provided it is finite. But if e is exactly zero, then clearly Eq. (1) possesses only solutions of the type (2). This circumstance leads one to suspect that the non-physical solutions (3) must depend in a singular way on e as $e\to 0$. An inspection of (3) immediately confirms this, for as $e\to 0$, $a\to\infty$ and the solution (3) contains an essential singularity at $e=0$. It is for this reason that (3) cannot be expanded as a series in ascending powers of e. We have therefore found a new criterion for distinguishing the physical from the non-physical solutions. The physical solutions are those which are continuous functions of e as $e\to 0$ and can therefore be expanded as series in ascending powers of e; the non-physical solutions are essentially singular functions of e as $e\to 0$, and cannot be expanded as series in ascending powers of e.

It can be seen at once from dimensional considerations that this criterion is still valid when the point particle possesses a dipole or higher multipole moment, exact equations for which can always be found as proved by Bhabha and Harish-Chandra (1944, 1946). Suppose the particle possesses a multipole of order 2^n with an interaction constant g_n having the dimension charge times length to the power n. The radiation reaction terms in the translational

equations of motion are quadratic in g_n and hence contain derivatives of order $2n+2$ with respect to τ. Similarly, the radiation reaction terms in the rotational equations of motion of the spin contain $2n+1$ derivatives with respect to τ. The appearance of these higher derivatives in the equations again has the consequence that they possess non-physical solutions which are essentially singular functions of g_n at $g_n=0$ since no such solutions exist if $g_n=0$. The exact classical equations for a point dipole illustrate this point (Bhabha, 1940, Eqs. (30), (36); Bhabha and Corben, 1941, Eqs. (101), (103), and (106)). We are therefore led to the following general theorem:

The exact equations of motion of point particles possess two types of solutions; the first type, called the physical solutions, are continuous functions of the interaction constants at the point where the values of these constants is zero, and hence can be expanded as series in ascending powers of the constants; the second type, called the non-physical solutions, have an essential singularity at the point where the values of the interaction constants is zero, and hence cannot be expanded as series in ascending powers of the interaction constants.

Hitherto it has been customary to exclude the non-physical solutions by postulating that the allowed solutions are those which do not become infinite in the infinitely distant future. The theorem stated above now permits one to exclude the non-physical solutions by postulating that the allowed solutions shall be continuous functions of the interaction constants as the value of these constants tends to zero. This implies *ipso facto* that it must be possible to expand any allowed solution as a series in ascending powers of the interaction constants.

The situation mentioned above is of so general a nature that we should also expect it to hold in any quantum theory which is a quantization of a classical theory of the type mentioned. Thus, one could exclude the non-physical solutions in quantum theory by simply postulating that the allowed solutions shall be continuous functions of the interaction constants as the values of the latter tend to zero. Indeed, the usual perturbation method of solving problems in quantum mechanics as a series in ascending powers of the interaction constants automatically excludes the non-physical solutions. Our discussion shows that the expansibility of solutions as series in ascending powers of the interaction constants is not so much a property susceptible of proof or disproof, but rather a postulate which allows one to select the physical and exclude the non-physical solutions.

References

H. J. Bhabha, Proc. Ind. Acad. Sci. **A11**, 247–267, 467 (1940).

H. J. Bhabha and H. Chandra, Proc. Roy. Soc. **A183**, 134–141 (1944); **185**, 250–268 (1946).

H. J. Bhabha and H. C. Corben, Proc. Roy. Soc. **A178**, 273–314 (1941).

P. A. M. Dirac, Proc. Roy. Soc. **A167**, 148–169 (1938).

PHYSICAL REVIEW VOLUME 70, NUMBERS 9 AND 10 NOVEMBER 1 AND 15, 1946

Resonance Fluorescence of Nuclei

L. I. SCHIFF
Department of Physics, University of Pennsylvania, Philadelphia, Pennsylvania
(Received October 28, 1946)

EXCITED states several million volts above the normal state have been discovered in several of the light nuclei by means of radiations that accompany reactions in which these nuclei are end products. This note discusses an alternative method for locating such states which may extend the amount of data available in nuclear spectroscopy, both through the discovery of additional states and through the determination of the breadths of these states. The process to be employed is that of resonance fluorescence: the nucleus under investigation is exposed to a continuous gamma-ray spectrum, as from a betatron, and the radiation scattered at a large angle ($\sim 90°$) with the primary beam is analyzed. This will consist of sharp lines corresponding to excited states that can make radiative transitions to the ground state, and a continuous background. The intensity of each line depends on the breadth Γ of the state from which it arises, so that this method can in principle yield a value for Γ as well as for the energy E of the state. It is also possible that in favorable cases the scattered energy that is concentrated in the line is enough greater than that in the background so as to provide a useful source of mono-energetic gamma-radiation.

We restrict our attention here to excited states of light nuclei for which $E \gg mc^2$, which however lie low enough so that particle emission cannot occur. Also, we shall not consider explicitly the effect of competition from other radiative transitions; the results can readily be extended to include this, and the orders of magnitude obtained below are not altered. The Breit-Wigner single level dispersion formula gives for the integrated total cross section: $\int \sigma dE = 0.91 \times 10^{-26} \Gamma/E^2$ cm^2·Mev, where Γ is measured in volts and E in Mev, and statistical weight factors of order unity are omitted; the angular distribution is characterized by the electromagnetic partial wave that excites the transition. If the radiation is of electric quadrupole character and has a breadth of 10^{-3} volt for $E \approx 1$ Mev,[1] this becomes about $10^{-29}E^2$; if it is of magnetic dipole character, as is probably the case with the O^{16} 6.2-Mev line,[2] a simple estimate shows that the integrated total cross section is roughly $2 \times 10^{-29} E$.

The continuous background has two principal sources: coherent non-resonant nuclear scattering, and double processes in which high energy Compton recoil electrons produce bremsstrahlung (the similar pair processes are much less probable for light nuclei). The direct Compton scattered radiation is not of great importance, for although it is fairly intense (cross section per unit solid angle $\approx 2 \times 10^{-26} Z/E$ at 90°) all of the quanta have about 0.5 Mev energy and can be filtered out. With reasonable assumptions about the dispersion properties of light nuclei, it appears that the dominant term in the non-resonant scattering is the classical Thomson scattering by the nucleus as a whole, which is about $10^{-31} Z$ cm^2 (this assumes that the atomic weight A equals about twice the atomic number Z).

The effective cross section for double processes is the product of four terms: (1) the Compton scattering cross section, (2) the bremsstrahlung cross section, (3) the number of nuclei per cm^2 encountered by the recoil electron, and (4) a dimensionless factor that takes account of the large angle between incident and outgoing gamma-quanta. This background may be reduced by requiring, for example, that the degradation of the gamma-rays not exceed about 1 Mev, which means that the excited state under investigation is to be within 1 Mev of the maximum gamma-ray energy of the betatron source. The value of (1) for recoil electron kinetic energy within 1 Mev of the primary gamma-ray energy is $1.8 \times 10^{-25} Z/E$ cm^2, where E is in Mev. Similarly, the value of (2) for secondary gamma-ray energy within 1 Mev of the electron kinetic

[1] V. Weisskopf, Phys. Rev. 59, 318 (1941).
[2] L. I. Schiff, Phys. Rev., to be published.

energy is roughly $6\times10^{-27}Z^2/E$ cm². (3) is the product of the number N of nuclei per cm³ and the effective range R of the recoil electron. This range will be either a typical linear dimension of the scattering sample, or the distance in which the electron loses about 1 Mev of its energy, whichever is smaller. The latter is about $0.23A/\rho Z$, where ρ is the density, and hence is of the order of a few mm. Thus for samples of reasonably large size, NR is a constant equal to about $1.4\times10^{23}/Z$. The angular spreads of both the energetic recoil electrons and the bremsstrahlung are of the order of a few degrees for the conditions of interest here. Thus (4) must be caused either by deflection of the recoil electron by multiple Coulomb scattering before it loses 1 Mev of its energy, or by large angle bremsstrahlung (because of the conservation laws, a recoil electron of definite energy has a definite direction). Both of these are improbable, but the latter much less so than the former at such a large angle as 90°. The fraction of the total number of energetic gamma-quanta radiated per unit solid angle at 90° may be estimated[3] to be $1/16\pi E^2$. Thus the cross section for such double processes is about $3\times10^{-30}Z^2/E^4$.

Comparison between the formulas given above for the resonance and the background cross sections indicates that the resonance should stand out clearly against the background. Thus for the 6.2-Mev oxygen state, the integrated resonance cross section per unit solid angle at 90° is about 1 to 2×10^{-29} cm²-Mev; the background cross section for production of scattered gamma-rays within 1 Mev of the resonance if the betatron is run at a slightly higher energy is about 10^{-30} cm². Since the background cross section does not increase with sample size when it is more than a few mm in linear dimensions, it is desirable to use as large a sample as is otherwise convenient in order to increase the over-all intensity.

[3] A. Sommerfeld, *Atombau und Spektrallinien* (Vieweg, Braunschweig, 1939), Vol. 2, p. 551.

PHYSICAL REVIEW VOLUME 70, NUMBERS 9 AND 10 NOVEMBER 1 AND 15, 1946

On the High Pressure Bands of Carbon and the Formation of C_2 Molecules

G. HERZBERG
Yerkes Observatory, Williams Bay, Wisconsin
(Received October 30, 1946)

IN several previous publications[1-3] it was stated that the so-called high pressure bands of carbon belong to the Swan bands of the C_2 molecule. In view of several recent inquiries concerning this matter it appears desirable to amplify the previous statements.

It has been shown by Johnson and Asundi[4] that the high pressure carbon bands represent a $^3\Pi-{}^3\Pi$ transition just as the Swan bands and that the two band systems have the lower state (presumably the ground state of the C_2 molecule) in common. Using Jevons' formula[5] for the band heads of the Swan system (in which a term in $v'v''$ takes account of the rather large change of the distance between head and origin) one obtains for $v'=6$ and $v''=0,\ 1,\ \cdots 11$ the wave numbers given in the second column of Table I

TABLE I. High pressure bands of carbon.

v''	ν_{head}(calculated)	ν_{head}(observed)	Estimated intensity
0	29164	(29241)*	1
1	27560	(27620)*	1
2	25977	—	1
3	24417	24426	2
4	22879	22883	7
5	21362	21361	15
6	19867	—	1
7	18395	18394	5
8	16944	16946	10
9	15515	15518	8
10	14108	14114	6
11	12723	12731	4

* These values are band centers whereas all others are band heads.

[1] J. G. Fox and G. Herzberg, Phys. Rev. **52**, 638 (1937).
[2] G. Herzberg, Astrophys. J. **89**, 290 (1939).
[3] G. Herzberg, *Molecular Spectra and Molecular Structure I. Diatomic Molecules* (New York, 1939), p. 472.
[4] R. C. Johnson and R. K. Asundi, Proc. Roy. Soc. **A124**, 668 (1929).
[5] W. Jevons, *Report on Band Spectra of Diatomic Molecules* (London, 1932), p. 61.

which should be compared to Johnson and Asundi's wave numbers of the heads of the high pressure bands given in the third column. Except for the first two very faint bands (for which band centers rather than band heads were measured and for which a large separation head-origin is expected) the agreement with the values calculated on the assumption that the high pressure bands represent the $v'=6$ progression of the Swan system is just as good as can be expected particularly if it is remembered that the term in $v'v''$ does not completely account for the variation of the distance head-origin, and that the position of the vibrational level $v'=6$ may well be a few cm^{-1} off the extrapolated value.

A further strong argument, if such were needed, for the proposed identity is supplied by the intensity distribution. The intensities of the high pressure bands as estimated by Johnson and Asundi are given in column 4 of Table I. The two intensity maxima occur precisely at the places where they would be expected by extrapolating the Condon parabola of the observed Swan bands to $v'=6$, namely at $v''=5$ and 8. Even apart from this agreement the presence of two intensity maxima, according to well-established principles, excludes the possibility that the upper state is a $v'=0$ level of a different electronic state.

Johnson and Asundi have measured the fine structure of only the R branches of the high pressure bands. Therefore a precise determination of the rotational constants is not possible. However, a rough determination using the data for the lower state from the bands of Fox and Herzberg[1] yields $B'=1.59$ cm^{-1} for the upper state of the high pressure bands, a value that fits well into the B' *versus* v' curve of the Swan bands.

According to all these arguments the identity of the high pressure bands with the $v'=6$ progression of the Swan bands must be considered as proven. It is well known that the high pressure bands may occur when no trace of the ordinary Swan bands is observed.[6-8] Asundi and Pant[8] have considered this as conclusive evidence against our assumption. However other cases of selective excitation of certain band progressions are known, for example the excitation of certain progressions of the first positive group of nitrogen in the afterglow of active nitrogen or the excitation of a single progression of H_2 bands in a discharge through argon and hydrogen.[9,10] The question is what is the mechanism of the selective excitation in the present case.

Since the high pressure bands are observed in carbon monoxide and since the other Swan bands do not simultaneously appear it seems certain that the selective excitation is connected with the formation of C_2 molecules from carbon atoms which in turn are formed by the dissociation of CO in the discharge. This is confirmed by the observation that the bands occur usually outside the direct path of the discharge. In a previous publication[2] it was suggested that the recombination is one by triple collision, the dissociation energy being used to excite the newly formed molecule to the $v'=6$ level. However it is difficult to account in this way for the great selectivity of the excitation. It seems much more likely that the mechanism consists in an inverse predissociation leading to a recombination in a two-body collision. Indeed the observation that the Swan bands ordinarily break off with $v'=5$ suggests strongly that the $v'=6$ level is predissociated. Therefore an inverse predissociation is also possible, that is, two C atoms colliding with the proper kinetic energy on the potential curve of the state that causes the predissociation may jump over to the potential curve of the upper $^3\Pi_g$ state of the Swan bands. Only the predissociating vibrational level $v'=6$ can be formed in this way. Once in this state the molecule may go over into the ground state with emission of the high pressure bands or it may predissociate again, and the process will repeat itself until a stable molecule is formed. On this basis the selectivity in the excitation of the Swan bands is immediately accounted for at least if the lifetime of the $v'=6$ state is sufficiently small that collisions during the lifetime are unimportant.

[6] T. R. Merton and R. C. Johnson, Proc. Roy. Soc. **A103**, 383 (1923).
[7] G. Herzberg, Zeits. f. Physik **52**, 815 (1929).
[8] R. K. Asundi and D. D. Pant, Curr. Sci. **10**, 520 1941).
[9] E. E. Witmer, Phys. Rev. **28**, 1223 (1926).
[10] H. Beutler, Zeits. f. Physik **50**, 581 (1928).

The only other well-established case of inverse predissociation is the observation by Stenvinkel[11] of the emission of the predissociated lines of AlH under conditions that strongly favor formation of AlH molecules from Al and H atoms in two-body collisions.

Independent of the specific mechanism of the recombination process it follows that the dissociation energy of the C_2 molecule is less than the excitation energy of the $v'=6$ level and larger than that of the $v'=5$ level that is between the limits 3.4 and 3.6 volts—probably closer to the upper limit. This value depends of course on the correctness of the assumption of a recombination process for the explanation of the selective emission of the $v'=6$ progression of the Swan bands (i.e., the high pressure carbon bands).

[11] G. Stenvinkel, Zeits. f. Physik 114, 602 (1939).

PHYSICAL REVIEW VOLUME 70, NUMBERS 9 AND 10 NOVEMBER 1 AND 15, 1946

Racetrack Stability*

D. M. DENNISON AND T. BERLIN
Randall Laboratory of Physics, University of Michigan, Ann Arbor, Michigan

(Received October 25, 1946)

IN a recent Letter to the Editor, Serber[1] has pointed out that the existence of the straight, field-free sections of the racetrack synchrotron introduces a condition for the stability of the orbits which depends upon (a) the ratio of the length of a straight section to the radius of curvature of the circular portions of the orbit and (b) upon the frequencies of oscillation in the circular portions. These latter, the frequencies of the Z and of the radial motion, are proportional to $(n)^{\frac{1}{2}}$ and to $(1-n)^{\frac{1}{2}}$, respectively, where n is the coefficient determining the fall-off law for the magnetic field.

The calculation made by Serber was for a racetrack with two equal straight sections, and it was found that the proposed dimensions of the Michigan racetrack, while leading to stable orbits, were uncomfortably close to a region of instability.

We have reexamined the problem and have extended the formulas to include the case of N equal straight sections, each of length L, connected by N circular arcs of length $2\pi r/N$. The method of solution was as follows. Consider the mth passage of the electron through a circular portion of the orbit. Let the coordinate describing the particle motion within the tube be x and let the frequency of oscillation be ω. (x may be identified with either the Z or the radial displacement from equilibrium.)

$$x=A_m \sin\omega t+B_m \cos\omega t.$$

At the end of the mth circular portion of the orbit the electron enters the mth straight section. Throughout this section $\dot{x}$ remains constant but the particle has received a displacement of amount $L\dot{x}/v$ where v is its forward velocity. The particle now enters the $(m+1)$th circular portion and will again be described by

$$x=A_{m+1} \sin\omega t+B_{m+1} \cos\omega t.$$

Recursion formulas connecting A_{m+1} and B_{m+1} with A_m and B_m may be easily found and solved.

$$A_m=A \sin m\pi\mu+B \cos m\pi\mu,$$
$$B_m=C \sin m\pi\mu+D \cos m\pi\mu,$$

where A, B, C, and D are constants which are related through recursion formulas.

It is thus seen that the amplitudes vary sinosoidally and that the motion of the x coordinate approximates to that of a modulated wave. This statement would be rigorously correct if m increased uniformly with the time. Actually m is an integer and therefore discontinuous. However the orbit, which is in reality composed of short sinusoidal arcs connected by straight lines, will closely resemble a modulated sine

* The work described in this letter has been supported by the Bureau of Ordnance, U. S. Navy, under contract NOrd-7924.

[1] R. Serber, Phys. Rev. 70, 434 (1946).

curve. The frequency of modulation may be determined through the quantity $\pi\mu$ and the equation which fixes its value also constitutes the stability condition, since $\cos\pi\mu$ must lie between ± 1. In agreement with Serber,[1] we find,

$$\cos\pi\mu = \cos\pi\nu - p\sin\pi\nu.$$

In this expression $\nu = 2n^{\frac{1}{2}}/N$ and $p = n^{\frac{1}{2}}L/d$ for the Z motion where d is twice the radius of curvature of the circular arcs. For the radial motion $\nu = 2(1-n)^{\frac{1}{2}}/N$ and $p = (1-n)^{\frac{1}{2}}L/d$. From our earlier study[2] it appears that the magnetic fall-off parameter n should lie in the range from 0.56 to 0.75. In the following calculations a value of $n = \frac{3}{5}$ has been used. For the number of straight sections, $N = 2$, 3, 4, 6, and 8, the ratio L/d must be less than 0.363, 1.06, 1.64, 2.69, and 3.69, respectively, if the resulting orbits are to be stable. Originally the design of the Michigan synchrotron called for a ratio $L/d = 0.30$ which is therefore just inside the range of stability for the case of $N = 2$. When the number of gaps is increased to 3 or more, however, it is clear that $L/d = 0.30$ is far from the instability region and indeed may be somewhat increased with safety.

A second way of viewing the phenomenon is to calculate the degree of modulation. This quantity, R, may be defined as the ratio of the greatest amplitude of oscillation which the particle achieves to its least amplitude. As L/d is decreased, R will increase and become infinite at the point of instability. A calculation yields the formula,

$$R^2 = (\sin\pi\nu + p\cos\pi\nu + p)/(\sin\pi\nu + p\cos\pi\nu - p).$$

In the following table R is listed for various values of N and for both the radial and Z motions. It has been assumed that $L/D = 0.30$ and $n = \frac{3}{5}$.

N	R (Z motion)	R (radial motion)
2	2.45	1.21
3	1.30	1.19
4	1.27	1.22
6	1.32	1.28
8	1.38	1.35

Since the final yield of high energy electrons will probably be greatest when R is the least, the logical choice for the number of gaps is 4, and the Michigan synchrotron will be so constructed.

A study has been made to show how the stability is affected by an inequality in the lengths of the straight sections. It was assumed that the racetrack contains two opposite sections of lengths L_1 and two sections of lengths L_2, each section being connected by a quadrant of circular arc. The stability condition becomes,

$$|2(\cos\pi\nu - p_1\sin\pi\nu)(\cos\pi\nu - p_2\sin\pi\nu) - 1| < 1,$$

where for the Z motion $\nu = \frac{1}{2}n^{\frac{1}{2}}$, $p_1 = L_1 n^{\frac{1}{2}}/d$ and $p_2 = L_2 n^{\frac{1}{2}}/d$. A new region of instability is thus revealed, namely when the values of p_1 and p_2 bracket $\cot\pi\nu$. It would appear easy to use dimensions for the 4-gap track so as to avoid this region. (Incidentally the value $p = \cot\pi\nu$ is just that point where instability sets in for the 2-gap racetrack.)

[2] D. M. Dennison and T. Berlin, Phys. Rev. 69, 542 (1946).

Letters to the Editor

PROMPT publication of brief reports of important discoveries in physics may be secured by addressing them to this department. The closing date for this department is the third of the month. Because of the late closing date for the section no proof can be shown to authors. The Board of Editors does not hold itself responsible for the opinions expressed by the correspondents. Communications should not in general exceed 600 words in length.

The Magnetic Moments of the Neutron and the Deuteron

WAYNE R. ARNOLD AND ARTHUR ROBERTS*
Argonne National Laboratory, Chicago, Illinois
October 3, 1946

ON the basis of the measurement of the quadrupole moment of the deuteron by Rabi and his co-workers,[1] Rarita and Schwinger[2] calculated that the predominantly $^3S_1$ ground state of the deuteron must contain an admixture of 3.9 percent $^3D_1$ state. On the simple assumption that the proton and the neutron retain, when combined in the deuteron, the magnetic moments they possess when free, these authors predicted from the known magnetic moments of the proton and the deuteron that the magnetic moment of the free neutron should be -1.911 nuclear magneton. Because of the contribution of the orbital angular momentum of the ^3D state, this is different from the simple numerical difference between the proton and deuteron moments, which is -1.933 nuclear magneton. The predicted value is not inconsistent with the experimental value for the magnetic moment of the neutron obtained by Alvarez and Bloch,[3] which is -1.935 ± 0.03. It is clear, however, that greater precision in the measurement of the neutron magnetic moment is desirable.

Recently, Purcell, Torrey, and Pound,[4] and Bloch, Hansen, and Packard[5] have described closely-related radiofrequency resonance methods for measuring the gyromagnetic ratios of nuclei in matter in the solid or liquid state. We have now taken advantage of the method of Purcell, Torrey, and Pound, the technique of Bloch *et al*,[6] in polarizing and analyzing neutron beams by passage through ferromagnets, and the availability of an intense source of well-thermalized neutrons in the Argonne heavy water pile, to measure carefully the ratios of the deuteron magnetic moment and the neutron magnetic moment to the magnetic moment of the proton.

In the case of the neutron, the magnetic field was adjusted for proton resonance, using an arbitrary radiofrequency near 30 Mc/sec. Without changing the magnetic field, the water sample used for proton resonances was removed from the r-f coil in the magnetic field, a neutron beam sent through the coil, and the neutron resonance found by varying the radiofrequency applied to the coil. The drop in intensity of the neutron beam at resonance was between five and eight percent. The ratio of the magnetic moments, since the spins of both proton and neutron are one-half, is then the ratio of the two radiofrequencies.

For the deuteron, the magnetic field was adjusted to resonance at a fixed frequency with a heavy water sample. Ordinary water was then substituted and the frequency varied until the proton resonance was found.

The mean of seventeen observations of the neutron-proton ratio gives the value 0.68479. Four observations on the deuteron-proton ratio give the value 0.30702. The internal consistency of these observations alone yields the probable errors 0.0002 and 0.00002, respectively. A search for possible systematic error in the proton resonance was made. The proton resonances in tap water, distilled water, benzene, paraffin, and 1.5 percent $FeCl_3$ solution could not be separated and were all within 0.01 percent in frequency. The magnetic field was homogeneous to better than 0.05 percent, and to a first approximation the inhomogeneity introduces no error in the ratios. Since the possibility of systematic error cannot be excluded, however, we regard the final values as 0.68479 ± 0.0004 for the neutron-proton ratio and 0.30702 ± 0.0001 for the deuteron-proton ratio. Taking the magnetic moment of the proton as *exactly* 2.7896 nuclear magnetons, since the theory depends only upon relative values, we obtain for the neutron, inserting a minus sign, -1.9103 ± 0.0012 nuclear magneton, and for the deuteron 0.85647 ± 0.0003. Rabi and his co-workers[7] give for the deuteron-proton ratio 0.30703 ± 0.0001, and for the absolute value of the magnetic moment of the deuteron 0.8565 ± 0.0004.

Rarita and Schwinger's predicted value for the neutron moment, corrected to use Rabi's latest values, is -1.9108. Conversely, using our measured values for the neutron-proton and deuteron-proton ratios, we find in the ground state of the deuteron an admixture of 4.0 percent $^3D_1$ state, as compared with 3.9 percent deduced from the quadrupole moment.

We wish to acknowledge with thanks the cooperation extended by personnel of the Argonne National Laboratory, and especially the encouragement and assistance of the Director, Dr. W. H. Zinn.

* Department of Physics, State University of Iowa, Iowa City, Iowa.
[1] J. M. B. Kellogg, I. I. Rabi, N. F. Ramsey, and J. R. Zacharias, Phys. Rev. **57**, 677 (1940).
[2] W. Rarita and J. Schwinger, Phys. Rev. **59**, 436 (1941).
[3] L. W. Alvarez and F. Bloch, Phys. Rev. **57**, 111 (1940); Phys. Rev. **57**, 352A (1940).
[4] E. M. Purcell, H. C. Torrey, and R. V. Pound, Phys. Rev. **69**, 37 (1946).
[5] F. Bloch, W. W. Hansen, and Martin Packard, Phys. Rev. **69**, 127 (1946).
[6] F. Bloch, M. Hamermesh, and H. Staub, Phys. Rev. **64**, 47 (1943).
[7] J. M. B. Kellogg, I. I. Rabi, N. F. Ramsey, and J. R. Zacharias, Phys. Rev. **56**, 728 (1939).

The Maximum Inversion Temperatures of Helium, Hydrogen, and Neon

JOSEPH JOFFE
Newark College of Engineering, Newark, New Jersey
October 9, 1946

J. R. ROEBUCK and H. Osterberg in their work on the Joule-Thomson effect of helium[1] estimate the maximum inversion temperature of helium as 23.6°K by using their experimental value for air and assuming that the

reduced temperature (T/T_c) is the same for helium as for air, in accordance with the law of corresponding states. R. H. Newton has, however, shown[2] that in the correlation of activity coefficients and compressibility factors of gases in terms of reduced temperature and reduced pressure hydrogen, helium, and neon are exceptional. Experimental data for these three gases can be correlated successfully with data obtained from other gases provided that the critical temperatures and pressures for these three gases are replaced with pseudo-critical values, $T_c' = T_c + 8$ and $P_c' = P_c + 8$, in the calculation of reduced temperatures and pressures.[3]

It is probable that Newton's correction also applies in the correlation of inversion temperatures for the Joule-Thomson effect. The values of the reduced inversion temperatures for nitrogen, air, and hydrogen are known to be, respectively, 4.93, 4.55, and 5.89. It is seen that the value for hydrogen is high as compared with those for nitrogen and air. If, however, the pseudo-critical temperature is used in place of the critical temperature, the reduced temperature for hydrogen becomes 4.75, in good agreement with the observed values for nitrogen and air. If we now assume that the reduced maximum inversion temperature of helium is 4.75, as for hydrogen, then employing the pseudo-critical value we find that the absolute value of the inversion temperature for helium should be 62.7°K and not 23.6°K as estimated by Roebuck and Osterberg. If air instead of hydrogen is used in the computation, the maximum inversion temperature for helium becomes 60.1°K. With the aid of Newton's method of correlation it can also be predicted that the maximum inversion temperature of neon is in the neighborhood of 250°K.

[1] J. R. Roebuck and H. Osterberg, Phys. Rev. **43**, 60 (1933).
[2] R. H. Newton, Ind. Eng. Chem. **27**, 302 (1935).
[3] H. C. Weber, *Thermodynamics for Chemical Engineers* (New York, 1939), p. 111.

On the Detection of Meteors by Radio

L. A. MANNING, R. A. HELLIWELL, O. G. VILLARD, JR., AND W. E. EVANS, JR.
Department of Electrical Engineering, Stanford University, California
October 18, 1946

PIERCE has found isolated echoes on ionosphere virtual height-*versus*-time records and has identified them with the passage of meteors in the upper atmosphere.[1] Chamanlal and Venkatamaran have studied the Doppler whistles which can be heard under certain conditions on short wave radio signals during the passage of meteors.[2,3] The Federal Communications Commission has measured bursts of signal from f-m stations in the 40–50 megacycle band at distances beyond the range of the ground wave, and has attributed them to reflections from trails of ionization produced by meteors.[4] Lastly, Ferrell has noted radar reflections from meteoric ionization trails.[5]

Further evidence bearing on these observations was obtained during the Giacobini-Zinner meteor shower of October 9, 1946. Two radio signals were used to detect the passage of meteors: one from a 15-megacycle short wave broadcasting station of 100 kilowatts power 72 miles distant, and the other from a 29-megacycle continuous-wave transmitter of 0.7-kilowatt power located one mile away from the receiving point. The antennas used at the receiving and transmitting stations were horizontal half-wave dipoles mounted one quarter-wave above ground, and having a figure eight pattern in the horizontal plane. Direct signal from the local transmitter was reduced to a very low value at the receiver by mounting the two antennas in such a way as to take advantage of the nulls.

Doppler whistles of the type reported by Chamanlal and Venkatamaran were plainly heard on both emissions, both during and after the meteor shower. Doppler whistles occurring simultaneously with visually observed meteors were noted.

Doppler whistles on both frequencies were often followed by a burst of signal strength. On the 20-megacycle frequency, however, many bursts not accompanied by whistles were heard. These bursts were usually shorter in duration and weaker in amplitude than those accompanying the whistles. Observations showed that a continuous gradation existed, from very weak bursts without whistles, all the way to strong bursts accompanied by strong whistles.

By listening to the 15- and 29-megacycle signals simultaneously, it was established that in every case when a burst without a whistle was observed on the latter signal, a whistle could plainly be heard on the former. This would appear to be evidence that the whistles and the bursts are both caused by meteors, and that both bursts and whistles may be used as indications of the passage of a meteor.

During the height of the meteor shower, the bursts occurred so frequently on the 29-megacycle signal that they overlapped, producing a nearly continuous meteor-reflected signal several times stronger than the reference signal.

Previous investigators in the field of meteor detection by radio have made use of radio transmitting equipment of 10–100 kilowatts power, such as high power, short wave broadcasting stations. However, it will be found that even those fortunate enough to be located near such stations will have difficulty in using them for meteor detection studies for these reasons:

(1) The transmitted program tends to obscure meteor whistles.

(2) The unstable "long scatter" signals, returned to regions in the vicinity of the transmitter from scattering sources beyond the edge of the skip zone, tend both to drown out Doppler whistles and to obscure bursts of signal strength caused by meteors.

(3) The stations operate on an intermittent schedule and usually go off the air during the early morning hours when meteors are most plentiful.

A locally-generated continuous wave signal offers advantages in addition to controllable time of operation and lack of program modulation. Selection of an operating frequency slightly higher than the highest at which long distance communication can be maintained at any given time, automatically eliminates the "long scatter" signal. It is desirable to use the lowest possible operating fre-

quency, since as frequency is increased a greater degree of ionization is required for a given amplitude of reflection from a given meteor trail.

The fact that meteors can be detected by means of signals from radio equipment of roughly one kilowatt power in the 30-megacycle frequency range, should, therefore, be of interest to astronomers and other investigators who do not have access to radio transmitting equipment of very high power.

[1] J. A. Pierce, Phys. Rev. 59, 625 (1941).
[2] Chamanlal and Venkatamaran, Electrotech. 14, 28 (1941).
[3] O. G. Villard, Jr., Q.S.T. 30, 59 (1946).
[4] Electronics 18, 105 (January, 1945).
[5] O. P. Ferrell, Phys. Rev. 69, 32 (1946).

Confirmation of Assignment of 2.6 *h* Ni to a Mass Number of 65

E. E. Conn, A. R. Brosi, and J. A. Swartout
Monsanto Chemical Company, Clinton Laboratories, Oak Ridge, Tennessee
and
A. E. Cameron, R. L. Carter, and Douglas G. Hill
Tennessee Eastman Corporation, Oak Ridge, Tennessee
October 18, 1946

THE assignment of the 2.6 *h* Ni activity to a mass number of 65 which was recently reported on the basis of (n, p) reactions with copper samples of different isotopic abundances[1] has been independently confirmed using nickel preparations of various isotopic abundances.

Samples of NiO enriched in Ni^{62} and Ni^{64} were prepared with the calutron, purified, and analyzed mass-spectrographically by the Tennessee Eastman Corporation. Comparisons were made of the relative amounts of 2.6 *h* beta-activity produced during exposure of a sample enriched in Ni^{62}, a sample enriched in Ni^{64}, and nickel of natural isotopic abundance to the neutron flux of the Clinton pile. As is shown in Table I the relative activities agree with the relative amounts of Ni^{64} bombarded.

Table I. Evidence for production of 2.6 *h* Ni by the reaction: $Ni^{64}(n, \gamma)Ni^{65}$

	Natural Ni	Enriched Ni^{64}	Enriched Ni^{62}
Percentage of Ni^{64}	0.88[a]	85.1 ± 1	$1.8^{+0.2}_{-1.8}$
Percentage of Ni^{62}	3.8[a]	$1.0^{+0.1}_{-0.2}$	94.2 ± 0.2
2.6 *h* beta-activity (c/m/mg Ni at 100% geom.)	5.3×10^8	4.2×10^8	6.8×10^6
Specific activity (c/m/mg Ni^{65} at 100% geom.)	6×10^8	5×10^8	4×10^7

[a] G. E. Valley, Phys. Rev. 59, 836 (1941).

Although the value for the specific activity from the enriched Ni^{62} sample is of low accuracy corresponding to the large uncertainty in the mass-spectrographic analysis for Ni^{64}, it is in agreement with the assignment to a mass number of 65.

This paper is based on the results of research performed under Contracts W-35-058-eng-71 and W-7401-eng-23, with the Manhattan Project, Oak Ridge, Tennessee.

[1] J. A. Swartout, G. E. Boyd, A. E. Cameron, C. P. Keim, and C. E. Larson, Phys. Rev. 70, 232 (1946).

The Representation of Single Particle Operators in Two-Particle Form

Eugene Feenberg
Washington University, St. Louis, Missouri
October 25, 1946

LET p_i and q_i be any pair of classical quantities or quantum-mechanical operators for the ith particle of a system of N particles and

$$P=\Sigma p_i, \qquad Q=\Sigma q_i$$

the corresponding quantities for the complete system. A small circle between the symbols denotes a generalized multiplication for which the distributive law is assumed to hold. Then

$$\begin{aligned} QoP &= \sum_{ij} q_i o p_j \\ &= N\Sigma q_i o p_i - \sum_{i<j} q_{ij} o p_{ij}, \end{aligned}$$

in which $p_{ij}=p_i-p_j$, $q_{ij}=q_i-q_j$. Consequently

$$\Sigma q_i o p_i = \frac{1}{N}\sum_{i<j} q_{ij} o p_{ij} + \frac{1}{N} QoP. \tag{1}$$

It is the purpose of this note to direct attention to three relations of the form (1) which may find a useful field of application in the development of the theory of nuclear structure.

(a) $p_i=q_i=\nabla_i$, the vector gradient operator. Equation (1) becomes

$$\Sigma \nabla_i^q = \frac{1}{N}\sum_{i<j} \nabla_{ij}^q + \frac{1}{N}(\Sigma \nabla_i)^q. \tag{2}$$

If now the center of mass of the system is at rest, the last term in the right-hand member of Eq. (2) may be omitted leaving the relation

$$\Sigma \nabla_i^q = \frac{1}{N}\sum_{i<j} \nabla_{ij}^q. \tag{3}$$

Equation (3) represents the internal kinetic energy of N isobaric particles in terms of the relative kinetic energy of pairs of particles.

(b) $p_i=\nabla_i$, $q_i=\mathbf{r}_i$, $o \equiv x$ (the vector product). Then

$$\Sigma \mathbf{r}_i x \nabla_i = \frac{1}{N}\sum_{i<j} \mathbf{r}_{ij} x \nabla_{ij} + \frac{1}{N}\Sigma \mathbf{r}_i x \Sigma \nabla_j. \tag{4}$$

With the center of mass at rest, Eq. (4) reduces to

$$\Sigma \mathbf{r}_i x \nabla_i = \frac{1}{N}\sum_{i<j} \mathbf{r}_{ij} x \nabla_{ij}. \tag{5}$$

Equation (5) states that the internal orbital angular momentum of an assemblage of particles can be expressed in terms of the relative angular momentum of pairs of particles. Both (4) and (5) remain valid if the multiplication operation is interpreted as the scalar product.

(c) $p_i=q_i=\mathbf{r}_i$ the vector distance from a fixed point. Then[1]

$$\Sigma r_i^q = \frac{1}{N}\sum_{i<j} r_{ij}^q + \frac{1}{N}(\Sigma \mathbf{r}_i)^q. \tag{6}$$

Consider now a system of N identical particles bound to-

gether by elastic forces between pairs of particles. Equation (6) establishes a correspondence between the energy levels and wave functions of this system and those of the simpler system composed of N identical particles bound to a fixed point in space by elastic forces.

Returning to the discussion of theorem (a), the existence of the linear momentum integral enables the kinetic energy operator of a system of isobaric particles to be expressed in the two-body form commonly assumed for the potential energy operator. The formal uniformity thus achieved suggests that, in nuclear systems, an actual similarity exists in the symmetry dependence of the diagonal matrix elements of the kinetic and potential energy operators. The proof or disproof of the suggested similarity is important because of its bearing on theories of nuclear binding energy and stability.[2]

Equation (1) does not exhaust the possibilities under the heading of this note. A simple example of physical interest is supplied by the dipole moment operator of a nuclear system:

$$P_x=\sum_{i=1}^{Z}x_{pi}-\frac{Z}{A}\left[\sum_{i=1}^{Z}x_{pi}+\sum_{i=1}^{N}x_{ni}\right]$$
$$=\frac{1}{A}\sum_{i=1}^{Z}\sum_{j=1}^{N}(x_{pi}-x_{nj}),\quad A=N+Z. \tag{7}$$

The application of Eq. (7) to isobaric nuclei which are located symmetrically about the line $N=Z$ yields an interesting result without further computation. Under the hypothesis of charge independent (symmetrical) forces these isobaric nuclei possess the same energy levels, i.e., the level system of one can be superimposed upon that of the other by a suitable displacement along the energy axis. It is evident then that corresponding electric dipole transition probabilities should be equal in pairs of isobaric nuclei such as Li^7, Be^7 and Be^{10}, C^{10}.

[1] This relation and also the classical equivalent of Eq. (2) appear in Jacobi's *Vorlesungen über Dynamic*, p. 22 (see E. T. Whittaker, *Analytical Dynamics*, fourth edition, p. 342).
[2] E. P. Wigner, Phys. Rev. 51, 947 (1937); W. H. Barkas, Phys. Rev. 55, 691 (1939).

Transition Effects of the Soft Component of Cosmic Rays

S. N. Vernov and O. N. Vavilov*
P. N. Lebedev Physical Institute, Academy of Sciences of the U.S.S.R., Moscow, Russia
October 20, 1945

THE existence of the hard and soft components becomes evident on examination of the absorption of the cosmic radiation in lead.[1,2] The properties of the soft component may be described by the cascade theory if, as is usually supposed, this component is composed chiefly of photons and electrons.

According to this theory, on transition from air to lead an appreciable transition maximum should be observed, similar to that observed in the stratosphere. The existence of such a maximum follows simply from the fact that in air the average energy of particles of the cascade component (which is of the order of the critical energy) exceeds by more than ten times the average energy of these particles in lead.

Calculations show that cascade multiplication should increase the number of the electrons by 4–6 times in comparison with the initial value. It should be mentioned that the latest calculations of S. Z. Belenky,[3,4] which we employ here and in which account is taken of the variation of the photon absorption coefficient with energy and of scattering, introduce appreciable corrections in the cascade curves for heavy elements. These calculations flatten out the theoretical transition curves and bring them more nearly into agreement with those experimentally observed by us.

The transition curves obtained previously by Schindler,[5] Street and Young,[2] and others in general do not exhibit any appreciable transition maximum. D. V. Skobelzyn[6] pointed out that the results of these experiments sharply contradict the cascade theory. It was shown by one of us[7] that this discrepancy may be owing to scattered cosmic-ray electrons produced in the lead, which miss the measuring instrument. Computations carried out by Tamm and Belenky[8] indicate that a large fraction of the electrons produced in lead as a result of cascade processes possess very small energies (30 percent of the electrons have energies below 0.6 Mev and 75 percent below 7 Mev); thus these electrons are considerably scattered in lead and even in the comparatively thin walls of the measuring instruments they may be appreciably absorbed.

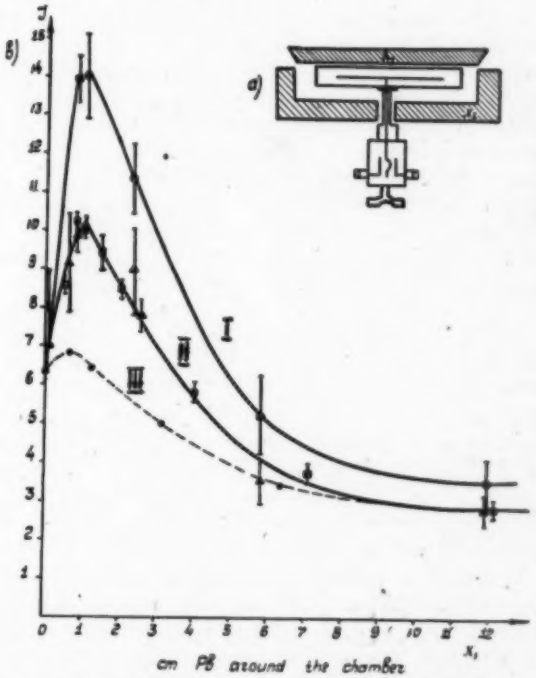

FIG. 1. Absorption curves of cosmic rays in lead at altitude of 3860 m. (a) Scheme of the apparatus, (b) ionization produced by cosmic rays in various chambers (ions per cm^3 per sec. N.T.P.). Circles indicate measurements with foil chamber, Pamir. Triangles are for chamber with 0.4 mm Al walls, Pamir (1944). Squares are for a similar chamber at Mt. Elbrus (1940). The dotted curve is from Street and Young (reference 2). Transition curve of Street and Young and that obtained at Mt. Elbrus are made comparable with Pamir results by equating the intensities of the soft component of the cosmic rays.

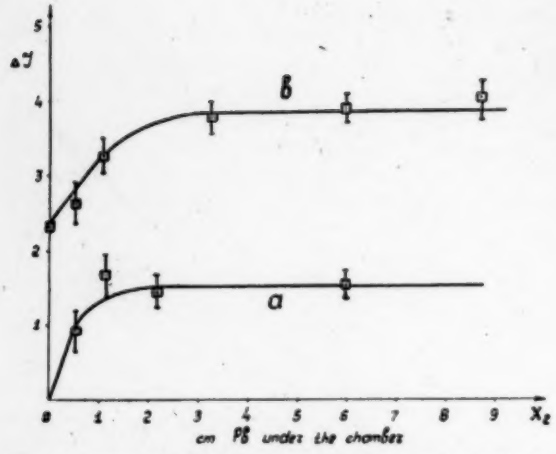

FIG. 2. Increase of ionization due to lead X_2 beneath the chamber (0.4 mm Al), Elbrûs glacier: (a) No lead above chamber ($X_1=0$), (b) 1 cm Pb above the chamber.

In order to observe transition curves not distorted by scattering, special methods of measurement must be applied. We used a measuring instrument (ionization chamber or counter) with thin walls and completely surrounded the instrument by a lead screen. Under these conditions the number of particles lost in the lead above the apparatus will be compensated by those scattered upwards from the lead.

Measurements of the transition curves of the soft component by this method were carried out by one of us at an altitude of 4200 m on Mt. Elbrus[4] (1940) and at an altitude of 3860 m in the Pamir Mountains (1944). In the Pamirs three instruments were operated simultaneously: two flat ionization chambers (40×40×5 cm) with aluminum walls of 0.4 and 0.02 mm thickness and a counter 2 cm long, 0.7 cm in diameter and with 0.3 mm Al walls. On Mt. Elbrus measurements (with the first chamber) were carried out on a glacier and this permitted us completely to exclude the influence of radioactivity on the ionization currents measured. The results are shown in Fig. 1.

The transition curves obtained by us have a very sharp maximum and in this respect strongly differ from those of Schindler and Young and Street (Curve III of Fig. 1). Under 1 cm of lead the intensity of the soft component obtained by using a foil chamber exceeds by a factor of 3.8 the value obtained when no lead is placed above and below the chamber. In the chamber with 0.4 mm Al walls the increase in the maximum turned out to be 2.1 while the counter yielded an increase of 2.6 times.

The result of measurements of the "back current" (increase of ionization when lead is placed below the chamber) carried out in 1940 on a glacier at Mt. Elbrus are shown in Fig. 2. These measurements clearly illustrate the importance of the scattered radiation from lead which increases the ionization in the 0.4 mm Al chamber by almost 40 percent of that of the soft component when no lead is employed; this result accords with the theory.[9]

On transition from lead to aluminum a considerable decrease of intensity should take place because absorption of cascade electrons in thin layers of aluminum is much stronger than their reproduction by photons. It can be seen from Fig. 1 that the intensity of the soft component under the lead appreciably decreased when the wall thickness of the ionization chamber was changed from 0.02 to 0.4 mm Al (Curves II and III of Fig. 1). Special investigations of the lead-to-aluminum (thin layers) transition effect carried out in the Pamirs are in good agreement with the cascade theory calculations of Tamm and Belenky.[8,10]

The air-to-lead transition curve obtained by using the counter is similar to that obtained with the ionization chamber (of approximately the same wall thickness), its maximum, however, being somewhat higher. This may indicate that an appreciable part of the ionization of the soft component in air is owing to heavily ionizing particles.

According to Alichanov[11] an even greater fraction of the ionization by the soft component should be ascribed to heavy particles. On the other hand, comparison of the experimental transition curve obtained with the foil chamber with the cascade curves computed on basis of present knowledge of the electron spectrum in air[8,12] permits one to estimate the upper limit of the fraction of ionization due to non-multiplying heavy particles at about 50 percent of the total soft component.

Measurements carried out in aerostats to altitudes of 8–9 thousand meters showed that on surrounding the ionization chamber by 1 cm of lead the intensity of the soft component increased by 2 times (the thickness of the chamber walls being 0.4 mm Al). Multiplication was insignificant when the lead absorber covered a solid angle of only about one steradian.

This once more points to considerable scattering of the soft component in lead and the necessity of taking this scattering into account in all experiments in which the soft component is investigated.

* Deceased.

[1] P. Auger, L. Leprince-Rinquet, and P. Ehrenfest, Comptes rendus 200, 1747 (1935); J. de phys. et rad. 7, 58 (1936).
[2] R. T. Young and J. S. Street, Phys. Rev. 52, 550 (1937).
[3] S. Belenky, J. Phys. U.S.S.R. 8, 305 (1944).
[4] O. N. Vavilov, Comptes Rendus Acad. Sci. U.S.S.R. 33, 203 (1941).
[5] H. Schindler, Zeits. f. Physik 72, 625 (1931).
[6] D. V. Skobelzyn, Bull. Acad. Sci. U.S.S.R., ser. Phys. NI, 129 (1938).
[7] S. N. Vernov, Comptes Rendus Acad. Sci. U.S.S.R. (Doklady) 24, 860, 864 (1939).
[8] J. E. Tamm and S. Belenky, J. Phys. 1, 177 (1939); Phys. Rev. 70, 660 (1946).
[9] S. Z. Belenky, J. Phys. U.S.S.R. 8, 347 (1944).
[10] S. Z. Belenky, in press.
[11] A. Alichanov and A. Alichanian, J. Phys. U.S.S.R. 8, 314 (1944); 8, 1272 (1944).
[12] H. E. Stanton, Phys. Rev. 66, 48 (1944).

Evidence for the Reaction $O^{17}(n, \alpha)\, C^{14}$

E. P. HINCKS
National Research Council of Canada, Division of Atomic Energy, Chalk River, Ontario, Canada
September 30, 1946

IN 1944 a search was made by A. N. May and the writer for the reaction $O^{17}(n, \alpha)C^{14}$ by exposing oxygen samples in a pressure ionization chamber to a high thermal neutron flux. Two samples were compared, one being en-

riched (3 times normal) and the other impoverished (0.5 times normal) in the isotope O^{17}. The pulses produced in the chamber were amplified and counted by a kicksorter or pulse amplitude analyzer. Differences between runs with the two samples showed a significant increase in the number of pulses between 1 and 2 Mev in the case of the enriched sample, with a peak at about 1.4 Mev. The effect proved to be caused by thermal neutrons, and has been attributed to the above reaction.

With air in the ionization chamber, the pulses due to the reaction $N^{14}(n, p)C^{14}$ were counted, thus permitting the cross section for the oxygen effect to be determined in terms of the nitrogen cross section. We found a value $\sigma_O/\sigma_N=(1.1\pm0.3)\times10^{-4}$, where σ_O is the cross section per atom of natural oxygen. Lapointe and Rasetti[1] have found a value 1.2×10^{-24} cm² for σ_N which, however, is based on a value of 600×10^{-24} cm² for σ_B, the neutron capture cross section of boron. On the basis of a recently published value of $\sigma_B=710\times10^{-24}$ cm²,[2] the above value of σ_N should be increased to 1.4×10^{-24} cm². Assuming this figure, the cross section for the (n, α) reaction in O^{17} is then $(1.6\pm0.4)\times10^{-28}$ cm² per atom of natural oxygen, or $(0.38\pm0.09)\times10^{-24}$ cm² per atom of O^{17}.

Using the masses of O^{17} and C^{14} given by Mattauch,[3] we find that the reaction $O^{17}(n, \alpha)C^{14}$ should be exothermic, with $Q=+1.72$ Mev, in approximate agreement with our results.

A full account of the experiment will be submitted for publication to the *Canadian Journal of Research*.

[1] C. Lapointe and F. Rasetti, Phys. Rev. **58**, 554 (1940).
[2] John Marshall, Phys. Rev. **70**, 107 (1946).
[3] J. Mattauch, *Kernphysikalische Tabellen* (Verlagsbuchhandlung Julius Springer, Berlin, 1942).

Three Unusual Cosmic-Ray Increases Possibly Due to Charged Particles from the Sun

SCOTT E. FORBUSH
Department of Terrestrial Magnetism, Carnegie Institution of Washington, Washington, D. C.
October 10, 1946

SEVERAL world-wide decreases in cosmic-ray intensity have been observed[1,2] during magnetic storms. These decreases have been ascribed[3] to ring currents, or their equivalents, required to account for the observed world-wide magnetic changes.

In about 10 years of continuous records of ionization in Compton-Bennett meters (shielded by 11-cm Pb) three obviously unusual increases in ionization have been noted. For Cheltenham, Maryland, geomagnetic latitude, $\Phi=50°$ N, these are shown in Fig. 1, in which the bi-hourly means were corrected for barometric pressure. Curves very similar to the upper one in Fig. 1 obtain[2] simultaneously for Godhavn, Greenland, $\Phi=78°$ N; and for Christchurch, New Zealand, $\Phi=48°$ S. Except for the absence of significant increases on February 28, 1942; March 7, 1942; and July 25, 1946, the curves for Huancayo, Peru, $\Phi=1°$ S, are otherwise quite similar to those for Cheltenham.

Figure 1 indicates each of the three unusual increases in cosmic-ray intensity began nearly simultaneously with a solar flare (bright chromospheric eruption) or radio fadeout (indicating a solar flare). Original records for February 28 and March 7, 1942, indicate increases in ionization which began within 0.3 hour after the commencement of the radio fadeout. The record for Cheltenham on July 25, 1946, first indicated an increase in ionization 1.0 hour after the reported commencement of the solar flare and fadeout. All three fadeouts were complete for about five hours and the flare was reportedly observed for three hours until clouds obscured it.

Magnetic records from several observatories indicate that the magnetic changes during these fadeouts or flares were probably caused by an augmentation of the diurnal variation.[4] Thus the magnetic changes do not appear ascribable to a ring current as first supposed.[3] Magnetic records on the night side of the Earth indicate no significant change in field at the time of the fadeouts yet the cosmic-ray records show the increases occurred simultaneously on the day and night side.

The known small diurnal variation[5] in cosmic-ray intensity excludes the possibility that these increases could have been caused by an augmentation in magnetic diurnal variation.

During a period of several hours on March 7, 1942, when the cosmic-ray ionization at Cheltenham increased to well above normal, that at Huancayo was sub-normal. Also the

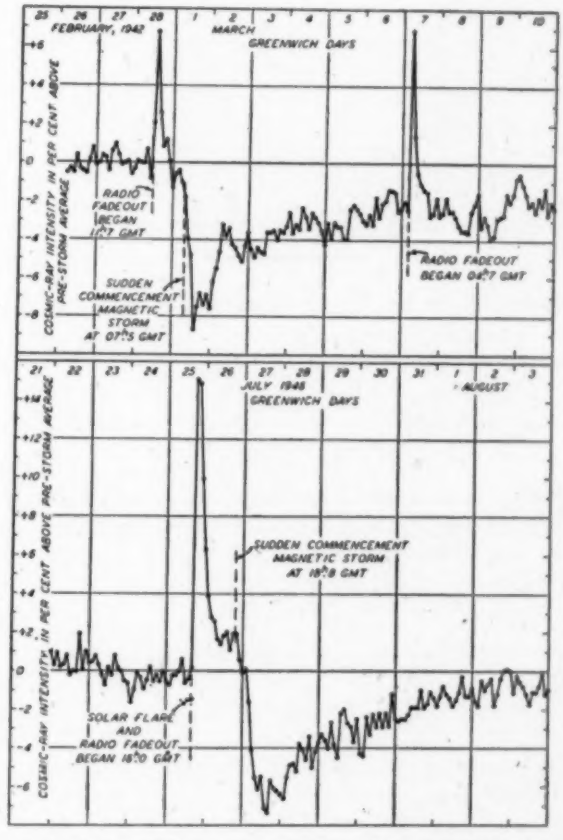
FEBRUARY, 1942
MARCH
GREENWICH DAYS
COSMIC-RAY INTENSITY IN PER CENT ABOVE PRE-STORM AVERAGE
RADIO FADEOUT BEGAN 1717 GMT
SUDDEN COMMENCEMENT MAGNETIC STORM AT 0715 GMT
RADIO FADEOUT BEGAN 0427 GMT
JULY 1946
AUGUST
GREENWICH DAYS
SUDDEN COMMENCEMENT MAGNETIC STORM AT 1818 GMT
SOLAR FLARE AND RADIO FADEOUT BEGAN 1800 GMT

FIG. 1. Three unusual increases in cosmic-ray intensity at Cheltenham, Maryland, during solar flares and radio fadeouts.

intensity at Cheltenham, Godhavn, and Christchurch was sub-normal before and after the unusual increase on March 7, 1942. Thus the mechanism responsible for the cosmic-ray increase on March 7, 1942, must have been distinct from that responsible for the otherwise sub-normal intensities during this period which have been ascribed[3] to ring currents.

These circumstances might suggest a change in the Sun's magnetic moment, arising perhaps from transient fields, as a possible cause[6] for the three unusual increases in cosmic-ray intensity. However, the effectiveness of such a mechanism should be independent of whether a particularly active area on the Sun was oriented toward the Earth. That each of the three fadeouts was followed, within about a day, by a magnetic storm, indicates that the three cosmic-ray increases did occur when a particularly active area on the Sun was preferentially oriented toward the Earth.

These considerations suggest the rather striking possibility that the three unusual increases in cosmic-ray intensity may have been caused by charged particles actually being emitted by the Sun with sufficient energy to reach the Earth at geomagnetic latitude 48° but not at the equator. It is recognized that particles of this energy should not escape from low latitudes on the Sun except in the absence of the much-disputed permanent solar magnetic field.

W. F. G. Swann[7] considered one mechanism for accelerating charged particles which involved changing magnetic fields of sunspots (near which observed flares occur) or stellar spots.

[1] E. B. Berry and V. F. Hess, Terr. Mag. 47, 251–256 (1942).
[2] S. E. Forbush and Isabelle Lange, Terr. Mag. 47, 331–334 (1942).
[3] S. E. Forbush, Terr. Mag. 43, 203–218 (1938).
[4] A. G. McNish, Terr. Mag. 42, 109–122 (1937).
[5] S. E. Forbush, Terr. Mag. 42, 1–16 (1937).
[6] M. S. Vallarta, Nature 139, 839 (1937).
[7] W. F. G. Swann, J. Frank. Inst. 215, 273–279 (1933).

Remarks on Dr. Ma's "Redundant Zeros in the Discrete Energy Spectra in Heisenberg's Theory of Characteristic Matrix"

W. Opechowski
Natuurkundig Laboratorium der N. V. Philips' Gloeilampenfabrieken, Kastanjelaan, Eindhoven
September 4, 1946

CONTRARY to the opinion expressed by Dr. Ma in his recent letter,[1] there are no redundant zeros in the case considered by him. The only zeros are given by his condition—I use his notations here—:

$$J_{2aki}[2a(u_0)^{\frac{1}{2}}]=0. \qquad (I)$$

It is easily seen that Dr. Ma's condition for redundant zeros,

$$1/\Gamma(-2aki+1), \qquad (II)$$

leads to a contradiction. Condition (II) would mean, indeed, that $2aki$ is an integer. But for the integer values of $2aki$ the solution given by Dr. Ma,

$$u=c\{J_{-2aki}[2a(u_0)^{\frac{1}{2}}]J_{2aki}[2a(u_0x)^{\frac{1}{2}}] - J_{2aki}[2a(u_0)^{\frac{1}{2}}]J_{-2aki}[2a(u_0x)^{\frac{1}{2}}]\}, \qquad (III)$$

vanishes identically,[2] while it is implicitly assumed in his derivation of (II) that this solution does not vanish identically.

Dr. Ma has apparently overlooked the fact that J_{2aki} and J_{-2aki} do not form a fundamental system of solutions of the Bessel differential equation when $2aki$ is an integer.[2] The correct procedure is, of course, to take instead of (III) the solution

$$u=c\{N_{2aki}[2a(u_0)^{\frac{1}{2}}]J_{2aki}[2a(u_0x)^{\frac{1}{2}}] - J_{2aki}[2a(u_0)^{\frac{1}{2}}]N_{2aki}[2a(u_0x)^{\frac{1}{2}}]\}, \qquad (IV)$$

where N_p is a Neumann function (as is well known, N_p and J_p do form a fundamental system of solutions with no restrictions on p). One finds then that the solution (IV) represents a closed state only when k is imaginary and when, as above stated,

$$J_{2aki}[2a(u_0)^{\frac{1}{2}}]=0 \qquad (I)$$

for all values of $2ak$, the integer values included; on the contrary, one does not find any supplementary condition such as (II).

[1] S. T. Ma, Phys. Rev. 69, 668 (1946).
[2] For integer values of p one has: $J_{-p}=(-1)^pJ_p$.

Half-Life Determination of Carbon (14) with a Mass Spectrometer and Low Absorption Counter

L. D. Norris
Clinton Laboratories, Oak Ridge, Tennessee
AND
M. G. Inghram
Argonne National Laboratories, University of Chicago, Chicago, Illinois
August 28, 1946

A DETERMINATION of the half-life of carbon (14) has been made by counting small, weighed amounts of barium carbonate containing known amounts of carbon (14) determined by mass spectrometric measurement. The carbon (14) was prepared in the Clinton Laboratories by L. D. Norris and A. H. Snell using neutron bombardment of an ammonium nitrate solution to yield carbon (14) by the reaction $N^{14}(n, p)C^{14}$. The mass spectrometric measurement of the abundance of the carbon (14) in the barium carbonate was made by M. G. Inghram, and the activity of the barium carbonate was determined by L. D. Norris.

Two separate samples were analyzed with a Nier type mass spectrometer. The samples were prepared for analysis by heating the outgassed barium carbonate in a quartz tube to about 1100°C to evolve CO_2. The CO_2 was then introduced into the mass spectrometer and the ratio of the carbon (12) to the carbon (14) determined by measuring the ratio of the mass 44 ($C^{12}O^{16}O^{16}$) to the mass 46 ($C^{14}O^{16}O^{16}$) peaks. Appropriate corrections were applied for the O^{17} and O^{18} contributions to the mass 46 peak. The two samples of barium carbonate were thus shown to have 3.23 percent and 3.35 percent carbon (14). Incidental to the abundance determination was the direct mass spectrometric verification of the mass of the long-lived radioactive carbon.

Small, finely ground portions of these samples (approximately 150 μ g) were weighed on a microbalance, and after being mounted on 0.001" aluminum, the beta-rays were counted in a low absorption, windowless counter. The geometry of the counter was determined by using aliquots of solutions of $UX_{1,2}$, the UX_1 having been quantitatively separated from old uranium solutions by coprecipitation with lanthanum. The UX samples were mounted on films of zapon (<0.1 mg/cm²), for which the backscattering is negligible. Since the carbon (14) was mounted on 0.001" aluminum, a backscattering correction was obtained by mounting samples of the carbon on zapon film, counting, and then recounting after inserting 0.001" aluminum behind the zapon film, less than 0.5 mm from it. This amounted to 21 percent in this counting arrangement. Other scattering has been assumed to be negligible, and self-absorption corrections have been neglected because the amounts contained less than 0.2 mg/cm² of the sample. As the counter had no window, the only other correction to be made concerns the weight of the counting mixture between the sample and the active portion of the counter tube (0.8 mg/cm²).

A very rough preliminary value of 6100 years was announced at the June meeting of the American Physical Society. A number of mounts have now been prepared from both of the analyzed samples and a half-life of 5300 years obtained, which is appreciably below the previously accepted values. The uncertainty in this value is no more than 15 percent.

Penetrating Cosmic-Ray Bursts

E. P. GEORGE
Birkbeck College, London
AND
L. JANOSSY
The University, Manchester, England
October 15, 1946

IN order to see whether ionization bursts contain a penetrating component, we have recently performed measurements with the set shown schematically in Fig. 1. B is a small ionization chamber of 1.5 liters capacity, filled with pure argon to a pressure of 40 atmospheres. Under the chamber was placed a fourfold counter set C, and the bottom counters of this set were screened in all directions with lead to a thickness of 15 cm. The burst pulses from B were amplified and recorded photographically in a normal manner. Similarly, the fourfold counter coincidences were recorded in the usual way. Finally, in the event of a fourfold counter coincidence occurring simultaneously with a burst pulse, a small lamp was energized and was registered on the film recording the bursts.

TABLE I. Observed burst rate.

Thickness of lead at A	No. of bursts with 4-fold coincidences	Time	Rate	Rate of 4-fold coincidences	Rate of bursts of size >20
7 cm	18	36	0.5±0.1 (0.02) per day	45.5±1 per day	8.5 per hour
0	2	12.5 days	0.16±0.1 (0.004) per day	30.0±1.6 per day	2.7 per hour

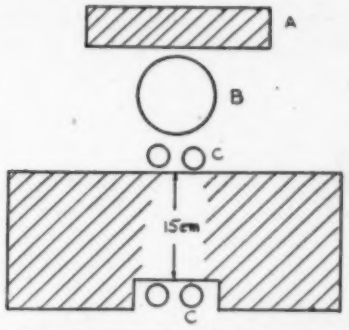

FIG. 1. Counter arrangement for burst measurements.

The minimum size of burst recorded was one of 20 rays through the chamber B.

The results of our measurements are given in Table I. In the fourth column of Table I, we show in parentheses the accidental rates of burst-shower coincidences, evaluated from the known resolving time of the circuits involved. The accidental rates are seen to be negligible.

It may be shown that the coincidences with 7-cm Pb at A cannot be caused by cascades, or to double knock-ons by mesons. The following processes may be thought of to account for the results: (a) the initial collision that forms the pinnacle of a cascade in the lead, also produces several mesons at the same time, (b) a small percentage of bursts is composed entirely of mesons, (c) all bursts are normal cascades which produce mesons during their development.

The size distribution of penetrating bursts

$$B(>N)=a \log (400/N),\ a=0.78/\text{day} \qquad (1)$$

shows that (b) is unlikely.

A fuller account of the experiment will be published shortly.

Measurements of Nuclear Quadrupole Moment Interactions†

W. A. NIERENBERG, N. F. RAMSEY, AND S. B. BRODY*
Columbia University, New York, New York
October 22, 1946

THE molecular beam magnetic resonance method[1-4] has been applied in the present work to a study of the resonance minima associated with the sodium nucleus in NaBr, NaCl, and NaI. Comparison of the results with the theory of Lamb and Feld[4] indicates that the predominant observed phenomena are caused by the interaction of the electrical quadrupole moment of the sodium nucleus with the inhomogeneous electric field of the molecule and provides a measurement of this interaction energy.

Previous measurements in this laboratory[3] of the deuteron quadrupole moment were made with D_2 and HD in the first rotational state in which case the resonance minima from the different orientation states were separately resolved enabling a very direct determination of

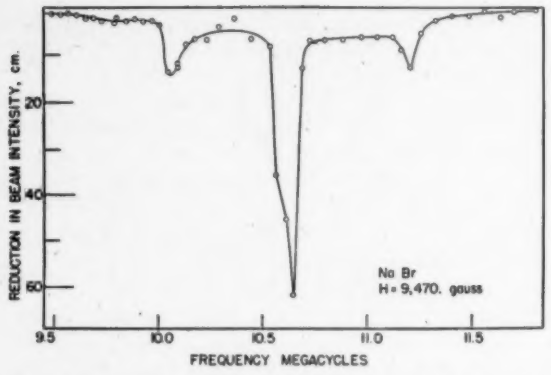

FIG. 1. The radiofrequency spectrum of Na^{23} (in NaBr) in a strong magnetic field. The central resonance corresponds to the g value for Na^{23}. The measured total beam is 1630 cm and the r-f current is 4 amperes.

the nature of the interaction to be made. In the present experiments, however, a large number of rotational states are excited so that the resonance minima from each orientation state are not separately resolved and a statistical theory developed by Lamb and Feld[4] must be used in accounting for the results. Previous measurements by Millman and Kusch[2] with the Na_2 molecule indicated the existence of a quadrupole interaction in this molecule, but no suitable statistical theory was available at the time of their measurements to allow a detailed interpretation.

The apparatus used in this work was rebuilt from one originally constructed and described by Millman and Kusch.[1] In the sodium halides, with high values of the homogeneous magnetic field, resonance minima similar to those shown in Fig. 1 for NaBr were obtained when the beam intensity was plotted as a function of the frequency at a fixed magnetic field. The central resonance minimum is at the position predicted for the nuclear g value of Na^{23}; and if measurements are made at different values of the magnetic field, the frequency at the central resonance is proportional to the magnetic field. The positions of the two subsidiary resonances, however, are not proportional to the field but, to the first approximation, are at a fixed frequency away from the central resonance minimum, indicating that they are separated from the central minimum because of an interaction within the molecule rather than a magnetic interaction with the externally applied field.

Figure 1 is very similar to the theoretical prediction in Fig. 5 of Lamb and Feld[4] for the shape of the resonance minima for a nucleus of spin $\frac{3}{2}$ possessing an electrical quadrupole moment and in a molecule of which many rotational states are excited. The major discrepancies can be accounted for by the approximations used in the Lamb and Feld treatment. According to Lamb and Feld the separation of the side resonance minima from each other should be equal to $e^2qQ/2h$ cycles where Q is the nuclear electrical quadrupole moment[3,4] in cm^2 and q is a measure of the gradient of the electric field at the position of the nucleus as defined exactly in earlier papers.[3-5] Consequently the measurement of these resonance minima provide a direct measurement of the product qQ. The values obtained for $e^2qQ/2h$ in NaBr, NaCl, and NaI from measurements with high magnetic fields are given in the rows accompanying high field values in Table I.

TABLE I. Separations of resonance minima.

Substance	External magnetic field (gauss)	$e^2qQ/2h$ (megacycles)
NaBr	9740.	1.17
NaBr	<4	1.22
NaCl	9305.	1.35
NaCl	<4	1.42
NaI	8490.	0.97
NaI	<4	0.99

The measurements have also been extended to a resonance minima of a type not previously observed, namely, minima for which the external magnetic field is almost equal to zero (less than 4 gauss). In this case the central position of the resonance is due to the electrical quadrupole interaction. The theory of these minima was also worked out by Lamb and Feld,[4] who give $e^2qQ/2h$ for the predicted frequency of the resonance. These resonances have been observed for NaBr, NaCl, and NaI and a typical one is shown in Fig. 2. Values of $e^2qQ/2h$ obtained in this way are shown in Table I in rows accompanying low magnetic fields. There is a small but apparently consistent difference between the values of $e^2qQ/2h$ obtained at high fields and at low. The latter are from 2 to 5 percent high. All values in the table are taken from the location of the minima in the resonance curves.

Observations have also been made at magnetic fields in the neighborhood of 300 gauss in which case the resonance minimum centered at $e^2qQ/2h$ is spread an amount proportional to the external magnetic field as predicted by Lamb and Feld.

Since the shapes of the resonance minima at high magnetic fields and the number of resonances at low magnetic fields depend on the spin of the nucleus concerned, this

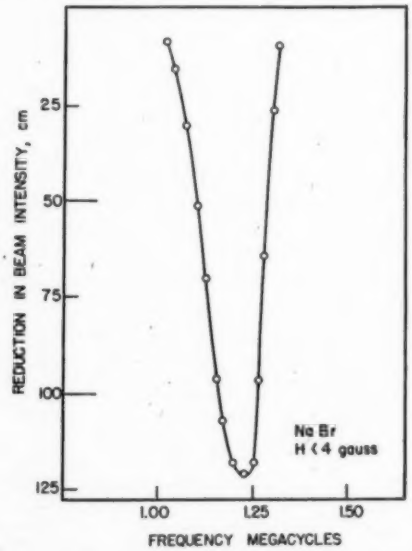

FIG. 2. The radiofrequency spectrum of Na^{23} (in NaBr) in a weak magnetic field. The position of the resonance agrees very closely with the difference in frequency of the positions of the subsidiary minima of Fig. 1. The measured total beam is 2730 cm and the r-f current is 3 amperes.

method should provide a means of measuring the nuclear spin. The present results are in agreement with the well-established spin of $\frac{3}{2}$ for Na^{22}. It is planned to extend the method to nuclei of spins other than $\frac{3}{2}$ using the molecular beam technique. This method of measuring spins and quadrupole interactions may also be applicable to the resonance absorption[6,7] and nuclear induction[8] methods.

The authors wish to thank Drs. Millman, Kusch, Rabi, and Trischka for their advice and assistance in this work.

† Publication assisted by the Ernest Kempton Adams Fund for Physical Research of Columbia University, New York, New York.

* Sarah Lawrence College.

[1] I. I. Rabi, S. Millman, P. Kusch, and J. R. Zacharias, Phys. Rev. 55, 526 (1939).
[2] P. Kusch, S. Millman, and I. I. Rabi, Phys. Rev. 55, 1176 (1939).
[3] J. M. B. Kellogg, I. I. Rabi, N. F. Ramsey, Jr., and J. R. Zacharias, Phys. Rev. 57, 677 (1940).
[4] B. T. Feld and W. E. Lamb, Jr., Phys. Rev. 67, 15 (1945).
[5] A. Nordsieck, Phys. Rev. 58, 310, (1940).
[6] E. M. Purcell, H. C. Torrey, and R. V. Pound, Phys. Rev. 69, 37 (1946).
[7] William E. Good, Phys. Rev. 70, 213 (1946).
[8] F. Bloch, W. Hansen, and M. Packard, Phys. Rev. 69, 127 (1946).

Plastic Flow of Metals

J. H. HOLLOMON AND J. D. LUBAHN
General Electric Research Laboratory, Schenectady, New York
October 7, 1946

ONE of the most important problems connected with the plastic flow of metals is the one of determining the combined effects of strain, strain rate, and temperature on the stress required for plastic flow. In general, these relations should apply to plastic flow in situations when the stress distribution is complex; as well as for the case of deformation under the action of simple tensile stress. However, this note will describe only the relations between the variables for the case of simple tension.

It has been found[1] that at a constant strain rate and temperature, the stress (σ) and strain (ϵ) are related by the following equation:

$$\sigma = K(\epsilon)^m, \tag{1}$$

where K and m are constants that may depend upon the strain rate and temperature. Further, an empirical relation[2] between stress and strain rate (α) has also been developed:

$$\sigma = K_1(\alpha)^n, \tag{2}$$

where K_1 and n may depend upon the strain and temperature. In addition to these relations, another has been found giving all combinations of temperature and strain rate that correspond to a given stress at a fixed strain.[3-5] The relation can be written in the following forms:

$$l = \alpha/\alpha_1 e^{Q/RT}, \tag{3}$$

or

$$Q/R = -T \ln \alpha/\alpha_1, \tag{3a}$$

where α_1 may be a function of the strain, Q a function of stress and strain, and R is the gas constant.

From these three equations, a general relation connecting all four variables has been derived:

$$\sigma = C(\alpha/\alpha_0)^{DT} e^{(E-FT \ln \alpha/\alpha_0)} \tag{4}$$

where α_0, C, D, E, and F are constants of the material.

Two important consequences of this equation can be described briefly. The equation can be rewritten in logarithmic form:

$$\frac{\ln \sigma - \ln C - E \ln \epsilon}{F \ln \epsilon - D} = -T \ln \alpha/\alpha_0. \tag{4a}$$

Upon comparison with Eq. (3a) it is found that Q should vary linearly with the logarithm of the stress. This relation is in disagreement with the ideas of Becker,[6] Kauzmann,[7] and Dushman *et al.*[8] However, upon replotting the recalculated[3] values of Q, obtained from Dushman's data against the logarithm of the stress, straight lines are obtained.

Furthermore, it is seen from (4a) that the logarithm of the stress should vary directly with the temperature, the slope being a linear function of the logarithm of the strain rate. By replotting data obtained by Nadai and Manjoine,[9] these relations have been confirmed.

The problem of determining the entire plastic behavior of a metal in the range of temperature, strain rate, and strain in which it undergoes no phase changes becomes only a question of evaluating the five constants of Eq. (4). There are many conclusions that may be drawn from it. It has important applications to the problem of creep and to the theory of plastic flow. These relations will be discussed further in papers now in preparation.

[1] J. H. Hollomon, Metals Tech. 12, No. 4 (1945).
[2] J. H. Hollomon, Supplement J. Am. Welding Soc., Sept. (1945).
[3] C. Zener and J. H. Hollomon, J. App. Phys. 17, 69–82 (1946).
[4] C. W. MacGregor and J. C. Fisher, J. App. Mech. 12, A217–A227 (1945).
[5] C. W. MacGregor and J. C. Fisher, J. App. Mech. 13, A11–A16 (1946).
[6] R. Becker, Zeits. f. tech. Physik 7, 547 (1926).
[7] W. Kauzmann, Trans. A.I.M.E. 143, 57 (1941).
[8] S. Dushman, L. W. Dunbar, and H. Huthsteiner, J. App. Phys. 15, 108 (1944).
[9] A. Nadai and M. J. Manjoine, Trans. A.S.M.E. 63, A–77 (1941).

The Inversion Spectrum of Ammonia

B. BLEANEY AND R. P. PENROSE
The Clarendon Laboratory, Parks Road, Oxford, England
October 23, 1946

WHILE our detailed analysis of this spectrum awaits publication in the *Proceedings of the Royal Society*, the paper of the above title by W. E. Good[1] calls for the following comments.

1. The splitting of the inversion spectrum of ammonia, according to the theory of Sheng, Barker, and Dennison,[2] should be represented by a formula of the type

$$\bar{\nu} = \bar{\nu}_0 - A(J^2+J) + BK^2, \tag{1}$$

where the terms involving the rotational quantum numbers J, K correspond to the first term in the expansion of an exponential function. In our letter[3] of February 12, 1946, to *Nature*, we suggested a formula which, after correcting the $\bar{\nu}_0$ term for an error in the sign of the reduction of the wave numbers to a vacuum, becomes

$$\bar{\nu} = 0.7935 - 0.0050_5(J^2+J) + 0.0070_4K^2 + 0.63\{-0.0050(J^2+J) + 0.0070K^2\}^2 \text{ cm}^{-1} \text{ (vacuum)}, \tag{2}$$

exponential expansion. The extra term involves no further empirical coefficients, since the 0.63 is merely (1/2)/0.7935.

In his letter[4] the 20th of April, 1946, to *The Physical Review*, written before the author had seen our publication, Good suggested the formula

$$\tilde{\nu}=0.7932-0.0048(J^2+J-K^2)+0.0020K^2.$$

The expression now obtained by Good[1] is

$$\tilde{\nu}=0.79347-0.005048(J^2+J)+0.007040K^2+0.00001546(J^2+J)^2-0.00004260(J^2+J)K^2+0.00002920K^4, \quad (3)$$

where all the coefficients are empirical. On multiplying out, (2) becomes

$$\tilde{\nu}=0.7935-0.0050_8(J^2+J)+0.0070_4K^2+0.000016_1(J^2+J)^2-0.000044_9(J^2+J)K^2+0.000031_2K^4. \quad (2a)$$

It is surprising that Good made no comment on the close agreement between the two expressions. It should be noted that the accuracy of the measurement of frequency is the same in the two experiments, since the ±5. Mc/sec. claimed by Good corresponds to our ±0.02 percent. We did not feel justified, however, in evaluating the coefficients to greater accuracy, since even third-order terms would be appreciable for some lines.

2. The comparison of the relative intensities of the lines made by Good assumes that the widths of the different lines are all the same. The widths of 17 lines measured by us vary as $3[K^2/(J^2+J)]^{\frac{1}{2}}$, and from these widths the absolute intensities can be calculated. Our measured intensities agree with the calculated values within ±5 percent, while the intensities shown in Good's Fig. 5 are considerably smaller. For instance we find 0.044 db/meter for the line (6, 3), whereas Good's value appears to be less than 0.01 db/meter. The calculated value is 0.042 db/meter.

3. The following factors affect the change of intensity with temperature, in addition to those enumerated by Good.

(a) The change in the relative populations of the two levels of the inversion doublet causes the intensity to vary as $1/T$, corresponding to the fact that the cancellation of the absorption by induced emission is less at low temperature.

(b) At a given pressure the lines become broader, not sharper, as stated by Good, as the temperature is lowered, because the number of molecules per cc varies as $1/T$, while the molecular velocity varies only as $\sqrt{T}$.

4. Good suggests that the fall in intensity at low pressures shown in his Fig. 4 is owing to the interruption of the absorption by collision with the walls of the wave guide, which would ultimately cause the collision frequency to become independent of the pressure. At room temperature in a wave guide with the usual narrow dimension of 4.5 mm, however, an ammonia molecule would collide with the walls about $13\cdot10^4$ times per second giving a line-breadth constant ($\Delta\nu$) of $13\cdot10^4/2\pi\cdot10^6=0.02$ Mc/sec. The value of $\Delta\nu$ for the line (3, 3), estimated from Good's Fig. 4a, is, however, 0.4 Mc/sec. which must therefore be attributed to collisions between molecules. This indicates that the collision cross section for this absorption is considerably greater than the kinetic theory value; our measurements of the width of this line show that the ratio of the two cross sections is actually 14.

5. We suggest that the diminution in the intensity as the pressure is reduced may be owing to disturbance of thermal equilibrium, as the absorption of energy tends to equalize the populations of the upper and lower levels. We have observed this effect by determining the absorption coefficient at various energy densities in a resonant cavity, and find that the reduction in the intensity is in close agreement with that calculated from the measured energy density. In a wave guide of cross-sectional area A through which a power W is flowing, the attenuation γ should be less than that (γ_0), which would be observed if thermal equilibrium were preserved, by a factor

$$\gamma/\gamma_0=\frac{2}{a}\left(1-\frac{1}{(1+a)^{\frac{1}{2}}}\right),$$

where

$$a=\frac{16\pi(\mu mn)^2}{3(hc)^2(\Delta\tilde{\nu})^2}\cdot\left(\frac{\lambda g}{\lambda}\right)\cdot\frac{W}{Ac}.$$

Inserting our measured value for the line breadth constant ($\Delta\tilde{\nu}$) we find that a power of one milliwatt would be sufficient to reduce the intensity of the line (3, 3) by a factor of 3 at a pressure of $1.5\cdot10^{-2}$ mm Hg. The usual types of oscillator give 20–30 mw; allowing 10 db of attenuation and 3 db for the division of power between the two guides, it would seem quite possible that a milliwatt of power was flowing through the ammonia. Thus the disturbance of thermal equilibrium appears a likely explanation for the drop in the intensity at low pressure and may also explain the abnormally low intensities shown in Fig. 5 of Good's paper.

[1] W. E. Good, Phys. Rev. **70**, 213 (1946).
[2] Hsi-Yin Sheng, E. F. Barker and D. M. Dennison, Phys. Rev. **60**, 786 (1941).
[3] B. Bleaney and R. P. Penrose, Nature **157**, 339 (1946).
[4] W. E. Good, Phys. Rev. **69**, 539 (1946).

Additional Cosmic-Ray Measurements with the V-2 Rocket

S. E. Golian, E. H. Krause, and G. J. Perlow
The Naval Research Laboratory, Washington, D. C.
November 1, 1946

ANOTHER cosmic-ray experiment has been done in a V-2 rocket, fired on October 10 at White Sands, New Mexico (Geom. $\lambda=41°$N). Measurements were made with the counter arrangement shown in Fig. 1, of the ratio of total intensity as measured in the threefold telescope 1, 2, 3, to the intensity below 15.2 cm of lead as measured by the fourfold coincidences 1, 2, 3, (6+7+8). The quantities included in the parentheses were electronically paralleled for this measurement. Because of space limitations, it was not possible to make the solid angle of the fourfold set completely include that of the threefold. The ratio of these solid angles was determined to be 0.37 by a ground calibration. A third channel measured sixfold coincidences 1, 2, 3, 6, 7, 8. Each of these three channels was protected against the shower rays found in a previous experiment[1]

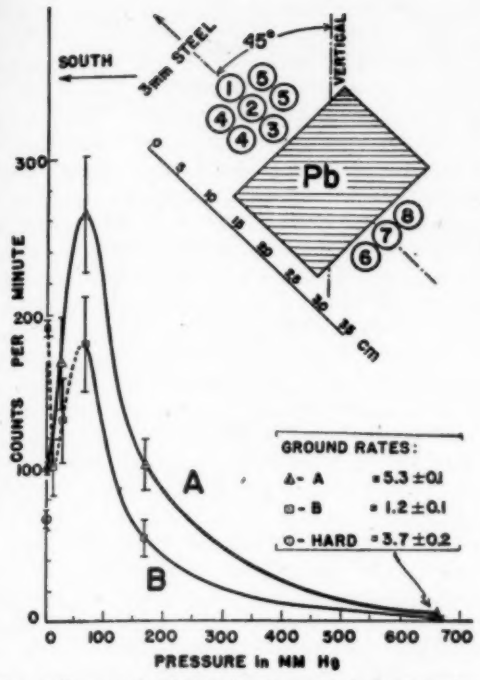

FIG. 1. Curve *A*, total intensity. Curve *B*, shower intensity. Circled points, intensity of penetrating component.

by anticounters 4 and 5 all operating in parallel. In a fourth channel, unprotected coincidences 1, 2, 3 were transmitted. The differences between these data and the similar, protected data give a measure of the showers.

The counters used had 0.8-mm brass walls. Resolving times for each channel were $\sim 5\times10^{-6}$ sec. Data were transmitted to ground by the same radio system used in the previous flight. The altitude attained was in excess of 160 km.

The telescope axis pointed south at a zenith angle of 45° through a 3-mm steel "window." Both zenith angle and azimuth were preserved through the atmosphere, but the telescope axis precessed about the zenith in free space. "Free space" is taken as the region of less than 2 mm Hg pressure.

Curve *A* in Fig. 1 shows the altitude dependence of the protected total intensity. It is seen that the counting rate in free space (based on 252 counts) was about $\frac{1}{3}$ that at the maximum (based on 22 counts). For the hard component, however, the counting rate within the atmosphere was too low to permit drawing a curve. Only two points are shown; the ground point determined by several hours of calibration, and the point in free space for which 150.6 seconds of operation (63 counts) was used. It is seen that the penetrating component amounts to about 70 percent of the total radiation. The shower rate in free space (480 counts) was again high as may be noted by curve *B* which is the difference between the unprotected and protected coincidences 1, 2, 3. The validity of the dip in this curve at 12 mm Hg is questionable. Of the 63 hard counts in free space 13 were associated with showers below the lead.

In the experiment of Schein, Jesse, and Wollan,[2] it was reported that very few of the particles penetrating 4 cm of lead produced showers under 2 cm. The present results would appear to be consistent with that data if the non-penetrating radiation were fairly soft. Further experimental work is in progress.

The writers wish to acknowledge the aid of their colleagues in the Rocket Sonde Research Section of the Naval Research Laboratory, and are especially indebted to Professor J. A. Wheeler, Princeton University, for helpful discussion.

[1] S. E. Golian, E. H. Krause, and G. J. Perlow, Phys. Rev. **70**, 223 (1946).
[2] M. Schein, W. P. Jesse, and E. O. Wollan, Phys. Rev. **59**, 615 (1941).

The Magnetic Field of the Galaxy

LYMAN SPITZER, JR.
Yale University, New Haven, Connecticut
October 24, 1946

THE force which galactic radiation pressure exerts on minute dust grains in interstellar space will give these grains a drift velocity of about 10^4 cm/sec. relative to the interstellar atoms.[1] On the average, this velocity should be directed away from the galactic center. The Coriolis force of galactic rotation will deflect these grains, and give them also a drift velocity at right angles to the direction of the galactic center. Thus the dust grains rotate more slowly about the galactic center than do the interstellar atoms and electrons. It is believed that each dust grain has an electric charge of roughly 100 electrons. Therefore, the differential rotation of the dust grains produces an electrical current circling the galactic center. This result requires that the number of dust grains per cm^3 be constant in the galactic plane along any circle of constant radius about the galactic center. While most of the observed galactic dust is concentrated in isolated clouds, present evidence indicates a "substratum" of more nearly uniform distribution.[2] On the assumption that the density of this substratum is 6×10^{-26} gram/cm^3, the primary galactic current, computed without regard to the important secondary effects discussed below, is about 10^{17} amperes. Since the effective radius of this circular current is between 5000 and 10,000 parsec., the magnetic field resulting is between 10^{-5} and 10^{-6} gauss.

This computed field is so large that secondary effects of the magnetic field on the primary galactic current must be taken into account. A field of 10^{-5} gauss would provide a deflecting force on the dust grains which would be about 10^6 times as great as the Coriolis force. A detailed study of this interaction is still in progress, but preliminary results indicate that the magnetic field in most of the galaxy will be no greater than is required to nearly cancel the Coriolis force, thus reducing the primary galactic current to a low value. Secondary effects on atomic ions must also be considered. The computations show that the resultant magnetic field is probably in the general neighborhood of 10^{-12} gauss. This tentative result is subject to very considerable revision as more complete information on the interstellar medium becomes available.

A field of 10^{-12} gauss would have several interesting effects. Its value agrees with the 10^{-11} to 10^{-13} gauss which Alfvén has assumed[3] to confine most of the observed cosmic rays within the galaxy. Protons and electrons from outside the galaxy could not reach the galactic plane near the sun unless their energies exceeded about 10^{13} electron volts. The rotation of the galaxy in this magnetic field would produce a slight separation of electrical charges, with a resultant radial electrical field of about 10^9 volts per 1000 parsec.; this field would cancel the magnetic force on a charge revolving in a circular orbit around the galactic center. Since the interstellar ions have thermal motions superimposed on their revolution about the galactic center, their paths relative to axes rotating with the galaxy would be curved by the magnetic field; at a mean thermal velocity corresponding to about 10,000°K, the radii of curvature for electrons and protons would be 0.2 and 8 astronomical units, respectively. The rotation of interstellar clouds containing ionized gas would tend to be slowed down by the eddy currents generated, thus facilitating the formation of stars. While these effects require further study, there is little question but that the possible presence of a galactic magnetic field must be taken into account in discussions of interstellar phenomena.

[1] L. Spitzer, Jr., Astrophys. J. **94**, 232 (1941).
[2] F. Seares, Astronom. Soc. Pac. **52**, 80 (1940).
[3] H. Alfvén, Zeits. f. Physik **107**, 579 (1937).

Discovery, Identification, and Characterization of 2.8*d* Ru^{97}*

W. H. Sullivan,** N. R. Sleight, and E. M. Gladrow
Plutonium Project, Iowa State College, Ames, Iowa
November 1, 1946

DURING the course of a series of investigations, which sought to disentangle many inaccuracies concerning the mass and element assignments of radioactive isotopes of Ru and Rh, a new Ru activity was discovered.

The observation of this isotope was made possible by examining deuteron and neutron-bombarded Ru samples after decay of the 4.5*h* Ru^{105} (i.e., formation of 36.5*h* Rh^{105} daughter activity) was practically complete (76 hours after bombardment) and after purification of Ru by distilling it as RuO_4 from fuming $HClO_4$ solution. This Rh-free Ru fraction showed a complex decay and graphical resolution of the decay curve gave 42*d* and ~3 day components. The 42*d* activity was shown in other experiments to be a Ru isotope, identical with the 45*d* Ru produced in fission.[1,2]

The characterization of the half-life and radiations of this short-lived activity was accomplished by using differential absorption-decay curve techniques. In these experiments, two families of decay curves, which used 25 different thicknesses of Al (from 0 added absorber to 1.51 g/cm² Al) and 8 different thicknesses of Pb (from 0.161 g/cm² Pb to 3.96 g/cm² Pb), were measured for a period of about 80 days. Each of the 33 decay curves was plotted and graphically analyzed into a 42*d* and a short-lived component. The average half-life value of the short-lived component was found to be 2.8±0.3 days.

By plotting an isochron*** from data for the 2.8*d* activity and resolving this absorption curve into its components, intense 18.$_2$ kev x-rays (150 mg/cm² Al half-value thickness) weak 0.2 Mev electrons (6–7 mg/cm² Al initial half-value thickness, 40–60 mg/cm² Al range), and 0.23-Mev gamma rays (0.9 g/cm² Pb half-value thickness) were found to be present. The relative intensities of these three types of radiation at zero added absorber (~20 mg/cm² total absorber) were 26:24:6.

The assignment of this isotope to mass 97 was based on the following considerations. By slow neutron activation only radio-isotopes Ru^{97}, Ru^{103}, and Ru^{105} would be produced. The 4.5*h* Ru→36.5*h* Rh decay chain, which was formed in slow neutron and deuteron-irradiated Ru and which was found to emit only negatrons, was assigned to mass number 105, since no other mass assignment would permit chain decay by negatron emission. The assignment of the 42*d* isotope to mass number 103 was based; (1) on Livingood's observation[3] that a 46*d* activity in deuteron-bombarded Ru emitted only negatrons; (2) on our observation that these negatrons were nuclear beta-radiations; (3) on arguments concerning the observed gamma-ray intensity ratio, $I_{2.8d/42d}=\sim 2$, at the end of bombardment. Using the assumption that the activation cross sections for Ru^{98} and Ru^{102} did not differ greatly and that the bombardment time was effectively "indefinitely short," it was found that the observed and predicted ratios were in much closer agreement for the assignments 2.8*d* Ru^{97} and 42*d* Ru^{103}, than for the assignments, 42*d* Ru^{97} and 2.8*d* Ru^{103}.

From the foregoing facts, observations, and deductions, the most probable decay process for Ru^{97} appeared to be *K* capture since the x-ray/γ-ray ratio of ~4 and the presence of low energy electrons (~0.2 Mev) pointed to partial conversion of the 0.23 Mev γ-ray rather than low energy positron emission, which could be the alternate mechanism. Also, the 18.$_2$ kev x-ray energy corresponded to that expected for element 43 formed by *K* electron capture in Ru.

A search for the daughter 43 activity of the 2.8*d* Ru^{97} did not give conclusive results since 42*d* Ru^{103} contaminated the element 43 fraction, isolated as the tetraphenyl arsonium salt. However, the data indicated 43^{97} must be long-lived and from absorption measurements in a windowless counter there was evidence that a very soft beta-ray was present. It was considered likely that this radiation was due to the 0.097-Mev electrons from the 90*d* isotope discovered by Cacciopuoti.[4]

This document is based on work performed under contract No. W-7405-ENG-82 for the Manhattan Project and the information covered in this document will appear in Division IV of the Manhattan Project Technical Series, as part of the contribution of the Iowa State College.

* The information presented here is abstracted from Plutonium Project Reports CC-921, issued September 15, 1943 and CC-1493, issued March 8, 1944.
** The present address of the writer is Clinton Laboratories, Oak Ridge, Tennessee.
*** The term, isochron, as used here, may be defined as an absorption curve obtained at any specified time from a family of decay curves through selected absorbers.

[1] Y. Nishina, T. Yasaki, K. Kimura, and M. Ikawa, Phys. Rev. **59**, 323 (1941).
[2] Y. Nishina, T. Yasaki, K. Kimura, and M. Ikawa, Zeits. f. Physik **119**, 195 (1942).
[3] J. J. Livingood, Phys. Rev. **50**, 425 (1936).
[4] B. N. Cacciopuoti and E. Segrè, Phys. Rev. **52**, 1252 (1937).

A Thermodynamic Criterion for the Fracture of Metals—Reply to a Criticism

EDWARD SAIBEL
Carnegie Institute of Technology, Pittsburgh, Pennsylvania
September 18, 1946

IN the note referred to above,[1] the author described a criterion for fracture of isotropic substances in simple tension. Zener[2] has chosen to criticize the criterion by citing some examples to which it was not intended to apply. The general principles necessary for handling the cases which he brought up have been treated in the main paper. This has been submitted for publication.

The author would like, however, to clear up, in a general way, the difficulties under which Zener is laboring. He asserts that the criterion is in contradiction to certain well-established principles regarding fracture. There are no well-established principles regarding fracture which are generally agreed upon. However, it is presumed that what is meant is that there is a contradiction between the theory and certain facts regarding fracture. The first of these mentioned is: the strain energy absorbed prior to fracture is dependent upon the conditions of test, for example, upon stress system, temperature, and rate of deformation.

The extent to which this is true is quite limited, and this point is not as important as it is made out. The fact is, these variables have a much greater effect on the ductility and stress at fracture than they do on the energy absorbed up to fracture. The last quantity is measured by the area under the flow curve and it is interesting to note in this connection that the author's opinion is shared by Vivian,[3] who states: "If the argument adopted in the writer's recent paper can be accepted, the curve is not only steeper, but is also shorter, to correspond with basic thermodynamic considerations. The consequence would be that the areas under the curves at different loading rates will tend to be constant, and will only differ owing to differences in the loss by the radiation and conduction of heat from the points at which straining is taking place."

The theory does take the variables into account. Their influence is reflected in the manner in which they affect the flow curve. If the flow curve is changed and the material is to fracture when the area under the flow curve reaches a certain critical value, calculated *a priori*, there must be a change in the ordinate and in the abscissa at fracture. This means physically a change in the fracture stress and in the ductility. That the proposed theory shows this, is evident from Table II of the original paper.[1]

The second so-called principle mentioned is that, under constant test conditions, the strain energy at fracture is very structure sensitive. The expression, structure sensitive, has been used in the literature to mean several widely different things. In the sense in which Zener used the term, namely: two steels, one of which is temper brittle and the other not, may have precisely the same flow stress and yet under severe test conditions the ductility and, hence, the strain energy of fracture of the latter may be many times that of the former, has been explained in the main paper on the basis of an initial energy density existing in the temper brittle specimen. It is true that it is difficult to estimate the initial energy density in a specimen, but that is hardly a reflection on the theory. One calculable case, the determination of the fracture stress of a specimen pulled in tension under a superimposed hydrostatic pressure, has been worked out in the main paper, and the results are in good agreement with experimental findings.

In the case of torsion, it can only be said that no completely satisfactory solution of the state of stress and strain in a solid cylindrical specimen twisted beyond the elastic limit has been worked out as yet. Consequently, it is not known just how the complicated distribution of stress and strain and the consequent effect on the energy density affects the fracture problem.

[1] E. Saibel, Phys. Rev. **69**, 667 (1946).
[2] C. Zener, Phys. Rev. **70**, 225 (1946).
[3] A. C. Vivian, Engineering p. 423 (June 2, 1944).

Mass Spectrographic Confirmation of the Isotopic Assignment for the Long-Lived Radioactivity in Beryllium

A. K. PIERCE AND F. W. BROWN, III
Radiation Laboratory, Department of Physics, University of California, Berkeley, California
August 13, 1946

IN a recent paper by McMillan and Ruben[1] the existence of a long period beryllium activity, presumed to be Be^{10}, has been shown. We have confirmed this mass assignment by observing the activity of samples separated by a mass spectrograph.

This material used was part of sample *C* of reference 1, which had been activated and purified in 1940. This material was in the form of BeO; it was mixed with powdered charcoal, heated to 600°–700°C, and chlorine gas passed over it to generate $BeCl_2$ vapor which was carried into the ion source arc by the gas stream. The measurements on samples collected at the mass 9 and mass 10 positions were:

Be^9:	
Weight of Be collected =	9.8 ± 0.3 mg
Counting rate =	20.3 ± 0.7 counts/min.
Background =	21.6 ± 0.4 counts/min.
Activity =	-1.3 ± 0.8 count/min.
Be^{10}:	
Counting rate =	62.2 ± 0.9 counts/min.
Background =	21.6 ± 0.4 counts/min.
Activity =	44.6 ± 1.0 counts/min.

From counts of the original BeO sample under the same counting conditions the expected counting rate for the collected Be^{10} sample should be 56.5 ± 2.4 counts/min. if all the activity were owing to Be^{10}. Therefore, we can ascribe the β-activity to Be^{10}.

The sample used in this determination was furnished through the courtesy of Professor E. M. McMillan.

This work is part of a general program of the isotopic assignment of radioactivities initiated by Dr. B. J. Moyer; it was done under the auspices of the Manhattan District under Contract No. W-7405-Eng-48.

[1] E. M. McMillan and S. Ruben, Phys. Rev. **70**, 123 (1946).

The "Two-Step" Isomeric Transition in Te^{121}

P. T. BITTENCOURT* AND M. GOLDHABER
Department of Physics, University of Illinois, Urbana, Illinois
October 31, 1946

IT was recently shown here that the metastable state of Te^{121} (125–143d) decays by a "two-step" isomeric transition, where one step corresponds to an energy of ~50 kev and the other to an energy of ~225 kev.[1] The order in which these steps take place could not be decided in the previous work. The transitions were found to follow each other within a mean time shorter than the resolving time of the coincidence circuit used (0.8×10^{-6} sec.). Using the method of "delayed coincidences" and a circuit with a smaller resolving time (0.45×10^{-6} sec.), we have been able to establish the order in which these transitions take place, as well as the half-life time of the lower excited state. A short-lived metastable state, following β-decay of Hf^{181} into Ta^{181*} (22 μsec.), was first studied by de Benedetti and McGowan[2] with the help of delayed coincidences.

Our experimental procedure, which permits the measurement of half-life times which are of the same order of magnitude as the uncertainty in the "firing time" of a Geiger counter, was the following: The 50-kev transition was detected through the Te K x-ray emitted when it is internally converted, and the 225-kev transition through the unconverted γ-ray. The x-rays were identified with the help of critical absorbers and the γ-rays by Pb absorbers. The pulse from either the x-ray or the γ-ray Geiger counter could be delayed by a known time interval with the help of a delay line. The resolving time of the coincidence circuit, as determined from chance coincidences, was found to be 0.45×10^{-6} sec. This is approximately one-half of the mean width of the curve obtained for the delayed coincidences when UX_2 β-rays were sent through both counters. These measurements served to calibrate the arrangement for "zero time delay" (Curve 1, Fig. 1). The curve for the $x-\gamma$ delayed coincidences (curve 2) shows a definite shift relative to the UX_2 calibration curve indicating that the 50-kev transition preceeds the 225-kev transition. The tail of the right part of curve 2 follows approximately an exponential curve corresponding to a half-life time of $(5\pm2)\times10^{-6}$ sec. for the excited state of Te^{121} of 225-kev energy.

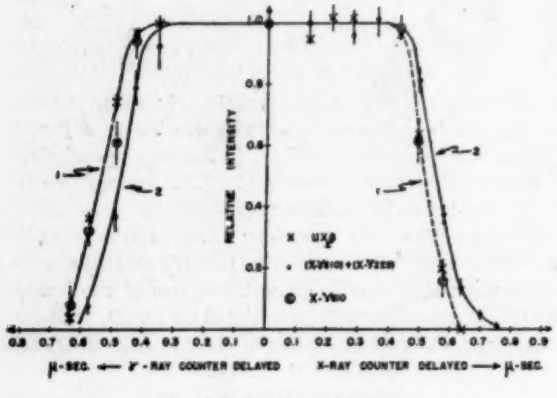

FIG. 1. Delayed coincidences.

The ground state of Te^{121} (16–17d) decays by K-electron capture to Sb^{121} which is usually left in an excited state of 610-kev energy. With the 225-kev γ-rays practically removed by a Pb absorber, $\frac{1}{16}$" thick, delayed coincidences between the 610-kev γ-rays and Sb K x-rays were studied. No delay between these γ-rays and the x-rays could be detected (see Fig. 1). From this we can conclude that the lifetime of the excited state of Sb^{121} is $<2\times10^{-8}$ sec.

Our thanks are due Mr. Oscar Sala for valuable help in carrying out these measurements.

* Rockefeller Fellow of the University of São Paulo, São Paulo, Brazil.
[1] S. B. Burson, P. T. Bittencourt, R. B. Duffield, and M. Goldhaber, Phys. Rev. **70**, 566 (1946).
[2] S. de Benedetti and F. K. McGowan, Phys. Rev. **70**, 569 (1946).

The Microwave Spectrum of Ammonia

LAWRENCE N. HADLEY AND D. M. DENNISON
Randall Laboratory of Physics, University of Michigan, Ann Arbor, Michigan
October 31, 1946

RECENTLY a number of excellent determinations have been made of the fine structure of the inversion band of ammonia at $\nu=0.8$ cm^{-1}. The experiments were performed independently by Bleaney and Penrose,[1] by Townes,[2] and by Good[3] and are all in substantial agreement. Approximately 30 lines were observed and these were fit by a formula containing the rotational quantum numbers J and K. The formula given by Good contains a power series up through the quartic terms but it will be sufficient for our purpose to include only the quadratic terms. Experimentally,

$$\nu/hc=0.79347-0.005048(J^2+J)+0.007040K^2.$$

The splitting of the next higher pair of ammonia levels was determined from infra-red measurements by Sheng, Barker, and Dennison.[4] For these excited levels, they found,

$$\nu/hc=35.9-0.17(J^2+J)+0.23K^2.$$

The existence of the terms in J^2+J and in K^2 were attributed by S., B., and D. to the influence of centrifugal forces which effectively produce a slight change in the potential hill separating the two minima and hence affect the splitting of the levels. A theory was developed which, for the first excited states, gave the very satisfactory result,

$$-0.162(J^2+J)+0.222K^2.$$

The splitting of the ground states was also calculated and it was found that the coefficients of J^2+J and of K^2 were so small as to be virtually unobservable in the infra-red. The wonderful dispersion now attainable in the microwave region makes the influence of these terms easily measurable. The numerical agreement between the observations and the predictions of S., B., and D. was, however, poor. We have reexamined the problems and have found that numerical errors had been made in evaluating the formulas, particularly for the ground state levels.

Our recomputation yields the following values[5]

$$\begin{array}{ll} \textit{First Excited States} & -0.156(J^2+J)+0.219K^2, \\ \textit{Normal States} & -0.0035(J^2+J)+0.0053K^2. \end{array}$$

The agreement between theory and experiment for the excited states is still good; but for the ground states, where the experimental data are the best, it is only fair.

We have reexamined the theory and have attempted certain variations. (a) the Manning double minimum potential was replaced by a parabolic double minimum[6] but no substantial change was found. (b) The paths of the hydrogen particles throughout the motion were originally determined through the potential constants of the molecule. These are not known with too great accuracy and some variation in path could be used. Unfortunately, a change that helps the agreement for the normal states, tends to produce disagreement for the excited states. As an example we took a path where $(dr/d\alpha)_{\alpha=\alpha_0}=0.20$. (The value used by S., B., and D. was 0.10.) We find,

$$\begin{array}{ll} \textit{First Excited States} & -0.21(J^2+J)+0.24K^2, \\ \textit{Normal States} & -0.0047(J^2+J)+0.0059K^2. \end{array}$$

On the whole these results are moderately satisfactory. It appears to us that the remaining discrepancies may be attributed in part to the approximate character of the theory and in part to a lack of knowledge of the details of the molecular forces in ammonia.

[1] B. Bleaney and R. P. Penrose, Nature **157**, 339 (1946).
[2] C. H. Townes, Phys. Rev. **70**, 109(A) (1946).
[3] W. E. Good, Phys. Rev. **70**, 213 (1946).
[4] H. Sheng, E. F. Barker and D. M. Dennison, Phys. Rev. **60**, 786 (1941).
[5] In a private communication Dr. Townes informed us that he also has recalculated certain of the splittings. His results appear to be in substantial agreement with ours.
[6] D. M. Dennison and G. E. Uhlenbeck, Phys. Rev. **41**, 313 (1932).

Solar Ultraviolet Spectrum to 88 Kilometers

W. A. Baum, F. S. Johnson, J. J. Oberly, C. C. Rockwood, C. V. Strain, and R. Tousey
Naval Research Laboratory, Washington, D. C.
November 1, 1946

THE ultraviolet spectrum of the sun below 3400A was photographed to altitudes up to 88 km by means of a spectrograph mounted in the tail fin of a V-2 rocket. The rocket was fired on October 10, 1946 by Army Ordnance at the White Sands Proving Grounds, New Mexico, and reached an altitude in excess of 160 km. A series of 35 spectra was obtained during the ascent. Solar spectra above 88 km were not photographed because the rocket turned the spectrograph away from the sun, and excessively rapid use of film produced by severe vibration earlier in the ascent prevented operation above 107 km.

The spectrograph was designed for the nose of the rocket and utilized an f:10, 40 cm radius, 15,000 line/inch grating in a Rowland mount. The grating was ruled on aluminum at the Johns Hopkins University. The film was Eastman 35-mm 103-0 ultraviolet sensitized, and was 20 feet long. As many as 100 exposures could be taken. An eight-second exposure cycle with separate exposures of 0.12, 0.66, and 3.6 seconds was provided. In place of a slit a 2-mm diameter sphere of lithium fluoride was used. This formed a small real image of the sun which acted as source and because of the astigmatism introduced by the grating produced a line spectrum. This system accepted sunlight over a wide field of view and was many times faster than a conventional slit of equivalent width covered with a diffusing plate. A second bead was placed diametrically opposite the first to provide a second channel, thereby doubling the chance of receiving sunlight as the rocket turned. A plane mirror on each side folded the two light paths to fit the conical nose. The dispersion was 44A/mm and the resolution about 3A. The spectrograph was evacuated by a port open to the atmosphere. The short wavelength limit of the spectrograph was set by the transmission limit of the lithium fluoride bead, and spectra to wavelengths as short as 1100A were produced in the laboratory.

Sample spectra are reproduced in Fig. 1. All exposures shown were 3.6 seconds and altitudes given are above sea level. Up to about 44 km the rocket was stabilized. Above this point it rolled and yawed and spectra F and G were taken with the sun well off axis. Consequently G, the highest solar spectrum taken to date, was so lightly exposed that it showed less ultraviolet than F. The spectra were shaded in printing to emphasize as much as possible the region of interest. Definition in E and F was reduced by vibration and by rotation of the rocket. It was a

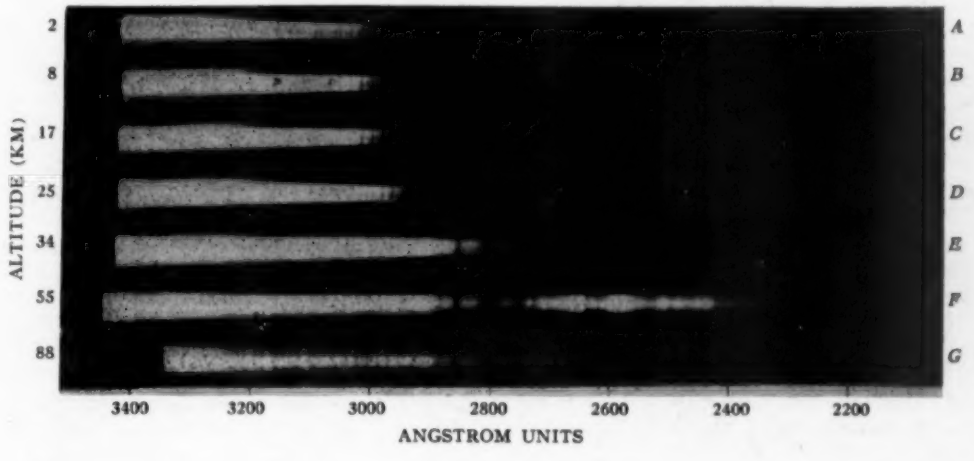

FIG. 1. Solar spectrum at various altitudes.

characteristic of the bead slit system that the spectra moved slightly, mainly along the lines, as the rocket rolled. The effect appears in spectra *F* and *G* which show the spectrum displaced somewhat along the lines during exposure.

Preliminary examination of the spectra showed a progressive extension of the spectrum into the ultraviolet. At 25 km the spectrum was photographed to 2925A. Spectrum *E* taken at 34 km extended to 2650A and showed measurable blackening from approximately 2100 to 2260A which may be lost in reproduction. At 24 km therefore there was still enough ozone above to prevent recording the spectrum in the central region of the Hartley band of ozone, but transmission in the window between the Hartley band and the oxygen absorption at shorter wavelengths was observed. At 55 km sufficient ozone was passed through to permit photographing the spectrum throughout the Hartley band.

An analysis of the absorption features of the spectrum and a determination of the solar spectra intensity curve of the sun and of the details of the ozone distribution in the atmosphere are in progress.

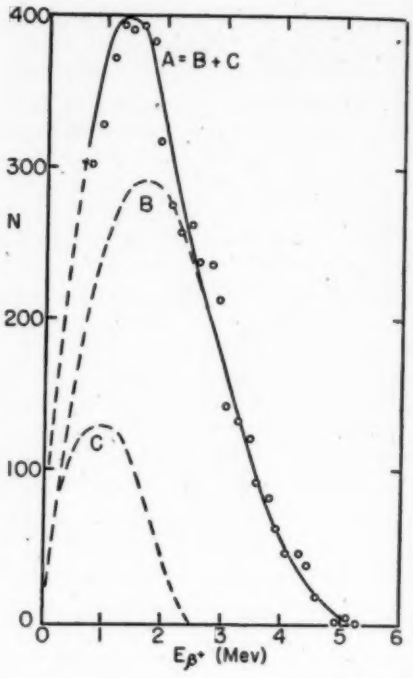

FIG. 1. Energy distribution of the positrons from Cl^{34}.

Disintegration of $_{17}Cl^{34}$

HO ZAH-WEI
Laboratoire de Chimie Nucléaire du Collège de France, Paris, France
October 2, 1946

THE β^+-spectrum of $_{17}Cl^{34}$ has been already studied by Sagane[1] by means of a Wilson chamber and its maximum energy has been estimated to be 3 Mev. On the other hand, Brandt,[2] using the absorption method, has obtained a value of 2.5 Mev. Neither author indicated any presence of γ-rays from the disintegration of $_{17}Cl^{34}$.

In order to obtain more accurate data on the energy and disintegration process of $_{17}Cl^{34}$, I have undertaken the experiment with a Wilson chamber of longer effective time. The source of $_{17}Cl^{34}$ which is relatively thin is prepared by the bombardment of CuS by fast deuterons, according to the reaction

$$_{16}S^{33}(d, n)_{17}Cl^{34}.$$

As S^{33} is a rare sulphur isotope (only 0.74 percent), the activity of Cl^{34} is relatively weak. The active chlorine is precipitated in the form of AgCl; purification and precipitation are repeated, until the source shows no other activity than that of 33-minute period from $_{17}Cl^{34}$.

The experimental conditions are as follows: The cloud chamber is filled with air at an initial pressure of 1.9 atmos., the magnetic field being 900 gauss. The source is placed outside the chamber. After traversing a mica window of 12 mm diameter, (3.94 mg/cm^2), the trajectories of the positrons are photographed stereoscopically.

In total, 2088 positron tracks with $H\rho > 3500$ gauss-cm ($E_\beta > 680$ kev) have been measured. Their energy distribution is shown in Fig. 1, curve *A*. The maximum energy of

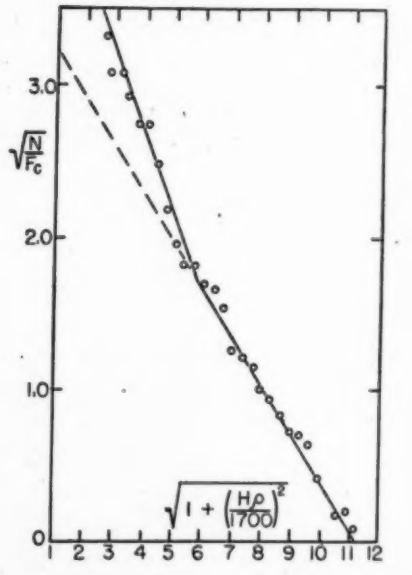

FIG. 2. Van der Held plot of the positron spectrum from Cl^{34}. The abscissa represents the energy, including the rest energy, of the positron in units of the rest energy of an electron.

β^+-spectrum is estimated to be 5.1 ± 0.3 Mev. In order to know whether the spectrum is simple or complex, analysis has been carried out according to Van der Held's method[3] which is a combination of the Fermi's and Konopinski-

Uhlenbeck's plots. It has the advantage that one can deduce the correct form of a single spectrum from the observed maximum energy. The result of analysis (Fig. 2) shows that the spectrum is not simple and is composed of at least 2 components with the maximum energy of 5.1 and 2.4 Mev, respectively. The ratio of their intensities is 4:1 (Fig. 1, curves *b* and *c*).

During the experiments, besides the positron tracks, about 200 recoil electrons have also been observed, which have their origin either in the mica window or in the glass wall of the chamber. The energy distribution (Fig. 3) indicates a maximum energy of 3.1 ± 0.3 Mev which corresponds to a γ-ray energy about 3.4 Mev.

In summary, $_{17}Cl^{34}$ emits a β^+-spectrum which is complex, composed probably of two components or more with maximum energies about 5.1 and 2.4 Mev, and emits besides, at least a γ-ray of energy about 3.4 Mev. According to the decay constant and the observed β^+ maximum energy, the disintegration of $_{17}Cl^{34}$ belongs to the forbidden transition (it lies on the second curve of the Sargent's diagram).

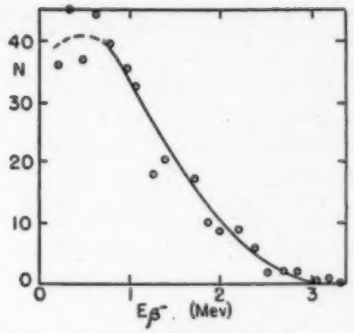

FIG. 3. Energy distribution of recoil electrons from gamma-rays from Cl^{34}.

[1] R. Sagane, Phys. Rev. **50**, 1141 (1936).
[2] H. Brandt, Zeits. f. Physik **108**, 726 (1938).
[3] E. F. M. Van der Held, Physica **8**, 196 (1941).

Proceedings of the American Physical Society

Addendum to the Minutes of the Meeting of July 12–13, 1946, at Berkeley

An oversight of which the Local Secretary for the Pacific Coast is innocent, led to the omission from the Minutes of the Berkeley meeting [Phys. Rev. **70**, 443 (1946)] of the names of the participants in the excellent Symposium and of the titles of their papers. This Symposium deservedly attracted an attendance surpassing by far the greatest hitherto recorded at our meetings on the West Coast, 500 persons being crowded into a room seating 380 while others could not even enter. Its title and its composition were as follows:

Symposium: The Production and Use of High Energy Particles

1. **Why Are We Interested in High Energy Particles?**
   J. Robert Oppenheimer, *University of California.*
2. **The Experimental Problem of Accelerating Charged Particles.**
   Ernest O. Lawrence, *University of California.*
3. **The Design of a Linear Accelerator for Protons.**
   Luis W. Alvarez, *University of California.*
4. **The Synchrotron.**
   Edwin M. McMillan, *University of California.*
5. **The 184" Cyclotron.**
   R. L. Thornton, *University of California.*

This Addendum is signed by the Secretary in order to remove all suspicion of blemish from the too-brief and now-ended career of R. T. Birge as Local Secretary for the Pacific Coast (1941–46). J. Kaplan now succeeds to this distinguished office.

Karl K. Darrow, *Secretary*
American Physical Society
Columbia University
New York 27, New York

Minutes of the Meeting of September 19–21, 1946 at New York

The 274th meeting of the American Physical Society was held at New York City, in the building of the Engineering Societies, on Thursday, Friday, and Saturday, September 19, 20, and 21, 1946. This was a meeting of unprecedented character in more than one respect. It was confined to papers on three topics: cosmic-ray phenonema, theories of elementary particles, and the design and operation of accelerators of nuclear particles and electrons. Disparate as these three subjects may appear to be, the trend of physics is rapidly uniting them. The ratio of invited to contributed papers was higher than normal, and a novel feature was introduced in the form of concerted prearranged discussions by distinguished authorities. Many guests from overseas were present, some of whom had timed their visits to the United States in order to attend our meeting, while we ourselves had timed the meeting so as to suit the convenience of others who came to attend the Princeton University conference on nuclear science. The halls were provided for us by the generosity of the American Society of Mechanical Engineers. We are grateful to this Society and to Miss Muriel England of its New York office, who handled many of the troublesome details. This excellent meeting owes its origin and most of its features to the initiative and labor of J. A. Wheeler, the head of the Local Committee.

Over a thousand people attended the meeting, and the great auditorium of the Engineering Societies was frequently jammed, in spite of tropical conditions indoors and outdoors; for the weather did not cooperate, inflicting upon us a heat-wave such as would have been excessive in midsummer. A large number of potent germs appear also to have attended the meeting, to judge from the colds which beset many of our members soon after.

The dinner was held on the evening of September 20 at the Mens' Faculty Club of Columbia University, which again could not accommodate the hosts of would-be diners. We shall

probably feel obliged to contract at our next New York meeting for a much larger hotel diningroom at a correspondingly greater cost. The after-dinner speech was delivered in the McMillin Theatre by P. M. S. Blackett on the topic "The Tradition of Science." The numerous other invited papers are listed hereinafter, with abstracts (another deviation from our practice). The discussion leaders were P. M. S. Blackett for cosmic-ray phenonema and C. G. Suits for accelerators.

The Society has lost through death B. O. Grönblom of Finland and S. Kalandyk of Poland, both victims of the war.

The Council, meeting on September 19, elected to Fellowship the 25 candidates and to Membership the 124 candidates whose names appear below.

Elected to Fellowship: H. H. Barschall, L. L. Beranek, Egon Bretscher, H. W. Emmons, Richard Feynman, T. L. Fowler, Otto Frisch, Darol Froman, S. L. Gerhard, D. T. Griggs, Morton Hamermesh, A. O. Hanson, Marshall Holloway, Joseph Keller, L. D. P. King, J. L. McKibben, Hugh Richards, R. D. Richtmeyer, B. W. Sargent, Otto Struve, Richard Taschek, Theodore von Karman, Ernst Weber, Royal Weller, and R. R. Wilson.

Elected to Membership: H. H. Abelew, D. F. Abell, Fay Ajzenberg, Marcelo Alonso, A. V. Baez, N. A. Baily, H. W. Baldwin, J. G. Beckerley, L. J. Berberich, R. W. Birge, R. R. Blackwood, E. A. Blasi, M. D. Blatt, D. L. Bobroff, L. R. Boyd, H. L. Bradt, G. H. Briggs, LeRoy S. Brooks, E. L. Bussell, Joseph Burnsweig, Jr., H. E. Carr, K. C. Clark, P. B. Cole, C. H. Collie, A. H. Cooke, A. R. Crooker, Leon Damas, Estrella A. M. de Mathov, R. J. Debs, R. J. Dery, W. J. Deshotels, Malcolm Dole, T. M. Donahue, B. D. Donn, L. D. Fallon, Jerone Fleeman, E. C. Fowler, J. S. Fraser, E. H. Gamble, E. D. Goddess, Edith Goldfarb, J. I. Greenberger, L. R. Greene, Jay Gregory, W. L. Grube, W. G. Guindon, E. W. Guptill, T. M. Hahn, Jr., Theodore Hall, J. R. Hamilton, Michael Harold, W. D. Hartsough, A. E. Hayes, Jr., A. G. Hellfritzsch, E. P. Hincks, G. E. Holbrook, R. B. Holt, G. A. J. Homes, C. W. Huffman, R. I. Hulsizer, R. E. Johnson, Seymour Katcoff, R. F. Kingsbury, R. W. Keaton, A. P. King, M. J. Kofoid, Lew Kowarski, Sidney Krasik, J. J. Kyame, D. E. Lawrence, David Lazarus, L. M. Lederman, Leonard Lesensky, E. A. Long, G. H. Markstein, E. I. Mates, J. F. Mathison, R. S. Mathur, R. K. McCombs, J. R. Menke, Sydney Meshkov, C. H. Miller, G. E. Mueller, Ann Muzyka, J. A. Newth, L. D. Norris, Jr., C. J. Oberist, G. E. Ogden, A. O. Oliner, M. L. Oliphant, W. J. Ozeroff, C. L. Peacock, R. P. Penrose, Edward Peskin, V. Z. Peterson, E. R. Pounder, L. L. Pourciau, G. T. Reynolds, L. B. Robinson, W. J. Robinson, Jr., Basil Rose, George Schecter, J. M. Schwartz, Donna J. Seaman, Walter Selove, Lena Sharney, Martin Silverman, Miriam Skinner, R. C. Smith, H. M. Spivack, W. H. Stephens, A. B. Stewart, A. J. Stosick, W. G. Stroud, Jr., W. M. Strouse, K. R. Symon, C. S. Szegho, W. B. Van Horne, E. S. Van Valkenburg, D. S. Webber, F. A. White, R. W. Williams, J. W. Wise, and W. J. Wyatt.

KARL K. DARROW, *Secretary*
American Physical Society
Columbia University
New York 27, New York

ABSTRACTS OF PAPERS

Cosmic-Ray and Subnucleonic Physics

Invited Papers

C1. On the Determination of the Energy Spectrum and Sign of Primary Cosmic Radiation. M. S. VALLARTA, M. L. PERUSQUÍA AND J. DE OYARZABAL, *University of Mexico.*—One of us[1] suggested the measurement of the azimuthal effect of cosmic radiation as a means of determining the sign and the energy spectrum of primary cosmic rays. This experiment, of duration exceeding 100 days for each continuous run, has now been carried out in Mexico City (geomagnetic latitude 29° N, altitude 2250 m) using trains of triple coincidence counters. The zenith angle is kept constant throughout a given run and only the azimuthal angle is changed by rotating the apparatus around a vertical axis. The rotation and photographic recording is wholly automatic. The apparatus was designed and built by A. Baños, Jr. and M. L. Perusquía.[2] The theory of the experiment depends on the knowledge of the allowed cone and particularly of the so-called penumbra bands.[3] Since the length of atmospheric path traversed by cosmic rays is the same, it is assumed that the number of particles counted by the instrument in a given direction is a measure of the number of primary particles arriving outside the atmosphere from the same direction. The experiment as performed explores the energy band between 0.512 and 0.307 Störmer (14.5 and 6.3 Bev for protons). In this band the energy spectrum is best represented by the law K/E^c, where K is a constant, E is the energy and c varies between 3.7 for low energies and 2.4 for high energies. There is no indication of negative particles. Possibly the results could also be explained by a line spectrum of positive particles alone, with sharp lines corresponding to energies around 0.35, 0.38 and 0.45 Störmer (6, 8 and 13 Bev for protons), but only much better resolution could finally settle this

point. The present results agree satisfactorily with those derived from the experiments of Gill,[4] carried out in Lahore (Punjab, India, 22° geomagnetic latitude).

[1] M. S. Vallarta, Rev. Mod. Phys. 11, 239 (1939).
[2] An account of the design, construction and operation of this instrument by A. Baños, Jr. and M. L. Perusquía, will be submitted shortly to the *Review of Scientific Instruments*.
[3] R. A. Hutner, Phys. Rev. 55, 15 (1939); 55, 614 (1939).
[4] P. S. Gill, Phys. Rev. 67, 347 (1945).

C2. The Periodic Orbits of Cosmic-Ray Particles at High Magnetic Latitudes. CARLOS GRAEF-FERNÁNDEZ, *Institutos de Física y de Matemáticas de la Universidad Nacional de México, and Observatorio Astrofísico de Tonanzintla, Puebla.*—The forms of the trajectories of primary cosmic-ray particles are analyzed in the large, starting with the differential equations of motion. It is found that the distribution of points of inflection and flat points along an orbit is essential in determining its form. From purely geometrical considerations it follows that all periodic orbits of the primary cosmic radiation cut the geomagnetic equator. An important physical consequence of this result is the fact that, since there are no periodic orbits which remain at a high magnetic latitude, charged cosmic particles cannot stay in those regions moving periodically around the dipole. When the sun has an outburst of charged particles which arrive at the vicinity of the earth, these can form an equatorial ring-current which lasts a short time, but they can never form ring-currents at high magnetic latitudes. Thus it is a sufficient approximation to consider an equatorial ring current in dealing with magnetic storms due to moving charged particles, as Vallarta has suggested.

C3. Attempt of an Analysis of Some Cosmic-Ray Phenomena. R. P. FEYNMAN AND H. A. BETHE, *Cornell University.*—Schein, Jesse and Wollan[1] have suggested that the primary cosmic radiation consists predominantly of protons, and have given evidence for this hypothesis. They assume that the protons produce mesons by collisions with the nuclei of the air, and that the mesons decay into electrons and neutrinos, thus giving rise to the soft component. We wish to develop this hypothesis more quantitatively, without making specific assumptions about the theory of the processes involved. The following experimental data were used: (1) The intensity of the hard component as a function of altitude[1] (see also private communication by Dr. Schein). (2) The ratio of soft to hard component up to 4300 meters.[2] (3) The total vertical intensity as a function of altitude from 4300 meters up, measured by coincidences.[3,4] (4) The energy distribution of mesons at sea level.[5] (5) The energy distribution at Echo Lake.[6] Curves representing a consolidation of these data will be presented. In addition, we made the following assumption, based both on theoretical and experimental evidence: (6) A proton produces, in general, several mesons in a collision with a single nucleus, and loses almost all its energy in this process. The cross section for such collisions is about the geometrical size of the nucleus, so that protons in air will be absorbed to $1/e$ in a distance of about 60-cm water equivalent. The conclusions we have reached so far are the following: (1) In spite of the multiple meson production, there need not be a maximum in the total intensity of the hard component as a function of altitude. This is because the meson decay is proportional to the distance traveled, whereas the production is proportional to the amount of material traversed. No maximum in the intensity has been observed. From this it can be concluded that the average multiplicity of production, ν, is smaller than $A+1$ where A is related to the average decay of the mesons. Assuming Rossi's measurement of the lifetime,[6] $A=1$ Bev/E where E is an average meson energy. Near the magnetic equator, the intensity as a function of altitude might have a maximum, because either the average multiplicity of production or the average energy of the mesons would be higher. (2) The increase in the soft component below the top of the atmosphere should at first be linear until, at about 4-cm Hg, shower multiplication becomes important. The initial rate of increase of the *total* intensity should be $\nu-1$ times the rate of decrease of the primary protons, because each decaying meson produces one electron. Present evidence indicates that ν is greater than 1 but probably less than 4. Together with the shape of the curve for the hard component (point 1), this indicates that the average meson energy is somewhat, but not much, below 1 Bev. (3) Schein's data on the hard component, assuming the primary protons to decay with a 60-cm water equivalent mean free path, give the number of mesons at each altitude. The energy released by the decay of these mesons can be calculated directly and gives 2 Bev per incident primary particle. If half of this energy is liberated as neutrinos, we should expect the total energy in the soft component to be 1 Bev. The ionization loss of the hard component above ground is 0.6 Bev. Thus the total ionization losses above ground should be 1.6 Bev per incident primary. However, a direct integration of the curves for the total vertical intensity gives 2.0 Bev lost per incident primary showing that the intensity in the soft component (1.4 Bev) is larger than can be accounted for by meson decay (1.0 Bev). (4) From the latitude distribution[3] the average energy of the incident particles at 50° N latitude is calculated to be about 9 Bev. This is in serious disagreement with the 2.0-Bev loss measured directly. The discrepancy is somewhat reduced if we assume that all the soft component (1.4 Bev) comes from meson decay; then the unobservable neutrinos produced would carry an additional 1.4 Bev, and adding the loss of energy (about 0.6 Bev per incident primary) by mesons below ground an energy of 4 Bev per incident primary can be accounted for, but this appears still to be definitely below the 9 Bev expected from the latitude effect. This may indicate that there are fewer incident protons than is indicated by extrapolating Schein's curve, or that energy is carried away by neutral mesons, or by some other component of cosmic rays which carries appreciable energy. Powell[7] has suggested from cloud-chamber photographs of stars that the star producing radiation (probably neutrons) carries a very appreciable fraction of the total cosmic-ray energy. (5) The energy distribution of mesons at sea level[5] is in good

agreement with the assumption that they are produced near the top of the atmosphere with an energy distribution of the form $E^{-2.9}dE$ and are subject to ionization loss and decay in the atmosphere. However, the energy distribution at Echo Lake[6] contains too many slow mesons for such a hypothesis. It is difficult to account for these slow mesons by production near the top of the atmosphere (where they would have energies of about 1.5 Bev). It seems likely that the slow mesons are produced at lower elevations by photons whose energy distribution would explain the predominance of slow mesons. The cross section for production by photons would be of the order of 10^{-27} cm^2 per nucleon. Some direct evidence for such production has been obtained.[8] (6) The intensity of soft radiation at any given elevation is due partly to decay of mesons while in motion, partly to decay of mesons which have been stopped. The number of electrons in the soft component above 20 Mev which would be expected to arise in this way agrees roughly with the number measured by Greisen as a function of altitude. (7) The large number of processes necessary to produce the soft component, plus the large scattering of the electrons by the air atoms, will decrease the correlation between the direction of the primaries and that of most of the shower electrons. This may explain the smaller East-West effect observed for soft as compared with hard component at high altitude—provided this observation proves correct.

[1] Schein, Jesse, and Wollan, Phys. Rev. **59**, 615 (1941).
[2] K. Greisen, Phys. Rev. **61**, 212 (1942).
[3] Millikan, Neher, and Pickering, Phys. Rev. **61**, 397 (1942); **63**, 234 (1943).
[4] Carmichael and Dymond, Proc. Roy. Soc. **171**, 321 (1939).
[5] This has been measured indirectly with a cloud chamber by Haydn Jones, Rev. Mod. Phys. **11**, 235 (1939), and indirectly by absorption in lead of various thickness by Nielson, Ryerson, Nordheim, and Morgan, Phys. Rev. **59**, 548 (1941), and in the earth, J. Clay, Physica **6**, 184 (1939), and V. C. Wilson, Phys. Rev. **53**, 337 (1938).
[6] Rossi, Stearns, Froman, and Koontz, Phys. Rev. **61**, 675 (1942).
[7] W. H. Powell, Phys. Rev. **69**, 385 (1946).
[8] See, for example, Schein, Jesse, and Wollan, Phys. Rev. **57**, 847 (1940).

C4. Multiple Production of Mesons by Protons. H. A. BETHE, *Cornell University.*—Heitler, Hamilton, and Peng[1,2] have calculated the production of mesons by collisions between two nucleons, using the Weiszaecker-Williams method and a calculated cross section for the scattering of mesons by nucleons. We shall in this paper assume their scattering cross section to be correct. H. H. P. assume that in a collision between two nucleons only *one* meson can be produced. Any multiple production of mesons in collisions between a proton and a nucleus is attributed to the fact that the nucleus contains many nucleons which can be struck successively by the proton.[3] A result of the theory is that the multiplicity of production is small, that the cross section is considerably greater than the geometric cross section of the nucleus, and that protons (or neutrons) of considerable residual energy may emerge from the collision. We believe that actually *several* mesons can be produced even in a collision between two individual nucleons. In the Weiszaecker-Williams method, we consider the passage of two nucleons at a certain distance b (impact parameter). One nucleon is considered as carrying a field of virtual mesons, any one of which may be scattered by the other nucleon and thereby be converted into a real meson. Now the various virtual mesons can be scattered quite independently, subject only to the condition that the sum of their charges compensates the change of charge of the nucleons. Because of the large coupling between mesons and nucleons, a close passage ($b<\hbar/\mu c$ where μ=meson mass) will in general lead to the emission of several mesons of different energy. In the theory of Heitler and Peng this fact appears in the form that for small b the probability of meson emission is greater than one. This fact, whose correct interpretation is multiple production, was overlooked by the authors and, after integration over the impact parameter b, gave rise to their excessive cross sections. In the analogous process of Bremsstrahlung, the emission of several quanta in one collision is, of course, very unlikely because of the small coupling. However, in principle, the emission of several quanta is certainly possible.[4] In a collision between two nucleons, then, the close passages ($b<\hbar/\mu c$) lead to multiple production while the more distant passages give an exponentially decreasing probability of production. The total cross section is of the order of $(\hbar/\mu c)^2$. In a collision between a nucleon and a heavy nucleus, the multiplicity suggested by Jánossy, i.e., that due to successive collision with several nucleons in the nucleus, is superposed upon that in the elementary process. Therefore the incident nucleon (and any nucleon ejected from the nucleus) will, in general, lose a very large fraction of its energy and will emerge with such low energy that it can hardly produce any further mesons in another nucleus. This makes cascade processes very unlikely. The number of mesons produced in the collision of a very fast ($>10^{10}$ ev) nucleon with a very heavy nucleus is very large; an estimate gave a result of 10–20. The cross section, on the other hand, is nearly equal to the geometric cross section of the nucleus because distant collisions give a negligible probability of meson production. This picture is in reasonable agreement with experimental evidence. Jánossy, Rochester, and others[5] have obtained considerable evidence for multiple production of mesons. Schein (private communication) has found that the absorption of the meson-producing radiation (presumed to be protons) in air corresponds nearly to the geometric cross section of the nitrogen nucleus, i.e., the intensity falls by a factor e in 60–100-cm water equivalent. Multiple production in an elementary process is in agreement with the general arguments of Heisenberg[6] concerning the "fundamental length" in quantum theory, and we believe this conclusion to be correct independently of the special assumptions on the meson scattering cross section.

[1] W. Heitler and H. W. Peng, Proc. Roy. Irish Acad. **49**, 101 (1943).
[2] J. Hamilton, W. Heitler, and H. W. Peng, Phys. Rev. **64**, 78 (1943).
[3] L. Jánossy, Phys. Rev. **64**, 345 (1943); W. Heitler and P. Walsh, Rev. Mod. Phys. **17**, 252 (1945).
[4] See, e.g. Bloch and Nordsieck, Phys. Rev. **52**, 56 (1937).
[5] Jánossy and Rochester, Proc. Roy. Soc. **182**, 180 (1943); **183**, 186 (1944); and further literature quoted here.
[6] W. Heisenberg, Ann. d. Physik **32**, 20 (1938).

C5. On the Production of Groups of Mesons and Nucleons. GLEB WATAGHIN, *Universidade de Sao Paulo, Brazil.*—Showers of penetrating particles in the penetrating particles in the cosmic rays were observed by a group of physicists in Sao Paulo (1939–1946) and independently

in England (by L. Jánossy, P. Ingleby, and G. D. Rochester). The experimental techniques used in Sao Paulo are described and discussed. An attempt to determine the average number of mesons in the core of the shower is made. Some theoretical problems concerning the production and the absorption of mesons (including the absorption in great depths) are discussed. If n indicates the number of mesons produced by a collision of the nucleon P with a nucleus A, and a relation is assumed to hold between n and the total energy (E_P+E_A) measured in the frame of the centrum of masses of both particles, then a Lorentz transformation to the frame in which the nucleus A is at rest, gives the corresponding functional dependence of n from the primary energy E_P' of the nucleon P. An argument based on the observation of mesons at great depths seems to support the relation $n\sim\sqrt{E_P'}$. [See *Symposium sobre raios cosmicos, Rio de Janeiro*, 1941 (Imprensa Nacional, 1943) p. 132.]

C6. Cosmic-Ray Effects at High Altitudes. C. D. ANDERSON, *California Institute of Technology.**—It is proposed to discuss the absorption and production of cosmic-ray particles with particular reference to those effects which give rise to particles more massive than electrons. Such effects occur principally at the higher altitudes. Among the questions which have not received a complete answer are: (1) nature of the particles and the mechanism responsible for the production of mesotrons, (2) nature of the particles which produce and are produced by the disintegration characterized by the ejection of several particles from one center, (3) relationship between the above phenomena and cascade showers, and (4) mass of the mesotrons.

* 20-minute paper.

C7. Some Problems in the Study of Cosmic-Ray Mesons. BRUNO ROSSI, *Massachusetts Institute of Technology, Cambridge.**—Through the study of cosmic-ray mesons the following facts have been established: (1) Most of the mesons observed near sea level have a mass of the order of 200 electron masses. (2) Mesons are unstable and their mean lifetime is approximately 2 microseconds. (3) Mesons are not part of the primary cosmic radiation but are produced in the atmosphere, directly or indirectly, by primary rays which are for the most part positively charged. Many fundamental questions concerning cosmic-ray mesons, however, still remain unanswered or have only received a tentative answer. Among these questions the most important are: (1) Do all mesons have the same mass? (2) Do all mesons have the same spin, and if so, what is the value of the spin? (3) Do all mesons undergo disintegration, and if not, what happens to the mesons which do not disintegrate? (4) What are the processes by which mesons are produced; what is the nature and what are the properties of the meson producing radiation? The following experimental data bearing on the questions listed above are discussed in the present paper. (1) *Cloud chamber determinations of the meson mass.* While most of the measurements give masses of the order of 200 electron, some pictures have been interpreted as showing the existence of mesons with much smaller or much larger masses. (2) *Ionization chamber data on bursts associated with the hard component of cosmic rays.* These bursts are interpreted as the result of radiation processes of mesons. Experiments at sea level are in agreement with the hypothesis that mesons have spin 0 or ½, while experiments in the mountains may be interpreted as indicating the existence of a certain number of mesons of spin 1 at high altitude. (3) *Experimental data on the ratio between the numbers of electrons and mesons in the atmosphere.* The value of this ratio at sea level is moderately well in agreement with the hypothesis that all electrons are produced by disintegration or collision processes of mesons if one assumes that each meson disintegrates into an electron and a neutrino. (This incidentally seems to rule out the possibility of mesons having spin ½.) The above hypothesis, however, does not explain the observed rapid increase of the ratio of electrons to mesons with altitude, unless one assumes the existence at high altitude of mesons with a lifetime considerably shorter than 2 microseconds. These short-lived mesons might well be identical with the mesons of spin 1, discussed in connection with the experiments on bursts. Another possible explanation of the experimental results, of course, is that not all of the electrons observed at high altitude are produced by mesons. (4) *Experiments on the disintegration of mesons at rest.* These experiments seem to indicate that only half of the mesons which have been brought to rest, undergo disintegration. There is some evidence to the effect that the mesons which disintegrate are the positive ones. (5) *Experiments on the variation of meson intensity with height.* These experiments seem to indicate that all mesons are subject to decay, while traveling in the air. This result may be reconciled with that of the experiments mentioned above if one assumes that negative as well as positive mesons are unstable but that negative mesons, when brought to rest, may be absorbed by a competitive nuclear process before having a chance to disintegrate. The experiments on the variation of meson intensity with height do not seem to reveal the existence of any appreciable number of short lived mesons up to an altitude of about 4000 meters. (6) *Experimental data on the production of mesons, including cloud-chamber observations, counter experiments on the production of meson showers, counter experiments showing the production of penetrating rays by penetrating non-ionizing radiation.* These data seem to indicate that the meson producing rays (protons? neutrons?) have a mean free path roughly of the order of 100 g/cm², and independent of atomic number. The experimental picture concerning the production of mesons, however, is by no means clear or free from contradictions.

* 20-minute paper.

C8. Origin of Cosmic-Ray Mesons. MARCEL SCHEIN, *University of Chicago.**—In a series of balloon experiments carried out by the Chicago group, it was found that charged particles capable of penetrating 18 cm of Pb are present in large numbers close to the top of the atmosphere (at pressures of 1.8 cm of Hg). The majority of these particles consists of mesons since their absorption in atmospheric layers is considerably higher than in equivalent thick-

nesses of solid material. Because of the large cross section required for the production process of mesons at pressures below 8 cm of Hg (maximum of the electronic transition curve) electrons and photons are excluded as a major factor of producing cosmic-ray mesons. It is assumed that they originate from primary protons interacting with air nuclei. This assumption is supported by experiments showing that practically all the multiple mesons observed under a few centimeters of paraffin are produced by ionizing rays. The multiple production of mesons in paraffin was still observable at an atmospheric pressure of 17 cm Hg. This demonstrates that mesons are produced over a considerable depth of the atmosphere.

* 20-minute paper.

C9. On the Recoil of the Nucleus in Beta-Decay. J. C. JACOBSEN, *Institute of Theoretical Physics, Copenhagen.*—To obtain a quantitative determination of the recoil energy in a β-transformation the active substance must be a monatomic gas at a pressure which is so low that the mean free path is large compared with the dimensions of the apparatus. Then the recoil atoms remain charged before their collisions with the walls, and the recoil energy can be determined by a retarding field. If the daughter substance formed in the transformation is radioactive, the number of recoil atoms passing through the retarding field can be simply determined. The use of a monatomic gas is necessary because a recoil atom which forms part of a molecule will share its energy with the other atoms of the molecule. In the experiments ^{85}Kr, formed by uranium fission, was used, the total pressure in the apparatus being of the order of 10^{-4} to 10^{-3} mm Hg. The recoil atoms, being ions of ^{85}Rb, could by a simple procedure be separated from all other Rb and Cs isotopes formed in the fission process. The upper limit of energy for the recoil atoms from ^{85}Kr was found to 51.5 ± 2 ev. The upper limit of energy for the β-spectrum is 2.4 Mev, to which corresponds a recoil energy of 50 ev; the agreement between the two values is as good as could be expected from the accuracy of the results. The method does not give a determination of the recoil energy in individual transformations; only the energy distribution of the recoil atoms can be determined. From a comparison of the measured energy distribution with that to be expected from the β-spectrum it was found that (1) the emission of a neutrino must be assumed, (2) the neutrino is probably emitted mainly in the same direction as the β-particle. To settle this last point definitely further refinements in the experiments are necessary.

C10. Recent Cloud-Chamber Observations of the Soft Component of Cosmic Rays. WAYNE HAZEN, *University of California.*—Recent observations at the University of California have permitted comparisons with theory that are more exacting than previously possible for the origin of the soft component at sea level and for its interactions with matter. The intensity (from angles near the zenith) of electrons relative to mesotrons has been determined by B. Lombardo from observations with a cloud chamber that contained lead plates. Electrons were differentiated from mesotrons by their scattering and ionization in the case of high energies. From range-energy relationships for the lower energies and shower curves for the higher energies, an energy distribution was assigned to the electrons. The production of high energy secondary electrons by mesotrons in decay or collision events appears to account for all of the observed electrons. The production of collision electrons has been studied separately for the case of lead by S. Nasser and an energy distribution obtained. In order to eliminate the uncertainties resulting from the translation of the observations to the case of air, experiments are in progress for determining the production of collision electrons in water where the atomic number is close to that for air. The collision loss in the production of ions by cosmic-ray electrons in air has been determined by simultaneous ionization and momentum measurements. The relativistic rise in ionization has been verified quite accurately up to a point where the ionization has increased by more than one-third. More recent observations by E. Clement indicate the expected twofold ionization at energies of roughly 1000 Mev. The absolute values of the ionization as well as the relative values are in accord with the theory. Radiation loss by cosmic-ray electrons has been studied indirectly from observations of cascade showers in lead by S. Nassar. The energies of electrons with $E<25$ Mev were determined by curvatures in a magnetic field; thus, although the energy of the initiating electron could not be measured directly, considerable information on the energy distribution among shower particles, the shape of the cascade curve, etc., was obtained. In the range of initiating energies that was studied (roughly, from 150 to 1000 Mev), the usual approximations of cascade theory are not good in the case of lead and hence detailed comparison with theory is difficult. Finally, suppose we consider specifically nuclear interactions of the soft component, of the photons in particular. From counter studies, considerable evidence has been presented in the past for production of penetrating particles (mesotrons?) by non-ionizing rays that were presumed to be photons. Cloud-chamber observations at elevations of 10,000–14,000 feet, on the other hand, have indicated no association between multiple production of penetrating particles and photons and hence the producing agents are presumed to be neutrons. Recent observations of multiple production of very energetic penetrating particles at sea level by W. Fretter, however, show strong association with energetic cascade radiation. Most of these latter observations were not inconsistent with a production of penetrating particles by photons but an alternative process of production of both the penetrating particles and also the energetic cascade radiation by a third type of radiation (energetic protons or neutrons) seems more likely.

C11. Range-Momentum Measurements of Particles Emitted in Nuclear Disintegrations Induced by 100-Mev X-Rays. G. S. KLAIBER, E. A. LUEBKE, AND G. C. BALDWIN, *General Electric Company.**—The masses of the particles have been determined by the measurement of magnetic curvatures and ranges of tracks originating from bombardment with 100-Mev x-rays of the glass wall of a

cloud chamber. The cloud chamber was 30 cm in diameter and was filled with air or hydrogen at one atmosphere. The effective visible range was extended by the use of a set of six aluminum foils of thickness successively increasing from 0.004" to 0.080" in logarithmic steps to a total of 730-cm air equivalent. The method avoids any evaluation of density of ionization along the tracks. The magnetic field of 2650 gauss permits particles of intermediate mass to be readily distinguished from protons. An additional series of photographs was taken without magnetic field to investigate the possible influence of scattering. At the present writing, 2730 photographs are available with magnetic field. Of 163 heavily ionizing tracks observed, it is possible to determine the ranges of 98 tracks which stop in the gas or in the plates. The balance pass out of the illuminated region of the chamber. None of the tracks exhibit negative curvature. There is no evidence from this series of photographs for particles of intermediate mass. A study of 68 heavily ionizing tracks in 800 photographs without magnetic field showed examples of apparent curvature due to scattering sufficient to explain the few deviations from protonic mass that appear in the above analysis. There are examples of protons stopping in each of the plates and of particles passing through all of them. A range distribution will be presented.

* 25-minute paper.

C12. Radiochemical Search for Gamma-Meson Reactions Induced by 100-Mev X-Rays. G. FRIEDLANDER, M. PERLMAN AND L. PEPKOWITZ, *General Electric Company.**—In view of earlier work[1] indicating that mesons may be produced by 100-Mev x-rays, an attempt was made to find radiochemical evidence for a gamma-meson reaction. The reaction $Cu^{63}(\gamma,\mu)Zn^{63}$ was chosen for investigation. The Cu_2O used as target material was specially purified from traces of zinc to eliminate the production of Zn^{65} by the reaction $Zn^{64}(\gamma,n)Zn^{63}$. After each bombardment, zinc was separated chemically from copper, cobalt, nickel, iron, and manganese, and in each case the zinc fraction contained some activity decaying with the 38-minute half-life characteristic of Zn^{63}. However, evidence will be presented indicating that much or all of this activity is made by the reaction $Cu^{63}(p,n)Zn^{63}$ induced by protons produced in the thick cuprous oxide target. The upper limit for the cross section of the reaction $Cu^{63}(\gamma,\mu)Zn^{63}$ estimated from these experiments is several orders of magnitude lower than the cross section for meson production indicated by the original cloud chamber data of Schein and co-workers.[1] Other cases of hypothetical γ- μ^- reactions are being investigated. An attempt is being made to decide whether a γ- μ^+ reaction is responsible for the production of Mg^{27} by bombardment of Al^{27} with 100-Mev x-rays.[1]

* 15-minute paper.
[1] Papers presented by M. Schein, G. S. Klaiber, A. J. Hartzler, and G. S. Baldwin at Annual Meeting of American Physical Society, New York, January, 1946.

C13. Disintegration of Mesons at Rest. F. RASETTI, *Laval University.*—After the hypothesis of the instability of the meson had been advanced in order to explain the atmospheric absorption effect, it was felt highly desirable that the disintegration process should be observed in the laboratory. Williams obtained the first evidence for this process, as he succeeded in photographing two meson tracks ending in the gas of the cloud chamber. A thin track is seen to begin at the end of the heavier meson track, and is interpreted as the track of the disintegration electron. The first evidence for the disintegration of mesons at rest by means of a counter arrangement was published by the writer. In these experiments mesons previously selected by a counter telescope were absorbed in a metal layer, and it was shown that particles emitted from the absorber gave delayed coincidences with the incident mesons. The circuits were designed to supply an approximate value of the mean lifetime, which was found to be about two microseconds, in agreement with the results from the atmospheric absorption effect. Similar experiments were later described by Auger, Maze, and Chaminade. Rossi and Nereson studied the effect with an improved system of circuits, designed to give a complete disintegration curve. They obtained a beautiful exponential decay curve, and the mean lifetime was established as 2.15 ± 0.07 microseconds. Besides the determination of the lifetime, another important result aimed at in these experiments was to decide what exactly happens of the mesons that have been brought to rest by collision energy losses. Tomonaga and Araki have assumed on theoretical grounds that positive mesons should decay freely in dense matter as in empty space with their normal lifetime, while negative mesons should be expected to be captured by nuclei and give rise to excitation processes. If we assume that the energy equivalent to the mass of the meson (about 90 Mev) is shared between two disintegration products (electron or positron and neutrino), then the disintegration of the positive meson should give rise to an easily detectable 45-Mev positron. However, the capture of a negative meson by a nucleus and the consequent nuclear excitation are expected to produce only particles of relatively low energy not detectable in the above-described experiments. In the writer's experiments an evaluation was made of the number of decay electrons per meson, and gave a value of about one-half, hence consistent with the assumption that only half of the mesons (probably the positive ones) undergo free decay. The same conclusion was indicated by the experiments of Rossi and Nereson. Recently, Conversi, Pancini, and Piccioni attempted an ingenious experiment to settle this point. A set of magnets in which the deflection of a charged particle in the magnetized iron was used, permitted them to concentrate either the positive or the negative mesons. On these selected particles, an experiment similar to the writer's was performed. They obtained a definite indication of decay electrons in the case of the positive mesons but none for the negative mesons. The great difficulty of these experiments resides in the exceedingly small number of events that can be observed within a reasonable time with the available intensity of the mesons at sea level. Under these conditions it seems difficult to improve much on the experiments that have been performed, but there is little doubt that further important results could be gathered from similar experiments at high altitudes, where the number of slow mesons is much higher.

C14. An Attempt to Observe the Radioactivity of the Neutron. E. F. SHRADER,* D. SAXON, AND A. H. SNELL, *Clinton Laboratories, Oak Ridge, Tennessee.*—On the assumption that the neutron undergoes radioactive decay to the proton with a half-life of about 30 minutes, at least three possible means of observation of the effect present themselves: (1) collection of the hydrogen in a chamber immersed for a long time in a high slow neutron flux; (2) observation of the beta-particles; (3) electrical counting of the protons formed. Experimental work is being done on the third. A highly collimated beam of slow neutrons emerging from the Clinton chain-reacting pile is allowed to pass through thin aluminum windows into and out of an evacuated chamber, and protons formed in a defined volume are electrostatically collected and accelerated to 10 kv in a direction perpendicular to the primary neutron beam. They are then allowed to fall on the first plate of an electron multiplier tube of the type developed by J. S. Allen. Backgrounds will be measured with boron absorbers interrupting the beam, and different geometries, window thicknesses, pressures, etc., will be studied in an attempt to eliminate spurious effects. It is hoped that results will be at hand by the time of the meeting. Determination of the half-life depends on evaluation of the efficiency with which the protons are collected and counted.

* On leave from Case School of Applied Science, Cleveland, Ohio.

C15. Application of a Bent Crystal Neutron Spectrometer to Measurements of Resonance Absorption. R. B. SAWYER, E. O. WOLLAN, K. C. PETERSON, AND S. BERNSTEIN, *Clinton Laboratories, Oak Ridge, Tennessee.*—With the high neutron fluxes now available, the diffraction of neutrons by crystals has become a useful tool for the study of neutron absorption as a function of energy. To increase the intensity and hence the energy range over which these measurements can be made with good resolution, we have constructed a transmission type crystal spectrometer for neutrons. The transmission method has the advantage that large crystal apertures can be used at the small angles encountered in neutron diffraction without sacrificing on the resolution of the instrument. A cadmium Soller slit system forms an inportant part of this instrument. As set up for our work it gives a convergent beam of neutrons which passes through a NaCl crystal bent to a curvature of about 60 cm. With this arrangement diffracted beams can be measured to within a fraction of a degree of the direct beam. The resolution depends only on the accuracy of the slits and is independent of the imperfections of the crystal. The instrument gives good resolution of neutron resonance peaks of about 0.1-ev width at half-maximum at energies up to 1 ev and satisfactory work can be done up to energies of several ev. As examples of work done with this instrument the absorption curves for Cd and for Ir will be shown. The Breit-Wigner one level formula gives a good fit with the experimental data.

C16. The Mass of the Mesotron as Determined by Cosmic-Ray Measurements. DONALD J. HUGHES, *Argonne National Laboratory, Chicago.*—All quantitative determinations of the masses of individual cosmic-ray mesotrons have been based on cloud-chamber photographs involving measurements of magnetic curvature plus ionization density, range, or energy of knock-on electrons. The errors involved in the different methods will be discussed as well as the possibility of reducing these errors by the choice of experimental conditions. A review of the mass determinations which have been reported shows that the errors involved are often much larger than estimated by the experimenters themselves. In spite of the large errors inevitable in the methods used, it is concluded that the spread in mass values exceeds the experimental errors, and that it is extremely likely the mesotron does not possess a unique mass. It is certain that the reality of the large spread in mass values can be definitely established by present methods with the incorporation of relatively minor improvements. The recent betatron findings on the mesotron mass will not be described, but if available at the meeting the betatron results can be compared with the present review as the basis for a discussion of the identity of the cosmic-ray and the betatron mesotron.

C17. Mass of Cosmic-Ray Mesotrons. W. B. FRETTER AND R. B. BRODE, *University of California, Berkeley, California.*—Data on the masses of mesotrons were collected in an experiment which involved the use of two vertically in line cloud chambers which were simultaneously expanded by counter control. The upper chamber was 30 cm in diameter and was in a magnetic field of 5300 gauss. The lower chamber was 40 cm in diameter and contained eight ½-inch thick lead plates. Particles which stop in the lower chamber after penetrating one or more of the lead plates are sufficiently curved in the magnetic field (H) to permit accurate measurement of their radius of curvature (ρ). If only ionization losses are involved in stopping a particle, its mass may be determined from its range and $H\rho$.[1] The uncertainty in $H\rho$ is approximately 10 percent, while the uncertainty in range is ½ inch of lead. These lead to an uncertainty in the mass of $\pm 30\ m_e$. One mass determination per operating day is usually obtained. The results of the observations to date have consistently indicated a mass between 160 and 200 m_e. The straggling in range which was found by Street in a similar experiment[2] does not seem to be a serious cause of error and possibly could be explained by the large angle scattering which has occasionally been observed in the present experiment.

[1] J. A. Wheeler and R. Ladenburg, Phys. Rev. **60**, 754 (1941).
[2] J. C. Street, J. Frank. Inst. **227**, 765 (1939).

C18. Measurement of Meson Masses by the Method of Elastic Collision. Probable Existence of a Heavy Meson (1000 m_0) in the Cosmic Radiation. L. LEPRINCE-RINGUET, *Laboratoire de l'Ecole Polytechnique.*—During the years 1940–1945, with the aid of Messrs. Gorodetzky, Theritier, Nageotte, Richard-Foy, a systematic study of the method of elastic collision for determining masses of high energy particles in the cosmic radiation was carried out. A first value obtained with a Wilson chamber and a field of 2600 gauss gave us $M = 240\ m_0 \pm 10$ percent. During a long series of experiments (more than ten thousand usable negatives), a stereoscopic picture of a collision observed under good

conditions (the incident particle losing practically all its momentum) gave us a mass of 990 $m_0 \pm 12$ percent. This picture shows, provided the collision is elastic, that there exist in the cosmic radiation particles of mass about four times that of the normal meson, or approximately half that of the proton. The observed particle is positive. Other Wilson chamber photographs not showing collisions but exhibiting, for a known curvature, ionization less than that of a proton and more than that of a meson of mass 200 also favor the existence of particles of mass intermediate between the meson of mass 200 and the proton.

C19. Cosmic-Ray Bursts in a Large and in a Small Ion Chamber at Sea Level and in a Small Ion Chamber under 30 Meters of Clay. H. CARMICHAEL AND C. N. CHOU, *University of Cambridge.*—Bursts have been recorded for about 3000 hours underground and for about 1000 hours at sea level in a 1.1 liter thin-walled ion chamber containing argon at 85 atmos. pressure, and at sea level for some 2000 hours in a 175 liter thin-walled ion chamber. The effect of placing shields of lead and aluminum of various thicknesses above these ion chambers has been studied. Although this work came to an end in 1939, only parts of it have so far been published, in the *Proceedings of the Royal Society*,[1] in a short note to *Nature*,[2] and in a relatively inaccessible paper in China.[3] The results given in *Nature* were recently quoted by Kingshill and Lewis[4] who gave an interesting explanation of a marked discontinuity in the size-frequency curves obtained with the ion chambers unshielded. The size-frequency curve obtained with a lead shield above the large ion chamber has a second discontinuity which appears to be due to a very rare type of burst of large size.

[1] Hugh Carmichael, Proc. Roy. Soc. **A154**, 223 (1936).
[2] H. Carmichael and C. N. Chou, Nature **144**, 325 (1939).
[3] C. N. Chou, *Collected Papers* (College of Science and Engineering, University of Amoy, 1943), Vol. 1, No. 1.
[4] K. L. Kingshill and N. G. Lewis, Phys. Rev. **69**, 159 (1946).

C20. Ionization Chamber Measurements on Cosmic-Ray Air Showers. LLOYD G. LEWIS, *Princeton University and the University of Chicago*, AND KONRAD L. KINGSHILL AND J. M. BENADE, *University of Chicago.*—The authors wish to call attention to the following several papers concerning bursts of ionization in unshielded ionization chambers, in order to promote discussion of the interesting work of Carmichael and Chang-Ning Chou presented in the preceding abstract: H. Carmichael and Chang-Ning Chou, Nature **144**, 325 (1939); H. Euler, Zeits. f. Physik **116**, 73 (1940); J. Clay, Physica, 's Grav. **9**, 897 (1942); R. E. Lapp, Phys. Rev. **64**, 129 (1943); L. G. Lewis, Phys. Rev. **67**, 228 (1945); J. Clay, Physica, 's Grav. **11**, 311 (1945); L. Wolfenstein, Phys. Rev. **67**, 237 (1945); and K. Kingshill and L. G. Lewis, Phys. Rev. **69**, 159 (1946). These several papers point out the lack of agreement between the cascade theory of air showers applied to primary electrons at the top of the atmosphere and the experimental results. The several observers have suggested different mechanisms to explain their results. In addition, unpublished work of E. Hoffmann who worked with Professor Steinke at Freiburg University, as well as data obtained recently with a modification of the thin-walled chambers used by the Chicago group, will be discussed.

C21. Total Cross Section of Hydrogen for Neutrons of Energies from 35 to 490 kev. DAVID H. FRISCH, *Massachusetts Institute of Technology.*—The total cross section of hydrogen has been measured at mean neutron energies of 35 ± 5, $95 + 5$ to -10, $265 + 5$ to -10, and $490 + 5$ to -10 kev. Protons from the smaller Wisconsin electrostatic generator at Los Alamos, collimated to a $\frac{3}{32}''$ diameter beam, bombarded a lithium target of 5 to 10 kev stopping power. The nearly monoenergic neutrons emerging forward were scattered out of a proton recoil proportional counter by graphite and polythene disks. Source intensity was monitored by a small sensitive fission counter between source and scatterer. A polythene shadow cone reduced the counting rate to about 2 percent. The errors given for the corrected data include estimates of error in scatterer thickness and in geometric corrections (only single scattering corrections have been made) in addition to the statistical error given for the uncorrected data. The values obtained are, respectively: uncorrected $16.15 \pm .25$, corrected 16.74 ± 41; $13.04 \pm .26$, $13.46 \pm .39$; $8.87 \pm .15$, $9.12 \pm .24$; $6.19 \pm .15$, $6.33 \pm .21$. This data and higher energy data by Williams *et al.* and Bretscher *et al.* have been fitted by Bohm and Richman with a potential consisting of a deep square well with a wide shallow square tail.

Discussion

Does the primary radiation contain in appreciable quantities more than one kind of particle? Are the cosmic-ray mesons produced singly or in multiple? What primary energies are required for such processes?

Discussion Leader: P. M. S. BLACKETT, *Victoria University, Manchester, England*

H. A. BETHE, *Cornell University.*
H. J. BHABHA, *Tata Research Institute, Bombay.*
M. SCHEIN, *University of Chicago.*
R. B. BRODE, *University of California.*
C. D. ANDERSON, *California Institute of Technology.*
W. F. G. SWANN, *Bartol Research Foundation*

Theories of the Elementary Particles

Contributed Papers

T1. A Convergent Quantum Electrodynamics. THEODORE A. WELTON, *Massachusetts Institute of Technology.*—An attempt has been made to obviate the characteristic divergences of quantum electrodynamics by omitting the quantized electromagnetic field from the formalism. We assert that the variables of the quantized electron-positron field alone can be made to give a complete description of electrodynamic phenomena. To accomplish this, we write the usual equations of motion for these variables with the addition of non-linear terms so that electrons always change their states in pairs, as is observed. It is found that the theory can be consistent only if advanced and retarded interactions between electrons are included on an equal footing. The theory here proposed is then seen to be a possible quantization of the classical theory recently proposed by Wheeler and Feynman.[1] The formalism is somewhat cumbersome, but leads to the Möller scattering formula in a natural fashion. More complicated phenomena are in process of calculation. The vacuum polarization divergences of the positron theory seem to remain.

[1] J. A. Wheeler and R. P. Feynman, Rev. Mod. Phys. 17, 157 (1945).

T2. On the Theory of the Electron. C. JAYARATNAM ELIEZER, *University of Ceylon.*—Dirac's classical theory of the electron, while it satisfactorily removes the difficulty of infinite self-energy, meets with the circumstance that the equations of motion do not always have physically understandable solution. There is evidence to suggest that the signs of certain terms do not fit appropriately. To bring about the necessary alterations in sign, the author has abandoned the assumption that the field of a moving particle is given by its retarded field alone, and adds to this field a multiple, k, of the difference between retarded and advanced fields. The force of radiative reaction is then $(2k+1)$ times the usual value. When $k \leqq -\frac{1}{2}$, the results show agreement with familiar physical ideas. This classical theory is translatable into the quantum theory by following Dirac's method of field quantization, using the λ limiting process and negative-energy photons. On the basis of this electrodynamics, the interaction with a radiation field of a free electron or an electron bound by a Coulomb field is found to be free from divergence to any order of approximation in the perturbation theory, provided one uses only those solutions which correspond to outgoing waves of the electron.

T3. The Two-Particle Problem in the Theory of Action at a Distance. JOHN A. WHEELER, *Princeton University.*—Reformulation of classical electrodynamics consistently with the theory of action at a distance, with a force on each particle uniquely determined by half the sum of advanced and retarded fields of all other particles, is known to eliminate the usual infinities in the electromagnetic energy of a system of point charges, and appears, at first sight, to dispose also of the infinite number of degrees of freedom of the field. The latter infinity has led in quantum theory to the divergence of the zero-point energy of the field, and came from the underlying classical theory: the super-position of any number of plane waves on a particular solution of Maxwell's equations was considered to represent an acceptable state of the field. However, a closer analysis discloses that even two particles coupled by the Tetrode-Fokker law of action at a distance constitute a system with an infinite number of degrees of freedom because of the non-instantaneous nature of the forces. The character of these degrees of freedom is analyzed to the first order of small deviations from the primary motion, and their physical significance is discussed.

T4. Blackbody Radiation in the Theory of Action at a Distance. GILBERT N. PLASS AND JOHN A. WHEELER, *Princeton University.*—The usual and well verified theory of blackbody radiation is based on Rayleigh's counting of the degrees of freedom of the field. The number of vibrations up to any given frequency—and consequently the energy of the field at a given temperature—is proportional to the volume of the container, and independent of the number, N, of particles which constitute the container. To account for this result in the theory of action at a distance appears at first sight difficult because the number of degrees of freedom of a system of N particles is independent of the volume occupied by the particles. However, this conclusion depends on the existence of instantaneous forces between the particles and is not valid for half-advanced, half-retarded forces. For illustration, the characteristic frequencies are calculated for a system of many particles distributed uniformly through the interior of a sphere. A self-consistent solution is found for the equations of motion of any particle in the sphere. The requirement that the fields be half-advanced, half-retarded, plus the usual boundary conditions at the surface of the sphere for the electric and magnetic fields, gives a distribution of allowed vibration frequencies which is identical with that of Rayleigh.

T5. Electron Waves in the Magnetic Dipole Field of a Neutron. CHARLES L. CRITCHFIELD, *George Washington University.*—The relativistic wave functions for an electron moving in the field of a central magnetic dipole are studied. When the central spin is $\frac{1}{2}\hbar$, states of total angular momentum $F\hbar$ can be formed with electron states of two different angular momenta, $j\hbar$, *viz.*, $j=F-\frac{1}{2}$ and $j=F+\frac{1}{2}$. These two electron waves are coupled by the magnetic interaction so that, except for $F=0$, there are four, first-order, coupled differential equations for the radial dependence of the electron waves, instead of the usual two. The equations for $F>0$ are equivalent to two coupled Schroedinger equations having a positive definite potential energy operator. Thus, solutions may be found without cutting off the magnetic interaction and there are no

bound states of the system. For $F=0$, however, the equations are equivalent to a single Schroedinger equation in which the potential energy is positive at all radii only for the electron-neutron interaction. The positron-neutron potential becomes strongly negative in a small region near a separation of the order of e^2/Mc^2, where M is the mass of the neutron. This attraction is sufficient to form a bound $P_{\frac{1}{2}}$-state of the positron. Asymptotic forms of solutions are found for the states with $F=0$ and $F=1$.

T6. Relativistic Wave Equations. E. P. WIGNER, *Princeton University.*—The relativistic wave equations describe the properties of single particles or of systems which are in one definite quantum state. They can be developed from two points of view: by investigating wave equations in the ordinary sense and imposing the condition that they be relativistically invariant. This line has been followed by numerous investigators, most recently and most completely by Bhabha. An alternate procedure is to investigate invariant linear manifolds and find afterwards equations the solutions of which these manifolds represent. This attack has been followed. It yields the ordinary relativistically invariant wave equations for finite mass and spins 0, ½, 1, ⅔, ... For 0 rest mass it yields, in addition to the well known equations with spin 0, ½, 1, ⅔, . . ., two more equations which were not considered before. The spin is infinite for both of these in the sense that there are infinitely many states associated with any linear momentum. The wave function is single-valued in one case and two-valued in the other case. These equations represent a new type of particle if they exist and cannot be decomposed into equations of the above well-known types. The advantage of the second type of treatment is that it gives definite results, free from arbitrariness. On the other hand, it is entirely possible, as suggested by Bhabha, that the first treatment gives connections between the equations, which although arbitrary from the point of view of invariants, are valuable from the point of view of physics.

T7. Relativistic Wave Equations. H. J. BHABHA, *Tata Research Institute.*—Those relativistic wave equations are investigated which contain only the first-order derivatives of the wave function with respect to space and time coordinates; i.e., have the general appearance of Dirac's electron equations. It is postulated also that no auxiliary conditions be imposed on the wave function such as are, for instance, the equations requiring that the divergence of the electro-magnetic field intensity varies in a vacuum. There is a great variety of equations satisfying the above two conditions and an attempt is made to correlate these equations with the various elementary particles.

T8. Difficulties of the Meson Theories of Nuclear Forces. SHUICHI KUSAKA, *Princeton University.*—Since the discovery of the meson in the cosmic rays, extensive work has been done in trying to formulate a satisfactory theory of nuclear forces based on the idea that they arise from the interaction of the meson with the nucleon. Various types of mesons and the different charge possibilities of charged, neutral, and symmetrical theories have been investigated according to two approximate methods of calculation. However no single theory has been able to account for all phenomena. Generally speaking, the weak coupling theories suffer from the inadequacy of the basic assumption that the coupling between the meson field and the nucleon is small, and the divergence difficulties inherent in the present formulation of the quantum field theories. The strong coupling theories, on the other hand, are unable to explain the observed values for the magnetic moments of the proton and neutron, and face difficulties with the saturation properties and the stability of heavy nuclei. Furthermore both theories give rise to anisotropy in the scattering of fast neutrons by protons which is opposite to that observed. It therefore seems now that there is no possibility of formulating a satisfactory theory of nuclear forces based on the conventional meson field theories.

T9. Conservation Theorems and Invariance Properties of the Lagrangian. L. ROSENFELD, *Dublin Institute for Advanced Studies.*—The general equations of the electromagnetic and gravitational fields involve a current-charge density vector and an energy-momentum tensor, respectively, which describe the sources of the fields and obey conservation laws. If the field equations are derived from a Lagrangian by the usual variation principle, the expressions of the source tensors follow directly in terms of the variables characterizing the material fields which interact with the electromagnetic and gravitational ones. It will be shown that the structure of such general expressions, as well as the corresponding conservation laws, is intimately related to the invariance properties of the Lagrangian; in fact, one can say, more generally, that the invariance of the Lagrangian with respect to any group of transformations implies a corresponding conservation theorem. Some applications to cases of actual interest (such as meson fields) will be discussed.

T10. Resonance Fluorescence of Nuclei. L. I. SCHIFF, *University of Pennsylvania.*—The possibility of studying excited states of nuclei through the process of gamma-ray resonance fluorescence is discussed. It is desirable that the atomic number Z of the nucleus be as small and the excitation energy E as large as possible so long as particle emission cannot occur. Assuming quadrupole transitions for which the breadth is 10^{-3} volt at 1 Mev, with no competition from lower excited states, the total fluorescence scattering cross section integrated over energy is $\sim 10^{-30} \cdot E^3$ cm²—Mev, where E is in Mev. Other processes that would tend to mask this effect are: (1) Compton scattering, (2) non-resonant nuclear scattering, (3) conversion to an electron with subsequent radiation. By observing the fluorescent gamma-rays at large angles, the shielding is simplified and (1) is minimized. The cross section for (1) is roughly $10^{-26} \cdot Z/E$ at 90° and all the scattered quanta are below 0.5 Mev. In practical cases, (3) has a larger cross section than (2), about $10^{-30} \cdot DZ^3/E$, where D is a specimen dimension in cm. The fluorescent radiation should be detectable with a cloud chamber when a 20-Mev betatron is used as a primary source, and could be enhanced by running the betatron slightly above E.

Invited Papers

T11. Electrodynamics without Point Singularities. R. E. PEIERLS AND H. MCMANUS, *University of Birmingham.*—Relativistic invariance is compatible with the assumption that the elementary particles (e.g. electrons) have a finite extension in space provided one admits the occurrence in the equations of integral operators which connect the behavior of field quantities at one time directly with those at times different by amounts of the order r_0/C, where r_0 is the electron radius. This programme can be carried out in classical theory and leads to equations without singularities but agreeing with the present equations as regards radiation damping, etc. The quantization of these equations so far still meets with formal difficulties.

T12. Relations of Dirac's New Method of Field Quantization to Older Theories. DAVID BOHM, *University of California.*—By means of a simple transformation, Dirac's new theory[1] can be obtained directly from the quantum electrodynamics of Heisenberg and Pauli, provided that one introduces the auxiliary B potentials of Dirac, defined to satisfy the wave equation everywhere, and to be equal initially to the actual A potentials, both in magnitude and in rate of change. With suitable changes in commutation rules for the B potentials, the Hamiltonian of the radiation field may be taken as the difference between actual and initial energies, so that the Hamiltonian now has negative eigenvalues. In the Fourier analysis of $M=(A+B)/2$, and $N=(A-B)/2$, operators appear, which have the same commutation relations as emission and absorption operators, but which are not complex conjugates. Yet a representation can be found in which these operators have matrix expressions similar to those of true emission and absorption operators. The eigenfunctions representing different numbers of positive and negative photons are not, however, orthogonal in the usual sense, but instead, show an orthogonality property only when integrations are carried out with a special weighting function, which is not positive definite. This weighting function makes possible unique expressions in terms of these eigenfunctions. The state of zero photons in this representation turns out to yield the initial condition described above, namely that the A and B fields are equal. In terms of the usual representation, this state involves infinite excitation of each normal mode. The effects of fluctuations involving emissions are then cancelled by these involving absorption from the infinite background, represented by Dirac as emission of negative energy photons. Finite self-energies and transition probabilities are the result of a special relation between initial and final conditions, analogous to that which in the classical Dirac theory led to the elimination of infinite self-acceleration. Because of the possibility of fluctuation in the quantum theory, the incident background needed to prevent infinite reactions must also be infinite. Probabilities of transition are found by first solving a corresponding problem in the radiation filled world, starting always with the zero state described above. While emission of a positive photon is given its usual meaning, emission of a negative photon is regarded as equivalent to absorption of a photon actually present initially in the real world. Thus, initial and final states are obtained simultaneously, by solution of a finite problem. Re-interpretation in terms of the actual world is naturally ambiguous, but from applications to simple problems, it is hoped that a unique correlation may be obtained. A characteristic ambiguity appears in the solution for Compton scattering to order e^4, in which the value of the radiation reaction is found to depend on the contour of integration about certain singularities introduced by secular terms in the second order. This ambiguity corresponds physically to an ambiguity in the ingoing or outgoing character of the waves at infinity, which is not known *a priori* in the hypothetical world. With a choice of contour corresponding to the presence of nothing but outgoing waves in the higher order terms, the radiation reaction disappears, but a symmetrical combination of ingoing and outgoing waves may be chosen which yields the correct radiation reaction in the low velocity limit. Whether this method can be extended to Coulomb scattering with radiation is now being investigated.

[1] P. A. M. Dirac, Proc. Roy. Soc. **A180**, 1 (1942); W. Pauli, Rev. Mod. Phys. **15**, 175 (1943).

T13. Quantum Theory of Damping. W. HEITLER, *Dublin Institute for Advanced Studies.*—The divergencies, which so far have prevented an unambiguous application of the quantum theory of fields, can be eliminated in a relativistically invariant way. This is done by putting all the divergent integrals occurring there equal to zero. One obtains in the first place a theory that can be applied to calculate all collision cross sections including those describing the creation and annihilation of new particles. This theory differs from the usual first approximation by the inclusion of the damping which is very large in processes involving mesons. The results for meson collisions seem to be in good agreement with the (very scanty) experiments. The cross section for the scattering of a meson by a nucleon increases from zero to a maximum at an energy $\epsilon=1/G$ (G^2 is of the order of the meson-nucleon coupling constants, *i.e.*, $G^2\sim 1/10$). For higher energies the cross section decreases like ϵ^{-2} and is asymptotically $4\pi/\epsilon^2$. This agrees well with the experiments by Code, Shutt, and more recently by Sinha. The primary meson can also split up into two mesons (multiple process). The cross section also increases first for small ϵ, and has a maximum at $\epsilon\sim 1/G$. This maximum value is however 10–20 times smaller than that for the single scattering. For still higher energies the cross section decreases very rapidly (ϵ^{-6}), and is entirely negligible compared with that for ordinary scattering. The theory thus leads to reasonable results for multiple processes which have none of an "explosive" character. Applications to the production of mesons in P-P collisions show that at least the right order of magnitude is obtained, and a reasonable account of meson production in the atmosphere can be given. Mathe-

matical difficulties prevent very accurate calculations. The theory fits exactly into the scheme proposed recently by Heisenberg. In fact it provides a definite and general proposal for the S-matrix which Heisenberg suggested to be the fundamental quantity in the quantum theory of fields. By analytic continuation of S into the complex plane also questions concerning the bound states consisting of several particles and quanta can be answered. It can for instance be shown that in the above theory of damping a bound state exists consisting of a proton (neutron) and a positive (negative) meson with an excitation energy of $\sim$15 Mev (proton isobars with charge 2, -1). Similarly a very few isobar states with charge 1 or 0 exist, if the charge symmetrical meson theory is used. The results concerning the isobars can be interpreted by saying that in this theory the spin and isotopic spin inertias are not quite zero but decrease rapidly with energy. The existence of isobars depends very sensitively on S. A slight change of S giving rise to no appreciable change in the cross section may make these isobar states disappear. As the whole theory is of a preliminary character the existence of isobars must therefore not be taken for granted. Problems concerning the structure of the elementary particles themselves, for instance the magnetic moment of the proton and neutron, still remain unsolved.

T14. Reaction of Radiation on Electron Scattering, and Heitler's Theory of Radiation Damping. J. R. OPPENHEIMER, *University of California*, AND H. A. BETHE, *Cornell University*.—W. Heitler and his collaborators[1] have recently developed a theory of fundamental processes which takes into account radiation damping. This theory has been applied to many problems concerning the scattering and the production of mesons and has been successful in eliminating the divergences at high energy which normally appear in meson theory. We have tried to test this theory by applying it to the problem of the reaction of radiation on the scattering of electrons. This problem leads to the well-known "infra-red catastrophe," *viz.*, to an infinite probability for emission of quanta of extremely low energy. In the ordinary theory, this difficulty was solved by Bloch and Nordsieck,[2] who showed that the large probability for scattering with radiation is compensated by a reduction of the probability of radiationless scattering. The simplest way of obtaining this result consists in considering the radiation enclosed in a box of very large but finite dimensions; then not more than one quantum will in general be emitted in one collision; the cross section with emission of one quantum, $\delta_r\sigma$, is finite and proportional to log L where L is the size of the box, and the radiationless scattering is reduced by an amount $\delta_e\sigma$ which is equal to $\delta_r\sigma$ and is caused by the perturbation due to states containing *virtual* quanta of very low energy. However, as Pauli and Fierz[3] (non-relativistic) and Dancoff[4] (relativistic) have shown, the inclusion of the perturbation owing to virtual quanta causes divergence at the high energy end. Beyond the Duane-Hunt limit $h\nu = E$ (energy of the incident electron), the *emission* of quanta is impossible but virtual quanta of such energy must still be taken into account. The compensation therefore no longer exists, and the total scattering cross section diverges as some function of the maximum frequency of virtual quanta taken into account. Moreover, Dancoff has shown that this divergence depends in a senseless way on the particular relativistic theory used. In Heitler's theory of radiation damping, the difficulty is shifted back to the infra-red end. It is the basis of this theory that every process be calculated only in the lowest order in which a non-vanishing result is obtained, and in this way the usual divergences at the high energy end are avoided. However, in our case, the correction to the radiationless scattering caused by virtual quanta of *low* energy must also be omitted: The compensation of the scattering with radiation by an equal reduction of the radiationless scattering therefore no longer occurs, and the infra-red catastrophe re-appears. We had hoped that this difficulty might be remedied by the formalism of Heitler's theory in which the matrix element of the Hamiltonian does not directly give the transition probability but must first be corrected by the damping. In this way, the scattering with radiation does give a correction $\delta_e\sigma$ to the radiationless scattering. Unfortunately, this correction is much too small: The scattering with radiation is proportional to $e^2\sigma$ where e is the electronic charge and σ the scattering cross section without radiation, whereas the correction $\delta_e\sigma$ to the radiationless scattering is of the order $e^2V^2\sigma$ where V is the (suitably normalized) matrix element of the scattering potential. V will, in general, be smaller than one, and will in any case depend on the particular problem. Therefore there will, in general, be no compensation of $\delta_r\sigma$ and $\delta_e\sigma$. This discussion shows that no recipe as simple as complete inclusion or complete exclusion of higher approximations in the matrix element will lead to a finite result for this simple problem. One should include the virtual quanta of low frequency and exclude those of high frequency. There must therefore be some limiting frequency. This is probably not the Duane-Hunt limit whose introduction at this place would almost certainly give results in disagreement with the correspondence principle. Dancoff has shown that the relativistic limit $h\nu = mc^2$ does not give a satisfactory cutoff. We therefore believe that a new limit must be involved which may be given by Heisenberg's fundamental length and above which the interaction between matter and radiation must be modified in an essential way.

[1] W. Heitler and H. W. Peng, Proc. Camb. Phil. Soc. **38**, 296 (1942).
[2] F. Bloch and A. Nordsieck, Phys. Rev. **52**, 54 (1937).
[3] W. Pauli and M. Fierz, Nuovo Cimento **15**, No. 3, 1 (1938).
[4] S. M. Dancoff, Phys. Rev. **55**, 959 (1939).

T15. Some General Aspects of the Self-Energy Problem. A. PAIS, *Institut for teoretisk Fysik Copenhagen*.—It is impossible to overcome the self-energy difficulties by subjecting a divergence-free classical theory to quantization, because the quantization itself introduces new divergences due to the field fluctuations which are essential for the interpretation of field measurements (Bohr and Rosenfeld). If the dualistic character of quantum theory is maintained in future theory, field self-energies W should be very small compared with the total particle mass which then cannot be derived from "universal constants of the first kind"

(Heisenberg: e, h, c and a universal length) by using $W = mc^2$. The only scheme which till now with some success could be applied in accordance with hole theory, taking account of fluctuations and yielding adequately small self-energies, is the introduction of l as the range of a neutral (scalar) "f-field" created by the electron.[1] Requiring the compatibility of electron, proton, and neutron "convergence relations"[1] unambiguously yields the inseparability of electric and f-charge, making the proton-neutron mass difference amenable to interpretation. The introduction of l as field range generally leads to the introduction of a universal time: the lifetime of the field quanta for negatron-positron decay. "f-bremsstrahlung" of electrons with energy $> \hbar l^{-1} c$ is practically equivalent with $e^* \rightarrow 2e^* + e^*$ as a one-act process.

[1] A. Pais, Phys. Rev. **68**, 227 (1945).

Accelerators

Contributed Papers

A1. Electrostatic Generator for Nuclear Research. R. J. Van de Graaff, W. W. Buechner, W. M. Woodward, L. R. McIntosh, E. A. Burrill, and A. Sperduto, *Massachusetts Institute of Technology, Cambridge, Massachusetts.*—A description will be given of the design of an electrostatic generator now under construction at Massachusetts Institute of Technology. At a number of other laboratories copies of this particular design with suitable adaptations are under way. The apparatus is housed in a vertical pressure tank 5.5 feet in diameter and 16 feet long. The insulating medium is nitrogen at 400 pounds per square inch gauge pressure, storage tanks being provided so that the same gas can be used repeatedly. Subsequently, partial pressures of sulphur hexafluoride gas will also be used. Two accelerating tubes will be provided, one for positive ions and one for electrons. When positive ions are being accelerated, the electron tube will be used for differential pumping to reduce the flow of gas from the ion source into the main part of the positive ion tube. On the basis of previous tests[1] with other generators, an output of about five million volts is expected. It is a pleasure to acknowledge the support of The Rockefeller Foundation which made this work possible.

[1] Buechner, Van de Graaff, Sperduto, Burrill, McIntosh, and Urquhart, Abstract J6, Bull. Am. Phys. Soc. Cambridge Meeting, April, 1946.

A2. Electron Injection Technique for Betatrons.* E. C. Greanias, *USNR*, and E. O. Wukasch, *USNR, United States Naval Research Laboratory, Washington, D. C.*—The gamma-ray yield obtained with the betatron is much less than the yield to be expected from the maximum possible electron current which can exist in the orbit. Injection technique was studied to see if the actual current, and consequently the yield, could be increased. Step-shaped injection voltage pulses which would give longer total acceptance periods, and thus introduce more electrons into the oribit, were tried. These pulses were relatively narrow (3 to 4 microseconds), and required very critical timing. This timing difficulty could not be entirely overcome and the yields obtained with short rectangular pulses were only 80 percent of the value obtained with longer pulses (40 microseconds). However when the step pulses were tried, an increase in yield was observed. One, two, and three step pulses were tried and an increase of approximately 15 percent per step was observed—thus the long pulse yield was exceeded. The yield obtained with all narrow pulses was very erratic and required constant manipulation of the timing controls. If this timing difficulty can be overcome, shaped injection pulses may prove to be very valuable.

* To be read by title only.

A3. The Synchro-Betatron Electron Accelerator Guide Fields. H. F. Kaiser and E. C. Greanias, *United States Naval Research Laboratory, Washington, D. C.*—The authors have recently suggested[1] the possibility that the ultimate electron energy of a given betatron or synchrotron may be extended by supplying the guide field of the unit with a super guide field synchronized in operation with the high frequency electric acceleration and produced by various types of conductors placed within the unit or used independently to replace the conventional system. The magnetic fields produced by proximate conductors in which the two currents flow in opposite directions are strong between these and of the order of magnitude of the current but diminish rapidly outside. Such conductors also afford a coil system of low inductance giving a time constant of the order of 10^{-3} second for a 20-cm coil radius. The field shapes and intensity *vs.* radius relations of several such coil systems are examined and also the effect of iron near them. The possibility of using such conductor systems as cavities or wave guides is examined and an accelerator design for the use of these is described.

[1] H. F. Kaiser and E. C. Greanias, Phys. Rev. **69**, 536 (1946).

A4. Preliminary Studies on the Purdue Microwave Electron Accelerator. R. O. Haxby, E. S. Akeley, A. Ginzbarg, R. N. Smith,* H. W. Welch and R. M. Whaley, *Purdue University.*—The construction of a microwave linear accelerator for electrons has been started. An eighteen section accelerating tube has been constructed using loading every half-wave-length. Measurements of other modes showed that the only interfering mode is one having seventeen half-waves in the eighteen sections. This may be removed by symmetrical feeding. Since, for longer

tubes, other modes will also become troublesome, experiments are being continued, using different loading, every third or every quarter-wave-length. Because of the difficulty of obtaining sufficiently high speed electrons, experiments have been performed on tube sections with heavier loading and a short tube has been constructed for use in accelerating electrons with entering velocity less than c.

* Now at Boeing Aircraft, Seattle, Washington.

A5. Design of a 70-Mev Synchrotron. H. C. POLLOCK, R. V. LANGMUIR, F. R. ELDER, J. P. BLEWETT, A. M. GUREWITSCH AND R. L. WATTERS, *General Electric Company.*—The synchrotron[1] under construction in the Research Laboratory of the General Electric Company is designed to operate with an equilibrium orbit 29.2 cm in radius. Peak fields of 8300 gauss at the orbit will permit acceleration of electrons to peak energies of 70 Mev. The magnet resembles a conventional betatron magnet except that the main core is replaced by a small core capable of carrying flux sufficient for betatron type acceleration up to about 5 or 6 Mev. At this point, the core begins to saturate and 163-Mc radiofrequency acceleration is initiated. The high frequency resonator is a quarter-wave coaxial structure whose inner and outer conductors are separated by the glass vacuum envelope. The inner and outer conductors of this resonator are thin films of silver which are divided by parallel scratches into narrow segments so that magnetic field distortions caused by eddy currents will be reduced to negligible proportions. Power is fed to this resonator from a master oscillator-power amplifier system. Timing and injection circuits will be discussed and tests on the various components of the machine will be described.

[1] V. Vekler, J. Phys. U.S.S.R. 9, 153 (1945). E. M. McMillan, Phys. Rev. 68, 143 (1945).

A6. The Transition from Betatron to Synchrotron Operation.* J. P. BLEWETT, *General Electric Company.*—The differential equations describing the motion of electrons in the synchrotron are sufficiently complex that, as yet, no general analytical solution has been evolved. During acceleration the radius of the electron orbit undergoes a large number of cycles of oscillation about its equilibrium orbit. The frequency of this oscillation after the initial transient can be calculated approximately and is not constant. The amplitude has been shown by a number of workers to decrease slowly with time so that the motion is stable. The present paper describes a mechanical solution, using a differential analyzer, of the equations of motion in the transition range between betatron "injection" and synchrotron operation. The small errors introduced by the analyzer will be discussed and shown to have negligible effects on the solution in this range. The results of this study indicate that all, or almost all, of the electrons in the initial betatron orbit will be trapped in stable synchrotron orbits, provided that the radiofrequency is within 1 or 2 percent of the correct value. The rate of rise of the radiofrequency envelope is not critical; rise times of 1 to 10 microseconds yield very similar results under the conditions which obtain in the General Electric synchrotron.

* The work described in this abstract and in the preceding one is supported by the U. S. Navy Office of Research and Invention under Contract N5ORI-178.

A7. Theoretical Considerations on Bringing the Beam out of a Betatron. E. D. COURANT AND H. A. BETHE, *Cornell University.*—It is proposed to use simple electrostatic deflection to bring the electron beam out of the betatron, synchrotron, or similar accelerating devices. To start with, the electron orbit is expanded by rapidly reducing the magnetic field at the orbit. Without any further devices, this would give an electron spray emerging in all directions. The electrons then enter the electrostatic field at the radius $r=r_0$ at which Hr (H=magnetic field) has its maximum as a function of r. At this point, adjacent orbits are rather widely separated. The separation is proportional to the $\frac{2}{3}$ power of the rate of reduction of the magnetic field; for a rate of one percent per microsecond, the separation is about one percent of the radius which is amply sufficient. (Near the original orbit of the electrons, the separation would be only about 0.07 percent.) The oscillations of the electrons about their stable orbit may also help the separation of orbits. The angular spread of the emerging beam is proportional to the orbit separation at the deflector, and also to $(H/E)^{\frac{1}{2}}$; for the separation calculated above, and for $H=4000$ gauss, $E=50{,}000$ volts/cm, the spread is about 5 degrees. The emerging beam can be refocused by an auxiliary magnetic field.

Invited Papers

A8. Electron Radiation in High Energy Accelerators. JULIAN SCHWINGER, *Harvard University.**—The only fundamental limitation to the attainment of very high energy electrons in devices such as the betatron and synchrotron is the radiative energy loss accompanying the circular motion. For an electron of energy $E \gg mc^2$, moving in a circular path of radius R, the energy radiated per revolution is

$$\delta E = \frac{4\pi}{3}\frac{e^2}{R}\left(\frac{E}{mc^2}\right)^4$$

which amounts to roughly 30 kev for an electron of 1 Bev in a magnetic field of 10^4 gauss. The radiation spectrum consists of harmonics of the rotation angular frequency

$\omega = c/R$. The intensity in the nth harmonic is independent of E and varies as $n^{\frac{1}{3}}$ for $n < (E/mc^2)^3$, decreasing rapidly for higher frequencies. Thus the spectrum extends into the x-ray region for $E = 1$ Bev. The radiation is emitted in the direction of electron motion, within a narrow cone of angle $\theta \sim mc^2/E$ (0.03° for $E = 1$ Bev). In addition to the individual or incoherent radiation effects of the electrons, there exists, in the synchrotron, a coherent radiation arising from the electron bunching along the circular trajectory. This type of radiative energy loss is independent of E, for the coherent spectrum is limited by the length of the electron bunch. Since the latter is not a small fraction of the orbit circumference, the coherent radiation is emitted at long wave-lengths, and may be effectively suppressed by metallic shielding. Radiative energy loss in a conventional betatron results in an adiabatic decrease in the oribit radius, which is already appreciable for $E = 10^8$ ev. No difficulty is encountered in a synchrotron provided the radiofrequency voltage is adequate to supply the radiation losses. However, the required radiofrequency voltage reaches formidable proportions for energies in excess of 3 Bev. A further effect of importance at such high energies is a radiative damping of phase oscillations which is a stabilizing influence, however, only if the magnetic field index $n (H \sim r^{-n})$ is less than $\frac{3}{4}$.

* 15-minute invited paper.

A9. The Design of Linear Accelerators. J. C. SLATER, *Massachusetts Institute of Technology.*—Theoretical features of linear accelerator design are similar for positive ions at relatively low frequencies, such as Alvarez is working on, and for electron acceleration at microwave frequencies, as at Massachusetts Institute of Technology and the General Electric Company. The main problems are (1) production of an accelerating tube furnishing the desired r.f. field; (2) feeding r.f. power into the tube from many suitably phased oscillators; (3) study of electron or ion dynamics to produce proper bunching and acceleration of electrons or ions; (4) focusing methods to counteract the defocusing resulting inevitably from the bunching. (1) Two forms of accelerating tubes have been studied: a cylinder containing circular irises, and one containing hollow cylinders spaced along the axis, with gaps between. For tubes of moderate length, it seems desirable to use a standing wave, which can be analyzed into a traveling wave with the same velocity as the ions, which accelerates them, and another in the opposite direction, which produces unimportant perturbations. The tube with irises is more easily adaptable to velocities near that of light, and that with cylinders to lower velocities. Both types contain undesired modes of oscillation, corresponding to different phase velocities, which must be avoided. (2) In the M.I.T. project the tube is to be fed with a series of 10-cm magnetrons. We have studied the problem of feeding n magnetrons into $n-1$ highly resonant loads, in the same phase, or into a long accelerating tube. A solution has been found by Halpern and Everhart, though it is unfortunately very critical to the various adjustments. (3) A simple analytical treatment, similar to the theory of the synchrotron, describes the bunching phenomenon and the acceleration of the bunches. Originally unbunched beams become bunched in the initial part of the accelerator, particularly if the field is applied gradually. Thereafter the bunches tend to maintain the proper phase relation with respect to the wave. The bunching will not be effective, however, unless the accelerator is designed so that the ions receive less than the maximum possible acceleration at each gap. (4) Study of the transverse fields shows that electrons or ions falling off the axis of the tube, in such a phase as to be bunched, will be defocused. The magnitude of this defocusing decreases as the velocity approaches the velocity of light. For electrons, it seems possible to counteract the defocusing by a longitudinal magnetic field, which should be of the order of magnitude of a few hundred or thousand gauss. For positive ions, the field would be prohibitively large, and one is led to foil focusing, of the type considered by Alvarez, Serber, and others at Berkeley. The M.I.T. program so far has been exploratory, is directed at present toward electrons, and has not yet led to the production of an actual accelerator. It is being carried on under the Research Laboratory of Electronics.

A10. The Design of a Proton Linear Accelerator. LUIS W. ALVAREZ, *University of California.*—Protons are to be injected into an r-f resonant system from a pressure Van de Graaff generator at about 4 Mev. The resonator will be built in 40-foot lengths with a 1-meter inside diameter. The copper skin of the resonator does not support a vacuum, but rests in a 4-foot diameter steel tank which is split longitudinally for access. The operating wave-length is 1.5 meters. Acceleration takes place in gaps between cylinders placed on the axis of the resonator. The cylinders are $0.75\,\beta\lambda$ long and the gaps $0.25\beta\lambda$. The shunt resistance of this system has been determined by integrating the measured value of dB/dt over a plane containing the axis of the resonator. For 80-kw per foot, the peak $\int E \cdot dl$ is 1.3 Mv per foot. The first 40-foot section will be powered by 30 radar transmitters of 100-kw peak output each. It is hoped that later sections will be driven by one or two magnetrons of 5 megawatts each. No touble has been experienced in phasing large numbers of self-excited oscillators in one high Q load. Tests on a 3-foot long vacuum model have shown no electrical breakdown occurs at 1 Mv/foot, the maximum attained so far. This corresponds to a maximum field in the gap of about 1 Mv per inch. Models on 10 and 30 cm have shown it possible to align many cylinders on the axis of the resonator so that a single uniform mode can be excited over the whole resonator. This is essentially an E_0 wave guide mode at cut-off, perturbed by the "drift tubes." The circulating magnetic field at the edge of the resonator is uniform along the 40-foot length and is everywhere in phase. It will be shown that if hollow cylinders are used as accelerating electrodes, it is impossible to have simultaneously phase dependent radial focusing, and phase stability of the ions relative to the r-f fields. This difficulty will be overcome by passing the protons through a thin beryllium foil as they enter each electrode. Scattering of the protons in these foils

spreads the beam to a diameter between 1 and 2 inches, and this diameter is independent of the frequency of the r.f. This fact controls the choice of λ since if shorter λ is used, the drift tubes cannot be made large enough to pass the beam and larger λ merely increases the mechanical and vacuum problems. The oscillators are turned on 15 times per second, for 300 μsec., by a line type pulser. The ion source now gives a 500 μa resolved proton beam for the 500 μsec. pulses. This is expected to be realized in practice, as a diffusion and a mechanical pump are installed in the high potential electrode. Velocity modulation of the beam at high potential should allow 30 percent of the protons to be bunched into the proper phase for acceleration. Particle energy should be 1 Mev per foot, as energy is lost for three reasons: (1) foil loss, (2) transit phase must be less than 90° to provide phase stability, (3) transit time is finite, so the field varies during acceleration.

A11. Resonance Acceleration of Charged Particles. EDWIN M. MCMILLAN, *University of California.**—The most fruitful means now known for accelerating particles to very high energies are: (1) to give repeated small pushes by an alternating electric field, as in the cyclotron or linear accelerator, and (2) to give a steady push produced by a varying magnetic flux, as in the betatron. The first of these, which may be called "resonance acceleration," gives promise of reaching higher ultimate energies, and will be the subject of this paper. The problem of keeping the particles in step with the accelerating electric field for a very large number of cycles seems at first sight to be a formidable one, not only because of intrinsic difficulties such as the well-known relativistic limit of the cyclotron, but also because of practical limits on the accuracy of construction of machines. However, an appreciation of the property of "phase stability" shows the way to a simple solution of this problem. If the particle is moving in a circular orbit, the angular velocity must just match the applied electric frequency for resonance to be maintained; if the motion is in a straight line, there is a corresponding relation between the linear velocity and the product of the electrode repeat length by the frequency. It can now be shown that, in general, if the angular or linear velocity varies with the energy, it is not necessary to make the exact match mentioned above, since particles started sufficiently near the right velocity will fall into a stable motion in which the velocity, energy, and phase oscillate about equilibrium values. (The phase describes the time relation between the arrival of the particle at an acceleration gap and the field across the gap.) The equilibrium energy is that value which achieves the exact match between velocity and frequency. If this energy is now made to vary slowly by changing the frequency or magnetic field in the circular case, the stability will remain and the actual energy will oscillate about the varying equilibrium value. In the linear case, the variation is produced by the changing repeat length as the particle travels down the tube. Thus acceleration is accomplished with complete stability of the motion at all times, provided that the rate of variation is not too great, and that adequate focusing of the beam is provided. The focusing problem in the linear case has been discussed by Dr. Alvarez; in the circular case it is the same as in the cyclotron and betatron. This stability takes care of relativistic difficulties as well as tolerances in the machine. The circular orbit machines can be divided into three types: (1) magnetic field variation (synchrotron), which is most suitable for accelerating electrons; (2) frequency variation (synchro-cyclotron), most suitable for ions; and (3) variation of both quantities. The third type has the advantage that the size of the orbit can be held constant by maintaining a certain relation between the field and frequency, but it involves all the practical difficulties inherent in both of the other types. Methods of obtaining the variations and details of design will be illustrated by descriptions of the 300-Mev synchrotron and the 184" synchro-cyclotron now under construction at Berkeley. There will also be a discussion of future possibilities, leading to the eventual attainment of the billion-volt range.

* 40-minute paper.

A12. The Racetrack.* H. R. CRANE, *University of Michigan.*—A form of the synchrotron which appears to possess a number of practical advantages is that in which a "linear" type magnet is used, and in which the electron orbit tube has the form of an oval racetrack. The guiding field is confined to two half-cricles, which are connected by straight, field free sections. A synchrotron of this type, having 1 meter radius and 60-cm straight sections is being designed and will be constructed at the University of Michigan.[1] We believe that the advantages offered by the racetrack modification will assume much greater importance in the region of extreme energies than at moderate energies. Therefore we are attempting to work out all the features of design with an eye toward much higher energies. Calculations show that the electron orbits in the racetrack are stable, provided certain values of the fall-off exponent are avoided,[2] and provided the ratio of the length of the straight section to the radius of the half-circles does not exceed a critical value.[3] Neither of these limitations seems to be severe. One of the straight sections contains the injection box. Electrons will be accelerated through a potential difference of 500 kv, supplied by a high voltage transformer, and will be introduced into the orbit tube tangentially by electric deflection. The other straight section contains the radiofrequency accelerating cavity. In order to pick up the electrons at 500 Kev ($\beta=0.86$) and accelerate them to essentially the velocity of light without change in the radius of the equilibrium orbit, the radiofrequency has to be modulated between the limits 34.4 and 40 mc. A circuit which accomplishes this is in operation.[4] Two 10,000-mc reflex klystrons, one of which is frequency modulated through modulation of the reflector voltage, feed a mixer. The difference frequency, 34.4 to 40 mc, is amplified by a broad band amplifier whose final stage has 1-kw output. Double resonant circuits are used as coupling between stages and between the last stage and the cavity. A cavity having the required low Q can be made (a) small in volume with high lumped capacitance at the center or (b) large in volume with low lumped capacitance and a

resistance load at the center. The latter requires the smaller driving amplifier, for a given voltage and frequency deviation. Our cavity is about 8 feet in diameter. The magnet is being designed for 20 cycle per second continuous operation. The low frequency used will allow the coils to be made of $\frac{1}{8}''\times\frac{3}{8}''$ solid rectangular wire, compactly wound, with occasional layers of $\frac{1}{4}''$ copper tubing for water cooling, without appreciable loss due to eddy currents. At this frequency the dielectric loss in the capacitor bank is small (proportional to $1/f$), and this makes it possible to use d.c. capacitors rather than the more expensive power factor capacitors. The method of driving the magnet which at present seems to be the most promising is that of adding a small charge to the condenser bank at the top of each cycle, through a grid-controlled gas tube. The minimum frequency at which it is profitable to operate a synchrotron is determined mainly by the loss of electrons caused by gas scattering during the early part of the acceleration cycle. A high *rate* of acceleration ($2\pi f°E_{\text{final}}$) and a high injection energy are favorable in regard to loss by scattering. Calculations along these lines[5] indicate that 20 cycles per second is sufficiently high for the synchrotron under consideration.

* This work is supported by the Bureau of Ordnance, U. S. Navy, under Contract NOrd-7924.

[1] H. R. Crane, Phys. Rev. **69**, 542 (1946).
[2] D. M. Dennison and T. H. Berlin, Phys. Rev. **69**, 542 (1946).
[3] Robert Serber, private communication.
[4] R. W. Bogle, to be published.
[5] T. H. Berlin and D. M. Dennison, to be published.

Discussion

Relative Advantages of Proton and Electron Accelerators

Discussion Leader: C. G. SUITS, *General Electric Company*

L. ALVAREZ, *University of California*
E. O. LAWRENCE, *University of California*
J. LAWSON, *General Electric Company*
E. MCMILLAN, *University of California*
I. I. RABI, *Columbia University*
M. G. WHITE, *Princeton University*
R. R. WILSON, *Harvard University*
J. R. ZACHARIAS, *Massachusetts Institute of Technology*

Proceedings of the American Physical Society

MINUTES OF THE JOINT MEETING OF THE DIVISION OF HIGH-POLYMER PHYSICS WITH THE FIBER SOCIETY AT CHARLOTTESVILLE, VIRGINIA, SEPTEMBER 26–28, 1946

The third meeting of the Division of High-Polymer Physics, which was exclusively devoted to textile and fiber research, was held in Maury Hall, of the University of Virginia, on September 26–28, 1946. The meeting was sponsored conjointly with the Fiber Society. Approximately 105 members of the Division and the Fiber Society, and guests, registered at the meeting.

The program was arranged by a Joint Committee under the co-chairmanship of Lewis Larrick and W. A. Sisson. Dr. Larrick also headed the Local Committee, in which undertaking he was ably and enthusiastically assisted by the Staff of the Institute of Textile Technology, particularly in expediting activities during the actual meeting.

In addition to addresses of welcome by Ivy F. Lewis, Dean, University of Virginia, and Ward Delaney, President, Institute of Textile Technology, three addresses of non-technical nature were given in the course of the three-day meeting. P. Larose of the National Research Council, in Ottawa, spoke on Thursday afternoon on "Textile Research in Canada." Carl M. Conrad on Friday delivered a paper commemorating the life and work of the late Enoch Karrer, Fellow of the

A.P.S., and a pioneer in high polymer research. In the principal after-dinner speech Friday evening, H. Wickliffe Rose presented, with numerous slides, impressions of Japan and the Japanese textile industry, gained on a recent trip there.

Thirteen technical papers were presented. Titles and abstracts (where the latter have been provided) appear hereunder.

W. JAMES LYONS
Division Secretary

TITLES AND ABSTRACTS OF CONTRIBUTED PAPERS

1. Air and Water Vapor Permeability of Fabrics.* L. W. RAINARD, E. L. WILSON, AND A. L. NESTMANN, *Institute of Textile Technology.*

* Publication of portion on air permeability will appear in *Textile Research Journal*, October, 1946.

2. Moisture Transfer to and from Tire Cords Encased in GR-S. W. JAMES LYONS,* HILDA M. ZIIFLE, MARY L. NELSON AND TRINIDAD MARES, *Southern Regional Research Laboratory, New Orleans, Louisiana.*—Observations of moisture regain at room temperature have been conducted on GR-S test pieces in which cotton and rayon tire cords had been vulcanized. Test pieces consisting of thin pads containing the tire cord as flat fabric, and of blocks 1 inch thick, containing bundles of cords, were stored in jars at 100 percent relative humidity for periods extending up to one year. At the end of the humid-storage period for the thin pads, they were removed to desiccating jars containing calcium chloride. Observations of moisture absorbed or desorbed were made by weighing the test pieces at appropriate intervals during the storage periods. GR-S test pieces containing no fabric were carried through the experiments as controls, to provide data on moisture in the rubber of the actual fabric-containing test pieces. From the results, inferences are drawn concerning the percentage of moisture in the fabrics of actual tires under various humidity conditions of operation.

* Resigned April 24, 1945.

3. Curl in Woven Textile Fabrics. ROSS WHITMAN, *Kendall Mills, Walpole, Massachusetts.*—A theory is developed relating the tendency of yarns to untwist in the presence of a swelling agent with the tendency of woven fabric to curl. It is shown that, if the torsional forces in the warp yarns are balanced against those of the filling yarns, a woven fabric will not curl. Balance between these forces is achieved and a non-curling fabric obtained when the following equation is satisfied:

$$\left\{\frac{(M-N/66)E}{N^{3/2}}\right\}_{\text{warp}}=\left\{\frac{(M-N/66)E}{N^{3/2}}\right\}_{\text{filling}},$$

where: M = twist multiple, N = yarn count, and E = end count, cotton system.

4. Tricot. C. W. BENDIGO, *Textile World, McGraw-Hill Publishing Company.*

5. Tensile and Torsional Properties of Textile Fibers. L. G. RAY, JR., *Rayon Department, E. I. du Pont de Nemours & Co., Inc., Buffalo, New York.*—Textile fibers were considered to be specialized materials of construction, and their physical properties were investigated in terms of engineering principles. Correlations of fiber properties with fiber structure and with fabric behavior were attempted. The hysteresis which was observed when single filaments were strained and allowed to recover was compared in a general way to resiliency. The degree of compliance of single fibers to small longitudinal and torsional stresses was measured, and a comparison of these values was taken as a measure of the anisotropy of the fibers. The fibers investigated included, among others: wool, casein, cellulose acetate, cellulose, and nylon.

6. The Creep Behavior of Textile Fibers. M. T. O'SHAUGHNESSY,* *E. I. du Pont de Nemours & Co., Buffalo, New York.*—The explanation of the mechanical properties of textile fibers will require (1) the development of new mechanical analogies to replace the combinations of Hookian springs and Newtonian dashpots which have been satisfactory for amorphous, unoriented polymers and (2) interpretation of these analogies in terms of our molecular scale model of a fiber as a partially crystalline and partially oriented polymeric structure. The study of creep reveals some features of behavior apparently peculiar to the fibrous state. In viscose rayon, the elongation in a first creep experiment, at a moderate load, is at first recoverable but a non-recoverable component soon sets in, at a time varying inversely with the load. Plots of elongation/tension *vs.* log time for rayon reveal that the well-known non-linearity of fiber behavior is in this case a transition phenomenon between linear behavior at very short or very long times. The elongation recoverable in 24 hours is related to the total elongation in 24-hour creep by a function of the form

$$R=aE+b$$

over a very large range of E.

* Now at Brooklyn Polytechnic Institute.

7. Electron Microscopical Studies of Natural Cellulose Fibers. WILLIAM G. KINSINGER AND CHARLES W. HOCK, *Hercules Experiment Station, Hercules Powder Company, Wilmington, Delaware.*—Three recent developments in the techniques of preparing specimens for electron microscopy —metallic shadow-casting, surface replicas, and electron stains—have been applied to a study of the submicroscopic structure of natural cellulose fibers. By means of metallic

shadow-casting, beaten fibers were found to consist of fibrils whose diameters varied from 90 to 400A, depending on the sample. These fibrils were frequently found in sheets whose thickness corresponds to the thickness of growth rings in the fiber. By the use of thin film replicas of the surface of unbeaten fibers it has been demonstrated that such fibrils exist in the original fiber. A periodic structure at 150A along the fibril axis has been detected in specimens prepared by metallic shadow-casting and in specimens stained with lead acetate. The significance of this spacing or its relation to the crystalline structure of the fibril is not yet known.

8. The Measurement of Irregular Distances and its Use in Studying the Swelling of Cotton Fibers. ENOCH KARRER AND R. S. ORR, *Southern Regional Research Laboratory.*

9. Performance of Tensile Testing Machines. HERBERT F. SCHIEFER AND JOSEPHINE M. BLANDFORD, *National Bureau of Standards.*—Equations relating applied tension on specimen against time, based upon simple theoretical considerations, show the tension to be a periodic function for both pendulum and inclined plane tensile testers. Experiments made on different materials, in which an electric strain-gauge dynamometer was mounted in series with the test specimen and the tension recorded as a function of time, confirmed the theoretical conclusions. The rate of loading varied enormously during a test. The applied and indicated tensions differ considerably during a test. At rupture this difference depends upon the phase of the periodic term and also upon the overthrow of the pendulum which arises from the kinetic energy which the pendulum possesses at the instant of rupture. The applied tension, T, could be represented by the equation

$$T=a+bt+ce^{-kt}\cos 2\pi vt$$

where time t is in seconds and a, b, c, k, and v are constants. In tear testing the equation was

$$T=1800+1000e^{-1.08t}\cos 4.25\pi t \text{ grams.}$$

The electronic control developed by Demartini of G. E. to operate pendulum testers at constant rate of loading and to reduce inertia forces was found to operate the tester at essentially constant rate of loading when the extension of the specimen was low or when the extension per unit load remained substantially constant throughout the test.

10. Apparatus for Determining the Coefficient of Friction of Running Yarn. FRANCIS B. BREAZEALE, *The American Enka Corporation, Enka, North Carolina.*—An apparatus is described which, with certain auxiliary equipment, indicates the coefficient of friction of running yarn over materials of choice. The coefficient-of-friction indicator proper utilizes the classical formula:

$$T_1/T_2=e^{k\alpha},$$

where T_1 and T_2 = tension in the yarn after and before passing α radians over the circular surface under test, and k = coefficient of friction between the yarn and this surface. This ratio of tensions is indicated as coefficient of friction through the equilibrium position of two levers, attached at right angles and free to rotate about this point of junction, to the free ends of which the tensions T_1 and T_2 are applied. The principle auxiliary unit is a tensiometer which feeds into a conventional potentiometer type chart recorder, thus enabling the operator to see at a glance the tension obtaining in the yarn. Studies made with this assembly on a number of materials reveal an increase in the coefficient of friction with yarn speed, and a decrease with increased yarn tension.

11. Spun Nylon. L. L. LARSON, *E. I. du Pont de Nemours and Company, Inc.*

12. An Investigation of the Load-Deformation Characteristics of Celanese* and Wool with Particular Reference to the Use of These Materials in Carpet Pile. R. W. WORK, A. M. THORNE, AND M. R. LIVINGSTON, *Celanese Corporation of America, Cumberland, Maryland.*—The relationship between the load-deformation behavior of cellulose acetate yarns and wool yarns in carpet piles was studied. The bending load-deformation characteristics of the yarns and the compression load-deformation properties of the staple fibers used in carpets were determined. The effects of filament denier of the cellulose acetate yarns and the effects of source as well as denier of the wool fibers on their stiffness were determined. The data secured indicates that the stiffness of these fibers is an exponential function of the fiber denier, with the stiffness of the wool increasing more rapidly than that of the cellulose acetate with increasing fiber (filament) diameter. The recovery after removal of a deforming load is little affected by the fiber (filament) size, but rather appears to be a function of the material composing the yarn. The recovery of wool is more rapid than that of cellulose acetate yarn. Unlike synthetic filaments, the size distribution of wool fibers cannot be controlled and large ones are always present in the normal distribution. These may account for the bristly feel of wool carpet pile as compared with the softer feel of the carpet pile made cellulose acetate yarn.

* Registered U. S. Pat. Off.

13. The Design of Parachute Shroud Lines as Influenced by Fundamental Energy Absorption Properties.* E. R. KASWELL, *Fabric Research Laboratories, Inc.*

* Sponsored by U. S. Army Air Forces.